AUTOMATICA.IT 2022 **Cagliari, 1-3/9/2022**

TECHNICAL PROGRAM

September 1st, Thursday (Venue: Cittadella dei Musei)

09:00-11:00 - Parallel regular sessions

ThA1: Analysis and Control I (aula verde)

ThB1: Robotics (aula rossa)

09:00-11:00 **ThA1: Analysis and Control I – Chairs: Prof. Alberto Cavallo**
Prof. Guido Maione

09:00-09:15	ThA1.1: *A global finite-time first-order sliding mode strong observer design with certain semi-global fixed-time convergence characteristics* **Authors**: Alessandro Pilloni, Alessandro Pisano, Elio Usai
09:15-09:30	ThA1.2: *Data-driven Dynamic Relatively Optimal Control* **Authors**: Felice Andrea Pellegrino, Franco Blanchini, Gianfranco Fenu, Erica Salvato
09:30-09:45	ThA1.3: *The pseudo inversion paradigm and the definition of a new and more general 2DOF control scheme* **Authors**: Valentina Orsini
09:45-10:00	ThA1.4: *Data-driven mixed-sensitivity control with automatic weights design* **Authors**: Nicholas Valceschini, Mirko Mazzoleni, Simone Formentin, Fabio Previdi
10:00-10:15	ThA1.5: *On the use of SDC parameterisation in nonlinear systems for nonlinear optimal control problems* **Authors**: Giuseppe Antonio Scala, Andrea Bonci, Sauro Longhi
10:15-10:30	ThA1.6: *An indirect realization of non-integer order discrete-time Tustin operators for non-integer order controllers* **Authors**: Guido Maione
10:30-10:45	ThA1.7: *Further characterizations of integral input-to-state stability for hybrid systems* **Authors**: Antonio Russo. Alberto Cavallo
10:45-11:00	ThA1.8: *Stability Analysis of a Class of Discontinuous Discrete-Time Systems* **Authors**: Francesco Ferrante, Giorgio Valmorbida

09:00-10:45 **ThB1: Robotics – Chairs: Prof. Graziana Cavone** **Prof. Roberto Meattini**	
09:00-09:15	ThB1.1: *Multi-Trajectory Model Predictive Control for safe UAV Navigation in an Unknown Environment* **Authors**: Danilo Saccani, Leonardo Cecchin, Lorenzo Fagiano
09:15-09:30	ThB1.2: *Vision-Based Modal Analysis of the Built Environment with Multiple Drones* **Authors**: Michele Bolognini, Giovanni Izzo, Daniele Marchisotti, Lorenzo Fagiano, Maria Pina Limongelli, Emanuele Zappa
09:30-09:45	ThB1.3: *sEMG-driven HITL Robotic Grasping: Soft-DTW Neural Networks Allow Minimally Supervised Regression-based Myocontrol* **Authors**: Alessandra Bernardini, Roberto Meattini, Gianluca Palli, Claudio Melchiorri
09:45-10:00	ThB1.4: *Human-Robot Collaboration for Dental Implant Surgery Using Adaptive Virtual Fixture and Image guiding Method* **Authors**: Mohammad Hossein Hamedani, Fan Shao, Fanny Ficuciello
10:00-10:15	ThB1.5: *Safe and Ergonomic Human-Drone Interaction in Warehouses* **Authors**: Silvia Proia, Raffaele Carli, Graziana Cavone, Mariagrazia Dotoli
10:15-10:30	ThB1.6: *Motor Maps for legged locomotion control* **Authors**: Luca Patanè, Alessia Li Noce, Fabio Di Pietro, Paolo Arena
10:30-10:45	ThB1.7: *A UV-based disinfection mobile robot with microbiological experimental analysis* **Authors**: Andrea Borgese, Dario Calogero Guastella, Giovanni Muscato, Stefania Stefani, Stefano Stracquadanio, Giuseppe Sutera

11:30-13:00 - Parallel regular sessions

ThA2: Analysis and Control II (aula verde)

ThB2: Control Applications I (aula rossa)

11:30-13:00 **ThA2: Analysis and Control II – Chairs: Prof. Elena De Santis** **Prof. Alessandro Freddi**	
11:30-11:45	ThA2.1: *Security and Critical Observability of Finite State Machines under Cyber-attacks* **Authors**: Naeimeh Fakhr Shamloo, Elena De Santis, Maria Domenica Di Benedetto
11:45-12:00	ThA2.2: *Chance-constrained sets approximation: A probabilistic scaling approach* **Authors**: Martina Mammarella, Victor Mirasierra, Matthias Lorenzen, Teodoro Alamo, Fabrizio Dabbene
12:00-12:15	ThA2.3: *On the control of MIMO systems with uncertain control direction* **Authors**: Alessandro Pisano and Giorgio Bartolini
12:15-12:30	ThA2.4: *Distributed control invariant set: the linear affine case* **Authors**: Davide Liuzza, Angel Molina, Paolo Falcone, Luigi Glielmo
12:30-12:45	ThA2.5: *On Semi-Global Exponential Stability Under Sampling for Locally Lipschitz Time-Delay Systems* **Authors**: Mario Di Ferdinando, Pierdomenico Pepe, Stefano Di Gennaro
12:45-13:00	ThA2.6: *Modeling and Control of a Telescopic Quadrotor Using Disturbance Observer Based Control* **Authors**: Alessandro Baldini, Riccardo Felicetti, Alessandro Freddi, Sauro Longhi, Andrea Monteriù

11:30-13:00 **ThB2: Control Applications I – Chairs: Prof. Riccardo Caponetto Prof. Antonio Russo**	
11:30-11:45	ThB2.1: *Model-based selective image downsampling in remote driving applications* **Authors**: Maziar Ebrahimi Dehshalie, Francesco Prignoli, Paolo Falcone, Marko Bertogna
11:45-12:00	ThB2.2: *On the stability of a sampled-data Image-Based Visual Servoing Control Scheme* **Authors**: Marco Costanzo, Ciro Natale, Antonio Russo
12:00-12:15	ThB2.3: *New Automatic Motor Speed Reference Generators for Cruise and Lateral Control of Electric Vehicles with in-Wheel Motors* **Authors**: Cristiano Maria Verrelli, Mohamed El Arayshi
12:15-12:30	ThB2.4: *Road User Position Prediction using Averaging* **Authors**: Angelos Toytziaridis, Paolo Falcone, Jonas Sjöberg
12:30-12:45	ThB2.5: *Simultaneous Design of Passive and Active Spacecraft Attitude Control via Black-Box Optimization* **Authors**: Lorenzo Jr Sabug, Gian Paolo Incremona, Mara Tanelli, Fredy Ruiz, Lorenzo Fagiano
12:45-13:00	ThB2.6: *Implementation of a fully analog feedback loop with a Carbon-Black-based Fractional Order* **Authors**: Riccardo Caponetto, Luca Patanè, Maria Gabriella Xibilia

14:30-16:30 - Parallel regular sessions

ThA3: Identification and Estimation (aula verde)

ThB3: Learning (aula rossa)

14:30-16:30 **ThA3: Identification and Estimation – Chairs: Prof. Simone Paoletti Prof. Saverio Farsoni**	
14:30-14:45	ThA3.1: *Set-membership identification of continuous-time systems through model transformation* **Authors**: Vito Cerone, Sophie Fosson, Simone Pirrera, Diego Regruto Tomalino
14:45-15:00	ThA3.2: *Variational Bayes Moving Horizon Estimation* **Authors**: Xiangxiang Dong, Giorgio Battistelli, Luigi Chisci, Yunze Cai
15:00-15:15	ThA3.3: *Switching Observer for Finite State Machines and Its Application to Opacity* **Authors**: Naeimeh Fakhr Shamloo, Elena De Santis, Maria Domenica Di Benedetto
15:15-15:30	ThA3.4: *Data-driven Output Regulation via Gaussian Processes and Luenberger Internal Models* **Authors**: Lorenzo Gentilini, Michelangelo Bin, Lorenzo Marconi
15:30-15:45	ThA3.5: *An iterative optimization-based approach to piecewise affine system identification* **Authors**: Simone Paoletti, Andrea Garulli, Antonio Vicino
15:45-16:00	ThA3.6: *LS-SVM Identification of LPV Systems: Solution in Primal and Dual Space* **Authors**: Luca Cavanini, Francesco Ferracuti, Sauro Longhi, Andrea Monteriù
16:00-16:15	ThA3.7: *Physics Informed Gaussian Process Regression Methods for Robot Inverse Dynamics Identification* **Authors**: Giulio Giacomuzzo, Alberto Dalla Libera, Diego Romeres, Ruggero Carli
16:15-16:30	ThA3.8*: Safe and physically-consistent identification of robot payload in collaborative applications: an approach exploiting dynamic motion planning, mixed-reality and sensor fusion* **Authors**: Saverio Farsoni, Jacopo Rizzi, Marcello Bonfè, Silvio Simani

14:30-16:30 **ThB3: Learning – Chairs: Prof. Franco Angelini Prof. Giacomo Baggio**	
14:30-14:45	ThB3.1: *Learning-Based Model Predictive Control Using Expected Sarsa Algorithm* **Authors**: Hoomaan Moradimaryamnegari, Marco Frego, Angelika Peer
14:45-15:00	ThB3.2: *Deep Reinforcement Learning for Visual Active Exploration and Tracking* **Authors**: Alberto Dionigi, Gabriele Costante, Alessandro Devo, Leonardo Guiducci
15:00-15:15	ThB3.3: *Learning and control of Networked Control systems* **Authors**: Luis Felipe Florenzan Reyes, Francesco Smarra, Alessandro D'Innocenzo
15:15-15:30	ThB3.4: *Functional Iterative Learning Control for Linear Systems* **Authors**: Franco Angelini, Cosimo Della Santina
15:30-15:45	ThB3.5: *Learning with Bayesian Frequentist Bounds* **Authors**: Giacomo Baggio, Algo Carè, Anna Scampicchio, Gianluigi Pillonetto
15:45-16:00	ThB3.6: *Switched ARX models: stability analysis and learning with guarantees* **Authors**: Vittorio De Iuliis, Francesco Smarra, Costanzo Manes, Alessandro D'Innocenzo
16:00-16:15	ThB3.7: *Sparse learning with concave regularization: relaxation of the irrepresentable condition* **Authors**: Vito Cerone, Sophie Fosson, Diego Regruto
16:15-16:30	ThB3.8: *On Multi-Agent Cognitive Cooperation: a Reinforcement Learning Decentralized Multi-Agent Control Approach* **Authors**: Salvatore D'Avella, Gerardo Camacho-Gonzalez, Carlo Alberto Avizzano, Paolo Tripicchio

September 2nd, Friday (Venue: Cittadella dei Musei)

09:00-11:00 - Parallel regular sessions

FrA1: Control Applications I (aula verde)

FrB1: Multi-agent systems and Networks I (aula rossa)

09:00-11:00	**FrA1: Control Applications I – Chairs: Prof. Cecilia Pasquale** **Prof. Michele Roccotelli**
09:00-09:15	FrA1.1: *Intrusion Detection System (IDS) for connected Electric and Autonomous Vehicles to prevent Vehicular ad hoc networks (VANET) Attacks* **Authors**: Wasim Ali, Michele Roccotelli, Maria Pia Fanti
09:15-09:30	FrA1.2: *Optimal control of electric and autonomous buses on intercity lines based on traffic prediction* **Authors**: Cecilia Pasquale, Simona Sacone, Silvia Siri, Antonella Ferrara
09:30-09:45	FrA1.3: *Optimization-Based Coordination of Mixed Traffic at Unsignalized Intersections Based on Platooning Strategy* **Authors**: Muhammad Faris, Paolo Falcone, Jonas Sjöberg
09:45-10:00	FrA1.4: *A distributed optimization based architecture for management of interconnected energy hubs* **Authors**: Giulio Ferro, Michela Robba, Rabab Haider, Anuradha Annaswamy
10:00-10:15	FrA1.5: *A discrete event approach for EVs' charging optimal scheduling* **Authors**: Luca Parodi, Michela Robba, Giulio Ferro, Riccardo Minciardi
10:15-10:30	FrA1.6: *Traffic-light control in urban environment exploiting drivers' reaction to the expected red lights duration* **Authors**: Matteo Scandella, Arnob Ghosh, Michelangelo Bin, Thomas Parisini
10:30-10:45	FrA1.7: *MARTe2 porting for the ARM Architectures Design and challenges: towards novel generations of magnetic fusion plants* **Authors**: Giuseppe Avon, Arturo Buscarino, Andrè Neto, Filippo Sartori, Fabio Zanon, Eliana De Marchi
10:45-11:00	FrA1.8: *Energy-aware black box MIMO model identification of wood chips refining process operating in closed loop* **Authors**: Roberto Boffadossi, Marco Leonesio and Lorenzo Fagiano
09:00-11:00	**FrB1: Multi-agent systems and Networks I – Chairs: Prof. Diego Deplano** **Prof. Agostino M. Mangini**
09:00-09:15	FrB1.1: *A new connection protocol for multi-consensus of discrete-time and sampled-data systems* **Authors**:Mattia Mattioni, Salvatore Monaco, Dorothee Normand-Cyrot
09:15-09:30	FrB1.2: *Can Competition Outperform Collaboration? The Role of Malicious Agents* **Authors**: Luca Ballotta, Giacomo Como, Jeff S. Shamma, Luca Schenato
09:30-09:45	FrB1.3: *Decision Modeling in Markovian Multi-Agent Systems* **Authors**: Carl-Johan Heiker, Paolo Falcone
09:45-10:00	FrB1.4: *Type-K Monotone Systems and Consensus in Multi-Agent Networks* **Authors**: Diego Deplano, Mauro Franceschelli, Alessandro Giua

10:00-10:15	FrB1.5*: A Consensus Protocol for Connecting Automated Vehicles at Signal-Free Intersection* **Authors**: Gianvito Difilippo, Maria Pia Fanti, Agostino Marcello Mangini
10:15-10:30	FrB1.6: *Distributed Estimation of All Distinct Eigenvalues of the Laplacian Matrix via Data-Driven Consensus Optimization* **Authors**: Claudia Congiu, Diego Deplano, Alessandro Giua, Mauro Franceschelli
10:30-10:45	FrB1.7: *Bearing Rigidity Theory Applied to Robotic Formations* **Authors**: Giulia Michieletto, Angelo Cenedese
10:45-11:00	FrB1.8: *Distributed Constrained Connectivity Keeping Supervision Scheme in the Presence of Static Obstacles* **Authors**: Alessandro Casavola, Vincenzo D'Angelo, Ayman El Qemmah, Francesco Tedesco, Franco Angelo Torchiaro

11:30-13:00 - Parallel regular sessions

FrA2: Control Applications III (aula verde)

FrB2: Optimization (aula rossa)

11:30-13:00 **FrA2: Control Applications III – Chairs: Prof. Pasquale Palumbo**
Prof. Silvia Maria Zanoli

11:30-11:45	FrA2.1: *A coarse-grain model for cellular growth accounting for ribosome synthesis* **Authors**: Massimiliano d'Angelo, Pasquale Palumbo, Stefano Busti, Marco Vanoni
11:45-12:00	FrA2.2: *Model Predictive Control System for Slug Flow in Microfluidics* **Authors**: Samuele Moscato, Giovanna Stella, Maide Bucolo
12:00-12:15	FrA2.3: *Symbolic Control Design of an Artificial Pancreas for Type-2 Diabetes* **Authors**: Alessandro Borri, Giordano Pola, Pierdomenico Pepe, Maria Domenica Di Benedetto, Pasquale Palumbo
12:15-12:30	FrA2.4: *Water resources systems control and optimization: real case studies* **Authors**: Silvia Maria Zanoli, Crescenzo Pepe
12:30-12:45	FrA2.5: *Potential evaluation of Model Predictive Control applied to Variable Speed Variable Displacement Pump systems* **Authors**: Leonardo Cecchin, Stefan Gering, Maximilian Manderla, Adrian TrachteMoritz Diehl
12:45-13:00	FrA2.6: *Mechanical Fault Detection of CNC Milling Machines* **Authors**: Marino Pavone, Nicola Epicoco, Giordano Pola, Elena De Santis, Maria Domenica Di Benedetto

11:30-13:00 **FrB2: Optimization – Chairs: Prof. Raffaele Carli**
Prof. Mauro Franceschelli

11:30-11:45	FrB2.1: A surrogate-based scheme for black-box and preference-based optimization with a controller calibration application **Authors**: Davide Previtali, Mirko Mazzoleni, Antonio Ferramosca, Fabio Previdi
11:45-12:00	FrB2.2: *Clarke's Local Generalized Nash Equilibria with Nonconvex Coupling Constraints* **Authors**: Paolo Scarabaggio, Raffaele Carli, Sergio Grammatico and Mariagrazia Dotoli
12:00-12:15	FrB2.3: *Resilient Constrained Optimization in Multi-Agent Systems* **Authors**: Mojtaba Kaheni, Elio Usai and Mauro Franceschelli
12:15-12:30	FrB2.4: *Internal Model-Based Online Optimization* **Authors**: Nicola Bastianello, Ruggero Carli and Sandro Zampieri
12:30-12:45	FrB2.5: *Tracking-based Distributed Aggregative Optimization for Cooperative Robotics*

	Authors: Andrea Camisa, Guido Carnevale and Giuseppe Notarstefano
12:45-13:00	FrB2.6: *Job Shop Sequencing in Manufacturing Plants by Timed Coloured Petri Nets and Particle Swarm Optimization* **Authors**: Gaetano Volpe, Agostino Marcello Mangini and Maria Pia Fanti

14:30-16:30 - Parallel regular sessions

FrA3: Control Applications IV (aula verde)

FrB3: Multi-agent systems & Networks II (aula rossa)

14:30-16:30 **FrA3: Control Applications IV – Chairs: Prof. Stefano Panzieri** **Prof. Enrico Zero**	
14:30-14:45	FrA3.1: *Avalanche victim search via robust observers* **Authors**: Nicola Mimmo, Pauline Bernard and Lorenzo Marconi
14:45-15:00	FrA3.2: *Modeling and Control of Multilevel Flying-Capacitor Converters* **Authors**: Davide Tebaldi and Roberto Zanasi
15:00-15:15	FrA3.3: *Distributed robust control in a quadruple tank system* **Authors**: Alessandro Bozzi, Simone Graffione, Simona Sacone, Roberto Sacile and Enrico Zero
15:15-15:30	FrA3.4: *Advanced Intrusion Detection System for Industrial Cyber-Physical Systems* **Authors**: Valeria Bonagura, Chiara Foglietta, Stefano Panzieri and Federica Pascucci
15:30-15:45	FrA3.5: *MPC-Based Process Control of Deep Drawing: An Industry 4.0 Case Study in Automotive* **Authors**: Graziana Cavone, Augusto Bozza, Raffaele Carli and Mariagrazia Dotoli
15:45-16:00	FrA3.6: *AI-powered Distributed Stochastic MILP for Microgrid Control* **Authors**: Andrea Camisa, Giuseppe Notarstefano
16:00-16:15	FrA3.7: *Generalized Simulink Model of PMSMs* **Authors**: Davide Tebaldi
16:15-16:30	FrA3.8: *Towards autonomous soft grasping of deformable objects using flexible thin-film electro-adhesive gripper and online capacitance measure* **Authors**: Salvatore D'Avella, Ion-Dan Sîrbu, Marco Fontana, Rocco Vertechy, Paolo Tripicchio
14:30-16:30 **FrB3: Multi-agent systems & Networks II – Chairs: Prof. Alessandro Colombo** **Prof. Giulia Fracastoro**	
14:30-14:45	FrB3.1: *Distributed Optimal Control of Discrete-Time Linear Systems over Sensor Networks* **Authors**: Massimiliano d'Angelo, Stefano Battilotti and Filippo Cacace
14:45-15:00	FrB3.2: *Control of Dynamic Financial Networks* **Authors**: Giuseppe Calafiore, Giulia Fracastoro and Anton Proskurnikov
15:00-15:15	FrB3.3: *Stability analysis of wireless control networks via Markov jump systems theory* **Authors**: Anastasia Impicciatore, Yuriy Zacchia Lun, Alessandro D'Innocenzo and Pierdomenico Pepe
15:15-15:30	FrB3.4: *Robust Control Invariance for Networked Control Systems with Output Feedback* **Authors**: Masoud Bahraini, Mario Zanon, Alessandro Colombo and Paolo Falcone
15:30-15:45	FrB3.5: *A Multi-Agent Trust and Reputation Mechanisms for the Management of Smart Urban Lighting Systems* **Authors**: Alessandro Casavola, Giuseppe Franzè, Gianfranco Gagliardi and Francesco Tedesco
15:45-16:00	FrB3.6: *Handling complexity in large scale complex systems through distributed computation*

	Authors: Lucrezia Manieri, Alessandro Falsone and Maria Prandini
16:00-16:15	FrB3.7: *Distributed Mode Computation in Open Multi-Agent Systems* **Authors**: Zoreh Al Zahra Sanai Dashti, Gabriele Oliva, Carla Seatzu, Andrea Gasparri and Mauro Franceschelli
16:15-16:30	FrB3.8: *Distributed Game-theoretical Control for EV-integrated Energy Communities* **Authors**: Nicola Mignoni, Raffaele Carli and Mariagrazia Dotoli

17:00-18:30 - Round Table

"*Energia: Scenari Attuali e Futuri e Transizione Ecologica: il ruolo dell'Automatica*" (aula verde)

Chair: Prof. Elio Usai (Università degli Studi di Cagliari)

Speakers

– Domenico Villacci (*Università degli Studi del Sannio*)
Prof. Ordinario di Sistemi Elettrici per l'Energia. Presidente del Consorzio Ensiel.

– Fabrizio Pilo (*Università degli Studi di Cagliari*)
Prof. Ordinario di Sistemi Elettrici per l'Energia. Prorettore per il territorio e l'innovazione.

– Chiara Vergine (*Terna S.p.A*)
Dispacciamento e Conduzione, Real Time Operation.

– Marco Barbagelata (*Stam Srl*)
Business Area Manager.

Can Competition Outperform Collaboration? The Role of Malicious Agents

Luca Ballotta[1], Giacomo Como[2], Jeff S. Shamma[3] and Luca Schenato[1]

Extended Abstract

From smart grids managing energy consumption, to fleets of autonomous vehicles for intelligent transportation, everyday life depends more and more on control of network systems.

While the latter bring numerous benefits, a major drawback is that malicious agents can locally intrude from any point in the system, and cause major damage at global scale. Such a concern, which has been classically addressed in computer engineering and telecommunication, has also been involving control applications for a few years now, such as smart grids or vehicular platoons [1]. Other concerns for safety and security are cascading failures originating from single nodes and propagating to neighbors, with notable example across many scenarios, from electricity blackouts to collisions within crowded automated systems such as robot formations.

To deal with such issues, research efforts have split into mainly two directions. A body of work develops control techniques to overcome fragility in specific applications, such as power outage in smart grids [2], cascading failures in cyber-physical systems [3], denial of service [4]. From a methodological perspective, control and optimization communities have been focusing on robustness of distributed algorithms and control protocols to a fraction of misbehaving agents. This model can tailor either intentionally malicious cyber-attacks, or simply faulty agents. In particular, *resilient consensus* aims to achieve consensus among normally behaving agents in the face of unknown adversaries. With regard to this, the most popular approach is based on the filtering technique referred as "Mean Subsequence Reduced" (MSR), whereby agents discard suspicious incoming data from local updates. In particular, seminal work [5] introduced a weighted version (W-MSR) and the notion of r-*robustness*, which is roughly related to the ability of a network to spread information among its nodes, and enables theoretical guarantees for W-MSR. Among the many variants and adaptations of this protocol, [6] studies resilient control for double integrators, [7] tackles mobile adversaries, and [8] considers the more general distributed optimization framework.

Other approaches proposed in literature move resilience requirements from update protocol to agent capabilities. For example, [9] employs a buffer to store all values received from other agents and replaces the thresholding mechanism with a voting strategy followed by dynamical updates, while [10] studies algorithmic robustness enabled by trusted agents.

Unfortunately, while the above methods have been shown to be effective in many scenarios, the communication network needs to be minimally connected (r-robust) for theoretical guarantees to hold, which may result in either strong requirements on the network itself, or in computational infeasibility of checking such requirements. While algorithms might still work, the lack of theoretical guarantees may be undesired in certain applications, where a more conservative but safer approach may be preferred. Moreover, while in some applications agents may just agree upon a common decision, *average consensus* is key in several other tasks. Thus, we depart from classical MSR-based strategies, aiming to design algorithms that can offer theoretical guarantees in a broader sense – while still ensuring certain level of resilience.

Towards this goal, we set the stage with two key steps. Firstly, instead of focusing on conditions for achieving consensus, we consider the cost of a distributed quadratic optimization problem. Secondly, we draw inspiration from game theory. Distributed cooperative control and games, despite their apparent contrast, are linked from several perspectives which have been largely explored in literature [11], [12]. In particular, our starting point is [13], where the authors discuss the connection between consensus and potential games. Stepping forward, we propose a novel approach to resilient distributed quadratic optimization based on the celebrated Friedkin-Johnsen (FJ) dynamics. One key feature of this model is a tunable parameter $\lambda \in [0, 1]$ which allows to smoothly transition from *full collaboration*, where each normally behaving agent puts equal trust in all agents in the network (including itself), leading to standard average consensus, to *full competition*, whereby agents do not trust each other, *i.e.,* they regard all other agents as adversaries.

Such a mixed approach allows to explore the performance trade-off that arises from different choices of agents that may decide to trust their neighbors or not, which turns out to be crucial in the presence of adversaries. In fact, we observe a fundamental *competition-collaboration trade-off*: in general, **the optimal choice to achieve resilience is a hybrid strategy that makes agents trust neighbors only partially**, as illustrated in Fig. 1. In particular, the global cost function (solid blue) is the sum of two conflicting contributions, representing respectively deception due to collaboration with malicious agents (dashed red) and inefficiency caused by competition against agent's neighbors (dash-dotted yellow). To achieve analytical intuition, we discuss such

[1]Department of Information Engineering, University of Padova, 35131 Padova, Italy {ballotta, schenato}@dei.unipd.it.

[2]Department of Mathematical Sciences, Politecnico di Torino, Corso Duca degli Abruzzi 24, 10129, Torino, Italy giacomo.como@polito.it.

[3]Industrial and Enterprise Systems Engineering (ISE), University of Illinois Urbana-Champaign, Illinois, USA jshamma@illinois.edu.

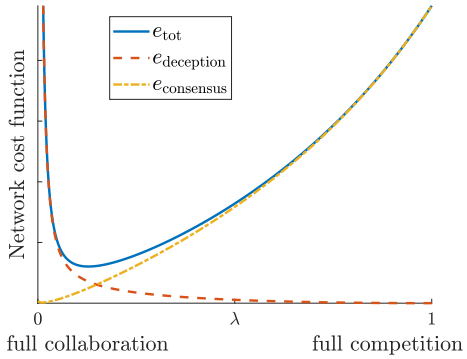

Fig. 1: Competition *vs.* collaboration in distributed quadratic optimization. The global cost e_{tot} is the sum of two contributions, that reflect two contrasting attitudes of normally behaving agents: $e_{\text{deception}}$ is caused by trusting (erroneously) adversarial agents, which yields a drift from nominal average consensus, while $e_{\text{consensus}}$ is due to inter-agent competition, in an attempt to mitigate potential attacks from neighbors, but doing so prevents agents to reach consensus. The tunable parameter $\lambda \in [0, 1]$ allows normal agents to shift smoothly from full collaboration, where they trust equally all agents in the network, to full competition, where they trust only themselves, inducing a richer spectrum of behaviors at both local and global scale.

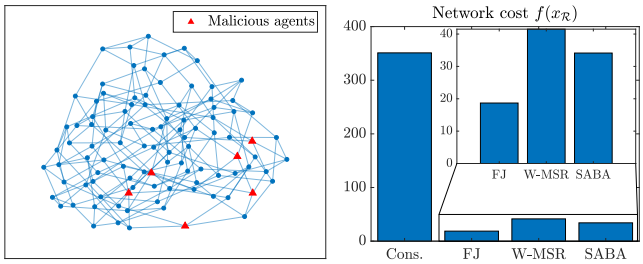

Fig. 2: Communication network with malicious agents (left) and network costs obtained with standard consensus, FJ, W-MSR, and SABA (right).

competition-collaboration trade-off using tools drawn from *opinion dynamics*, in particular the *social power* that arises through the FJ model, shedding light on the role of malicious agents and parametrization of agent dynamics on optimization performance. Further, we thoroughly study the addressed cost function both analytically and numerically, showing that even the trivial protocol instance with $\lambda = 1$ (full competition) can outperform the standard consensus protocol under some technical conditions. In fact, the optimal parameter λ^* (that minimizes the error function) is shown to lie in the open interval $(0, 1)$ under some mild assumptions which essentially encode "non-degenerate" distribution of the initial agents' conditions and network connections. Finally, our analytical study involves dependence of both cost function and optimal parameter λ^* on the parameters quantifying intensity of attacks. Even though an analysis precisely targeting the minimizer is not possible because of the structure of the cost function, we achieve analytical intuition about its behavior through formal results, which is substantiated by numerical tests with various sets of parameters.

We also carry out some comparisons with state-of-the-art W-MSR and the recently proposed SABA [9], showing that our approach can be especially effective with sparse networks whose structure may hamper performance of such algorithms (Fig. 2). In particular, we observe that the real parameter λ can adapt the network behavior to achieve a good trade-off between performance and resilience, enforcing more or less collaboration according to the attack scenario.

After characterizing and validating the proposed competition-based protocol, we fix agent update rule and shift attention to the network topology, in order to assess how the latter impacts performance of regular agents with respect to distributed optimization. In particular, we use regular graphs to numerically show that network connectivity can hamper malicious attacks from both standpoints of global cost function and attacker energy (interpreted as control effort), and observe how performance varies when the topology gets sparser through progressive removal of edges. In particular, we heuristically observe that not only high connectivity, but also degree balance across agents is useful to tame unknown adversaries, that could intuitively exploit highly connected agents to disrupt the optimization at network level.

The full version of this extended abstract, that extends the preliminary conference version [14], is soon-to-be submitted for review to IEEE Transactions on Automatic Control, and a preprint is available online at [15].

References

[1] S. Raskin. (2021) Energy secretary says enemies are capable of shutting down us power grid. (web).

[2] C. Huang, R. Zhang, and S. Cui, "Optimal power allocation for wireless sensor networks with outage constraint," *IEEE Wireless Communications Letters*, vol. 3, no. 2, pp. 209–212, 2014.

[3] Z. Huang, C. Wang, M. Stojmenovic, and A. Nayak, "Characterization of cascading failures in interdependent cyber-physical systems," *IEEE Transactions on Computers*, vol. 64, no. 8, pp. 2158–2168, 2015.

[4] Q. Yan, F. R. Yu, Q. Gong, and J. Li, "Software-defined networking (sdn) and distributed denial of service (ddos) attacks in cloud computing environments: A survey, some research issues, and challenges," *IEEE Communications Surveys Tutorials*, vol. 18, no. 1, pp. 602–622, 2016.

[5] H. J. LeBlanc, H. Zhang, X. Koutsoukos, and S. Sundaram, "Resilient asymptotic consensus in robust networks," *IEEE Journal on Selected Areas in Communications*, vol. 31, no. 4, pp. 766–781, 2013.

[6] S. M. Dibaji and H. Ishii, "Consensus of second-order multi-agent systems in the presence of locally bounded faults," *Systems & Control Letters*, vol. 79, pp. 23–29, 2015.

[7] Y. Wang, H. Ishii, F. Bonnet, and X. Défago, "Resilient consensus against mobile malicious agents," *IFAC-PapersOnLine*, vol. 53, no. 2, pp. 3409–3414, 2020, 21st IFAC World Congress.

[8] L. Su and N. H. Vaidya, "Byzantine-resilient multiagent optimization," *IEEE Trans. Autom. Control*, vol. 66, no. 5, pp. 2227–2233, 2021.

[9] S. M. Dibaji, M. Safi, and H. Ishii, "Resilient distributed averaging," in *American Control Conference*, 2019, pp. 96–101.

[10] W. Abbas, A. Laszka, and X. Koutsoukos, "Improving network connectivity and robustness using trusted nodes with application to resilient consensus," *IEEE Transactions on Control of Network Systems*, vol. 5, no. 4, pp. 2036–2048, 2018.

[11] N. Li and J. R. Marden, "Designing games for distributed optimization," *IEEE Journal of Selected Topics in Signal Processing*, vol. 7, no. 2, pp. 230–242, 2013.

[12] A. V. Proskurnikov and R. Tempo, "A tutorial on modeling and analysis of dynamic social networks. part i," *Annual Reviews in Control*, vol. 43, pp. 65–79, 2017.

[13] J. R. Marden, G. Arslan, and J. S. Shamma, "Cooperative control and potential games," *IEEE Transactions on Systems, Man, and Cybernetics, Part B (Cybernetics)*, vol. 39, no. 6, pp. 1393–1407, 2009.

[14] L. Ballotta, G. Como, J. S. Shamma, and L. Schenato, "Competition-based resilience in distributed quadratic optimization," in *Proceedings of the 61th IEEE Conference on Decision and Control*, 2022, (to appear), *arXiv preprint* arXiv:2203.14099 (pdf).

[15] ——, "Can competition outperform collaboration? The role of malicious agents," *arXiv e-prints*, 2022, page arXiv:2207.01346 (pdf).

Learning-Based Model Predictive Control Using Expected Sarsa Algorithm

Hoomaan MoradiMaryamnegari
Faculty of Science and Technology
Free University of Bozen-Bolzano
Bolzano, Italy
Hoomaan.MoradiMaryamnegari@natec.unibz.it

Marco Frego
Faculty of Science and Technology
Free University of Bozen-Bolzano
Bolzano, Italy
Marco.Frego@unibz.it

Angelika Peer
Faculty of Science and Technology
Free University of Bozen-Bolzano
Bolzano, Italy
Angelika.Peer@unibz.it

***Abstract*—The potential of reinforcement learning (RL) algorithms in tuning the parameters of model predictive controllers (MPC), including the weights of the cost function and the unknown model parameters, has been highlighted in recent studies. An open problem is to find a framework for an easy and straightforward implementation that allows training in a contained number of episodes and overcomes the need for additional constraints. We apply the Expected Sarsa RL algorithm using a nonlinear MPC as a function approximator. The results obtained in simulation and on a coupled tanks system confirm that the proposed algorithm allows the tuning of the MPC over a reduced number of episodes compared to other methods.**

***Index Terms*—Model Predictive Control, Reinforcement Learning, Expected Sarsa Algorithm, Model-Based Learning Method.**

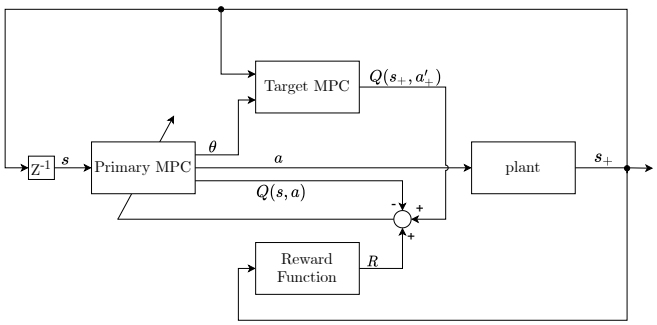

Fig. 1. MPC with Expected Sarsa

I. Introduction

Model predictive control (MPC) is a powerful and established technique, but it requires an accurate model and a proper tuning of the parameters to be effective. Recently, machine learning (ML) methods have been introduced and combined with MPCs to mitigate the effects of inaccurate models and non optimal parameters, [1]. In particular, reinforcement learning (RL) has demonstrated considerable performance when combined with MPC. However, the problem of requiring a significant effort and time to train the model still remains. One of the prominent works that combines RL with MPC is [2], where the Q-Learning algorithm is employed to tune the parameters of an economic nonlinear MPC (ENMPC), so that the algorithm produces the optimal output even when the MPC model is not exact. MPC has been used as a function approximator for RL, parameterized with the weights of its cost function and with the unknown parameters of its model. The Q-Learning algorithm finds the unknown parameters of the MPC by exploring the environment based on a reward function. More in detail, in the MPC-based Q-Learning formulation adopted in [2], [4], the target policy is defined as a typical MPC, where the first element of the output control vector is applied to the system with the delay of one sampling time. Hence, the primary policy in the next sampling time, which is the primary MPC, must be constrained with the action obtained by the target policy in the previous sampling time. This yields an additional input constraint. Since the primary policy usually acts exploratory, [3], the whole exploration capability of the algorithm is reduced. Although it has been a significant step to combine MPC with RL, it is still possible to improve the performance of this family of techniques at least in two directions. Firstly, finding an MPC-RL framework trainable in a reduced number of episodes; secondly, it is possible to remove the extra constraint on the first input for the primary MPC in the MPC-Q-Learning method, which is responsible for the performance degradation.

II. Parametrized Model Predictive Control as Function Approximator (PMPCFA)

In this study, a value-based RL method is presented to tune the MPC's parameters. The advantages are twofold: the online training process is fast, and it provides an easier and more straightforward framework for the implementation on a real system, due to the elimination of the extra constraint on the first input. To this end, we used an RL algorithm called Expected Sarsa. It has been proven that given the same amount of experience, Expected Sarsa outperforms Sarsa, [6], since the variance is eliminated by selecting the random action in the target value function. Our solution, Parametrized Model Predictive Control (MPC) as Function Approximator (PMPCFA, [5]), assumes that the whole MPC, together with its equality and inequality constraints, is the value function approximator. In this way, the MPC parameters are found by adopting the Expected Sarsa algorithm, see Fig. 1. The MPC parameterized in the weights of the cost function and model

parameters, is considered as the action value function of the Expected Sarsa algorithm and is defined as:

$$Q_\theta(\boldsymbol{s},\boldsymbol{a}) = \min \sum_{i=0}^{N} \gamma^i [(\boldsymbol{x}_i - \boldsymbol{x}_{\text{ref}_i})^2_{\boldsymbol{\theta_x}} + (\boldsymbol{u}_i - \boldsymbol{u}_{\text{ref}_i})^2_{\boldsymbol{\theta_u}} + \boldsymbol{\theta}^T_{\boldsymbol{w}} \boldsymbol{\sigma}_i] + \gamma^N [(\boldsymbol{x}_N - \boldsymbol{x}_{\text{ref}_N})^2_{\boldsymbol{\theta}_{\boldsymbol{x}_f}} + \boldsymbol{\theta}^T_{\boldsymbol{w}_f} \boldsymbol{\sigma}_N], \tag{1}$$

subject to $\boldsymbol{x}_{i+1} = f^{\text{model}}_{\boldsymbol{\theta}_m}(\boldsymbol{x}_i, \boldsymbol{u}_i),\ \boldsymbol{x}_0 = \boldsymbol{s}$, and

$$\boldsymbol{g}(\boldsymbol{u}_i) \leq 0,\ \ \boldsymbol{h}(\boldsymbol{x}_i, \boldsymbol{u}_i) \leq \boldsymbol{\sigma}_i,\ \ \boldsymbol{h}^f(\boldsymbol{x}_N) \leq \boldsymbol{\sigma}_N,$$

with the slack variables $\boldsymbol{\sigma}_{0,\cdots,N} \geq 0$. The function $Q_{\boldsymbol{\theta}}(\boldsymbol{s},\boldsymbol{a})$ is the action value function estimator at the current state $\boldsymbol{s}$ and action $\boldsymbol{a}$; $\boldsymbol{x}_i$, $\boldsymbol{u}_i$ and $\boldsymbol{\sigma}_i$ are the predicted state, control input, and slack variable at the sampling time i, respectively; $\boldsymbol{x}_{\text{ref}}$ and $\boldsymbol{u}_{\text{ref}}$ are the set points of the state and action, N is the prediction horizon, $\boldsymbol{g}(\boldsymbol{u}_i)$ is the input constraint, $\boldsymbol{h}(\boldsymbol{x}_i, \boldsymbol{u}_i)$ is the mixed constraint, $\boldsymbol{h}^f(\boldsymbol{x}_i)$ is the final constraint, the discount factor is $0 < \gamma \leq 1$; $f^{\text{model}}_{\boldsymbol{\theta}_m}$ is the model of the system with unknown parameters $\boldsymbol{\theta}_m$. Parameters $\boldsymbol{\theta_x}$, $\boldsymbol{\theta_u}$, $\boldsymbol{\theta_w}$, $\boldsymbol{\theta}_{\boldsymbol{x}_f}$, and $\boldsymbol{\theta}_{\boldsymbol{w}_f}$ are the weights of cost function terms including the tracking error, control input, slack variables, final tracking error, and final slack variable, respectively. The parameter vector $\boldsymbol{\theta} = [\boldsymbol{\theta}_m, \boldsymbol{\theta_x}, \boldsymbol{\theta_u}, \boldsymbol{\theta_w}, \boldsymbol{\theta}_{\boldsymbol{x}_f}, \boldsymbol{\theta}_{\boldsymbol{w}_f}]$ is found online during the interaction of the system with the environment. The solution of the above optimization problem leads to a sequence of control outputs, $[\boldsymbol{u}_1, \boldsymbol{u}_2, \ldots, \boldsymbol{u}_N]$, at each sampling time. The policy is defined to choose with probability 1 the first element of the control output and apply it to the system. In this way, the temporal difference error δ_k is rewritten as follows [7]:

$$\delta_k = R + \gamma Q_{\boldsymbol{\theta}}(\boldsymbol{s}_+, \boldsymbol{a}'_+) - Q_{\boldsymbol{\theta}}(\boldsymbol{s}, \boldsymbol{a}),$$

where R is the reward received by the environment, $\boldsymbol{a}'_+$ is the action computed in state $\boldsymbol{s}_+$ by the target MPC after applying $\boldsymbol{a}$ to the system by the primary MPC. To optimize the expected reward, one option is to compute the difference between the current state and the reference input.

Based on the Expected Sarsa algorithm presented in [3], after initializing $\boldsymbol{\theta}$ and $\boldsymbol{s}$, we need to solve the primary MPC (1) in order to obtain optimal $\boldsymbol{x}_i$, $\boldsymbol{u}_i$ and $\boldsymbol{\sigma}_i$ at each sampling time. Doing this, the MPC cost function is computed and defined as the value of $Q_{\boldsymbol{\theta}}(\boldsymbol{s},\boldsymbol{a})$. Afterwards, according to the mentioned policy, the first element of $\boldsymbol{u}$ is applied to the real system so that the next state, $\boldsymbol{s}_+$, and the reward value, R, can be observed. In order to approximate the target action value function, the target MPC (1) needs to be solved when $\boldsymbol{x}_0 = \boldsymbol{s}_+$, so that $Q(\boldsymbol{s}_+, \boldsymbol{a}'_+)$ is obtained. Finally, it is possible to compute the error δ_k and use it to update the MPC.

III. Results

We applied the algorithm in simulation and to a real system of coupled tanks, in which the water level of the upper and the lower tanks (see x_1 and x_2 in Fig. 2) were set to 10 cm. The control input was the voltage of the pump that filled the upper tank, which then flowed inside the lower tank. The proposed PMPCFA converged after 4 training episodes to the reference signal. Fig. 2 shows the achieved performance of the algorithm obtained with 4, 5 and 6 episodes. It also illustrates the convergence to the set point in case of disturbances, i.e., when randomly adding water in both tanks, (see the jumps in the plot) indicating that the system quickly converged also in this case to the set point. As a comparison, PMPCFA requires just few episodes to be trained, whereas the MPC-based Q-learning method was about 100 episodes slower.

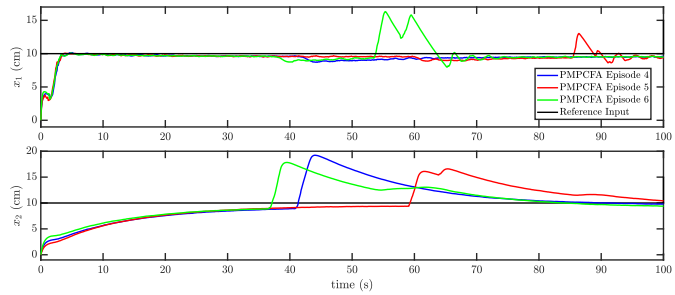

Fig. 2. PMPCFA performance to control the levels of a coupled tanks system.

IV. Conclusion

Compared to MPC-based Q-Learning, the advantage of the proposed algorithm based on Expected Sarsa is that the extra constraint on the first input of the primary MPC is eliminated. Indeed, forcing the primary MPC to start from a specific input, has a negative effect on the performance of MPC-based Q-Learning. Thanks to this improvement, the proposed algorithm has a faster convergence compared to MPC-based Q-Learning methods. Therefore, the training phase becomes shorter and more efficient, due to the wider variation between primary and target MPC. However, in both algorithms, the horizon needs to be chosen short enough to reduce the computational cost, since two MPCs have to be solved in each sampling time.

References

[1] Bin Chen, Zhiwu Huang, Rui Zhang, Weirong Liu, Heng Li, Jing Wang, Yunsheng Fan, and Jun Peng. Data-Driven Koopman Model Predictive Control for Optimal Operation of High-speed Trains. *IEEE Access*, 2021.

[2] Sébastien Gros and Mario Zanon. Data-driven Economic NMPC using Reinforcement Learning. *IEEE Transactions on Automatic Control*, 65(2):636–648, apr 2019.

[3] Seijen Harm van, Hasselt Hado van, Shimon Whiteson, and Marco Wiering. A theoretical and empirical analysis of expected sarsa. *2009 IEEE Symposium on Adaptive Dynamic Programming and Reinforcement Learning, ADPRL 2009 - Proceedings*, pages 177–184, 2009.

[4] Arash Bahari Kordabad, Hossein Nejatbakhsh Esfahani, Anastasios Lekkas, and Sébastien Gros. Reinforcement Learning based on Scenario-tree MPC for ASVs. *European Control Conference (ECC)*, mar 2020.

[5] Hoomaan MoradiMaryamnegari, Marco Frego, and Angelika Peer. Model Predictive Control-Based Reinforcement Learning Using Expected Sarsa. *under review*, xx:1–16, 2022.

[6] Richard S. Sutton and Andrew G. Barto. Reinforcement Learning, Second Edition: An Introduction. *The MIT Press*, pages 1–3, 2018.

[7] Csaba Szepesvári. Algorithms for reinforcement learning. *Synthesis Lectures on Artificial Intelligence and Machine Learning*, 9:1–89, 2010.

Security and Critical Observability of Finite State Machines under Cyber-attacks

Naeimeh Fakhr Shamloo, Elena De Santis, *Senior Member, IEEE*, and Maria Domenica Di Benedetto, *Life Fellow, IEEE*

***Abstract*—In many applications, security is a serious issue due to the high risk of cyber-attacks. Detecting any malicious activity is necessary to cover up its negative effects and make the system operate reliably. In this work, we propose a new approach to analyzing the security and critical observability of a Finite-state machine (FSM) under multiple attacks. Different kinds of attacks are modeled by an FSM and the composition of the nominal and attack model can express all the effects of possible attacks on the given system. We define different concepts of security and give conditions under which detectability of the attacks is possible. Moreover, critical observability of an FSM affected by multiple attacks is characterized.**

I. Introduction

In recent years, failing to detect attacks early in systems operations has caused significant financial losses to industries all over the world. In this work, we focus on systems described by Finite State Machines (FSM). For this class of systems, Gao et. al. [1] considered a system subject to two different classes of attacks, a constant attack where the intruder can only select one attack and a switching attack where different kinds of attacks may be chosen. However, most studies in this field focus on the design of controllers in the presence of attacks. Carvalho et. al. [2] proposed a defense strategy that aims at preventing damage from the attack, which can add/erase data in sensors/actuators, and disables all controllable events after an attack is detected. Necessary and sufficient conditions for the existence and synthesis of robust supervisors against general classes of sensor deception attacks, called all-out attack strategy, are considered in [3].

In this work, we introduce different notions of security and propose a novel method to assess security of an FSM under different kinds of attacks. The attacker is described by an FSM model and the interaction between the attacker and the nominal system is captured by their parallel composition. This way of representing the attacked system is very similar to the one the authors in [3] use. However, [3] is concerned with designing a robust supervisor in the presence of sensor attacks, while we focus on attack detection and observability of the system under attack. Another key feature distinguishing our work is that we adopt a fairly simple and general attack model that has no restrictions on the type of attacks , called the man-in-the-middle attack [4], where the attacker can replace, remove and inject symbols in the output executions. The methodologies used in [1] are based on constructing observers and diagnosers, which are exponential in the number of states of the FSM, while in [5] a polynomial mechanism verifies whether there exists a sensor attacker for a given plant and supervisor such that the supervisor fails to keep the plant within the specification.

Another property that we investigate is “critical observability", which corresponds to the possibility of detecting whether the current state belongs to a “critical set", i.e. a set containing specific states of interest such as unsafe states. When the system is not under attack, this problem was studied in [6] for linear switching systems. In this work, the preliminary results on critical observability presented in [7], where the attack can inject or replace only one symbol in the output executions, are extended to check the critical observability of FSMs under multiple different kinds of attacks.

A. Abbreviations and Acronyms

The following standard notations are used in this paper. For $a, b \in \mathbb{Z}$, $[a, b] = \{x \in \mathbb{Z} : a \leq x \leq b\}$ where $\mathbb{Z}$ denotes the set of nonnegative integer numbers and for a string σ, $\sigma|_{[a,b]}$ is the string $\sigma(a)\sigma(a+1)...\sigma(b)$. The null output is denoted by ϵ, and represents the situation where a state does not produce any output, i.e. it is a silent state. For a set $Y \subset X$, the symbol $\subset$ has to be understood as "subset" of Y in X.

II. Main Results

Consider an FSM M defined as

$$M = (X, X_0, Y, H, \Delta) \tag{1}$$

where:

- X is the finite set of states;
- $X_0 \subset X$ is the set of initial states;
- Y is the finite set of outputs;
- $H : X \to Y$ is the output function;
- $\Delta \subset X \times X$ is the transition relation.

Let $\mathcal{X}$ be the set of all finite and infinite state executions of the FSM M, and Υ be the set of strings with symbols in Y. Define $\mathrm{y} : \mathcal{X} \to \Upsilon$, the function that associates with a state execution the corresponding output execution as $\mathrm{y}(x) = H(x(1))...H(x(n))$ where $n = |x|$. Let $\Pi = \{(i, j) \in X \times X : H(i) = H(j)\}$. Finally, $\mathrm{y}^{-1}(\mathrm{y}(x)) = \{\hat{x} \in \mathcal{X} : \mathrm{y}(\hat{x}) = \mathrm{y}(x)\}$, $x \in \mathcal{X}$.

Naeimeh Fakhr Shamloo, Elena De Santis and Maria Domenica Di Benedetto are with the Department of Information Engineering, Computer Science and Mathematics, Center of Excellence DEWS, University of L'Aquila. (e-mail: {naeimeh.fakhrshamloo, elena.desantis,mariadomenica.dibenedetto}@univaq.it)

The research leading to these results has been partially supported by the Center of Excellence DEWS.

The FSM M is said to be *under attack* if an *attacker*, denoted A, replaces and/or removes the output of some states, and/or injects output symbols in the output string. Moreover, output symbols may be replaced with the symbol ϵ, so that we can speak in general of replacement, and the removal is a particular case of a replacement. If during a state execution $x \in \mathcal{X}$ an attack occurs, the resulting output execution is called *corrupted* if it is different from the nominal output string $\mathrm{y}(x)$. For a finite string x, if an injection occurs after the last symbol $x(|x|)$, the corrupted string produced by x is $\mathrm{y}(x)b$ where b is the injected symbol. For a string $x \in \mathcal{X}$, let Υ^x be the set of all the output strings (corrupted or not corrupted) produced by x. The symbol $(\Upsilon^x)^{-1}\Upsilon^x$ denotes the set $\{x' \in \mathcal{X} : \Upsilon^{x'} \cap \Upsilon^x \neq \emptyset\}$. The symbol Υ^x_a denotes the set of corrupted strings produced by x, hence $\Upsilon^x_a \subset \Upsilon^x$.

We model the behavior of the attacker with an FSM, as

$$M^A = (X_A, X_{0A}, E_A, Y_A, H_A, \Delta_A) \tag{2}$$

Let $X_A = X_{A,off} \cup X_{A,on}$, where $X_{A,off}$ is the set of states in which the attacker is off, $X_{A,on} = X^R_A \cup X^I_A$ where X^R_A, X^I_A represent the set of states in which the attacker makes a replacement and an injection attack, respectively.

In this work, we consider two problems. First, we focus on detecting the occurrence of an attack and analyze the security of FSMs. Then, we investigate observability of critical states despite the presence of attacks.

Three different aspects of security are defined in this paper. If there does not exist any corrupted output execution caused by the attack equal to the nominal output executions of the system (immediately or after some steps) the property is called "Security". Given an infinite execution $x \in \mathcal{X}$ of M, we denote by $\hat{k}$ the minimum value of k such that the output corresponding to $x(k)$ is replaced or such that an injection occurs between $x(k)$ and $x(k+1)$.

Definition 1. *(Security) An FSM M is said to be* secure *with respect to the attacker A, if there exists $d \in Z$, such that for all $x' \in \mathcal{X}$, and for all infinite $x \in \mathcal{X}$*

$$\mathrm{y}(x') \notin \Upsilon_a^{x|_{[1,\hat{k}+d+1)}} \tag{3}$$

The FSM M is called strongly secure *if $d = 0$.*

When the attack cannot be detected neither immediately nor with some delay, the FSM is called "unsecure":

Definition 2. *(Unsecurity) The FSM M is* unsecure *with respect to the attacker A if, for all infinite executions $x \in \mathcal{X}$ and for all $\hat{\mathrm{y}} \in \Upsilon^x_a$, there exists $x' \in \mathcal{X}$ such that*

$$\mathrm{y}(x') = \hat{\mathrm{y}} \tag{4}$$

If some of the corrupted outputs can be detected and some cannot, the property is called "weak-security":

Definition 3. *(Weak-security) The FSM M is* weak-secure*, if it is neither secure nor unsecure with respect to A.*

In some applications, and for some specific goals, it is important for the designer to detect if a state belongs to a "critical set", i.e. a set that can represent faulty or unsafe states, more than to detect the attack. This idea was first proposed for safety critical applications in [7]. In this paper, we investigate "critical observability" for the FSM M under attack:

Definition 4. *(Critical observability under attack) The FSM* (1) *is critically observable under attack w. r. t. a set $\Omega \subset \mathrm{X}$ (shortly, critically Ω-obs under attack), if for any finite string $x \in \mathcal{X}$ ending in Ω, it follows that any string $\hat{x} \in (\Upsilon^x)^{-1}\Upsilon^x$ ends in Ω.*

The complete analyze of the problems mentioned in the previous section, is presented in the full version of this work. All the effects of a given attack model on the nominal FSM can be represented by an FSM

$$M^E = (X_E, X_{0E}, Y_E, H_E, \Delta_E) \tag{5}$$

which can be obtained by parallel composition of the nominal FSM and the attack model ($M^E = M||M^A$):

$$M^E = Ac\,(X \times X_A, X_0 \times X_{0A}, Y \cup Y_A, H_E, \Delta_E) \tag{6}$$

where $Ac(.)$ denotes the accessible part

III. Conclusions

In the first part of this work, we proposed security properties for an FSM. Different kinds of attacks were modeled by an FSM, which enabled us to take advantage of composition rules to capture all the interactions of the attacker. The effects of all possible kinds of attacks were analyzed and conditions were given for the FSM's security in the complete version of this report. In the second part of the work, critical observability of FSM under attacks, a property that is equivalent to the immediate detection of any attack that the system may suffer from, was investigated. Conditions were given under which this property holds despite the attacks in the full version.

References

[1] C. Gao, C. Seatzu, Z. Li and A. Giua, "Multiple attacks detection on discrete event systems," *Proc. IEEE International Conference on Systems, Man, and Cybernetics (SMC)*, pp. 2352-2357, Oct. 2019.

[2] L. K. Carvalho, Y.- C. Wu, R. Kwong, S. Lafortune, "Detection and mitigation of classes of attacks in supervisory control systems," *Automatica*, vol. 97, 2018, pp. 121-133.

[3] R. Meira-Góes, S. Lafortune, and H. Marchand, "Synthesis of supervisors robust against sensor deception attacks," *IEEE Transactions on Automatic Control*, vol. 66, no. 10, 2021, pp. 4990-4997.

[4] P. M. Lima, M. V. S. Alves, L. K. Carvalho, M. V. Moreira, "Security of Cyber-Physical Systems: Design of a Security Supervisor to Thwart Attacks," *IEEE Transactions on Automation Science and Engineering*, vol. 19, no. 3, pp. 2030-2041, July 2022.

[5] Y. Tong, Y. Wang, A. Giua, "A polynomial approach to verifying the existence of a threatening sensor attacker*,"*Control Systems Letters*, Early Access.

[6] E. De Santis, M. Di Benedetto, S. Di Gennaro, A. DInnocenzo, G. Pola, "Critical observability of a class of hybrid systems and application to air traffic management," *Lecture Notes in Control, Information Sciences*, Blom and Lygeros Eds., vol. 337, 2006, pp. 141-170.

[7] N. F. Shamloo, E. De Santis, M. D. Di Benedetto, "Critical observability of finite state machines under attacks," *in Proc. 29th Mediterranean Conference on Control and Automation (MED)*, Bari, Italy, June 2021.

Control of Dynamic Financial Networks

Giuseppe Calafiore, Giulia Fracastoro, and Anton V. Proskurnikov

In this work we consider the problem of mitigating the effects of financial contagion via targeted and optimized interventions. We start from the setup of the multi-step model developed in [1] and introduce in the model an external control term representing corrective cash injections at nodes to be performed by a ruling authority. The rationale is that a ruling authority, perhaps public, may intervene with minimal and targeted cash injections at certain nodes in order to prevent catastrophic cascaded failure events. We show that such control problem can be cast and efficiently solved as a linear program. We refer the interested reader to [2] for an extended version of this work.

We consider n financial nodes (banks) who are subject to mutual liabilities $\bar{p}_{ij} \geq 0$, where $\bar{p}_{ij}$ represents the payment due from node i to node j. We also consider a discrete time horizon $t = 0, 1, \ldots, T$, with periods of fixed duration (e.g., one day, or one month, etc.), where $T \geq 0$ represents the final time of the horizon. The interbank liabilities constitute the *liability matrix* $\bar{P} \in \mathbb{R}^{n\times n}$, such that $[\bar{P}]_{ij} = \bar{p}_{ij}(t)$ for $i \neq j = 1, \ldots, n$, and $[\bar{P}]_{ii} = 0$ for $i = 1, \ldots, n$. Also, nodes may receive cash from external entities, which are not part of the network, and we denote by $e(t) \in \mathbb{R}^n_+$ the vector whose ith component $e_i(t) \geq 0$ represents the total cash inflow from the external sector to node i at time t. We also consider an additional term $u(t) \geq 0$, where $u_i(t)$ represents a "control inflow" injected at node i at time t by the control authority. Thus, the total cash inflow from external entities is $c(t) = e(t) + u(t) \geq 0$. We further assume that payments towards external entities are made to a fictitious node that owes no liability to the other nodes (the corresponding row of $\bar{P}(t)$ is zero). In normal situations, at the end of each time period t each node i is able to pay its liabilities in full, which means that each node i receives an inflow of liquidity $c_i(t) + \sum_{k\neq i} \bar{p}_{ki}$ and pays out its liabilities by a total amount of $\bar{p}_i \doteq \sum_{k\neq i} \bar{p}_{ik}$. Due to limited liability, the outflow cannot exceed the inflow. A critical situation instead occurs when (due to, e.g., a drop in the external in-flow $c_i(t)$) some bank i cannot fully pay its debt. In this situation, the actual payments to other banks have to be less than their nominal due values $\bar{p}_{ij}$. We let $P(t) \in \mathbb{R}^{n\times n}$, $t = 0, \ldots, T$, denote the actual payment matrix at time t. A matrix of mutual payments $P(t)$, with $0 \leq P(t) \leq \bar{P}$, is said to be *admissible* if at each node $i = 1, \ldots, n$ the outflow $p_i(t) = \sum_{k\neq i} p_{ik}(t)$ does not exceed the inflow $c_i(t) + \sum_{k\neq i} p_{ki}(t)$. If the nominal liabilities $\bar{P}$ are admissible then payments $P(t) = \bar{P}$ are such that all mutual obligations are met while maintaining the net worth of each node nonnegative, and no default arises. If instead $\bar{P}$ is not admissible, then some nodes are in *default*, and all nodes must agree on a different set of admissible payments $P(t)$, which are upper bounded by $\bar{P}$, since no node should pay more than due. Moreover, when a node is in default, it must pay out all of its cash inflow to the creditor nodes. So each node i either pays out $\bar{p}_i$, or it pays out its whole inflow. Therefore, a *clearing payment matrix* $0 \leq P(t) \leq \bar{P}$ obeys the relation

$$P(t)\mathbf{1} = \min(\bar{P}\mathbf{1}, c(t) + P^\top(t)\mathbf{1}). \tag{1}$$

In practice, payments under default are subject to further regulations. A commonly used "local fairness" rule is that the outstanding claims should be redistributed based on a proportionality (pro-rata) rule. We define the relative proportion of payment due nominally by node i to node j as

$$a_{ij} \doteq \begin{cases} \dfrac{\bar{p}_{ij}}{\bar{p}_i} & \text{if } \bar{p}_i > 0 \\ 1 & \text{if } \bar{p}_i = 0 \text{ and } i = j \\ 0 & \text{otherwise.} \end{cases} \tag{2}$$

Computing these proportions for all i, j we form the *relative liability* matrix $A = [a_{ij}]$. The so called *pro-rata rule* imposes that payments are due in proportion to the rates fixed in matrix A, that is

$$p_{ij}(t) = a_{ij} p_i(t), \quad \forall i, j, \tag{3}$$

where $p_i(t) = \sum_{k\neq i} p_{ik}(t)$ is the out-flow defined from node i. Since $p(t) \doteq P(t)\mathbf{1}$, the pro-rata rule imposes a set of linear equality constraints on the entries of $P(t)$, namely $P(t) = \text{diag}(P(t)\mathbf{1})A = \text{diag}(p(t))A$. Under the pro-rata rule, the full payment matrix $P(t)$ is determined by $p(t)$.

In this work we can deal indifferently with models with full payment matrices, or with matrices constrained by the pro-rata condition: in this latter case we shall simply include the linear equality constraint $P(t) = \text{diag}(p(t))A$ on the payment matrices, where $p(t) \doteq P(t)\mathbf{1}$. The net worth $w(t)$ evolves in accordance to

$$w(t+1) = w(t) + c(t) + P^\top(t)\mathbf{1} - P(t)\mathbf{1}, \tag{4}$$

for $t \in \mathcal{T}$, where we define $\mathcal{T} \doteq \{0, \ldots, T-1\}$. The limited liability condition requires that $w(t) \geq 0$ at all t. It may therefore happen that a payment $p_{ij}(t)$ has to be lower than the corresponding liability $\bar{p}_{ij}(t)$ in order to guarantee $w_i(t) \geq 0$. When this happens at some $t < T$, instead of declaring default and freezing the financial system, we allow

The authors are with the Department of Electronics and Telecommunications, Politecnico di Torino, Turin, Italy. E-mails:{giuseppe.calafiore, giulia.fracastoro, anton.proskurnikov}@polito.it.

operations to continue up to the final time T, updating the due payments according to the equation

$$\bar{P}(t+1) = \alpha\left(\bar{P}(t) - P(t)\right), \quad t \in \mathcal{T}, \tag{5}$$

where $\alpha \geq 1$ is the interest rate applied on past due payments. The recursions (4) and (5) are initialized with $w(0) = 0$, $\bar{P}(0) = \bar{P}$, where $\bar{P}$ is the initial liability matrix. The payment matrices $P(t)$ are subject to the constraints

$$0 \leq P(t) \leq \bar{P}(t) \quad \forall t \in \mathcal{T}, \tag{6}$$

$$P(t)\mathbf{1} \leq w(t) + c(t) + P(t)^\top \mathbf{1} \quad \forall t \in \mathcal{T}. \tag{7}$$

Conditions (6), (7) can be made explicit by eliminating the variables $w(t)$ and $\bar{P}(t)$:

$$P(t) \geq 0, \tag{8}$$

$$\sum_{k=0}^{t} \alpha^{t-k} P(k) \leq \alpha^t \bar{P} \tag{9}$$

$$C(t) + \sum_{k=0}^{t} \left(P(k)^\top - P(k)\right)\mathbf{1} \geq 0 \tag{10}$$

$$\forall t \in \mathcal{T},$$

where $C(t) \doteq \sum_{k=0}^{t} c(k) = \sum_{k=0}^{t} e(k) + u(t)$. In the case when pro-rata is enforced the above conditions can be rewritten in terms of the outflow vectors only:

$$p(t) \geq 0, \tag{11}$$

$$\sum_{k=0}^{t} \alpha^{t-k} p(k) \leq \alpha^t \bar{p} \tag{12}$$

$$C(t) + \sum_{k=0}^{t} \left(A^\top p(k) - p(k)\right) \geq 0 \tag{13}$$

$$\forall t \in \mathcal{T},$$

where $\bar{p} \doteq \bar{P}\mathbf{1}$ is the initial outflow liabilities and A is defined according to the initial liabilities $\bar{P}$.

For brevity, we denote $[P] \doteq (P(0), \ldots, P(T-1))$, $[p] \doteq (p(0), \ldots, p(T-1))$, and similarly $[c] \doteq (c(0), \ldots, c(T-1))$, $[u] \doteq (u(0), \ldots, u(T-1))$, etc. We say that a payment sequence $[P]$ is feasible for a *given* $[c]$, if it satisfies (8)–(10). Analogously, under pro-rata, a sequence $[p]$ is feasible for given $[c]$, if it satisfies (11)–(13). We now introduce a system-level cost criterion:

$$\delta(t) \quad \doteq \quad \sum_{i,j=1}^{n} \left(\bar{p}_{ij}(t) - p_{ij}(t)\right) = \mathbf{1}^\top \left(\bar{P}(t) - P(t)\right)\mathbf{1}.$$

We next consider the problem of controlling the financial network by optimal injections of cash $[u] = (u(0), \ldots, u(T-1))$ at nodes. The cumulative amount of cash injected from 0 to t is

$$B(t) \doteq \sum_{\tau=0}^{t} \mathbf{1}^\top u(\tau), \quad t \in \mathcal{T}.$$

The control problem is then stated as follows:

$$\min_{[P],[u]} \; (1-\eta)\sum_{t=0}^{T-1} \delta(t) + \eta \mathbf{1}^\top \bar{P}(T)\mathbf{1} + \gamma B(T-1) \tag{14}$$

$$\begin{aligned} \text{s.t.:} \quad & [P] \geq 0, \quad [u] \geq 0 \\ & \textstyle\sum_{k=0}^{t} \alpha^{t-k} P(k) \leq \alpha^t \bar{P}, \; t \in \mathcal{T} \\ & C(t) + \textstyle\sum_{k=0}^{t} \left(P(k)^\top - P(k)\right)\mathbf{1} \geq 0, \; t \in \mathcal{T} \\ & B(t) \leq F(t), \end{aligned}$$

where $\gamma \geq 0$ is a given penalty on the total control cash, $\eta \in [0,1]$ is a weight on the terminal cost, and $F(t) \geq 0$ is a given *nondecreasing sequence* that represents the maximum budget available up to time t for controlling the network. Problem (14) is an LP and can therefore be solved efficiently for the global optimum.

Under the pro-rata rule the control problem simplifies to

$$\min_{[p],[u]} \; (1-\eta)\textstyle\sum_{t=0}^{T-1} \mathbf{1}^\top (\bar{p}(t) - p(t)) + \eta \mathbf{1}^\top \bar{p}(T) + \gamma B(T-1)$$

$$\begin{aligned} \text{s.t.:} \quad & [p] \geq 0, \quad [u] \geq 0 \\ & \textstyle\sum_{k=0}^{t} \alpha^{t-k} p(k) \leq \alpha^t \bar{p}, \; t \in \mathcal{T} \\ & C(t) + \textstyle\sum_{k=0}^{t} \left(A^\top p(k) - p(k)\right) \geq 0, \; t \in \mathcal{T} \\ & B([u]) \leq \bar{B}. \end{aligned}$$

The above problems can be extended to the case where the inflows are known only up to some interval of uncertainty:

$$e(t) = \hat{e}(t) + d(t), \quad t = 0, \ldots, T-1,$$

where $\hat{e}(t) \geq 0$ is the nominal predicted value of the external cash inflow at t, and $d(t)$ is an unpredictable uncertainty on this value, assumed to bounded in magnitude so that

$$|d_i(t)| \leq r_i(t) \doteq \epsilon(t)\hat{e}_i(t), \quad i = 1, \ldots, n; \; t = 0, \ldots, T-1,$$

where $\epsilon(t) \in (0,1)$ is the given relative error level at t.

Let us now focus on the case of proportional payments. The decision variables $[p], [u]$ are assumed to be prescribed by a reactive policy that allows adjustments in consequence to deviation of the external inflows from their nominal values: for all $t \in \mathcal{T}$ we let

$$\begin{aligned} p(t) = \quad & \hat{p}(t) + \Theta(t)(e(t) - \hat{e}(t)) = \hat{p}(t) + \Theta(t)d(t) \\ u(t) = \quad & \hat{u}(t) + \Gamma(t)(e(t) - \hat{e}(t)) = \hat{u}(t) + \Gamma(t)d(t). \end{aligned} \tag{15}$$

and $[\hat{p}], [\hat{u}]$ are now the new decision variables, together with the collections of reaction matrices $[\Theta], [\Gamma]$. The control problem is now cast in a worst-case setting as follows

$$\min_{[\hat{p}],[\hat{u}],[\Theta],[\Gamma]} \quad \max_{[d]\in\mathcal{D}} J([p],[u])$$

$$\begin{aligned} \text{s.t.:} \quad & \min_{[d]\in\mathcal{D}} [p] \geq 0, \quad \min_{[d]\in\mathcal{D}} [u] \geq 0 \\ & \max_{[d]\in\mathcal{D}} \sum_{k=0}^{t} \alpha^{t-k} p(k) \leq \alpha^t \bar{p}, \; t \in \mathcal{T} \\ & \min_{[d]\in\mathcal{D}} C(t) + \sum_{k=0}^{t} \left(A^\top p(k) - p(k)\right) \geq 0, \; t \in \mathcal{T} \\ & \max_{[d]\in\mathcal{D}} B(t) \leq F(t), \; t \in \mathcal{T}, \end{aligned}$$

where $\mathcal{D} = \{[d] : |d_i(t)| \leq r_i(t), i = 1, \ldots, n; t = 0, \ldots, T-1\}$.

Numerical examples show that the proposed control model can significantly reduce the default propagation by applying small targeted cash injections.

References

[1] G. C. Calafiore, G. Fracastoro, and A. V. Proskurnikov, "Clearing payments in dynamic financial networks," *arXiv preprint arXiv:2201.12898*, 2022.

[2] ——, "Control of dynamic financial networks," *IEEE Control Systems Letters*, 2022.

Intrusion Detection System (IDS) for connected Electric and Autonomous Vehicles to prevent Vehicular ad hoc networks (VANET) Attacks

Wasim A. Ali, Michele Roccotelli, and Maria Pia Fanti

The challenges of managing In the era of the fourth industrial revolution, named Industry 4.0, even more smart factories are growing worldwide. In this context, the Electric vehicles (EV) industry is transforming the transportation system manufacturing field. Today, most of the EV's features and services are realized through smart technology. Conventional vehicles using an internal combustion engine consume fossil fuels and emit gases such as carbon oxides and hydrocarbons, which is the main reason for the environmental crisis. To overcome this issue, EVs have been introduced, developed, and improved over the past few years [1]. Vehicles will become smart objects using sensors that form the basis for the IoT networks. Improving the EV user experience relies on three basic components, the physical entities in the real world, the virtual models, and the data-driven by these models. Integrating these components requires a simulation framework to simulate large-scale traffic scenarios [2]. The distribution of charging points, EV volume, and all dynamic operations in the EVs network should be managed effectively and safely. For this goal, a simulation platform can be introduced to simulate the EV's network components and the interaction between each other. The simulation of operations could help us understand the nature of the physical product in each stage and collect information about the product characteristics, which can be helpful in the development process. Most simulation platforms support the concept of Digital Twin (DT), which provides a great capability to simulate the real-world entity in the industrial environment. DT concept is a virtual replica of a real-world object that can give the ability to study the development of physical objects in a digital situation/environment. DT was considered one of the world's ten strategic latest innovations in 2019, providing autonomous objects (e.g., self-driving cars), immersive technologies such as virtual reality (VR), augmented reality (AR), and quantum computing [3].

Digital data can improve an engineering system's intelligence concerning analytical evaluation, extrapolative diagnosis, and performance optimization. Then, the results of the analyses can be used to make the product or process run better in the physical environment [4]. In particular, DTs are used in a wide range of applications, including transportation, manufacturing, medicine, business, education, and more.

Integrated machine-driven, electrical, and computer software systems can be simulated in the virtual workspace through DT technology [5]. One important example of such a systems is EV, for which new technology is needed to optimize vehicle performance continuously.

Integrating big data analytics, IoT, and Artificial Intelligence (AI) techniques with DT leads to new significance, prospects, and challenges. Furthermore, an intelligent DT model can only be created using advanced AI techniques applied to the data [6]. The importance of DT is also proved in the security and monitoring systems. Lu et al. [11] presented a DT-enabled anomaly detection system based on industry foundation classes for asset monitoring solutions.

The automotive industry has seen significant changes due to rapid advancements in computing and electronics. A new generation of vehicles has emerged: autonomous vehicles (AV). The communication medium in these vehicles is an ad hoc vehicular network known as VANET. The network comprises ad hoc infrastructure and mobile vehicles communicating via open wireless channels. Shared wireless medium, high mobility and lack of centralized security services make VANET more susceptible to attacks. According to current research, external communication networks (V2X) have encountered security and privacy issues. However, the current detection techniques have much-limited prevention. They are designed for a set of known attacks, which is difficult to avoid the recent attacks designed to penetrate existing security systems. Therefore, the need for

Intrusion detection systems has been increased to protect V2X communication in autonomous vehicles from potential and updated attacks. And deploying IDS for VANET should be essential in the network architecture.

Some authentication methods, such as the Intrusion Presentation System (IPS), detect unauthorized users and prevent them from accessing the network. However, an IPS can be bypassed by a skilful intrusion. Therefore, an IDS can be the second layer of security to detect these types of intrusions. The role of an intrusion detection system (IDS) is to continuously network activity and collect relevant data for further analysis to make appropriate decisions in different situations.

We intend to build IDS to detect the intrusions and attacks on VANET such as DOS, DDOS, Botnet and Probe attacks that cause network issues, taking into account some parameters such as packet delivery, dropped, and delays, and latency of the network. We started our research and divided the work into three phases to build and evaluate our IDS as follows:

We started our research and divided the work into three phases to build and evaluate our IDS as follows:

1-Mobility and traffic simulation

We need the mobility simulator to enhance the realism degree in simulations with VANET. It will build realistic traces of vehicular mobility to be used as an input for the second stage (network simulator). Here we can define the scenario parameters (i.e., maximum vehicle speed, Driving pattern, Weather and traffic conditions and departure dates, etc.). Simulation of Urban Mobility (SUMO) is used in our research, and SUMO is an open-source traffic simulation designed to handle large road networks.

2- Network simulation

The network simulator simulates the network with the traces generated by the vehicular mobility simulator (SUMO) to achieve more practical results. Here we will simulate VANET and the communication between vehicles to vehicles (V2V) and vehicles to infrastructure (V2I). Once the network has been implemented, the model will be ready for the next step. We also chose an open-source network simulation called (Objective Modular Network Testbed in C++) OMNET++. Basically, it has been created for the communication networks simulation and extended to wireless and ad-hoc network simulations. OMNET++ has enormous libraries and frameworks available to develop various applications with simulation. In our research, we will work with the Vehicles in Network Simulation (VEINS). VEINS is a framework which runs for vehicular network simulations and combines the OMNET++ file and SUMO file to offer a comprehensive suite of models of Inter-Vehicle Communication (IVC)

3- Building an Intrusion detection system

In this stage, we will create some security attack scenarios, and applying an algorithm can help evaluate the network's behaviour. After collecting the previous statistics and scenarios, we need to build an IDS model using a Machine learning tool and choose a suitable method to identify network intruders.

References

[1] X. Lü, X., Wu, Y., Lian, J., Zhang, Y., Chen, C., Wang, P., Meng, L. (2020). Energy management of hybrid electric vehicles: A review of energy optimization of fuel cell hybrid power system based on genetic algorithm. Energy Conversion and Management, 205, 112474.

[2] Rassõlkin, A., Vaimann, T., Kallaste, A., Kuts, V. (2019, October). Digital twin for propulsion drive of autonomous electric vehicle. In 2019 IEEE 60th International Scientific Conference on Power and Electrical Engineering of Riga Technical University (RTUCON) (pp. 1-4). IEEE.

[3] Gartner. (2018) Gartner top 10 strategic technology trends for 2019. [Online]. Available: https://www.gartner.com/en/documents/3904573-top-10-strategic-technology-trends-for-2019-a-gartner-tr

[4] Qi Q. L. and F. Tao F., "Digital twin and big data towards smart manufacturing and industry 4.0: 360 degree comparison," IEEE Access,vol.6, pp. 3585–3593, Jan. 2018.

[5] WeyerS.,Meyer T.,Ohmer M.,Gorecky D.,andZuhlke D., "Future ¨ modeling and simulation of CPS-based factories: An example from the automotive industry," IFAC PapersOnLine, vol. 49, no. 31, pp. 97–102, 2016, doi: 10.1016/j.ifacol.2016.12.168.

[6] Rathore, M. M., Shah, S. A., Shukla, D., Bentafat, E., &Bakiras, S. (2021). The Role of AI, Machine Learning, and Big Data in Digital Twinning: A Systematic Literature Review, Challenges, and Opportunities. IEEE Access, 9, 32030-32052.

Stability analysis of wireless control networks via Markov jump systems theory

Anastasia Impicciatore, Yuriy Zacchia Lun, Alessandro D'Innocenzo, Pierdomenico Pepe

***Abstract*—In this note, we present stability analysis of wireless control networks. We adopt Markov jump system theory to model wireless control network scenarios. We present a threefold contribution. Firstly, we extend Lyapunov characterization of Input-to-state stability (ISS) to discrete-time nonlinear Markov jump systems. Secondly, we consider wireless control network scenarios with double sided packet-loss links modeled via finite-state Markov channels (FSMCs). We prove that the separation principle holds also in this case with FSMCs under a TCP-like communication scheme. Finally, we show that the FSMC can be also exploited to study suitable conditions guaranteeing secrecy against eavesdropping over Markov wireless links.**

Keywords: Markov Jump Systems, Lyapunov theorems, Wireless control networks, FSMCs

I. Introduction

Discrete-time Markovian switching nonlinear systems are particularly useful for modeling systems subject to abrupt changes such as Wireless Control Networks (WCNs). Indeed, a wireless channel may suffer from packet-losses [1], [2], and Markov chains allow to model bursts of packet losses, which is not possible using Bernoulli random variables [3]. Moreover, the FSMC model allows performance improvement in stabilizing control synthesis [4].

One side of our research focuses on the general class of discrete-time switching nonlinear systems [5] adding the Markovian switching rule [6], [7]. In this setting, we study exponential mean square input-to-state stability (ISS) [6], that is an ISS notion involving the second moment of the state. We provide necessary and sufficient Lyapunov conditions guaranteeing exponential mean square ISS [8].

Another interesting insight related to Markovian switching systems is their application to the study of wireless control network scenarios with double sided packet-loss wireless links modeled via finite-state Markov channels (FSMCs) [4]. In this framework, we adopt Markov jump linear systems (MJLSs) theory extending the results in [9]: we present novel detectability notions [10] and solve the optimal output-feedback control (OFC) problem (under a TCP-like communication scheme) [11].

The authors are with the Department of Information Engineering, Computer Science and Mathematics, University of L'Aquila, L'Aquila 67100, Italy (e-mails: anastasia.impicciatore@graduate.univaq.it, yuriy.zacchialun@univaq.it, alessandro.dinnocenzo@univaq.it, pierdomenico.pepe@univaq.it)

The FSMC can be also exploited to study suitable conditions guaranteeing secrecy against eavesdropping over Markov wireless links [12].

In this note, we will use the following acronyms: *MS* stands for mean-square, *MSS* stands for *MS* stable or *MS* stability, *MSD* stands for *MS* detectable or *MS* detectability, *EMS-ISS* stands for exponential *MS* input-to-state stability or exponentially *MS* input-to-state stable.

II. Lyapunov characterization of EMS-ISS

Consider the following discrete-time Markovian switching nonlinear system,

$$\begin{cases} x(k+1) = f_{r(k)}(x(k), u(k)), & k \in \mathbb{N}, \\ x(0) = \xi \in \mathbb{R}^n, & r(0) = i \in \mathcal{S}, \end{cases} \tag{1}$$

where $x(k) \in \mathbb{R}^n$ is the state of the system, $u(k) \in \mathbb{R}^m$ is the input signal, and $\{r(k)\}_{k\in\mathbb{N}}$ is a Markov chain (hereafter, MC). For any $i \in \mathcal{S}$, $f_i : \mathbb{R}^n \times \mathbb{R}^m \to \mathbb{R}^n$, is a locally bounded function satisfying $f_i(0,0) = 0$, continuous at zero.

We report in the following the definition of *EMS-ISS* [6].

Definition 1. *The system described by* (1) *is EMS-ISS if there exist positive constants $\theta, \zeta \in \mathbb{R}^+$ with $\theta \geq 1$, $0 < \zeta < 1$, and a $\mathcal{K}$-function η, such that for any initial condition $\xi \in \mathbb{R}^n$, for any $i \in \mathcal{S}$, and for any input signal $u \in \mathcal{U}$, $\mathbb{E}\left[\|x(k,\xi,i,u)\|^2\right]$ satisfies the following inequality, for any $k \in \mathbb{N}$:*

$$\mathbb{E}[\|x(k,\xi,i,u)\|^2] \leq \theta\zeta^k\|\xi\|^2 + \eta\left(\sup_{s=0,\dots,k-1}(\|u(s)\|)\right), \tag{2}$$

where the second term of the sum in the right-hand side of (2) *is taken equal to zero for $k = 0$.*

The following theorem states necessary and sufficient conditions for *EMS-ISS* of a given discrete-time Markov jump nonlinear system as the one considered in [8].

Theorem 1. *The system described by* (1) *is EMS-ISS if and only if there exist a locally bounded function $V : \mathbb{R}^n \times \mathcal{S} \to \mathbb{R}^+$ such that $V(\xi, i)$ is continuous at $\xi = 0$, for any $i \in \mathcal{S}$, positive real numbers α_l, $l = 1, 2, 3$, and a function α_4 of class $\mathcal{K}$, such that the following inequalities hold for all $i \in \mathcal{S}$, $\xi \in \mathbb{R}^n$, $u \in \mathbb{R}^m$,*

$b_1)$ $\alpha_1\|\xi\|^2 \leq V(\xi, i) \leq \alpha_2\|\xi\|^2$;
$b_2)$ $\mathcal{L}V(\xi, u, i) \leq -\alpha_3\|\xi\|^2 + \alpha_4(\|u\|)$,

with $\mathcal{L}V(\xi, u, i)$ linear operator defined in [6].

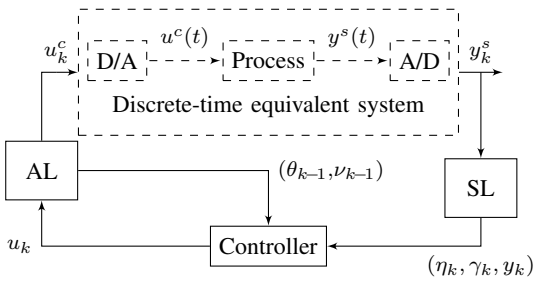

Fig. 1: Remote output-feedback architecture.

III. Optimal OFC for WCNs

Consider the remote architecture depicted in Fig. 1, where, for $k \in \mathbb{N}$, ν_k and γ_k are binary random variables describing the occurrence of packet losses over actuation link (AL) and sensing link (SL), respectively. The variables θ_k and η_k describe the channel mode of AL and SL, respectively. The information ν_{k-1}, θ_{k-1} is obtained by the controller through acknowledgement messages, that are typical of a TCP-like architecture as the one considered. Obviously, the ack message is received after the transmission, so there is one time-step delay [2]. As explained with more details in [10] and [11], the remote OFC architecture depicted in Fig. 1 can be modeled by a MJLS $\mathcal{G}$. Through the use of MJLS theory, by developing novel detectability notions and conditions [10], [11], it is possible to state a separation principle, as follows.

Theorem 2. *Given a MJLS $\mathcal{G}$, the closed-loop system dynamics can be made MSS if and only if the MJLS $\mathcal{G}$ is both MSD and MS stabilizable with one time-step delayed AL mode observation.*

IV. System state privacy

Finally, we show that the FSMC can be also exploited to study system state privacy [12]. The secrecy against eavesdropping is obtained when a legitimate user estimation mean square error (MSE) converges while the MSE of a malicious eavesdropper diverges. The design of a secrecy mechanism guaranteeing this condition over FSMCs is presented in [12].

V. Numerical case study

This section presents the wireless OFC of an inverted pendulum on a cart [10], controlled remotely over TCP-like lossy SL and AL (see Fig. 2).

VI. Conclusions

This note illustrates two research lines: the first one is a Lyapunov characterization for *EMS-ISS* of discrete-time Markovian switching nonlinear systems. The second one states a separation principle for WCNs modeled via MJLSs generalizing the results from [9]. Future research directions concern investigations of UDP-like WCN scenarios and converse Lyapunov theorems for discrete-time nonlinear systems with Markovian delays.

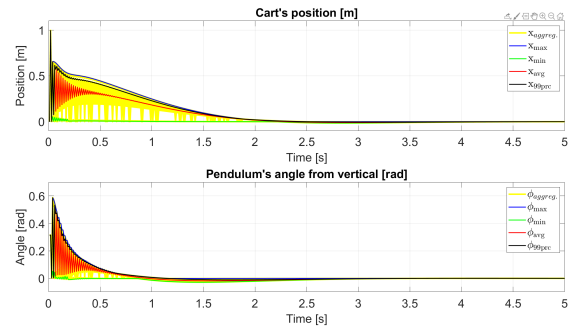

Fig. 2: Traces of the closed-loop system state of the inverted pendulum on a cart [10].

References

[1] O. L. V. Costa, M. D. Fragoso, and R. P. Marques, *Discrete-Time Markov Jump Linear Systems*. Springer-Verlag London, 2005.

[2] Y. Zacchia Lun and A. D'Innocenzo, "Stabilizability of Markov jump linear systems modeling wireless networked control scenarios," in *Proc. IEEE 58th Conf. Decis. Control*, 2019, pp. 5766–5772.

[3] P. Sadeghi, R. A. Kennedy, P. B. Rapajic, and R. Shams, "Finite-state Markov modeling of fading channels - a survey of principles and applications," *IEEE Signal Process. Mag.*, vol. 25, no. 5, pp. 57–80, 2008.

[4] Y. Zacchia Lun, C. Rinaldi, A. Alrish, A. D'Innocenzo, and F. Santucci, "On the impact of accurate radio link modeling on the performance of WirelessHART control networks," in *IEEE Conf. Computer Commun. (INFOCOM)*, 2020, pp. 2430–2439.

[5] P. Pepe, "Converse Lyapunov Theorems for Discrete-Time Switching Systems with Given Switches Digraphs," *IEEE Trans. Autom. Control*, vol. 64, no. 6, pp. 2502–2508, 2019.

[6] A. Impicciatore, A. D'Innocenzo, and P. Pepe, "Sufficient Lyapunov conditions for *p*th moment ISS of discrete-time Markovian Switching Systems," in *Proc. IEEE 59th Conf. Decision Control (CDC)*. IEEE, Dec. 2020.

[7] P. Patrinos, P. Sopasakis, H. Sarimveis, and A. Bemporad, "Stochastic model predictive control for constrained discrete-time Markovian switching systems," *Automatica*, vol. 50, no. 10, pp. 2504–2514, 2014.

[8] A. Impicciatore, P. Pepe, and A. D'Innocenzo, "Lyapunov characterizations of exponential mean square input-to-state stability for discrete-time Markovian switching nonlinear systems," *IEEE Trans. Autom. Control. Conditionally accepted as Paper*, 2022.

[9] L. Schenato, B. Sinopoli, M. Franceschetti, K. Poolla, and S. S. Sastry, "Foundations of Control and Estimation Over Lossy Networks," *Proceedings of the IEEE*, vol. 95, no. 1, pp. 163–187, 2007.

[10] A. Impicciatore, Y. Zacchia Lun, P. Pepe, and A. D'Innocenzo, "Optimal output-feedback control and separation principle for Markov jump linear systems modeling wireless networked control scenarios," in *Amer. Control Conf. (ACC)*, 2021, pp. 2700–2706.

[11] ——, "Optimal output-feedback control over Markov wireless communication channels," *IEEE Trans. Autom. Control. Under Review*, 2022.

[12] A. Impicciatore, A. Tsiamis, Y. Zacchia Lun, A. D'Innocenzo, and G. J. Pappas, "Secure state estimation over Markov wireless communication channels," *IEEE 61st Conf. Decis. Control. Accepted*, 2022.

A global finite-time first-order sliding mode strong observer design with certain semi-global fixed-time convergence characteristics

Alessandro Pilloni, Alessandro Pisano, Elio Usai

***Abstract*— For uncertain linear systems subjected to uniformly bounded unknown inputs we proposed a framework for the development and analysis of globally finite-time stable first-order sliding-mode observers. The design comprises of two exponentially convergent sliding-mode strong observers in the canonical form, modified by the presence of certain fixed-time injection terms, and a delayed output allowing the estimation of the unmeasurable state in a prescribed fixed-time since the sliding-motion is established. Finite-time and fixed-time stability arguments are exploited to formally study the convergence characteristics of the proposed strong observer, and regardless the unknown input influence. Numerical simulations illustrate the scheme effectiveness.**

***Index Terms*— State estimation, fixed-time stability, unknown input observer, sliding mode control, linear systems**

I. Introduction

State estimation in the presence of unknown inputs is supported by a well established theory [1]–[3]. Nevertheless, design techniques for *unknown input observers* (UIOs) are constantly evolving due to the variety of applications where they can be employed, such as output feedback control and fault detection/tolerant applications [1]–[3], and the monitoring of cyber-physical networks [4]. Condition for the UIO existence is the plant is *strongly detectable* (it doesn't possess unstable invariant zeros and fulfill the so-called *rank condition*). This is the case of *first-order sliding mode observers* (FOSMOs) [1], which however guarantee only exponential estimation rates. If the invariant zeros' set is empty, the system is called *strongly observable*. Then, finite-time *higher-order sliding mode observers* (HOSMOs) [3], or finite-time homogeneous UIOs, or fixed-time *arbitrary-order differentiators* [5] can be designed. However, except for the *suboptimal* HOSMO, which can be applied only to second-order dynamics [2], HOSMOs and homogeneous UIOs can compensate only Lipschitz UI, whereas the lasts only guarantee practical stability characteristics [5].

Thus, from a robust control perspective FOSMOs appear superior to others in the sense they can reject discontinuous UIs. Nonetheless, they can only guarantee the exponential state estimation, whereas other schemes may achieve it in finite- and/or fixed-time. Thus motivated, we propose a novel FOSMO design to guarantee: **a)** the global finite-time stability of the estimation errors; **b)** the insensitivity to uniformly bounded UIs. Moreover, since the proposal guarantees the unmeasurable state estimation in a prescribed-time since the sliding-motion is established, we further show: **c)** it possesses semi-global fixed-time convergence characteristics.

The research leading to these results has received funding by the Fondazione di Sardegna with grants: "IQSS-Information Quality aware and Secure Sensor networks for smart cities" (CUP:F75F21001400007), "ARGOSAT-Microsatellite cluster for the observation of optical transients in Astronomy (CUP:F74I19001070007)"; and by the Sardinian Regional Government with grant "POR SARDEGNA FSE 2014-2020-Asse III, Azione:10.5.12, "Avviso di chiamata per il finanziamento di Progetti di ricerca Anno 2017". A. Pilloni, A. Pisano, and E. Usai are with Department of Electrical and Electronic Engineering, University of Cagliari, Italy.

Corresponding author email: alessandro.pilloni@unica.it.

II. Problem formulation and preliminaries

Consider an uncertain linear dynamical system of the form

$$\dot{\mathrm{x}}(t) = \mathrm{A}\mathrm{x}(t) + \mathrm{B}u(t) + \mathrm{D}\xi(t,\mathrm{x},u), \quad \mathrm{x}(0) = \mathrm{x}_0 \tag{1}$$

$$y(t) = \mathrm{C}\mathrm{x}(t) \tag{2}$$

with state $\mathrm{x} \in \mathbb{R}^n$, input $u \in \mathbb{R}^m$, output $y \in \mathbb{R}^p$ and UI $\xi \in \mathbb{R}^q$. In accordance with theory of strong observers [1] we assume:

- **A1** The pair (A,C) of (1)-(2) is observable;
- **A2** Matrices $\mathrm{C} \in \mathbb{R}^{p\times n}, \mathrm{D} \in \mathbb{R}^{n\times q}$ in (1)-(2) are full-rank, with $p > q$, and $\mathrm{rank}(\mathrm{CD}) = q$;
- **A3** The triplet $(\mathrm{A},\mathrm{D},\mathrm{C})$ do not posses invariant zeros;
- **A4** The UI ξ satisfies $\|\xi(t,\mathrm{x},u)\|_\infty \leq \mu\|u\| + \rho(t,y)$ with known $\mu > 0$ and $\rho : \mathbb{R}_{\geq 0} \times \mathbb{R}^p \mapsto \mathbb{R}_{>0}$.

Problem: Let $\hat{\mathrm{x}}(t)$ be the estimate of $\mathrm{x}(t)$, and $\mathrm{T}(\mathrm{x}_0) : \mathbb{R}^n \mapsto \mathbb{R}_{\geq 0}$ the error settling time, we aim to design a finite-time UIO regardless the effects of nonsmooth UIs, i.e., such that

$$\exists\, \mathrm{T}(\mathrm{x}_0) : \hat{\mathrm{x}}(t) - \mathrm{x}(t) = 0 \quad \forall\, \mathrm{x}_0,\, \xi,\, t \geq \mathrm{T}(\mathrm{x}_0). \tag{3}$$

Moreover, let $z(t)$ be the unmeasurable part of $\mathrm{x}(t)$ such that $\mathrm{x}(t) \mapsto (z(t); y(t))$, if the additional assumption $z(0)$ remains in a-priory known in size compact region $\mathscr{Z} \subset \mathbb{R}^{n-p}$ is verified, whose size Z could also be arbitrarily large, i.e.,

$$\exists\, Z \,:\, \|z(0)\| \leq Z \quad \forall\, u \in \mathbb{R}^m,\, t \geq 0. \tag{4}$$

Then, $\mathrm{x}(t)$ is reconstructed in a fixed-time, namely,

$$\exists\, \mathrm{T}_{\max} : \hat{\mathrm{x}}(t) - \mathrm{x}(t) = 0 \quad \forall\, \mathrm{x}_0,\, \xi,\, t \geq \mathrm{T}_{\max}, \tag{5}$$

thus showing semi-global fixed-time stability characteristics. From **A1**-**A4**, and [1, Lemma 6.1], (1) can be decomposed as

$$\begin{bmatrix} \dot{z} \\ \dot{y} \end{bmatrix} = \underbrace{\left[\begin{array}{c|c} A_{11} & \mathscr{A}_{12} \\ \hline \begin{matrix}\mathscr{A}_{211} \\ \mathscr{A}_{212}\end{matrix} & \mathscr{A}_{22} \end{array}\right]}_{\mathscr{A}=T\bar{A}T^{-1}} \begin{bmatrix} z \\ y \end{bmatrix} + \underbrace{\begin{bmatrix} \mathscr{B}_1 \\ \mathscr{B}_2 \end{bmatrix}}_{\mathscr{B}=TB} u + \underbrace{\begin{bmatrix} 0_{n-q,q} \\ 0_{p-q,q} \\ \mathscr{D}_2 \end{bmatrix}}_{\mathscr{D}=TD} \xi. \tag{6}$$

III. Proposed strong observer

Let $i = 1,2$, consider the pair of canonical state observers

$$\dot{r}_i = A_{11} r_i + \mathscr{A}_{12} w_i - R_i(w_i - y) + \mathscr{B}_1 u + \tilde{L}_i v_i \quad (7)$$

$$\dot{w}_i = \mathscr{A}_{21} r_i + \mathscr{A}_{22} w_i - W_i(w_i - y) + \mathscr{B}_2 u + v_i \quad (8)$$

where $v_i \in \mathbb{R}^p$ is a discontinuous output injection vector

$$v_i = -a \operatorname{sig}^{\alpha}(w_i - y) - b \operatorname{sig}^{\beta}(w_i - y) - c(t,y,u) \operatorname{sign}(w_i - y), \quad (9)$$

with parameters $\mathrm{a} > 0, b > \mathrm{b}/p^{\frac{\beta-1}{2}}, \mathrm{b} > 0, \alpha \in (0,1)$, and $\beta > 1$, and $c(t,y,u)$ is any scalar function satisfying

$$c(t,y,u) \geq \|\mathscr{D}_2\|(\mu\|u\| + \rho(t,y) + \eta) \quad (10)$$

for some scalar $\eta > 0$. Then, the observer design matrices are

$$R_i = \mathscr{A}_{12} + \tilde{L}_i(\mathscr{A}_{21}\tilde{L}_i - \mathscr{A}_{22}^*) + F_i\tilde{L}_i,\ \tilde{L}_i = \left[L_i\ ,\ 0_{n-p,q}\right],$$
$$F_i = A_{11} - L_i\mathscr{A}_{211}, \quad W_i = \mathscr{A}_{22} + \mathscr{A}_{21}\tilde{L}_i - \mathscr{A}_{22}^*, \quad (11)$$

where $\mathscr{A}_{22}^*$ and $L_i \in \mathbb{R}^{(n-p)\times(n-q)}$ are selected satisfying

$$\Re(\lambda_j(F_2)) < \Re(\lambda_\ell(F_1)) \in \mathbb{R}_{<0} \quad \forall\ j,\ell \leq n-p, \quad (12)$$
$$\Re(\lambda_j(\mathscr{A}_{22}^*)) \in \mathbb{R}_{<0} \quad \forall\ j \leq p. \quad (13)$$

Finally, by stacking the states of (7)-(8) as $r = (r_1; r_2)$ and $w = (w_1; w_2)$, and by introducing a constant delay $\tau > 0$, the observer outputs (the estimation of z and y of (6)) are

$$\hat{z}(t) = K\left[r(t) - \mathrm{e}^{F\tau} r(t-\tau)\right] \quad (14)$$
$$\hat{y}(t) = Q^{\mathsf{T}} w(t) \quad (15)$$

with constant matrices designed as next

$$K = \left[I_{n-p}\ ,\ 0_{n-p,n-p}\right]\left[H\ ,\ \mathrm{e}^{F\tau}H\right]^{-1} \in \mathbb{R}^{(n-p)\times 2(n-p)}, \quad (16)$$
$$F = \begin{bmatrix} F_1 & 0_{n-p,n-p} \\ 0_{n-p,n-p} & F_2 \end{bmatrix}, H = \begin{bmatrix} I_{n-p} \\ I_{n-p} \end{bmatrix}, Q = \tfrac{1}{2}\begin{bmatrix} I_p & I_p \end{bmatrix}.$$

IV. Main results

Lemma 1. *Consider* (6)*, and let* ***A1-A3*** *hold. If* L_1*,* L_2 *in* (11) *satisfy* (12)*,* $\exists\ \left[H \quad \mathrm{e}^{F\tau}H\right]^{-1}$ *in* (16) *for almost all* $\tau > 0$*.*

Proof. Thank to **A1-A3**, and [1, Lemma 6.1.a] $(A_{11}, \mathscr{A}_{211})$ is observable and F_1, F_2 can be chosen as in (12). Note that

$$\det\left(\left[H \quad \mathrm{e}^{F\tau}H\right]\right) = (-1)^{n-p}\det\left(\mathrm{e}^{F_1\tau} - \mathrm{e}^{F_2\tau}\right)$$
$$= (-1)^{n-p}\det\left(\mathrm{e}^{F_1\tau}\right)\det\left(I_{n-p} - \mathrm{e}^{-F_1\tau}\mathrm{e}^{F_2\tau}\right), \quad (17)$$

which has a zero for $\tau = 0$. Since $\mathrm{e}^{F_2\tau} = o(\mathrm{e}^{-F_1\tau})$, while $\det\left(\mathrm{e}^{F_1\tau}\right) \to 0$ as $\tau \to \infty$, (17) does not vanish identically because the last determinant tends to 1. Thus, due to the *Principle of isolated zeros* we conclude $\exists\ \tau > 0 : \left[H \quad \mathrm{e}^{F\tau}H\right]^{-1}$. □

Theorem 1 (**Global finite-time stability**)**.** *Consider* (6) *and let* ***A1-A4*** *hold. Consider the UIO* (7)-(9) *with outputs* (14)-(15)*, and parameters as in* (10)-(13)*. Then* (3) *is verified* $\forall$ $a \geq 0$*,* $\mathrm{b} \geq 0$*,* $\alpha \in (0,1)$*,* $\beta > 1$*,* $\eta > 0$ *and almost all* $\tau > 0$*.*

Sketch of the Proof. Firstly, the estimation error global quadratic stability for (7)-(8) is proved, showing $\exists\ t \leq \mathrm{T}(\mathrm{x}_0) : \hat{y}(t) - y(t) = 0,\ \forall\ \mathrm{x}_0, \xi$. Thus, in the sliding motion results

$$\dot{r}_i \overset{\text{eq}}{=} A_{11} r_i + \mathscr{A}_{12} y + \mathscr{B}_1 u - L_i\mathscr{A}_{211}(r_i - z) \quad \forall\ t > \mathrm{T}(\mathrm{x}_0).$$

Then, after manipulations, note that $\frac{d}{dt}(r - Hz) \overset{\text{eq}}{=} F(r - Hz)$, which implies $r(t) - Hz(t) = \mathrm{e}^{F\tau}\left[r(t-\tau) - Hz(t-\tau)\right]$. From that, and (14), and the fact by construction $KH = I_{n-p}$ and $K\mathrm{e}^{F\tau}H = 0_{n-p,n-p}$, one can finally conclude that

$$\hat{z}(t) = K[r(t) - \mathrm{e}^{F\tau}r(t-\tau)] + z(t) - KHz(t) + K\mathrm{e}^{F\tau}Hz(t-\tau) = z(t)$$

i.e, $\exists\ t \geq \mathrm{T}(\mathrm{x}_0) + \tau : \hat{z}(t) = z(t)$, regardless its initialization.□

Theorem 2 (**Semi-global fixed-time stability**)**.** *Consider* (6) *and let* ***A1-A4*** *hold. Further assume* $z(t) \in \mathscr{Z} \subset \mathbb{R}^{n-p}$*, and there exists a known* $Z > 0$ *such that* (4) *holds. Consider the UIO* (7)-(9) *with outputs* (14)-(15) *and parameters as in* (10)-(13) *where* $\eta > \|\mathscr{A}_{211}Z\|_\infty / \|\mathscr{D}_2\|_1$*. Then* (5) *is verified* $\forall$ $a > 0$*,* $\mathrm{b} > 0$*,* $\alpha \in (0,1)$*,* $\beta > 1$*, and almost all* $\tau > 0$*.*

Sketch of the Proof. If Z in (4) is known, we can choose $\eta > \|\mathscr{A}_{211}Z\|_\infty / \|\mathscr{D}_2\|_1$. Then, thank to [6], we prove $\exists\ t \leq \mathrm{T}' = 2/(a(1-\alpha)) + 2p^{\frac{\beta-1}{2}}/(b(\beta-1)) : \hat{y} - y = 0,\ \forall\ \mathrm{x}_0, \xi$. Thus, one finally conclude that $\hat{z} = z\ \forall\ t \geq \mathrm{T}' + \tau$.□ Although the UIO (7)-(15) is well-posed for every initialization, until $\hat{y} - y = 0_p$ is established, overshoots on $\hat{z}(t)$ can be observed. To avoid overshoots, (14) can be replaced by

$$\hat{z}(t) : \begin{cases} Qr(t), & \text{if } [\ \|w - 1_2 \otimes y\|_1 \geq \lambda\ \wedge\ t < \mathrm{T}_{\max} + \tau\ ] \\ K\left[r(t) - \mathrm{e}^{F\tau}r(t-\tau)\right], & \text{otherwise} \end{cases} \quad (18)$$

where $\lambda > 0$ is a threshold aimed to detect the sliding-regime.

Numerical results Consider the inverted pendulum with a cart [1, Sect 5.6.3] with the input channel corrupted by a noisy uniformly bounded ξ, and linearized it around its unstable equilibrium. Consider the UIO (7)-(16) with $a = 100$, $\mathrm{b} = 30$, $\rho = 2$, $\alpha = 0.2$, $\beta = 3$, $\tau = 0.01$, and $L_1 = \begin{bmatrix} 0 & 19.8547 \end{bmatrix}$, $L_2 = \begin{bmatrix} 0 & 20.8547 \end{bmatrix} : F_1 = -20 > F_2 = -21$, and $\mathscr{A}_{22}^* = \operatorname{diag}(-20, -21, -22)$, and where $\mathrm{T}' = 2/(a(1-\alpha)) + 2p^{\frac{\beta-1}{2}}/(b(\beta-1)) = 0.125$, and $\mathrm{T}' + \tau = 0.135$.

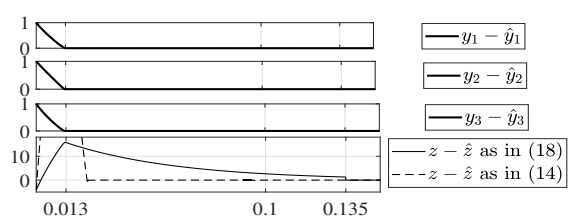

Fig. 1: Fixed-time convergence of the state estimation errors.

References

[1] C. Edwards and S. Spurgeon, *Sliding mode control: theory and applications*. Crc Press, 1998.

[2] J. Davila, A. Pisano, and E. Usai, "Finite-time state observation for nonlinear uncertain systems via higher order sliding modes," *Int. J. Control, 82(8):1564-1574, 2009*.

[3] A. Chalanga, S. Kamal, L. M. Fridman, B. Bandyopadhyay, and J. A. Moreno, "Implementation of super-twisting control: Super-twisting and higher order sliding-mode observer-based approaches," *IEEE TIE, 63(6):3677–3685, 2016*.

[4] S. Nateghi, Y. Shtessel, and C. Edwards, "Resilient control of cyber-physical systems under sensor and actuator attacks driven by adaptive sliding mode observer," *INT. J. RNC, 31:(15):7425–7443, 2021*.

[5] J. A. Moreno, "Arbitrary order fixed-time differentiators," *IEEE TAC, 67(3):1543-1549, 2022*.

[6] A. Polyakov, "Nonlinear feedback design for fixed-time stabilization of linear control systems," *IEEE TAC, 57(8):2106–2110, 2011*.

A coarse-grain model for cellular growth accounting for ribosome synthesis

Massimiliano d'Angelo[†,*], Pasquale Palumbo[‡,†], Stefano Busti[†,‡], and Marco Vanoni[†,‡]

Abstract

Protein synthesis in eukaryotes is carried out by ribosomes, large RNA–protein complexes consisting of a small and a large subunit. In this work (accepted for presentation at the 61-st IEEE Conference on Decision and Control - Dec. 6-9, 2022, in Cancún, Mexico) we present a mathematical model for cellular growth comprising both protein production and ribosome synthesis, properly accounting for both small and large subunits dynamics. The qualitative analysis of the model is carried out according to a simplifying assumption on the proportion of the two ribosomal subunits in stationary growth conditions; such hypothesis is based on a reasonable biological ground. Conditions are given on the model parameters in order to ensure exponential growth and the corresponding growth rate is straightforwardly computed from the model parameters. These results are validated by numerical simulations carried out according to a set of biologically meaningful model parameters. The modified model is better suited to host molecular blow-up of ribosomal synthesis and cell growth within a modular whole-cell model able to act as a scaffold connecting metabolism, growth and cycle.

Mathematical model of ribosome-protein synthesis and the computation of the exponential growth rate

We start from the ribosome-protein synthesis model of [1], which considers the following couple of ODEs

$$\dot{R} = k(\rho P - R)^+ - \gamma R, \tag{1}$$

$$\dot{P} = k_p R - \gamma_p P, \tag{2}$$

where R is the copy number of ribosome and P refers to protein accumulation in terms of polymerized amino acids copy numbers, whilst $(\cdot)^+$ is the function of the positive part and $k, \gamma, \kappa_p, \gamma_p$ are positive parameters.

We expand the latter model by considering the fact that ribosomes consist of two major components: the Small and Large ribosomal Sub-Units (SSU and LSU). In particular, during protein synthesis, both SSU and LSU bind to the mRNA strand to form an active ribosomal unit [4]. Our model expands the mathematical description of the ribosome, thus state variables of our model are:

$$R_{\text{SSU}}: \quad \text{copy number of the free SSUs} \tag{3}$$

$$R_{\text{LSU}}: \quad \text{copy number of the free LSUs.} \tag{4}$$

$$R: \quad \text{copy number of the active translating ribosomes.} \tag{5}$$

$$P: \quad \text{copy number of polymerized amino acids.} \tag{6}$$

where

$$R_{\text{SSU}} + R_{\text{LSU}} \underset{k_{\text{off}}}{\overset{\tilde{k}_{\text{on}}}{\rightleftharpoons}} R. \tag{7}$$

*current affiliation: Dipartimento di Ingegneria Informatica Automatica e Gestionale, Sapienza University, Rome, Italy.
†Dipartimento di Biotecnologie e Bioscienze, Università Milano-Bicocca, Milan, Italy.
‡SYSBIO- ISBE, 20126 Milan, Italy.

The new model can be derived and it is expressed by the following set of ODEs:

$$\dot{R}_{\mathrm{SSU}} = k_{\mathrm{SSU}}\left(\rho P - R_{\mathrm{tot}}\right)^{+} - \gamma_{\mathrm{SSU}} R_{\mathrm{SSU}} - k_{\mathrm{on}} \frac{R_{\mathrm{SSU}} R_{\mathrm{LSU}}}{P} + k_{\mathrm{off}} R, \tag{8}$$

$$\dot{R}_{\mathrm{LSU}} = k_{\mathrm{LSU}}\left(\rho P - R_{\mathrm{tot}}\right)^{+} - \gamma_{\mathrm{LSU}} R_{\mathrm{LSU}} - k_{\mathrm{on}} \frac{R_{\mathrm{SSU}} R_{\mathrm{LSU}}}{P} + k_{\mathrm{off}} R, \tag{9}$$

$$\dot{R} = k_{\mathrm{on}} \frac{R_{\mathrm{SSU}} R_{\mathrm{LSU}}}{P} - k_{\mathrm{off}} R, \tag{10}$$

$$\dot{P} = K_2 R - \gamma_p P, \tag{11}$$

with $R_{\mathrm{tot}} = R + \min\{R_{\mathrm{SSU}}, R_{\mathrm{LSU}}\}$.

The model is validated through numerical simulation with reference to budding yeast, and a closed formula for the exponential growth rate of the cell is derived through an approximated model. In particular, by considering some simplifications, and by denoting with the subscript SU mean parameters between the two subunits, we have the following theorem.

Theorem 1 *Let the following conditions hold true*

$$\sqrt{\frac{k_{\mathrm{off}}\gamma_p}{k_{\mathrm{on}} K_2}} < \rho - \frac{\gamma_p}{K_2} \tag{12}$$

$$k_{\mathrm{SU}} > k_{\mathrm{off}} \tag{13}$$

$$(k_{\mathrm{SU}} + \gamma_{\mathrm{SU}})\sqrt{\frac{k_{\mathrm{off}}\gamma_p}{k_{\mathrm{on}} K_2}} + \frac{k_{\mathrm{SU}}\gamma_p}{K_2} \leq \rho k_{\mathrm{SU}} \tag{14}$$

$$\rho(K_2\rho - \gamma_p) - (K_2\rho - \gamma_{\mathrm{SU}})\tilde{\beta} \geq 0 \tag{15}$$

with $\tilde{\beta}$ provided by

$$\tilde{\beta} = \frac{-(2K_2\rho + k_{\mathrm{off}} - \gamma_p) + \sqrt{\Delta}}{2(k_{\mathrm{on}} - K_2)} \qquad \text{and} \tag{16}$$

$$\Delta = (k_{\mathrm{off}} - \gamma_p)^2 + 4\rho k_{\mathrm{on}}(k_{\mathrm{off}} - \gamma_p + \rho K_2) \geq 0. \tag{17}$$

There exists exponential growth at regime

$$\frac{R_{\mathrm{SU}}}{P} = \beta \tag{18}$$

where β is the unique solution of

$$\psi(\beta) = \rho\, k_{\mathrm{SU}} \qquad \text{with} \tag{19}$$

$$\psi(\beta) = k_{\mathrm{on}}\beta^2 + \big(\lambda_+(\beta) + k_{\mathrm{SU}} + \gamma_{\mathrm{SU}}\big)\beta + \frac{(k_{\mathrm{SU}} - k_{\mathrm{off}})\big(\lambda_+(\beta) + \gamma_p\big)}{K_2} \tag{20}$$

and

$$\lambda_+(\beta) = \frac{-(k_{\mathrm{off}} + \gamma_p) + \sqrt{(k_{\mathrm{off}} - \gamma_p)^2 + 4\beta^2 k_{\mathrm{on}} K_2}}{2}. \tag{21}$$

is the exponential growth rate shared by R_{SU}, R and P at regime.

We stress that this model is intended to be a functional module of a whole-cell model of budding yeast ([3, 2, 5]) dealing with main cellular activities such as metabolism, growth and cycle. Finally, such a coarse-grained module is conceived to be expanded into a finer version detailing for the many assembly factors and ribosomal proteins involved in the ribosome assembly.

References

[1] L. Alberghina, L. Mariani, and E. Martegani. Cell cycle modelling. *Biosystems*, 19(1):23–44, 1986.

[2] T.M. Earnest, J. Lai, K. Chen, M.J. Hallock, J.R. Williamson, and Z. Luthey-Schulten. Toward a whole-cell model of ribosome biogenesis: kinetic modeling of ssu assembly. *Biophysical journal*, 109(6):1117–1135, 2015.

[3] Jonathan R Karr, Jayodita C Sanghvi, Derek N Macklin, Miriam V Gutschow, Jared M Jacobs, Benjamin Bolival Jr, Nacyra Assad-Garcia, John I Glass, and Markus W Covert. A whole-cell computational model predicts phenotype from genotype. *Cell*, 150(2):389–401, 2012.

[4] S. Klinge and J.L. Woolford. Ribosome assembly coming into focus. *Nature reviews Molecular cell biology*, 20(2):116–131, 2019.

[5] P. Palumbo, M. Vanoni, F. Papa, S. Busti, M. Wortel, B. Teusink, and L. Alberghina. An integrated model quantitatively describing metabolism, growth and cell cycle in budding yeast. In *Italian Workshop on Artificial Life and Evolutionary Computation*, pages 165–180. Springer, 2017.

Avalanche victim search via robust observers

Nicola Mimmo, Pauline Bernard*and Lorenzo Marconi†

July 26, 2022

Abstract

This paper deals with the problem of victim localization in avalanches by using controlled UAVs equipped with an electromagnetic sensor (known as ARVA) typically adopted in these Search & Rescue (S&R) scenarios.

1 Introduction

Within S&R in high mountain, a sensor technology that is typically adopted is the so-called ARVA. The system ARVA consists of two elements: a *transmitter* and a *receiver*. The transmitter is worn by the victims and emits an electromagnetic signal detectable by the receiver, which is held by the rescuers. The rescuers are trained to interpret the ARVA data to move closer to the victim location. Unfortunately, although this technique is common and quite efficient, it requires a non negligible amount of time due to the difficulties in walking in avalanche terrains. In this context, drones represent a valid alternative to humans resulting in a faster and safer research.

2 System description

The ARVA system relies on a transmitter device that generates a magnetic field modelled as a dipole. Let p_r, p_t be the receiver and transmitter positions, then the magnetic field intensity is given by (see [1])

$$\|h\| = \frac{1}{4\pi\|p\|^3}\sqrt{1+3\cos^2\Theta} \tag{1}$$

where $p \in \mathbb{R}^3$ denotes the error $p_r - p_t$, and $\Theta \in \mathbb{R}$ models the radiation pattern. The idea is to approximate $\sqrt{1+3\cos^2\Theta}$ with an equivalent function that makes (1) inversely proportional to a polynomial of p. This paper adopts this approximation

$$\frac{1}{\sqrt[3]{1+3\cos^2\Theta}} \approx \frac{1}{a^2}\cos^2\Theta + \frac{1}{b^2}\sin^2\Theta \tag{2}$$

with $a, b > 0$. Let $p := (x, y, z)^\top$, then the (1) becomes

$$\|h\| \approx \frac{1}{4\pi}\left(\frac{a^2b^2}{b^2x^2 + a^2(y^2+z^2)}\right)^{\frac{3}{2}} \tag{3}$$

from which it is possible to obtain the following linear regression model

$$\eta(\|h\|) = \Phi^\top(p_r)\,\mathrm{x}(x_t) \tag{4}$$

in which $\eta(\cdot)$, $\Phi(\cdot)$, and $\mathrm{x}(\cdot)$ are smooth functions of intensity $\|h\|$, the receiver positions $p_r \in \mathbb{R}^3$, and the transmitter state $x_t := (p_t, R_t)$, where $R_t \in SO(3)$ represents the attitude.

The receiver is assumed to be rigidly installed on a quadcopter, whose dynamics is given in [2]. Let $\dot{p}_t, \dot{R}_t = 0$, the goal is to control the UAV to estimate the position p_t of the victim as precisely as possible.

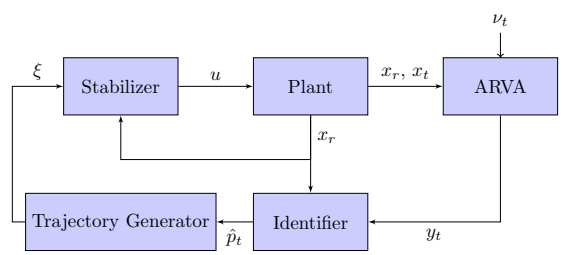

Figure 1: Representation of the closed-loop system.

3 Proposed Solution

Figure 1 depicts the proposed overall control scheme whose elements are detailed in the following sections.

3.1 Identifier

The role of the identifier is to provide an estimation of the victim position by properly processing the ARVA

*P. Bernard is with the Systems and Control Centre of MINES ParisTech, Université PSL, 60 Boulevard Saint-Michel, 75006 - Paris, France. e-mail: pauline.bernard@mines-paristech.fr.

†N. Mimmo and L. Marconi are with the Department of Electrical, Electronic and Information Engineering, University of Bologna, Italy, Viale del Risorgimento 2, 40136 - Bologna (BO). e-mail: {nicola.mimmo2, lorenzo.marconi} @unibo.it.

signal. This paper adopts the Recursive Least Square (RLS) with forgetting factor detailed in [3] and hereafter briefly recalled in its differential version. Given the ARVA measurement η, the RLS algorithm is given by

$$\begin{cases} \dot{R} &= -\rho\, R + \dfrac{\phi\phi^\top}{1+\phi^\top\phi} \\ \dot{Q} &= -\rho\, Q - \dfrac{\phi\,\eta}{1+\phi^\top\phi} \\ \dot{\hat{\mathrm{x}}} &= -\Gamma\left(R\hat{\mathrm{x}} + Q\right) \end{cases} \quad , \quad \hat{p}_t = \Upsilon\left(\hat{\mathrm{x}}\right) \quad (5)$$

in which, for easiness of notation, ϕ denotes the known signal $\Phi(p_r)$, $\rho > 0$ represents the forgetting factor, the matrix $\Gamma = \Gamma^\top > 0$ is a scaling matrix, and the initial conditions of R and Q are taken for instance as $R(0) = I$, $Q(0) = 0$. If the vector $\Phi(p_r)$ is persistently exciting and in the ideal case where $y_t = \Phi(p_r)^\top \mathrm{x}(x_t)$, it is a well-known fact ([3]) that the origin of the estimation error $\hat{\mathrm{x}} - \mathrm{x}(x_t)$ is globally exponentially stable, and therefore $\lim_{t\to+\infty} \hat{p}_t(t) = p_t$.

3.2 Reference Trajectory Generator

In order to use the identifier defined above, we need $\Phi(p_r)$ bounded and persistently exciting, and $p = p_r - p_t$ becoming sufficiently small to reduce the impact of the noise on the estimation error $\tilde{\mathrm{x}}$. The idea is therefore to make p_r follow a reference trajectory ξ composed of an exciting part ξ_e and a "slow" part ξ_s steering p_r to p_t, i.e., reducing p. In order to guarantee boundedness of trajectories, we saturate the slow component ξ_s outside a bounded region where the victim is known to be.

More precisely, the reference trajectory generator is represented by a dynamic system described by the following equations

$$\dot{\xi}_s = f_s(\hat{p}_t - \xi_s) \ , \quad \xi = \mathrm{sat}(\xi_\mathrm{s}) + \xi_\mathrm{e} \qquad (6a)$$

with $\xi_s(t_0) = p_r(t_0)$,

$$\xi_e(t) = (A_1 \sin \varpi_1 t,\ A_2 \sin \varpi_2 t,\ A_3 \sin \varpi_3 t)^\top \qquad (6b)$$

and where $f_s(\cdot)$ is defined as (with $K > 0$)

$$f_s(v) = f_{s_\mathrm{max}} \frac{K\|v\|}{\sqrt{1+K^2\|v\|^2}} \frac{v}{\|v\|}. \qquad (7)$$

4 Main result

We now analyse the stability of the whole interconnection shown in Figure 1. The following theorem claims that if the time scales of the references ξ_e and ξ_s are sufficiently different (namely if $f_{s_{max}}$ is taken sufficienly small in relation to the ϖ_is), then the estimation error of the victim position practically converges to zero with a practical region that is affected by the amplitude of the exciting signal. Such property, indeed, holds as long as the receiver remains sufficiently close to the victim in relation to the noise features.

Theorem 1. *Let the identifier and the reference signal be fixed as in Sections 3.1 and 3.2. Define with $\hat{p}_t$ the estimated transmitter position. Then, there exist $f^\star_{s_{max}} > 0$ and $\varepsilon > 0$ such that if $f_{s_{max}} \le f^\star_{s_{max}}$, there exists a class-$\mathcal{K}$ function γ such that any trajectory of the UAV, the identifier, and the reference generator is bounded and verifies*

$$\limsup_{t\to\infty} \|p_r(t) - p_t(t)\| + \|\hat{p}_t(t) - p_t(t)\| \le \gamma(\|\xi_e\|_\infty + \varepsilon)$$

The boundedness of all trajectories, guaranteed by the saturation of ξ_s, ensures that the drone remains in a predefined zone containing the avalanche area. The size of this region depends on the chosen saturation, the amplitude of the excitation, and the tracking performance ε of the UAV controller.

5 Conclusions

This paper presented an identification scheme for the problem of automatic estimation of the position of avalanche victims who wearing an electromagnetic transmitter (commercially known as ARVA). Due to the peculiar properties of the output map associated to the ARVA receiver, rigidly attached to a quadcopter, the identification process, provided by the implementation of a recursive least square algorithm and supported by a control system which steers the receiver toward the transmitter, solve the problem.

References

[1] P. Piniés and J. D. Tardós, "Fast localization of avalanche victims using sum of gaussians," in *Proceedings 2006 IEEE International Conference on Robotics and Automation, 2006. ICRA 2006.* IEEE, 2006, pp. 3989–3994.

[2] R. Naldi, M. Furci, R. G. Sanfelice, and L. Marconi, "Robust global trajectory tracking for underactuated vtol aerial vehicles using inner-outer loop control paradigms," *IEEE Transactions on Automatic Control*, vol. 62, no. 1, pp. 97–112, 2016.

[3] P. A. Ioannou and J. Sun, *Robust adaptive control.* Courier Corporation, 2012.

Deep Reinforcement Learning for Visual Active Exploration and Tracking

Alberto Dionigi[1] Alessandro Devo[2] Leonardo Guiducci[3] Gabriele Costante[1]

***Abstract*— The development of visual tracking systems is becoming a major goal for the Robotics community. Most of the works dealing with this topic focus exclusively on passive tracking, where the target is confined within the camera's field of view. Only a minority propose active approaches, capable not only of identifying the object to be tracked but also of producing motion control actions to maintain visual contact with it. However, all the methods introduced so far assume that the target is initially in the immediate proximity of the tracker. This represents an undesirable constraint on the applicability of these techniques, and it is to overcome this limitation that we propose a novel End-to-End Deep Reinforcement Learning based system, capable of both exploring the surrounding environment to find the target and then of tracking it. Through different experiments, we demonstrate the effectiveness of our approach and its superior performance with respect to current state-of-the-art (SotA) methods.**

I. INTRODUCTION

The growing interest in various robotics applications, such as autonomous driving, robot manipulation, and many others, encourages new research into the development of Visual Tracking (VT) systems. Despite the advances in the fields of Deep Learning and Computer Vision, in most works, these technologies have only been applied to *passive* tracking [1], [2]. This scenario is particularly limited since it assumes that the target to be tracked is always within the camera field-of-view (FoV).

To overcome this limitation, a recent line of research, focusing on Visual *Active* Tracking (VAT) [3], [4] is gaining increasing interest. In the active tracking scenario, the target is no longer constrained within the FoV; instead, it is necessary for the algorithm to dynamically adjust the position of the camera (or a mobile robot, as in our case), in order to maintain visual contact with it.

Although VAT can be addressed by combining a passive tracking module (*e.g.,* an object detector) with a separate one controlling the robot's motion, this approach has drawbacks [5], [6]: i) the two modules are not jointly optimized and not specifically designed for VAT; ii) combining them is not trivial and requires hyper-parameter tuning.

For this reason, much attention is shifting towards approaches based on end-to-end Deep Reinforcement Learning (DRL). Recent works [3], [4] have shown that DRL can also be effectively applied to produce robust VAT algorithms.

[1] The authors are with the Department of Engineering, University of Perugia, 06125 Perugia, Italy alberto.dionigi@studenti.unipg.it, gabriele.costante@unipg.it.

[2] The author is with the Red Lynx Robotics S.r.l., 06125 Perugia, Italy alessandro.devo@redlynxrobotics.com.

[3] The author is with the DISPOC, University of Siena, 53100 Siena, Italy leonardo.guiducci@unisi.it.

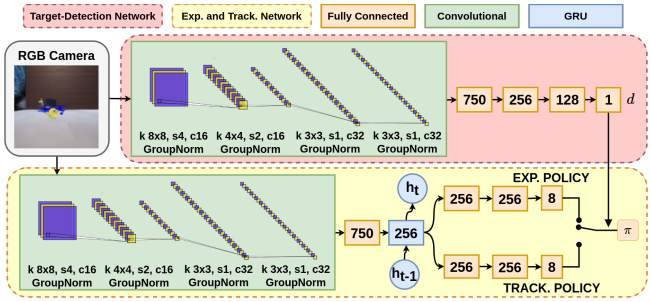

Fig. 1: The exploration and tracking architecture. The red block corresponds to the *Target-Detection* network, while the yellow one refers to the *Exploration and Tracking Network*. Both the sub-networks are fed with the RGB image of the current timestep. The output of the *Target-Detection* is used to switch between the exploration and the tracking policy.

Despite the impressive results achieved, these approaches assume that the target is initially positioned within the tracker's FoV. This assumption does not consider the case where the surroundings have first to be explored to discover the position of the target. Therefore, in our research, we propose *E-VAT*, an approach aimed to develop an active tracker that can explore a possibly unknown environment to find and track a specified target. Through different experiments, in simple, complex, and photo-realistic simulated environments, we show that our approach can effectively explore an unknown environment, find the target and track it. Furthermore, we demonstrate that despite our approach simultaneously solves two tasks, it matches and even outperforms the tracking performance of other SotA methods that, instead, have no exploration capabilities and make the simplifying assumption of having the target initially positioned in front of the tracker.

II. APPROACH AND TASK DETAILS

Given a specified possibly moving target, the goal of our approach is to explore the environment, detect the target and, once found, produce motion maneuvers to maintain it within its FoV by using only visual inputs. We define the tracker as an RL agent, which, by repeatedly interacting with an environment E, over a series of independent episodes and through discrete timesteps, receives input observations o_i, rewards r_i, and produces actions a_i.

Specifically, we assume that both tracker and target are free to move on a 2D plane. The tracker receives only the image stream from the front camera, and its action space is discrete. When an episode starts, the tracker and the target are randomly placed in an unknown indoor environment, and until it ends, the tracker has to explore the scenario, find the

target, and track it.

Following the recent works on DRL, we exploit Deep Neural Network (DNN) approximators and use the *actor-critic* formulation [3], [4]. Specifically, we aim to learn an *actor* model, which provides the optimal policy to fulfill the given task, and a *critic* model, which evaluates such a policy. The former acts only during the training phase, while the latter is the actual model used at test time to provide the action policies.

Contrary to the classical *symmetric actor-critic* implementations that require the two networks to share the same inputs, we adopt an asymmetric structure [7]. This strategy allows us to design the *Actor Network* to require only RGB inputs, while much more supervision information (that is more difficult to obtain at test time) can be exploited and provided to the *Critic Network*.

In our setting, target tracking can only start after the tracker has explored the environment and found it. Therefore, an end-to-end optimization of the agent penalizes the tracking sub-task, leading to poor performance. To this aim, we design a new training algorithm that differs from the classical actor-critic framework for 3 main features:

a) Sub-tasks decoupling and Agents splitting: we divide the problem into two fully decoupled tasks. The former starts from a condition in which the *tracker* and the *target* are distant, and the goal is to explore the environment until the *target* is found. The latter begins with the *target* in front of the *tracker*, and the goal is to maintain the desired distance and angle between the *tracker* and the *target*.

b) Actor with branches: To also decouple the sub-tasks at the model level, the Actor Network is designed with two different branches, focusing on the exploration and tracking policy separately. During training, each branch update is computed by using trajectories collected by the respective agent group only (*i.e.,* exploration or tracking). At test time, the switching between the policies is handled by the *Target-Detection Network*, depending on whether it has detected the target or not.

c) Critic with focused inputs: since each branch only handles one sub-task, the critic must be able to discriminate between the tasks and judge the policies separately. To this aim, we forced the critic to focus only on a subset of inputs (the task-specific ones) by setting to zeros all the others.

The simulated environments used during the training phase are built by using the photo-realistic graphics engine Unreal Engine 4 (UE4)[1]. The environment consists of a large unfurnished floor divided into rooms that are connected by corridors. At the start of each episode, the *tracker* is randomly spawned in a room of the floor, and, depending on whether it belongs to the exploration or tracking agent group, the *target* is randomly placed in a different room or in front of the *tracker*, respectively.

Since our model is trained in simulation only, we apply *domain randomization* [8] to achieve generalization also to more complex and photo-realistic contexts.

[1]https://www.unrealengine.com

TABLE I: RESULTS in DIFFERENT SCENARIOS

Scenario	Model	Target Found	Score Angle	Score Distance	Score Mean
Unfurnished	*E-VAT*	75%	0.66	0.88	0.77
	AD-VAT+	10%	0.63	0.74	0.69
	AOT	5%	0.93	0.78	0.86
Photo-realistic	*E-VAT*	40%	0.40	0.53	0.46
	AD-VAT+	10%	0.30	0.23	0.27
	AOT	10%	0.30	0.23	0.27

III. EXPERIMENTS

Experiments are designed to evaluate the ability of the agent to explore the environment, find the target, and keep it at the desired distance and at the center of the FoV.

Tests are performed both on simple scenarios, similar to those used for training and on more complex and photo-realistic contexts to evaluate the generalization capabilities of our model.

The results reported in Table I show that our approach outperforms all the baselines with respect to the exploration metric. This result is a direct consequence of the learned exploration policy. Specifically, the model has learned the *wall-following* policy, which is optimal in environments with connected walls.

Considering the tracking task, our model shows better performance, or at least similar, with respect to all the baselines in the unfurnished environments. Furthermore, even if as expected we found a performance drop in the photo-realistic environment, our model achieves better results compared to the baselines in all metrics.

IV. ACKNOWLEDGEMENTS

This research has been partially funded by HiPeRT s.r.l. within a research project with the Autonomous and Robotics Research (ARR) Center of the UAE Technology Innovation Institute (TII)

REFERENCES

[1] D. Zhang, H. Maei, X. Wang, and Y.-F. Wang, "Deep reinforcement learning for visual object tracking in videos," *arXiv preprint arXiv:1701.08936*, 2017.

[2] S. Pu, Y. Song, C. Ma, H. Zhang, and M.-H. Yang, "Deep attentive tracking via reciprocative learning," in *Advances in Neural Information Processing Systems*, 2018, pp. 1931–1941.

[3] F. Zhong, P. Sun, W. Luo, T. Yan, and Y. Wang, "Ad-vat+: An asymmetric dueling mechanism for learning and understanding visual active tracking," *IEEE transactions on pattern analysis and machine intelligence*, 2019.

[4] A. Devo, A. Dionigi, and G. Costante, "Enhancing continuous control of mobile robots for end-to-end visual active tracking," *Robotics and Autonomous Systems*, vol. 142, p. 103799, 2021.

[5] D. Murray and A. Basu, "Motion tracking with an active camera," *IEEE transactions on pattern analysis and machine intelligence*, vol. 16, no. 5, pp. 449–459, 1994.

[6] D. K. Das, M. Laha, S. Majumder, and D. Ray, "Stable and consistent object tracking: An active vision approach," in *Advanced Computational and Communication Paradigms*. Springer, 2018, pp. 299–308.

[7] L. Pinto, M. Andrychowicz, P. Welinder, W. Zaremba, and P. Abbeel, "Asymmetric actor critic for image-based robot learning," *arXiv preprint arXiv:1710.06542*, 2017.

[8] J. Tobin, R. Fong, A. Ray, J. Schneider, W. Zaremba, and P. Abbeel, "Domain randomization for transferring deep neural networks from simulation to the real world," in *2017 IEEE/RSJ international conference on intelligent robots and systems*, 2017, pp. 23–30.

Towards autonomous soft grasping of deformable objects using flexible thin-film electro-adhesive gripper and online capacitance measure

Salvatore D'Avella[1], Ion-Dan Sîrbu[1], Marco Fontana[1], Rocco Vertechy[2], Paolo Tripicchio[1]

Autonomous robotic grasping is a topic of great interest in the research community since it is fundamental in many applications like service robots, pick and place in manufacturing and logistics, and others. Though, it is a challenging problem as it requires many steps to succeed, ranging from detecting the target location to selecting the grasp pose configuration to have a stable grasp. In this context, the perception of the robot can involve vision, touch, and proprioception that give different information about the task. Most of the approaches in the literature rely only on visual cues since vision is useful to get global information from the scene, needed to compute the grasping points. On the contrary, vision is not suited to detect local information regarding the contact phase and the gripper-target interaction, especially in terms of the forces exerted during the grasping. Instead, the sense of touch is effective to acquire such information as well as the physical attributes of the target like the friction coefficient of its surface or its stiffness.

Grasping fragile objects or objects is a more complex task with respect to the traditional pick and place of solid objects relying only on visual information. Even though the research in that field is progressing fast, robots typically do not have a reliable sense of touch, and traditional robotic grippers are designed to grasp specific types of objects. In the case of fragile or soft objects, a retention action is typically preferred over a compression force in order to avoid damaging the objects. In this work [1] we propose a robotic grasping system that employs a gripper realized with the flexible thin-film electro adhesive (EA) pads technology (Fig. 1) that is controlled through a vision pipeline based on an RGB-D camera to detect the grasp pose configuration. The advantage of using such kind of system is that vision is the only perception cue needed to successfully grasp the target without damaging it, thanks to the properties of the EA gripper. Indeed, the gripper can automatically adapt its shape to the surface of the target delicately wrapping its two fingers around the object. The grasping action of the gripper relies on the electrostatic force induced by an electric field generated applying a voltage across a couple of electrodes embedded between dielectric substrates. Several tests have been done to assess the capabilities of the proposed robotic system, picking and placing deformable objects, comparing the EA gripper with a traditional parallel jaw gripper. In particular, we use compliant single layer cardboard boxes that are typically employed in medical and pharmaceutical packaging.

The obtained results showed that with the proposed approach, we were able to successfully complete grasping tasks that were not possible to accomplish with a conventional parallel jaw gripper that fails because of the large compliance of the walls of the boxes even though it implements a force feedback control based on the returned current (Fig. 2). Additionally we demonstrated the high robustness of the grasping of the EA gripper in presence of loads that have offset with respect the center of the grasping area. i.e. that induces shearing rotational torques.

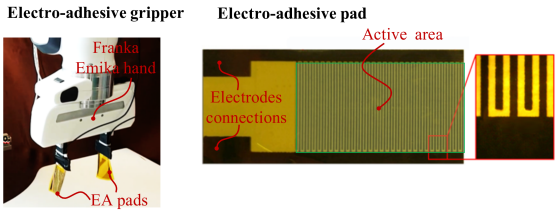

Fig. 1: Gripper equipped with two ED pads (left). Geometry of the EA pad showing the electrode shapes and the active area (right).

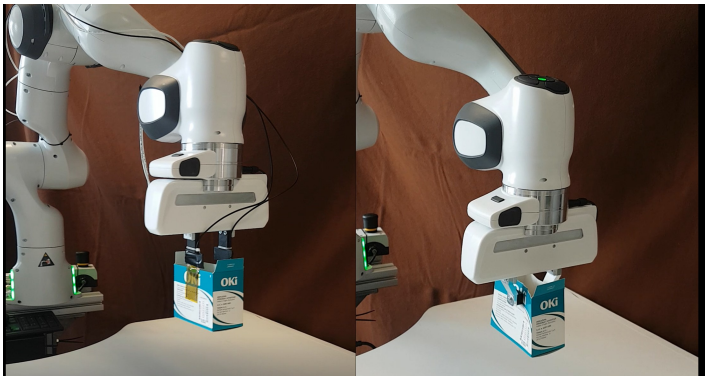

Fig. 2: Grasping of opened medicine box. On the left, the EAD gripper successfully grasp the box without altering its geometry. On the right, the classic parallel-jaw gripper deforms the box during grasping.

Furthermore, we propose a novel low-cost sensing architecture that makes it possible to detect the successful creation of EAD adhesion force and detect the possible loss contact with the adhering objects [2]. The proposed principle leverages on the intrinsic variation of capacitance that is associated with the capacitive coupling established between the elector-adhesive device EAD and the adhering object. Thus the measurement of capacitance during the operation of the EAD allows to identify several important adhesion parameters without any additional sensors and can be used as a checking mechanism that the grasping task has been successfully completed. Such a variation is dependent upon the material of the adhering object, the surface quality, and the presence of remaining air gaps at the interface. The non-trivial aspect of this measuring system relies on the high-voltage (usually in the range of several kilovolts) required for the

[1]Salvatore D'Avella, Ion-Dan Sîrbu, Marco Fontana, and Paolo Tripicchio are with the Perceptual Robotics Laboratory, Department of Excellence in Robotics & AI, Institute of Mechanical Intelligence, Scuola Superiore Sant'Anna salvatore.davella@santannapisa.it

[2]Rocco Vertechy is with the Department of Industrial Engineering, University of Bologna

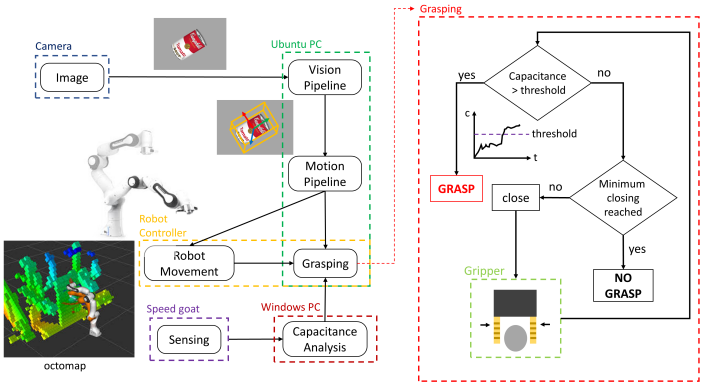

Fig. 3: Schematic describing the complete pipeline with the connections among the components

operation of EAD. The proposed Capacitance Sensing Circuit is based on a custom low-cost circuit that provides a direct analog output signal proportional to the capacitance value and does not need expensive high bandwidth high voltage amplifiers. The system is based on the injection of a low voltage sinusoidal signal obtained through filtering capacitors combined with a precision rectifier.

The system has been realized as a component-based designed architecture. In particular, the vision and planning pipeline run in the ROS (robotic operating system) Noetic environment containerized in a docker machine with Ubuntu 20.04 LTS. The gripper controller executes on a Speedgoat Baseline real-time target machine, and the capacitance analysis runs on another PC with Windows and MATLAB Simulink 2021a. All the computing units are interconnected by employing a switch: the Speedgoat talks directly with the Windows PC, which sends the closing information to the main Ubuntu PC via ROS messages from Simulink. Fig. 3 depicts a schematic of the complete working pipeline with the necessary connections among the components.

The vision system uses a Realsense D435 RGB-D camera positioned on top of the working table, looking down at the object to be manipulated. In order to show the grasp capabilities of the electroadhesive gripping system and to demonstrate the possibility of recognizing instant in which electradhesion become effective, single object scenarios have been considered. The vision pipeline exploits the registered depth information for segmenting the scene and detecting the pose of the target. In particular, the algorithm extracts the principal axes, the centroid, and builds the bounding box. As a first step, the RGB image is converted to grayscale to perform a thresholding operation to get the mask of the target object. Then, the Suzuki algorithm is used to find the contour, and the Principal Component Analysis (PCA) is applied to that contour. PCA is a statistical procedure that extracts the most important features of a data set and allows for dimensionality reduction by finding the direction along which the data varies the most. Therefore, the PCA on the contour returns the two eigenvectors that represent the principal components of the data and are used to identify the object orientation. The size of each eigenvector is encoded in the corresponding eigenvalue, which indicates how much the data vary along with the principal component or, in other words, it represents the length of the side of the enclosing 2D bounding box. The beginning of the eigenvectors is the center of all points in the data set, a.k.a.,

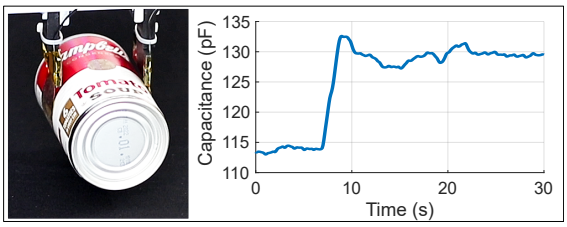

Fig. 4: Capacitance variation during the adhesion of the pads onto a curved surface of a metallic can.

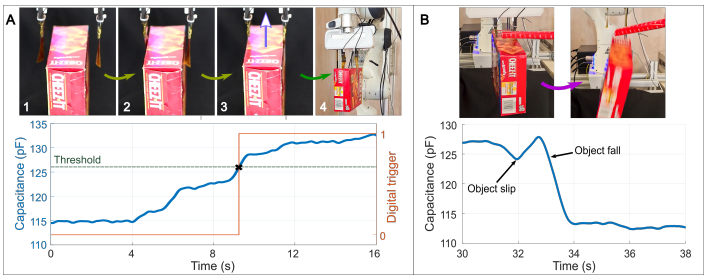

Fig. 5: Capacitance variation during manipulation of a cardboard box

the centroid. Therefore, the result of the PCA provides the centroid of the target ($p = [m_u, m_v, 1]^T$) where m_u, m_v are pixel coordinates, and the x and y-axis (f_x, f_y) of the object frame w.r.t. the camera frame. Assuming the object lays horizontally on the working table, the rotation matrix can be built by considering f_z pointing inside the working table to be orthonormal to f_x and f_y that lay on the plane. Being K the intrinsic camera matrix and H the homogeneous extrinsic matrix representing the camera frame in the world coordinate, it is possible to obtain the centroid of the object in world coordinates. Then, the vision pipeline builds the 3D cuboid of the object deriving the height, width, and depth of the object. In particular, the height and the width can be obtained from the magnitude of the eigenvalues and the depth can be computed by reading the depth information provided by the camera as the difference between the depth value of the centroid and the depth of the working table. Finally, the algorithm searches for the two smallest parallel surfaces that are below the gripper clearance to compute the grasping pose of the robot. The grasping happens with a purely vertical movement, with the gripper opened at its maximum clearance, in order to minimize possible causes of errors. The grasping phase is a closed-loop signal procedure. During the grasping, the main Ubuntu PC commands the gripper to close until it receives feedback from the Windows PC that the capacitance has surpassed a threshold which has been calibrated empirically on the used objects. Fig. 4 and 5 show two grasping attempts using the self sensing mechanism. In particular, 5 depicts the possibility to understand if the object drops down during the transportation phase.

References

[1] Salvatore D'Avella, Marco Fontana, Rocco Vertechy, and Paolo Tripicchio. Towards autonomous soft grasping of deformable objects using flexible thin-film electro-adhesive gripper. In *2022 IEEE 18th International Conference on Automation Science and Engineering*. IEEE, 2022.

[2] Ion-Dan Sîrbu, Marco Bolignari, Salvatore D'Avella, Lorenzo Agostini, Paolo Tripicchio, Rocco Vertechy, Lucio Pancheri, and Marco Fontana. Adhesion state estimation for electrostatic gripper based on online capacitance measure. *IEEE Access*, 2022.

Robust Control Invariance for Networked Control Systems with Output Feedback

Masoud Bahraini, Mario Zanon, Alessandro Colombo, and Paolo Falcone

July 22, 2022

1 Extended Abstract

A system whose feedback loop is closed through a wireless communication channel is called a wireless networked control system (NCS). Recently, NCSs have gained more attention due to their advantages, such as less wiring cost and more flexible structure. However, closing the control loop through a communication channel may lead to impaired control performance or even instability due to the communication-channel imperfections. Hence, explicit consideration of the communication impact on control stability and performance is needed. Furthermore, the control may also be designed to enhance the communication performance, such as reduced energy usage, or meet some additional limitations, such as reducing the communication demand in a shared medium scenario.

Recently, robust control and scheduling design for multi-agent NCSs with safety critical applications has been studied, where safety conditions are presented as state and input constraints for each system. In [1], a linear control feedback is considered where constraint satisfaction is guaranteed through guaranteeing robust invariance for each system. The robust invariance is in turn guaranteed through communication scheduling such that each system's feedback loop is closed frequently enough. While this communication schedule design is offline and for a NCS with single shared channel, it has been extended to design online schedules with more general communication structures [2, 3]. Furthermore, model predictive control (MPC) has been employed in this setting in order to minimize the communication demand for each system while preserving the robust invariance [4, 5].

In this paper, we consider robust output feedback for a class of multi-agent NCSs with a shared communication link and in presence of state and input constraints for the systems. Consider the multi-agent setting shown in Figure 1, where the local control loops receive the sensor measurements through a shared wireless channel, with limited communication capacity. The central scheduler is

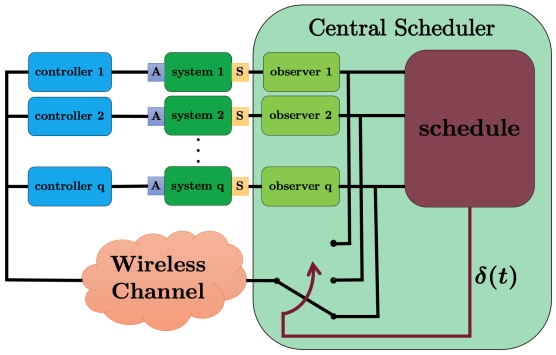

Figure 1: A set of agents sharing a common channel to exchange state measurements data based on decisions of the Central Scheduler.

in charge of scheduling the measurement updates for each local controller to guarantee that state and input constraints are respected. To this end, we estimate the states using a Luenberger observer. The state-estimate and an invariant set for the state-estimation error are then used in control

Table 1: Numerical simulation results

Observer/Control	K_1	K_2	MPC
L_1	3	5	5
L_2	5	8	8
L_3	4	6	19

design. We first consider a linear feedback policy with a constant feedback gain and show that the communication demand minimization with respect to the feedback gain is hard to solve. Then, we find the minimum attainable communication demand, with respect to a given observer gain, and formulate an MPC problem to design a corresponding control policy. We show that the second approach is less difficult and yields lower communication demand in comparison to the linear feedback case. We also propose a heuristic to minimize the communication demand with respect to the observer gain and control.

We provide a numerical example to illustrate the proposed methods. Table 1 provides the simulation results, where rows indicate different observer gains and columns indicate different controllers. The numbers indicate the so called *safe time intervals, which are the longest period during which the system's feedback loop needs to get closed once. Hence, a larger number indicates a lower communication demand. As one can see from the table, the observer gain has in impact on the safe time interval and given an observer gain, MPC outperforms other controllers. Figure 2 shows the approximated minimal invariant sets for the state-estimation error. Note that while the corresponding invariant set to the observer gain L_2 is the largest, it yields less communication demand in comparison to the observer gain L_1.*

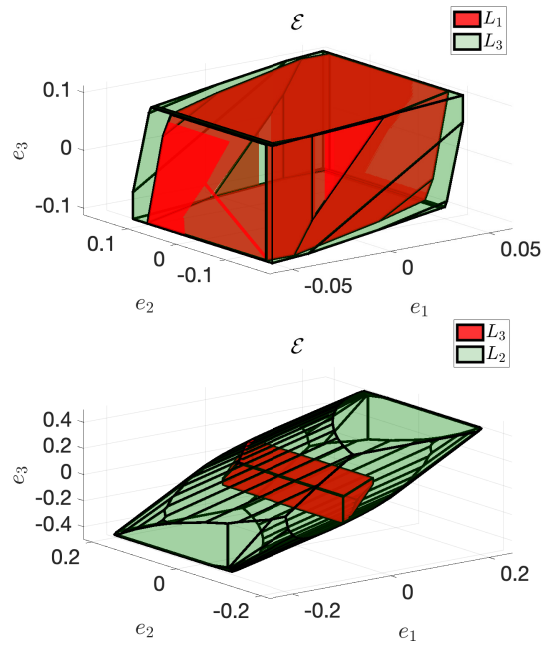

Figure 2: A set of agents sharing a common channel to exchange state measurements data based on decisions of the Central Scheduler.

References

[1] *Colombo, Alessandro, Masoud Bahraini, and Paolo Falcone. "Measurement scheduling for control invariance in networked control systems." 2018 IEEE Conference on Decision and Control (CDC). IEEE, 2018.*

[2] *Bahraini, Masoud, et al. "Receding-horizon robust online communication scheduling for constrained networked control systems." 2019 18th European Control Conference (ECC). IEEE, 2019.*

[3] *Bahraini, Masoud, et al. "Scheduling and Robust Invariance in Networked Control Systems." IEEE Transactions on Automatic Control (2021).*

[4] *Bahraini, Masoud, et al. "Optimal Control Design for Perturbed Constrained Networked Control Systems." IEEE Control Systems Letters, 2020.*

[5] *Bahraini, Masoud, et al. "Optimal scheduling and control for constrained multi-agent networked control systems." OCAM, 2021.*

Modeling and Control of Multilevel Flying-Capacitor Converters

Davide Tebaldi, Roberto Zanasi

Abstract

This extended abstract addresses the modeling and the control, through the proposal of a new variable-step algorithm, of multilevel flying-capacitor converters.

1. Introduction

Multilevel flying-capacitor converters require particular attention when dealing with capacitor voltages balancing [1]-[3]. Such converters have full floating capacitors voltage balancing capability if the number of output voltage levels m equals the number of capacitors n plus one. However, the n-dimensional multilevel flying-capacitor converter can go up to 2^n levels in "extended operation" [4]-[5]. If $m > n+1$, the full voltage balancing capability is lost and a suitable closed-loop control technique becomes paramount [5]. In this contribution, the modeling and the proposal of a new variable-step algorithm for properly controlling multilevel flying-capacitor converters are addressed [6].

2. Converter Modeling

The n-dimensional model of the converter is [6]:

$$\begin{cases} \mathbf{C}\dot{\mathbf{V}}_c = \mathbf{A}\mathbf{V}_c - \mathbf{S}_j^{\mathrm{T}} I_{out} + \mathbf{B} V_{in}, \\ V_{out} = \mathbf{S}_j \mathbf{V}_c, \end{cases} \quad \mathbf{C} = \left[\begin{array}{c|ccc} C_1 & 0 & \cdots & 0 \\ \hline 0 & C_2 & \cdots & 0 \\ \vdots & \vdots & \ddots & \vdots \\ 0 & 0 & \cdots & C_n \end{array}\right],$$

$$\mathbf{A} = \left[\begin{array}{c|ccc} \frac{-1}{R_{in}} & 0 & \cdots & 0 \\ \hline 0 & 0 & \cdots & 0 \\ \vdots & \vdots & \ddots & \vdots \\ 0 & 0 & \cdots & 0 \end{array}\right], \mathbf{V}_c = \begin{bmatrix} V_1 \\ V_2 \\ \vdots \\ V_n \end{bmatrix}, \mathbf{S}_j^{\mathrm{T}} = \begin{bmatrix} s_1 \\ s_2 \\ \vdots \\ s_n \end{bmatrix}, \mathbf{B} = \begin{bmatrix} \frac{1}{R_{in}} \\ 0 \\ \vdots \\ 0 \end{bmatrix}. \tag{1}$$

Davide Tebaldi and Roberto Zanasi are with the Department of Engineering "Enzo Ferrari", University of Modena and Reggio Emilia, Modena, Italy. `davide.tebaldi@unimore.it`, `roberto.zanasi@unimore.it`

3. Variable-Step Control of the Converter

The scheme of the new proposed variable-step control is shown in Fig. 1. Its main features are:

- At each activation time t_k, the algorithm computes the two configuration vectors $\mathbf{S}_H$, $\mathbf{S}_L$ (which are in a one-to-one correspondence with the transistors switching states [6]) and the duty cycle V_{dc} to be applied in the following PWM time interval $[t_k \quad t_k + T_{PWM}]$.
- N_s defines the *maximum level-to-level distance*.
- The current values of the upper level α_H, lower level α_L and duty cycle d_c are computed. If α_H and α_L are admissible, then the sets $\mathscr{S}_{\alpha_H}$ and $\mathscr{S}_{\alpha_L}$ of the admissible configuration vectors $\mathbf{S}_{Hi}$ and $\mathbf{S}_{Lj}$ and the corresponding vectors $\overline{\mathbf{S}}_{CHi}$ and $\overline{\mathbf{S}}_{CLj}$ are computed.
- The distance vectors $\Delta\overline{\mathbf{V}}_{cij}$ for each possible combination of the configuration vectors $\mathbf{S}_{Hi}$ and $\mathbf{S}_{Hj}$ belonging to the two sets $\mathscr{S}_{\alpha_H}$ and $\mathscr{S}_{\alpha_L}$ are computed.
- If the norm of the distance vector $\Delta\overline{\mathbf{V}}_{cij}$ is smaller than the current minimum norm N_m, then the algorithm updates the value of parameter N_m.
- The algorithm ends its minimum distance vector search either when the maximum level-to-level distance N_s is achieved, or when the current minimum distance N_m is lower than the initial one, or if N_m is lower than radius $V_{r0}N_{si}$, where V_{r0} is the input basic radius and N_{si} is the current level-to-level distance. Radius $V_{r0}N_{si}$ represents the varying radius of an hypersphere in the $(n-1)$-dimensional space.
- The new concept of "*variable level-to-level distance*", exemplified in Fig. 2, is introduced.

4. Simulations

In the considered simulation case study, the considered converter with $n = 3$ capacitors is supposed to be working in a configuration generating eight voltage levels. At some point, an unfavorable condition is supposed to occur, i.e. the required output voltage is supposed to be constant for a certain time interval. From the results in Fig. 3, it is possible to see that capacitors voltage trajectories divergence due to a constant

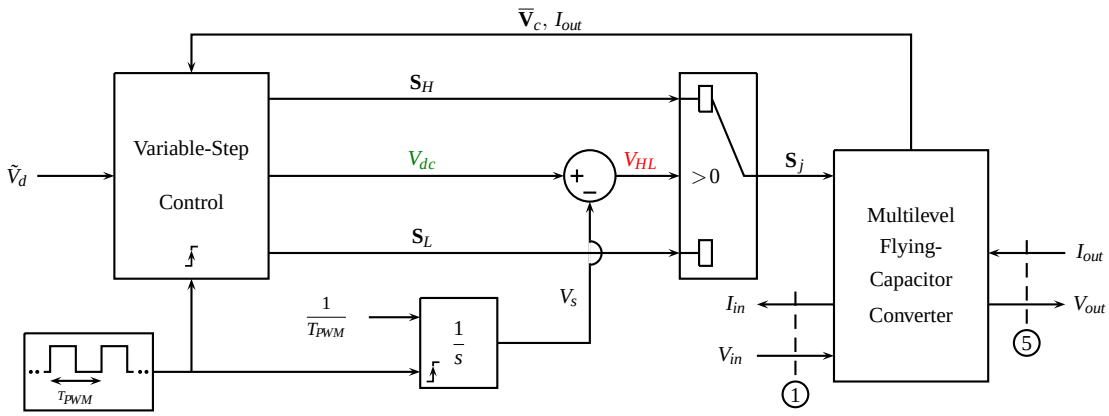

Figure 1: Variable-Step Control of the Multilevel Flying-Capacitor Converter.

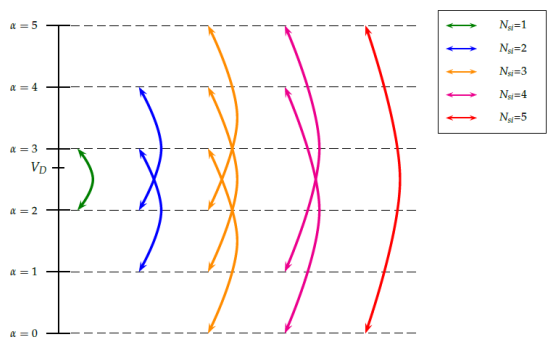

Figure 2: Variable level-to-level distance concept.

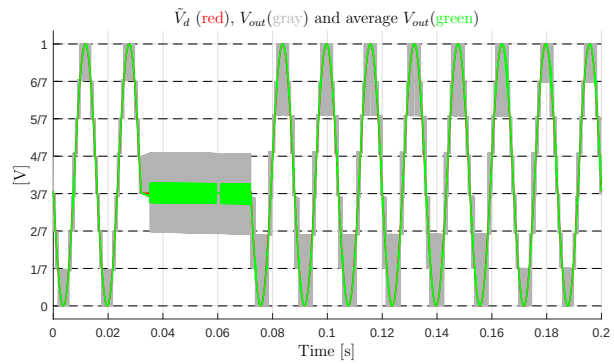

Figure 3: Results of the simulation case study.

required output voltage is effectively prevented by extending the level-to-level distance to two, while the normal converter operation is eventually reestablished.

5. Conclusions

The ability to dynamically change the level-to-level distance in the proposed variable-step control algorithm for multilevel flying-capacitor converters represents a powerful feature allowing to effectively prevent capacitors voltage trajectories divergence. This is thanks to an effective use of the available redundancy, and ensures the correct converter operation even under particularly unfavorable operating conditions, such as a constant required output voltage or a sudden load current change for example.

References

[1] H. Tian and Y. W. Li, “Carrier-Based Stair Edge PWM (SEPWM) for Capacitor Balancing in Multilevel Converters With Floating Capacitors”, IEEE Trans. Ind. Appl., vol. 54, no. 4, pp. 3440-3452, Jul.-Aug. 2018.

[2] B. P. McGrath and D. G. Holmes, “Enhanced Voltage Balancing of a Flying Capacitor Multilevel Converter Using Phase Disposition (PD) Modulation”, EEE Trans. Power Electron., vol. 26, no. 7, pp. 1933-1942, Jul. 2011.

[3] D.-W. Kang, B.-K. Lee, J.-H. Jeon, T.-J. Kim and D.-S. Hyun, “A Symmetric Carrier Technique of CRPWM for Voltage Balance Method of Flying-Capacitor Multilevel Inverter”, IEEE Trans. Ind. Electron., vol. 52, no. 3, pp. 879-888, Jun. 2005.

[4] X. Kou, K. A. Corzine and Y. L. Familiant, “Full binary combination schema for floating voltage source multilevel inverters”, IEEE Trans. Power Electron., vol. 17, no. 6, pp. 891-897, Nov. 2002.

[5] J. Huang and K. A. Corzine, “Extended operation of flying capacitor multilevel inverters”, IEEE Trans. Power Electron., vol. 21, no. 1, pp. 140-147, Jan. 2006.

[6] R. Zanasi, D. Tebaldi, Modeling Control and Robustness Assessment of Multilevel Flying-Capacitor Converters, Energies, 2021, 14(7), 1903.

Job Shop Sequencing in Manufacturing Plants by Timed Coloured Petri Nets and Particle Swarm Optimization

Gaetano Volpe * **Agostino Marcello Mangini** *
Maria Pia Fanti *

* *Polytechnic of Bari, Department of Electrical and Information Engineering, Via Orabona 4, 70126 Bari Italy (e-mail: gaetano.volpe@poliba.it, agostinomarcello.mangini@poliba.it, mariapia.fanti@poliba.it).*

1. INTRODUCTION

The increasing demand of diversified products in the market poses major challenges to producers. On the one hand, in order to be competitive, each company is required to offer the widest possible product range. On the other hand, that has to be achieved with as few machines as possible to optimize spaces and costs. However, the optimization of job scheduling in such field, that is known in literature as Flexible Job Shop Scheduling Problem (FJSSP), is one of the most difficult combinatorial optimization problems (Zhao et al., 2015) and it is NP-hard in general (Garey et al., 1976). Some of the typical objectives of that problem are the throughput maximization and the consequent minimization of job and machine waiting time. This paper considers manufacturing systems for the mass production of different types of jobs through a sequence of operations performed by a set of flexible working machines. Moreover, each machine can perform simultaneously multiple operations on different job types. The problem is determining the optimal sequence of job types and the number of jobs for each job type to be processed, in order to maximize the throughput of the system.

2. TCPN MODEL OF A MANUFACTURING PLANT

In this section, we describe the TCPN model of a production system consisting of CNC machines connected in a production line and capable of working, at the same time, a finite number of jobs. The jobs are of different types characterized by different raw material and by the required different processing tools.

Let us consider a set of N CNC machines $M = \{M_1, M_2, M_n, \ldots, M_N\}$, connected in a line production system. Let us also consider a set of features $F = \{f_1, f_2, f_i, \ldots, f_{|F|}\}$, where each feature f_i can represent a raw material or a tool in the CNC machine devoted to a particular operation. Note that symbol $|A|$ denotes the cardinality of the generic set A. Figure 1 shows an example of the TCPN model of a system composed by $N = 3$ CNC machines. Each CNC machine n is modeled by a TCPN with three places $p_{n,i}$ with $i = 1, 2, 3$ and two transitions. More precisely, place $p_{n,1}$ is the jobs input buffer where jobs wait to be processed, $p_{n,2}$ is the storage area that provides a limited set of processing tools, $p_{n,3}$ is the working cell in which jobs are processed. Each machine is modeled also by two transitions $t_{n,i}$ with $i = 1, 2$: $t_{n,1}$ denotes the beginning of the operation of the job in the CNC machine n and $t_{n,2}$ denotes the end of the operation and the entering in the subsequent machine. In addition, t_{start} is a source transition that feeds the system with a new job by firing at predetermined time intervals and p_{end} is the place collecting the completed jobs.

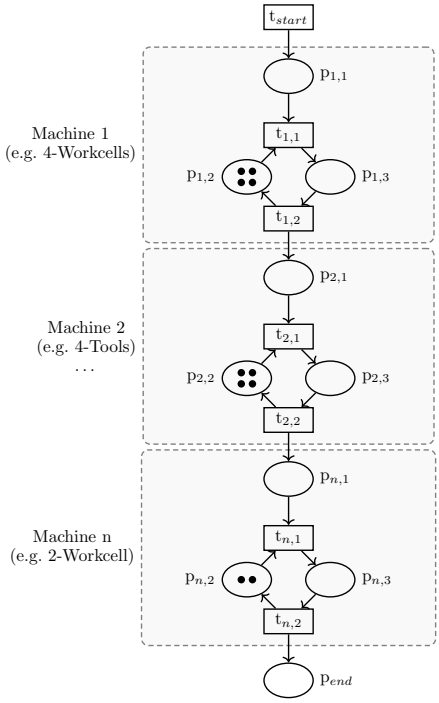

Fig. 1. Model of a line production system with 3 CNC machines

3. JOB SEQUENCING BY PARTICLE SWARM OPTIMIZATION

In this section, we define the job sequencing problem and we propose the optimization approach based on the PSO applied to the CTPN simulation. We assume that in the considered manufacturing system, the daily production is continuous and consists of a predetermined repeated sequence of job types. The objective of the optimization

problem is to find the sequence of the job types and the number of the jobs pertaining to each job type that have to enter the system to maximize the output throughput TH. Denoting by Ω the set of the possible permutations of the elements in J, we define the following decision variables:

- $\omega_h \in \Omega$ is a permutation of the elements of J that indicates the sequence in which the job types enter the production system;
- δ_i is the number of jobs of type $J_i \in J$ for $i = 1, ..., m$ in the sequence ω_h.

We assume that for each $i = 1, ..., m$, the number of jobs δ_i is in an interval $[\delta_{mini}, \delta_{maxi}]$ with $\delta_{mini} > 0$.

The problem is formulated as follows:

$$TH_{MAX} = \max_{X} TH(X) \tag{1}$$

with $X = \{\omega_h, \delta_1, \ldots, \delta_i, \ldots, \delta_m\}$, $\omega_h \in \Omega$ and $0 < \delta_{mini} \leq \delta_i \leq \delta_{maxi}$.

In the considered application context, we implement a PSO technique because the search space has a straightforward representation using PSO particles, thus avoiding complex encoding and decoding operations. Moreover, the evaluation of the objective function requires a limited number of simulations that are typically time consuming.

4. CASE STUDY

We consider as a case study an ophthalmic lenses mass production system in a firm consisting of three CNC machines: the first one is a lens-blocker with four work-cells and can process up to four jobs at the same time, regardless of the raw material. The second one is a lens-generator characterized by four different finishing tools and can process up to to four jobs simultaneously, supposed that that each job requires a different tool. The third machine is a lens polisher having two work-cells that concludes the lens generation process and can process up to two jobs at a time. We implement the TCPN simulation and the PSO optimization in a Matlab environment.

As shown in Figure 3, we achieve the best result by simulation 16, in which the optimization process starts from 227 jph and converges to 407 jph when we feed the system cyclically with the computed sequence. Similar results are obtained by simulations 35, 21 and 96. However, the worst result is achieved in simulation 51 that converges to 356 jph. The optmized job sequences for all considered simulations are depicted in Figure 2. In order to show the efficiency of the proposed method, we simulate the TCPN arranging the job types according to two well-known techniques: SPT (Shortest Processing Time) and LPT (Longest Processing Time) (Blackstone et al., 1982). Figure 4 shows that by using the best solution of the proposed method the firm is able to increase the throughput of about 23% (i.e., 77 jobs) per hour with respect to the LPT and SPT techniques.

5. CONCLUSION

This paper proposes a meta-heuristic approach based on Timed Coloured Petri Nets (TCPN) and Particle Swarm Optimization (PSO) to maximize the throughput of jobs in a production system by computing the optimal sequence

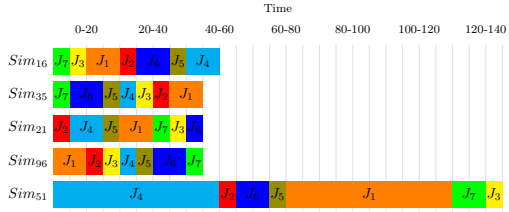

Fig. 2. Optimized Jobs Sequences to cyclically feed the system through t_{start}

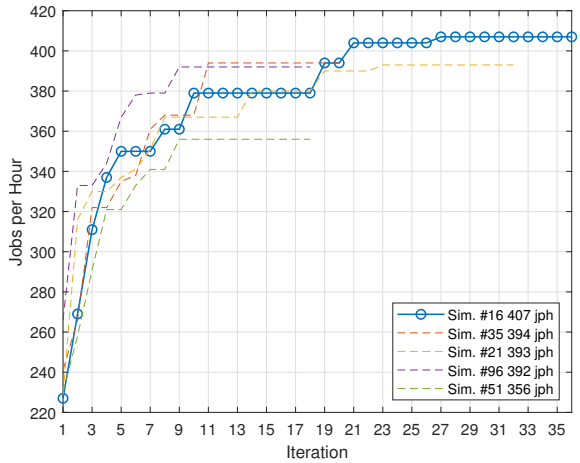

Fig. 3. Throughput obtained at each PSO iteration optimization

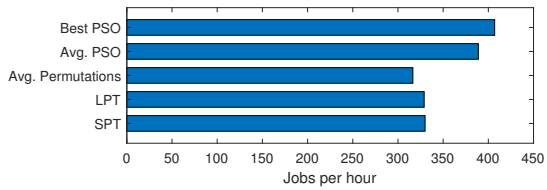

Fig. 4. Throughput comparison between PSO and other methods

of job types and the amount of units of each type. The computed sequence represents the order by which the jobs enter the system in a cyclical way. This work has been accepted for presentation at WODES 2022, 16th IFAC Workshop on Discrete Event Systems, that will be held in Prague, Czechia, September 7-9, 2022. Future developments concern an extended generalization of the modeling approach to include more complex job routing and larger number of CNC machines to optimize the job sequences.

REFERENCES

Blackstone, J.H., Phillips, D.T., and Hogg, G.L. (1982). A state-of-the-art survey of dispatching rules for manufacturing job shop operations. *International Journal of Production Research*, 20(1), 27–45.

Garey, M.R., Johnson, D.S., and Sethi, R. (1976). The complexity of flowshop and jobshop scheduling. *Mathematics of operations research*, 1(2), 117–129.

Zhao, F., Zhang, J., Zhang, C., and Wang, J. (2015). An improved shuffled complex evolution algorithm with sequence mapping mechanism for job shop scheduling problems. *Expert Systems with Applications*, 42(8), 3953–3966.

A Multi-Agent Trust and Reputation Mechanisms for the Management of Smart Urban Lighting Systems

Alessandro Casavola, Giuseppe Franzè, Gianfranco Gagliardi, Francesco Tedesco

DIMES, Università della Calabria, Via Pietro Bucci, Cubo 42-C, Rende (CS), 87036, ITALY ({alessandro.casavola, giuseppe.franze, francesco.tedesco}@unical.it, g.gagliardi@dimes.unical.it)

In this paper, an adaptive urban smart lighting architecture allowing municipalities to manage and control public street lighting lamps is developed. In order to reduce energy consumption, the system is designed to autonomously adapt street lamps' brightness on the basis of the presence of vehicles in specific segments of the streets/roads of interest. To this end, a hybrid traffic model is here proposed to estimate in each segment of the road the number of vehicles crossing the segment. The estimation task is carried out by means of a bank of switching observers and corresponding sensors. One observer at a time is selected from the bank and put in order. Such a selection is based on a recently developed multi-agent reputation mechanism for a class of networked systems. As one of its merits, this methodology is capable to reveal those sensors that have the highest information contents (Quality of Service) on the basis of their reputation (trust) shared among agents.

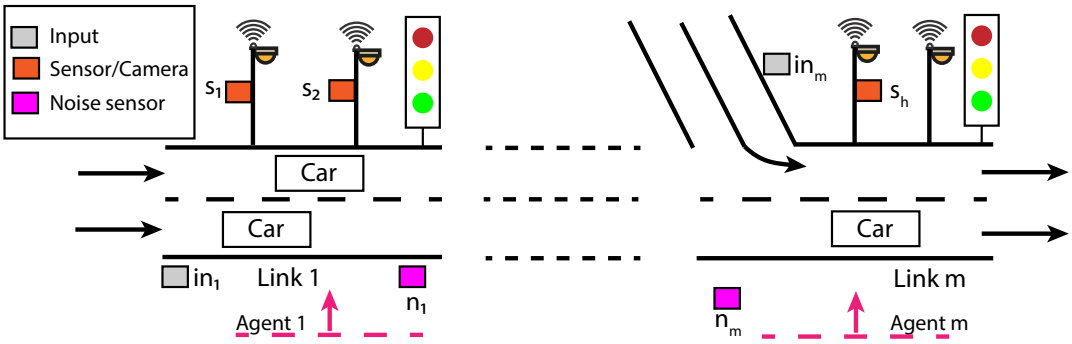

Figure 1: Road schematic: each link j of the road is endowed with a sensor group $\mathcal{S}_j$ and is associated to one agent a_j

With reference to Figure 1 and by taking inspiration from the field of hydrodynamical applications [Homolova(2005)] the traffic dynamics of the j-th link can be described by exploiting the basic idea that in any link, the number of vehicles there lying both depends on such a quantity estimated at the previous time instant and on the algebraic sum of entering and outgoing cars. In order to maximize the energy saving, each link j of the road is associated to one *agent* a_j (control entity) that is instructed to establish the optimal lighting profile $I_j(Y_{r_j}(t))$, $j = 1, \ldots, N$, on the basis of the traffic volume $Y_{r_j}(t)$. This latter is computed on the basis of traffic queue length ($\xi_j(t)$) and the number of incoming cars ($in_j(t)$) on j-th link. Unfortunately, ξ_j is not directly available. Therefore, it has to be estimated by using the information θ_{jk} provided by a camera s_k to the agent a_j. Because θ_{jk} can be subject to Quality of Service (QoS) issues it is required to choose a performance criterion capable to give a measure of the effectiveness of the estimation process with respect to the agent task. According to this, it is assumed that auxiliary measurements, obtained by acoustic sensors (n_j) *ad-hoc* placed along the road, are available to each agent a_j. These sensors are assumed no subject to QoS issues and in normal conditions the amplitude $\phi_j(t)$ of the signal conveyed by the sensor n_j is proportional to $I_j(\xi_j)$. The quantity $\phi_j(t)$ can be used to set a reference light profile $I_\phi(\phi_j(t)) = I_j(Y_\phi(\phi_j(t)))$ and to indirectly assess the quality of the estimate $\hat{\xi}_j$. Hence, by denoting with $\hat{Y}_j(t)$ traffic volume estimate at agent side, the idea is at comparing the chosen light profile $I_j(\hat{Y}_j)$ to the approximate one $I_\phi(\phi_j(t))$ by enforcing, during

real-time operations, the constraint $\Gamma_{\min} \leq |I_j(\hat{Y}_j(t)) - I_\phi(\phi_j(t))| \leq \Gamma_{\max}$, $j = 1, \ldots, N,$, that can be satisfied by minimizing a properly defined performance index $J_j(t) : \mathbb{R} \to \mathbb{R}^+, j = 1, \ldots, N$, [Casavola(2022)]. Then, based on the above discussion, the main goal is to design a trust based estimation selection architecture exploiting switching observers to compute the state estimates ($\hat{x}_j(t)$, $j = 1, \ldots, N,$), a distributed reputation mechanism and a sensor selection logic in charge to determine the most trustworthy sensors.

In order to demonstrate the effectiveness of the proposed architecture a scenario consisting of five road links , seven identical groups of cameras and five agents has been accounted. The proposed test considers a simulation period of approximately 3,5 hours (12.800s) and corrupted sensor camera information. Figure 2 report the results related to the road link 2: notice that the adopted architecture is always capable to identify the sensor group providing the *best* state estimate of each agent. The performance of the smart lighting architecture, designed according to the

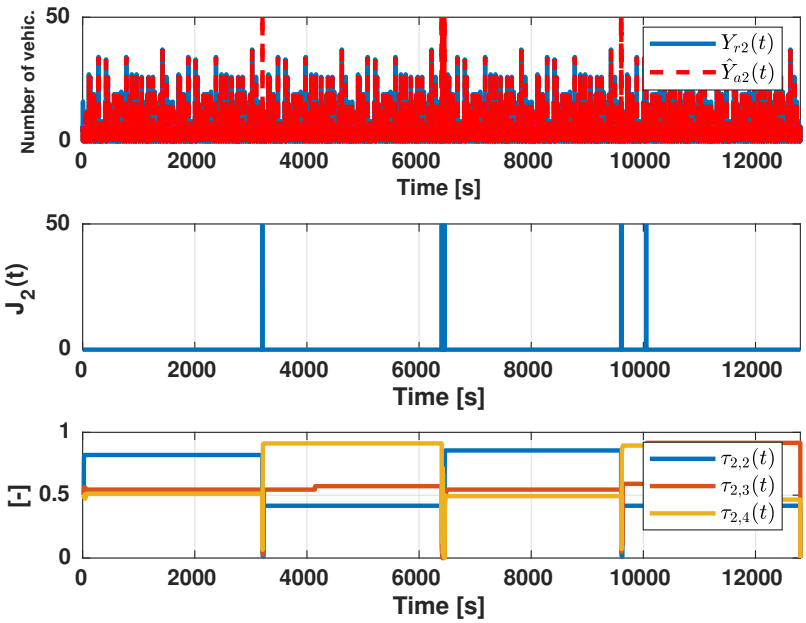

Figure 2: link 2: system state and its estimate computed at agent side (top), performance index (middle) and trust realizations trend (down).

infrastructure presented in [Gagliardi(2020)], are evaluated in terms of energy consumption and savings with respect to a standard lighting system (namely High-Pressure Sodium lamp-based system) and standard LED configuration. As expected, the smart lighting system allows one to save a huge amount of energy: 78,31 [%] w.r.t. a standard lighting system equipped with 100 [W] HPS lamps and 56,62 [%] w.r.t. a LED lighting system equipped with 50 [W] LED lamps.

References

[Homolova(2005)] Homolova J. and Nagy I., "Traffic model of a microregion", *16th Triennal IFAC World Congress,* , Prague, Czech Republic, 4-8 July 2005.

[Casavola(2022)] A. Casavola, G. Franzè, G. Gagliardi and F. Tedesco, "Improving Lighting Efficiency for Traffic Road Networks: A Reputation Mechanism Based Approach," in *IEEE Transactions on Control of Network Systems*, 2022, doi: 10.1109/TCNS.2022.3182026.

[Gagliardi(2020)] Gagliardi G., Lupia M., Cario G., Cicchello Gaccio F., Lo Scudo F., Tedesco F. and Casavola A., "Advanced Adaptive Street Lighting Systems for Smart Cities", *Smart Cities*, Special Issue on "Feature Papers for Smart Cities", Vol. 3, N. 4, pp. 1495-1512, 2020.

Vision-Based Modal Analysis of the Built Environment with Multiple Drones

Michele Bolognini, Giovanni Izzo,Daniele Marchisotti, Lorenzo Fagiano, Maria Pina Limongelli, Emanuele Zappa

***Abstract*—Unmanned Aerial Vehicles are employed for vision-based modal analysis of civil infrastructure, as they overcome the range limitations of fixed cameras and can measure the oscillations of a structure up close. Nevertheless they are often piloted manually and one at a time, though a single drone is usually unable to capture the motion of a whole structure with high spacial resolution. An approach is presented that employs multiple drones simultaneously to estimate natural frequencies and modal shapes of a structure, by synchronizing the footage they record. The ability of the method to detect modal parameter variations is assessed, such that it can identify anomalies in the structure, when paired with a damage detection procedure.**

I. Introduction

Unmanned Aerial Vehicles (UAVs) are increasingly being adopted as tools in many sectors, such as agriculture [1], military [2], natural asset management [3] and construction [4]. Besides the recent decreasing trend of their cost, their ease of use makes previously cumbersome tasks much simpler. In fact, they can reach remote places and hold a diverse array of payloads, hosting for example RGB and thermal cameras for visual inspections, LiDARs and depth cameras for mapping and 3D scanning, or gas sensing systems [5]. Thanks to these features, the use of UAVs in public infrastructure monitoring is promising. As a consequence, any tool that could help lower at least some of the costs is worth investigating.

In the state of the art, we note the absence of drone-enabled vision-based vibration modal analysis techniques that can capture the response of an entire structure at once with high spacial accuracy. By using multiple drones it is possible to perform measurements of the whole structure at the same time, thus also overcoming time limit of battery charge and the need to maintain a continuous external forcing input for a prolonged time. We propose a novel system to perform video-based modal analysis through multiple cameras mounted on collaborative drones, that measure natural frequencies and estimate modal shapes. Our approach exploits the idea of overlapping the target areas measured by two different cameras to perform *a posteriori* signal synchronization. The problem at hand is to obtain modal parameters of a structure, namely natural frequencies ω_i and modal shapes $\mathbf{\Phi}_i$, where $i = 1, ..., n$ is an index that identifies the different modes, up to the n-th. This is to be done through vision only, syncrhonizing multiple footage sources

II. Proposed Method

The structure is excited with a kinetic hammer and its oscillation is recorded with drone-mounted cameras. In order to track the displacement of an object, *i.e.* the movement of the targets across pixels in consecutive frames, we first apply the Harris corner detection algorithm [6] to find features

Fig. 1. The structure used for vibration tests. Spot markers are present alongside ArUco ones, but they were not exploited in these procedures.

within the gray-scale version of the first frame. Some of those features are manually selected for tracking. Tracking is then performed through the Kanade-Lucas-Tomasi (KLT) algorithm [6], which formulates an optimization problem to estimate the displacement d of single pixels in consecutive pictures as optical flow.

We apply a Fast Fourier Transform (FFT) to obtain the spectrum of frequency components of the signal. In commercially available drones, ours included, cameras are mounted on active gimbals, capable of compensating some of these disturbances, and the contribution of the rotating blades is outside the range considered here. We verify experimentally that the noise does not contain high frequency components that could corrupt the signal. Therefore, we can apply a high-pass filter to separate the natural frequencies of the structure from the frequency components introduced by the motion of the camera. In order to obtain the modal shapes, we take the signals two at a time and estimate the transfer function between them. Evaluating the phase of such transfer function at the natural frequencies yields the phase delay between each feature pair:

$$\Delta\phi_{i,a-b} = \arg\left(G_{a-b}(j\omega_i)\right), \tag{1}$$

where j is the imaginary unit, $G_{a-b}(j\omega_i)$ is the value of the continuous-time transfer function between the signals describing the displacement of features a and b, evaluated at point $j\omega_i$. To calculate pair-wise phase delays between features appearing in different video sources, we first synchronize them through cross-correlation of the high-pass filtered displacement measurements of a feature or marker appearing in both videos, in the overlapping region. We then estimate the transfer function between signals extracted from the two different but synchronized recordings.

III. Experimental Results and Conclusion

A test was carried out where two UAVs were used to record the displacement. The structure was excited with a rubber hammer and the drones were hovering in front of it at a 1 m distance. After calculating and correcting the delay between the two videos, through oversampling and cross-correlation of the displacement of the overlapping marker, the pairwise relative phase delays between markers can be computed. Synchronized displacements were treated as if they were recorded by the same camera, and yielded the results shown in Table I. The error is calculated as the absolute value of the difference with respect to the phase delays estimated with a single camera. Phase delays between non-consecutive markers can be computed as

$$\Delta\phi_{i,a-c} = \Delta\phi_{i,a-b} + \Delta\phi_{i,b-c}, \tag{2}$$

and they are comparable to the ones obtained both with a single flying camera and with the accelerometers.

In order to ascertain the ability of this procedure to detect variations in modal parameters, a second series of tests was carried out after gradually adding masses to the protruding end of the cantilever. Another one was conducted after removing the additional masses and loosening one of the clamps that held together the structure. Results were compared to the base case to find out if the measured modal parameters differ significantly, and they are collected in Table II. Figure 2 shows the effect of gradually adding mass to the structure. As expected, the natural frequencies decrease, since they are, in general, proportional to the square root of the ratio between the modal stiffness and mass. Nevertheless, they maintain the same ratio. No significant differences emerge in the modal shape analysis. The effect of a tampered clamp, on the other hand, is noticeably different: Here the natural frequencies are still impacted, as the second one drops to 8.19 Hz, while the first does not, thus the ratio is not maintained. This decrease in frequency is likely due to an overall reduction of the stiffness of the structure. The modal shape is still the same, though some phase delays increase with respect to the base scenario, indicating that bending of the cantilever beam is probably starting to happen due to the loosened clamp, with a modal shape that is not symmetric. We also note that all measurements performed with cameras are compatible with the same measurements taken with accelerometers.

A. Conclusion

We described and tested a method to conduct vision-based modal analysis through the use of measurements acquired simultaneously by multiple airborne cameras. We measured the natural frequencies and calculated the modes of vibration of a metal structure and showed that accurate displacement measurements can be carried out based on features occurring on the surface of the target structure, without markers. Despite the limited bandwidth due to rather low FPS cameras, we deem this solution feasible and convenient when accelerometers are not already present and their installation is difficult, including real-world cases like modal analysis of flexible structure (metallic and slender buildings, pedestrian bridges, ...) and vision-based estimation of tension force in cables, such as those in stadiums, cable-ways, power transmission systems and cable-stayed bridges.

ω_i	$\Delta\phi_{i,1-2}$ (err.)	$\Delta\phi_{i,1-3}$ (err.)	$\Delta\phi_{i,1-4}$ (err.)
5.05 Hz	−1.17° (0.07°)	−1.87° (2.48°)	−2.73° (2.49°)
11.17 Hz	−3.02° (3.77°)	−2.21° (1.99°)	−2.23° (2.79°)

TABLE I. Phase delays estimated with two drone-mounted cameras and synchronization

Mode	ω_i	$\Delta\phi_{i,1-2}$	$\Delta\phi_{i,2-3}$	$\Delta\phi_{i,3-4}$
$i = 1$	4.96 Hz	3.51°	0.50°	−2.75°
$i = 2$	8.19 Hz	4.32°	0.81°	−4.95°

TABLE II. Estimated phase delays after tampering

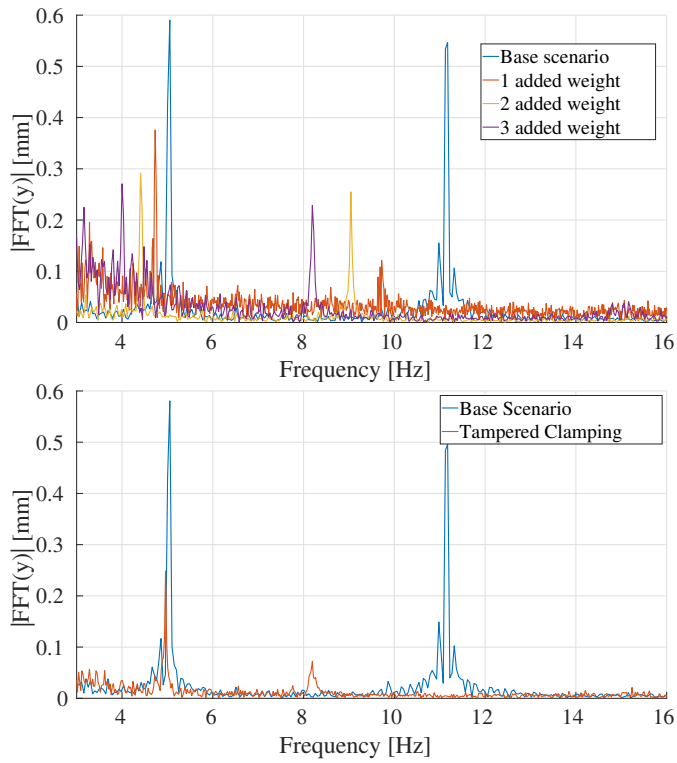

Fig. 2. Effect of increasing mass (top) and of loosening a clamp (bottom) on natural frequencies.

References

[1] M. Kulbacki, J. Segen, W. Knieć, R. Klempous, K. Kluwak, J. Nikodem, J. Kulbacka, and A. Serester, "Survey of drones for agriculture automation from planting to harvest," in *2018 IEEE 22nd International Conference on Intelligent Engineering Systems (INES)*. IEEE, 2018, pp. 000 353–000 358.

[2] S. K. Chaturvedi, R. Sekhar, S. Banerjee, and H. Kamal, "Comparative review study of military and civilian unmanned aerial vehicles (uavs)," *Bulletin of the National Institute for Aerospace Research" Elie Carafoli"*, vol. 11, no. 3, pp. 183–198, 2019.

[3] M. J. Sousa, A. Moutinho, and M. Almeida, "Thermal infrared sensing for near real-time data-driven fire detection and monitoring systems," *Sensors*, vol. 20, no. 23, p. 6803, 2020.

[4] R. Ali, D. Kang, G. Suh, and Y.-J. Cha, "Real-time multiple damage mapping using autonomous uav and deep faster region-based neural networks for gps-denied structures," *Automation in Construction*, vol. 130, p. 103831, 2021.

[5] M. Rossi, D. Brunelli, A. Adami, L. Lorenzelli, F. Menna, and F. Remondino, "Gas-drone: Portable gas sensing system on uavs for gas leakage localization," in *SENSORS, 2014 IEEE*. IEEE, 2014, pp. 1431–1434.

[6] C. Tomasi and T. Kanade, "Detection and tracking of point," *International Journal of Computer Vision*, vol. 9, pp. 137–154, 1991.

Distributed robust control in a quadruple tank system

Alessandro Bozzi, Simone Graffione, Roberto Sacile, Simona Sacone, Enrico Zero

I. Introduction

The goal of this work is to propose a distributed robust control approach to react to unpredictable disturbances in a System of Systems (SoS). The case study is referred to four water tanks, defined as a quadruple-tank plant (QTP), connected by several tubes which manage the water flows among the tanks according to the activation of electrical pumps in order to maintain a predefined optimal level of liquid. This problem has been proposed in [1] where the authors defined the input flows in order to control the liquid tank levels by varying the valves setting. This case study also represented a control benchmark in [2] where the authors proposed a multivariable internal model control for feedback control of the tank levels in the lower two tanks of the system by manipulating pump speed. The proposed approach for the nonlinear QTP control problem is based on a distributed robust control strategy. The main objective of the control law is to react to disturbances either caused by model imperfection or by external input in an optimal way, by a set of distributed agents with a partial observation of the state.

II. System definition

Let a system *G* be composed by a set of *N* interconnected subsystems G_i, $i = 1, 2, .., N$. Let each subsystem G_i be characterized at instant *k*, $k = 0, 1, .., T-1$ by a state variable $x_{i,k}$. Each state variable is defined as a variation with respect to a given desired working state $\hat{x}_i$. The subsystem interconnection is supposed to be modeled by linear interactions defined by parameters $a_{i,j} \in \mathbb{R}^+$ where $a_{i,j}$ represents the magnitude of $x_{j,k}$ to affect the working state $x_{i,k}$, at each instant *k*.
We introduce the problem to control the system *S* in a distributed way, considering that each subsystem is subject to a stochastic disturbance. A set of *M*, $M \leq N$ agents has the possibility to get partial information on the overall system state. The control vector $\underline{u}_k$ can affect the vector $\underline{x}_{k+1}$, which in turn is also conditioned by a disturbance $\underline{\omega}_k$. The overall goal is to minimize the maximum quadratic deviation of the control from zero, and of the states $x_{i,k}$ from the desired working value weighted by a parameter related to the importance of the subsystem in the overall system of systems architecture. This deviation is normalized by the magnitude of the disturbance defined by the square Euclidean norm of the disturbance.
More formally, we introduce the following SoS distributed robust control problem (SoS-DRCP).

All the authors are from the Department of Informatics, Bio-engineering, Robotics and Systems Engineering (DIBRIS), University of Genoa.

Let a system *G* be defined by the following linear dynamics:

$$\underline{x}_{k+1} = A\underline{x}_k + B\underline{u}_k + \underline{\omega}_k \tag{1}$$

where:

- $\underline{x}_k \in \mathbb{R}^N$ is the system state vector at instant $k = 0, 1, .., T$
- $\underline{u}_k \in \mathbb{R}^M$ is the control state vector in time interval $[k, k+1)$, $k = 0, 1, .., T-1$
- $\underline{\omega}_k \in \mathbb{R}^N$ is a generic noise affecting each subsystem in time interval $[k, k+1)$, $k = 0, 1, .., T-1$
- $A \in \mathbb{R}^{N\text{x}N}$ is the matrix modeling the linear interdependencies between subsystems
- $B \in \mathbb{R}^{N\text{x}M}$ is the matrix related to the available control on the different subsystems.

Let the *j*-th agent, $j = 1, 2, .., M$ have the capability to get partial information on the overall system state $\underline{x}_k$. Specifically, let $\underline{y}_{j,k} \in \mathbb{R}^{N_j}$ the measure of the state $\underline{x}_k$ which can be taken at instant *k* by the *j*-th agent:

$$\underline{y}_{j,k} = C_j \underline{x}_k \tag{2}$$

In general, a subset of the whole state is available, i.e. $N_j \leq N$, where $C_j \in \mathbb{R}^{N_j, N}$. The SoS-DRCP aims to find the function $\mu_{j,k}$ related to the closed loop control problem computing:

$$u_{j,k} = \mu_{j,k}(y_{j,k}) \quad j = 1, 2, ..., M \qquad k = 0, 1, .., T-1 \tag{3}$$

allowing to optimize the following cost function:

$$\inf_{\underline{\mu}_k} \sup_{0 \neq \underline{\omega}_k} J(\underline{x}_k, \underline{u}_k) \tag{4}$$

The function $J(\underline{x}_k, \underline{u}_k)$ is a function defined by:

$$J(\underline{x}_k, \underline{u}_k) = \frac{\sum_{k=0}^{T-1} \begin{pmatrix} x_k \\ u_k \end{pmatrix}' \begin{pmatrix} Q_{xx} & Q_{xu} \\ Q_{ux} & Q_{uu} \end{pmatrix} \begin{pmatrix} x_k \\ u_k \end{pmatrix}}{\sum_{k=0}^{T-1} ||\underline{\omega}_{k-1}||^2} \tag{5}$$

where $\underline{\omega}_{-1} = \underline{x}_0$ and and $Q_{uu} > 0$. The following Theorem allows the computation of the optimal control law that is demonstrated to be linear.

Theorem 1. *Consider the SoS-DRCP defined by (1) - (5) for T=1. The following statements are true:*

- $\mu_{j,1}(\cdot)$ *is linear, and* $\mu_{j,1}(y_{j,1}) = L_j y_{j,1}$, $L_j \in \mathbb{R}^{M\text{x}N_j}$ $j = 1, ..., M$
- *Defining* $C = [C'_M, C'_{M-1}, \ldots, C'_1]'$, $C \in \mathbb{R}^{MN_j\text{x}N}$ *and* $L = diag(L_M, \ldots, L_1)$, $L \in \mathbb{R}^{M^2\text{x}\sum_{j=1}^{M} N_j}$ *computed solving the follow inequality*

$$\min_{\gamma, L} \gamma$$

s.t.

$$\begin{pmatrix} Q_{xx} - \gamma I + Q_{xu}LC + C'L'Q_{ux} & C'L' \\ LC & -Q_{uu}^{-1} \end{pmatrix} \leq 0 \quad (6)$$

Proof. The problem becomes a static minmax team problem and the proof is based on Theorems 1 and 2 in [3]. It can be generalized to T > 1 considering the linearity of the system. □

III. Case Study

In our case study, we consider a QTP system partially filled by water, where all the tanks are identical cylinders characterized by:

- a cross-sectional area S,
- outlet pipelines with section area s allowing water to flow out by the tanks

Specifically, the four tanks are positioned in couples, one couple above the other as shown in Fig.1. Each couple at the same level is linked by a communicating pipeline, so that each couple form communicating vases. The state variables are the levels of water in each tank $x_i(t)$ $i = 1..4$. Three control variables $u_j(t)$ $j = 1..3$ are controlled by three pumps allowing water to be pumped in both directions. Specifically, $u_1(t)$ and $u_2(t)$ can pump water respectively to/from tank 1 and tank 3 with a pipeline connected to an additional tank, external to the system, which is supposed always to have water available. The control $u_3(t)$ can pump water to/from tank 2 from/to tank 4. As a convention, positive flows for the controls $u_j(t)$ $j = 1..3$ are respectively in direction of tank 1, 4, and 2. The system G can be subject to external disturbance represented by $w_i(t)$ $i = 1..4$.

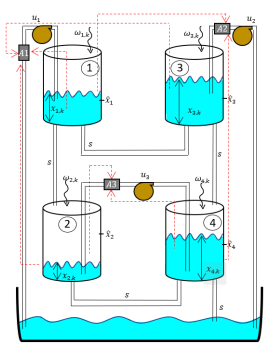

Fig. 1. The QTP model used in this work. A1, A2, and A3 are the three agents respectively controlling u_1,u_2,u_3.

The tank state equations are shown below

$$\frac{dx_1(t)}{dt} = -sign(x_1(t) - x_3(t))(\frac{s_c\sqrt{2g}}{S}\sqrt{|x_1(t) - x_3(t)|}) + \\ -\frac{s\sqrt{2g}}{S}\sqrt{x_1(t)} + u_1(t) + \omega_1(t) \quad (7)$$

$$\frac{dx_2(t)}{dt} = -sign(x_2(t) - x_4(t))\frac{s_c\sqrt{2g}}{S}\sqrt{|x_2(t) - x_4(t)|} + \\ +\frac{s\sqrt{2g}}{S}\sqrt{x_1(t)} - u_3(t) + \omega_2(t) \quad (8)$$

$$\frac{dx_3(t)}{dt} = +sign(x_1(t) - x_3(t))\frac{s_c\sqrt{2g}}{S}\sqrt{|x_1(t) - x_3(t)|} + \\ -\frac{s\sqrt{2g}}{S}\sqrt{x_3(t)} + u_2(t) + \omega_3(t) \quad (9)$$

$$\frac{dx_4(t)}{dt} = +sign(x_2(t) - x_4(t))\frac{s_c\sqrt{2g}}{S}\sqrt{|x_2(t) - x_4(t)|} + \\ +\frac{s\sqrt{2g}}{S}\sqrt{x_3(t)} - \frac{s\sqrt{2g}}{S}\sqrt{x_4(t)} + u_3(t) + \omega_4(t) \quad (10)$$

The system is nonlinear, with stochastic components and can be linearised around an equilibrium ($\underline{\hat{x}}$,$\underline{\hat{u}}$) as:

$$\frac{d\Delta\underline{x}(t)}{dt} = A\Delta\underline{x}(t) + B\Delta\underline{u}(t) \quad (11)$$

where $\Delta\underline{x}(t) = \underline{x}(t) - \underline{\hat{x}}$ and $\Delta\underline{u}(t) = \underline{u}(t) - \underline{\hat{u}}$. Matrixes A and B can be easily computed by the Jacobian. In our case study, we consider a linearisation where $\hat{x}_1 > \hat{x}_3$ and $\hat{x}_2 > \hat{x}_4$. The goal of the system is to control the levels according to the cost function defined in (4) in a distributed way by three agents associated to related pumps with the partial observation of the whole system.

IV. Results

The results will be shown during the conference. As a qualitative result, Fig. 2 shows the performance defined by (4) on time interval of 1 second over 1 hour of simulation subject to different disturbance. One important characteristic of this approach is that the maximum value of the cost function (4) can be a priori computed so defining the worst performance of the system. In addition upper outliers can represent undesired emergent behaviours of this SoS.

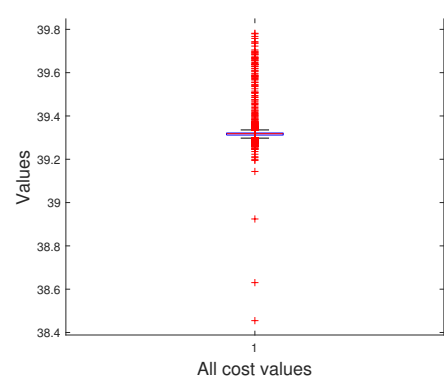

Fig. 2. Boxplot of the cost function values over 1 hour of simulation. The number of upper outliers is 156. It represents 4.3% of all values.

References

[1] K. Johansson, "The quadruple-tank process: a multivariable laboratory process with an adjustable zero," *IEEE Transactions on Control Systems Technology*, vol. 8, no. 3, pp. 456–465, 2000.

[2] E. P. Gatzke, E. S. Meadows, C. Wang, and F. J. Doyle Iii, "Model based control of a four-tank system," *Computers & Chemical Engineering*, vol. 24, no. 2-7, pp. 1503–1509, 2000.

[3] A. Gattami, B. M. Bernhardsson, and A. Rantzer, "Robust team decision theory," *IEEE Transactions on Automatic Control*, vol. 57, no. 3, pp. 794–798, 2012.

On the stability of a sampled-data Image-Based Visual Servoing Control Scheme

Marco Costanzo, Ciro Natale, and Antonio Russo

1 Introduction

With reference to Image-Based Visual Servoing (IBVS), due to the limited camera frame rate, actuation delays and the time needed for computations, the sampling time of the visual control system is not negligible and its intrinsic sampled-data nature should be taken into account to pursue the objective of improving the visual servoing quality and the overall robotic system performance, while ensuring stability. The sampled-data designs appeared in the literature so far are based on the approximation of the feature dynamic model derived via the forward Euler method. However, the obtained discrete-time model does not retain the rigid motion constraint, which is the base of the continuous time model. Furthermore, the discrete-time IBVS model obtained via the forward Euler method approximates the continuous-time model with a relatively good degree of accuracy only in a neighbourhood of the desired equilibrium point. This, in turn, implies that any stability analysis based on such a discrete-time model can be performed only locally.

In this presentation, we firstly propose an exact nonlinear sampled-data model of the feature dynamics by suitably exploiting the properties of the interaction matrix. Then, we inspect the stability properties of the error dynamics equilibrium points. Extending the results presented in [1], we prove that, for a suitable choice of the sampling time and control parameters, the sampled-data IBVS closed-loop system exhibits a desired equilibrium point being *almost globally asymptotically stable* [2], implying that the only trajectories not converging to it are those starting from zero Lebesgue measure sets. Furthermore, a novel control algorithm aimed at improving the accuracy and the execution speed of the visual servoing task is proposed. The algorithm is based on the discrete-time Lyapunov analysis and it allows the designer to guarantee end-effector Cartesian velocity constraints, depending on the robot configuration and joint velocity limits. Moreover, the algorithm enforces the constraint of monotonic convergence of the feature error over time, i.e., it does not exhibit any hidden oscillations, and it guarantees a prescribed smooth approach of the camera towards the target configuration. These control objectives are achieved through adaptation of the control gain obtained as the solution of a constrained optimization problem.

The proposed IBVS control schemes are experimentally evaluated in a lab-scale emulated in-store logistic scenario, where pick&place operations for shelf replenishment are executed by a robot in collaboration with a human partner, by utilizing object handover as well as dexterous handling maneuvers [3].

The authors are with the Dipartimento di Ingegneria, Università degli Studi della Campania "Luigi Vanvitelli", 81031 Aversa (CE), Italy e-mail: {marco.costanzo, ciro.natale, antonio.russo1}@unicampania.it.

2 IBVS Model

In this section we firstly recall notations and the continuous-time dynamics of the IBVS, then the corresponding exact nonlinear sampled-data model is derived. We assume that the 3D feature vectors of the captured RGB image, indicated hereafter with $\boldsymbol{s}_i$, are composed of the 3D coordinates of the points. The IBVS approach aims at designing a closed-loop control scheme that regulates the current image feature $\boldsymbol{s} \in \mathbb{R}^{3n}$ to a given target $\boldsymbol{s}^\star \in \mathbb{R}^{3n}$ of an image acquired beforehand, i.e., the objective is to bring the error $\boldsymbol{e} = \boldsymbol{s} - \boldsymbol{s}^\star$ to zero.

Denote with $\boldsymbol{v} = \begin{bmatrix}\mathbf{v}^\top & \boldsymbol{\omega}^\top\end{bmatrix}^\top \in \mathbb{R}^6$ the body velocity screw of the camera. Then, the link between the rate of $\boldsymbol{e}(t)$ and $\boldsymbol{v}(t)$ is described by the following relationship

$$\dot{\boldsymbol{e}}(t) = \boldsymbol{L}_{\boldsymbol{e}}\boldsymbol{v}(t). \tag{1}$$

where $\boldsymbol{L}_{\boldsymbol{e}} \in \mathbb{R}^{3n\times 6}$ is the so-called *interaction matrix* [4].

By exploiting the structure of the interaction matrix and relying on the results in [5] on the dynamics of switched systems, we can derive the sampled-data feature error dynamics as

$$\boldsymbol{e}_{k+1} = \boldsymbol{e}_k + \boldsymbol{P}_k\boldsymbol{L}_{\boldsymbol{e}_k}\boldsymbol{v}_k, \tag{2}$$

where $\boldsymbol{P}_k \in \mathbb{R}^{3n\times 3n}$ is defined as

$$\boldsymbol{P}_k = \boldsymbol{P}(\boldsymbol{\omega}_k) = \int_0^T e^{-\bar{\boldsymbol{S}}(\boldsymbol{\omega}_k)\sigma}\,\mathrm{d}\sigma, \tag{3}$$

and $\bar{\boldsymbol{S}}(\boldsymbol{\omega}_k) = \boldsymbol{I}_n \otimes \boldsymbol{S}(\boldsymbol{\omega})$, being $\boldsymbol{S}(\cdot)$ the skew-symmetric operator of the vector product. Let the velocity control law in (2) be defined as

$$\boldsymbol{v}_k = -\lambda\boldsymbol{L}_{\boldsymbol{e}_k}^\dagger\boldsymbol{e}_k, \tag{4}$$

with, again, λ being either a positive constant or a positive time-varying scalar. Then, the expression of the sampled-data closed-loop feature error dynamics in (2) becomes

$$\boldsymbol{e}_{k+1} = (\boldsymbol{I}_{3n} - \lambda\boldsymbol{P}_k\boldsymbol{L}_{\boldsymbol{e}_k}\boldsymbol{L}_{\boldsymbol{e}_k}^\dagger)\boldsymbol{e}_k, \quad \boldsymbol{e}_0 = \boldsymbol{e}(0). \tag{5}$$

3 Stability Properties

We will study stability not only of the desired equilibrium $\boldsymbol{e} = \mathbf{0}$, but also of the well-known undesired equilibria $\hat{\boldsymbol{e}}$ [1]. Denote with e_{Mk} the mean square error $e_{Mk} = \|\boldsymbol{e}_k\|/\sqrt{n}$, with e_L and e_H two positive scalars such that $e_L < e_H$ and let $\mu \in (0, 1]$, let $q(\cdot)$ be a fifth-order polynomial whose coefficients are determined such that the first and second order derivatives are zero at the extremes of the interval $[0, 1]$ and $q(0) = 0$, $q(1) = 1$ and denote with $\boldsymbol{\omega}_k^1 = -\begin{bmatrix}\mathbf{0}_3 & \boldsymbol{I}_3\end{bmatrix}\boldsymbol{L}_{\boldsymbol{e}_k}^\dagger\boldsymbol{e}_k$, let define the following functions

$$\pi(\boldsymbol{e}_k, \lambda_k T) = -\lambda_k T\left(2l(\boldsymbol{e}_k) - \alpha_k\lambda_k T\left\|\boldsymbol{\omega}_k^1\right\| - \lambda_k T\right), \tag{6}$$

$$l(\boldsymbol{e}_k)=\begin{cases}\mu & \text{if } e_{Mk}\le e_L\\ 1 & \text{if } e_{Mk}\ge e_H\\ \mu+(1-\mu)q(\frac{e_{Mk}-e_L}{e_H-e_L}) & \text{otherwise}\end{cases}, \tag{7}$$

where $\alpha_k = \|\boldsymbol{e}_k\|/\|\boldsymbol{e}_{Ik}\|$, being $\boldsymbol{e}_{Ik}$ the projection of $\boldsymbol{e}_k$ in the image of $\boldsymbol{L}_{\boldsymbol{e}_k}$.

The following statements on the sampled-data dynamics can be proven

1) With reference to the system (5), the only trajectories $\boldsymbol{e}_k$ that asymptotically converge to $\hat{\boldsymbol{e}}$ are those starting from $\boldsymbol{e}_0$, such that $\boldsymbol{s}_0 \in \mathcal{N} = \{\boldsymbol{s}\,|\,\boldsymbol{s} = \hat{\boldsymbol{e}} + \boldsymbol{s}^\star + \Delta\bar{\boldsymbol{p}}\}$, with any translation $\Delta\bar{\boldsymbol{p}}$, if and only if $0 < \lambda T < 2$.
2) Consider the sampled-data closed-loop system (5) with $\lambda = \lambda_k$. If λ_k is selected such that
$$0 < \lambda_k T < \frac{2}{1+\alpha_k\|\boldsymbol{\omega}_k^1\|},\ \forall k \in \mathbb{N}_0, \tag{8}$$
then, the desired equilibrium point $\boldsymbol{e} = \boldsymbol{0}$ of system (5) is *almost globally asymptotically stable*.
3) Consider the sampled-data closed-loop system (5) with $\lambda = \lambda_k$. Assuming $\boldsymbol{s}_0 \notin \mathcal{N}$, if the gain λ_k is determined, for each sampling time interval, by solving
$$\min_{\lambda_k T}\quad \pi(\boldsymbol{e}_k, \lambda_k T) \tag{9a}$$
$$\text{s.t.}\quad 0 < \lambda_k T < \frac{2l(\boldsymbol{e}_k)}{1+\alpha_k\|\boldsymbol{\omega}_k^1\|} \tag{9b}$$
$$\|\boldsymbol{\omega}_k\| \le \omega_k^M,\quad \|\mathbf{v}_k\| \le \mathrm{v}_k^M \tag{9c}$$
then:
   a) the equilibrium point $\boldsymbol{e} = \boldsymbol{0}$ of the sampled-data closed-loop system is *almost globally asymptotically stable*;
   b) the feature error norm $\|\boldsymbol{e}(t)\|$ exhibits a monotonic decrease over the time t.

The stability can be proven through Lyapunov argument by selecting as Lyapunov function candidate $V(\boldsymbol{e}_k) = \boldsymbol{e}_k^\top\boldsymbol{e}_k$, yielding

$$\Delta V_k \le -\lambda_k T\big(2\|\boldsymbol{e}_{Ik}\| - \lambda_k T\alpha_k\|\boldsymbol{\omega}_k^1\|\|\boldsymbol{e}_{Ik}\| + - \lambda_k T\|\boldsymbol{e}_{Ik}\|\big)\|\boldsymbol{e}_{Ik}\|. \tag{10}$$

4 Experiments

The visual servoing algorithm has been tested in a collaborative in-store logistic scenario for shelf replenishment tasks. A video of few experiments carried out with the proposed control law is available at: https://youtu.be/unNwifaBD4A.

The robot is commanded to pick an object and place it on a selected shelf. Two experiments are executed, in the first one the robot performs the pick&place task autonomously. In the second one the object pose is perturbed by a human operator during the visual servoing sub-task. Figure 1 shows the results of the two experiments. The top plot reports the root mean square error e_M while the bottom one the control gain λ_k. The blue lines represent the results obtained when the object pose is not perturbed by the human partner. The red lines represent the perturbed case. At about 0.5 s the human partner moves the object to be grasped to avoid the collision between the robot and another object present on the picking desk. The object position perturbation lasts 0.5 s and ends at $t = 1$ s. During this time interval, the robot follows the moving object and the root mean square error is almost constant. When the perturbation ends, the error decreases and converges towards zero.

When the root mean square error e_M reaches the prescribed value of 2 mm the visual servoing sub-task is considered completed, the robot grasps the object, moves it to reach the target location and places it on the destination shelf to complete the pick&place task. The placing trajectory, after the visual servoing phase, has been planned offline by using the motion planners available in MoveIt!.

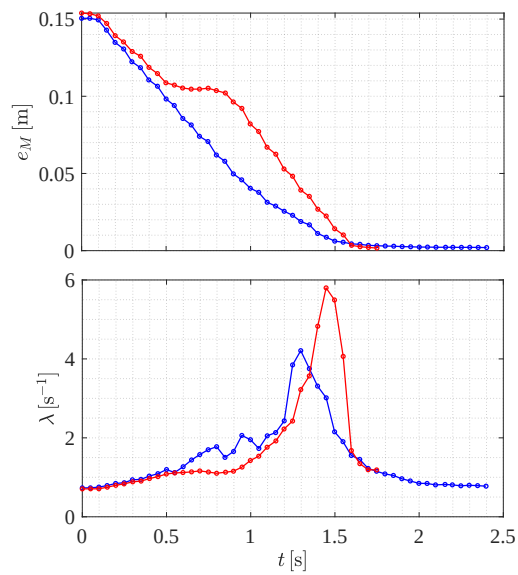

Fig. 1. Pick&Place experiment. Top plot - root mean square errors: unperturbed experiment (blue curve), perturbed one (red curve).

5 Conclusion

In this paper we presented a novel image-based visual servoing with three dimensional features. A sampled-data model is presented to describe the exact closed-loop dynamics in the sampling times.

The control design, suggested by a discrte-time Lyapunov stability analysis, is aimed at improving the robotic system performances in terms of accuracy and execution speed. The input to the robot controller has been synthesized by adapting the control gain solving a constrained optimization problem, ensuring that robot velocity limits are fulfilled.

The accompanying video shows that the robot exhibits a high accuracy in grasping and placing the objects, and behaves, in terms of speed of execution, in a way comparable to the human operator, satisfying the requirement for the optimal sharing of a collaborative logistic task.

References

[1] F. Schramm, G. Morel, A. Micaelli, and A. Lottin, "Extended-2d visual servoing," in *IEEE International Conference on Robotics and Automation, 2004. Proceedings. ICRA '04. 2004*, vol. 1, 2004, pp. 267–273 Vol.1.
[2] A. Rantzer, "A dual to lyapunov's stability theorem," *Systems & Control Letters*, vol. 42, no. 3, pp. 161–168, 2001.
[3] M. Costanzo, G. De Maria, and C. Natale, "Two-fingered in-hand object handling based on force/tactile feedback," *IEEE Transactions on Robotics*, vol. 36, no. 1, pp. 157–173, Feb 2020.
[4] E. Cervera, A. P. del Pobil, F. Berry, and P. Martinet, "Improving image-based visual servoing with three-dimensional features," *The International Journal of Robotics Research*, vol. 22, no. 10-11, pp. 821–839, 2003.
[5] D. Liberzon and A. Morse, "Basic problems in stability and design of switched systems," *IEEE Control Systems Magazine*, vol. 19, no. 5, pp. 59–70, 1999.

Distributed Game-theoretical Control for EV-integrated Energy Communities

Nicola Mignoni, Raffaele Carli, and Mariagrazia Dotoli

I. Introduction

The recent proliferation of electric vehicles (EVs) is adding high variability to the demand side of modern power grids. Nevertheless, EVs can be used for ancillary services, in order to regulate the network dynamics when generation/load imbalances occur. Also, when parked, EVs can be used to mimic the functionality of energy storage systems (ESSs), by using their battery as a temporary energy buffer [1]. In order to leverage on the benefits of the integration of EVs into the grid, numerous studies analyze the problem under the lenses of game theory [2]–[4] and model predictive control (MPC) [5], [6]. However, the existing literature does not address the simultaneous vehicle-to-grid (V1G) and vehicle-to-building (V2B) capability, under the realistic assumption of EV's stochastic parking and recharging time, which is essential for a robust design of ancillary service-based energy communities (ECs).

In this context, we propose a novel MPC-based control strategy for the optimal scheduling of an EC constituted by prosumers and equipped with V1G and V2B capabilities. In particular, V2B services are provided by long-term parked EVs thus used as temporary storage systems by prosumers, who in turn offer the V1G service to EVs provisionally plugged to charging stations. Some of the results presented in this talk have been published in a conference paper [7] and are being extended for submission to a peer-reviewed international journal [8].

II. System Model

The EC model comprises the following agents:

• *Charging EVs* (cEVs) - These are EVs that are temporarily plugged to charging stations of the EC and connected to the grid with the only aim of recharging their own batteries. Each cEV has a given battery capacity and arrives at the charging station with an initial battery level. For each time slot in the control horizon, each cEV can buy energy from the retailer, or from the i-th prosumer.

• *Trading EVs* (tEVs) - These are non-resident EVs that are long-term parked in the parking spots of the EC and connected to the grid with the aim of renting their free battery capacity to prosumers as a temporary ESS. However, from the prosumers' point of view, the drawback of the tEVs' storage usage is that the latter may leave the parking spot with part of the energy being held for prosumers. Hence, we introduce the *leaving fee*, representing the "refund" tEVs are willing to pay to prosumers for every unit of lost storage. In addition, tEVs have to incur costs related to the battery physical degradation, modeled by a quadratic term depending on the battery technological coefficient.

• *Retailer* - This is a passive agent, responsible for selling energy both to prosumers and cEVs as well as buying energy from prosumers, at any moment in time, with fixed pricing curves. Its presence is needed in order to guarantee the energy balance in the EC.

• *Prosumers* - These are the community members equipped with autonomous generation systems (e.g., photovoltaic, eolic sources), and characterized by a local energy demand. On the one hand, in the case of energy surplus, the prosumers can buy the energy supplied by the retailer and retrieve stored energy, discharged by the tEVs. On the other hand, in case of energy deficit, they can sell the energy to the retailer and/or to cEVs, for recharging purpose, and/or store it using tEVs capacity.

EVs have a stochastic behavior, since owners may move their vehicles from the parking spots, in the case of tEVs, or from the recharging stations before the charging is finished, in the case of cEVs. Nevertheless, each EV has local knowledge of its parking and charging time distribution, which is shared with prosumers when the former arrive at the parking spot or recharging station. For the generic EV, we assume that the probability of being parked/recharging follows a truncated normal distribution.

III. The Proposed Control Strategy

Each agent $n \in \mathcal{N}$ acts selfishly, determining the best strategy which ensures that its cost function is minimized and local constraints are satisfied.

Formally, this agreement means finding the Nash equilibrium (NE) of the non-cooperative game $\mathcal{G}(\mathcal{N}, \mathcal{X}, \mathcal{J})$, where $\mathcal{X} = \prod_{n\in\mathcal{N}} \mathcal{X}_n(\boldsymbol{x}_{-n})$ is the set of strategies, $\mathcal{X}_n(\boldsymbol{x}_{-n})$ is the strategy set of the n-th agent, and $\boldsymbol{x}_n$ and $\boldsymbol{x}_{-n}$ are the strategies of the n-th agent and of all the remaining agents in $\mathcal{N} \setminus \{n\}$, respectively. Lastly, $\mathcal{J} = \{J_n(\boldsymbol{x}_n),\ n \in \mathcal{N}\}$ is the set of objective functions. The optimal strategies $(\boldsymbol{x}_n^*)_{n\in\mathcal{N}}$ of all agents result from the following inter-dependent optimization problems:

$$\boldsymbol{x}_n^* = \underset{\boldsymbol{x}_n \in \mathcal{X}_n(\boldsymbol{x}_{-n}^*)}{\arg\min} \ J_n(\boldsymbol{x}_n), \quad \forall n \in \mathcal{N}. \tag{1}$$

Note that, due to the presence of the coupling constraints arising from $\mathcal{X}_n(\boldsymbol{x}_{-n})$, the above defined problem is a (GNEP). There exists a class of GNEPs which can be treated

N. Mignoni, R. Carli, and M. Dotoli are with the Department of Electrical and Information Engineering of the Polytechnic of Bari, Italy. (e-mail: {nicola.mignoni, raffaele.carli, mariagrazia.dotoli}@poliba.it).

as a variational inequality (VI) problem. Given a convex closed set $\mathcal{K} \subseteq \mathbb{R}^n$ and a continuous function $\boldsymbol{F} : \mathcal{K} \to \mathbb{R}^n$, solving the variational problem $VI(\mathcal{K}, \boldsymbol{F})$ means finding a vector $\boldsymbol{x} \in K$ such that $\boldsymbol{F}(x)^\top(\boldsymbol{x} - \boldsymbol{y}) \geq 0, \quad \forall \boldsymbol{y} \in K$. If $\boldsymbol{F} = (\nabla_{\boldsymbol{x}_1} J_1(\boldsymbol{x}_1)^\top, \ldots, \nabla_{\boldsymbol{x}_N} J_N(\boldsymbol{x}_N)^\top)^\top$, the following proposition holds.

Proposition 3.1: Every solution of the $VI(\mathcal{X}, \boldsymbol{F})$ formulation of $\mathcal{G}(\mathcal{N}, \mathcal{X}, \mathcal{J})$ is also a solution of the GNEP.

Following [9], we employ the so-called accelerated distributed agumented Lagrangian method (ADALM). The basic idea consists of iteratively minimizing the Lagrangian of the cost function $J_n(\boldsymbol{x}_n)$ for each agent n, whose general form is:

$$\mathcal{L}_n(\boldsymbol{x}_n, \boldsymbol{\lambda}_n) = J_n(\boldsymbol{x}_n) + \boldsymbol{\lambda}_n^\top \boldsymbol{c}_n + \frac{\rho}{2}\|\boldsymbol{c}_n\|^2 \tag{2}$$

where $\boldsymbol{c}_n$ represents the *shared constraints* and $\boldsymbol{\lambda}_n$ is the associated vector of Lagrange multipliers. The ADALM-based iterative process is summarized as follows

$$\tilde{\boldsymbol{x}}_n^{(\tau)} = \underset{\boldsymbol{x}_n \in \mathcal{K}_n}{\arg\min}\, \mathcal{L}_n\left(\boldsymbol{x}_n, \boldsymbol{\lambda}_n^{(\tau-1)}\right) \tag{3}$$

$$\boldsymbol{x}_n^{(\tau)} = \boldsymbol{x}_n^{(\tau-1)} + \chi\left(\tilde{\boldsymbol{x}}_n^{(\tau)} - \boldsymbol{x}_n^{(\tau-1)}\right) \tag{4}$$

$$\boldsymbol{\lambda}_n^{(\tau)} = \boldsymbol{\lambda}_n^{(\tau-1)} + \rho\chi \boldsymbol{c}_n^{(\tau)} \tag{5}$$

with $\chi \in \mathbb{R}_+$ being the step-size, $\rho \in \mathbb{R}_+$ is the regularization strength and $\tau \in \mathbb{N}$. The convergence properties are formally addressed by the following:

Proposition 3.2: For any $\chi \in (0, 1/2)$, the sequence $\boldsymbol{x}_n^{(\tau)}$ converges to $\boldsymbol{x}_n^*$ for each $n \in \mathcal{N}$.

On the one hand, the MPC plant is constituted by the agents trading energy in the EC, i.e., the tEVs, cEVs, and prosumers. On the other hand, the core of the MPC is represented by the distributed mechanism (i.e., the ADALM algorithm) solving the online optimization problem (1). Agents participate to the game-based energy market through ADALM, which yields the control strategies over the whole control horizon. Results are applied to all agents in a closed-loop control fashion.

IV. Numerical Results

The conducted experiments refer to a 3 day simulation, with a time step of 1 hour and a control horizon of 1 day, thus allowing prosumers to consider both the lower and higher generation periods in the scheduling problem. Figure 1 shows the results in terms of average energy inflow and outflow. This shows that the market has economically sustainable capabilities, meaning that the energy exchange is not polarized towards the static buyer (i.e., the retailer) but involves all the agents in the EC. The consequences on the environmental sustainability of systems are impactful, since a significant percentage of EVs energy supply comes from local RESs. Data and source code are fully available [10].

V. Conclusions

A non-cooperative distributed control framework is proposed, where an energy community provides recharging services to electric vehicles (EVs), while exploiting the energy storage capabilities of long-term parked EVs. An MPC strategy is defined based on a quadratic optimization model, that is solved in a distributed fashion leveraging on the accelerated distributed augmented Lagrangian method (ADALM), whose convergence properties are guaranteed.

Future work will focus on extending the architecture to different settings and ensuring the correct operation of the control framework in case of untrustworthy EVs.

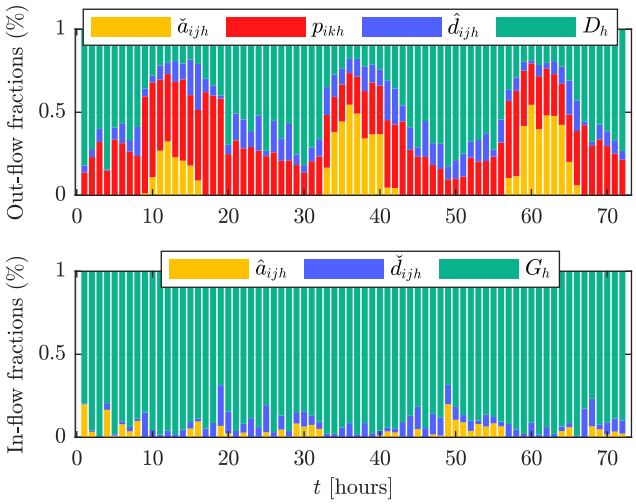

Fig. 1. Average composition of prosumers' in-flow and out-flow

References

[1] N. Mignoni, P. Scarabaggio, R. Carli, and M. Dotoli, "Control frameworks for transactive energy storage services in energy communities," *Control engineering practice (in review)*.

[2] M. H. K. Tushar, A. W. Zeineddine, and C. Assi, "Demand-side management by regulating charging and discharging of the ev, ess, and utilizing renewable energy," *IEEE Transactions on Industrial Informatics*, vol. 14, no. 1, pp. 117–126, 2017.

[3] J. Dominguez-Navarro, R. Dufo-Lopez, J. Yusta-Loyo, J. Artal-Sevil, and J. Bernal-Agustin, "Design of an electric vehicle fast-charging station with integration of renewable energy and storage systems," *International Journal of Electrical Power & Energy Systems*, vol. 105, pp. 46–58, 2019.

[4] J. Zhang, L. Che, L. Wang, and U. K Madawala, "Game-theory based v2g coordination strategy for providing ramping flexibility in power systems," *Energies*, vol. 13, no. 19, p. 5008, 2020.

[5] R. Iacobucci and R. Bruno, "Cascaded model predictive control for shared autonomous electric vehicles systems with v2g capabilities," in *2019 IEEE SmartGridComm*. IEEE, 2019, pp. 1–7.

[6] A. Karimi and M. Haeri, "Game theory meets distributed model predictive control in vehicle-to-grid systems," in *2019 11th ELECO*. IEEE, 2019, pp. 764–768.

[7] N. Mignoni, P. Scarabaggio, R. Carli, and M. Dotoli, "Game theoretical control frameworks for multiple energy storage services in energy communities," in *2022 8th International Conference on Control, Decision and Information Technologies (CoDIT)*. IEEE, 2022.

[8] N. Mignoni, R. Carli, and M. Dotoli, "Distributed stochastic V1G/V2B mpc for charging services and long-term parked electric vehicles," *IEEE Transactions on Control System Technology, (submitted)*.

[9] N. Chatzipanagiotis, D. Dentcheva, and M. M. Zavlanos, "An augmented lagrangian method for distributed optimization," *Mathematical Programming*, vol. 152, no. 1, pp. 405–434, 2015.

[10] N. Mignoni, R. Carli, and M. Dotoli. (2022) Data and source code. https://github.com/nicomignoni/EVS-MPC.git. GitHub repository.

Data-driven Dynamic Relatively Optimal Control

Felice Andrea Pellegrino[1], Franco Blanchini[2], Gianfranco Fenu[1] and Erica Salvato[1]

***Abstract*— We show how the recent works on data driven open-loop minimum-energy control for linear systems can be exploited to obtain a stabilizing state feedback compensator (actually deadbeat) (i) that does not require feedforward or state initialization, (ii) which relies only on collected experimental data (without the need for a mathematical formulation of the model), and (iii) that is optimal for the nominal initial condition. The result is a data-driven dynamic relatively optimal controller (ROC). As an example, we apply the proposed approach in a point-to-point cart and pole control task. The results show the effectiveness of the proposed data-driven dynamic ROC.**

Model-based control (MBC) approaches have been widely exploited over the years, exhibiting their ability to provide effective and reliable control laws in a large variety of control tasks. However, their implementation is strictly constrained on the existence of a dynamical model of the system to be controlled, not often easy to derive or identify. To overcome this intrinsic limitations of MBC approaches, the control community is recently focusing on the so called *data-driven control* (DDC), i.e., the family of model-free control solutions in which the synthesis of controllers is entirely based on input-output data collections.

The key issue in DDC is how to replace process models with data. A first solution in this regard was postulated, in case of linear systems, by Willems *et al.* [1], who states that a linear system can be dynamically represented by a finite set of system trajectories, provided that these trajectories come from sufficiently excited dynamics. This lemma has been more or less explicitly exploited for the design of data-driven controls.

In [2], for example, authors propose an off-line approach leading to optimal open-loop input sequences from data-batch collected in preliminary experiments. Here, explicit formulas for the open-loop minimum energy control problem, based entirely on experimental data, are derived for linear, unconstrained discrete-time systems. A less restricted experimental framework is presented in [3], while some applications on complex systems, such as power-grid networks and brain networks, are reported in [4].

Data-driven closed-loop solutions are instead proposed in [5], [6] where linear quadratic regulator (LQR) problems are faced respectively with infinite and finite optimization time horizons. Further results on the data-driven LRQ approach applied on nonlinear systems, and in case of data corrupted by noise, can be find in [7], [8]. Data-driven solutions to address the model predictive control (MPC) problem are instead proposed in [9], [10], [11], [12].

In the present work, we deal with open-loop optimal control sequences obtained by the sole experimental data, and specifically, by sequences of inputs and the corresponding states. The aim is to exploit such open-loop sequences to get a closed-loop control law.

In [13] we proved that, given the experimental input and state data, collected during N experiments lasting $2K$ steps:

$$\underbrace{u(2K-1)^\top, \dots, u(K)^\top}_{\hat{u}_i^\top}, \underbrace{u(K-1)^\top, \dots, u(0)^\top}_{u_i^\top}$$

$$x(1), \dots, \underbrace{x(K)}_{x_i}, x(K+1), \dots, \underbrace{x(2K)}_{\hat{x}_i},$$

we can compute both the optimal open loop control sequence, and the respective state trajectory following:

$$u^* = \left(XU^\dagger\right)^\dagger \left(XU^\dagger \hat{U} - \hat{X}\right) X^\dagger x_{\text{ini}}, \tag{1}$$

$$x(k) = \left(\hat{X}_k - R_k \hat{U}_k\right) X_k^\dagger x_{\text{ini}} + R_k u_k^* \tag{2}$$

for each $k = 1, \dots, K$, where

$$U = [u_1, \dots, u_i, \dots, u_N], \qquad \hat{U} = [\hat{u}_1, \dots, \hat{u}_i, \dots, \hat{u}_N]$$

$$X = [x_1, \dots, x_i, \dots, x_N], \qquad \hat{X} = [\hat{x}_1, \dots, \hat{x}_i, \dots, \hat{x}_N],$$

are suitably constructed matrices.

Then, relying on the state-space partitioning technique described in [14], we get a *static*, nonlinear, state-feedback controller having the property (besides being stabilizing) of guaranteeing the achievement of the optimal trajectory when starting from the same initial condition of the optimal open loop trajectory.

Here, relying on the above stated results, and based on the dynamic relatively optimal control (ROC) theory of [15], we present an approach able to synthesize a linear *dynamic* controller having the same properties of the static ROC [13], [14]. In particular, following [15], the relatively optimal compensator

$$z(k+1) = Qz(k) + Rx(k) \tag{3}$$

$$u(k) = Sz(k) + Tx(k), \tag{4}$$

guaranteeing optimality from the set of initial conditions $x_{\text{ini}}^{(i)}$, $i = 1 \dots r$, is given by the unique solution of:

$$\begin{bmatrix} \mathcal{ZP} \\ \mathcal{U} \end{bmatrix} = \begin{bmatrix} Q & R \\ S & T \end{bmatrix} \begin{bmatrix} \mathcal{Z} \\ \mathcal{X} \end{bmatrix}, \tag{5}$$

*This work has been partially supported by the Italian Ministry for Research in the framework of the 2017 Program for Research Projects of National Interest (PRIN), Grant no. 2017YKXYXJ.

[1]Department of Engineering and Architecture, University of Trieste, Italy. {fenu,fapellegrino}@units.it, erica.salvato@dia.units.it

[2]Dipartimento di Scienze Matematiche, Informatiche e Fisiche, Università degli Studi di Udine, Via delle Scienze 206, 33100 Udine, Italy. blanchini@uniud.it

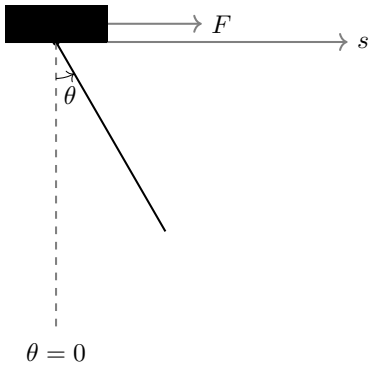

Fig. 1. Cart and pole system

where $\mathcal{X}$ and $\mathcal{U}$ contain, respectively, the optimal state and input sequences obtained following Equations (1) and (2), $\mathcal{Z}$ is any matrix such that: $M = \begin{bmatrix} \mathcal{Z} \\ \mathcal{X} \end{bmatrix}$ is invertible, and $\mathcal{P} = \operatorname{diag}\left\{\mathcal{P}^{(i)}\right\}$ is a diagonal block matrix whose blocks have the form:

$$\begin{bmatrix} 0 & 0 & \dots & 0 & 0 \\ 1 & 0 & \dots & 0 & 0 \\ 0 & 1 & \dots & 0 & 0 \\ \vdots & \vdots & \dots & \vdots & \vdots \\ 0 & 0 & \dots & 1 & 0 \end{bmatrix}. \tag{6}$$

As a result, we get a dynamic ROC which is data-driven, in the sense that it can be synthesized directly form the collected data.

We report the simulation results obtained applying the proposed data-driven ROC approach to a cart and pole system (Figure 1). We denote by $x = \begin{bmatrix} s & \dot{s} & \theta & \dot{\theta} \end{bmatrix}^\top$ the state vector, where s, $\dot{s}$, θ, $\dot{\theta}$ denote, respectively, the position and the speed of the cart, and the angular position and the angular speed of the pole. The goal is to determine a compensator able to move the cart and pole system from an initial state x_{ini} towards the null state $x_0 = \begin{bmatrix} 0 & 0 & 0 & 0 \end{bmatrix}^\top$. We perform 20 experiments, starting from x_0, and applying randomly chosen inputs thus lasting $2K = 18$ steps. The closed-loop trajectories obtained by applying the compensator, solution of the data-driven ROC problem, starting from two linearly independent initial states $x_{\text{ini}}^{(1)} = \begin{bmatrix} 1 & 0 & 0 & 0 \end{bmatrix}^\top$, and $x_{\text{ini}}^{(2)} = \begin{bmatrix} 0 & 0 & 0 & 1 \end{bmatrix}^\top$, are reported respectively in blue and in red in Figure 2, and exhibit the desired behavior. Indeed for both initial conditions the system goes towards zero in the desired number of time-steps.

The proposed approach can handle more than a single initial condition and, differently from the static approach [13], is not based on the partition of the state space, thus it is suitable for high order systems.

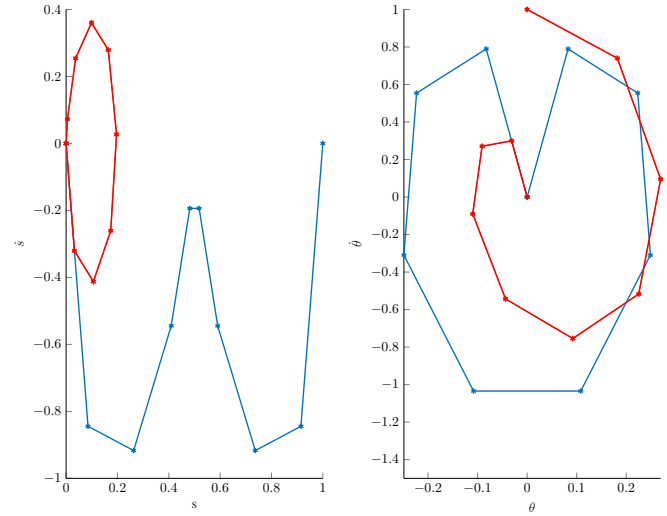

Fig. 2. Optimal trajectories obtained solving the data-driven ROC problem on the cart and pole system (Figure 1) starting from the two linearly independent initial conditions $x_{\text{ini}}^{(1)} = \begin{bmatrix} 1 & 0 & 0 & 0 \end{bmatrix}^\top$ (blue), and $x_{\text{ini}}^{(2)} = \begin{bmatrix} 0 & 0 & 0 & 1 \end{bmatrix}^\top$ (red).

References

[1] J. C. Willems, P. Rapisarda, I. Markovsky, and B. L. De Moor, "A note on persistency of excitation," *Systems & Control Letters*, vol. 54, no. 4, pp. 325–329, 2005.

[2] G. Baggio, V. Katewa, and F. Pasqualetti, "Data-driven minimum-energy controls for linear systems," *IEEE Control Systems Letters*, vol. 3, no. 3, pp. 589–594, 2019.

[3] G. Baggio and F. Pasqualetti, "Learning minimum-energy controls from heterogeneous data," in *2020 American Control Conference (ACC)*. IEEE, 2020, pp. 3991–3996.

[4] G. Baggio, D. S. Bassett, and F. Pasqualetti, "Data-driven control of complex networks," *Nature Communications*, vol. 12, no. 1, p. 1429, 2021.

[5] C. De Persis and P. Tesi, "Formulas for data-driven control: Stabilization, optimality, and robustness," *IEEE Transactions on Automatic Control*, vol. 65, no. 3, pp. 909–924, 2019.

[6] M. Rotulo, C. De Persis, and P. Tesi, "Data-driven linear quadratic regulation via semidefinite programming," *IFAC-PapersOnLine*, vol. 53, no. 2, pp. 3995–4000, 2020.

[7] C. De Persis and P. Tesi, "Designing experiments for data-driven control of nonlinear systems," *arXiv preprint arXiv:2103.16509*, 2021.

[8] C. De Persis and P. Tesi, "Low-complexity learning of linear quadratic regulators from noisy data," *Automatica*, vol. 128, p. 109548, 2021.

[9] H. Yang and S. Li, "A data-driven predictive controller design based on reduced hankel matrix," in *2015 10th Asian Control Conference (ASCC)*. IEEE, 2015, pp. 1–7.

[10] J. Coulson, J. Lygeros, and F. Dörfler, "Data-enabled predictive control: In the shallows of the deepc," in *2019 18th European Control Conference (ECC)*. IEEE, 2019, pp. 307–312.

[11] ——, "Regularized and distributionally robust data-enabled predictive control," in *2019 IEEE 58th Conference on Decision and Control (CDC)*. IEEE, 2019, pp. 2696–2701.

[12] J. Berberich, J. Köhler, M. A. Müller, and F. Allgöwer, "Data-driven model predictive control with stability and robustness guarantees," *IEEE Transactions on Automatic Control*, vol. 66, no. 4, pp. 1702–1717, 2020.

[13] F. A. Pellegrino, F. Blanchini, G. Fenu, and E. Salvato, "Closed-loop control from data-driven open-loop optimal control trajectories," in *submitted to European Control conference*, 2022.

[14] F. Blanchini and F. A. Pellegrino, "Relatively optimal control: A static piecewise-affine solution," *SIAM Journal on Control and Optimization*, vol. 46, no. 2, pp. 585–603, 2007, cited By 10.

[15] ——, "Relatively optimal control and its linear implementation," *IEEE Transactions on Automatic Control*, vol. 48, no. 12, pp. 2151–2162, 2003, cited By 24.

The pseudo inversion paradigm and the definition of a new and more general 2DOF control scheme

Valentina Orsini

I. Long abstract

While attaining closed-loop stability and exact steady-state tracking for a feedback control system is a relatively simple task [1], [2], inherent limitations on transient performance make it difficult to obtain an accurate transient tracking, especially for non-minimum phase systems. In general, a significant improvement of transient performance can be only achieved through a proper feedforward action which is designed separately from the feedback controller. In this regard, many methods are based on the model stable inversion [3], [4], [5], which allows exact tracking through an infinite preactuation interval starting from null initial conditions. The practical unfeasibility of this solution motivated the use of approximated preview-based techniques with a bounded pre-actuation interval,[6], [7], [8], [9]. All the above papers assume that the system is hyperbolic, namely without zeros on the boundary of the stability region (the imaginary axis or the unitary circumference). For systems with non-minimum phase zeros near the boundary of the stability region (near non-hyperbolic systems), the pre-actuation interval becomes very large and tends to infinite for zeros lying on the boundary (non-hyperbolic systems) [10], [11].

To alleviate the serious limitations present in these techniques, a completely different approach has been proposed by reformulating the problem of stable inversion of the model as an optimal control problem (whence the name of pseudo-inversion), [12], [13], [14], [15]. The pseudo-inversion is not aimed at yielding an exact inversion even if the plant is exactly known. The inverse problem consists in determining a reference input such that when it is applied to the model yield an output that is an optimal approximation (in the mean least square sense) of the desired one.

The main merits of the pseudo-inversion approach with respect to the other methods for accurate tracking based on the classical stable inversion approach are: 1) the initial conditions can be arbitrary and possibly uncertain; 2) the method does not require pre-actuation; 3) the method can also be applied to the class of non-hyperbolic systems; 4) the approach allows the definition of a functional multi-objective for the simultaneous fulfillment of multiple control requirements; 5) he technique is robust with respect to parametric uncertainties; 6) the method can be directly extended to deal with the more general tracking problem of an output, which is required to track a repeatedly and non-periodically switching set point, and only a limited preview information is available.

Using B-splines to model the reference input and the control effort allows an efficient implementation of the pseudo-inversion method. This is because B-spline functions are continuously differentiable universal approximators which admit a parsimonious parametric representation and belong to the convex hull defined by the relative control points. These properties significantly reduce the number of parameters (the control points) with respect to which the quadratic cost functional is minimized. They also allow the minimization procedure to be formulated as a robust least square estimation problem where both the design matrix and observations are not exactly known due to plant uncertainty.

The pseudo inversion paradigm also allows the definition of a new 2DoF control architecture to achieve enhanced trajectory tracking performance. [16]. The most widely used 2DoF control architectures based on inverse control are classified into two main categories: FeedForward Plant Inversion (FFPI) and FeedForward Closed Loop Inversion (FFCLI). The achievable tracking accuracy of both control schemes depend on the specific application and on the amount of uncertainty affecting the plant. The performances of the two architectures have been discussed and compared by several authors in [17], [18], [19]. As each of the two architectures has advantages over the other, depending on the specific problem, it is not possible to state the best scheme independently of the particular application. This problem can not be solved with the guidelines stated in the above papers because they refer to some definite applications and their qualitative nature makes it difficult any generalization. Hence, it would be very useful to define a more general 2DoF control architecture optimally combining the FFPI and FFCLI control actions The proposed inversion procedure is a way to settle this issue : the resulting control law is always given by an optimal combination of the FFPI and FFCLI control actions, independently of the particular application and, as a consequence, it outperforms both FFPI and FFCLI. Robustness with respect to polytopic uncertainty is obtained using a min-max optimization approach. The main, notable advantage of this new solution is to relieve the designer of the often difficult choice of the most appropriate 2DOF control scheme to be adopted.

This new architecture is referred to as FeedForward Optimally Balanced Inversion (FFOBI), (see Fig 1).

The block Σ_f is the feedback connection of a (possibly

Dipartimento di Ingegneria dell'Informazione,UNIVPM, Ancona, Italy. vorsini@univpm.it

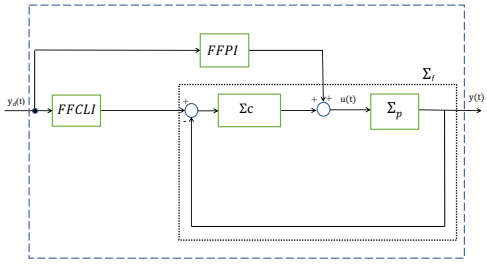

Fig. 1. The FFOBI control scheme

non-minimum phase and/or with non hyperbolic internal dynamics) LTI polytopic plant Σ_p with an LTI robustly stabilizing dynamic output feedback controller Σ_c.

A. Numerical results

The linearized model (1) is the unstable, non minimum phase with near non hyperbolic internal dynamics system considered in [10]. It represents an aircraft trimmed at a nominal $5°$ pitch attitude, with a mid-range weight, a mid-position center of gravity and operating in-ground effect at near sea level. The model is described by

$$\dot{x}_p(t) = A_p x_p(t) + B_p u(t),\ y(t) = C_p x_p(t) \tag{1}$$

where

$$x_p = \begin{pmatrix} U \\ W \\ Q \\ V \\ P \\ R \\ \theta \\ \chi \end{pmatrix} = \begin{pmatrix} \text{forward velocity} \\ \text{vertical velocity} \\ \text{pitch rate} \\ \text{lateral velocity} \\ \text{roll rate} \\ \text{yaw rate} \\ \text{pitch attitude} \\ \text{roll attitude} \end{pmatrix},\ y = \begin{pmatrix} U \\ W \\ V \\ R \end{pmatrix}$$

$$u = \begin{pmatrix} \delta_C \\ \delta_B \\ \delta_A \\ \delta_P \end{pmatrix} = \begin{pmatrix} \text{collective} \\ \text{longitudinal cyclic} \\ \text{lateral cyclic} \\ \text{tail rotor collective} \end{pmatrix}$$

The vectors $y(t) \in \mathbb{R}^q$, $u(t) \in \mathbb{R}^m$, $q = m = 4$, represent the controlled and manipulated variables respectively. The entries of A_p and B_p can be found in [10]. With respect to [10] a polytopic dynamical matrix is here assumed. As in [10], the forward velocity and the yaw rate are to be kept at zero $\forall t \in \mathbb{R}^+$, while the desired behavior of W and V is the smooth function converging to the constant value 0.2 in the interval $[0, 13)$, as shown in Fig. 2. The same figure confirms that the best tracking performance is given by the FFOBI configuration. A measure of the improvement provided by the FFOBI has been calculated as the percentage of reduction of $\|e(t)\|_2$ (2-norm of the tracking error) with respect to FFCLI and FFPI. These percentages are 20.93% and 82.68% respectively.

References

[1] Francis, B. A., O. A. Sebakhy, W. M. Whonam. Synthesis of Multivariable regulators: the internal model principle. Applied Mathematics and Optimization, 1974,16, 64?86.

[2] Desoer, C. A. , Y. T. Wang. LinearTime- Invariant Robust Servomechanism Problem: A Self Contained Exposition. Control and Dynamical Systems, 1980, 16, 81-90, Ed. Leondes, Academic Press, N.Y.

[3] Devasia S, Chen D, Paden B. Nonlinear inversion based output tracking. IEEE Transactions on Automatic Control 1996, 41, 930-942.

[4] Hunt LR, Meyer G, Su R. Non-causal inverses for linear systems. IEEE Transactions on Automatic Control,1996, 41, 608-611.

[5] Marro, G., D. Prattichizzo, E. Zattoni. Convolution profiles for right inversion of multivariable non-minimum phase discrete-time systems. Automatica, 2002, 38,1695-1703.

[6] Zou Q, Devasia S. Preview-based stable-inversion for output tracking of linear systems. Journal of Dynamic Systems, Measurement, and Control 1999; 121(4):625?630.

[7] Piazzi A, Visioli A. Using stable input-output inversion for non minimum-time feedforward constrained regulation of scalar systems. Automatica 2005; 41(2):305?313.

[8] Zou Q. Optimal preview-based stable-inversion for output tracking of nonminimum-phase linear systems. Automatica 2009; 45(1):230?237.

[9] Devasia S. Nonlinear minimum-time control with pre-and post actuation. Automatica 2011; 47(7):1379?1387.

[10] Devasia, S.. Output tracking with nonhyperbolic and near nonhyperbolic internal dynamics: helicopter hover control, AIAA J. Guid. Control Dynamics, 1997, 20,573-580.

[11] Huang, J. , C. F. Lin. Output regulation of nonlinear systems with nonhyperbolic zero dynamics. IEEE Trans. Autom. Control, 1995, 40, 1497-1500.

[12] Jetto L, Orsini V, Romagnoli R. A mixed numerical-analytical stable pseudo-inversion method aimed at attaining an almost exact tracking. International Journal of Robust and Nonlinear Control 2015, 25, 809-823.

[13] Jetto L, Orsini V, Romagnoli R. Spline based pseudo-inversion of sampled data non-minimum phase systems for an almost exact output tracking. Asian Journal of Control 2015, 17, 1866-1879.

[14] Jetto L, Orsini V, Romagnoli R. Accurate output tracking for nonminimum phase nonhyperbolic and near nonhyperbolic systems. European Journal of Control 2014,20, 292-300.

[15] L. Jetto, V. Orsini, R. Romagnoli. A B-spline-based pseudo-inversion approach for constrained optimal output transition, International Journal of Control,2018,91,2332-2344.

[16] L.Jetto, V.Orsini. Enhanced trajectory tracking using optimally combined feedforward plant inversion and feedforward closed loop inversion, European Journal of Control, 2022, 63,223-231.

[17] B. P. Rigney, L. Y. Pao, D. A. Lawrence. Model inversion architectures for settle time applications with uncertainty. in Proc. 45th IEEE Conf. Decis. Control, San Diego, CA, USA, 2006, 6518-6524

[18] J. A. Butterworth, L. Y. Pao, D. Y. Abramovitch. A comparison of control architectures for atomic force microscopes. Asian J. Control,2009, 11,175-181.

[19] G. M. Clayton, S. Tien, K. K. Leang, Q. Zou, S. Devasia. A review of feedforward control approaches in nanopositioning for high-speed SPM. J. Dyn. Syst., Meas., Control, 2009, 131.

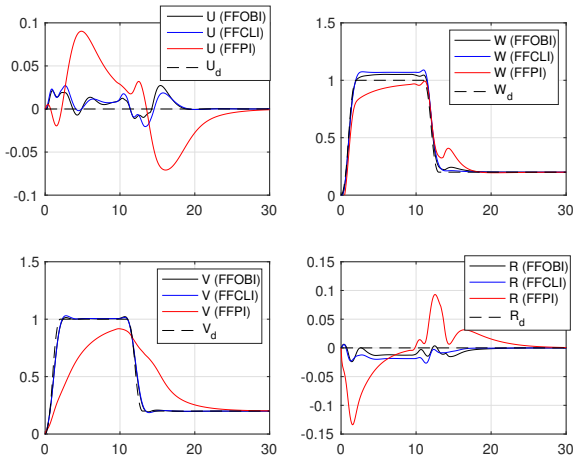

Fig. 2. The trajectories of $y_d(t) \triangleq [U_d(t)\ W_d(t)\ V_d(t)\ R_d(t)]^T$ (black dashed lines) and of the controlled output $y(t) \triangleq [U(t)\ W(t)\ V(t)\ R(t)]^T$ produced by FFOBI (black lines), FFCLI (blue lines) and FFPI (red lines) schemes respectively.

Set-membership identification of continuous-time systems through model transformation

V. Cerone, S. M. Fosson, S. Pirrera, D. Regruto

***Abstract*— In this paper, we consider the identification of continuous-time linear-time-invariant systems from sampled input-output data corrupted by unknown but bounded noise. We formulate the problem in the set-membership identification framework and we select the parameter estimate from the feasible parameters set by computing the solution to a polynomial optimization problem.**

I. INTRODUCTION

System identification (SI) deals with the problem of building mathematical models of dynamical systems from input-output (I/O) experimental data. Since such data are typically collected by sampling the I/O sequences, most of the approaches available in the literature look for a discrete-time (DT) description. However, identification of continuous-time (CT) models is sometimes preferable over discrete-time (DT) ones for different reasons: first, most physical systems are actually described in terms of differential equations; second, many common control system design procedures are formulated in a CT setting and, finally, the identified parameters does not depend on the sampling time. In the literature, we find different approaches to CT SI. Most of them involves pre-processing of the input-output data through a linear dynamic operator in order to recast the problem into an algebraic one; see, e.g. [1] for an overview.

In this work we address CT identification in the set-membership (SM) framework, where both the input and the output collected data samples are assumed to be corrupted by unknown but bounded additive noise. In this context, all models consistent with available data, errors' bounds and assumed model structure are considered as feasible solutions to the problem (see, e.g., [2]). SM identification of DT models has been developed in, e.g., [3]. In contrast, SM identification of CT transfer functions has not received considerable attention so far.

In this work, we develop a mathematical formulation of the CT SM identification problem starting from the model transformation proposed in [4], leading to a polynomial optimization problem (POP) solved through suitable convex relaxation techniques. The effectiveness of the proposed approach is shown by means of numerical simulation.

II. PROBLEM FORMULATION

We consider a SISO LTI dynamical system, described by the CT transfer function

$$H(s) = \frac{\sum_{i=0}^{n-1} \beta_i s^i}{s^n + \sum_{i=0}^{n-1} \alpha_i s^i} \tag{1}$$

where s is the Laplace variable and $\theta = [\alpha_0, \dots, \alpha_{n-1}, \beta_0, \dots, \beta_{n-1}]$ are the unknown parameters to be identified.

We assume that input $u(t)$ and output $y(t)$ are sampled at constant rate, with sampling period T_s, and are corrupted by additive noise. For $k = 1, \dots, N$, we use the notation $\tilde{u}(k) = u(k) + \epsilon(k)$, $\tilde{y}(k) = y(k) + \eta(k)$, where $\eta(k)$ and $\epsilon(k)$ are the noise sequences, which are bounded as $\underline{\Delta_\eta}(k) \leq \eta(k) \leq \overline{\Delta_\eta}(k)$ and $\underline{\Delta_\epsilon}(k) \leq \epsilon(k) \leq \overline{\Delta_\epsilon}(k)$.

According to the standard approach in SM estimation, we define the feasible parameter set (FPS) $\mathcal{D}$ as

$$\begin{aligned} \mathcal{D} = \{\theta \in \mathbb{R}^{2n} : & \, y(t) = h(t) * u(t) \quad \forall t, \\ & y(k) = y(kT_\mathrm{s}), u(k) = u(kT_\mathrm{s}), \\ & \tilde{u}(k) = u(k) + \epsilon(k), \quad \tilde{y}(k) = y(k) + \eta(k), \\ & \underline{\Delta_\eta}(k) \leq \eta(k) \leq \overline{\Delta_\eta}(k), \quad \underline{\Delta_\epsilon}(k) \leq \epsilon(k) \leq \overline{\Delta_\epsilon}(k)\} \end{aligned} \tag{2}$$

where $h(t)$ is the impulse response of the CT system to be identified. The purpose of this work is to provide a method to optimally select a parameter estimate θ^* among all the parameter vectors $\theta \in \mathcal{D}$. Specifically, we consider:

$$\theta^* = \arg\min_{\theta \in \mathcal{D}} \mathcal{L}(\theta) \tag{3}$$

where the objective function $\mathcal{L}(\theta)$ is a multivariate polynomial in θ that accounts for the simulation error.

III. A POLYNOMIAL APPROACH FOR THE COMPUTATION OF THE OPTIMAL ESTIMATE

In this section, we present a method to solve the optimization problem (3). For this purpose, we retrieve the algebraic reformulation of $H(s)$ in [4], defining the transformation $s = \frac{1-\lambda}{\tau\lambda}$, where τ is a parameter to be tuned.

By applying this operator, the original transfer function $H(s)$ defined in (1) is re-written as

$$H_0(\lambda|\alpha, \beta) = \frac{\sum_{j=1}^{n} \tilde{\beta}_j \lambda^j}{1 + \sum_{j=1}^{n} \tilde{\alpha}_j \lambda^j} \tag{4}$$

where $\tilde{\alpha}$ and $\tilde{\beta}$ are new parameters depending on α, β as

$$\begin{aligned} \tilde{\beta}_j &= \sum_{i=0}^{n-1} \beta_i \tau^{n-i} c_{n-j+1}^{(i)} \\ \tilde{\alpha}_j &= c_{n-j+1}^{(n)} + \sum_{i=0}^{n-1} \alpha_i \tau^{n-i} c_{n-j+1}^{(i)} \qquad j = 1, \dots, n. \end{aligned} \tag{5}$$

where $c_j^{(i)}$ are properly defined constants. See [5] for details.

$H(\lambda|\tilde{\alpha},\tilde{\beta})$ relates filtered inputs with filtered outputs signals. To establish the relation between a signal $x(t)$ and his filtered version $\lambda x(t)$, we compute the DT filter $F(z) = \dfrac{f_1 + f_2 z^{-1}}{1 + f_3 z^{-1}}$ by discretization of $F(s)$. Next, we apply $F(z)$ to the sequences $u(k), y(k), u^{(j)}(k), y^{(j)}(k)$ for $j = 1, \ldots, n-1$, obtaining

$$\begin{aligned} x^{(i)}(k) + f_3 x^{(i)}(k-1) = f_1 x^{(i-1)}(k) + \\ + f_2 x^{(i-1)}(k-1) + \delta_x^{(i)}(k). \end{aligned} \tag{6}$$

where $x(t)$ represents either $u(t)$ or $y(t)$ and $\delta_u^{(i)}(k), \delta_y^{(i)}(k)$ are discretization errors. Neglecting such discretization errors and putting together the above equations, we get an explicit description of $\mathcal{D}$ in terms of polynomials in the variables $\alpha, \beta, \tilde{\alpha}, \tilde{\beta}, u, y, \ldots, u^{(n)}, y^{(n)}$. See [5] for the complete polynomial expression of the FPS. Since constraints are bilinear in the optimization variables, and $\mathcal{L}$ is assumed to be a polynomial, problem (3) is recast to a POP, which can be solved through semidefinite programming relaxation techniques (see, e.g., [6]).

IV. ACCOUNTING FOR THE DISCRETIZATION ERROR

When we identify a CT system from sampled data, we have to cope with discretization error, which is always introduced by any digital procedure. However, most of the existing CT identification approaches either neglect it or simply account for it by introducing a generic additive equation error. As a result, the identification algorithm may often lead to incorrect parameter estimates, even in the noise-free case.

In the SM approach proposed in this work, we introduce discretization errors by replacing $F(s)$ with $F(z)$. If such errors are neglected, the formulated POP may potentially be infeasible. To take into account the presence of the discretization error, we assume that they are bounded by a constant Δ_δ such that $|\delta_y^{(i)}(k)| \leq \Delta_\delta$ and $|\delta_u^{(i)}(k)| \leq \Delta_\delta$. If Δ_δ is known, it is possible to reformulate $\mathcal{D}$ replacing constraints of the kind of (6) with the following inequalities

$$\begin{aligned} -\Delta_\delta \leq x^{(i)}(k) + f_3 x^{(i)}(k-1) - f_1 x^{(i-1)}(k) + \\ - f_2 x^{(i-1)}(k-1) \leq \Delta_\delta \end{aligned} \tag{7}$$

where $x(t)$ represents either $u(t)$ or $y(t)$. However, in practice, Δ_δ is usually not a-priori known and the problem of its estimation from the data arises. An algorithm for computing the smallest possible value of Δ_δ such that $\mathcal{D} \neq \emptyset$ is proposed in this work.

V. SIMULATION STUDY

In this section, we present a simulation experiment performed to show the effectiveness of the proposed method. Input-output data are generated by simulating a CT system described by a second order transfer function $H(s)$ excited by a multi-sine input signal with amplitudes and phases randomly generated according to $\mathcal{N}(0,1)$ and frequencies between $0\,\mathrm{rad\,s^{-1}}$ and $15\,\mathrm{rad\,s^{-1}}$.

	θ_{true}	θ_{SM}	θ_{SRIVC}
α_0	16.3	16.654	16.972
α_1	2.2	2.2923	2.2734
β_0	-21	-21.848	-21.139
β_1	10.5	10.487	10.328
$\mathcal{L}_{\mathrm{test}}$	$-$	140.71	244.17

TABLE I

RESULTS WITH $T_s = 0.02\,\mathrm{s}$

Then, input and output sampled signals are corrupted by additive noise sequences $\eta(k)$ (bounded by $\Delta_\eta = 1.5$), and $\epsilon(k)$ (bounded by $\Delta_\epsilon = 0.5$). We select the squared ℓ_2-norm of the simulation error's residuals $\mathcal{L} = \|y - \tilde{y}\|_2^2$ as a cost function of the optimization problem and we set $\tau = 2\,\mathrm{s}$. All the solutions are obtained by means of SDP relaxation of the corresponding POPs with order of relaxation 2.

Neglecting the discretization error, the problem turns out to be infeasible. Instead, by adopting the procedure suggested in Section IV, we obtain upper bounds on the minimum discretization error as $2.2573e-4$. Using such value, we get the parameter estimates θ_{SM}. For the sake of comparison, we apply to the same data the SRIVC algorithm provided in the CONTSID toolbox obtaining estimates θ_{SRIVC}.

Finally a test dataset is generated by applying to $H(s)$ a square wave input signal. Then, the CT models corresponding to the parameter estimates θ_{SM} and θ_{SRIVC}, are compared with the true output evaluating $\mathcal{L}_{\mathrm{test}}$, the squared ℓ_2-norm of the simulation error. The true parameters, the estimates θ_{SM} and θ_{SRIVC} and $\mathcal{L}_{\mathrm{test}}$ are reported in table I.

VI. CONCLUSIONS

In this paper, we introduce an original approach for performing SM identification of SISO CT transfer functions from sampled input-output data corrupted by bounded noise. We provide a mathematical description of the feasible set in terms of polynomial constraints, and we show how to optimally select a model from such a set through convex relaxation of a polynomial optimization problem. In the proposed procedure we also provide a method to explicitly account for the effect of the unavoidable discretization error. Reported numerical results show the effectiveness of the proposed approach.

REFERENCES

[1] H. Garnier, M. Mensler, and A. Richard, "Continuous-time model identification from sampled data: Implementation issues and performance evaluation," *International Journal of Control - INT J CONTR*, vol. 76, pp. 1337–1357, 09 2003.

[2] M. M., N. J., P.-L. H., and W. É., *Bounding Approaches to System Identification*. Springer US, 1996.

[3] V. Cerone, D. Piga, and D. Regruto, "Set-membership error-in-variables identification through convex relaxation techniques," *IEEE Transactions on Automatic Control*, vol. 57, no. 2, pp. 517–522, 2012.

[4] R. Johansson, "Identification of continuous-time models," *IEEE Transactions on Signal Processing*, vol. 42, no. 4, pp. 887–897, 1994.

[5] V. Cerone, S. M. Fosson, S. Pirrera, and D. Regruto, "Set-membership identification of continuous-time systems through model transformation," *accepted for presentation at IEEE CDC 2022*, 2022.

[6] J. Lasserre, *Moments, Positive Polynomials and Their Applications*. Imperial College Press, Optimization series, Vol. 1, 2010.

Human-Robot Collaboration Using Fuzzy Adaptive Virtual Fixture Method for Dental Implant Surgery

Mohammad Hossein Hamedani*, Fan Shao, Fanny Ficuciello

Abstract

The purpose of this work is to develop a methodology to improve human-robot collaboration for robot-aided dental implant placement. In this study, a human-robotic implant system (HRIS) is designed according to a hand-guiding control to increase the accuracy and stability of osteotomy drilling based on the surgeon's decision, and robot motion during the implant placement. The proposed method is able to guide the surgeon's hand according to the pose of the desired placement. To guide and modify the pose of the surgeon's hand, the virtual fixture method is used as the main control approach. To verify the performance of the introduced method, the KUKA MED robot is used to perform the dental implant placement using the presented approach on a phantom head with a 3D jaw bone model. Additionally, the results between free-hand drilling and HRIS controlled drilling according to the apical center and head center of the implant placement are compared to evaluate the performance of the introduced method.

1 Introduction

Over the past years, the cooperation of robots and humans is becoming an important field of robotic application. The robotic assistance for Dental Implant Surgery (DIS) can be considered as a known application of human-robot cooperation. In Dental Implant Surgery (DIS), a missing tooth is replaced with dental implants. In this surgery, a dental prosthesis fixed in the jaw bone using an osseointegrated implant is defined as the direct structural connection between the bone and surface of an implant [1, 2]. According to Fig. 1, the dental implant should be placed first into the jawbone, and then a dental prosthesis is attached to the implant. The accuracy of some items such as position, angle, and depth within the jawbone has a direct impact on the quality of the dental implantation [3, 4]. Using the surgical robots in the DIS enables us to have a better view of the operative field and improve efficiently the surgical operation. According to Fig. 1, this study aimed to propose a method for human-robot collaboration using a hands-on approach to perform dental implant surgery. In

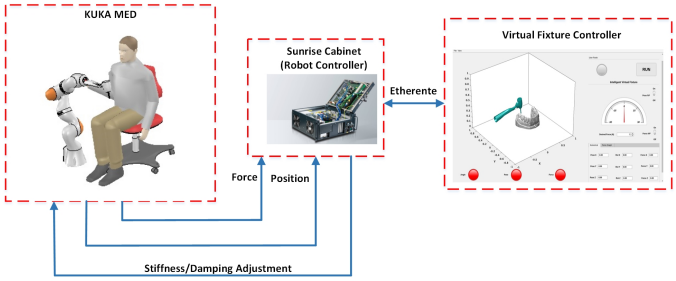

Figure 1: Proposed high-level controller structure. According to the virtual fixture method, the position and force interaction between the robot and human are received by the developed application software using Ethernet protocol and then the desired stiffness and damping are applied to manipulator.

addition, the virtual fixture approach is used as the main controller to modify the surgeon's hand. The main idea of the presented approach is that whenever the surgeon deviates from the desired path, the robot will try to revise the motion of the surgeon's hand by changing the stiffness and making a constraint in order to return the surgeon's hand to its desired path. To verify the performance of the introduced method, the KUKA MED robot is used to perform the dental implant placement using the presented approach on a phantom head with a 3D jaw bone model.

1.1 Dental Implant Robotic Systems

In implant surgery, a proper prosthesis should be planted abutment on dental parts lost to make people have a healthy mouth [5]. Accordingly, the accuracy of the insertion of the root specified the failure or success of the implant surgery. The implant surgery includes two processes: Pre-operative and intra-operative. The pre-operative is a process to establish surgery plans such as CT scan, guide manufacturing, and virtualization. In the intra-operative, the surgery is performed using the manufacturing guide. In general, three surgical approaches that can be used for dental implant placements consists of free-hand operation, static surgical template guided surgery, and online video navigated surgery [6], each of the mentioned methods has advantages and disadvantageous. Accordingly, the latter two increase the accuracy of the implant placement using guidance system and preoperative planning [7]. On the other hand, because of the complicated anatomy of the jawbone and insufficient visual field in intra-oral operations, the free-hand method has some concerns about the accuracy and safety of the dental implant placement [6]. Additionally, the preoperative planning and static surgical guide improve the accuracy of the operation, however, and because of the exciting inherent errors in the Computed Tomography (CT) image and 3D model reconstruction, there is the probability of deviation from the planned bone structure and resulting the useless of the surgical guide [7]. In order to use the navigation system for dental implant placement, the

surgeon should observe the real-time position of the drill on the screen and lead to increase the learning time for the surgeons with fewer experience [8, 9].

Using the robotic system for medical application in dental implant surgery has been widely addressed and investigated since 2000 [10, 11]. According to some recent studies such as [12, 13, 14], using the robotic system for dental implants could increase the quality of the intra-operative of the performance and improve the safety and accuracy of complex cases for example zygomatic implants. Recently, a robotic system name Yomi is developed as the robotic-assisted dental surgical system by the Neocis [13]. This robot includes a robotic manipulator and the process of the drilling and implant placement are performed by collaborating between surgeons and the operational arm. There is another robotic system is designed and developed by Yiming Zhao to conduct the implant placement and drilling autonomously using the preoperative plan with an optical navigation system [15].

1.2 Hands-on Robotic Surgery and Virtual Fixtures

Computer Integrated Surgery (CIS) technologies by combining the preoperative planning, robotic systems, innovative algorithms, video navigation, sensors, and human-machine interface (HMI) can increase the stability and robustness of the medical processes. CIS systems have been widely used in dental implants [16, 17]. Generally speaking, there are two main approaches including teleoperated system [18, 19] and hands-on technique [20, 21] to perform the surgical operations in terms of the semi-autonomous control structure for the robotic systems. In the case of the teleoperated method, the surgeon is quite in charge of the control the motion of the robot. The structure of this system is complex and includes three parts; slave manipulators, a master controller and sensory such as vision system to feedback information to the user [16]. According to the vision (and haptic) data, the surgeon moves the master controller and data transfer directly to the salve parts. There are many research addresses using teleoperated robots such as the Da Vinci system for surgical operation [22, 23, 24] However, in the hands-on approach, the human is always in contact with the robot, and therefore it is possible for the surgeon to supervise and control the motion of the robot directly. In addition, the robot is able to regulate intelligently the motion of the human. This method is often used to perform micromanipulation procedures, such as eye [25] or brain operations, urology, and microvascular. A hands-on robotic system can provide a balance between direct human control and autonomy.

The virtual fixture (or virtual constraint) method, according to its name, is a constraint obtained via software which limit the tool motion, imitating a mechanical constraints but with inherent flexibility [26, 27]. In the virtual fixture, software constraints are applied in order to increase safety by keeping the robot from entering a dangerous region of the workspace. Generally, the virtual fixture methods are classified into two main categories including Guidance Virtual Fixtures (GVF) and Forbidden Region Virtual Fixtures (FRVF). In the GVF approach, constraints keep the robot on the desired surfaces or path. Alterna-

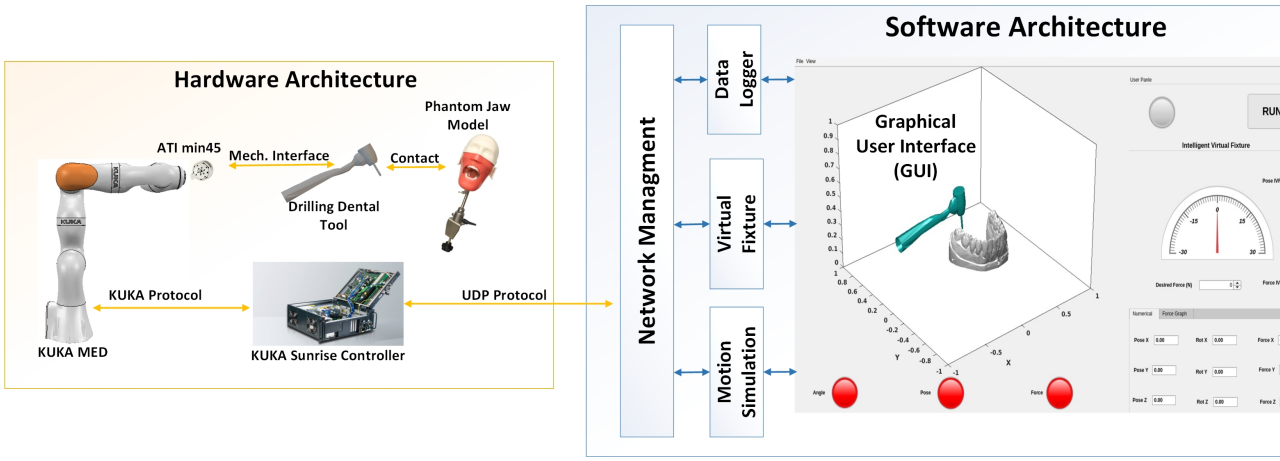

Figure 2: Proposed CIS structure for dental implant surgery

tively, FRVF keeps the robot out of the forbidden regions of the workspace [28]. In [29], a vision-based system is proposed for forbidden region virtual fixtures generation used to collision avoidance in robotic surgery. In [30], both GVF and FRVF are used to present a highly precise and safe polyp dissection surgery. In [31], a hands-on robotics craniotomy system using virtual restraint and safe isometric surfaces is presented to achieve efficiently, high accurate, and minimally invasive, and safe craniotomy.

In this work and according to the proposed controller structure illustrated in Fig. 1., a hands-on synergistic robotic with human-machine collaboration system is developed to perform the dental implant surgery. The proposed approach combines virtual fixture methods and impedance control of the robot to increase efficiently the accuracy of the implant positioning placement. In addition, a fuzzy mechanism is developed to tune the parameter of the virtual fixture. Therefore, the virtual fixture method is adapted according the task execution. In the rest of the paper, the architecture of the proposed hands-on system is introduced in section 2. In addition, the model of the robot and impedance profile, and proposed adaptive virtual fixtures is introduced in section 3. The passivity of the system is evaluated and guaranteed according to the method discussed in section 4.3. In the last section 5, the performance of the proposed controller is verified using the KUKA Med system and GUI developed for dental implant surgery.

2 The architecture of the proposed System

The proposed structure and experimental setup for the CIS are constructed as shown in Fig. 2, and a jaw model phantom is adopted for the operational test. KUKA Med, a lightweight robot manipulator from KUKA Company, is selected

as the surgeon fellow. It has a working range of 850mm and a load capacity of 7 kg, suitable for the requirements of dental implant placement. Because of the cooperation between the robot and surgeon, the robot is able to correct the human position and the user is able to supervise and control the motion of the robot. As result, the proposed CIS method for the dental implant can increase simultaneously both the safety and accuracy of the dental implant surgery. In Fig. 2, the drilling tool can be attached to the robot end-effector using the mechanical interface which is designed to mount and fix the drilling tool at the end of the robot arm. A head phantom is assembled to a fixed place.

The software application is developed using the MATLAB App Designer (v2021a) from MathWorks. To control the robot, the software application is connected to the controller interface of the robot using the UDP protocol. In addition, the developed app includes five main software tasks: Graphical User interface (GUI), Motion simulation, Network management, Datalogger, and last but not the least Virtual Fixture Controller.
GUI designed in order that the user easily enables and disables the cooperation of the robot and human only by clicking the specified button. In addition, there are some alarm lamps and gauges that are considered to illustrate the error position of the tool, accordingly the surgeon is able to track the error. One of the most important sections of the GUI is the tool motion simulator. Using this software task, the surgeon is able to observe the motion and place of the tool in the 3D space to control the tool to the desired tooth position for drilling operation.
Other features of the designed app are network management and data logger. The former is used to receive data including the position or force sensor and send the command data such as desired stiffness and damping of the robot. The latter software task is developed in order to the loge the required data such as the position of the tool and applied force on the tool. By using logged data, the performance of the surgeon during the dental implant surgery can be analyzed or used to train the other users.

3 Robot Controller Method

The KUKA Med is a 7DOF robot that provides a steady robotic manipulator for different applications. According to the end-effector of the robot, different tools can be attached to the robot using various mechanical interfaces. The hands-on robotic system enables surgeons to perform tremor-free surgical maneuvers. The robot and user both keep the surgical instruments and move them collaboratively to achieve desired surgical control goals.

3.1 Model of Hands-on Robotic system

In this section, the model of the hands-on robotic system is presented. In addition, the impedance control structure is discussed. The dynamics model of

the robot manipulator in the Cartesian space can be considered as [32],

$$\mathbf{M}(\mathbf{x})\ddot{\mathbf{x}} + \mathbf{D}(\mathbf{x}, \dot{\mathbf{x}})\dot{\mathbf{x}} + \mathbf{g}(\mathbf{x}) = \mathbf{u} - \mathbf{f_h}\,, \tag{1}$$

where $\mathbf{x}$ is the displacement vector of link pose. $\boldsymbol{u} \in \mathbb{R}^{N\times 1}$ is the applied signal control at each joint of manipulator. $\mathbf{M}(\mathbf{x}) \in \mathbb{R}^{N\times N}$ is the inertia matrix, $\mathbf{D}(\mathbf{x}, \dot{\mathbf{x}}) \in \mathbb{R}^{N\times N}$ is the Coriolis and centrifugal matrix, and $\mathbf{g}(\mathbf{x}) \in \mathbb{R}^{N\times 1}$ is the gravitational vector. In addition, $\mathbf{f_h} \in \mathbb{R}^{N\times 1}$ is the external forces vector applied by human at the end-effector. It is assumed that the states $\mathbf{x}$, $\dot{\mathbf{x}}$ as well as human force $\mathbf{f_h}$ are available for feedback.
The contact model of the robot and human hands is shown in Fig.3. In this work, to have a simple case, we consider the interaction force applied by human's hand to the end-effector of the robot is modeled by a single spring as

$$\mathbf{f_h} = \mathbf{K_h}(\mathbf{x} - \mathbf{x_h})\,, \tag{2}$$

where $\mathbf{x_h}$ is the human hand's pose. $\mathbf{K_h} \in \mathbb{R}^{N\times N}$ is the diagonal stiffness matrix of human hand.

3.2 Impedance Control

Impedance control is a classical control approach that can be used as indirect force control method. Hogan in [33] presented the main concept of the impedance controller method and using impedance parameters such as inertia, stiffness, and damping it can adapt the modulated the end-effector behavior according to desired interaction with the external environment. In order to interact with an unknown environment is required that the impedance parameters can be tuned in order to perform various tasks. In this work, the impedance parameter should be adapted according to the algorithm of the virtual fixture. The desired impedance model of the robot can be considered as

$$\mathbf{M}\ddot{\mathbf{e}} + \mathbf{B}\dot{\mathbf{e}} + \mathbf{K}\mathbf{e} = \mathbf{e_f}\,, \tag{3}$$

where $\mathbf{e} = \mathbf{x_d} - \mathbf{x_c}$ and $\tilde{\mathbf{e}_f} = \mathbf{f_d} - \mathbf{f_h}$ are the pose error and force error, receptively. $\mathbf{x_d} \in \mathbb{R}^{\mathbf{N}\times\mathbf{1}}$ and $\mathbf{x_c} \in \mathbb{R}^{\mathbf{N}\times\mathbf{1}}$, are the desired and command position vector. In addition, $\mathbf{M}$, $\mathbf{B}$, and $\mathbf{K} \in \mathbb{R}^{\mathbf{N}\times\mathbf{N}}$ are the inertia, damping and stiffness gains, receptively, and are considered as a positive diagonal matrix.

Assumption 1. *It can be assumed that if the robot has a tight position control then* $\mathbf{x} = \mathbf{x_c}$.

Without loss of generality and because of the diagonal matrices of desired impedance profile in (3) , let us take one dimension of impedance model as:

$$m\ddot{e} + b\dot{e} + ke = e_f\,. \tag{4}$$

The impedance model of the robot and human hand as an interaction environment is illustrated in Fig. 3.

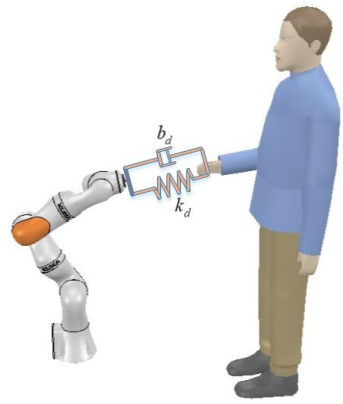

Figure 3: Impedance model of the robot and user

3.3 Impedance Profile for Hands-on Collaboration

According to section 3.2, the desired trajectory x_d is the human hand position. In fact, the robot should be able to follow human hands' motion in order that the robot keeps in contact with the user's hand.
To track the hand, we consider the position of the human as the desired trajectory $x_d = x_h$ and according to assumption 1, we rewrite the (3) as

$$\mathbf{M}(\ddot{\mathbf{x}}_\mathbf{h} - \ddot{\mathbf{x}}) + \mathbf{B}(\dot{\mathbf{x}}_\mathbf{h} - \dot{\mathbf{x}}) + \mathbf{K}(\mathbf{x}_\mathbf{h} - \mathbf{x}) = \mathbf{e}_\mathbf{f}\,. \tag{5}$$

where $e = x_h - x$. If both the desired and hand force are supposed to be zero $\mathbf{e}_f = 0$, then it can be observed from (5) that $x \to x_h$ for the steady-state. In fact, the robot tracks the human hand.

4 Proposed Adaptive Virtual Fixture

To adapt the desired impedance profile according to the desired goal, a virtual fixture method is presented. The proposed method is able to increase efficiently the accurate and stable osteotomy drilling based on the surgeon's decision and robotic manipulators motion during the implant placement. As discussed in the introduction, the virtual fixture can be classified into two main classes: FRVF and GVF. In general, GVF is suitable to guide the robot end-effector towards the desired path, a FRVF is used for the constraining surfaces or delicate region that the robot is forbidden to enter.

4.1 Kinematics of the System

In this work, the focus is on the GVF method. Usually, two quantities are required to describe a GVF: its geometry and the constraint enforcement method.

For the geometry of the GVF, the robot should follow human motion. Therefore, the desired geometry path is defined by the human hand. However, the desired point is the tooth position considered for drilling. According to the Fig. 4, three main frames are considered including $\{F_W\}$, $\{F_T\}$, and $\{F_D\}$ which are the world frame, tool frame, and desired frame, receptively. In addition, the pose/rotation of each frame can be defined as:

$$\mathbf{x_i} = [x_P^T \; x_R^T]^T \qquad i = 1, 2, 3 \tag{6}$$

where $x_P \in \mathbb{R}^{3\times1}$, and $x_R \in \mathbb{R}^{3\times1}$ are the position and orientation parameters measured in the world frame. According to Fig. 4, it can be written:

$$\mathbf{x_1} = \mathbf{x_2} - \mathbf{x_3} \tag{7}$$

The both vectors of the $\mathbf{x_2}$ and $\mathbf{x_3}$ are available. The $\mathbf{x_2}$ can be obtained by the direct kinematics equations of the KUKA Med robot and the $\mathbf{x_3}$ is measured by the camera or any other methods. In addition, it can be defined:

$$\mathbf{e} = \mathbf{x_1} \tag{8}$$

where $\mathbf{e}$ is the same as the symbol used in the (3).

4.2 Fuzzy Adaptive Virtual Fixture

According to the GVF structure to have an attractive behavior towards the desired path, a constraint enforcement approach including a spring-damper force needs to be considered. In fact, the $\mathbf{f_d}$ should be designed in order that the robot applies the required force on the human hand to modify the motion. Therefore, the constraint force can be presented as

$$\mathbf{f_{vf}}(\mathbf{e}, \dot{\mathbf{e}}) = -\mathbf{K}_{vf}\mathbf{e} - \mathbf{B}_{vf}\dot{\mathbf{e}} \tag{9}$$

where $\mathbf{K}_{vf} \in \mathbb{R}^{N\times N}$ and $\mathbf{D}_{vf} \in \mathbb{R}^{N\times N}$ are positive definite matrices and properly designed diagonal. By considering the GVF defined in (9) such that $\mathbf{f_d} = \mathbf{f_{vf}}$ and impedance profile (3), the closed loop behavior can be obtained as:

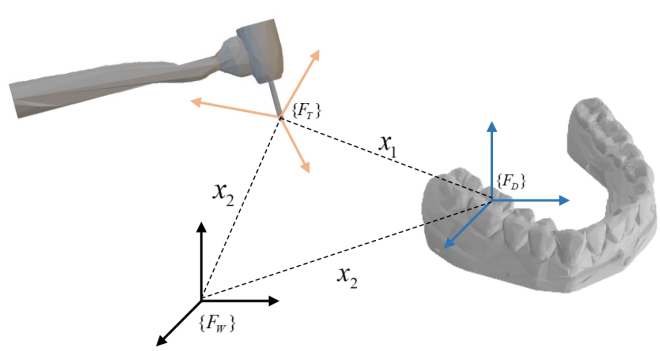

Figure 4: Guidance Virtual Fixture (GVF) geometry and desired path.

$$\mathbf{M_d}\ddot{\mathbf{e}} + \mathbf{B_d}\dot{\mathbf{e}} + \mathbf{K_d}\mathbf{e} = \mathbf{f_h}\,, \tag{10}$$

where $\mathbf{B}_d = \mathbf{B}_c + \mathbf{B}_{vf}$ and $\mathbf{K}_d = \mathbf{K}_c + \mathbf{K}_{vf}$. According to the (10), the combination of the GVF and general impedance profile is similar to variable impedance control approach.
To adapt GVF enforcement constraint in (9) for the human-robot collaboration, a nonlinear and varying stiffness profile is considered for the adapting $\mathbf{K}_{vf}$. Accordingly, each diagonal elements of the stiffness matrix to be

$$k_{vf,ii}(e,\dot{e}) = \beta(e,\dot{e})K_{max} \qquad \forall i = 1,...,N \tag{11}$$

where $k_{vf,ii}$ is the diagonal element of the $\mathbf{K}_{vf}$ matrix, $\beta(e,\dot{e})$ is the impedance shaping function, and finally e is the $i-th$ component of the vector $\mathbf{e}$. In addition, t is the time and K_{max} denotes the maximum value for the adapting the stiffness. Using $\beta(e,\dot{e})$ function, the robot is enable to adapt its impedance parameters to modify and correct human motion. We can propose $\beta(e,\dot{e})$ as

$$\beta(e,\dot{e}) = \begin{cases} 0 & |e| \geq l \\ k_s(e,\dot{e}) & otherwisel \end{cases} \tag{12}$$

where the $k_s(e,\dot{e})$ is adapted using the fuzzy rules in Table 1. One of the main properties of the fuzzy logic is that the rules are set in natural language. The fuzzy logic leads to make an inference system in which decisions are flexible, nonlinear, and without discontinuities which closer to human manner than classical logic is [34, 35, 36]. Positive, Zero, and Negative are considered as the

Table 1: Proposed Fuzzy Rules To Tune k_s

Rule No.	IF	THEN
$\mathbf{R_1}$	$\mathbf{e}$ is Positive and $\dot{\mathbf{e}}$ is Positive	$\mathbf{k_s}$ is Large
$\mathbf{R_2}$	$\mathbf{e}$ is Positive and $\dot{\mathbf{e}}$ is Negative	$\mathbf{k_s}$ is Small
$\mathbf{R_3}$	$\mathbf{e}$ is Zero and $\dot{\mathbf{e}}$ is Negative	$\mathbf{k_s}$ is Large
...	...	...
$\mathbf{R_n}$	$\mathbf{e}$ is Negative and $\dot{\mathbf{e}}$ is Positive	$\mathbf{k_s}$ is Small

linguistic terms of the If part of the fuzzy rules, and Small, Medium, and Large are the linguistic terms of the consequence part. According to the mentioned linguistic term for the fuzzy rules, all membership functions of their corresponding fuzzy sets are Gaussian functions such as:

$$\mu_m(x) = e^{-\frac{(x-c_m)^2}{2\sigma_m}} \tag{13}$$

where x is the input of the membership function and takes the value $\mathbf{e}$ and $\dot{\mathbf{e}}$ as the position and rate of position error. Additionally, m is used to distinguish the membership function for each of the linguistic terms. The scalar parameters of c_m and σ_m in (13) are chosen based on the knowledge about the constrained robot and controlling of the manipulator.

4.3 Passivity Analysis

In this section, the passivity of the closed loop system is evaluated. According to definition of the passivity a dynamical system as [35] :

$$\begin{cases} \dot{\mathbf{x}} = f(x) + g(x)u \\ y = p(x) \end{cases} \tag{14}$$

where x is the state, u is the input and y is output of the system, is passive if there exists a positive semi-definite (lower bounded function) and continuously differentiable V such that:

$$\mathbf{V}(\mathbf{x}(\mathbf{t})) - \mathbf{V}(\mathbf{x_0}) \leq \int_{\mathbf{0}}^{\mathbf{t}} \mathbf{y}(\tau)^{\mathbf{T}}\mathbf{u}(\tau)\,\mathbf{d}\tau \tag{15}$$

By considering the derivative form of (15) yields:

$$\mathbf{V}(\dot{\mathbf{x}}(\mathbf{t})) \leq y^T u \tag{16}$$

It can be observed that the model structure presented in (10) is not guaranteed the passivity of the system. Therefore, in this work, the thank theory is used to guarantee passivity. Accordingly, the energy function of the system is considered as:

$$\mathbf{V}(\mathbf{e}, \dot{\mathbf{e}}) = \frac{\mathbf{1}}{\mathbf{2}}\dot{\mathbf{e}}^{\mathbf{T}}\mathbf{M_d}\dot{\mathbf{e}} + \frac{\mathbf{1}}{\mathbf{2}}\mathbf{e}^{\mathbf{T}}\mathbf{K_d}\mathbf{e} \tag{17}$$

Now, the time derivative of (17) is:

$$\dot{\mathbf{V}} = \dot{\mathbf{e}}^T\mathbf{M_d}\ddot{\mathbf{e}} + \mathbf{e}^{\mathbf{T}}\mathbf{K_d}\dot{\mathbf{e}} + \frac{\mathbf{1}}{\mathbf{2}}\mathbf{e}^{\mathbf{T}}\dot{\mathbf{K}}_{\mathbf{d}}\mathbf{e} \tag{18}$$

By substituting the dynamic of (10) in (17), it yields:

$$\dot{\mathbf{V}} = \dot{\mathbf{e}}^T\mathbf{f_h} - \dot{\mathbf{e}}^{\mathbf{T}}\mathbf{B_d}\dot{\mathbf{e}} + \frac{\mathbf{1}}{\mathbf{2}}\mathbf{e}^{\mathbf{T}}\dot{\mathbf{K}}_{\mathbf{vf}}\mathbf{e}. \tag{19}$$

It can easily be observed that $\dot{\mathbf{K}}_{vf}$ can be positive or negative definite. As a result, the sign of the (19) is not definite. One of the solutions for this problem is to design a passivity preserving controller that follows the desired stiffness profile while restricting the changes by considering the (16). In order to reformulate the desired impedance profile by considering the passivity, it is required to define the α parameters for the variable stiffness of the system as:

$$\mathbf{K}_d = \alpha\mathbf{K_{vf}} \tag{20}$$

The parameter of α is defined after introducing the dynamic of the tank system. Using the concept of the energy tanks, introduced in [37], which goal at recovering the dissipated energy of the system to implement a less conservative impedance variation without violating the overall passivity of the system. In

the tank impedance control, a first-order dynamic system, as a reservoir (tank), is considered in parallel with impedance profile to observe the passivity of the system. Accordingly, the manipulator is responsible to store energy according to the following function:

$$\mathbf{T} = \frac{1}{2}z^2 \tag{21}$$

Now, the energy of the system with the tank can be rewritten as:

$$\mathbf{V}(\mathbf{e}, \dot{\mathbf{e}}, z) = \frac{1}{2}\dot{\mathbf{e}}^T\mathbf{M_d}\dot{\mathbf{e}} + \frac{\mathbf{1}}{\mathbf{2}}\mathbf{e^T}\mathbf{K_d}\mathbf{e} + \frac{1}{2}z^2 \tag{22}$$

and its derivative is:

$$\mathbf{V}(\mathbf{e}, \dot{\mathbf{e}}, z) = \dot{\mathbf{e}}^T\mathbf{f_h} - \dot{\mathbf{e}}^\mathbf{T}\mathbf{B_d}\dot{\mathbf{e}} + \frac{\mathbf{1}}{\mathbf{2}}\mathbf{e^T}\dot{\mathbf{K}}_\mathbf{vf}\mathbf{e} + \dot{z}z \tag{23}$$

and dynamic of the tank is described as:

$$\dot{z} = \frac{\phi}{z}\dot{\mathbf{e}}^T\mathbf{B_d}\dot{\mathbf{e}} - \frac{\alpha}{2z}\mathbf{e^T}\dot{\mathbf{K}}_\mathbf{vf}\mathbf{e} \tag{24}$$

where $z \in \mathbb{R}$ is the only scalar state of the tank and $\phi, \alpha \in \{0, 1\}$ are parameters used to enforce the upper stored energy bound in the tank $\bar{T}$. In addition, a lower threshold δ must be consider for the thank energy when the $z = 0$. The value of ϕ and α are specified as the following:

$$\alpha = \begin{cases} 1 & T \geq T_{min} \\ 0 & otherwisel \end{cases} \tag{25}$$

$$\phi = \begin{cases} 1 & T \leq T_{max} \\ 0 & otherwisel \end{cases} \tag{26}$$

where the value of the T_{min} and T_{max} are the design parameters and specified by the user. Accordingly, the energy function of the system with the tank and defined parameters is:

$$\mathbf{V}(\mathbf{e}, \dot{\mathbf{e}}, z) = \dot{\mathbf{e}}^T\mathbf{f_h} - (\mathbf{1} - \phi)\dot{\mathbf{e}}^\mathbf{T}\mathbf{B_d}\dot{\mathbf{e}} + \frac{\mathbf{1}}{\mathbf{2}}(\mathbf{1} - \alpha)\mathbf{e^T}\dot{\mathbf{K}}_\mathbf{vf}\mathbf{e} \tag{27}$$

When the $\alpha = 1$, the tank exchange the energy to the impedance profile using term $\mathbf{K_{vf}}$. In addition, $\alpha = 0$ means that the energy of th tank approaches to lower bound and the effect of the $\mathbf{K_{vf}}$ in not considered in the system. As a result, the passivity of the system is guaranteed by this method.

5 Experimental Results

In this section, the experimental setup is described and the proposed Fuzzy virtual fixture experiments are presented. To verify the performance of the

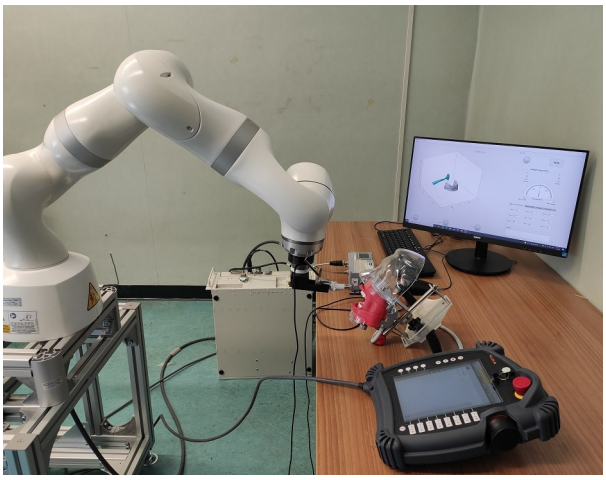

Figure 5: Experimental setup to verify the proposed approach

proposed controller, the experimental setup in Fig. 5 is considered. According to Fig. 5, the robot is equipped with the dental drilling tool using the mechanical interface. In addition, a min45 ATI force sensor is used to measure the force. There are two software programmers is developed for the robot. The software is run by the controller of the robot (sunrise cabinet) and is developed by the java programming language. Another software is a GUI application using MATLAB and run by the client computer. The main task of the controller of the robot is to receive the impedance parameters from the client computer and apply them to the robot a another task is that to send the pose, force, and time measurement of the robot in order to synchronize with the client computer. In this setup. the client computer is responsible to perform the main controller method of the robot including, the Monitoring system, GUI, Fuzzy adaptive VF method. All the hardware including the force sensor, the sunrise cabinet, and the client computer are connected together using User Datagram Protocol (UDP) network. In addition, Fig.6 depicts the hands-on robotic collaborative in which the user can easily control the motion of the tool and robot.

5.1 Implementation Algorithm

To implement hands-on robotic collaboration, the robot is responsible to correct the motion of the human hand in two directions: X and Y. According to the Algorithm 1, the implementation algorithm includes four main phases. In the first phase named free motion, the robot has low stiffness in all directions and can move easily in space. When the robot is approaching the desired goal position, the algorithm is changed to the next phase. In the second phase, the robot increases the stiffness in the Z and Y directions, and the surgeon is able to correct the X direction by using the GUI designed for simulation of the location

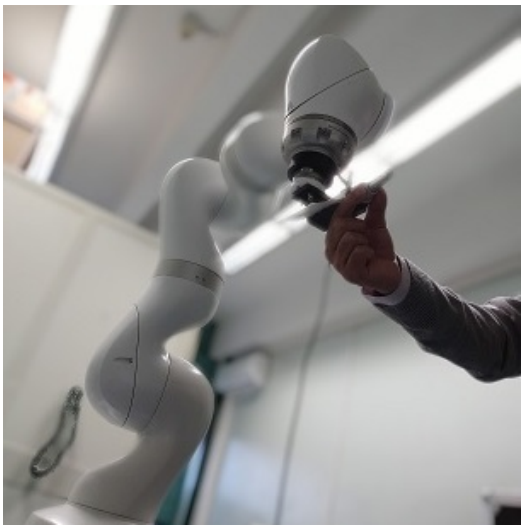

Figure 6: Hands-on robotic collaborative

of the tool and desired tooth. After modifying the X direction, the phase of the algorithm is changed to the third step. In this step, the stiffness in the Z and X directions rises, and the Y direction of the robot should be modified. In the fourth phase as the last step, the robot is only able to move in the Z direction to implement the drilling task. In addition, the fuzzy surface rule for the case study in the next section is illustrated in Fig. 7.

5.2 Case Study

Two scenarios are considered: smooth motion, and tremor motion. In the case of the smooth motion, the user moves the robot according to the monitoring error alarm to the desired point. However, in the tremor motion, the user deliberately moves the robot in a different direction to insert variable stiffness to the end-effector of the robot. In this case, the fuzzy rules are fired and it can be able to evaluate the fuzzy control method and passivity of the system. In both scenarios, the tank energy is enabled and according to the Algorithm 1, four main steps are considered. For the free motion, the stiffness of all directions (X,Y,Z) is considered $500N/m$. For the X modification, the stiffness in the direction X is specified by the fuzzy rules, and for the Y and Z direction, the stiffness is constant value $3000N/m$. For the Y modification phase, the stiffness for Y is specified by the fuzzy rules, and in the directions of X and Z, the stiffness is constant value $3000N/m$. Finally, for the Z motion, the stiffness of the robot in the Z direction is $500N/m$ and for the two others direction is $3000N/m$.
For the Smooth motion, the error position, stiffness, and tank energy are depicted in Figs. 8, 9, and 10, respectively. According to Fig. 9, the stiffness for each of the phases includes (1) Free motion, (2) Modification of X Direction, (3)

Algorithm 1 Modification X and Y direction of the surgeon hands

Require: End-effector Position (X,Y,Z)
  $Distance = \sqrt{X^2 + Y^2 + Z^2}$
  if $Distance < Minmum$ **then**
    Increasing the Stiffness in the Y and Z direction.
    Modifying the X Position using Fuzzy Virtual Fixture.
  end if
  if $XErrorPostion < MinmumError$ **then**
    Increasing the Stiffness in the X and Z direction.
    Modifying the Y Position using Fuzzy Virtual Fixture.
  end if
  if $YErrorPostion < MinmumError$ **then**
    while *VF is Enable* **do**
      Increasing the Stiffness in the X and Y direction.
      Decreasing the Stiffness of Z and robot is only able moving in the Z direction
    end while
  end if

Modification of Y Direction, and (4) Z Free motion are depicted and specified by the arrows. Changing the value of the stiffness are performing according to the presented Algorithm 1. By considering Fig. 8, using the proposed adaptive fuzzy VF, error position converges to zero.
For the tremor motion, the error position, stiffness, and tank energy are presented in Figs. 11, 12, and 13, respectively. According to Fig. 12, the stiffness for each of phases including: Free motion, Modification of X Direction, Modification of Y Direction, and Z Free motion are illustrated by the arrows. It can be observed that by moving the hand's motion in the different direction, the fuzzy rules enable and by changing the value of the stiffness and inserting forces try to keep the surgeon hand in the right direction. In addition, the tank energy is depicted in the Fig. 13 and the energy of the tank decreases by starting changing the stiffness of the manipulator around the 0.5s. At the end of the task around 2.5s, the tank energy return back to the a constant level. The results approve that the proposed approach and algorithm used to perform dental implant surgery can modify the surgeon's hand motion.

6 Conclusion

In this article, a hands-on robotic system using fuzzy adaptive virtual fixtures control is introduced for dental implant surgery. The proposed method generates the desired impedance profile to interact with the human hand. The introduced adaptive approach is used to adapt the impedance parameter. Using the proposed adaptive online approach, the stiffness parameters are updated to specify the new impedance profile to enhance the position tracking efficiency.

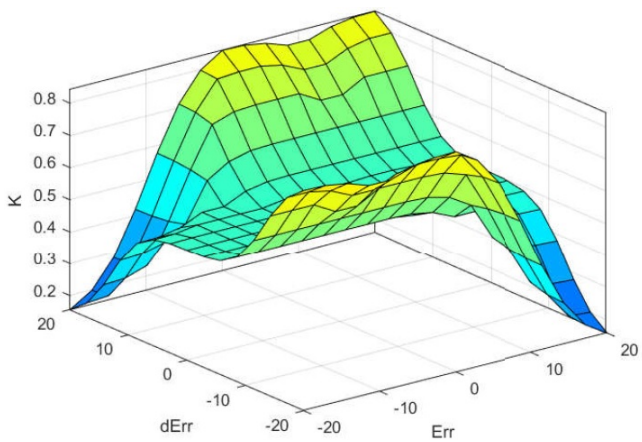

Figure 7: Fuzzy Surface Rules

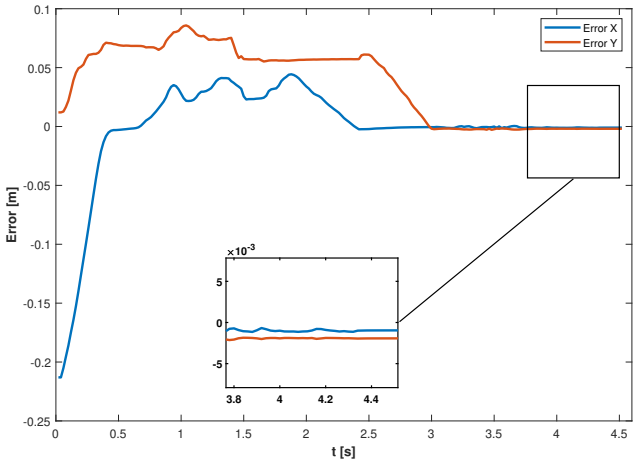

Figure 8: Error Position for the Case 1

The conditions of the stability of the closed-loop system are evaluated using the tank-energy passivity approach. To verify the performance of the proposed approach, experimental studies are conducted. The introduced approach is not only can be applied for dental implant surgery, but it can also be used for any hands-on robotic surgical operation that required accurate position control. As a result, the proposed adaptive virtual fixtures provide a more effective approach for hands-on robotic collaborative control.

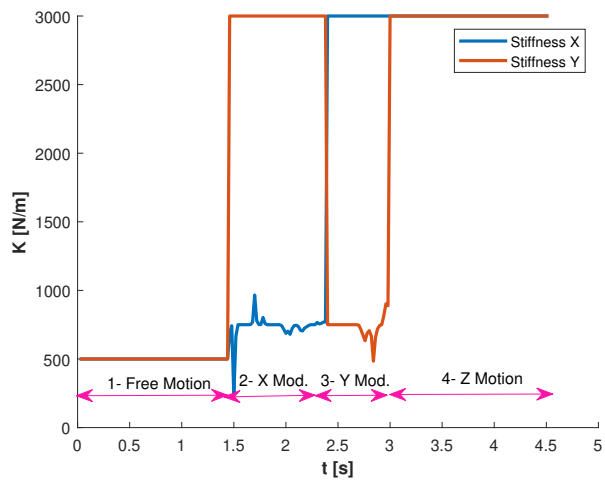

Figure 9: Stiffness for the Case 1

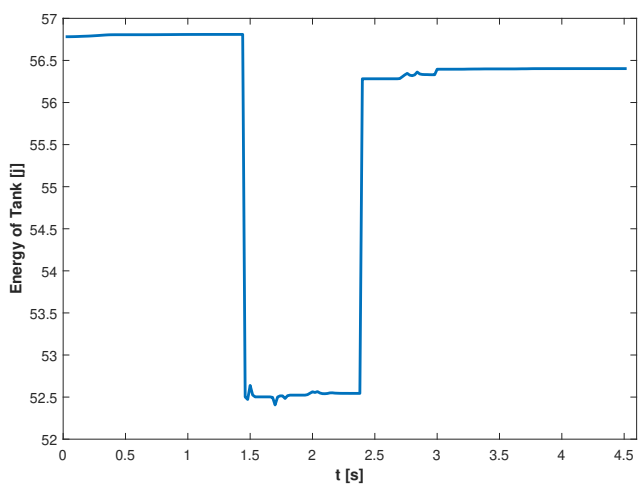

Figure 10: Tank Energy for the Case 1

References

[1] K.-j. Cheng, T.-s. Kan, Y.-f. Liu, W.-d. Zhu, F.-d. Zhu, W.-b. Wang, X.-f. Jiang, and X.-t. Dong, "Accuracy of dental implant surgery with robotic position feedback and registration algorithm: An in-vitro study," *Computers in Biology and Medicine*, vol. 129, p. 104153, 2021.

[2] T.-s. Kan, K.-j. Cheng, Y.-f. Liu, R. Wang, W.-d. Zhu, F.-d. Zhu, X.-

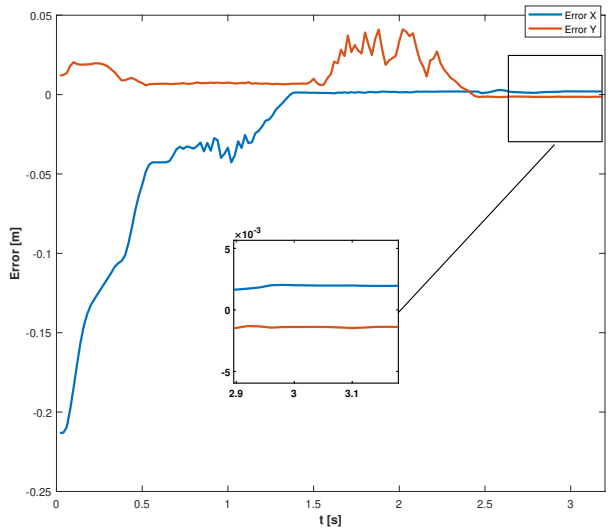

Figure 11: Error Position for the Case 2

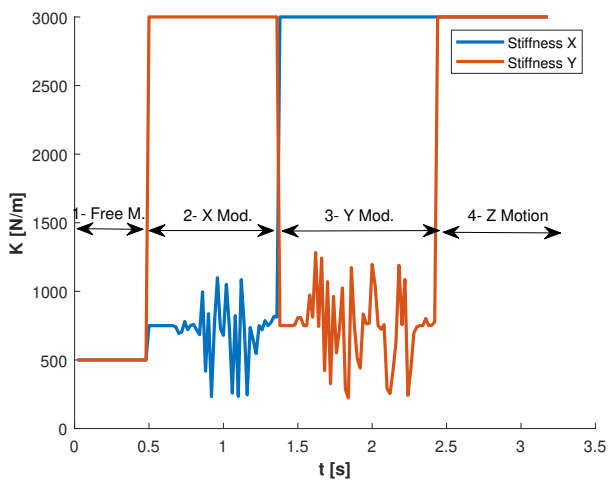

Figure 12: Stiffness for the Case 2

f. Jiang, and X.-t. Dong, "Evaluation of a custom-designed human–robot collaboration control system for dental implant robot," *The International Journal of Medical Robotics and Computer Assisted Surgery*, p. e2346, 2021.

[3] C. Monaco, A. Arena, L. Corsaletti, V. Santomauro, P. Venezia, R. Cavalcanti, A. Di Fiore, and G. Zucchelli, "2d/3d accuracies of implant posi-

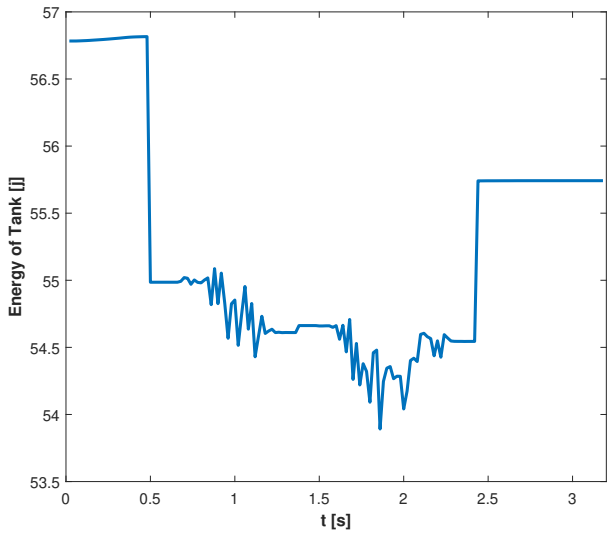

Figure 13: Tank Energy for the Case 2

tion after guided surgery using different surgical protocols: A retrospective study," *Journal of prosthodontic research*, vol. 64, no. 4, pp. 424–430, 2020.

[4] T. Fortin, G. Champleboux, S. Bianchi, H. Buatois, and J.-L. Coudert, "Precision of transfer of preoperative planning for oral implants based on cone-beam ct-scan images through a robotic drilling machine: An in vitro study," *Clinical Oral Implants Research*, vol. 13, no. 6, pp. 651–656, 2002.

[5] G. Kim, H. Seo, S. Im, D. Kang, and S. Jeong, "A study on simulator of human-robot cooperative manipulator for dental implant surgery," in *2009 IEEE international symposium on industrial electronics*. IEEE, 2009, pp. 2159–2164.

[6] N. Panchal, L. Mahmood, A. Retana, and R. Emery, "Dynamic navigation for dental implant surgery," *Oral Maxillofac Surg Clin North Am*, vol. 31, no. 4, pp. 539–47, 2019.

[7] J. Gargallo-Albiol, S. Barootchi, O. Salomó-Coll, and H.-l. Wang, "Advantages and disadvantages of implant navigation surgery. a systematic review," *Annals of Anatomy-Anatomischer Anzeiger*, vol. 225, pp. 1–10, 2019.

[8] T.-M. Sun, H.-E. Lee, and T.-H. Lan, "The influence of dental experience on a dental implant navigation system," *BMC Oral Health*, vol. 19, no. 1, pp. 1–11, 2019.

[9] A. Jorba-García, R. Figueiredo, A. González-Barnadas, O. Camps-Font, and E. Valmaseda-Castellón, "Accuracy and the role of experience in dynamic computer guided dental implant surgery: An in-vitro study," *Medicina oral, patologia oral y cirugia bucal*, vol. 24, no. 1, p. e76, 2019.

[10] D. Senkal, "Haptic surgical aid system with magnetorheological brakes for dental implants," Ph.D. dissertation, Citeseer, 2009.

[11] W. Korb, R. Marmulla, J. Raczkowsky, J. Mühling, and S. Hassfeld, "Robots in the operating theatre—chances and challenges," *International journal of oral and maxillofacial surgery*, vol. 33, no. 8, pp. 721–732, 2004.

[12] N. J. Vickers, "Animal communication: when i'm calling you, will you answer too?" *Current biology*, vol. 27, no. 14, pp. R713–R715, 2017.

[13] S. Rawal, D. E. Tillery Jr, and P. Brewer, "Robotic-assisted prosthetically driven planning and immediate placement of a dental implant." *Compendium of continuing education in dentistry (Jamesburg, NJ: 1995)*, vol. 41, no. 1, pp. 26–30, 2020.

[14] Z. Cao, C. Qin, S. Fan, D. Yu, Y. Wu, J. Qin, and X. Chen, "Pilot study of a surgical robot system for zygomatic implant placement," *Medical engineering & physics*, vol. 75, pp. 72–78, 2020.

[15] Z. Haidar, "Autonomous robotics: A fresh era of implant dentistry... is a reality!" *Journal of Oral Research*, vol. 6, no. 9, pp. 230–231, 2017.

[16] T. Haidegger, B. Benyó, L. Kovács, and Z. Benyó, "Force sensing and force control for surgical robots," *IFAC Proceedings Volumes*, vol. 42, no. 12, pp. 401–406, 2009.

[17] R. A. Faust, *Robotics in surgery: history, current and future applications*. Nova Publishers, 2007.

[18] K. Chandrasekaran, A. Somayaji, and A. Thondiyath, "Design of a flexure-based compliant grasper for the master arm of a surgical robot," in *Frontiers in Biomedical Devices*, vol. 84812. American Society of Mechanical Engineers, 2021, p. V001T12A007.

[19] T. B. Sheridan, "Telerobotics," *Automatica*, vol. 25, no. 4, pp. 487–507, 1989.

[20] T. Kastritsi and Z. Doulgeri, "A controller to impose a rcm for hands-on robotic-assisted minimally invasive surgery," *IEEE Transactions on Medical Robotics and Bionics*, vol. 3, no. 2, pp. 392–401, 2021.

[21] M. Jakopec, S. J. Harris, F. R. y Baena, P. Gomes, and B. L. Davies, "The acrobot® system for total knee replacement," *Industrial Robot: An International Journal*, 2003.

[22] C. D'Ettorre, A. Mariani, A. Stilli, F. Rodriguez y Baena, P. Valdastri, A. Deguet, P. Kazanzides, R. H. Taylor, G. S. Fischer, S. P. DiMaio *et al.*, "Accelerating surgical robotics research: A review of 10 years with the da vinci research kit," *IEEE Robotics and Automation Magazine*, 2021.

[23] A. A. Remirez, M. F. Rox, T. L. Bruns, P. T. Russell, and R. J. Webster III, "A teleoperated surgical robot system," *Neurosurgical Robotics*, pp. 49–61, 2021.

[24] F. Loschi, N. Piccinelli, D. Dall'Alba, R. Muradore, P. Fiorini, and C. Secchi, "An optimized two-layer approach for efficient and robustly stable bilateral teleoperation," in *2021 IEEE International Conference on Robotics and Automation (ICRA)*. IEEE, 2021, pp. 12 449–12 455.

[25] A. Ebrahimi, M. Urias, N. Patel, R. H. Taylor, P. L. Gehlbach, and I. Iordachita, "Adaptive control improves sclera force safety in robot-assisted eye surgery: A clinical study," *IEEE Transactions on Biomedical Engineering*, 2021.

[26] L. B. Rosenberg, "Virtual fixtures: Perceptual tools for telerobotic manipulation," in *Proceedings of IEEE virtual reality annual international symposium*. IEEE, 1993, pp. 76–82.

[27] S. A. Bowyer, B. L. Davies, and F. R. y Baena, "Active constraints/virtual fixtures: A survey," *IEEE Transactions on Robotics*, vol. 30, no. 1, pp. 138–157, 2013.

[28] S. Payandeh and Z. Stanisic, "On application of virtual fixtures as an aid for telemanipulation and training," in *Proceedings 10th Symposium on Haptic Interfaces for Virtual Environment and Teleoperator Systems. HAPTICS 2002*. IEEE, 2002, pp. 18–23.

[29] R. Moccia, C. Iacono, B. Siciliano, and F. Ficuciello, "Vision-based dynamic virtual fixtures for tools collision avoidance in robotic surgery," *IEEE Robotics and Automation Letters*, vol. 5, no. 2, pp. 1650–1655, 2020.

[30] J. Feng, X. Li, X. Xiao, B. Ouyang, and J. Fang, "Virtual fixtures assistance for safe polyp dissection in minimally invasive robotic surgery," in *2021 5th International Conference on Automation, Control and Robots (ICACR)*. IEEE, 2021, pp. 150–155.

[31] C. Xu, L. Lin, Z. Mar Aung, G. Chai, and L. Xie, "Research on spatial motion safety constraints and cooperative control of robot-assisted craniotomy: Beagle model experiment verification," *The International Journal of Medical Robotics and Computer Assisted Surgery*, vol. 17, no. 2, p. e2231, 2021.

[32] O. Khatib, E. Demircan, V. De Sapio, L. Sentis, T. Besier, and S. Delp, "Robotics-based synthesis of human motion," *Journal of physiology-Paris*, vol. 103, no. 3-5, pp. 211–219, 2009.

[33] N. Hogan, "Impedance control: An approach to manipulation: Part i—theory," 1985.

[34] F. Dernoncourt, "Introduction to fuzzy logic," *Massachusetts Institute of Technology*, vol. 21, 2013.

[35] M. Selvaggio, G. A. Fontanelli, F. Ficuciello, L. Villani, and B. Siciliano, "Passive virtual fixtures adaptation in minimally invasive robotic surgery," *IEEE Robotics and Automation Letters*, vol. 3, no. 4, pp. 3129–3136, 2018.

[36] M. H. Hamedani, M. Zekri, F. Sheikholeslam, M. Selvaggio, F. Ficuciello, and B. Siciliano, "Recurrent fuzzy wavelet neural network variable impedance control of robotic manipulators with fuzzy gain dynamic surface in an unknown varied environment," *Fuzzy Sets and Systems*, vol. 416, pp. 1–26, 2021.

[37] F. Ferraguti, C. Secchi, and C. Fantuzzi, "A tank-based approach to impedance control with variable stiffness," in *2013 IEEE international conference on robotics and automation*. IEEE, 2013, pp. 4948–4953.

iNGEGNERIA
DIPARTIMENTO DI ECCELLENZA

Department of Engineering

ROMA TRE
UNIVERSITÀ DEGLI STUDI

MCIPLab.it

ADVANCED INTRUSION DETECTION SYSTEM FOR INDUSTRIAL CYBER-PHYSICAL SYSTEMS

Valeria Bonagura

In collaboration with Stefano Panzieri, Federica Pascucci, Chiara Foglietta

Detection of Industrial Threats

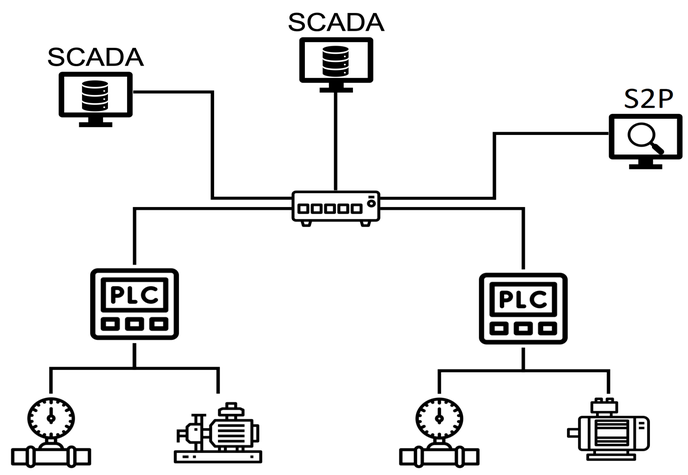

The integration of physical and cyber layers causes possible issues such as the increased surface of cyber-attacks

Smart Security Probe (S2P) is an innovative solution for detecting anomalies in the industrial world.

S2P is **database-centric**, where all the information are collected.

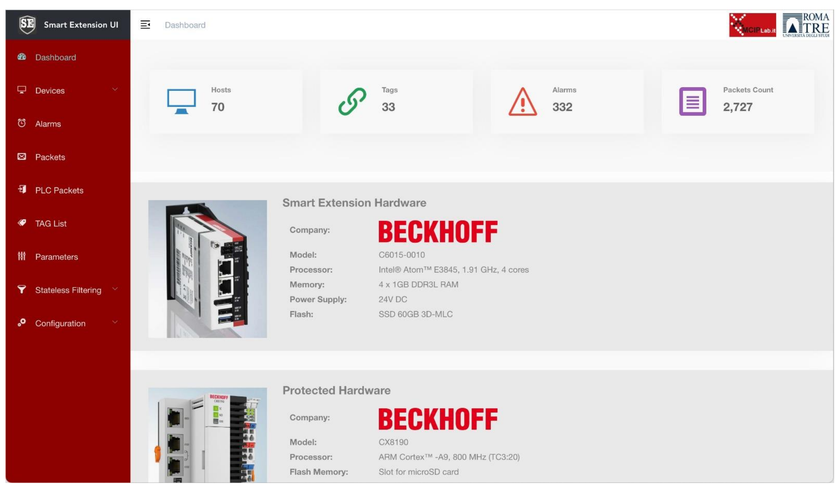

Anomaly-Based Approach

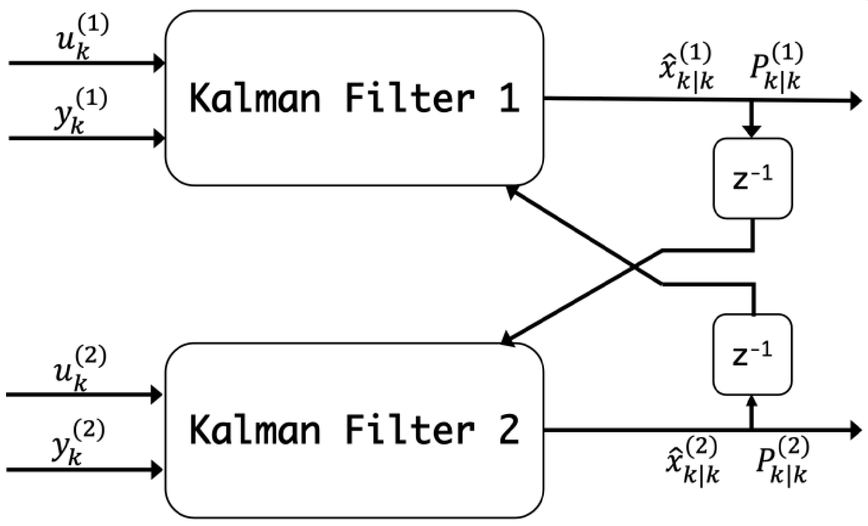

The **Interlaced Extended Kalman Filter** approach allows to **reduce computational load** of the estimation process for a class of nonlinear system.

IEKF consists of p **parallel Interlaced Kalman filters** implementations, each one is used to estimate only a **subset of state variables**.

IEKF is applied to systems where the **state space variables** can be **partitioned**.

At each k-th step, each filter forms a **prediction** exploiting both **its own estimation and the estimations provided by the other filter** at the k-1-th step

$$\begin{aligned} \hat{x}_{k|k-1}^{(i)} &= f^{(i)}\left(\hat{x}_{k-1|k-1} + u_k^{(i)}\right) \\ P_{k|k-1}^{(i)} &= F_k^{(ii)} P_{k-1|k-1}^{(i)} F_k^{(ii)} + F_k^{(ij)} P_{k-1|k-1}^{(j)} F_k^{(ij)} + Q^{(i)} \end{aligned}$$

The **correction** phase is conducted separately**.** There is no a priori exchange of information among the IEKF because subsystems are **considered not correlated in the matrix H**, which is the Jacobian of the observations.

$$\begin{aligned} K_k &= P_{k|k-1} H_k^T \left[H_k P_{k|k-1} H_k^T + R\right]^{-1} \\ \hat{x}_{k|k} &= \hat{x}_{k|k-1} + K_k \left(z_k - h(\hat{x}_{k|k-1})\right) \\ P_{k|k} &= (I - K_k H_k) P_{k|k-1} \end{aligned}$$

Using S2P to exchange informations among the Interlaced Kalman Filters

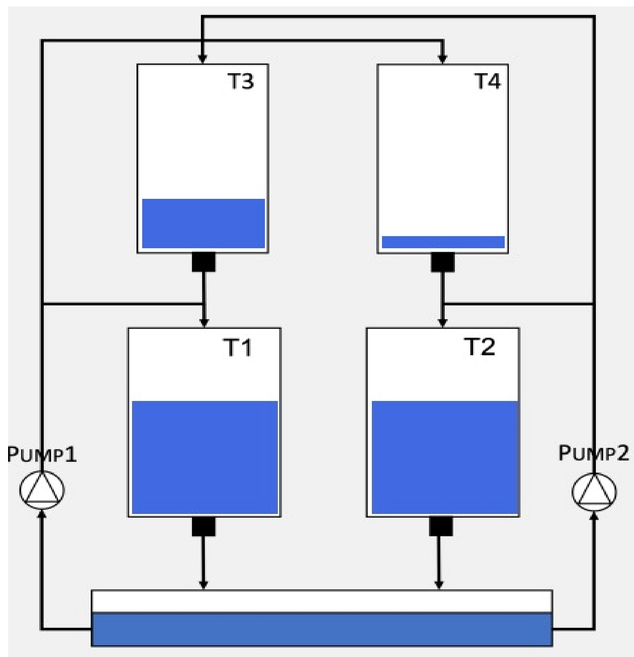

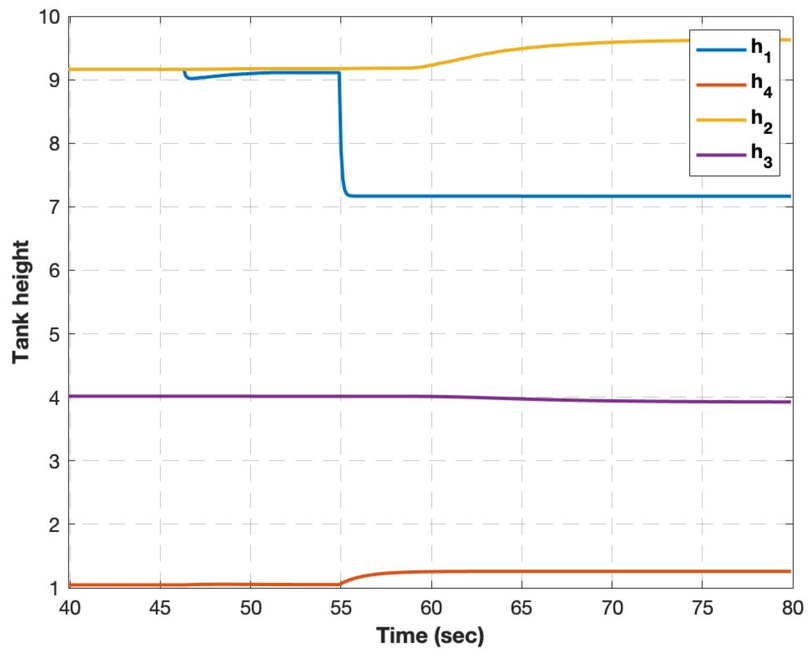

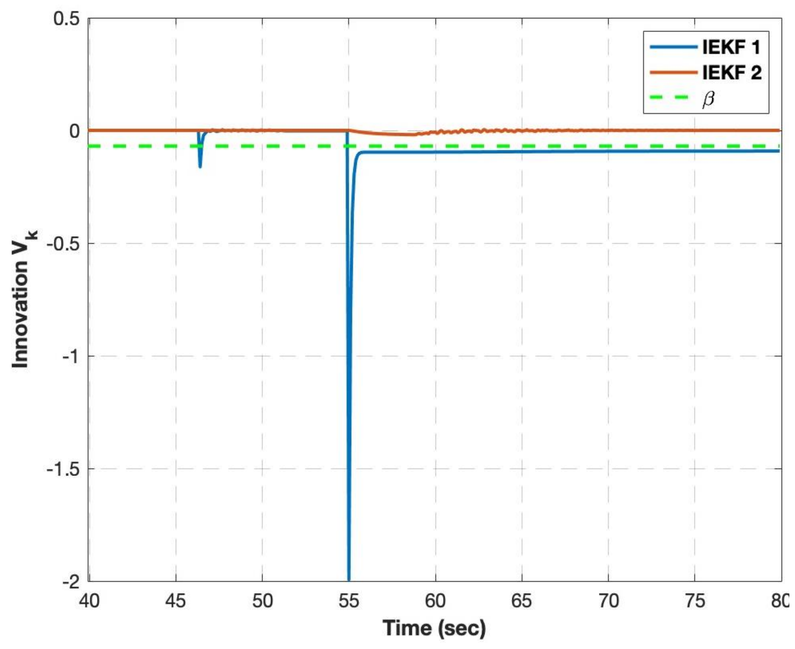

The physical process is composed of **four interconnected tanks**, **with two pumps**. Each PLC controls a pump.

Each IEKF forms a prediction of the height of the tanks under its control and communicates the a **posteriori state estimate and estimate covariance** to the other IEKFs exploiting the S2P database.

This way, the **Innovation** remains a **significative indicator** of the occurrence of an anomaly.

Starting from around 55 seconds **a stream of false data** related to the height of the tank 1 is injected into the system.

The implemented detector recognizes a very low level of **innovation with a spike around the moment of the attacker start**.

In this way, the IEKF **can detect false data injection** reducing also the complexity of the algorithm.

Bonagura Valeria, Chiara Foglietta, Stefano Panzieri, and Federica Pascucci. [2022], *Advanced Intrusion Detection System for Industrial Cyber-Physical Systems, Submitted to COSY 2022*

Handling complexity in large scale complex systems through distributed computation

Lucrezia Manieri, Alessandro Falsone, Maria Prandini

I. Introduction

The operation of large scale complex systems like those arising in the manufacturing, energy, and transportation domains is calling for efficient modeling and optimization frameworks. In this respect, *Mixed Logical Dynamical* (MLD) systems [1] represent an extremely powerful and versatile class of models, which can describe the behaviour of processes involving interleaved physical laws and logical rules subject to linear operating constraints. They include linear hybrid systems, finite state machines, and piecewise linear, possibly constrained, dynamical systems. If the performance of an MLD system is measured through a linear cost function J of the state and/or input, its optimal operation can be formulated as a *Mixed-Integer Linear Program* (MILP)

$$\min_{x} \quad J = c^\top x \tag{1a}$$

$$\text{subject to:} \quad Ax \leq b \tag{1b}$$

$$x \in \mathbb{R}^{n_c} \times \mathbb{Z}^{n_d} \tag{1c}$$

where x is the decision vector, with n_c continuous and n_d discrete components, vector $c \in \mathbb{R}^{n_c+n_d}$ defines the objective function, while matrix $A \in \mathbb{R}^{q\times(n_c+n_d)}$ and vector $b \in \mathbb{R}^q$ allow to express in compact form the q linear inequalities defining the operational constraints of the system. All values of x that satisfy the constraints (1b) and (1c) are *feasible* solutions of the MILP. A feasible $x^\star$ that attains the minimum of the objective function is an *optimal* solution to (1).

Unfortunately, MILPs have an intrinsic combinatorial complexity due to the presence of discrete variables. For this reason, finding an optimal solution becomes prohibitive as the size of the problem increases. One may, then, head for a feasible – although sub-optimal – solution by resorting to heuristic strategies tailored to the specific application, see e.g. [2] and [3].

In this work, we focus on MILPs with the following multi-agent structure that arises when addressing the optimal operation of multiple MLD systems coupled by shared resources:

$$\min_{x_1,\dots,x_m} \quad J = \sum_{i=1}^{m} c_i^\top x_i \tag{2a}$$

$$\text{subject to:} \quad \sum_{i=1}^{m} E_i x_i \leq f \tag{2b}$$

$$x_i \in X_i, \quad i = 1,\dots,m, \tag{2c}$$

The authors are with the Dipartimento di Elettronica Informazione e Bioingegneria, Politecnico di Milano, Via Ponzio 34/5, 20133 Milano, Italy. Email: name.surname@polimi.it.

where, for all $i = 1,\dots,m$, x_i is the decision vectors related to agent i, $X_i = \{x_i \in \mathbb{R}^{n_{c,i}} \times \mathbb{Z}^{n_{d,i}} : D_i x_i \leq d_i\}$ is its compact mixed-integer polyhedral constraint sets, and c_i its contribution to the cost function. Matrices $E_i \in \mathbb{R}^{p\times(n_{c,i}+n_{d,i})}$, $i = 1,\dots,m$, and vector $f \in \mathbb{R}^p$ model the usage of shared resources and couple the agents decisions.

In particular, we present an iterative resolution scheme to obtain a feasible solution through distributed computation. A bound on the possible performance degradation can also be provided which gets tighter as the ratio between the number of coupling constraints p and the number of agents m decreases. Details are omitted here due to space limitations.

Resolution of the monolithic, possibly non-structured, MILPs in (1) can also be addressed by combining the proposed resolution scheme with the decomposition procedure in [4], which turns (1) into (2), if possible, by permuting rows and columns of the A matrix in (1b). Superiority of the introduced resolution scheme with respect to its competitors [5], [6] is shown on a case study on plug-in electric vehicles charging, originally proposed in [5].

II. Proposed resolution scheme

A computationally efficient algorithm for solving multi-agent MILPs of the form (2) has been presented in [5]. The idea is to combine *Lagrangian relaxation* to decompose the MILP in m smaller problems with a fictitious *tightening* of the coupling constraints (2b) to enforce feasibility. In particular, the coupling constraints are relaxed by introducing a vector $\lambda \in \mathbb{R}^p$ of Lagrange multipliers and formulating the dual program

$$\max_{\lambda\geq 0} -\lambda^\top f + \sum_{i=1}^{m} \min_{x_i\in X_i} (c_i^\top + \lambda^\top E_i)x_i \tag{3}$$

which is easier to solve, since it is convex and the inner minimizations in (3) are decoupled. An optimal solution $\lambda^\star$ for (3) can be obtained through a decentralized scheme implementing the sub-gradient algorithm [7, Section 6.3]. A primal tentative solution $x(\lambda^\star) = [x_1(\lambda^\star)^\top \ \cdots \ x_m(\lambda^\star)^\top]^\top$ can be recovered from $\lambda^\star$ setting $\lambda = \lambda^\star$ in

$$x_i(\lambda) \in \arg\min_{x_i\in X_i} (c_i^\top + \lambda^\top E_i)x_i, \quad i = 1,\dots,m. \tag{4}$$

However, $x(\lambda^\star)$ is not guaranteed to satisfy the coupling constraints and the recovery procedure used in the convex case can't be used in presence of discrete decision variables.

In [5], it is shown under suitable assumptions that tightening of the resource vector can be used to enforce feasibility of

the recovered primal solution. Let $\tilde{\rho} \in \mathbb{R}^p$ have components

$$[\tilde{\rho}]_s = p \max_{i \in \{1,\dots,m\}} \left\{ \max_{x_i \in X_i} [E_i]_s x_i - \min_{x_i \in X_i} [E_i]_s x_i \right\} \quad (5)$$

for $s = 1, \dots, p$, with $[M]_s$ denoting the s-th row of matrix M. Consider the tightened version of the primal and dual problems (2) and (3), where the resource vector f is replaced by $f - \tilde{\rho}$. If we denote by $\lambda^\star_{\tilde{\rho}}$ the solution to the tightened dual, then, any solution $x(\lambda^\star_{\tilde{\rho}}) = [x_1(\lambda^\star_{\tilde{\rho}})^\top \ \cdots \ x_m(\lambda^\star_{\tilde{\rho}})^\top]^\top$, with $x_i(\lambda^\star_{\tilde{\rho}})$ satisfying (4) with $\lambda = \lambda^\star_{\tilde{\rho}}$, is feasible for the original problem (2).

Inspired by [6], we propose the decentralized resolution scheme with adaptive tightening described in Algorithm 1. At each iteration the central unit and the agents solve the tightened dual problem given the current value of ρ (cf. Step 4) via decentralized sub-gradient, agents then compute in parallel the sets $\hat{\mathcal{X}}_i$, $i = 1, \dots, m$, of primal solutions associated with the current optimal value of λ (cf. Step 6), and the central unit determines a candidate primal solution x by selecting the elements in $\hat{\mathcal{X}}_i$ attaining the minimum violation of the coupling constraints (cf. Step 8) to possibly halt the algorithm if the violation is zero and, hence, x is feasible (cf. Step 11). If the violation vector has some non-zero components, then, the central unit increases the corresponding components of the tightening vector ρ (cf. Step 14), until saturation to $\tilde{\rho}$. If all non-zero components of the violation vector correspond to saturated components of ρ, then, some (small) quantity Δ is added to all components (cf. Step 16) so as to avoid an impasse of the procedure.

The adopted progressive tightening aims at reducing conservativeness and improving the quality of the obtained solutions by using a less aggressive strategy in the ρ update with respect to the one in [6]. Indeed, it does not update ρ based on far-from optimal tentative solutions $x_i(\lambda)$ computed when λ has not converged yet, but uses instead the converged value of λ before computing $x_i(\lambda)$.

Algorithm 1 Proposed decentralized resolution scheme

1: $\rho(0) = 0$
2: $\Delta(0) = \max_{s=1,\dots,p} [\tilde{\rho}]_s$
3: **for** $k = 0, 1, \dots$ **do**
4: $\quad \lambda^\star_{\rho(k)} \in \arg\max_{\lambda \geq 0} \left\{ \lambda^\top (\rho(k) - f) + \sum_{i=1}^m \min_{x_i \in X_i} (c_i^\top + \lambda^\top E_i) x_i \right\}$
5: $\quad$ **for** $i = 1, \dots, m$ **compute**
6: $\quad\quad \hat{\mathcal{X}}_i(k) \subseteq \arg\min_{x_i \in \mathrm{vert}(X_i)} (c_i^\top + {\lambda^\star_{\rho(k)}}^\top E_i) x_i$
7: $\quad$ **end for**
8: $\quad [x_1(k)^\top \ \cdots \ x_m(k)^\top]^\top \in \arg\min_{\{x_i \in \hat{\mathcal{X}}_i(k)\}_{i=1}^m} \left\| \left[\sum_{i=1}^m E_i x_i - f \right]_+ \right\|_\infty$
9: $\quad v(k) = \left[\sum_{i=1}^m E_i x_i(k) - f \right]_+$
10: $\quad$ **if** $v(k) = 0$ **then**
11: $\quad\quad$ **return** $x(k) = [x_1(k)^\top \ \cdots \ x_m(k)^\top]^\top$
12: $\quad$ **end if**
13: $\quad$ **if** $(\tilde{\rho} - \rho(k))^\top v(k) > 0$ **then**
14: $\quad\quad \rho(k+1) = \min\{\tilde{\rho}, \rho(k) + v(k)\}$
15: $\quad$ **else**
16: $\quad\quad \rho(k+1) = \min\{\tilde{\rho}, \rho(k) + \Delta(k)\mathbb{1}\}$
17: $\quad$ **end if**
18: $\quad \Delta(k+1) = \min\{\Delta(k), \min_{s:[v(k)]_s > 0} [v(k)]_s\}$
19: **end for**

III. Simulation results

We tested the proposed approach on the Plug-In Electric Vehicles (PEVs) charging problem described in [5], where an aggregator has to determine an optimal overnight charging/discharging schedule for a fleet of m vehicles exchanging power with the same electricity distribution grid in a Vehicle-to-Grid (V2G) set-up. Vehicles are subject to both local operational constraints (e.g. final state of charge) and some network-wide limitations to avoid congestion of the grid.

Let $J^\star_{\lambda^\star}$ be the lower-bound on the optimal cost obtained solving the dual problem (3). The performance of a solution achieving a cost J can be assessed based on its relative performance gap $\Delta J_\% = \frac{J - J^\star_{\lambda^\star}}{|J^\star_{\lambda^\star}|}$. In Figure 1 we report $\Delta J_\%$ re-scaled by the number of vehicles m to assess the rate with which it vanishes to zero as m tends to infinity (see the discussion after Theorem 3.3 in [5]) for m ranging in $[250, 10000]$. As anticipated, Algorithm 1 achieves better performance than the algorithms in [5] and [6] in all tests.

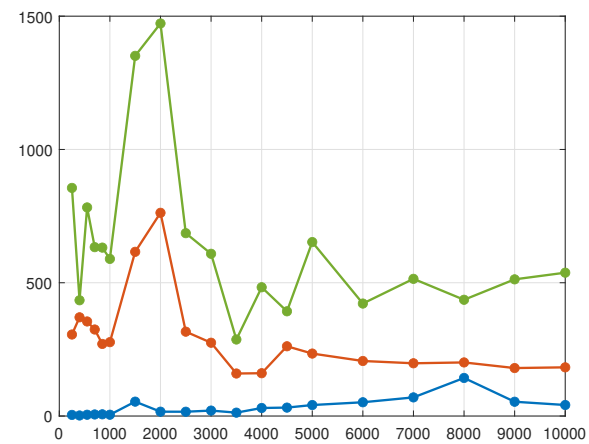

Fig. 1. Re-scaled performance gap $\Delta J_\% \cdot m$ obtained by Algorithm 1 (blue line) and its competitor algorithms in [5] (green line) and [6] (red line) as a function of the number m of vehicles.

References

[1] A. Bemporad and M. Morari, "Control of systems integrating logic, dynamics, and constraints," *Automatica*, vol. 35, no. 3, pp. 407–427, mar 1999.

[2] D. Bertsekas, G. Lauer, N. Sandell, and T. Posbergh, "Optimal short-term scheduling of large-scale power systems," *IEEE Transactions on Automatic Control*, vol. 28, no. 1, pp. 1–11, 1983.

[3] N. J. Redondo and A. Conejo, "Short-term hydro-thermal coordination by lagrangian relaxation: solution of the dual problem," *IEEE Transactions on Power Systems*, vol. 14, no. 1, pp. 89–95, 1999.

[4] L. Manieri, A. Falsone, and M. Prandini, "Hyper-graph partitioning for a multi-agent reformulation of large-scale MILPs," *IEEE Control Systems Letters*, vol. 6, pp. 1346–1351, 2022.

[5] R. Vujanic, P. Mohajerin Esfahani, P. J. Goulart, S. Mariéthoz, and M. Morari, "A decomposition method for large scale MILPs, with performance guarantees and a power system application," *Automatica*, vol. 67, pp. 144–156, 2016.

[6] A. Falsone, K. Margellos, and M. Prandini, "A decentralized approach to multi-agent MILPs: Finite-time feasibility and performance guarantees," *Automatica*, vol. 103, pp. 141–150, 2019.

[7] D. P. Bertsekas, "Nonlinear programming," *Journal of the Operational Research Society*, vol. 48, no. 3, pp. 334–0334, 1997.

Data-driven mixed-sensitivity control with automatic weights design

Nicholas Valceschini*, Mirko Mazzoleni*, Simone Formentin+ and Fabio Previdi*

I. Introduction

We consider the problem of weight functions tuning in the SISO LTI mixed-sensitivity design of robust controllers under plant model uncertainty. The S/T mixed-sensitivity approach requires the definition of stable and proper transfer functions $W_T(z)$ and $W_S(z)$ that define stability and performance requirements of the feedback system, respectively.

Robust system identification aims to provide an estimate of the nominal plant along with an estimate of its uncertainty set, which can then be used to design a controller robust to modeling uncertainties [1]. Several approaches exist for characterizing the bias and variance of the plant model estimates, namely stochastic embedding (SE) and model-error modeling (MEM) in a stochastic setting and set-membership (SM) identification in a deterministic/worst case one [2]

When identification is motivated by robust-control design purposes, the model order has to be relatively low [2] so that undermodeling is prevalent. If not proper taken into account, the modeling bias can compromise the uncertainty region, so that the true system might not be contained in it, thus jeopardizing the robust control. As an alternative solution, kernel methods first identify an high-order low-bias model using all the available and prior information, and a low-order model can be subsequently derived by model reduction [3].

This works investigates the use of the uncertainty set provided by low-bias kernel methods for SISO LTI robust control design by a S/T mixed-sensitivity $\mathcal{H}_\infty$ approach. The derived set is used to determine the stability weight $W_T(z)$, based on which $W_S(z)$ is tuned by a multi-objective optimization for maximum attainable control performance.

II. Preliminaries

A. Problem statement. Consider the unknown stable LTI SISO plant $G_0(z)$ and two stable proper scalar weighting functions $W_S(z), W_T(z)$. The control aim considered in this work is to design a LTI fixed-order controller $K(z,\boldsymbol{\rho})$, parametrized by the parameters vector $\boldsymbol{\rho} \in \mathbb{R}^{n_\rho \times 1}$, so as to minimize

$$J(\boldsymbol{\rho}, G_0) := \left\| \begin{matrix} W_S(z)S(z,\boldsymbol{\rho}) \\ W_T(z)T(z,\boldsymbol{\rho}) \end{matrix} \right\|_\infty, \tag{1}$$

where $S(z,\boldsymbol{\rho}) = [1 + K(z,\boldsymbol{\rho})G_0(z)]^{-1}$ and $T(z,\boldsymbol{\rho}) = 1 - S(z,\boldsymbol{\rho})$. Let $\Delta(z)$ a stable transfer function satisfying $\|\Delta\|_\infty \leq 1$, and a multiplicative uncertainty model set

$$\Pi: \quad G_p(z) := \big(1 + \Delta(z)W(z)\big)G_0(z), \tag{2}$$

where $G_p(z)$ denotes a particular perturbed SISO plant model. Under these settings, $W(z) = W_T(z)$ and problem (1) is solved usually imposing that $\|J(\boldsymbol{\rho})\|_\infty < 1$, for robust stability and nominal performance or $\|J(\boldsymbol{\rho})\|_\infty < 1/\sqrt{2}$ for robust performance. Here we focus to the case where a data-driven model $\hat{G}(z)$ is identified from a set of of n input/output data $\mathcal{D} = \{u(t), y(t)\}_{t=1}^n$ collected from an open-loop experiment on the plat, so that

$$y(t) = G_0(z)u(t) + d(t), \tag{3}$$

where $d(t)$ is a random measurement noise, possibly stochastic and norm-bounded with $|d(t)| < \bar{\delta}_d$, $\forall t$.

B. Kernel-based identification. Consider (3) but with $d(t) \sim \mathcal{N}\left(0, \sigma^2\right)$, with σ^2 the Gaussian noise variance, and the FIR model of order n_g, that is $G(z,\boldsymbol{\theta}) = \sum_{i=1}^{n_g} g_i z^{-i}$, $\boldsymbol{\theta} = \left[g_1\, g_2\, \ldots,\, g_{n_g}\right]^\top$. Assume that a prior distribution $\boldsymbol{\theta} \sim \mathcal{N}(\mathbf{0}, \mathbf{K})$ is placed on $\boldsymbol{\theta} \in \mathbb{R}^{n_g \times 1}$, where $\mathbf{K} \in \mathbb{R}^{n_g \times n_g}$ is a covariance (kernel) matrix encoding prior information on parameters. The posterior distribution $\boldsymbol{\theta}|\boldsymbol{y}$ is then Gaussian

$$\boldsymbol{\theta}|\boldsymbol{y} \sim \mathcal{N}\left(\hat{\boldsymbol{\theta}}, \hat{\boldsymbol{\Sigma}}\right), \tag{4a}$$

$$\hat{\boldsymbol{\theta}} = \left(\mathbf{K}\boldsymbol{\Phi}^\top\boldsymbol{\Phi} + \sigma^2 I_{n_g}\right)^{-1}\mathbf{K}\boldsymbol{\Phi}^\top\boldsymbol{y}, \tag{4b}$$

$$\hat{\boldsymbol{\Sigma}} = \mathbf{K} - \mathbf{K}\boldsymbol{\Phi}^\top\left(\boldsymbol{\Phi}\mathbf{K}\boldsymbol{\Phi}^\top + \sigma^2 I_n\right)^{-1}\boldsymbol{\Phi}\mathbf{K}, \tag{4c}$$

$$\text{where } \boldsymbol{\Phi} := [\boldsymbol{\varphi}(1)\ \boldsymbol{\varphi}(2)\ \ldots\ \boldsymbol{\varphi}(n)]^\top \in \mathbb{R}^{n \times n_g}, \tag{4d}$$

$$\boldsymbol{\varphi}(t) := [u(t-1)\ \ldots\ u(t-n_g)]^\top\, \mathbb{R}^{n_g \times 1} \tag{4e}$$

$$\boldsymbol{y} := [y(1)\, y(2)\, \ldots\, y(n)]^\top \in \mathbb{R}^{n \times 1}. \tag{4f}$$

The identified nominal model is set as $\hat{G}(z) := G(z, \hat{\boldsymbol{\theta}})$.

III. Design of mixed-sensitivity weights

A. Design of the stability weight. Let $G_p(z) := G(z, \boldsymbol{\theta}_p)$, with $\boldsymbol{\theta}_p$ a random sample drawn from (4a). Define

$$\Omega\left(e^{j\omega}\right) := \max_p \left| \frac{G_p\left(e^{j\omega}\right)}{\hat{G}\left(e^{j\omega}\right)} - 1 \right|, \tag{5}$$

where $\hat{G}(z) := G(z, \hat{\boldsymbol{\theta}})$. Robust stability against the multiplicative uncertainty model (2) requires that [4, Chapter 9]

$$\Omega\left(e^{j\omega}\right) \leq \left|W_T\left(e^{j\omega}\right)\right|, \quad \forall \omega \in [0, \pi f_s] \tag{6}$$

where ω is specific pulse in rad/s and f_s is the sampling frequency. The magnitude of the least conservative $W_T(z)$ can be estimated evaluating (5) in a discrete grid of n_m frequencies $\mathcal{M} = \{\omega_1, \omega_2, \ldots \omega_{n_m}\} \subseteq [0, \pi f_s]$ for a set

* M. Mazzoleni, N. Valceschini and F. Previdi are with the Department of Management, Information and Production Engineering, University of Bergamo, Via G. Marconi 5, 24044 Dalmine (BG), Italy. Email to: mirko.mazzoleni@unibg.it.

+ S. Formentin is with the Department of Electronics, Information and Bioengineering, Politecnico di Milano, via G. Ponzio 34/5, 20133 Milano, Italy.

of n_p samples. A nonparametric sampled estimate of the magnitude of $W_T(z)$ is thus

$$\left|\hat{W}_T\left(e^{j\omega_m}\right)\right| = \Omega\left(e^{j\omega_m}\right), \quad \forall \omega_m \in \mathcal{M}. \tag{7}$$

A stable and proper parametric model $\hat{W}_T(z)$ can then be obtained by fitting a model of adequate (low) order to the magnitude frequency points (7).

B. Design of the performance weight. Consider a reference model $T_d(s)$ for the closed loop system $T(s)$

$$T_d(s) := \frac{\omega_n^2}{s^2 + 2\xi\omega_n s + \omega_n^2}. \tag{8}$$

where ω_n is the natural frequency of the poles and ξ is their damping factor, that can also be expressed, in a more interpretable way, as function of the closed-loop step response overshoot o and settling time ℓ. Let $T_d(z)$ be a discretized version of (8), that acts as reference for $T(z)$. A simple approach to define the performance weight $W_S(z)$ is to employ the discrete counterpart of the sensitivity function from the reference model (8), so that $W_S(z) := (1 - T_d(z, o, \ell))^{-1}$. Let $o_{\min}, \ell_{\min} \neq 0$ be user-defined minimum allowable overshoot level and settling time. The following multi-objective optimization problem is solved:

$$(\mathcal{O}, \mathcal{L}) = \arg\min_{o,\ell} (o, \ell) \tag{9a}$$

$$\text{s.t.} \min_{\boldsymbol{\rho}} J\left(\boldsymbol{\rho}, \hat{G}, \hat{W}_T, W_S(o, \ell)\right) < 1 + \gamma, \tag{9b}$$

$$o_{\min} < o < 1, \tag{9c}$$

$$\ell_{\min} < \ell < \ell_{\max}, \tag{9d}$$

where $(\mathcal{O}, \mathcal{L})$ are two sets of Pareto-optimal dominant solutions for the overshoot and settling time, respectively. Problem (9) is subject to the following constraints: (i) (9b) requires the satisfaction of the robust stability and nominal performance condition, based on the nominal model $\hat{G}(z)$ and the tuned stability weight $\hat{W}_T(z)$[1]; (ii) (9c) and (9d) bound the overshoot and settling time in feasible ranges. The value $\ell_{\max}$ can be defined by the user and it is not critical.

The estimates $(\hat{o}, \hat{\ell}) \in (\mathcal{O}, \mathcal{L})$ are chosen as the point closest to $(o_{\min}, \ell_{\min})$ in the space defined by overshoot and settling time. The tuned weight $\hat{W}_S(z)$ is set as[2]

$$\hat{W}_S(z) = \left(1 - T_d(z, \hat{o}, \hat{\ell})\right)^{-1}. \tag{10}$$

Using $\hat{G}(z)$, (7), (10), the controller is estimated by (1).

IV. Numerical Example

Consider the following benchmark system

$$G_0(z) = \frac{0.28261z + 0.50666}{D(z)}, \tag{11}$$

$D(z) = z^4 - 1.41833z^3 + 1.58939z^2 + 1.58939z^2 - 1.31608z + 0.88642$, sampled a $T_S = 0.01$ s. System (11) is excited with a white noise input simulating $n = 5000$ data, and noise was added as an Output Error (OE) system with SNR $= \text{var}[y(t)]/\text{var}[d(t)] = 25$. The FIR order for kernel identification is set as $n_g = 100$, followed by model reduction to order 15. We compared with PEM identification, using an OE model with orders from 1 to 10 selected by AIC. The number of sampled system is set as $n_p = 738$ following the Chernoff's bound, and the number of sampled frequency is $n_\omega = 600$ in $\left[10^{-3}, \pi f_s\right]$ rad/s.

We thus tested the conditions presented in Table I, by extracting $M = 200$ random open-loop systems from the Gaussian distributions of PEM and Kernel parameters, centered at the respective estimate $\hat{G}(z)$. Results in Figure 1 show how the proposed approach attains better Integral Absolute Error (IAE) and settling time of the closed-loop systems step response, with the designed controller for the PEM and kernel cases. The PEM approach performs better than the kernel method: this is due to the fact the the chosen PEM model structure contains the true system $G_0(z)$, thus acting as an "oracle" result.

	Kernel ident.	PEM ident.
Manual design of $W_S(z)$ and $W_T(z)$	K_{M1-M2}	P_{M1-M2}
Manual design of $W_S(z)$ and automatic design of $W_T(z)$	K_{M1-A2}	P_{M1-A2}
(Proposed.) Automatic design of $W_S(z)$ and $W_T(z)$	K_{A1-A2}	P_{A1-A2}

TABLE I

Control design configurations tested.

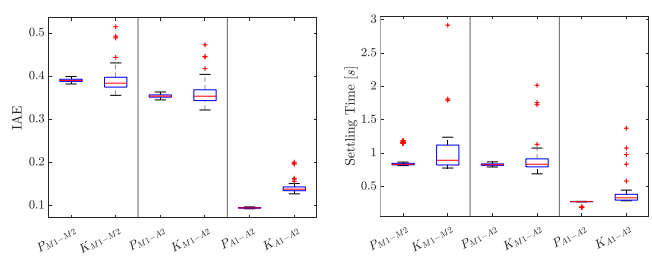

Fig. 1. Control performance results.

V. Conclusion and Final Remarks

We presented a model error approach based for tuning the weights in mixed-sensitivity control design for robust control, where the robust stability is defined with respect to the uncertainty set provided kernel identification procedures. From this, the performance weight is automatically optimized based on a fixed structure and solving a multi-objective optimization problem.

References

[1] P. Van den Hof, "Identification of experimental models for control design," in *IMTC 2001. Proceedings of the 18th IEEE Instrumentation and Measurement Technology Conference.*, vol. 2, pp. 1155–1162 vol.2, 2001.

[2] W. Reinelt, A. Garulli, and L. Ljung, "Comparing different approaches to model error modeling in robust identification," *Automatica*, vol. 38, no. 5, pp. 787–803, 2002.

[3] G. Pillonetto and G. De Nicolao, "A new kernel-based approach for linear system identification," *Automatica*, vol. 46, no. 1, pp. 81–93, 2010.

[4] K. Zhou, J. C. Doyle, and K. Glover, *Robust and Optimal Control*. USA: Prentice-Hall, Inc., 1996.

[1]Notice that $\gamma \in \mathbb{R}_{>0}$ denotes a small positive slack quantity that guarantees the feasibility of the optimization problem, also in spite of numerical inaccuracies.

[2]To ensure that $\hat{W}(s)$ is stable and proper, the same fitting procedure used for $\hat{W}_T(z)$ can be employed.

Variational Bayes Moving Horizon Estimation

Xiangxiang Dong, Giorgio Battistelli, Luigi Chisci, and Yunze Cai

***Abstract*—This contribution summarizes recent research results on single-sensor and distributed state estimation with unknown process and measurement noise covariance matrices [1], [2]. The unknown covariances are modeled with constrained inverse Wishart distributions and estimated together with the state trajectory within a moving horizon window by combining variational Bayes (VB) inference, Moving Horizon Estimation (MHE), and Monte Carlo integration with importance sampling. The proposed adaptive VB-MHE filter ensures mean-square boundedness of the estimation error with any number of importance samples and VB iterations, as well as for any window length. Simulation and experimental results on target tracking case-studies demonstrate the outperformance of the proposed VB-MHE filter compared to the state of the art.**

***Index Terms*—State estimation, moving horizon estimation, variational Bayes, sensor network, consensus.**

I. Problem Setting

Consider a linear discrete-time system

$$\begin{aligned} x_{t+1} &= Ax_t + w_t \\ y_t &= Cx_t + v_t \end{aligned}$$

where: t is the time index; x_t and y_t are the state and measurement vectors of dimensions n_x and n_y, respectively; A and C are the state transition and, respectively, measurement matrices; w_t and v_t denote mutually independent white process and measurement noises, assumed to be Gaussian with zero mean but unknown, possibly time-varying, covariances Q_t and R_t. In order to model possible prior knowledge on the structure of the unknown covariances, Q_t and R_t, they are supposed to belong to known sets $\mathcal{Q} \subseteq \mathbb{S}_+^{n_x}$ and $\mathcal{R} \subseteq \mathbb{S}_+^{n_y}$, respectively, where $\mathbb{S}_+^d$ denotes the set of real-valued positive definite $d \times d$ symmetric matrices. These sets can, for example, be specified in terms of upper and lower bounds on the unknown covariances, or in terms of more general matrix sets. Clearly, in case no prior knowledge is available, we do not consider any bound and simply take $\mathcal{Q} = \mathbb{S}_+^{n_x}$ and $\mathcal{R} = \mathbb{S}_+^{n_y}$.

Following a Bayesian approach, the process and measurement noise covariances are regarded as random matrices to be estimated together with the state trajectory. The initial state x_0 is assumed to be Gaussian-distributed with mean $\bar{x}_0$ and covariance $\bar{P}_0$, i.e.,

$$p(x_0) = \mathcal{N}\left(x_0; \bar{x}_0, \bar{P}_0\right).$$

For the unknown covariance of a Gaussian distribution, its conjugate prior is the inverse Wishart distribution, whose PDF is denoted as $\mathcal{W}^{-1}(G; \Delta, \gamma)$, indicating that the random matrix $G \in \mathbb{S}_+^d$ follows an inverse Wishart distribution with degree of freedom $\gamma > d+1$ and scale matrix $\Delta \in \mathbb{S}_+^d$. Since the unknown covariances Q and R are supposed to belong to the sets $\mathcal{Q}$ and $\mathcal{R}$, respectively, we take the priors for Q and R as constrained inverse Wishart distributions of parameters $(\bar{M}, \bar{m})$ and, respectively, $(\bar{S}, \bar{s})$, i.e.

$$\begin{aligned} p(Q) &\propto \mathcal{W}^{-1}\left(Q; \bar{M}, \bar{m}\right) \mathbf{1}_{\mathcal{Q}}(Q) \\ p(R) &\propto \mathcal{W}^{-1}\left(R; \bar{S}, \bar{s}\right) \mathbf{1}_{\mathcal{R}}(R) \end{aligned}$$

where $\mathbf{1}_{\mathcal{Q}}(Q)$ is the indicator function taking value 1 if $Q \in \mathcal{Q}$ and 0 otherwise.

II. Variationial Bayes Moving Horizon Estimation

To keep the computational complexity bounded over time, the proposed VB-MHE algorithm operates on a moving window of length T. More specifically, let $x_{t-T:t}$ denote the state trajectory from time $t-T$ to time t. Then, the VB-MHE algorithm computes, at each time t, a factorized approximation of the joint posterior probability density function of state trajectory and unknown covariances of the form

$$p_t\left(x_{t-T:t}, Q, R\right) \simeq q_{x,t}\left(x_{t-T:t}\right) q_{Q,t}\left(Q\right) q_{R,t}\left(R\right).$$

By following the VB approach, the factorized densities $q_{x,t}$, $q_{Q,t}$, $q_{R,t}$ are determined by solving the variational problem of minimizing the Kullback-Leibler divergence from the joint posterior

$$D_{KL}\left\{q_{x,t}\left(x_{t-T:t}\right) q_{Q,t}\left(Q\right) q_{R,t}\left(R\right) \,\middle\|\, p_t\left(x_{t-T:t}, Q, R\right)\right\},$$

i.e., by minimizing the loss of information due to the factorized approximation.

Then, it can be shown that the optimal solution of the resulting optimization problem takes a Gaussian bounded inverse Wishart form [1]

$$\begin{aligned} & p_t\left(x_{t-T:t}, Q, R\right) \\ & \propto \mathcal{N}\left(x_{t-T:t}; \hat{x}_{t-T:t|t}, P_{t-T:t|t}\right) \\ & \quad \times \mathcal{W}^{-1}\left(Q; M_t, m_t\right) \mathcal{W}^{-1}\left(R; S_t, s_t\right) \mathbf{1}_{\mathcal{Q}}(Q) \mathbf{1}_{\mathcal{R}}(R) \end{aligned}$$

where the quantities $\hat{x}_{t-T:t|t}$, $P_{t-T:t|t}$, M_t, and S_t can be computed by iterating solving a system of nonlinear equations via the fixed-point method estimating one parameter at a time while fixing the others.

Given the above factorized approximation, estimates of the unknown covariance matrices can be computed by means of the integrals

$$\begin{aligned} \hat{Q}_t &= \frac{\int_{\mathcal{Q}} Q\, \mathcal{W}^{-1}\left(Q; M_t, m_t\right) dQ}{\int_{\mathcal{Q}} \mathcal{W}^{-1}\left(Q; M_t, m_t\right) dQ} \\ \hat{R}_t &= \frac{\int_{\mathcal{R}} R\, \mathcal{W}^{-1}\left(R; S_t, s_t\right) dR}{\int_{\mathcal{R}} \mathcal{W}^{-1}\left(R; S_t, s_t\right) dR}. \end{aligned}$$

which can be approximated to any desired degree of accuracy by means of Monte Carlo integration with importance sampling.

As shown in [1], the resulting recursive estimation algorithm, under the assumption of bounded $\mathcal{Q}$ and $\mathcal{R}$ and detectability of the pair (A, C), turns out to be mean-square stable for any number of samples in the Monte Carlo integration, any number of fixed-point iterations, and any length of the moving horizon window.

III. Distributed VB-MHE

The proposed VB-MHE algorithm has been extended to a distributed setting in [2] by considering a set of N linear sensors providing measurements of the form

$$y_t^j = C^j x_t + v_t^j, \quad j = 1, \ldots, N,$$

where each sensor is characterized by an unknown measurement noise covariance matrix R_t^j. Each sensor j can collect measurement and also receive information from a subset $\mathcal{N}^j$ of nodes. We refer to $\mathcal{N}^j$ as the set of in-neighbors of node j. The overall sensor network can then be modelled as a graph $(\mathcal{N}, \mathcal{A})$ where $\mathcal{N} = \{1, 2, \ldots, N\}$ is the set of nodes and $\mathcal{A}$ is set of links such that $(i, j) \in \mathcal{A}$ if and only if $i \in \mathcal{N}^j$. In this setting, the problem of interest is to jointly estimate the state vector x_t and the unknown covariances Q_t and R_t^j, $j \in \mathcal{N}$, in a distributed way, so that each sensor j computes its

X. Dong and Y. Cai are with the Department of Automation; Key Laboratory of System Control and Information Processing of Ministry of Education; Key Laboratory of Marine Intelligent Equipment and System of Ministry of Education; Shanghai Jiao Tong University, Shanghai, 200240, China. (Email: js.danesir@sjtu.edu.cn; yzcai@sjtu.edu.cn)

G. Battistelli and L. Chisci are with the Dept. of Information Engineering, University of Florence, Florence, 50139, Italy. (Email: giorgio.battistelli@unifi.it; luigi.chisci@unifi.it)

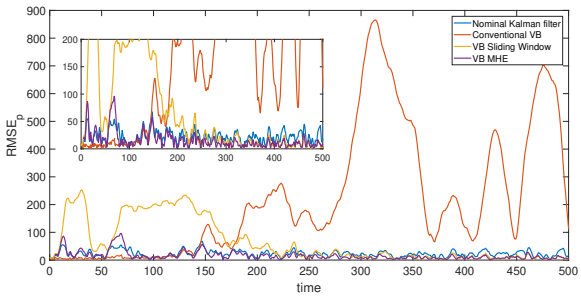

Fig. 1: Position RMSE in the case of a single sensor

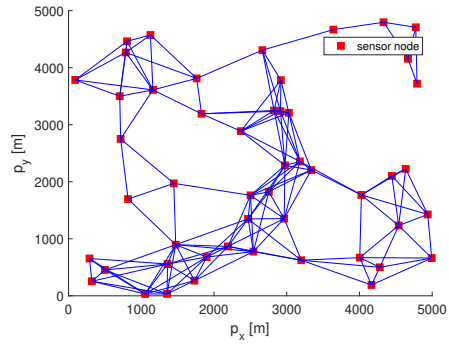

Fig. 2: Distributed Sensor Network

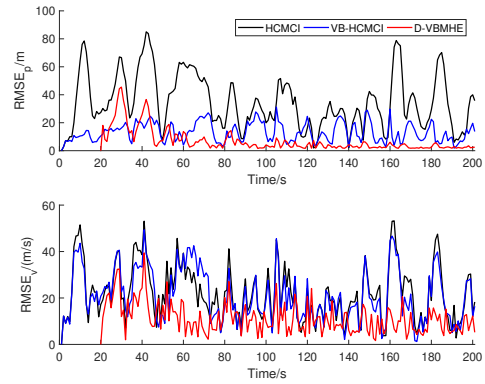

Fig. 3: Position and velocity RMSEs in the case of a sensor network

local estimates only on the basis of its own measurements and the information exchanged with its neighbors $i \in \mathcal{N}^j$.

To this end, each sensor runs locally the VB-MHE algorithm to compute estimates of the state trajectory in the moving window $x_{t-T:t}$, of the process noise covariance matrix Q_t, and of the local measurement noise covariance matrix R_t^j. Then, in order to diffuse the information through the network in a fully distributed way, the consensus algorithm is exploited. In particular, at each time instant three consensus tasks are performed in parallel. The first is consensus on the parameters of the process noise covariance matrix densities of each node by exploiting the distributed averaging of exponential family densities. To this end, a novel rule for the fusion of constrained inverse Wishart densities is provided in [2] . The other two consensus tasks (consensus on the prior information on the state trajectory over the moving window, and consensus on the measurements over the moving window) are carried out in order to get the estimated trajectory as well as the covariance and state for the next time moving horizon estimation recursion.

IV. Peformance evaluation

The performance of the proposed VB-MHE algorithm has been evaluated in several centralized and distributed target-tracking case studies using both simulated and experimental data. The objective is estimating the kinematic state $x = [p_x, p_y, \dot{p}_x, \dot{p}_y]^{\mathrm{T}}$, of a moving target given position measurements provided by the sensors (here p_x and p_y denote the positions along the coordinate axes, while $\dot{p}_x$ and $\dot{p}_y$ denote the corresponding velocities).

In the case of a single position sensor, the proposed VB-MHE filter has been compared with the nominal Kalman filter (NKF), the conventional VB filter of [3] and the sliding window variational Kalman filter (VB Sliding Window, VB-SW) of [4]. The *root mean square error* (RMSE) versus time for position and velocity (computed over 50 independent Monte Carlo runs) are provided in Fig. 1 demonstrating the outperformance of the proposed filter with respect to the others. In particular, the proposed VB-MHE filter provides improvement with respect to the conventional VB, NKF, VB-SW of is 91%, $13\%, 88\%$ in position RMSE and 45%, 12%, 36% in velocity, respectively.

In the distributed case, a network containing 50 position sensors has been considered as depicted in Fig. 2 In this case, the performance of the proposed D-VBMHE filter is compared to that of nominal consensus filter of [5] (referred to as Hybrid Consensus on Measurements and Consensus on Information, HCMCI) as well as that of the VB-HCMCI of [6]. The latter is an adaptive consensus filter that estimates the unknown covariances, while the HCMCI of [5] uses nominal covariances instead of the unknown true ones. Fig. 3 plots the position and velocity RMSEs (computed over 50 independent Monte Carlo runs) versus time for HCMCI, VB-HCMCI and distributed VB-MHE. It can be seen that the proposed approach provides improvements, with respect to HCMCI, of 81% in position RMSE and 50% in velocity. The improvements with respect to VB-HCMCI are 49% in position and 47% in velocity, respectively.

The interested reader is referred to [1], [2] for a detailed description of the considered scenarios as well as for additional simulation and experimental results (including an experimental case-study on a real-world dataset [7] concerning the problem of tracking the target, one robot, by 4 sensors, other robots equipped with cameras, that provide measurements of range and bearing).

References

[1] X. Dong, G. Battistelli, L. Chisci, and Y. Cai, "A variational bayes moving horizon estimation adaptive filter with guaranteed stability," *Automatica*, vol. 142, p. 110374, 2022. [Online]. Available: https://www.sciencedirect.com/science/article/pii/S0005109822002242

[2] ——, "Consensus variational bayesian moving horizon estimation for distributed sensor networks with unknown noise covariances," *Signal Processing*, vol. 198, p. 108571, 2022. [Online]. Available: https://www.sciencedirect.com/science/article/pii/S016516842200113X

[3] Y. Huang, Y. Zhang, Z. Wu, N. Li, and J. Chambers, "A novel adaptive Kalman filter with inaccurate process and measurement noise covariance matrices," *IEEE Transactions on Automatic Control*, vol. 63, no. 2, pp. 594–601, 2018.

[4] Y. Huang, F. Zhu, G. Jia, and Y. Zhang, "A slide window variational adaptive kalman filter," *IEEE Transactions on Circuits and Systems II: Express Briefs*, vol. 67, no. 12, pp. 3552–3556, 2020.

[5] G. Battistelli, L. Chisci, G. Mugnai, A. Farina, and A. Graziano, "Consensus-based linear and nonlinear filtering," *IEEE Transactions on Automatic Control*, vol. 60, no. 5, pp. 1410–1415, 2015.

[6] X. Dong, G. Battistelli, L. Chisci, and Y. Cai, "An adaptive consensus filter for distributed state estimation with unknown noise statistics," *IEEE Signal Processing Letters*, vol. 28, pp. 1595–1599, 2021.

[7] K. Y. Leung, Y. Halpern, T. D. Barfoot, and H. H. Liu, "The Utias multi-robot cooperative localization and mapping dataset," *The International Journal of Robotics Research*, vol. 30, no. 8, pp. 969–974, 2011.

On the use of SDC parameterisation in nonlinear systems for nonlinear optimal control problems

Giuseppe Antonio Scala
Dip. di Ingegneria dell'Informazione
Universita' Politecnica delle Marche
Ancona, Italy
g.a.scala@pm.univpm.it

Andrea Bonci
Dip. di Ingegneria dell'Informazione
Universita' Politecnica delle Marche
Ancona, Italy
a.bonci@univpm.it

Sauro Longhi
Dip. di Ingegneria dell'Informazione
Universita' Politecnica delle Marche
Ancona, Italy
sauro.longhi@univpm.it

***Abstract*—The present short paper aims to illustrate some preliminary ideas and insights with which the authors intend to propose a way to investigate some theoretical aspects of nonlinear optimisation control problems by exploiting the SDC parameterisation of nonlinear systems.**

I. Introduction

Various methods can be used for analysis and design of nonlinear systems [1]. The State Dependent Coefficient (SDC) representation, also known as extended linearisation [2], proposes to factorise a nonlinear function $f(x)$ into a linear-like structure with State-Dependent matrices, where continuous, nonlinear matrix-valued function, $A(x)$, can always be obtained by mathematical factorisation. This makes it possible to represent the system with a structure similar to that of linear systems, while retaining their non-linear nature. In recent years, the authors of this short report have begun to investigate some of the characteristics of this type of representation, believing that it has been widely proposed over the last two decades in various application solutions, but has not been as thoroughly explored conceptually and methodologically for the purpose of solving non-linear optimal control problems. A widely known control method using SDC parameterisation is the State Dependent Riccati Equation (SDRE), that offers a hybrid alternative between the use of the linear optimal control theory and nonlinear dynamical system representation in SDC form. It extends the effectiveness of the Linear Quadratic Regulator (LQR) control to non-linear systems through the use of SDC matrices and SDRE control. This allows the system to be controlled over a wider range than a single operating point around which the system is linearised in the case of linear control. Despite the growing documentation on the SDRE technique, there is still a lack of significant theoretical justification for the choice of SDC matrices and their effectiveness in representing the system under all operating conditions or a wide range of them. The purpose of this short paper is to illustrate some preliminary ideas and insights with which we intend to investigate the theoretical aspects underlying these methods to be used to solve complex nonlinear optimisation control problems.

II. Brief overview on the SDC

Consider a nonlinear control problem affine in input

$$\begin{cases} \dot{x} = f(x) + g(x)u \\ y = h(x) \end{cases} \tag{1}$$

A continuous, nonlinear matrix-valued function, A(x), can always be obtained by mathematical factorization if:
a) $f(0) = 0$
b) $f(x) \in C^1$.
When these conditions are met, $f(x)$ can be factored as:

$$f(x) = A(x)x \tag{2}$$

In [3], Cloutier showed that the factorization in Eq. 2 is non-unique for $n > 1$. Furthermore, denoting $g(x) = B(x)$, the system in Eq. 1 becomes:

$$\dot{x} = A(x)x + B(x)u \tag{3}$$

which represents the SDC factorization of the nonlinear state equation of the system (1).

III. Preliminary nonlinear analysis of SDC reachability

Probably, due to the similarity of the representation (3) with that of linear systems, optimal control problems for SDC representations of the type (3) have been addressed by attempting to extend the structural properties of linear systems to the SDC representation of nonlinear systems as well. The results were mixed, sometimes proving validity for certain types of systems or with certain characteristics, while in other cases counterexamples undermined the general validity [5]. The problem can be traced back to the use of tools limited by point wise assumption of the dynamic behavior [6]. Since treating non-linear representations, the tools of non-linear analysis or differential geometry would be more appropriate and suitable for such studies. A brief preliminary analysis about the reachability of the SDC representation of a generic second order nonlinear system will highlight some aspects of the SDC that cannot be seen otherwise. Let us consider the first equation of (1) with the state vector x of dimension two and assume that $f(x)$ is represented as (2). The dimension of f is 2×1, and it can be rewritten as a sum of column vectors of $A(x)$, here called $a_i(x)$, $i = 1, 2$, as follows.

$$
\begin{aligned}
&f = A(x)x = a_1(x)x_1 + a_2(x)x_2 \\
&where,\ A(x) = [a_1(x)\ a_2(x)] = \begin{bmatrix} a_{11} & a_{12} \\ a_{21} & a_{22} \end{bmatrix}\ ed\ x = \begin{bmatrix} x_1 \\ x_2 \end{bmatrix}
\end{aligned} \tag{4}
$$

This allow us to compute the Lie brackets more easily. Recalling [4], the nonlinear local reachability of (1) is related to the following set

$$
\{g; [f; g]\} \tag{5}
$$

where, the square parenthesis represent Lie bracket operator. By evaluating (5) for the equation (4) we have

$$
\begin{aligned}
[f; g] = [Ax; g] = [(a_1x_1 + a_2x_2); g] = [a_1x_1; g] + [a_2x_2; g] = \\
= [a_1; g]x_1 - a_1\mathcal{L}_g(x_1) + [a_2; g]x_2 - a_2\mathcal{L}_g(x_2)
\end{aligned}
$$

this because

$$
\begin{aligned}
[a_ix_i; g] &= \frac{\partial g}{\partial x}a_ix_i - \frac{\partial(a_ix_i)}{\partial x}g = \\
&= \frac{\partial g}{\partial x}a_ix_i - \left(\frac{\partial a_i}{\partial x}x_i + a_i\frac{\partial x_i}{\partial x}\right)g = \\
&= \left(\frac{\partial g}{\partial x}a_i - \frac{\partial a_i}{\partial x}g\right)x_i - a_i\frac{\partial x_i}{\partial x}g = \\
&= [a_i; g]x_i - a_i\mathcal{L}_g(x_i)
\end{aligned}
$$

where, $\mathcal{L}_g$ is the Lie derivative, which in this case can be simply computed as:

$$
\begin{aligned}
\mathcal{L}_g(x_1) &= \frac{\partial x_1}{\partial x}g(x) = [1\ 0]\begin{bmatrix} g_1 \\ g_2 \end{bmatrix} = g_1 \\
[a_1; g] &= \frac{\partial g}{\partial x}a_1 - \frac{\partial a_1}{\partial x}g = J_ga_1 - J_{a_1}g
\end{aligned}
$$

Where $J_g(x)$ is the jacobian respect to x of the affine input function g. Similarly J_{a_i} is the jacobian respect to x of the i-th column of $A(x)$. The final equation can be rearranged as follows:

$$
\begin{aligned}
&(J_ga_1 - J_{a_1}g)x_1 - a_1g_1 + (J_ga_2 - J_{a_2}g)x_2 - a_2g_2 = \\
&J_g(a_1x_1 + a_2x_2) - (J_{a_1}x_1 + J_{a_2}x_2)g - (a_1g_1 + a_2g_2)
\end{aligned} \tag{6}
$$

Recalling that the partial derivative of f is related to the jacobian, the partial derivative of the SDC form gives rise to:

$$
\begin{aligned}
&\frac{\partial f(x)}{\partial x} = J(x) \\
&f(x) = A(x)x \\
&\frac{\partial f(x)}{\partial x} = \frac{\partial(A(x)x)}{\partial x} = \frac{\partial A(x)}{\partial x}x + A(x)\frac{\partial x}{\partial x} = \frac{\partial A(x)}{\partial x}x + A(x) \\
&J(x) = \frac{\partial A(x)}{\partial x}x + A(x)
\end{aligned} \tag{7}
$$

where,

$$
\frac{\partial A(x)}{\partial x}x = \left[\frac{\partial A(x)}{\partial x_1}x; \frac{\partial A(x)}{\partial x_2}x; \ldots; \frac{\partial A(x)}{\partial x_n}x\right]
$$

The result of (6) can be rewritten as follows:

$$
\begin{aligned}
&J_g(a_1x_1 + a_2x_2) - (J_{a_1}x_1 + J_{a_2}x_2)g - (a_1g_1 + a_2g_2) = \\
&J_g(Ax) - \left(\frac{\partial A}{\partial x}x\right)g - (Ag) = \\
&J_gAx - \left(\frac{\partial A}{\partial x}x + A\right)g = \\
&J_gAx - Jg = [f; g]
\end{aligned}
$$

Equation (6) can be generalised to a generic system of order n, and it results that

$$
\begin{aligned}
[f; g] = [Ax; g] &= \left(\sum_{i=1}^{n}[a_i; g]x_i\right) - \left(\sum_{i=1}^{n}a_i\mathcal{L}_g(x_i)\right) = \\
&= J_g\left(\sum_{i=1}^{n}a_ix_i\right) - \left(\sum_{i=1}^{n}J_{a_i}x_i\right)g - \left(\sum_{i=1}^{n}a_ig_i\right)
\end{aligned} \tag{8}
$$

Eq. (8) describes the nonlinear reacahability of the SDC representation as depending by three terms. The first one disappear in the linear case when g does not depends from x and the output Jacobian J_g is null. In the linearised case, the state equation (3) is approximated by the first order Taylor expansion of (3) in the origin, and the dynamic matrix of the linear system simply coincide with the system Jacobian $A = J = \frac{\partial f}{\partial x}$. Differently, in the nonlinear case, Eq. (7) shows that the SDC representation also depends by the term $\frac{\partial A(x)}{\partial x}x$, which represents the error made by approximating the nonlinear system jacobian with A(x) as usually happens in the point wise analysis. The approximation error increases the greater the rate of change of the system state $\dot{x}$. Care must be taken when using point wise tools that usually approximate the Jacobian matrix with the dynamic matrix in SDC form.

IV. Conclusion

In this short paper, a preliminary investigation into some theoretical aspects of the use of SDC parameterisation of non-linear systems for future use in non-linear optimal control problems is proposed.

References

[1] H. K. Khalil, Nonlinear Systems, 3rd ed. Prentice Hall, 2002.

[2] B. Friedland, Advanced Control System Design. Prentice Hall, 1996.

[3] J.R. Cloutier, C.N. D'Souza and C.P. Mracek, "Nonlinear regulation and nonlinear h¥ control via the statedependent riccati equation technique: Part 1, theory; part 2: Examples." Proceedings of the First International Conference on Nonlinear Problems in Aviation and Aerospace., pp. 117–141, 1996.

[4] Alberto Isidori, J van Schuppen, E Sontag, M Thoma, and M Krstic, "Communications and control engineering," in Nonlinear control systems. Springer, 1995.

[5] Evrin Bilge Erdem, Analysis and real-time implementation of statedependent Riccati equation controlled systems, University of Illinois at Urbana-Champaign, 2001

[6] James R Cloutier, Donald T Stansbery, and Mario Sznaier, "On the recoverability of nonlinear state feedback laws by extended linearization control techniques," in Proceedings of the 1999 American Control Conference (Cat. No. 99CH36251). IEEE, 1999, vol. 3, pp. 1515–1519.

Optimal control of electric and autonomous buses on intercity lines based on traffic prediction

C. Pasquale[a], S. Sacone[a], S. Siri[a], A. Ferrara[b]

[a] Department of Informatics, Bioengineering, Robotics and Systems Engineering, University of Genova, Italy
[b] Department of Electrical, Computer and Biomedical Engineering, University of Pavia, Italy

In this extended abstract, we present an optimal control scheme for electric and autonomous buses which have to follow a certain line (a route with a timetable) in extra-urban roads. Specifically, the goal of this controller is to optimally define the charging time and the speed profiles of intercity buses. The need to define the optimal speed profile of electric vehicles is an issue that has often been addressed in the literature. Typically the goal of this type of problem is to reduce energy consumption based on aspects related to vehicle motion and road characteristics, such as slope, traffic light intersections, and so on (see for example [1, 2]). Eco-driving strategies have also been applied for the optimal control of buses. However, many of these approaches aim to control buses in urban areas as done for instance in [3, 4, 5]. In these approaches the presence of reserved lanes allows to overlook the influence of surrounding vehicular traffic.

This work, being focused on intercity bus control, requires that the presence of traffic must be taken into account both for energy-saving reasons and for respecting time schedules. It is worth noting that the interaction between autonomous vehicles and the surrounding traffic is an important issue to be addressed also from a traffic-efficiency perspective, as done for instance in [6] for truck platoons and in [7] for electric and autonomous buses. Therefore, the control scheme we are presenting is based on real-time and predicted traffic measurements in order to react to unexpected events or disturbances. Furthermore, in this approach we assume that each bus has to visit specific stops in specific time windows and that all these stops are equipped with charging infrastructure so that the bus is recharged during its stop. Hence, the proposed optimal control scheme, whose general functioning is presented in Fig. 1, is composed of two modules:

1. the *traffic prediction model*, which allows to make a prediction of the traffic state in the extra-urban road for a given horizon; the model is initialized with the traffic state measured in real time;

2. the *optimal control* module, which allows to find the optimal values of the control variables (i.e. the stopping times and speeds for the buses). This optimal control module receives as inputs the average traffic speeds computed by the prediction model and the traffic state of buses measured in real time, i.e. the position and energy level of each bus.

Specifically, in the prediction module the traffic model METANET [8] is used to predict the traffic state evolution along the road and this prediction is the input of the optimal control problem in order to account for the impact of traffic on the behavior of buses. Note that defining the speed of buses by taking into account the real traffic conditions is a very important aspect. Indeed, neglecting the traffic conditions encountered by buses may lead to suggest speeds that cannot be implemented in practice. The optimal control problem is formulated as a mixed-integer linear quadratic problem whose goal is to find the state variables of each bus, i.e. position and energy level, and the control variables, i.e. dwell time at bus stops and speed profile, which minimize an objective function composed by three terms. More in detail, the first term is related to the deviation from the timetable. This term is multiplied by a weight which allows to properly weigh early arrivals and late departures from stops. The second cost term enables to smooth the speed profiles between two consecutive time steps, while the last term penalizes the final lack of energy for buses. Even the latter two terms are multiplied by weight parameters. Note that this is a high-level control scheme for a fleet of buses, and the tracking of the speed suggested as a reference signal by this scheme requires, for each bus, the development and implementation of a low-level controller based on a more detailed description of the bus dynamics.

This control scheme has been applied to a suburban bus line in Northern Italy, starting in the city of Savona and ending in the town of Finalborgo. The application to this case study showed that in

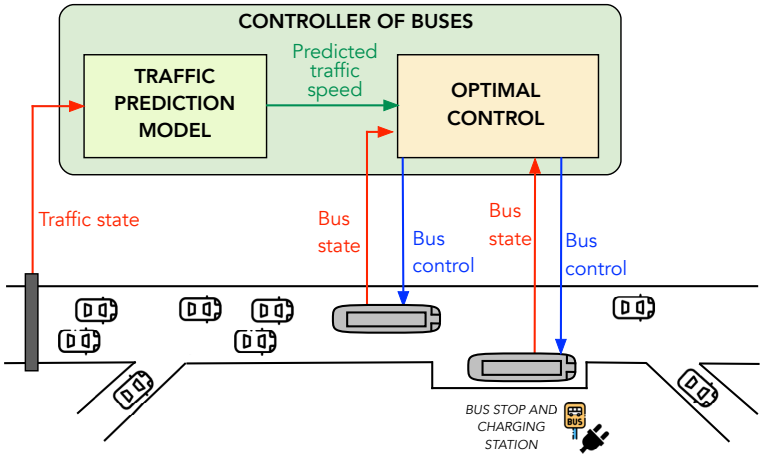

Figure 1: Sketch of the proposed control framework.

an extra-urban context the influence of traffic cannot be neglected. In addition, this case study also showed that the need to meet schedules and to recharge batteries may be in conflict, and the possible priority of either can be easily managed by correctly setting the weights in the objective function.

References

[1] A. Sciarretta, G. De Nunzio, L.L Ojeda (2015). Optimal ecodriving control: Energy-efficient driving of road vehicles as an optimal control problem. In *IEEE Control Systems Magazine*, vol. 35(5), 71–90.

[2] G.P. Padilla, S. Weiland, M.C.F. Donkers (2018). A global optimal solution to the eco-driving problem. In *IEEE Control Systems Letters*, vol. 2(4), 599–604.

[3] J. Flores Paredes, G. Padilla Cazar, M.C.F. Donkers (2019). A shrinking horizon approach to eco-driving for electric city buses: Implementation and experimental results. In *IFAC-PapersOnLine*, vol. 52(5), 556–561.

[4] S. Torabi, M. Bellone, M. Wahde (2020). Energy minimization for an electric bus using a genetic algorithm. In *European Transport Research Review*, vol. 12(1), 1–8.

[5] R. Lacombe, S. Gros, N. Murgovski, B. Kulcsr (2021). Bilevel Optimization for Bunching Mitigation and Eco-Driving of Electric Bus Lines. In *IEEE Transactions on Intelligent Transportation Systems*.

[6] C. Pasquale, S. Sacone, S. Siri, A. Ferrara (2018). A New Micro-Macro METANET Model for Platoon Control in Freeway Traffic Networks. In *Proc. of IEEE 21st International Conference on Intelligent Transportation Systems*, 1481–1486

[7] C. Pasquale, S. Sacone, S. Siri, A. Ferrara (2022). Optimal Charging and Speed Control of Electric Buses Based on Traffic Flow Predictions. Accepted to *6th IEEE Conference on Control Technology and Applications*

[8] A. Kotsialos, M. Papageorgiou, C. Diakaki, Y. Pavlis, F. Middelham (2002). Traffic Flow Modeling of Large-Scale Motorway Networks Using the Macroscopic Modeling Tool METANET. In *IEEE Transactions on Intelligent Transportation Systems*, 3, 282-292.

Optimization-Based Coordination of Mixed Traffic at Unsignalized Intersections Based on Platooning Strategy (Extended Abstract)

Muhammad Faris[1], Paolo Falcone[2], Jonas Sjöberg[1]

I. Introduction and Modeling

In the future, Connected and Automated Vehicles (CAVs) are expected to dominate traffic roads. CAVs are able to communicate and hence coordinate their decisions, facilitated by automatic intersection manager (IM). However, small portions of Human-Driven Vehicles (HDVs) may still exists. HDVs are known to be difficult to accurately predict and they may act non-cooperatively [1], which can challenge the traffic safety and efficiency, especially at unsignalized traffic junctions. Hence, coordination strategies specifically addressing mixed traffic scenarios are required. Here we leverage the idea of utilizing the CAVs as traffic *actuators* and *sensors* to somewhat control and observe the behavior of the HDVs [2].

Motivated by the aforementioned challenges, we develop a Model Predictive Control (MPC)-based algorithm for vehicle coordination at unsignalized intersections with mixed traffic. We leverage the concept of squeezing the HDVs among the CAVs forming a long virtual vehicle called a mixed platoon. Occupancy timeslot technique is utilized here to schedule the vehicles when accessing conflict zones (CZ) which are made flexible to accommodate HDVs uncertainties, hence safely avoiding collision and cut-in while attempting to gain traffic efficiency. Furthermore, the proposed algorithm employs two different HDV prediction models (car-following and constant velocity models) and compare them in numerical simulations with different models, added with uncertainties.

The CAVs can have three roles here. In *free-driving* mode, a CAV i is not joining any platoon and considered as a single agent. A *leader* CAV in a mixed platoon means that CAV i is immediately followed by one or several HDVs, with a *tail* CAV following the last HDV within the platoon. Hence, a mixed platoon has to be squeezed by a pair of CAVs.

Next, each vehicle motion along the paths is mathematically modeled as a linear discrete-time double integrator, with limitations on maximum/minimum allowed acceleration and velocity. For the HDVs, a human drivers behavior model is required for experiment and prediction purposes. In the experiment, we assume that a human driver switches between preferred velocity tracking and car-following, depending on the situation. For the prediction, we use and compare the car-following approach and constant velocity (measurements).

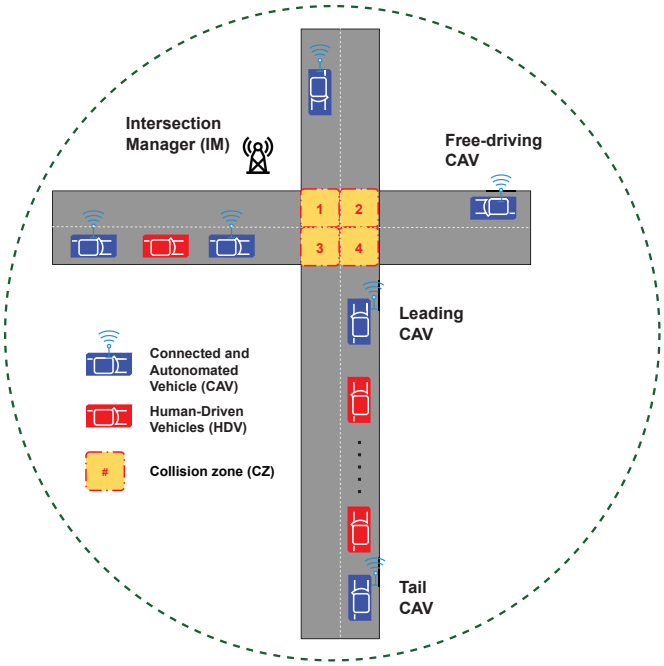

Fig. 1: Mixed platoons of CAVs and HDVs at an autonomous unsignalized intersection

In this work, we specifically consider a four-way unsignalized intersection with one lane is in each direction. The intersection area is divided into a set of conflict zones (CZs), as depicted in the four yellow squares in Fig. 1, which cannot be occupied by more than one vehicle at any time. Furthermore, for each CZ $z \in \mathcal{Z}$ the pair $\left(p_z^{\text{in}}, p_z^{\text{out}}\right)$ defines the entry and exit positions, respectively. It follows that, for every CAV i and CZ z an occupancy timeslot can be defined in terms of entry $\hat{t}_{i,z}^{\text{in}}$ and exit $\hat{t}_{i,z}^{\text{out}}$ times.

II. Problem Formulation and Control Algorithm

We next formulate the coordination problem as a bi-level constrained optimization problem. To avoid side collisions, each pair of vehicles traveling along paths intersecting at a CZ is subject to the timeslot (OR) constraints, which means for a pair $i,\ j$ of vehicles from different direction, either i or j is allowed to occupy the CZ z during $[\hat{t}_{i,z}^{\text{in}},\ \hat{t}_{i,z}^{\text{out}}]$. That is, the vehicle j is allowed to occupy the CZ either before or after the timeslot $[\hat{t}_{i,z}^{\text{in}},\ \hat{t}_{i,z}^{\text{out}}]$. Moreover, to avoid collision between adjacent vehicles moving in the same lane, a vehicle

*This work was supported by the Wallenberg Artificial Intelligence, Autonomous Systems and Software Program (WASP) funded by Knut and Alice Wallenberg Foundation.

[1]Muhammad Faris and Jonas Sjöberg are with Department of Electrical Engineering, Chalmers University of Technology, Gothenburg, Sweden. farism@chalmers.se, jonas.sjoberg@chalmers.se

[2] Paolo Falcone is with Department of Electrical Engineering, Chalmers University of Technology, Gothenburg, Sweden and and DIEF, Universita di Modena e Reggio Emilia, Italy. paolo.falcone@chalmers.se

must keep a *safe* distance from its immediate preceding vehicle.

The bi-level optimization consists of an upper-level planner and a lower-level controller. The goal of the upper-level optimization, represented by the IM, is to determine the intersection crossing order $\mathcal{O}$, which is to be broadcasted to the CAVs. The order is implicitly retrieved when solving the optimization problem.

In general, the objective functions in both upper and lower level is split into two terms. The first part is dedicated for the *free-driving* and *leader* CAVs, while the other one is for *tail* CAVs. For the former ones, the goal is to track a reference velocity while minimizing its acceleration/deceleration (control input). On the other hand, the objective of *tail* vehicles is slightly different as they have the additional task of accommodating the behavior of the preceding HDVs while minimizing their control inputs.

The objective function J^{lower} of the lower-level controller has a structure similar to that of the upper-level planner, since the goals are similar. However, it instead generates the control inputs U and timeslots $\hat{T}$ of all CAVs given the crossing order information. Both the upper-level and lower-level problems are regarded as Mixed-Integer Quadratic Programming (MIQP) Optimal Control Problem (OCP). Two different OCPs, each with the (1) car-following model and (2) constant velocity is deployed.

In practice, HDVs behavior are aleatory hence difficult to accurately predict. Consequently, achieving feasibility of some constraints can be challenging. To solve this issue, we soften some constraints such that extra margins are introduced. The soft constraints include rear-end safe distance between *tail* CAV and HDV, and entry and exit positions at CZ. The relaxation is done by adding slack variables to the constraints and penalty functions in the objective.

Model predictive control (MPC) approach [3] is selected to shape the closed-loop system behavior of the OCP. Thus, the MPC inherits the bi-level structure, and is formulated for the upper-level and lower-level modules. The algorithm is implemented in MATLAB with YALMIP and the Gurobi solver.

III. Numerical simulations

To evaluate the performance of the OCP, simulations are carried out. Evaluation metrics include safety aspects, e.g., no side/rear collision or cut-in occurs, and traffic efficiency, i.e., total intersection (CZ) clearance time of all vehicles. We consider a small-scale coordination case where a single CZ z is to be used by a single platoon consisting of a pair of *leader-tail* CAV and a single HDV in between, as well as a *free-driving* CAV.

Furthermore, we evaluate the performance of two OCPs, where the former utilizes car-following model while the other one adopts constant velocity model. In the car-following model, we fixed its coefficients to some constant, basically putting assumptions on how HDV would behave. In simulations, however, the switching mode is adopted for the HDV, where the coefficients are time-varying according to some Gaussian distribution. In addition, it is perturbed by an additive Gaussian disturbance, which models a deviation of a human driver from the models. Two scenarios are simulated where the variables and disturbance data are exactly the same, except in the 1st scenario, the v^{ref} has an average $\mu_v = 12.5$ m/s $(45$ km/h$)$ while in the 2nd one the average is $\mu_v = 16.67$ m/s $(60$ km/h$)$. In both scenarios, all vehicles start from certain locations around 150 meters from the CZ. The *free-driving* CAV is initially placed in such a way that it could arrive in the middle of the platoon coming from the other direction. Without the proposed algorithm, this would unfold into an unsafe cut-in situation. However, the IM lets *free-driving* CAV comes first then the platoon follows thereafter.

Furthermore, we see that the OCP problem with car-following model clears the CZ slightly faster (4.0 seconds) compared to the constant velocity model (4.1 seconds). This result is reasonable as the assumptions are much closer to the HDV behavior; hence, the prediction model can deliver better information. A contrast result in the second scenario where we run a similar simulation with the assumptions on the car-following model staying the same, but the HDV in the simulation decides to move faster instead. The constant velocity model clears CZ faster (2.0 seconds) than the car-following model (2.3 seconds), in which the time difference between those models here is more significant.

Even though the car-following model depends on measurements, it is nevertheless more sensitive toward the change of HDV behaviors and uncertainties, due to the applied certain assumption. On the other hand, we observe that the constant velocity model, which has the least assumption, performs more consistently by keeping reasonably safe distances with the HDV all the time, which is not too close, but is considered traffic efficient.

References

[1] X. Di and R. Shi, "A Survey on Autonomous Vehicle Control in the Era of Mixed-Autonomy: From Physics-Based to AI-Guided Driving Policy Learning," *Transportation Research Part C*, vol. 125, no. April, p. 103 008, 2021. arXiv: 2007.05156.

[2] D. Sadigh, S. S. Sastry, S. A. Seshia, and A. Dragan, "Information gathering actions over human internal state," *IEEE International Conference on Intelligent Robots and Systems*, vol. 2016-Novem, pp. 66–73, 2016.

[3] J. B. Rawlings, D. Q. Mayne, and M. M. Moritz, *Model predictive control: Theory, Computation, and Design 2nd Edition*. 2019, vol. 197, pp. 77–129, ISBN: 9780975937730.

Type-K Monotone Systems and Consensus in Multi-Agent Networks

Diego Deplano, Mauro Franceschelli, Alessandro Giua.

***Abstract*—This extended abstract presents recent advances on stability and convergence results of *type-K monotone* dynamical systems, firstly introduced by us for the discrete-time framework [1], [2] and now generalized to the continuous-time framework [3]. Remarkably, type-K monotonicity turns out to be equivalent to standard monotonicity in smooth systems evolving in continuous-time, subject of *monotone dynamical systems theory* [4], but not in discrete-time, subject of *nonlinear Perron-Frobenius theory* [5], thus suggesting its important role in bridging these two theories. Our research focuses on the stability analysis of type-K monotone systems that are also plus-homogeneous, which we call K-topical, and further investigates the consensus problem in K-topical multi-agent systems.**

I. Introduction

Dynamical systems whose trajectories preserve a partial order have represented a fruitful topic of research in numerous fields, especially in the modeling of biological, socio-economical, and transportation networks. Such systems are usually called *monotone*, i.e., given two ordered initial conditions $x(0)$, $z(0)$ the corresponding system's evolutions $x(t)$, $z(t)$ maintain the same order, i.e.,

$$x(0) \leq z(0) \quad \Rightarrow \quad x(t) \leq z(t), \qquad t > 0.$$

In the theory of *monotone dynamical systems* [4], emphasis is put on the class of continuous-time systems being strongly monotone, a subclass of monotone systems. Pioneering work in this field was done by Hirsch, who showed that if their solutions exist and are bounded, then they converge to a set of equilibrium points [6]. In contrast, in *nonlinear Perron–Frobenius* theory [5], one usually considers discrete-time dynamical systems that are only monotone, thus making unenforceable most of the theory of strongly monotone systems and, consequently, making necessary some additional assumptions. Indeed, Polavcik was among the first to show that trajectories of discrete-time systems may converge toward periodic orbits even under the strong monotonicity assumption [7]. In particular, attractive periodic orbits have been proven to be nonexistent for monotone systems in continuous-time systems, but may exist in discrete-time.

The monotone control community has recently recognized the importance of bridging the two above-mentioned approaches. Indeed, Angeli and Sontag studied continuous-time monotone systems satisfying an additional property that goes by the name of *plus-homogeneity*,

$$z(0) = x(0) + \alpha\mathbf{1} \;\Rightarrow\; z(t) = x(t) + \alpha\mathbf{1}, \quad t > 0,\, \forall \alpha \in \mathbb{R},$$

we call these systems *topical* after Gunardena and Kean [8].

D. Deplano, M. Franceschelli and A. Giua are with DIEE, University of Cagliari, 09123 Cagliari, Italy. Emails: {diego.deplano,mauro.franceschelli,giua}@unica.it

Under the strong monotonicity assumption, they have proved that convergence to equilibria is global for a suitable projection of the systems [9]. However, if one wishes to get a global convergence result only assuming that the dynamical system is monotone without a stronger assumption, one meets several difficulties when applying any known method used in the strongly monotone case. Concerning discrete-time systems, in his seminal works, Nussbaum showed that topical systems (without the strong monotonicity assumption) are nonexpansive under the sup-norm [10], whose trajectories are known to be either all unbounded or converging toward periodic orbits.

Our research aims at creating a more solid connection between these two theories by studying dynamical systems that satisfy a weaker property than strong monotonicity, which we call *type-K monotonicity*,

$$x(0) \leq z(0) \;\Rightarrow\; \begin{cases} x_i(t) \leq z_i(t) & \text{if } x_i(0) = z_i(0) \\ x_i(t) < z_i(t) & \text{if } x_i(0) < z_i(0) \end{cases} \quad t > 0.$$

and we call *K-topical* systems those being type-K monotone and plus-homogeneous.

II. Smooth monotone dynamical systems

One interesting and remarkable original result we have shown is that monotonicity and type-K monotonicity are equivalent properties for smooth dynamical systems evolving in continuous-time, while this is not the case for the discrete-time framework. It is clear that type-K monotonicity implies monotonicity, while the reverse implication is not true in general. However, if one considers a continuous-time system

$$\dot{x}(t) = f(x(t)), \qquad t \in \mathbb{R},$$

where f is C^1, monotonicity implies type-K monotonicity. This means that all results that apply to monotone systems apply to type-K monotone systems, given that the system evolves in continuous-time with a continuously differentiable vector field. When f is not C^1, this relation does not hold anymore, as shown by the following example with $x(t) \in \mathbb{R}$,

$$\dot{x}(t) = -\text{sign}(x(t)).$$

One can verify that this system is monotone but not type-K monotone. Conversely, if one considers a discrete-time system

$$\dot{x}(t+1) = f(x(t)), \qquad t \in \mathbb{N},$$

then monotonicity does not imply type-K monotonicity even if f is C^1. A simple counterexample is given by the system $x(t) \in \mathbb{R}^2$ with linear dynamics

$$x(t+1) = Ax(t), \quad A = \begin{bmatrix} 0 & 1 \\ 1 & 0 \end{bmatrix}.$$

One can verify that this system is monotone but not type-K monotone, whose trajectories lie on periodic orbits with a period equal to 2 for any initial condition.

III. Main convergence result and an application

The main convergence result we present in this abstract is that for smooth K-topical systems, each trajectory converges to some stable equilibrium point, if any exists. This result is as general as it appears: it applies to both continuous- and discrete-time systems and does not make any a priori assumption on the trajectories. Indeed, the proof of this result first shows that trajectories of K-topical systems exist and are unique at any time, then shows their convergence to periodic orbits by exploiting the nonexpansiveness property of topical systems. The last and most pivotal piece of the proof is that the type-K monotonicity constraints the systems' trajectories in a way that periodic orbits collapse to equilibrium points. In other words, type-K monotonicity avoids periodic behaviors of topical systems, thus creating the bridge we sought between continuous- and discrete-time systems.

A. Application to chemical reaction networks

An emblematic case of K-topical systems in continuous-time is that of well-mixed and isothermal chemical reactions [9]. The main result in Corollary 3.3 of [9] establishes convergence to a unique equilibrium of the reaction system exploiting the strong monotonicity of an equivalent system. However, strong monotonicity is shown to hold when the reaction system evolves on a forward invariant subset $\mathcal{X} \subset \mathbb{R}_{\geq 0}$ of the state-space, while for initial conditions not lying in this set, the authors provide an ad-hoc proof to establish the convergence of the system toward equilibrium points. By relaxing the assumption of strong monotonicity to that of type-K monotonicity, one can retrace the proof of Corollary 3.3 and prove the convergence of the system to an equilibrium point for any initial condition, namely $\mathcal{X} \equiv \mathbb{R}_{\geq 0}$. In other words, the type-K monotonicity allows generalizing the results in [9], by enabling one to study also the Michaelis-Menten type of reactions that may occur when some pairs of chemical species do not appear in the reaction.

IV. Consensus in Monotone Multi-Agent Systems

We have further investigated the exploitation of the result presented in the previous section in the context of K-topical Multi-Agent Systems (MASs). The focus of our research is precisely on understanding which kind of local couplings between agents make the global system K-topical, which would, in turn, prove the stability of the MAS; by stability is meant that all agents' states converge to an equilibrium point. Secondly, we focused on understanding under which conditions on the global network topology the set of equilibrium points coincide with those of consensus, i.e., equilibrium points such that all agents' states assume the same value, thus solving in this way the so-called *consensus problem* for the general class of nonlinear K-topical MASs.

An important step toward this direction is the derivation of necessary and sufficient conditions on the local coupling smooth functions between agents for both type-K monotonicity and plus-homogeneity, which is another original result of our research. First of all, we point out that plus-homogeneity is a common assumption in MASs, where the agents have usually no access to a common reference point, but they can only exchange relative information. This means that the coupling between any two agents does not depend on their specific state values, but rather on their state difference. This common assumption makes the MAS plus-homogeneous or, in other words, invariant with respect to a rigid translation along the direction of consensus. Concerning the type-K monotonicity, we proved that it is equivalent to a specific sign structure of the Jacobian matrix of the system dynamics. More precisely, in continuous-time a smooth system is type-K monotone iff the Jacobian is Metzler, whereas in discrete-time a system is type-K monotone iff the Jacobian is Metzler with a strictly positive diagonal. Clearly, such property can be verified locally by the agents and does not require knowledge of the overall dynamics of the system.

The second important result is that of providing sufficient conditions on the graph topology ensuring that the set of equilibrium points consists of only consensus states. Due to the plus-homogeneity property, if the origin is an equilibrium point, then all consensus states are necessarily equilibrium points, but not vice versa. We have shown that under the mild assumption of the presence of a globally reachable node in the directed graph, there no exists any other equilibrium point other than those of consensus.

The notable aspect of this work is that it avoids standard Lyapunov arguments in favor of nonlinear Perron-Frobenius and graph theories to prove the stability and consensus of MASs. Our results are thus a generalization to nonlinear dynamical system of nonnegative matrix theory applied to MAS.

References

[1] D. Deplano, M. Franceschelli, and A. Giua, "Lyapunov-free analysis for consensus of nonlinear discrete-time multi-agent systems," in *57th IEEE Conference on Decision and Control (CDC)*, 2018, pp. 2525–2530.

[2] ——, "A nonlinear perron–frobenius approach for stability and consensus of discrete-time multi-agent systems," *Automatica*, vol. 118, p. 109 025, 2020.

[3] ——, "Novel stability conditions for nonlinear monotone systems and consensus in multi-agent networks," *IEEE Transactions on Automatic Control*, under review.

[4] H. L. Smith, *Monotone Dynamical Systems: An Introduction to the Theory of Competitive and Cooperative Systems*, 41. American Mathematical Soc., 2008.

[5] B. Lemmens and R. Nussbaum, *Nonlinear Perron–Frobenius Theory*, ser. Cambridge Tracts in Mathematics. Cambridge University Press, 2012.

[6] M. W. Hirsch, "Stability and convergence in strongly monotone dynmamical systems," *Journal fur die reine und angewandte Mathmatik*, vol. 383, 1988.

[7] P. Poláčik and I. Tereščák, "Convergence to cycles as a typical asymptotic behavior in smooth strongly monotone discrete-time dynamical systems," *Archive for Rational Mechanics and Analysis*, vol. 116, no. 4, pp. 339–360, 1992.

[8] J. Gunawardena, "From max-plus algebra to nonexpansive mappings: A nonlinear theory for discrete event systems," *Theoretical Computer Science*, vol. 293, no. 1, pp. 141–167, 2003.

[9] D. Angeli and E. D. Sontag, "Translation-invariant monotone systems, and a global convergence result for enzymatic futile cycles," *Nonlinear Analysis: Real World Applications*, vol. 9, no. 1, pp. 128–140, 2008.

[10] R. Nussbaum, *Hilbert's Projective Metric and Iterated Nonlinear Maps*, Num. 388-391. American Mathematical Society, 1988.

An indirect realization of non-integer order discrete-time Tustin operators for non-integer order controllers

Guido Maione

Department of Electrical and Information Engineering, Politecnico di Bari, Italy

The interest in *non-integer order controllers* using differential and integral operators of non-integer order is continuously growing. Namely, these controllers may improve the trade-off between robust stability and dynamic performance with respect to integer order controllers. The seminal work was by Bode who conceived a non-integer order integrator as the ideal open-loop transfer function to obtain robustness to gain variations [1]. The basic idea is that the Bode phase diagram should be nearly "flat" around the gain crossover frequency. The literature often refers to fractional-order controllers as an application of fractional calculus, although the orders of differentiation and integration can be real or even complex, not just fractional numbers [2]. For example, the well-known $PI^{\lambda}D^{\mu}$-controllers have a transfer function $G_c(s) = K_p + \frac{K_i}{s^{\lambda}} + K_d s^{\mu}$, where s is the complex frequency, K_p, K_i, and K_d are the proportional, integral, and derivative gains, $0 < \lambda < 1$ and $0 < \mu < 1$ are the orders of integration and differentiation [3]. The additional degrees of freedom, λ and μ, provide more flexibility to match performance and robustness specifications. However, besides suitable design methods, implementation requires to "realize" the non-integer order operators $s^{-\lambda}$ and s^{μ}, which means to determine a rational transfer function approximating them over a given frequency interval [4]. The approximation models should be stable and minimum-phase. Direct and indirect approaches discretize the basic non-integer order operator s^{ν}, with $\nu = -\lambda$ or $\nu = \mu$, and allow implementation on digital control devices [5]-[8]. The first use a generating function, say $s = \psi(z^{-1})$, which depends on the sampling period T, and then truncate a power series expansion or a continued fraction expansion (CFE). Indirect approaches are in two steps: firstly, a frequency-domain fitting is applied to get an s-domain approximation; secondly, the fit s-transfer function is discretized by a suitable operator (Tustin, Euler, Al-Alaoui, etc.).

The author used a direct approach for approximating the non-integer order Tustin operator [8]. He showed that Laguerre CFE can be used to derive stable and minimum-phase transfer functions, with poles alternating with zeros (*interlacing* property). The issue is that transfer functions are computed by Euler-Wallis recurrence relations such as $A_i(x) = A_{i-1}(x) + a_i\, x\, A_{i-2}(x)$, where $a_i x$ are partial numerators in the CFE of the non-integer binomial function $(1+x)^{\nu}$. These relations can rapidly generate very large or very small coefficients in $G_n(x)$, which is the n-order approximation of $(1+x)^{\nu} \approx G_n(x)$. If overflow or underflow of the floating-point representation of the coefficients occur, then one must activate a new scaling of the recurrent relations at any iteration. This numerical problem is common to direct approaches. To avoid it, the author proposed an indirect two-steps approach for obtaining rational transfer functions not showing numerical problems [9]. Moreover, it's remarkable that the coefficients are expressed in a closed form, and stability, minimum-phase, and interlacing properties are guaranteed. The developed formulas avoid tedious algebraic s-to-z conversion operations of the usual indirect approaches.

In the first step, $(1+x)^{\nu}$ is approximated by $G_n(x) = \frac{\alpha_{n,0}\, x^n + \alpha_{n,1}\, x^{n-1} + \cdots + \alpha_{n,n-1}\, x + \alpha_{n,n}}{\beta_{n,0}\, x^n + \beta_{n,1}\, x^{n-1} + \cdots + \beta_{n,n-1}\, x + \beta_{n,n}}$ with coefficients expressed by:

$$\alpha_{n,i} = \binom{n}{k} P(n+k,k)\,(k+1+\nu)_{(n-k)} \quad \text{and} \quad \beta_{n,i} = \binom{n}{k} P(n+k,k)\,(k+1-\nu)_{(n-k)}$$

where $(k+1\pm\nu)_{(n-k)} = (k+1\pm\nu)(k+2\pm\nu)\cdots(n\pm\nu)$ are the Pochhammer symbols with $(n+1\pm\nu)_{(0)} = 1$ and $P(n+k,k) = (n+k)!/n!$, with $P(n,0) = 1$. Applying the transformation $x = 1/w$, using the equivalence with the Stieltjes CFE, and taking advantage of the Sturm sequence allows to prove that $G_n(x)$ has interlaced zeros and poles.

In the second step, $G_n(x)$ is converted into a rational discrete transfer function $H_n(z)$ modelling the non-integer order Tustin operator, with coefficients also given by formulas in closed form. To this aim, the transformation $x = 1/w = -\frac{2}{z+1}$ is applied such that the approximation is $\left(\frac{2}{T}\right)^{\nu}\left(\frac{z-1}{z+1}\right)^{\nu} \approx G_n(\nu,z) = \left(\frac{2}{T}\right)^{\nu} H_n(z) = \left(\frac{2}{T}\right)^{\nu} \frac{c_{n,0}\, z^n + c_{n,1}\, z^{n-1} + \cdots + c_{n,n-1}\, z + c_{n,n}}{d_{n,0}\, z^n + d_{n,1}\, z^{n-1} + \cdots + d_{n,n-1}\, z + d_{n,n}}$ with:

$$c_{n,i} = (n-i+1)_{(n)} \sum_{j=0}^{i} \frac{(-2)^{i-j}}{(i-j)!\,j!} (2n-i+1)_{(j)} (n-i+j+1+\nu)_{(i-j)}$$

$$d_{n,i} = (n-i+1)_{(n)} \sum_{j=0}^{i} \frac{(-2)^{i-j}}{(i-j)!\,j!} (2n-i+1)_{(j)} (n-i+j+1-\nu)_{(i-j)}$$

The coefficients can also be computed by $c_{n,i} = \sum_{k=n-i}^{n} (-2)^{n-k} \binom{k}{n-i} \alpha_{n,k}$ and $d_{n,i} = \sum_{k=n-i}^{n} (-2)^{n-k} \binom{k}{n-i} \beta_{n,k}$, where the recurrences $\alpha_{n,k} = \frac{(n+k)(n-k+1)}{k\,(k+\nu)} \alpha_{n,k-1}$ and $\beta_{n,k} = \frac{(n+k)(n-k+1)}{k\,(k-\nu)} \beta_{n,k-1}$ are useful. The obtained models have a characteristic zero-pole pattern. Namely, the (real and interlaced) zeros and poles of $H_n(z)$ are proven to be symmetrical with respect to the origin of the z-plane and belong to the interval (-1,1). As an example, consider $\nu = 0.4$, $T = 0.01$ s, and use $n = 4$. It holds:

$$G_4(0.4,z) = \left(\frac{2}{T}\right)^{0.4} H_4(z) = (200)^{0.4} \frac{1680\, z^4 - 672\, z^3 - 1324.8\, z^2 + 341.76 z + 118.8096}{1680\, z^4 + 672\, z^3 - 1324.8\, z^2 - 341.76\, z + 118.8096}$$

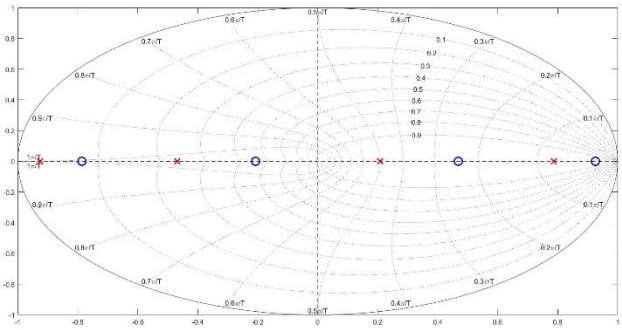

Fig. 1. Pole-zero map of the approximation $G(0.4, z)$ of $s^{0.4}$.

The sampling time is acceptable for the required computation time and reasonable for control applications. The zeros are 0.9254, -0.7864, 0.4685, -0.2075. The poles are -0.9254, 0.7864, -0.4685, 0.2075. Then zeros and poles are real (positive or negative), interlaced, and located inside the unit circle (stability and minimum-phase properties hold true). Moreover, they enjoy a special symmetry with respect to the origin, as shown in Fig. 1.

To evaluate the discrete rational model of the non-integer order Tustin operator with $\nu = 0.5$, other band-limited approximations of are considered, namely one based on the Al-Alaoui operator and another given in [10]. All approximations are obtained with $n = 4$. The Bode diagrams (Fig. 2) show that discretization based on the Tustin rule is affected by well-known larger errors at high frequencies, while other schemes improve the magnitude of the frequency response. However, the Tustin approximation has a phase diagram much closer to the constant phase of 45° associated to $s^{0.5}$, which is important for robust control. The left part of Fig. 3 shows that all approximations are stable and minimum-phase because zeros and poles are located inside the unit circle, however the Tustin approximation enjoys the peculiar symmetry of zeros and poles. The right part of Fig. 3 shows the responses of the approximations to the signal $u(t) = \sin(t)$, with frequency 1 rad/s belonging to the approximation range (see Fig. 2), and compares them to the ideal response specified by the 0.5-derivative of $u(t)$.

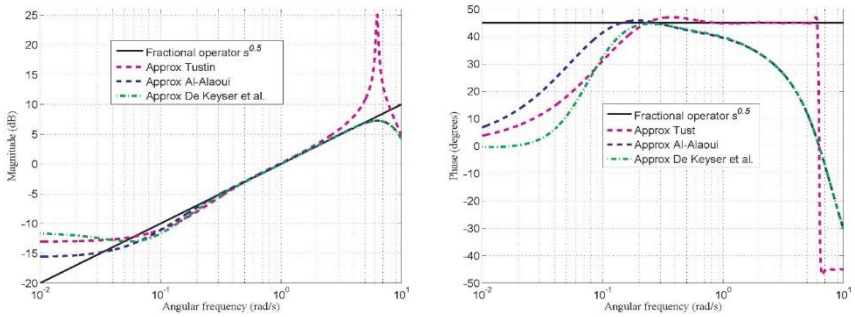

Fig. 2. Magnitude (left) and phase (right) Bode diagrams of the approximations of $s^{0.5}$.

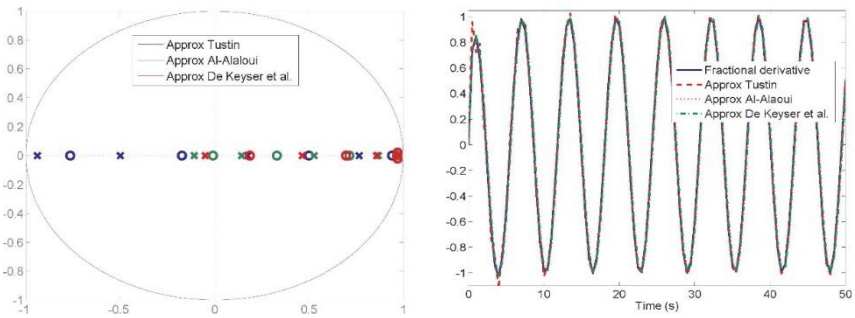

Fig. 3. Pole-zero maps of the approximations (left) and response to a sinusoidal signal (right).

To summarize, the proposed indirect discretization approach for approximating a non-integer order Tustin operator has the following characteristics:

- The coefficients of polynomials in the discrete transfer function can be easily and automatically computed by closed forms.
- Accuracy of the approximation is obtained with a reduced order n (a value equal to 4 or 5 is typically sufficient).
- The discrete transfer function (difference equation) can be implemented with numerical stability and limited round-off errors. Few and fast computations are necessary on input and output samples.
- It's possible to play with the non-integer order of differentiation/integration, ν, and the order of approximation, n.
- The approximation, and the controller developed on its basis, is stable and minimum-phase. Moreover, zeros and poles enjoy a symmetry with respect to the origin of the z-plane.

References

[1] H.W. Bode, *Network Analysis and Feedback Amplifiers Design*, Van Nostrand, New York, 1945.

[2] M.N. Kapetina, M.R. Rapaić, Z.D. Jeličić, P. Lino, G. Maione, “Complex-Order Models: A System Identification Point of View,” *Applied Sciences*, 12 (9): 4768, May 2022.

[3] I. Podlubny, “Fractional order systems and $PI^{\lambda}D^{\mu}$-controllers,” *IEEE Trans. Autom. Control*, vol. 44, no. 1, pp. 208–214, Jan. 1999.

[4] G. Maione, “Continued fractions approximation of the impulse response of fractional order dynamic systems,” *IET Control Theory and Applications*, vol. 2, no. 7, pp. 564–572, July 2008.

[5] I. Petráš, “Tuning and implementation methods for fractional-order controllers,” *Fract. Calculus Appl. Anal.*, 15: 282–303, 2012.

[6] Y. Q. Chen, B. M. Vinagre, and I. Podlubny, “Continued fraction approaches to discretizing fractional order derivatives – An expository review,” *Nonlinear Dynamics*, vol. 38, no. 1-2, pp. 155–170, 2004.

[7] G. Maione, “High-speed digital realizations of fractional operators in the delta domain,” *IEEE Trans. Autom. Control*, vol. 56, no. 3, pp. 697–702, Mar. 2011.

[8] G. Maione, “On the Laguerre rational approximation to fractional discrete derivative and integral operators,” *IEEE Trans. Autom. Control*, vol. 58, no. 6, pp. 1579–1585, June 2013.

[9] G. Maione, M.P. Lazarević, “On the symmetric distribution of interlaced zero-pole pairs approximating the discrete fractional Tustin operator”, *IEEE Int. Conf. on Systems, Man, and Cybernetics*, Bari, Italy, 6-9 Oct. 2019, pp. 2578-2583.

[10] R. De Keyser, C. I. Muresan, C. M. Ionescu, “An efficient algorithm for low-order direct discrete-time implementation of fractional order transfer functions,” *ISA Transactions*, vol. 74, pp. 229–238, 2018.

Safe and Ergonomic Human-Drone Interaction in Warehouses

Silvia Proia, Graziana Cavone, Raffaele Carli, and Mariagrazia Dotoli

***Abstract*— This paper presents an application of Human-Drone Interaction (HDI) for inventory management in a warehouse 4.0 that aims at improving the operators' safety and well-being together with increasing efficiency. The Speed and Separation Monitoring (SSM) methodology is applied for the first time to HDI, in analogy to the Human-Robot Interaction (HRI) ISO safety requirements as well as the Rapid Upper Limb Assessment (RULA), for evaluating the operator's ergonomic posture. With the aim of validating the proposed approach in a realistic scenario, a quadrotor is controlled to perform a pick and place task along a desired trajectory, from the picking bay to the palletizing area where the operator is located, avoiding collisions with the shelves by implementing the Artificial Potential Field technique (APF) for planning and the Linear Quadratic Regulator (LQR) and iterative LQR (iLQR) algorithms for tracking. The obtained results of the HDI architecture simulations are presented and discussed in detail proving the effectiveness of the proposed method.**

I. Introduction

Unmanned Aerial Vehicles (UAVs) play a fundamental role for advancing the complete automation of the warehouses 4.0 and Human-Drone Interaction (HDI) is emerging as a promising research field [1]. Until recently, most attention has been devoted to HDI in the outdoor context, while few contributions focus on HDI for indoor applications. In the current talk, a safe and ergonomic HDI is addressed in reference to the pick and place task in the intra-logistics sector, extending to this field the key requirements of Human-Robot Interaction (HRI). In fact, although there are notable differences between both fixed and mobile cobots and drones, there are similarities in the definition of HRI and HDI [1]. Therefore, by analogy with HRI where safety is the fundamental requirement, followed by the efficiency and the ergonomics targets [2], we apply the Speed and Separation Monitoring (SSM) approach [3] and the Rapid Upper Limb Assessment (RULA) index [4] to ensure an ergonomic posture of the operator. More specifically, our focus is to design an HDI architecture, which aims at increasing the efficiency of the pick and place task by planning, with the Artificial Potential Field (APF) algorithm, and tracking, with the iterative Linear Quadratic Regulator (iLQR), the shortest path for the quadrotor, while respecting ISO safety requirements and ergonomics in approaching the operator. The method effectiveness is validated through experiments and the results have been published in the conference paper [5] and are being extended for further journal submission.

S. Proia, R. Carli, and M. Dotoli are with the Department of Electrical and Information Engineering of the Polytechnic of Bari, Italy. (e-mail: {silvia.proia, raffaele.carli, mariagrazia.dotoli}@poliba.it).

G. Cavone is with the Department of Engineering, University of Roma Tre, Rome, Italy (e-mail: graziana.cavone@uniroma3.it).

II. Quadrotor Model and Tasks

The 2D quadrotor with 3 degrees of freedom (DOF) and 2 actuators (u_1, u_2) is modeled as a rigid body. In the ascent and descent mode and in the descent for HDI mode, the state vector is defined as: $\boldsymbol{s} = [x, z, \psi, \dot{x}, \dot{z}, \dot{\psi}]$, where x is the position of the quadrotor along the X axis, z along the Z axis, $\dot{x}$, $\dot{z}$ the linear velocities, ψ the angle of the quadrotor around the Z axis and $\dot{\psi}$ its angular velocity. In the free-flight mode, we consider the X-Y plane, thus the state vector is: $\boldsymbol{s} = [x, y, \psi, \dot{x}, \dot{y}, \dot{\psi}]$.

To apply the LQR in the ascent and descent mode and the iLQR in the free flight and descent for HDI modes, the non-linear quadrotor dynamics must be linearized. The system is linearized around a nominal point in the LQR and around a point over the nominal trajectory in the iLQR (see [5]).

For the development of our quadrotor automation, we consider three operating modes that are described as follows.

I) **Ascent and descent mode**: Ascent and descent are performed along a vertical axis by implementing an LQR controller. For ascent the quadrotor starts from a base raised from the ground and reaches a certain altitude where it begins to hover, while for descent the opposite occurs.

II) **Free flight mode**: In this mode, the quadrotor is in free flight and there is no contact with the floor. First, the shortest path that avoids collisions with the shelves is found with the APF algorithm. Then, an iLQR controller is implemented to ensure tracking of the desired planned trajectory.

III) **Descent for HDI mode**: Starting from a certain altitude with a non-zero velocity, the quadrotor descends along a vertical axis with a gradually decreasing velocity as it approaches the operator. To have greater control over the velocity, an iLQR is implemented instead of a LQR.

With the use of the quadrotor's operating modes listed above, it is possible to deliver items within the warehouse 4.0. In particular, a perfect HDI is obtained in six phases: (I) ascent without payload, (II) free flight without payload, (III) approaching the picking point, (IV) ascent with payload, (V) free flight with payload, and (VI) approaching the HDI point.

III. Descent for HDI Control Problem

In this section, the HDI crucial phase is described. Once the quadrotor has reached the palletizing area at a certain altitude, it begins to approach the HDI point along a vertical trajectory. The release of the payload by the drone must occur at an ergonomically optimal position for the operator, which is evaluated through the RULA index. Since in the HDI it is fundamental to ensure the operator's safety, we control the quadrotor's velocity applying the SSM.

The evaluation of the RULA index [4] is integrated as assessment tool in the HDI architecture with the aim of reducing the operator's work-related musculoskeletal disorders (MSDs). Following the procedure in [6], a design of experiments (DOE) is performed to determine the ergonomic operator's posture. The first phase consists in designing a manikin that simulates the operator in a fixed standing position. Then, a work volume $\mathcal{V}$ consisting of equidistant points reachable by the manikin's arm is defined in the work zone. For each point, the RULA index is evaluated and collected in a look-up table. Finally, for the sake of identifying the region in which the HDI point must be located, it is necessary to subdivide $\mathcal{V}$ into regions with constant RULA index and then choose the region with minimum value.

In addition to the evaluation of ergonomics, another goal is to respect the ISO safety requirements during the HDI. In particular, with the aim of preserving a safe separation distance between the operator and the quadrotor flying around the collaborative work zone, the SSM method measures the human-quadrotor distance that is compared with the authorized distance [3]. It can be assumed that the operator is safe when the quadrotor is moving outside a sphere of a certain radius, with the human in the center. Since the HDI occurs in the descent mode and we know the exact ergonomically optimal position of the operator in the X-Y plane, we are interested in controlling only the drone velocity along the Z axis, which is dangerous for the operator. Using the SSM method, when the separation distance tends to reduce below the authorized distance, and so when the quadrotor enters the collaborative work zone, the quadrotor must strongly decrease its linear velocity until it stops.

In particular, the minimum allowable quadrotor-human distance $S(t_0)$ is computed by using the equation in ISO/TS 15066 [7], that for our case study, in which the operator is located in the center of the sphere and the quadrotor flies around the work zone, can be rewritten as follow:

$$S(t_0) = (v_q T_q + v_q T_s) + B + C \tag{1}$$

where v_q is the quadrotor's velocity in the collaborative work zone, T_q is the quadrotor responding time in case of operator's presence, T_s is the time to stop the quadrotor motion, and C is an intrusion safety margin based on the expected human reach. B is computed as $v_q^2/2a$ and T_s as v_q/a with $v_q = \dot{z}$ being the maximum scalar quadrotor's velocity along the Z axis and a the worst-case deceleration value of the quadrotor during the stopping procedure.

IV. Case Study

The goal of our experiment is to efficiently and ergonomically perform a pick and place task in an Amazon-like warehouse (Fig. 1) by employing a quadrotor that, after leaving the charging area, transports an item, by finding the shortest path and avoiding collisions with the shelves (see [5]), from the picking bay to the palletizing area where the interaction with the operator takes place. More specifically, the experiment is conducted on a quadrotor modeled in accordance with the dynamic parameters in [8] and on a manikin that is a right-handed man with stature and weight percentile both equal to 50. The RULA analysis is executed with a payload of 0.8 kg for each equidistant point belonging to $\mathcal{V}$. From the DOE, it emerges that the HDI point must be located in the region $\mathcal{V}^*$ with minimum RULA equal to 3.

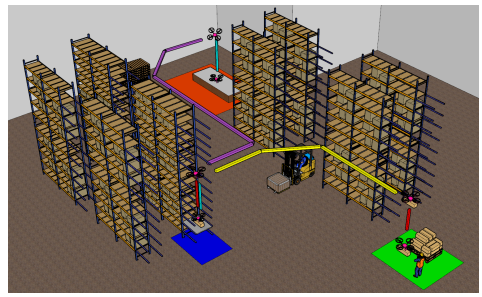

Fig. 1. 3D reconstruction of the warehouse environment where the quadrotor supports the operator in performing a pick and place task.

To evaluate the controllers effectiveness, we compute the root-mean-square error (RMSE) between the planned and the actual trajectory and the minimum distance from the shelves, which is equal to about 0.52 m. We remark that the operator's safety is guaranteed by the protective distance which is equal to 4.2 m. Finally, the ergonomics effectiveness is highlighted noting that the drone reaches the HDI point in $\mathcal{V}^*$ at a height of 1.3 m with an RMSE less than 0.001 m.

V. Conclusions and Outlooks

In this talk, a Human-Drone Interaction (HDI) application inside a warehouse 4.0 is presented. In particular, the quadrotor is used to transport an item from the picking bay to the palletizing area where the interaction with the operator takes place in a safe and ergonomic way. Future works will focus on enhancing the HDI architecture by considering the operator in motion instead of being standing still and forecasting the human movement, including collision avoidance with human workers and/or any kind of object in the ascent and descent phases, as well as analyzing the quadrotor model with a retractable gripper under more complex tasks.

References

[1] D. Tezza and M. Andujar, "The state-of-the-art of human–drone interaction: A survey," *IEEE Access*, 2019.

[2] S. Proia, R. Carli, G. Cavone, and M. Dotoli, "Control techniques for safe, ergonomic, and efficient human-robot collaboration in the digital industry: A survey," *IEEE Trans. Autom. Sci. Eng.*, 2021.

[3] J. A. Marvel and R. Norcross, "Implementing speed and separation monitoring in collaborative robot workcells," *Robot Comput. Integr. Manuf.*, vol. 44, pp. 144–155, 2017.

[4] L. McAtamney and E. N. Corlett, "Rula: a survey method for the investigation of work-related upper limb disorders," *Appl. Ergon.*, vol. 24, no. 2, pp. 91–99, 1993.

[5] S. Proia, G. Cavone, A. Camposeo, F. Ceglie, R. Carli, and M. Dotoli, "Safe and ergonomic human-drone interaction in warehouses," in *2022 IEEE/RSJ Int. Conf. Intell. Robots Syst. (IROS)*. IEEE, 2022, (accepted).

[6] S. Proia, R. Carli, G. Cavone, and M. Dotoli, "A trajectory planning optimization approach for a safe and ergonomic human-robot collaboration," in *2022 IEEE 18th Int. Conf. on Autom. Sci. and Eng. (CASE) (CASE)*. IEEE, 2022, (accepted).

[7] "International Organization for Standardization, ISO/TS 15066 (2016), Robots and Robotic Devices - Collaborative Robots."

[8] K. Yi, X. Liang, Y. He, L. Yang, and J. Han, "Active-model-based control for the quadrotor carrying a changed slung load," *Electronics*, vol. 8, no. 4, p. 461, 2019.

Learning and control of Networked Control systems

Luis Felipe Florenzan Reyes *, Francesco Smarra , and Alessandro D'Innocenzo

Department of Information Engineering, Computer Science and Mathematics. Università degli Studi dell'Aquila

Networked control systems (NCSs) are composed of spatially distributed sensors, actuators, and controllers communicating through wireless or wired networks. Despite their success in industrial monitoring applications, existing sensor-actuator network technologies face significant challenges in supporting control systems due to their lack of real-time performance and dynamic channel conditions in industrial plants. The inherent complexity of communication systems makes the physics-based modeling approach, in most cases, prohibitive in terms of cost and time constraints. Within our research, we derived novel methodologies by combining standard techniques in System Identification, Control systems, and Machine Learning to derive accurate control-oriented models of either wireless or wired channels. Our research activity proposes a novel methodology to learn a Markov model of a fading channel via historical data of the signal-to-interference-plus-noise-ratio (SINR). Such methodology is based on Regression Trees (RTs), and can be used to derive a Markov jump model of a wireless control network, and thus design a stochastic optimal controller that considers the interdependence between the plant and the wireless channel dynamics. Then, a complexity reduction methodology is proposed for a data-driven Switched Auto-Regressive eXogenous (SARX) model identification algorithm based on RTs.

Application to Wireless Networked Control systems. The method we proposed in [2], that we briefly recall in the next paragraph, leverages RTs to derive a Markov jump model of a wireless control network, and thus design a stochastic optimal controller that considers the interdependence between the plant and the wireless channel dynamics. The proposed method is validated by comparing its prediction accuracy and control performance with those of a stationary finite-state Markov chain derived assuming perfect knowledge of the physical channel model and parameters of a WirelessHART point-to-point communication based on the IEEE-802.15.4 standard.

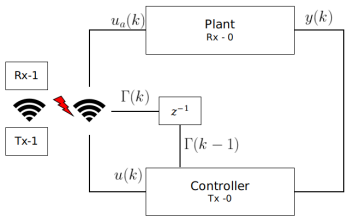

Figure 1: Wireless networked control system

From the automatic control perspective, we considered a nonlinear process with intermittent control packets due to a lossy communication channel described by the following equations:

$$\begin{cases} y(k+1) = f(y(k), u_a(k)), k \in \mathbb{N} \\ u_a(k) = \nu(k)u(k) \\ y(0) = y_0 \in \mathbb{R}^{n_y}, \end{cases} \tag{1}$$

where $y(k) \in \mathbb{R}^{n_y}$ is the output of the system and $u(k) \in \mathbb{R}^{n_u}$ is the input signal. $\{\nu(k)\}_{k\in\mathbb{N}}$ is a discrete-time Boolean process modeling the packet delivery of the control signals: if the packet is correctly delivered then $\nu(k) = 1$, otherwise $\nu(k) = 0$.

The control packet error probability (PEP) $\mathbb{P}(\nu(k) = 0)$ depends on the SINR of the communication $\Gamma(k)$, i.e.,

$$\mathbb{P}(\nu(k) = 0) = g(\Gamma(k)), \tag{2}$$

where $g : \mathbb{R} \to [0, 1]$ is a deterministic function defined by the communication standard.

We assume that the value of the SINR $\Gamma(k)$ is measurable and is sent to the controller via an acknowledgment (ACK). However, this ACK is available only after the current decision on the control

*Corresponding author.
E-mail: luisfelipe.florenzanreyes@graduate.univaq.it.

input to apply has been made and sent through the link, since the actual success of the transmission is not known in advance. Hence, at each time k the controller receives measurements of $y(k)$ and $\Gamma(k-1)$, as depicted in Fig. 1.

The main contribution of our research is a novel data-driven methodology, based on RTs, to identify such Markov chain abstraction. More precisely, we propose a novel methodology to model the PEP $\nu(k)$ on the basis of a Markov chain $\theta(k)$: each state of $\theta(k)$ is associated to a partition of $\mathbb{R}^{n_y+1}$ consisting of rectangular sets $\{R_i\}_{i=1}^{\ell}$, each representing the range of possible values of $\Gamma(k) \in \mathbb{R}$ and $y(k) \in \mathbb{R}^{n_y}$ at time k. We construct the transition probability matrix (TPM) of $\theta(k)$ as follows:

$$\begin{aligned} p(j \mid i) &\doteq \mathbb{P}(\theta(k+1) = j \mid \theta(k) = i) \\ &= \mathbb{P}(\theta(k+1) = j \mid (\Gamma(k), y(k)) \in R_i) \\ &= h(\Gamma(k), y(k)), \end{aligned} \tag{3}$$

where the identification from historical data of the function $h : \mathbb{R}^{n_y+1} \to [0,1]$, which depends on the current measurements $\Gamma(k)$ and $y(k)$, is the objective of the methodology proposed in [2]. Note that, given any two states i, j of the Markov chain, $p(j \mid i)$ also depends on the plant output: indeed, $y(k)$ may, for example, determine the distances between the transmitter, the receiver and the interferer, and this strongly affects the dynamics of $\Gamma(k)$.

Reduced SARX modeling and control via Regression trees. In [2], we leverage the techniques in [3] to construct a SARX model for the nonlinear plant f in (1) that can be directly combined with our Markov Jump model to setup a Stochastic Model Predictive Control problem for the system in (1). In particular, starting from a dataset $\mathcal{D} = \{(y(k), u(k))\}_{k=1}^{D}$ of D samples collected from the measurements of a physical system, respectively consisting of outputs $y(k) \in \mathbb{R}^{n_y}$ and inputs $u(k) \in \mathbb{R}^{n_u}$, we derive a model as follows:

$$y(k) = \theta_{\sigma(x(k))}^{\top} x(k), \tag{4}$$

where

$$\begin{aligned} x(k) \doteq [&y(k-1)^{\top}, \dots, y(k-\delta_y)^{\top}, \\ &u(k-1)^{\top}, \dots, u(k-\delta_u)^{\top}, 1]^{\top}, \end{aligned} \tag{5}$$

$\sigma : \mathbb{R}^{n_x} \to \{1, \dots, s\} \subset \mathbb{N}$ is a function that, on the basis of a partition $\{\mathcal{R}_i\}_{i=1}^{s}$ of $\mathbb{R}^{n_x}$, with $n_x = n_y\delta_y + n_u\delta_u + 1$, associates to each region $\mathcal{R}_i$ a discrete mode i and the corresponding parameters $\theta_i \in \mathbb{R}^{n_y \times n_x}$.

More precisely, the authors in [3] used the RTs learning algorithm algorithm to partition the dataset $\mathcal{D}$ to generate a partition of $\mathbb{R}^{n_x}$ consisting of hyper-rectangles $\{\mathcal{R}_i\}_{i=1}^{s}$ to be associated with the discrete modes of (4).

A lack of the methodology above is that the RTs learning algorithm partitions the features space by $\{\mathcal{R}_i\}_{i=1}^{s}$ to minimize the response variable variance in each region. The learning procedure corresponds to minimizing the prediction error performed by a constant estimator in each leaf; thus, it is generally not optimal anymore when ARX modeling is used instead of constant estimators. To address this issue, starting from the nominal SARX model in (4), we proposed in [1] to derive a procedure to learn a SARX model of the following form:

$$y(k) = \bar{\theta}_{\sigma(x(k))}^{\top} x(k), \tag{6}$$

where $\sigma : \mathbb{R}^{n_x} \to \{1, \dots, \bar{s}\} \subset \mathbb{N}$, with $\bar{s} << s$ and without compromising the model accuracy. In this respect, the idea is to apply a merge and discard procedure to all the ARX submodels. The *similarity* of the parameters of all submodels (not necessarily corresponding to adjacent regions $\mathcal{R}_i$) is quantified according to a metric: the samples associated to *similar* submodels are merged together, while if a submodel does not represent a relevant portion of the dataset it is discarded. Finally, the parameter vectors of the reduced model are recomputed based on the new partitioning.

References

[1] Luis Felipe Florenzan Reyes, Francesco Smarra, and Alessandro D'Innocenzo. Reduced sarx modeling and control via regression trees. In *2022 American Control Conference (ACC)*, 2022.

[2] Luis Felipe Florenzan Reyes, Francesco Smarra, Yuriy Zacchia Lun, and Alessandro D'Innocenzo. Learning markov models of fading channels in wireless control networks: a regression trees based approach. In *2021 29th Mediterranean Conference on Control and Automation (MED)*, pages 232–237, 2021.

[3] F. Smarra, G Di Girolamo, V. De Iuliis, A. Jain, R. Mangharam, and A. D'Innocenzo. Data-driven switching modeling for MPC using Regression Trees and Random Forests. *Nonlinear Analysis: Hybrid Systems*, 36:100882, 2020.

Distributed Optimal Control of Discrete-Time Linear Systems over Sensor Networks

Stefano Battilotti*, Filippo Cacace†, M. d'Angelo*

Abstract

In this paper (accepted for presentation at the 61-st IEEE Conference on Decision and Control - Dec. 6-9, 2022, in Cancún, Mexico) we consider the distributed Linear-Quadratic-Gaussian optimal control problem for discrete-time systems over sensor networks. In particular, the feedback controller is composed of local control stations, which receive some measurement data from the plant process and regulates a portion of the input signal. We provide a solution when the nodes have information on the structural data of the whole network but takes local actions, and also when only local information on the network are available to the nodes. The proposed solution is arbitrarily close to the optimal centralized one when the intermediate consensus steps are sufficiently large.

Problem Statement

We consider the general class of linear systems over networks described by

$$x_{k+1} = Ax_k + \sum_{i=1}^{N} B^{(i)} u_k^{(i)} + f_k, \tag{1}$$

$$y_k^{(i)} = C^{(i)} x_k + g_k^{(i)}, \quad i = 1, \ldots, N, \tag{2}$$

where $x_k \in \mathbb{R}^n$ is the state of the system, $y_k^{(i)} \in \mathbb{R}^{q_i}$, $q_i \geq 0$, is the measurement received by sensor i-th, $u_k^{(i)} \in \mathbb{R}^{p_i}$, $p_i \geq 0$, is the input signal sent by sensor i-th, and f_k and $g_k^{(i)}$, $i = 1, \ldots, N$, are zero-mean white noises, mutually independent with covariance respectively $Q \in \mathcal{P}_+(n)$, $R^{(i)} \in \mathcal{P}_+(q_i)$ $i = 1, \ldots, N$. The matrices Q and $R = \mathrm{diag}_i(R_i)$ are non-singular. Also $\bar{x}_0$ is random with mean $\bar{x}_0 := \mathbb{E}\{\bar{x}_0\}$ and covariance $\Sigma_{\bar{x}_0} := \mathbb{E}\{(x_0 - \bar{x}_0)(x_0 - \bar{x}_0)^\top\}$. In particular, different nodes, indexed by the label i-th(sensor and/or controller) communicate through an undirected graph $\mathcal{G} = (\mathcal{V}, \mathcal{E})$.

The infinite-horizon cost function is given by

$$J = \lim_{T \to \infty} \frac{1}{T} \mathbb{E} \left\{ \sum_{k=1}^{T} x_k^\top Q_c x_k + u_k^\top R_c u_k \right\}, \tag{3}$$

where Q_c and $R_c = \mathrm{diag}_i\{R_c^{(i)}\}$ are positive semi-definite matrices (strictly positive in the case of R_c). In order to design a distributed asymptotically optimal output-feedback control, we need the following assumptions.

Assumption 1 *The underlying graph $\mathcal{G}$ is undirected and connected.*

Assumption 2 *The couples (A, B) and (A, Q_c) are controllable, and the couples (C, A), (R_c, A) are observable.*

Assumption 3 *Matrices A, $B^{(i)}$, $C^{(i)}$, Q, $R^{(i)}$, Q_c, $R_c^{(i)}$ are available data for the node $i \in \{1, \ldots, N\}$ of the network.*

Assumption 2 is a standard global controllability/observability assumption, and we do not assume anything for the single pairs $(A, B^{(i)})$ and $(C^{(i)}, A)$. Assumption 3 is standard in this context and it requires the knowledge

*S. Battilotti and M. d'Angelo are with Dipartimento di Ingegneria Informatica Automatica e Gestionale, Sapienza University, Rome, Italy.

†F. Cacace is with Campus Bio-Medico di Roma, Rome, Italy.

of local input and output matrices and input cost, as well as of the systems matrices A, Q and cost Q_c. The aim of this paper is the following.

Goal: Find the distributed optimal output-feedback control policy $u_k^{(i)}$ for each sensor $i = 1, \ldots, N$, of system (1)–(2) such that the cost function J defined in (3) is minimized.

The term *distributed* explicitly refers to the constraints on communication local knowledge of the nodes (as specified by Assumption 3).

Main result

Theorem 1 *Given the system* (1)–(2) *with the cost function* (3)*, a network with the topology specified by a graph $\mathcal{G}$ with N nodes, let Assumptions 1, 2 and 3 hold true. Consider the distributed output-feedback control for $i = 1, \ldots, N$ given by*

$$u_k^{(i)} = \begin{cases} -L^{(i)}\hat{x}_k^{(i)}, & \text{if } B^{(i)} \neq 0 \\ 0, & \text{otherwise,} \end{cases} \tag{4}$$

with $L^{(i)}$ given by $L^{(i)} = {R_c^{(i)}}^{-1} B_i^\top S$, where S is obtained by solving

$$S = (I - SF)(A^\top SA + Q_c)(I - SF)^\top + SFS \tag{5}$$

with the term $F := BR_c^{-1}B^\top$ computed by each node $i \in \mathcal{V}$ through the Push-Sum algorithm, and $\hat{x}_k^{(i)}$ given, for some $\gamma \in \mathbb{N}$, by

$$v_k^{(i)} = -FS\hat{x}_k^{(i)} \tag{6}$$

$$\hat{x}_{k+1|k}^{(i)} = A\hat{x}_k^{(i)} + v_k^{(i)} \tag{7}$$

$$\begin{cases} z_{k+1,0}^{(i)} = & \hat{x}_{k+1|k}^{(i)} + K^{(i)}(y_{k+1}^{(i)} - C^{(i)}\hat{x}_{k+1|k}^{(i)}), \\ z_{k+1,h+1}^{(i)} = & z_{k+1,h}^{(i)} + \frac{1}{\delta}\sum_{j\in\mathcal{N}^{(i)}}(z_{k+1,h}^{(j)} - z_{k+1,h}^{(i)}) \end{cases} \tag{8}$$

$$\hat{x}_{k+1}^{(i)} = z_{k+1,\gamma}^{(i)}, \tag{9}$$

where $h = 0, \ldots, \gamma - 1$,

$$K^{(i)} := NP{C^{(i)}}^\top {R^{(i)}}^{-1}, \tag{10}$$

where P is the solution of

$$P = (I - PG)(APA^\top + Q)(I - PG)^\top + PGP \tag{11}$$

with the term $G := C^\top R^{-1}C$ computed by each node $i \in \mathcal{V}$ through the algorithm, $\delta > \lambda_N(\mathcal{L})$. Then the infinite-horizon cost function J of (3) *depending on the parameter $\gamma \in \mathbb{N}$ satisfies*

$$\lim_{\gamma\to+\infty} J = J^\star, \tag{12}$$

where $J^\star$ is the optimal cost of the centralized LQG Regulator.

We shall also present as a real-plant example an application to a water delivery system.

References

[1] S. Battilotti, F. Cacace, and M. d'Angelo. *A stability with optimality analysis of consensus-based distributed filters for discrete-time linear systems.* Automatica, vol. 129, p. 109589, 2021

[2] L. Orihuela, P. Millan, C. Vivas, and F. Rubio. *Distributed control and estimation scheme with applications to process control.* IEEE Trans. on Control Systems Technology, vol. 23, no. 4, pp. 1563–1570, 2015.

[3] S. Battilotti, F. Cacace, and M. d'Angelo. *Distributed infinite-horizon optimal control of continuous-time linear systems over network.* Inter- national Journal of Robust and Nonlinear Control, vol. 31, no. 6, pp. 2082–2096, 2021.

[4] Z. Ding and Z. Li. *Distributed adaptive consensus control of nonlinear output-feedback systems on directed graphs.* Automatica, vol. 72, pp. 46–52, 2016.

MPC-Based Process Control of Deep Drawing: An Industry 4.0 Case Study in Automotive

Graziana Cavone, Augusto Bozza, Raffaele Carli, and Mariagrazia Dotoli

***Abstract*— In this research work an innovative process control architecture based on Model Predictive Control (MPC) is developed for the industrial deep drawing process, which is an important metalworking process. In particular, we represent the process with a single-input multiple-output Hammerstein-Wiener model that relates the blank holder force (BHF) with the draw-in of different critical points around the die. Then, a single MPC regulator is designed to simultaneously control the draw-in of the multiple blank critical points by manipulating the BHF uniformly applied on the whole blank surface, avoiding workpiece defects that are due to the abnormal sliding of the metal sheet during the forming phase. The effectiveness of the proposed process controller is shown on a real case study in a digital twin framework, where the performance achieved by the MPC-based system is analyzed and discussed in detail.**

I. Introduction

Industrial deep drawing is the process used to impress a predefined shape to a metal sheet, which gets deformed plastically. Its core step is the forming phase, usually prone to several issues which could affect the quality of the stamped metal sheet [1]. To face the zero-defect manufacturing paradigm, automatic control techniques can be considered [2]. In deep drawing, process control [3] aims at monitoring specific forming variables (e.g., punch force, wrinkle height, draw-in, and friction force) during the formation phase in order to provide the correct blank holder force (BHF), which influences the forming stroke [4]. This results in a closed-loop control aiming at providing corrective actions in case of abnormal behaviors, thus ensuring a higher quality control of the whole process [5] as well contributing to disturbance rejection.

In this context, the goal of this talk, whose results have been published in [6], is twofold. On the one hand, differently from the state of the art, we model the forming stroke with a single-input multiple-output (SIMO) Hammerstein-Wiener (HW) model, providing a relationship between the BHF and the draw-in of n different monitored points around the die of the hydraulic press used for the process. On the other hand, we define a Model Predictive Control (MPC)-based architecture, where the regulator simultaneously controls the draw-in of the n different critical points by manipulating the BHF uniformly applied on the whole blank surface.

II. The Deep Drawing Process Model

Thanks to a system identification procedure, the deep drawing process is represented by a 2nd-order HW SIMO model having the BHF (uniformly distributed on the blank holder) –denoted as U_b– in input and the draw-in of n critical points of the metal sheet profile –denoted as $\boldsymbol{Y} = (Y_1, \ldots, Y_n)^\top$– in output. We represent its discrete-time nonlinear dynamics by means of a linear time-invariant dynamical subsystem sandwiched between two static nonlinear subsystems. The linear time-invariant block can be represented in accordance with its state-space representation:

$$\begin{cases} \boldsymbol{X_0}(k+1) = \boldsymbol{A}\boldsymbol{X_0}(k) + \boldsymbol{B}U_0(k) \\ \boldsymbol{Y}_0(k) = \boldsymbol{C}\boldsymbol{X_0}(k) + \boldsymbol{D}U_0(k) \end{cases} \tag{1}$$

where $\boldsymbol{X}_0 = (\boldsymbol{X}_1^\top, \boldsymbol{X}_2^\top, \ldots, \boldsymbol{X}_n^\top)^\top$ is the state variable vector with $\boldsymbol{X}_1 = (X_{11}, X_{12}, \ldots, X_{1q})^\top$, $\boldsymbol{X}_2 = (X_{21}, X_{22}, \ldots, X_{2q})^\top$, ..., $\boldsymbol{X}_n = (X_{n1}, X_{n2}, \ldots, X_{nq})^\top$, $\boldsymbol{A}$ is the $(n\,q) \times (n\,q)$ state matrix, $\boldsymbol{B}$ is the $(n\,q) \times 1$ input matrix, $\boldsymbol{C}$ is the $n \times (n\,q)$ output matrix, $\boldsymbol{D}$ is the $n \times 1$ input-output matrix, and q denotes the order of the HW model. Conversely, $U_0(k)$ and $\boldsymbol{Y}_0 = (Y_{01}, Y_{02}, \ldots, Y_{0n})^\top$ are the input and the outputs vectors of the SIMO linear subsystem, respectively. The former is defined through the input nonlinear function $\sigma_{in}(\cdot)$ applied to U_b, whilst the latter is used to compute the overall output of the whole system by means of the nonlinear function $\sigma_{out}(\cdot)$:

$$U_0(k) = \sigma_{in}\left(U_b(k)\right) \tag{2}$$

$$\boldsymbol{Y}(k) = \sigma_{out}\left(\boldsymbol{Y}_0(k)\right). \tag{3}$$

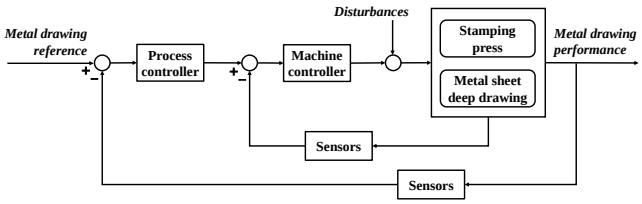

Fig. 1. Block diagram of a typical process control closed-loop.

III. The MPC-based Process Control

The proposed MPC-based closed-loop control system architecture, reported in Fig. 1, considers a single MPC block that simultaneously controls the draw-in of the n blank critical points by manipulating the BHF uniformly applied on the whole blank surface. At each sample time k, first, the controller computes the Control Variables (CVs), the State Variables (SVs), and the Output Variables (OVs) related to the given control horizon H_u and prediction horizon H_p respectively in the vector $\mathbf{u}(t) := (U_b(t+1)^\top, \ldots, U_b(t+H_u)^\top)^\top$, $\mathbf{x}(t) := (\boldsymbol{X}(t+1)^\top, \ldots, \boldsymbol{X}(t+H_p)^\top)^\top$, and

G. Cavone is with the Department of Engineering, University of Roma Tre, Rome, Italy (e-mail: graziana.cavone@uniroma3.it). A. Bozza, R. Carli, and M. Dotoli are with the Department of Electrical and Information Engineering of the Polytechnic of Bari, Italy. (e-mail: {augusto.bozza, raffaele.carli, mariagrazia.dotoli}@poliba.it).

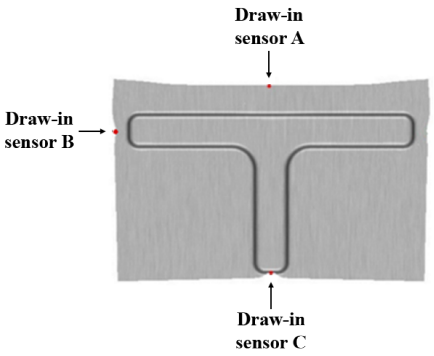

Fig. 2. 'T-shape' steel component with the critical points A, B, and C.

$\mathbf{y}(t) := (\boldsymbol{Y}_i(t+1)^\top, \ldots, \boldsymbol{Y}_i(t+H_p)^\top)^\top$. The values of CVs and OVs are subject to physical limitation, as indicated by the following constraints related to time step k:

$$U_b^{\text{lb}} \leq U_b(k) \leq U_b^{\text{ub}} \tag{4}$$

$$Y_i^{\text{lb}}(k) \leq Y_i(k) \leq Y_i^{\text{ub}}(k) \; \forall i \; = \; 1, \ldots, n \tag{5}$$

where U_b^{lb} and $Y_i^{\text{lb}}(k)$ and U_b^{ub} and $Y_i^{\text{ub}}(k)$ denote the lower and upper bounding for the CVs and the OVs, respectively. The MPC block has the following objective function:

$$\mathbb{J}(\mathbf{u}(t), \mathbf{y}(t)) = J_{\mathbf{y}}(\mathbf{u}(t), \mathbf{y}(t)) + J_{\boldsymbol{\Delta}\mathbf{u}}(\mathbf{u}(t), \mathbf{y}(t)). \tag{6}$$

$J_{\mathbf{y}}(\mathbf{u}(k), \mathbf{y}(k))$ is the term referring to the output reference tracking and it is defined as $J_{\mathbf{y}}(\mathbf{u}(t), \mathbf{y}(t)) = \sum_{k=t}^{t+H_p-1} \left(\sum_{i=1}^{n} w_i^y (Y_i(k+1) - Y_i^{\text{ref}}(k+1))^2 \right)$, while $J_{\boldsymbol{\Delta}\mathbf{u}}(\mathbf{u}(k), \mathbf{y}(k))$ is the term used for the move suppression of the MVs, defined as $J_{\boldsymbol{\Delta}\mathbf{u}}(\mathbf{u}(t), \mathbf{y}(t)) = \sum_{k=t}^{t+H_u-1} \left(w^{\Delta u} (U(k) - U(k-1))^2 \right)$. In both terms of the objective function (6) the parameters $w_j^{\mathbf{y}}$ and $w_l^{\boldsymbol{\Delta}\mathbf{u}}$ are suitable weighting factors. Then, the following optimization problem is solved by the MPC regulator:

$$\min_{\mathbf{u}(k), \mathbf{y}(k), \mathbf{x}(k)} (6)$$
$$\text{s. t.} \begin{cases} (2), (3), (1) \;\; \forall k = t+1, ..., t+H_p - 1 \\ (4) \, \forall k = t+1, ..., t+H_u \\ (5) \, \forall k = t+1, ..., t+H_p. \end{cases} \tag{7}$$

IV. Case Study

The proposed methodology is evaluated on a real 'T-shape' steel component, where three laser displacement sensors measure in real-time the draw-in of the metal sheet edge in three critical points (A, B, and C) during the stamping process (Fig. 2). The whole MPC-based control architecture is tested via a Monte Carlo simulation with 1000 runs, based on the Software-in-the-loop (SWIL) approach. In the SWIL simulation architecture both the designed MPC algorithm – implemented in the virtual Programmable Logic Controller Siemens S7-1500– and the press, machine controller, and three draw-in displacement sensors are deployed.

The effectiveness of the proposed control method is tested considering the closed-loop system trajectory tracking capability with respect to the desired draw-in. Thus, the

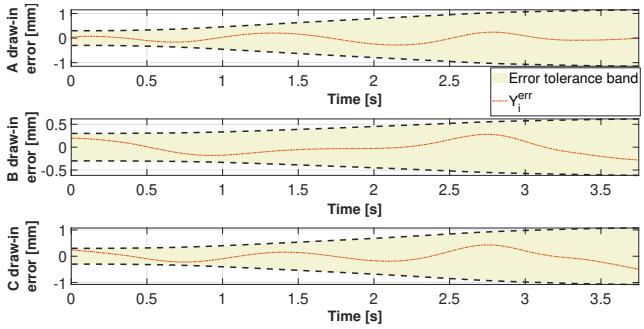

Fig. 3. Draw-in error profile of critical points A, B, and C vs. tolerance band obtained with the MPC-based control system.

error with respect to the reference value $\boldsymbol{Y}^{ref}$ is obtained as $\boldsymbol{Y}^{err} = (\boldsymbol{Y}^{ref} - \boldsymbol{Y})$. The experimental results are reported in Fig. 3, where the output error trajectory tracking is shown. The components of the error vector $\boldsymbol{Y}^{err}$ (i.e., Y_i^{err} for $i = \{1, 2, 3\}$ indicating the error between the actual and the reference draw-in at the critical points A, B, and C) get the mean values of 0.9%, 0.8%, and 0.7%, respectively. It is worthwhile noting that the obtained draw-in errors (indicated by dotted curves) are inside the tolerance band (represented by shaded area bounded by the dashed lines), thus ensuring that the stamped workpiece is defect free, despite the presence of the modeled external disturbances.

V. Conclusions and Future Works

An innovative MPC-based approach is proposed for the deep drawing control, aiming at optimizing the quality of the stamped part. The proposed approach achieves an excellent control quality solving a multivariable constrained optimization problem. The practical feasibility of the designed control system is demonstrated in a real-time SWIL-based simulation, despite the computational complexity and the fast dynamics of the involved process.

Extensions could regard the investigation of the proactive integration of the process controller within the prognostic and health management paradigm.

References

[1] M. E. Palmieri, V. D. Lorusso, and L. Tricarico, "Robust optimization and kriging metamodeling of deep-drawing process to obtain a regulation curve of blank holder force," *Metals*, vol. 11, no. 2, p. 319, 2021.

[2] M. Dotoli, A. Fay, M. Miśkowicz, and C. Seatzu, "An overview of current technologies and emerging trends in factory automation," *Int. J. Prod. Res.*, vol. 57, no. 15-16, pp. 5047–5067, 2019.

[3] A. Bozza, G. Cavone, R. Carli, L. Mazzoccoli, and M. Dotoli, "An mpc-based approach for the feedback control of the cold sheet metal forming process," in *2021 IEEE 17th Int. Conf. Autom. Sci. Eng.* IEEE, 2021, pp. 286–291.

[4] C. Su, K. Zhang, S. Lou, T. Xu, and Q. Wang, "Effects of variable blank holder forces and a controllable drawbead on the springback of shallow-drawn ta2m titanium alloy boxes," *Int. J. Adv. Manuf. Technol.*, vol. 93, no. 5, pp. 1627–1635, 2017.

[5] K. Siegert, M. Ziegler, and S. Wagner, "Closed loop control of the friction force. deep drawing process," *J. Mater. Process. Technol.*, vol. 71, no. 1, pp. 126–133, 1997.

[6] G. Cavone, A. Bozza, R. Carli, and M. Dotoli, "Mpc-based process control of deep drawing: An industry 4.0 case study in automotive," *IEEE Trans. Autom. Sci. Eng.*, vol. 19, no. 3, pp. 1586–1598, 2022.

Distributed Constrained Connectivity Keeping Supervision Scheme in the Presence of Static Obstacles

Alessandro Casavola [a], Vincenzo D'Angelo [a], Ayman El Qemmah [a], Francesco Tedesco [a], Franco Angelo Torchiaro [a],

[a] *Università della Calabria, Via Pietro Bucci, Cubo 42-c, Rende (CS), 87036, Italy*

Key words: Obstacle Avoidance, Distributed Command Governor, Constrained Control, Formation of Agents, Robot Operating System

Motion planning of dynamically feasible and safe trajectories is known to be a challenge for many autonomous systems [1]. In fact, when a vehicle follows a trajectory, a smooth motion is desirable while ensuring any potential collision avoidance with the obstacles located in the same environment. Traditional approaches [2], [3] usually envisage two operative phases: in the former, a path is determined by a basic reference planner, while in the second one, a safe robot trajectory complying with the vehicle dynamics is computed around the reference path using trajectory optimization [4]. Early works in this respect focused on static obstacles, in which autonomous systems sense the environment to avoid stationary obstacles and difficult situations using sophisticated techniques such as: path planning [14], decision trees [15], graph technique [16], heuristic search technique [17], potential fields technique [18] based algorithms. In [25] a more detailed summary is reported. However, such methods often suffer from significant replanning cycles when *a priori* unknown obstacles are present in the working space and formation keeping prescriptions are introduced among the vehicles for accomplishing more complicated tasks [5], [6].

On the other hand, recent advances in the field of distributed control of dynamic linear/non-linear systems, with input and/or state-related constraints, paved the way to novel solutions for the path-planning problems that are more attractive in order to deal with complex tasks. A common denominator among them relies upon recasting the problem requirements (e.g. bounds imposed on process variables to ensure safe and efficient system operation, and collision/obstacle avoidance conditions), in the form of pointwise-in-time set-membership state constraints. Some examples include mobile agents in proximity networks [7], partitioning [10], coverage [9], flocking [**?**]. Within this context, well-established control schemes are based on predictive control ideas [9]–[11] that present the benefit of explicitly taking into account the prescribed constraints while steering the vehicle to the planned desired trajectory.

Following these lines, this research activity addresses a novel multi-level supervision distributed architecture aimed at supervising a set of agents operating in a 2D space, subject to obstacle avoidance and connectivity-keeping constraints. In particular, the latter are introduced in order to guarantee the availability of a connected communication network for the agents. At the lower level, the architecture carries out a non-iterative non-cooperative distributed *Command Governor* (CG) algorithm [22] where agents not sharing the same constraints are grouped into particular sets and update their control actions in parallel on the basis of local information. For this reason, this procedure is denoted as *Turn-Based CG* and exploits the main features of the *Command Governor* approach [20] where a desired-set point is modified into a new one that complies with a set of operative constraints. The higher level represents the actual contribution of this work as it extends the *Turn-Based CG* to adequately deal with connectivity keeping and obstacle avoidance constraints.

In particular, by following ideas in [12], the communication network is modeled as a weighted time-varying graph and the algorithm enforces the existence of a specific spanning tree amongst all agents at each time in order to guarantee connectivity. Whenever more spanning trees are available, the scheme is instructed to select the minimum one with respect to the Euclidean distance among the agent position. The rationale behind this choice relies on the system performance enhancement associated to reference tracking. Anyway, the main differences with respect to the approach of [12] concern: i) the presentation of a novel algorithm for the minimum spanning tree computation that allows the supervision scheme to instantly and safely switch on

Email addresses: `a.casavola@dimes.unical.it` (Alessandro Casavola), `vincenzo.dangelo@dimes.unical.it` (Vincenzo D'Angelo), `elqemmah.ay@dimes.unical.it` (Ayman El Qemmah), `ftedesco@dimes.unical.it` (Francesco Tedesco), `franco.torchiaro@dimes.unical.it` (Franco Angelo Torchiaro).

the modified constraints structure arising from the new determined minimum spanning tree (please notice that in [12], such a switch is allowed only after a certain dwell time) *ii*) the presence of "static obstacles" that make the problem much more complicated. In this respect, the obstacle avoidance functionality introduced in this work makes use of a novel algorithm that exploits the *Hyperplane Separation Theorem* [13]. The latter has been traditionally used in robotics to generate collision free trajectories. See [24,26] and references therein for more details.

Main properties and, especially the feasibility of the control architecture, are formally proved. A simulation campaign involving a group of agents accomplishing several missions have been performed. Interesting enough, in certain simulations it is observed that the proposed scheme has the capability to get rid of undesired possible situations where agents get stuck when avoiding an obstacle. In fact, the induced self-coordination behavior translates into arbitrary circumnavigation maneuvers where the agents follow the same directions and are able to safely move toward the prescribed way-points.

References

[1] T. Fraichard and H. Asama, "Inevitable collision states - a step towards safer robots?" *Adv. Robot.*, vol. 18, no. 10, pp. 1001–1024, 2004.

[2] A. Ravankar, A. A. Ravankar, Y. Kobayashi, Y. Hoshino and C.C. Peng, "Path smoothing techniques in robot navigation: State-of-the-art, current and future challenges," *Sensors*, vol. 18, no. 9, 2018.

[3] S. M. LaValle, "*Planning Algorithms*" *Cambridge Univ. Press*, 2006.

[4] C. Richter, A. Bry and N. Roy, "Polynomial trajectory planning for aggressive quadrotor flight in dense indoor environments", *Springer Tracts in Advanced Robotics*, pp. 649–666, 2016.

[5] W. Ding, W. Gao, K. Wang and S. Shen, "An efficient b-spline-based kinodynamic replanning framework for quadrotors," *IEEE Trans. on Rob.*, vol. 35, no. 6, pp. 1287–1306, Dec 2019.

[6] J. Tordesillas, B. T. Lopez, M. Everett and J. P. How, "Faster: Fast and safe trajectory planner for navigation in unknown environments", *IEEE Trans. on Rob.*, pp. 1–17, 2021.

[7] M. Mesbahi, "On State-dependent dynamic graphs and their controllability properties", *IEEE Trans. on Aut. Contr.*, vol. 50, no. 3, pp. 387–392, 2005.

[8] J. A. Fax and R. M. Murray, "Information flow and cooperative control of vehicle formations", *IEEE Trans. on Aut. Contr.*, vol. 49, no. 9, pp. 1465–1476, 2004.

[9] J. Cortes, S. Martinez, T. Karatas and F. Bullo, "Coverage control for mobile sensing networks," *IEEE Trans. on Rob. and Autom.*, vol. 20, no. 2, pp. 243–255, 2004.

[10] M. Pavone, A. Arsie, E. Frazzoli and F. Bullo, "Distributed algorithms for environment partitioning in mobile robotic networks", *IEEE Transactions on Automatic Control*, vol. 56, no. 8, pp. 1834–1848, 2011.

[11] M. De Gennaro and A. Jadbabaie, "Decentralized control of connectivity for multi-agent systems", *IEEE CDC 2066*, pp. 3628–3633, 2006.

[12] T. Soleymani, E. Garone and M. Dorigo, "Distributed constrained connectivity control for proximity networks based on a receding horizon scheme", *Am. Control Conference*, pp. 1369-1374, 2015.

[13] K. Border, "*Separating hyperplane theorems*", Caltech, Tech. Rep., 2012.

[14] J. Bellingham, M. Tillerson, A. Richards and J.P. How, " Multi-task allocation and path planning for cooperating UAVs." *Cooperative Control: Models, Applications and Algorithms*, pp. 23–41, 2003.

[15] J. Minguez and L. Montano, "L. Nearness Diagram (ND) Navigation: Collision Avoidance in Troublesome Scenarios." *IEEE Trans. Robot. Autom.*, vol. 20, pp. 45–59, 2004.

[16] T. Perez-Lozano, "Spatial planning: A configuration space approach." *IEEE Trans. Comput.*, pp. 32, 1983.

[17] C.W. Warren, "Fast Path Planning Using Modified A* Method." *In IEEE Int. Conf. on Rob. and Aut.*, pp. 662–667, 1993.

[18] J. Cui, Y. Zhang, S. Ma, Y. Yi, J. Xin and D. Liu, " Path planning algorithms for power transmission line inspection using unmanned aerial vehicles." *In Proceedings of the 2017 29th Chinese Control And Decision Conference (CCDC)*, pp. 2304–2309, 2017.

[19] Z. Lin, M. Broucke and B. Francis, "Local Control Strategies for Groups of Mobile Autonomous Agents", *IEEE Trans. on Aut. Cont.*, vol. 49, pp. 622-629, 2004.

[20] E.G. Gilbert, I. Kolmanovsky and K. Tin Tan, "Discrete-time Reference Governors and the Nonlinear Control of Systems with State and Control Constraints", *Int. J. of Rob. and Nonlin. Contr.*, vol. 5, pp. 487-504, 1995.

[21] T. R. Jensen and B. Toft, "*Graph coloring problems*", John Wiley and Sons, 2010.

[22] A. Casavola, E. Garone and F. Tedesco. "A Distributed Command Governor Based on Graph Colorability Theory", *Int. J. of Rob. and Nonlin. Contr.* vol. 28, pp. 3056–3072, 2017.

[23] T. Schouwenaars et al., "Mixed integer Programming for Safe Multivehicle Cooperative Path Planning", *IEEE ECC*, 2001.

[24] S. Brossette and P. B. Wieber. "Collision avoidance based on separating planes for feet trajectory generation", *IEEE RAS International Conference on Humanoid Robots*, pp.509-514, Nov 2017.

[25] Ahmed S, Qiu B, Ahmad F, Kong C. and Xin H. "A State-of-the-Art Analysis of Obstacle Avoidance Methods from the Perspective of an Agricultural Sprayer UAV's Operation Scenario", *Agronomy*, vol. 11, no. 6, 2021.

[26] B. Sabetghadam, R. Cunha and A. Pascoal, "A Distributed Algorithm for Real-Time Multi-Drone Collision-Free Trajectory Replanning", *Sensors*, 22, 1855, 2022.

A distributed optimization based architecture for management of interconnected energy hubs

Giulio Ferro*, Michela Robba*, Rabab Haider** and Anuradha M. Annaswamy**

Department of Informatics, Bioengineering, Robotics and Systems Engineering, University of Genoa, Genoa, Italy (email: giulio.ferro@unige.it , michela.robba@unige.it)

Department of Mechanical Engineering, Massachusetts Institute of Technology, Cambridge, MA, 02141 USA (email: rhaider@mit.edu , aanna@mit.edu)

Significant effort has been expended across the globe to reduce greenhouse gas emissions and achieve sustainability, which in turn has led to a fundamental change in the management of resources and cities [1], [2]. In the case of the energy sector, the increase in the use of renewable resources and distributed generation, as well as the growing presence of electric vehicles, prosumers, microgrids, and other small-scale distributed resources, have enabled and accelerated restructuring of the electrical grid. In order to maintain a reliable and resilient grid, the emerging grid structure must be capable of dealing with intermittent and distributed production/loads, bidirectional flows, communication/structural faults, and large scale dispatching problems among others. In order to carry out optimal management of these distributed resources and address associated control problems, new models, methods, and technologies are necessary [3], [4]. The emergence of distributed energy resources at the edge and closer to the consumer has implications on the energy sector, not only at the grid level but also at a city level. A novel concept that has been recently introduced in the context of smart energy management in cities is that of an Energy Community (EC) and forms the focus of this work. An EC denotes a set of residential or small commercial agents, each acting as prosumer and generally including generation (electric and thermal), storage units such as batteries, and flexible loads [5].

This contribution pertains to a new systems architecture for EC, made of Energy Hubs (EHs) interconnected through electricity and heating networks. This architecture is proposed to be supervised by an Energy Community Manager (ECM).

An attractive property of an ECM is the inclusion of architecture for coordination. A P2P architecture is one in which all peers cooperate by trading or distributing a good or service that is of value to the entire community. In the context of ECs, the specific goods of interest are power and heat managed by an electrical network (E-N) and district-heating network (DH-N). The E-N includes all users and producers of electricity, as well as EVs that may either be individual vehicles or part of an EH. The DH-N includes generation units and storage elements. It is important to note that the development of a P2P market for energy exchange is made possible by underlying adequate P2P ICT architectures.

In this contribution, we consider an EC which consists of different EHs, including microgrids, smart buildings, and charging parks in a smart city (see Figure 1 for a schematic) and an ECM managing all EHs. The problem we consider is how the ECM will carry out energy exchanges among EHs, using a P2P market. In particular, we will consider how the ECM will ensure a fair sharing of costs and benefits across the entire EC, while minimizing the requisite objective function of each hub and ensuring that all underlying constraints are met. As each of the EHs is a complex cyber-physical system in itself, what is needed is an optimization approach that ensures data privacy and security while preserving plug and play modularity, i.e.,no system reconfiguration is needed when a player leaves or is added to the network, and optimal performance of the entire P2P network.

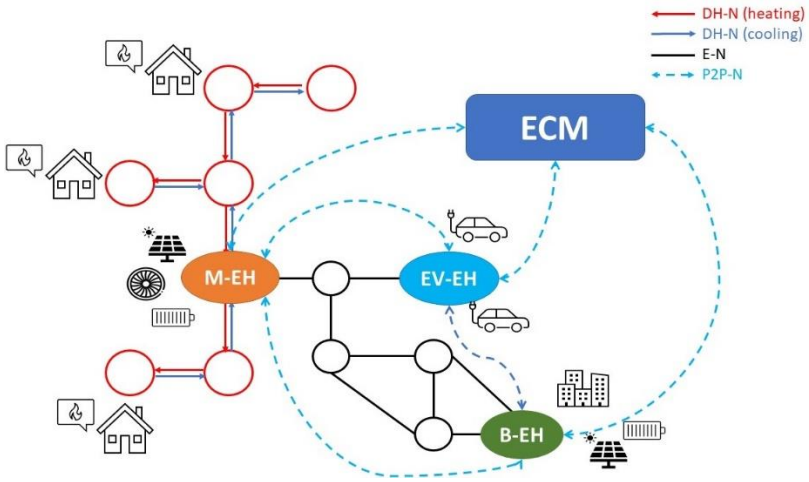

Figure 1 The overall systems architecture with an ECM managing an EC consisting of EHs including M-EH, B-EH, and EV-EH.

We propose to use a distributed optimization approach to carry out the energy management. This approach is based on Proximal Atomic Coordination (PAC) [6] with additional acceleration components based on the popular Nesterov method [7] and privacy preservation of both device setpoints and dual variables.

The main presented novelties are:

- A systems architecture that manages interconnected energy hubs in a smart city using an ECM. The ECM ensures a fair sharing of costs and benefits across the entire system, a near-optimal functioning of the individual hubs, and guarantees the satisfaction of physical constraints of the E-N and DH-N that interconnect the EHs;
- The introduction of a new distributed optimization-based solution to the optimization problem based on the PAC approach in [6] together with enhanced privacy properties (for both primal and dual variables) with the novelty based on the acceleration component of the Nesterov approach [7].

References

[1] M. A. Ahad, S. Paiva, G. Tripathi, and N. Feroz, “Enabling technologies and sustainable smart cities,” Sustainable Cities and Society, p. 102301,2020.

[2] Y. Wang, X. Wu, Y. Li, R. Yan, Y. Tan, X. Qiao, and Y. Cao, “Autonomous energy community based on energy contract,” IET Generation, Transmission & Distribution, vol. 14, no. 4, pp. 682–689, 2019.

[3] F. Delfino, G. Ferro, M. Robba, and M. Rossi, “An energy management platform for the optimal control of active and reactive powers in sustainable microgrids,” IEEE Transactions on Industry Applications, vol. 55, no. 6, pp. 7146–7156, 2019.

[4] M. Garcia, H. Nagarajan, and R. Baldick, “Generalized convex hull pricing for the ac optimal power flow problem,” IEEE Transactions on Control of Network Systems, vol. 7, no. 3, pp. 1500–1510, 2020.

[5] F. Moret and P. Pinson, “Energy collectives: a community and fairness based approach to future electricity markets,” IEEE Transactions on Power Systems, vol. 34, no. 5, pp. 3994–4004, 2018.

[6] J. J. Romvary, G. Ferro, R. Haider, and A. M. Annaswamy, “A proximal atomic coordination algorithm for distributed optimization,” IEEE Transactions on Automatic Control, 2021.

[7] Y. Nesterov, “A method of solving a convex programming problem with convergence rate o (1/k2),” in Sov. Math. Dokl, vol. 27.

Energy-aware black box MIMO model identification of wood chips refining process operating in closed loop

R. Boffadossi, M. Leonesio, L. Fagiano,

***Abstract*— The presentation will deal with the identification of a reduced black box LTI MIMO model of a wood chip refining process operating in closed loop. The specific fiber extraction process is dedicated to the production of Medium-density Fiberboard (MDF). The model is designed to predict the behavior of the two main quantities from the energy consumption perspective: the motor current of the refiner and the motor current of the plug screw. In the next steps, the obtained model will be employed for the economic multi-objective optimization of the process, which aims at minimizing energy consumption, maximizing the fiber quality, and ensuring compliance with the production constraint. This research activity is carried out within the EU project E2COMATION, *Life-cycle optimization of industrial energy efficiency*.**

***Index Terms*— Sustainable manufacturing, Model identification, Simulation Error Minimization, wood chip refiner**

I. INTRODUCTION

Energy efficiency plays a fundamental role in minimizing the environmental impact of production processes. It allows to achieve the same industrial objective with a reduction in natural resource consumption, which is an essential step to reaching the Sustainable Manufacturing (SM) goal [1]. From the product point of view, the SM definition evidences both the necessity of sustainable products and sustainable manufacturing processes. In particular, referring to the processes, the key aspects can be summarized in the reduction of negative impacts on the environment, energy and resources saving, reduction of waste, and recycling [2]. The pulp and paper industry is an excellent representation of the energy-intensive manufacturing process that needs urgently to become more efficient. This sector is one of the most extensive energy absorbing, it accounts for almost 6% of the total industrial energy consumption worldwide. In particular, the primary focus should be placed on the refining phase, which constitutes most of the energy consumption, close to 80% of the total [3].

In this project, we will cover the modeling of the two main elements affecting energy consumption in fiber extraction for Medium-density fiberboards (MDF) production. Those components are the refiner electric motor and the plug screw electric motor. Our final aim is to design a tool that is able to perform the economic real-time optimization of the process, in order to provide plant regulators and operators with the optimal set points, that at the same time minimize energy consumption, maximize the product quality and ensure the compliance with the production constraints. For these reasons, our goal is the identification of a reduced model of the refining process, whose parameters can be easily updated, and that features as input the plant signals manipulated by the operators.

Roberto Boffadossi and Marco Leonesio are with the Institute of Intelligent Industrial Technologies and Systems for Advanced Manufacturing (STIIMA), National Research Council, Milano. Lorenzo Fagiano is with the Dipartimento di Elettronica, Informazione e Bioingegneria, Politecnico di Milano.

Corresponding author: R. Boffadossi, roberto.boffadossi@stiima.cnr.it

The research activity is carried out within the EU project E2COMATION, this project has received funding from the European Union's H2020 research and innovation programme under Grant Agreement N 958410.

A. Wood chip refining process

The refining process consists of extracting fiber starting from raw wood chips. In MDF manufacturing, wood fibers are the main component on which product development is based. After being extracted, they are dried, glued, and compressed in order to obtain the final solid panels. The main steps of the process can be summarized in the following operations: different types of wood chips are gathered in the chip-bin, then pushed inside the digester through the plug screw, where the wood chips are pre-heated and exposed to high pressure, then the resulting mixture of steam and cooked wood chips is discharged and transported through the feed screw to the refiner inlet. At this stage, the material is pushed inside the grinding chamber, across two rotating plates, and the wood chips are fibered by the heat and the friction generated from the motion of the plates. This phase is the one mainly responsible for fiber quality and energy consumption.

Because of the difficulty in providing an accurate representation of the Thermo-Mechanical Pulping (TMP) process, it is problematic to design a rigorous controller that must operate in industrial conditions. The refining system is affected by the variation in raw material and operating conditions, and its dynamics are subject to change due to the wear of the refiner plates [4]. Moreover, the process is multivariate and characterized by strong coupling effects, making it very difficult to derive a consistent first principle model. For these reasons, the common practice consists of operating at constant refining intensity and monitoring online the fiber quality in order to correct the process parameters. In industrial applications, the most widespread parameter used to control the refining process is the Specific Energy Consumption (SEC). It provides a reliable measure of the refining intensity, being defined as the "amount of refining energy received by the specific amount of refined stock during a single pass through the refining zone" [5]. The refining SEC is computed by the ratio between the motor load and the production rate (i.e. the mass flow at the outlet of the refiner), and that definition makes it easier to employ this parameter with respect to the force-based characterization of refining intensity. Referring to the quantities involved in the computation of SEC, the motor load is affected by the distance between the rotating plates, which is usually changed automatically in order to track the SEC set point, while the production rate is regulated by varying the rotational speed of the discharge screw placed at the end of the digester. Furthermore, steam flow inside the digester is managed to increase the fiber quality as much as possible, indirectly affecting the motor load, as the consistency of the material is changed.

B. System identification

We performed the model identification using the signals gathered from a real plant operating in closed loop (i.e. plate position is controlled automatically w.r.t the SEC set point, and the plug screw rotational speed is controlled automatically in order to keep constant the material level inside the digester). Four quantities are identified as outputs of the process: the refiner motor current, the plug screw motor current, the production rate, and the fiber quality. This

research does not deal with the modeling of the fiber quality, while the production rate can be approximately considered proportional to the discharge screw rotational speed [6]. Thus, we identify the process as a MIMO system, whose output variables are the refiner motor current and the plug screw motor current, computed in order to predict energy consumption. The inputs of the process reflect quantities directly manipulated by the operators: discharge screw rotational speed, digester steam flow, SEC set point. The plate gap is automatically controlled by the embedded control system of the refiner. Therefore, this variable is considered an internal state of the closed-loop system, and it is discarded during the model identification. The digester level set point is discarded from the identification process because it is assumed to be a constant value.

We adopt the Simulation Error Minimization method, a data-driven approach that improves the consistency of the estimated model with the long-term system behavior. First of all, a fixed parametric model structure is defined. Then a constrained nonlinear optimization problem is set in order to estimate the parameter values that minimize the squared estimation error by simulating the model along one or more time windows. To perform the identification, we select a black box dynamic linear time-invariant fourth order MIMO model structure. The model involves two different outputs: the refiner motor current and the plug screw motor current, which are directly used for the computation of the related motor load. These quantities are modeled by adopting a MIMO model in order to represent the coupling effects between the two systems (i.e refiner and digester, both operating in closed loop). In addition, we formulate the following assumptions: a) the inputs delay is assumed small and negligible, b) the time-varying dynamics are considered as process disturbances (e.g. the plate wear), that are assumed to be correctly rejected by the controlles, and thus are held negligible in a closed-loop identification, c) the non-linear system behavior is considered negligible when the plant is working at a steady operational point.

The resulting comparison between the measured current values and the estimated ones in shown in fig. 1, where the sections in between the dotted lines (starting from the green one to the violet one) are the parts of the data-set that have been used for the identification of the parameters (i.e. almost 25% of the whole 117 hours data-set before the factory shutdown has been used for the identification). The identified model proved to be a good predictor of the motor current, both for the plug screw and the refiner, replicating correctly the measured value, except for the stochastic component of the signal. The mismatch from the measured values results in a mean absolute percentage error of 2.1% for the refiner motor current, and of 3% for the plug screw. The residual analysis shows that the model mismatch is very close to a Gaussian noise with zero mean. The residuals distribution is related to the fact that the model is not aware of the effect of the unmeasured quality of the raw material entering the refiner, (e.g. wood species, chip bulk density, chip solid content variability, obstructions. . .).

C. economic optimization

In validation, the obtained model proved to be sufficiently accurate to monitor the refiner energy consumption, and it will be adopted in the economic optimization tool, which is actually under development. The tool will perform a multi-objective optimization in order to find the best process operating points by computing the related steady-state value of the manipulable variables. It aims at minimizing energy consumption, maximizing the fiber quality, and ensuring compliance with the production rate constraint. In addition, the tool will be able to exploit the black box nature of the model and re-estimate in real-time the model parameters from recent signal measures, in order to update the model and to keep consistency with the real plant.

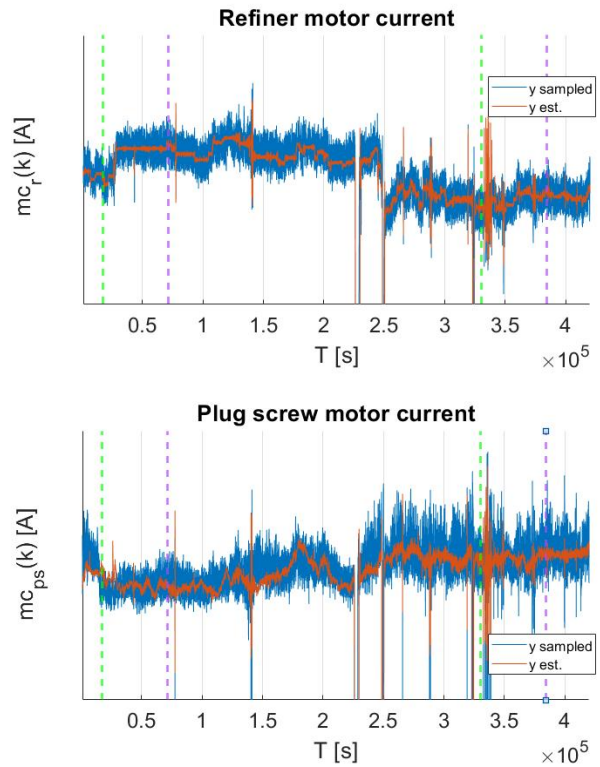

Fig. 1: Comparison between measured and estimated refiner motor current (upper figure) and comparison between measured and estimated plug screw motor current (lower figure).

II. REFERENCES

[1] A. D. Jayal, F. Badurdeen, O. W. Dillon, e I. S. Jawahir, «Sustainable manufacturing: Modeling and optimization challenges at the product, process and system levels», CIRP Journal of Manufacturing Science and Technology, vol. 2, n. 3, pag. 144–152, gen. 2010, doi: 10.1016/j.cirpj.2010.03.006.

[2] K. Gupta, R. F. Laubscher, J. P. Davim, e N. K. Jain, «Recent developments in sustainable manufacturing of gears: a review», Journal of Cleaner Production, vol. 112, pag. 3320–3330, gen. 2016, doi: 10.1016/j.jclepro.2015.09.133.

[3] B. Talebjedi, T. Laukkanen, H. Holmberg, E. Vakkilainen, e S. Syri, «Energy Efficiency Analysis of the Refining Unit in Thermo-Mechanical Pulp Mill», Energies, vol. 14, n. 6, pag. 1664, mar. 2021, doi: 10.3390/en14061664.

[4] H. Du e G. A. Dumont, «Constrained Multivariable Control of a Wood Chip Refiner», IFAC Proceedings Volumes, vol. 29, n. 1, pag. 6668–6673, giu. 1996, doi: 10.1016/S1474-6670(17)58753-4.

[5] K. Olejnik, «Impact of Pulp Consistency on Refining Process Conducted under Constant Intensity Determined by SEL and SEC Factors», BioResources, vol. 8, n. 3, pag. 3212–3230, mag. 2013, doi: 10.15376/biores.8.3.3212-3230.

[6] E. Harinath, L. T. Biegler, e G. A. Dumont, «Predictive optimal control for thermo-mechanical pulping processes with multi-stage low consistency refining», Journal of Process Control, vol. 23, n. 7, pag. 1001–1011, ago. 2013, doi: 10.1016/j.jprocont.2013.05.005.

A UV-based disinfection mobile robot with microbiological experimental analysis*

Andrea Borgese[1], Dario C. Guastella[1], Giovanni Muscato[1], Stefania Stefani[2], Stefano Stracquadanio[2], and Giuseppe Sutera[1]

[1]Dip. di Ingegneria Elettrica Elettronica e Informatica, Università degli Studi di Catania
[2]Dip. di Scienze Biomediche e Biotecnologiche, Università degli Studi di Catania
Corresponding author: dario.guastella@unict.it

1 Introduction

The persistence of COVID-19 pandemic calls for the adoption of effective methods and solutions for sanitizing those areas shared by several people. Ultraviolet germicidal irradiation (UVGI) is a common disinfection technique that relies on UVC radiation to inactivate a pathogen. However, UVC light can also be harmful for human eyes and skin and the damage entity depends on the exposure duration and the intensity of the irradiation. In this work, a mobile robotic manipulator exploiting UVGI is presented, which prevents the human operator from being accidentally exposed to UV light, as well as to the potential presence of pathogens. Experimental trials have been performed to assess the efficacy of the solution compared to common fixed-direction UV lamps through a microbiological analysis.

2 Related work

Several solutions based on contactless disinfection through UVGI have been proposed [1]. Some environmental disinfection processes with static omnidirectional UV lamps, either mounted on manually moved platforms [2] or on mobile robots [3], have been proposed. However, the main limitation of such solutions is related to the fixed emitting source that, albeit being on a mobile platform, often suffers from shadows, i.e. areas not directly reached by UV rays, thus reducing the disinfection efficacy [4]. Other recent works relying on mobile manipulators are either teleoperated [2] or do not fully exploit the dexterity of the arm [4].

*This work is funded by Ministero dell'Università e della Ricerca - FISR 2020 in the framework of the project "ARNOLD: AI-based full-coveRage AutoNOmous Local uv-Disinfection Robot" (proj. n.: FISR2020IP_02412) and by the University of Catania in the framework of the project Piano di incentivi per la ricerca di Ateneo 2020/2022 (Pia.ce.ri.) Linea 2D.

3 Proposed solution

We propose a UVGI-based disinfection solution which consists in a mobile robotic manipulator capable of computing the coverage trajectories of the emitting source online. To avoid non-direct exposure of the surfaces to UV light, we propose to adapt coverage path planning strategies to the problem of UV surface scanning. We address the problem as a sequential coverage of flat planar surfaces. We decompose the environment point cloud (acquired by an RGBD camera mounted on the arm) into a set of 2D flat surfaces, compute a back-and-forth coverage trajectory for each of them and finally merge these trajectories through a backtracking policy. We also take into account surface normals to keep the UV source perpendicular during the coverage.

The main contributions of this work are 1) the surface-aware motion and orientation of the emitting source through the arm, 2) the proposed 3D coverage path planning and 3) the microbiological experimental analysis of the virucidal efficacy compared to a fixed-direction emitting source.

4 Robotic platform

The prototype developed for assessing the goodness of the proposed method is shown in Fig. 1. The manipulator is a 6 d.o.f. robotic arm, the Aubo i5, which is mounted on a differential drive platform. The RGBD camera is a Microsoft Kinect which communicates with an Intel i9-based onboard computing unit. Robot Operating System (ROS) is used as a main software framework. To carry out the experimental comparison, two different types of UVC sources have been installed on the platform: 1) a LED UVC source made up of four modules arranged to form a square, 2) a fluorescent UVC lamp installed at the rear part of the mobile platform.

5 Microbiological analysis and results

We tested the disinfectant property of the two types of UVC sources by placing a set of Petri dishes on a

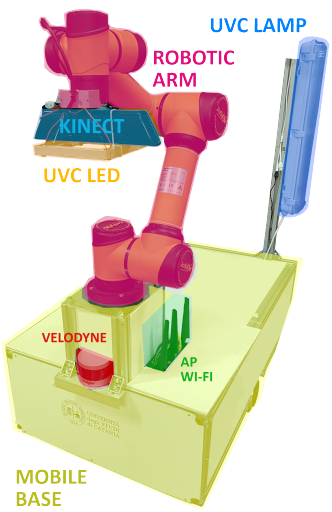

Figure 1: The prototype of mobile manipulator developed for the testing.

desk of an office-like scenario, as shown in Fig. 2. Two sets of dishes with different types of microorganisms have been used (namely Staphylococcus aureus and Acinetobacter baumannii).

The maximum distance of the scanning trajectory of the arm from the surface to sanitize has been set at 10 cm with an execution speed of 1 cm/s, thus obtaining an exposure time for a generic irradiated point of 16.5 seconds (taking into account the size of the LED square).

On the other hand, the translation motion of the UV lamp is obtained from a linear motion at a cruising speed of 1.5 cm/s of the mobile base in front of the considered area. This speed was calculated taking into account the power of the source.

The results of these tests highlighted the virucidal capacity of the UVC LEDs on both types of microorganisms with a reduction of the bacterial load of 6-8 logarithms. The effectiveness of the fixed UV lamp was comparable; however, a shadow area was observed in some Petri dishes partially hidden by objects on the desk, highlighted by the survival of the microorganism.

6 Conclusions

We presented a mobile robotic manipulator with a UVC source for the disinfection of indoor environments. The experimental results confirm the actual impact of the usage of a mobile manipulator in order to ensure exposure to the UVC source to all those areas that could potentially be hidden. The results suggest that the combination of both the actions of the fixed lamp and the movable arm offers a complete and effective solution to sanitize the surfaces of an environment.

Figure 2: Experimental setup for the microbiological analysis with Petri dishes.

References

[1] Y Shen, D Guo, F Long, L A Mateos, H Ding, Z Xiu, R B Hellman, A King, S Chen, C Zhang, and H Tan. Robots under COVID-19 pandemic: A comprehensive survey. *IEEE Access*, 9:1590–1615, 2021.

[2] D Conte, S Leamy, and T Furukawa. Design and map-based teleoperation of a robot for disinfection of COVID-19 in complex indoor environments. In *2020 IEEE Int. Symp. on Safety, Security, and Rescue Robotics*, pages 276–282. IEEE, 2020.

[3] L Tiseni, D Chiaradia, M Gabardi, M Solazzi, D Leonardis, and A Frisoli. UV-C mobile robots with optimized path planning: Algorithm design and on-field measurements to improve surface disinfection against SARS-CoV-2. *IEEE Robotics Automation Magazine*, 28(1):59–70, 2021.

[4] A G Sanchez and W D Smart. Towards verifiable COVID-19 aerosol disinfection using ultraviolet light with a mobile robot. In *The 14th PErvasive Technologies Related to Assistive Environments Conference*, pages 300–305, 2021.

Model-based selective image downsampling in remote driving applications

Maziar Ebrahimi Dehshalie*, Francesco Prignoli*, Paolo Falcone†, and Marko Bertogna‡

Remote driving is a technology that allows one to operate a vehicle without being physically present in it. This technology seems to be promising in accelerating full driving autonomy, but also it finds applications in industrial vehicles, such as trucks and agricultural machinery. Although remote driving is typically thought to be placed beside an autonomous driving system, other use cases exist, such as car sharing services, fleet managers, and services for helping people with reduced mobility.

Remote driving systems rely on: (1) vehicles equipped with actuators for the accelerator and braking pedals, and for the steering wheel; (2) a remote driver; (3) a wireless link, through which the vehicle receives (downlink) the driving commands and transmits (uplink) the video stream captured by the onboard cameras, other than the telemetry data.

However, the large-scale deployment of such technology can be obstructed by the large amount of video data that the vehicle transmits: both the limited capacity of the wireless channel and the latency introduced may prevent safely driving the vehicle. For this reason, we propose to tackle the challenge of reducing the size of the frames captured by onboard cameras, following an approach of *selective downsampling*. More in detail, we want to downsample the portions of each frame containing road users which are deemed not to conflict with the ego vehicle in the near future. On the opposite, we want to keep a full resolution for those portions including a road user that could conflict with the current trajectory of the ego vehicle. Thus, the selective downsampling approach requires assigning to each detected traffic participant a *relevance index*, which is a measure of the likelihood the road user will conflict with the ego vehicle in the near future. In this context, a road user is considered as not relevant for the remote operator if among all its possible trajectories (in a finite time horizon), none of them intersects that of the ego vehicle. More formally, this task is addressed by exploiting the reachability analysis framework. In addition, to compensate for the overhead due to the computation of the reachable sets, we resort to reachability analysis based on ellipsoidal sets [1], [2].

Figure 1 shows a demonstrative result of the implementation of our approach; the reference scenario is a T-junction, in which three road users (two vehicles and a pedestrian) are present, other than the ego vehicle. In the first case (Figure 1a) all the traffic participants are far enough to make null the intersections between their reachable sets (blue, cyan, yellow) and the ego vehicle trajectory (red); hence, both the left and right portions of the frame can be downsampled, since they contain road users considered as not relevant for the remote operator. On the opposite, in the second case (Figure 1c), the reachable set (blue) of the vehicle on the left intersects the trajectory of the ego vehicle. Thus the left portion of the frame should be kept at full resolution. It is interesting to note that the area possibly subject to be downsampled covers about 70% and 30% of the whole frame in the first (Figure 1b) and second case (Figure 1d), respectively. In addition, the measured computation time for the reachable sets is of the order of 1 millisecond per road user, where the time horizon has been set to 2 seconds.

At this stage, the results of this preliminary work show that the gain that the selective downsampling approach may bring in reducing the frame size can be high, although it strongly depends on the current scenario; indeed, crowded traffic conditions, such as urban driving, may worsen the overall gain. The real-time feasibility is assessed: the reachability analysis based on ellipsoid sets shown to be computationally

*The authors are with the Engineering Department of Enzo Ferrari, University of Modena and Reggio Emilia, Modena, Italy **{maziar_ebrahimi, f.prignoli, paolo.falcone}@unimore.it**

†The author is with the Mechatronics group at the Department of Electrical Engineering, Chalmers University of Technology, Gothenburg, Sweden **paolo.falcone@chalmers.se**

‡The author is with the Department of Physics, Informatics and Mathematics, University of Modena and Reggio Emilia, Modena, Italy **marko.bertogna@unimore.it**

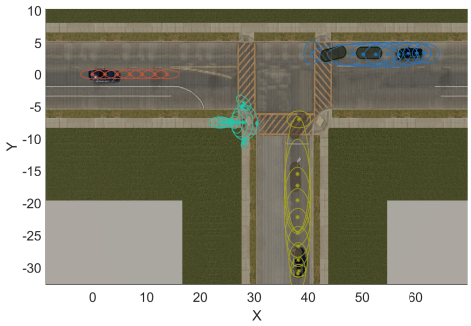

(a) Case 1: no conflicts

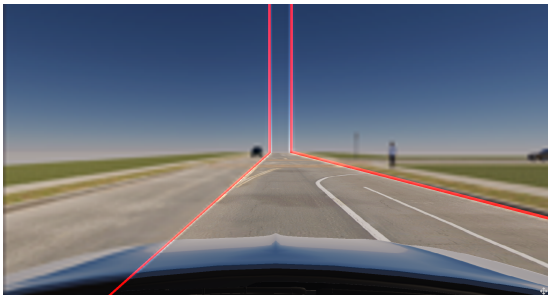

(b) The downsampled frame in scenario 1

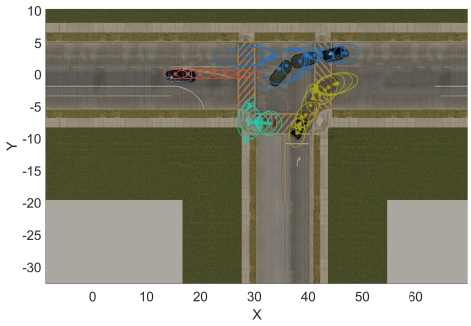

(c) Case 2: one conflict

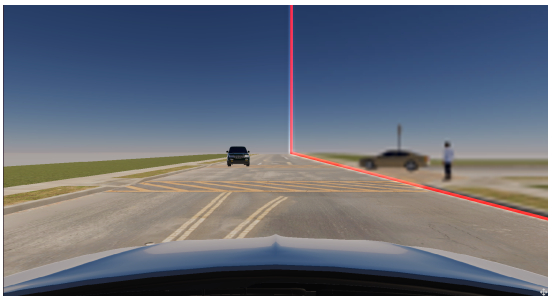

(d) The downsampled frame in scenario 2

Figure 1: An example showing how a frame can be downsampled depending on how relevant the information therein is for the remote driver.

efficient, but unusually high numbers of road users (i.e. crowds of people) could introduce unacceptable values of latency. However, these scenarios should be treated with clustering techniques, so that to drastically reduce the number of reachable sets to be computed.

The open problems ad future works include frame partitioning approaches and downsampling techniques. Also, we plan to study the reaction of the remote driver to the effect of the downsampling; it is important to remark that despite the lower resolution, a downsampled portion of the frame should still be visible, but with a lower level of details. Moreover, to have a more accurate model of the behavior of road users we should consider their interaction in the computation of reachable sets. Eventually, we plan to explore alternatives to ellipsoid-based reachability analysis: examples are reachability with zonotopes [3] and data-driven approaches, such as intent prediction [4] or deep neural networks.

References

[1] A. B. Kurzhanski and P. Varaiya, "Reachability under uncertainty and measurement noise," *Mathematical and Computer Modelling of Dynamical Systems*, vol. 11, no. 2, pp. 183–194, 2005.

[2] A. A. Kurzhanskiy and P. Varaiya, "Ellipsoidal toolbox (et)," in *Proceedings of the 45th IEEE Conference on Decision and Control*, IEEE, 2006, pp. 1498–1503.

[3] M. Althoff, "An Introduction to CORA 2015," in *Proc. of the Workshop on Applied Verification for Continuous and Hybrid Systems*, 2015, pp. 120–151. DOI: `10.29007/zbkv`.

[4] A. Toytziaridis, P. Falcone, and J. Sjöberg, "Road User Position Prediction in Urban Environments via Locally Weighted Learning," arXiv, Tech. Rep. arXiv:2201.12895, Apr. 2022, arXiv:2201.12895 [cs] type: article. [Online]. Available: `http://arxiv.org/abs/2201.12895`.

Clarke's Local Generalized Nash Equilibria with Nonconvex Coupling Constraints

Paolo Scarabaggio, Raffaele Carli, Sergio Grammatico, and Mariagrazia Dotoli

I. Introduction

In noncooperative games, a number of selfish agents with their individual dynamics and constraints aim at optimizing their objective functions, possibly in competition with each other. In many practical applications, from electricity markets to mobile-edge computing, the strategy that an agent can select depends not only on their preferences but also on those adopted by the others. A common way to define the solution of these noncooperative games is the *generalized Nash equilibrium* (GNE) [1]. From a control-theoretic perspective, the objective is to develop a coordination mechanism, namely, a discrete-time dynamical system for updating the strategies of the agents towards an equilibrium: the so-called *generalized Nash equilibrium problem* (GNEP), which is recently getting strong attention from researchers of different fields, since the presence of coupled feasible sets is widespread in real-world applications.

Most of the related literature focuses on games that have convex objective functions and feasible sets since this ensures the existence of equilibria and global convergence to solution algorithms [1]. Nevertheless, in many applications, convexity does not hold and thus some alternative approaches have been proposed [2], [3]. These approaches require local convexity, while the existence and convergence to such an equilibrium are not guaranteed.

Differently from the state of the art, we introduce a novel local equilibrium concept that we call *Clarke's local generalized Nash equilibrium* (CL-GNE). We define this equilibrium over Clarke's tangent cone and show that it satisfies the first-order optimality conditions of the optimization problems of the agents. By characterizing such equilibria, we also define variational CL-GNE (vCL-GNE), and thus locally fair, equilibrium points, showing their existence and local uniqueness. To compute a vCL-GNE, we design two discrete-time autonomous dynamics, or fixed-point iterations. We prove convergence of our proposed dynamics to an equilibrium under certain technical conditions, namely (strongly) monotone pseudo-gradient mapping of the game and proximally smooth feasible set.

Our theoretical results can be applied to several different control problems. For instance, this approach can be applied to power allocation games in cognitive radio networks due to nonconvex constraints on the transmit power, or to the operation of power systems, where the standard version of the well-known optimal power flow (OPF) problem corresponds to a set of nonlinear nonconvex equations.

The results presented in this talk have been submitted to a peer-reviewed international journal [4].

P. Scarabaggio, R. Carli, and M. Dotoli are with the Department of Electrical and Information Engineering of the Polytechnic of Bari, Italy. (e-mail: {paolo.scarabaggio, raffaele.carli, mariagrazia.dotoli}@poliba.it).

S. Grammatico is with the Delft Center for Systems and Control, TU Delft, The Netherlands. (e-mail: s.grammatico@tudelft.nl).

II. Problem Statement

We consider a game composed by a set of N agents $i \in \mathcal{N}$ each with decision variables $\mathbf{x}_i \in \mathbb{R}^n$. Moreover, we define $\mathbf{x}_{-i} \in \mathbb{R}^{(N-1)n}$ and $\mathbf{x} \in \mathbb{R}^{Nn}$, collecting the strategies of all agents different from i and the strategies of all agents, respectively. Each agent $i \in \mathcal{N}$ tries to minimize its cost function $f_i(\mathbf{x}_i, \mathbf{x}_{-i}) : \mathbb{R}^n \times \mathbb{R}^{(N-1)n} \to \mathbb{R}$ by choosing a strategy in its local feasible set $\mathbf{x}_i \in \Omega_i \subseteq \mathbb{R}^n$.

In addition, let us consider a finite number of constraints $m \in \mathcal{M}$, each denoted as $g_m(\mathbf{x}) \leq 0$, defining the coupled feasible set $\mathcal{X} = \prod_{i=1}^{N} \mathbf{\Omega}_i \cap \{\mathbf{x} \in \mathbb{R}^{Nn} \mid g(\mathbf{x}) \leq \mathbf{0}_M\}$ where $g(\mathbf{x}) := ((g_m(\mathbf{x}))_{m\in\mathcal{M}})$. By defining the set-valued mapping $\mathcal{X}_i(\mathbf{x}_{-i}) := \{\mathbf{y}_i \in \mathbb{R}^n \mid (\mathbf{y}_i, \mathbf{x}_{-i}) \in \mathcal{X}\}$, we have:

$$\forall i \in \mathcal{N}: \quad \begin{cases} \min\limits_{\mathbf{x}_i} & f_i(\mathbf{x}_i, \mathbf{x}_{-i}) \\ \text{s.t.} & \mathbf{x}_i \in \mathcal{X}_i(\mathbf{x}_{-i}). \end{cases} \tag{1}$$

The latter problem is a GNEP whose solution is the GNE, formally defined as follows.

***Definition* 1** *(Generalized Nash equilibrium):* A GNE is a collective strategy $\mathbf{x}^* \in \mathcal{X}$ such that:

$$\forall i \in \mathcal{N}: \; f_i(\mathbf{x}_i^*, \mathbf{x}_{-i}^*) \leq \inf\left\{f_i(\mathbf{x}_i, \mathbf{x}_{-i}^*) \,|\, \mathbf{x}_i \in \mathcal{X}_i(\mathbf{x}_{-i}^*)\right\}. \tag{2}$$

In this work, we analyze the case when $\mathcal{X}$ is nonconvex. Thus, let us first introduce some preliminary assumptions.

***Assumption* 1:** For each $i \in \mathcal{N}$ and for every $\mathbf{x}_{-i}$, the function $f_i(\cdot, \mathbf{x}_{-i})$ is convex and continuously differentiable.

***Assumption* 2:** For each $m \in \mathcal{M}$ and for every $\mathbf{x}_{-i}$, the function $g_m(\cdot, \mathbf{x}_{-i})$ is continuously differentiable (possibly nonconvex). The set $\mathcal{X}$ is nonempty, compact and satisfies the Mangasarian–Fromovitz constraint qualification.

III. Clarke's Local Generalized Nash Equilibria

To handle the case when the set $\mathcal{X}$ is nonconvex, let us propose a novel concept, namely *Clarke's local generalized Nash equilibrium problem* (CL-GNEP) and let us search for its possible solution, i.e., the *Clarke's local generalized Nash equilibrium* (CL-GNE). Our approach relies on the definition of Clarke's tangent cone $\tilde{\mathcal{X}}(\mathbf{x}) := \mathbf{x} + T_{\text{cl}}(\mathcal{X}, \mathbf{x})$ at a point $\mathbf{x}$ for the (nonconvex) set $\mathcal{X}$.

***Definition* 2** *(Clarke's local generalized Nash equilibrium):* A CL-GNE is a collective strategy $\mathbf{x}^* \in \mathcal{X}$ such that:

$$\forall i \in \mathcal{N}: \; f_i(\mathbf{x}_i^*, \mathbf{x}_{-i}^*) \leq \inf\left\{f_i(\mathbf{y}, \mathbf{x}_{-i}^*) \,|\, \mathbf{y} \in \tilde{\mathcal{X}}_i(\mathbf{x}_{-i}^*)\right\}. \tag{3}$$

A first approach to characterize a CL-GNE is employing the Clarke's normal cone $N_{\text{cl}}(\mathcal{X}, \mathbf{x}^*)$. For each agent $i \in \mathcal{N}$ the following optimality condition must be verified: $-\nabla f_i(\mathbf{x}_i^*, \mathbf{x}_{-i}^*) \in N_{\text{cl}}(\mathcal{X}_i(\mathbf{x}_{-i}^*), \mathbf{x}_i^*)$. Due to the difficulty of constructing the normal cone, let us characterize the CL-GNE by deriving the *Karush–Kuhn–Tucker* (KKT) conditions, hence, showing that these are satisfied at a CL-GNE.

***Theorem* 1:** Let Assumptions 1 and 2 hold. Then, the following statements are equivalent:

(i) $\mathbf{x}^* \in \mathcal{X}$ is a CL-GNE;

(ii) for each $i \in \mathcal{N}$, $-\nabla f_i(\mathbf{x}_i^*, \mathbf{x}_{-i}^*) \in N_{\text{cl}}(\mathcal{X}_i(\mathbf{x}_{-i}^*), \mathbf{x}_i^*)$;
(iii) for each $i \in \mathcal{N}$, there exists $\boldsymbol{\lambda}_i \in \mathbb{R}_{\geq 0}^M$ satisfying the KKT conditions. ■

In the related literature, convex games are usually solved by finding a solution to the associated variational inequality problem (VIP), since the resulting variational GNE not only exists but is also unique under certain conditions [1]. Similarly, by introducing the pseudogradient mapping $F(\mathbf{x}) = (\nabla_{\mathbf{x}_1} f_1(\mathbf{x}_1, \mathbf{x}_{-1}), ..., \nabla_{\mathbf{x}_N} f_N(\mathbf{x}_N, \mathbf{x}_{-N}))^\top$ we consider the following quasi-variational inequality (QVI) associated with the CL-GNEP in (1).

***Definition* 3** *(Quasi-variational inequality [5]):* Given the tangent cone $\tilde{\mathcal{X}}(\mathbf{x})$ and the mapping F, the *quasi-variational inequality problem QVIP*$(\tilde{\mathcal{X}}, F)$ consists in finding a vector $\mathbf{x}^* \in \tilde{\mathcal{X}}(\mathbf{x}^*)$, the so-called *quasi-variational equilibrium* (QVE), such that:

$$\inf_{\mathbf{y} \in \tilde{\mathcal{X}}(\mathbf{x}^*)} (\mathbf{y} - \mathbf{x}^*)^\top F(\mathbf{x}^*) \geq 0. \tag{4}$$

Thus, we can now introduce the following definition.

***Definition* 4** *(variational Clarke's local generalized Nash equilibrium):* A vCL-GNE is a CL-GNE in (3) that satisfies the QVIP in (4).

Note that, similarly to the relation between GNEP and VIP, not all solutions of the CL-GNEP are a solution of the QVIP; viceversa, a solution of the QVIP is always a solution of the original CL-GNEP. Furthermore, if we consider the KKT conditions, we have that the solutions of the CL-GNEP that are preserved passing to the QVIP are exactly those for which all agents have the same multipliers for the respective constraints, thus, the following results can be proven.

***Theorem* 2:** Let Assumptions 1 and 2 hold.

(i) Let $\mathbf{x}^*$ be a solution of the CL-GNEP in (1), where the KKT conditions for all agents hold with the same Lagrangian multipliers $\boldsymbol{\lambda} = \boldsymbol{\lambda}_i$, $\forall i \in \mathcal{N}$. Then, $\mathbf{x}^*$ is a solution of the QVI in (4) and thus it is a vCL-GNE.
(ii) Viceversa, let $\mathbf{x}^*$ be a solution of the QVI in (4) and thus be a vCL-GNE. Then, $\mathbf{x}^*$ is a solution of the CL-GNEP in (1) at which the KKT conditions hold with the same Lagrangian multipliers, $\boldsymbol{\lambda} = \boldsymbol{\lambda}_i$, $\forall i \in \mathcal{N}$. ■

IV. Existence and Convergence to a vCL-GNE

Since the projection onto a nonconvex set is not a nonexpansive operator, classical existence and convergence proofs do not apply to our setting. Let us thus focus on a class of nonconvex sets, namely *proximally smooth sets* which have some weaker projection properties that can be used to ensure the existence of a vCL-GNE when no assumptions are made on the pseudo-gradient mapping [6].

***Proposition* 1** *(Existence):* Let Assumptions 1 and 2 hold and let the set $\mathcal{X}$ be r-proximally smooth and simply connected. Then, the CL-GNEP in (1) has at least one vCL-GNE. ■

Regarding uniqueness, we cannot ensure that a vCL-GNE is globally unique, nevertheless, with an additional assumption on the mapping F, local uniqueness holds.

***Remark* 1** *(Local Uniqueness):* Under Assumptions 1 and 2, if the mapping F is strictly monotone, then the strict inequality holds in (4) and thus any vCL-GNE $\mathbf{x}^* \in \mathcal{X}$ is unique in its Clarke's tangent cone $\tilde{\mathcal{X}}(\mathbf{x}^*)$. ■

Requiring a nonconvex set to be simply connected is a rather strong assumption. To relax it, we strengthen assumptions on the pseudo-gradient mapping.

A. Strongly Monotone Pseudo-gradient Mappings

A popular algorithm for solving VIs with strongly monotone mappings is the projected pseudo-gradient method:

$$\mathbf{x}^{k+1} = \text{proj}_{\mathcal{X}}(\mathbf{x}^k - \gamma F(\mathbf{x}^k)). \tag{5}$$

By assuming that the mapping F is strongly monotone, we can prove the following result.

***Theorem* 3:** Let Assumptions 1–2 hold, F strongly monotone with constant $\mu > 0$ and Lipschitz continuous with constant $\ell > 0$, $\gamma \in (0, \min\{\frac{\sqrt{\ell^2 + p^2(\mu^2 - \ell^2)} + \mu p}{\ell^2 p}, \frac{r'}{1 + \bar{F}_{U(\mathcal{X}, r)}}\})$, such that $\mu \geq \ell$, and the set $\mathcal{X}$ is r-proximally smooth with $r' \in (0, r)$. Then:

(i) The CL-GNEP in (1) has at least one vCL-GNE;
(ii) The sequence generated by (5) converges to a vCL-GNE. ■

B. Monotone Pseudo-gradient Mappings

Inspired by the classical Korpelevich's method [7], let us propose a novel algorithm for computing a vCL-GNE:

$$\begin{cases} \mathbf{y}^k = \text{proj}_{\mathcal{X}}(\mathbf{x}^k - \gamma F(\mathbf{x}^k)) \\ \mathbf{x}^{k+1} = \text{proj}_{\tilde{\mathcal{X}}(\mathbf{y}^k)}(\mathbf{x}^k - \gamma F(\mathbf{y}^k) \end{cases} \tag{6}$$

By assuming that the mapping F is merely monotone, we can prove the following result.

***Theorem* 4:** Let Assumptions 1–2 hold, F monotone and Lipschitz continuous with constant $\ell > 0$, $\gamma \in (0, \min\{\frac{1}{\ell}, \frac{r}{4(1 + \bar{F}_{U(\mathcal{X}, r)})}\})$, and the set $\mathcal{X}$ is r-proximally smooth with $r' \in (0, r)$. Then:

(i) The CL-GNEP in (1) has at least one vCL-GNE;
(ii) The sequence generated by (6) converges to a vCL-GNE. ■

V. Conclusions

In this work, we have addressed the problem of solving a class of games with nonconvex coupling constraints. We have defined a local equilibrium concept presenting the conditions for optimality, existence and local uniqueness. Our technical contributions allow us, under certain conditions, to define two iterative schemes with global convergence guarantee toward this novel equilibrium concept.

This work can be extended proposing fully distributed algorithms to steer the strategies of agents to an equilibrium.

References

[1] G. Belgioioso and S. Grammatico, "Semi-decentralized generalized Nash equilibrium seeking in monotone aggregative games," *IEEE Transactions on Automatic Control*, 2021.
[2] J.-S. Pang and G. Scutari, "Nonconvex games with side constraints," *SIAM Journal on Optimization*, vol. 21, no. 4, pp. 1491–1522, 2011.
[3] L. J. Ratliff, S. A. Burden, and S. S. Sastry, "On the characterization of local Nash equilibria in continuous games," *IEEE Transactions on Automatic Control*, vol. 61, no. 8, pp. 2301–2307, 2016.
[4] P. Scarabaggio, R. Carli, S. Grammatico, and M. Dotoli, "Clarke's local generalized nash equilibria with nonconvex coupling constraints," *IEEE Transactions on Automatic Control* ***(under review)****, available at https://doi.org/10.36227/techrxiv.20079959*, 2022.
[5] J.-S. Pang and M. Fukushima, "Quasi-variational inequalities, generalized Nash equilibria, and multi-leader-follower games," *Computational Management Science*, vol. 2, no. 1, pp. 21–56, 2005.
[6] F. H. Clarke, R. Stern, and P. Wolenski, "Proximal smoothness and the lower-C2 property," *Journal of Convex Analysis*, vol. 2, no. 1-2, pp. 117–144, 1995.
[7] G. M. Korpelevich, "The extragradient method for finding saddle points and other problems," *Ekonomie i Mathematik Metody*, vol. 12, pp. 747–756, 1976, [English translation: Matecon 13 (1977) 35–49.].

Traffic-light control in urban environment exploiting drivers' reaction to the expected red lights duration

Matteo Scandella
Imperial College London

Arnob Ghosh
The Ohio State University

Michelangelo Bin
Imperial College London

Thomas Parisini
University of Trieste
Imperial College London

1 Introduction

Road traffic is related with many environmental, social, and financial problems that are caused by delays, congestion, and maintenance of the infrastructure. Furthermore, in 2010 the transport sector was responsible for approximately the 23% of the entire energy-related CO_2 emissions [1, Chapter 8]. Additionally, these problems worsen every year due to the continuous increase in traffic in almost all the major cities. For these reasons, it is necessary to rethink the way the traffic is managed and regulated in order to increase the efficiency and decrease the amount of congestion.

In this work, we focus on the urban settings. In particular, we propose a novel traffic light controller that regulates the traffic at the intersections. There exist an extensive literature on the topic developed in the last 50 years [3, 4, 2]. However, to the best of the authors' knowledge, the possibility of showing the drivers an information about the *Expected Red Time Duration* (ERTD from now on) for the foreseeable future is still unexplored. If the drivers know the ERTD, they can react accordingly and adjust their plan to reach the destination. For this reason, we propose to show the ERTD to the drivers in the queue at the intersections and to devise a traffic light controller that exploit their reaction to this additional information. In particular, in this work:

1. We develop a macroscopic model for the traffic flow that supports origin-destination pairs, finite links capacity, and rational route-planning that react to the information available.

2. Through simulations, we numerically find that showing the ERTD to the drivers always carries considerable improvement in the traffic flow even using a traffic-light controller that do not exploit the drivers' behavior.

3. We introduce a novel control policy for the traffic lights that exploits a model of the drivers' reaction to the new information to optimize the traffic-light schedule.

4. We validate the proposed controller numerically using simulations. In all the considered cases the proposed controller outperforms the previously used control scheme.

2 The Traffic Model

One of the main contributions of this work is a discrete macroscopic model for the traffic flow that supports origin-destination pairs, finite links capacity and more importantly the rational route-planning of the drivers using the ERTD information available.

The model is based on simplified road network modeled by a directed graph $(\mathcal{V}, \mathcal{E})$, where $\mathcal{V}$ is the set of nodes and $\mathcal{E} \subseteq \mathcal{V} \times \mathcal{V}$ is the set of edges. Nodes represent intersections, and each edge represents a single road connecting two different intersections. In particular, if $(i, j) \in \mathcal{E}$ then the junctions $i \in \mathcal{V}$ and $j \in \mathcal{V}$ are connected. Figure 1 shows an example of a road network where each node is represented with a gray square and each edge with a purple arrow. For each node $j \in \mathcal{V}$, we define a set $\mathcal{P}_j \subseteq \mathcal{V} \times \{j\} \times \mathcal{V}$ representing all the possible ways in which vehicles can cross the junction j. Specifically, if $(i, j, f) \in \mathcal{P}_j$, then a vehicle that comes from node i can go toward node f passing through node j. We define $\mathcal{P} := \bigcup_{j \in \mathcal{V}} \mathcal{P}_j$, and call its elements *paths*.

We assume that, with each path $(i, j, f) \in \mathcal{P}$, there is associated a unique traffic light regulating the traffic on it. Hence, with each path there is associated a unique queue of vehicles waiting to cross the intersection. Given a path $(i, j, f) \in \mathcal{P}$, a node $q \in \mathcal{V}$, and a time $t \in \mathbb{N}$, we define the *queue length* $N^t_{i,j,f,q} \in [0, \infty]$ is the amount of vehicles waiting in the queue (i, j, f) at the start of the t-th time interval that have q as final destination $g^t_{i,j,k}$ is the green time duration during the t-th time interval. Then, the value of $N^t_{i,j,f,q}$ evolves according to a model where the maximum amount of vehicle possible always depart at the start of the time instant.

The drivers select the route to follow in order to reach their destination. In particular, each flow is divided per destination of the drivers and at each intersection is split and then merged with other flows in order to reach its destination. The route that a flow follows is decided a priori without any knowledge of the traffic in the network by solving an optimization problem that trades off a rational term and an irrational one. Then, the drivers can adjust their route based on the local ERTD provided at each intersection. In particular, the fraction of drivers that decide to

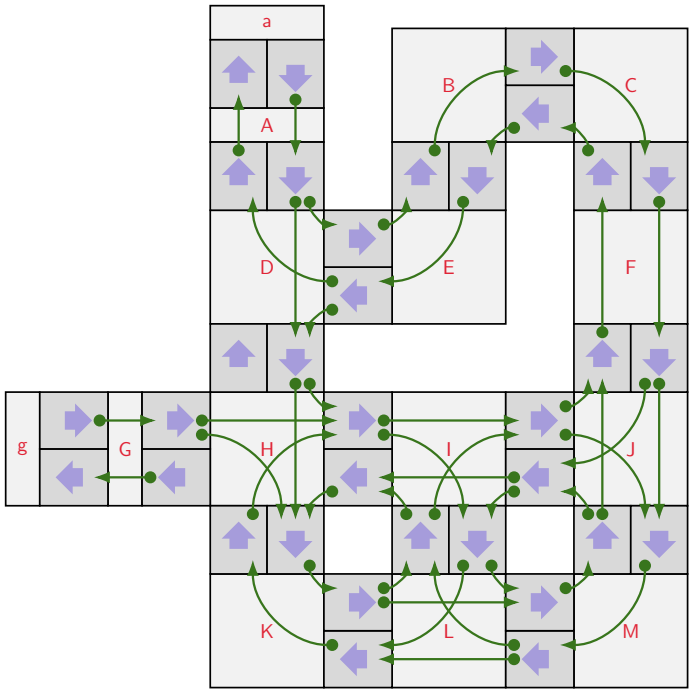

Figure 1: Example of traffic network.

change their pre-planned route is selected by solving an optimization problem that compromises between **(i)** a dispersion term that model the irrational behavior of some drivers; **(ii)** a stubbornness term that model the reluctance of some drivers to adjust their route; **(iii)** a rational term that depends on the queue length, the position of the driver in the queue, the ERTD (if it is communicated to the drivers) and network structure.

3 Traffic-Light Controllers

In order to evaluate the effectiveness of showing the ERTD to the drivers, we employ two different controllers: **NC** does not consider the possibility that the drivers can change route and **WC** that tries to exploit this possibility. Both controllers have access to the measurement of the *aggregated queue length* $N^t_{i,j,f}$, i.e. the sum of the queue lengths of each destination, the aggregated flows of vehicles that enter the network and the fraction of incoming vehicles that select a certain queue. Furthermore, we assume that the controllers are centralized, and they can access to all the measurements inside the entirety of the network. Then, both controllers are defined as finite-horizon MPC with cost function

$$J_c(g^t, t) = \sum_{\tau=t+1}^{t+m} \sum_{(i,j,f)\in\mathcal{P}} \left(N^\tau_{i,j,f}\right)^2,$$

where m is the finite horizon and $g^t = (g^t_{i,j,k})_{(i,j,k)\in\mathcal{P}}$ is the control variable that need to be selected. The optimization problem is constrained by two sets of constraints:

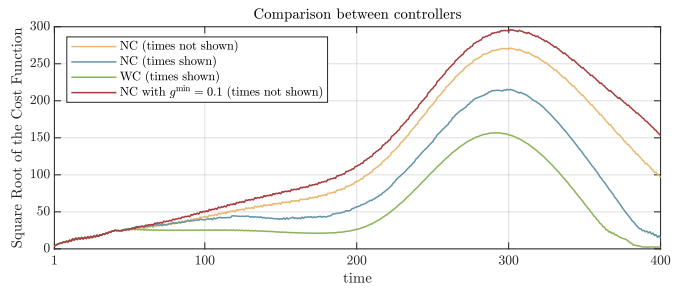

Figure 2: Comparison between different situation (the controllers start at $t = 40$).

(i) one that enforce the flow to not collide in the intersection; **(ii)** one that relate the aggregated queue length to the green time duration. The first set is the same for both controllers, while the second set is defined differently for the two controllers. In particular, **WC** utilizes a model where the route-replanning of the drivers in considered.

4 Numerical results

The effect of showing the ERTD with the two controllers in shown in Figure 2 where the results of the simulations on the network in Figure 1 are shown. The simulations clearly show that the performance of the controller **NC** significantly improves when the ERTD is shown to the drivers. Furthermore, the controller **WC** outperforms the controller **NC**.

References

[1] O. Edenhofer, R. Pichs-Madruga, Y. Sokona, E. Farahani, S. Kadner, K. Seyboth, A. Adler, I. Baum, S. Brunner, P. Eickemeier, B. Kriemann, J. Savolainen, S. Schlömer, C. von Stechow, T. Zwickel, and J.C. Minx, editors. *IPCC, 2014: Climate Change 2014: Mitigation of Climate Change. Contribution of Working Group III to the Fifth Assessment Report of the Intergovernmental Panel on Climate Change*. Cambridge University Press, Cambridge, United Kingdom and New York, NY, USA, 2014.

[2] Myungeun Eom and Byung-In Kim. The traffic signal control problem for intersections: a review. *European Transport Research Review*, 12(1):50, 2020.

[3] Clay McShane. The Origins and Globalization of Traffic Control Signals. *Journal of Urban History*, 25:379–404, 1999.

[4] M. Papageorgiou, C. Kiakaki, V. Dinopoulou, A. Kotsialos, and Yibing Wang. Review of road traffic control strategies. *Proceedings of the IEEE*, 91(12):2043–2067, 2003.

Modeling and Control of a Telescopic Quadrotor Using Disturbance Observer Based Control

Alessandro Baldini[1] Riccardo Felicetti[1] Alessandro Freddi[1] Sauro Longhi[1] Andrea Monteriù[1]

I. Short Introduction

Morphing multirotors are characterized by the capability to modify their shape during the flight, in order to negotiate narrow gaps without the need for miniaturization, thus preserving flight time and payload. The most common degrees of freedoms are represented by extendable arms [1] (telescopic or sliding arms) and rotating arms [2], also including X-geometry morphing mechanisms. In the state of the art solutions, the approach is that of continuously refreshing the position of the center of mass, the inertia, and the control effectiveness matrices, leading to a morphology dependent control. Many control solutions have been investigated, such as double loop structures involving proportional integral controllers, linear quadratic regulators, and active disturbance rejection control. Moreover, many estimation methods have been proposed in the literature to cope with external disturbances [3].

In this paper, we develop a control strategy to fly a morphing quadrotor under external additive disturbances given by the wind. In particular, we consider a quadrotor whose reconfiguration ability is represented by the telescopic arms (i.e. extendable arms), as the one shown in [1]. The time varying parameters due to morphing are modeled and updated online for the purposes of control and disturbance estimation. The effect of the external wind is estimated through a disturbance observer, and the estimation is feed-forwarded to a double loop composite controller, where the inner loop deals with the roll and pitch angles, whose dynamics are faster, while the outer loop manages position and orientation of the unmanned aerial vehicle.

This paper has been accepted and presented to the 30th Mediterranean Conference on Control and Automation [4].

II. Mathematical Model

The telescopic quadrotor is depicted in Fig. 1. The only allowed morphing ability is that of extendable arms. The geometry is assumed slowly varying, and the whole system can be considered as a collection of $N = 17$ rigid bodies subject to constraints. Considering an inertial earth fixed frame R_E and a body fixed frame R_B, the equations of motions are

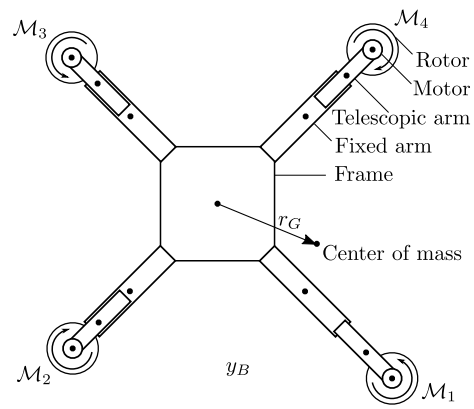

Fig. 1. Morphing quadrotor with telescopic arms.

$$
\begin{aligned}
m\ddot{p}_F &= -mR_B^E(\dot{\omega}\times r_G^B+\omega\times(\omega\times r_G^B))+F_g^E+R_B^E F_m^B+F_w^E \\
J\dot{\omega} &= -\omega\times J\omega+M_m^B \\
\dot{\eta} &= T(\eta)\omega,
\end{aligned} \tag{1}
$$

where $p_F = \mathrm{col}(x_F, y_F, z_F)$ is the position of R_B in R_E, r_G^B is center of mass in R_B, $\eta = \mathrm{col}(\varphi, \theta, \psi)$ is the vector composed by the roll, pitch, and yaw angles, J is the inertia matrix, m is the total system mass, R_B^E is the rotation matrix from R_B to R_E, ω is the angular velocity of R_B, $F_g^E = mge_3$ and F_w^E are the gravitational and wind forces, F_m^B and M_m^B are the thrust and torque due to the motors, $T(\eta)$ is the kinematic coordinate transformation. Since all the motors are collinear, F_m^B is of the form $F_m^B = \mathrm{col}(0, 0, f_z)$, and $\mathrm{col}(f_z, M_m^B) = Fu$, where $F \in \mathbb{R}^{4\times 4}$ is the arm-dependent allocation matrix. The center of mass r_G^B, the inertia matrix J, and the allocation matrix F are time varying, and they are calculated and updated online for the purpose of control [2].

III. Disturbance Observer

The estimation $\hat{F}_w^E$ of F_w^E is provided by the disturbance observer

$$\dot{s} = -Hs - H(\Phi + H\dot{p}_F) \tag{2}$$

$$\hat{F}_w^E = ms + mH\dot{p}_F, \tag{3}$$

where $s \in \mathbb{R}^3$ is the observer's state, $H \in \mathbb{R}^{3\times 3}$ is a gain matrix and Φ is a time varying known quantity. Provided that $-H$ is Hurwitz, the estimation error $\tilde{F}_w^E = F_w^E - \hat{F}_w^E$ exhibits a bounded input bounded output dynamics w.r.t. $\dot{F}_w^E$.

[1]All the authors are with the Department of Information Engineering, Università Politecnica delle Marche, Italy {a.baldini, r.felicetti, a.freddi, s.longhi, a.monteriu}@univpm.it

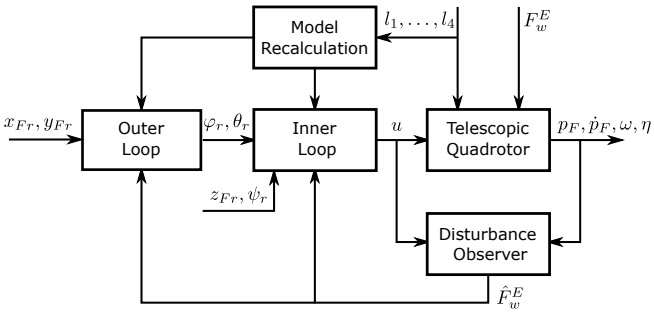

Fig. 2. Control scheme. The variables l_i denote the actual arm lengths.

IV. Inner and Outer Loops

Following the Disturbance Observer-Based Control (DOBC) approach [5], the feedback linearization-based composite controller for the inner loop is

$$u = F^{-1}A^{-1}\left(-\begin{bmatrix} b_z \\ b_\eta \end{bmatrix} - \begin{bmatrix} e_3^T \hat{F}_w^E \\ 0_{3\times 1} \end{bmatrix} + \begin{bmatrix} v_z \\ v_\eta \end{bmatrix}\right), \quad (4)$$

where b_z, b_η and A^{-1} are known time varying quantities (which belong to $\mathbb{R}^3$, $\mathbb{R}^3$ and $\mathbb{R}^{4\times 4}$, respectively), and the auxiliary inputs v_z, v_η are designed as stabilizing polynomials. In absence of estimation error, an exact linearization is achieved. The overall closed loop error system is bounded input bounded output with respect to $\dot{F}_w^E$, for which no assumption is made.

Assuming near hovering conditions (i.e. non-aerobatic flights), proper reference signals φ_r and θ_r can be generated by an outer loop as

$$\begin{bmatrix} \varphi_r \\ \theta_r \end{bmatrix} = \frac{m}{f_z} R_2(\psi)^T \left(-\begin{bmatrix} e_1^T \\ e_2^T \end{bmatrix}(\Gamma + \frac{1}{m}\hat{F}_w^E) + \begin{bmatrix} v_x \\ v_y \end{bmatrix}\right) \quad (5)$$

where Γ is a known time varying quantity (which belongs to $\mathbb{R}^3$), $R_2(\psi)$ is the two dimensional rotation matrix, and the auxiliary inputs v_x, v_y are designed as stabilizing polynomials. See Fig. 2 for the overall control scheme.

V. Numerical Simulations

Geometric dimensions and masses are approximately taken from real world components (DJI Flamewheel 450 for mechanics and T-Motor AirGear 350 for motors). Table I summarizes the most important system and design parameters. Additive white gaussian noise is applied to accelerations and angular rates according to the datasheet of the MPU-9250 IMU. During the simulation, the telescopic arms vary following an asymmetric pattern, as depicted in Fig. 3. The simulated wind acting on the frame is a constant plus the integral of a white noise whose standard deviation is set to $5 \cdot 10^{-3}$. The disturbance and its estimation are shown in Fig. 4. The tracking errors for the variables x_F, y_F, z_F, and ψ are reported in Fig. 5.

TABLE I

Parameters.

Parameter	Values	Meas. Unit
Total system mass (m)	1.448	$[kg]$
Lift coefficient (c_L)	$3.13 \cdot 10^{-5}$	$[N \cdot s^2]$
Drag coefficient (c_D)	$7.5 \cdot 10^{-7}$	$[N \cdot m \cdot s^2]$
Lift force range	$[0, 7.1]$	$[N]$
x_F, y_F closed loop poles	$-1, -2$	
z_F closed loop poles	$-1, -2.1$	
φ, θ closed loop poles	$-10, -20$	
ψ closed loop poles	$-1, -2$	
Observer gain matrix (H)	$4I_4$	

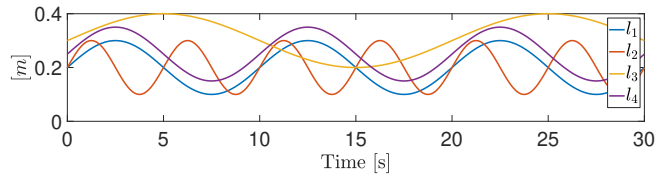

Fig. 3. Arm lengths.

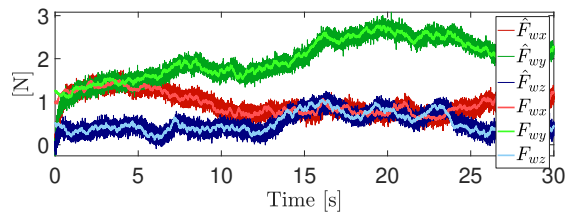

Fig. 4. Actual wind force acting on the vehicle $F_w^E = \mathrm{col}(F_{wx}, F_{wy}, F_{wz})$ and its estimation $\hat{F}_w^E = \mathrm{col}(\hat{F}_{wx}, \hat{F}_{wy}, \hat{F}_{wz})$.

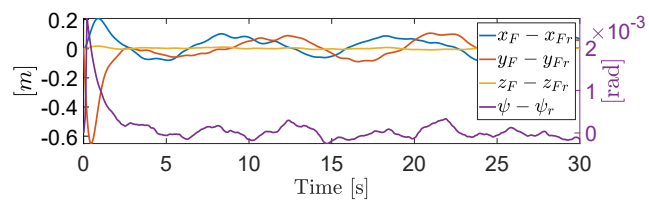

Fig. 5. Tracking performances.

VI. Conclusions

The tracking control problem for a telescopic quadrotor under wind conditions has been discussed using a DOBC approach. Investigation of an optimal control problem using the telescopic arms as additional degrees of freedom, as well as taking into account faults and failures, are future works.

References

[1] S. Brischetto, A. Ciano, and C. G. Ferro, "A multipurpose modular drone with adjustable arms produced via the fdm additive manufacturing process," *Curved and Layered Structures*, vol. 3, no. 1, 2016.

[2] D. Falanga, K. Kleber, S. Mintchev, D. Floreano, and D. Scaramuzza, "The foldable drone: A morphing quadrotor that can squeeze and fly," *IEEE Robotics and Automation Letters*, vol. 4, no. 2, pp. 209–216, 2018.

[3] T. Tomić, C. Ott, and S. Haddadin, "External wrench estimation, collision detection, and reflex reaction for flying robots," *IEEE Transactions on Robotics*, vol. 33, no. 6, pp. 1467–1482, 2017.

[4] A. Baldini, R. Felicetti, A. Freddi, S. Longhi, and A. Monteriù, "Modeling and control of a telescopic quadrotor using disturbance observer based control," in *2022 30th Mediterranean Conference on Control and Automation (MED)*. IEEE, 2022, pp. 1–6.

[5] S. Li, J. Yang, W. Chen, and X. Chen, *Disturbance Observer-Based Control: Methods and Applications*, ser. Disturbance Observer-based Control: Methods and Applications. CRC Press, Taylor & Francis Group, 2017.

Model Predictive Control System for Slug Flow in Microfluidics

S. Moscato[1], G. Stella[1], M. Bucolo[1]

[1] Department of Electrical Electronic and Computer Science Engineering, University of Catania, CT, Italy
giovanna.stella@phd.unict.it

In this work, a model predictive control system for slug flow in a micro-channel was designed, implemented and realized. The slug flow consists of an interlaced sequence of two immiscible fluids (liquid-liquid) that are circulating in a micro-system [1], in the so-called slug regime [2]. It was generated by the interaction of two fluids at a T-junction in the micro-channel. Nowadays, the study of slug flows in micro-channels has an important role in micro-nano technology, enabling the design of lab-on-chip devices in bio-medical field as well as in the chemical processes [3, 4]. In literature, different technologies have been presented to detect and control (passively or actively) slug flows [5], among those the optical approach offers the advantage of a wide range of measurements being minimally invasive [6]. Particularly, in recent studies carried out by the authors, the optical signals, acquired by monitoring the slug flows, were used to characterize the flow non linearity [7, 8] and to classify and identify the slug flow inside the micro-channel [9, 10]. Based on those results, it was possible the development of two platforms, the first for the real-time slug velocity detection [11] and the second for the feed-forward slug flow active control [12]. The possibility of a passive control of the slug flow was also investigated thanks to a chemical surface functionalization of the micro-channel [13]. In this context, the major challenge is to realize a system for the real-time detection and control of the microfluidics flows avoiding the optical bench equipment [14, 15]. In this direction, it is moving the recent research activity that has had two focal points. The first was to design a micro-optofluidics device that could be easily integrated in a control architecture suitable for the realization of low-cost embedded portable system. The second was to implement a control strategy adaptable to highly nonlinear microfluidics processes.

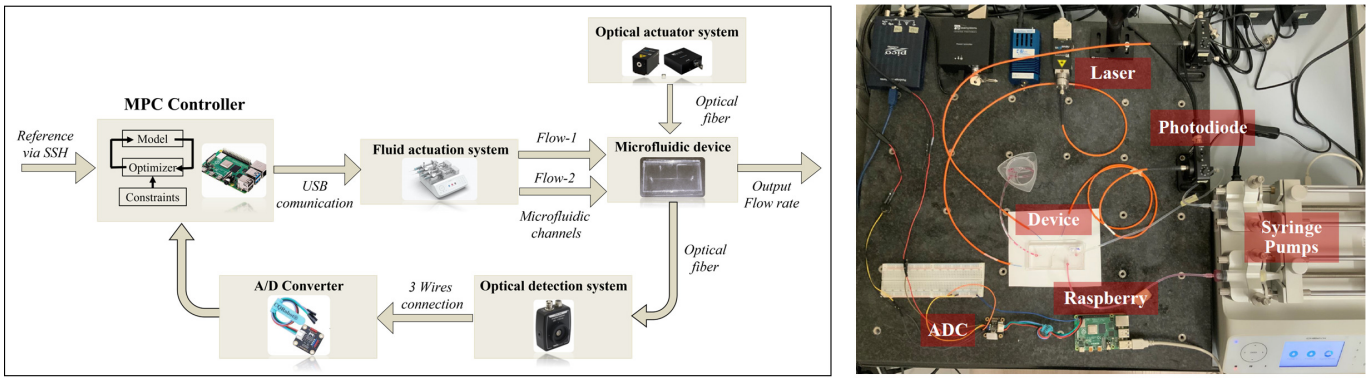

(a) (b)

Figure 1: (a) The block scheme and (b) the picture of the MPC system implemented for the slug flow in micro-channel.

The Poly-dimethylsiloxane (PDMS) micro-optofludics device, integrating a T-junction micro-channel for the generation of slug flow and an optical splitter (a combination of a mirror and two waveguides [18]) able to conduct and split the light in two points of the investigated area, was designed and manufactured by using an ad-hoc master-slave protocol based on 3D-Printing developed by the authors [16, 17]. The control architecture was designed as shown in the block scheme of Fig. 1(a). The core of the system is the micro-optofluidics device. Two fluids, deionized water and hexadecane oil, with defined input flow rates, were injected simultaneously at the inlets using a syringe pumps actuation system. The slug flow process, lighted by a laser source, was then monitored in an investigation area of the micro-channel by a photodiode pair. The optical signals detected from the photodiodes were sent to the analog-to-digital converter. The Raspberry pi board entirely manages the acquisition phase, the data analysis and the control action. Connected with the ADC converter, it analyses the optical signals to compute the actual frequency of the slug passage (representing the variable to be controlled) and determines with an MPC-based algorithm the new input flow rates to be imposed on the actuation system. A picture of the implemented experimental setup is shown in Fig. 1(b).

The model predictive control (MPC) strategy was chosen for its flexibility. Being the microfluidics processes highly nonlinear, a data-driven approach in the control design can be easily re-adapted in different experimental conditions. The possibility of obtaining a robust NARX model to identify the slug passage frequency was discussed in [19]. In this first attempt to realize a compact control architecture for the slug flow control, as a proof of concept a linear-MPC was implemented. In order to obtain the model, a first experimental campaign was performed by setting the two fluids flow-rates equal in the range $[0.05-0.3]$ ml/min. The acquired signals were used for the process characterization, and in particular the peak frequency obtained from the spectral analysis was correlated with the slug passage frequency per experimental condition. Using this information, a data-driven linear model (LMPC) was computed. A second experimental campaign was carried out to test the performance of the system globally. Initially, a desired single-reference slug frequency was imposed for a total of 6 experiments. Then, a sequence of five desired slug frequencies [25 Hz, 10 Hz, 5 Hz, 30 Hz and 45 Hz] was imposed. The results obtained in the second experimental campaign are shown in Fig. 2.

The first row of the figure shows both the control flow rates determined by the LMPC system and the peak frequency of the slug passage detected by the spectral analysis of the optical signals. The second row shows in details the optical signals acquired

during the control process for the desired frequency values of 25 Hz, 5 Hz and 45 Hz. The results obtained evidence the potentiality and the suitability of the presented MPC-based control system for the control of two-phase processes in microfluidics. The future improvements will be the implementation of the nonlinear MPC, which could significantly extend the use of the system to a variety of experimental applications.

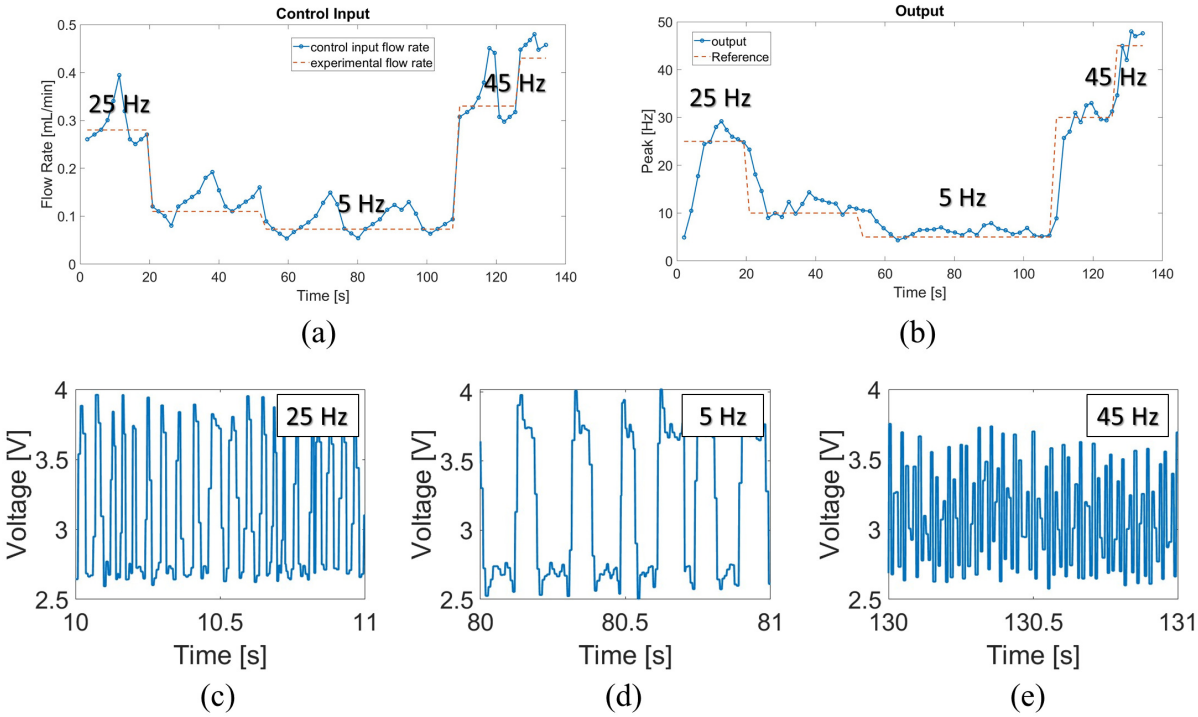

Figure 2: (a) Control input flow rates determined by the LMPC system. (b) Peaks frequency of the slug passage obtained from the spectral analysis of the optical signals. Trends of the optical signals acquired during the control process by setting the frequency values of (c) 25 Hz, (d) 5 Hz and (e) 45 Hz.

References

[1] P. Tabeling, "Introduction to microfluidics", Oxford University Press: New York, UK, USA, 2005.

[2] A. Serizawa,Z. Feng, K. Kawara, "Two-phase flows in microchannel", Exp. Therm. Fluid Sci., 26, 703-714, 2002.

[3] S. Mashaghi, A. Abbaspourrad, D.A. Weitz, A.M. van Oijen, "Droplet microfluidics: A tool for biology, chemistry and nanotechnology", Trends Anal. Chem., 82, 118-125, 2006.

[4] G.M. Whitesides, "The origins and the future of microfluidics", Nature, 442, 368-373, 2006.

[5] S. Pedersen, P. Durdevic, Z. Yang, "Review of slug detection, modeling and control techniques for offshore oil and gas production processes", Ifac-papersonline, 48(6), 89-96, 2015.

[6] P. Minzioni, "Roadmap on optofluidics", Journal of Optic 104195, 2017.

[7] F. Schembri, M. Bucolo, "Periodic input flow tuning nonlinear two-phase dynamics in a snake microchannel", Microfluid. Nanofluidic, 11, 189-197, 2011.

[8] F. Schembri, F. Sapuppo, M. Bucolo, "Experimental classification of nonlinear dynamics in microfluidic bubbles' flow", Nonlinear Dyn., 67, 2807-2819, 2012.

[9] F. Cairone, M. Bucolo, "Data-driven identification of two-phase microfluidic flows", In Proceedings of the 24th Mediterranean Conference on Control and Automation (MED), Athens, Greece, 21-24 June 2016.

[10] F. Cairone, S. Gagliano, M. Bucolo, "Experimental study on the slug flow in a serpentine microchannel", Int. J. Exp. Therm. Fluid Sci, 76, 34-44, 2016.

[11] S. Gagliano, G. Stella, and M. Bucolo, "Real-Time Detection of Slug Velocity in Microchannels", Micromachines, 11(3), 241, 2020.

[12] S. Gagliano, F. Cairone, A. Amenta, M. Bucolo, "A real time feed forward control of slug flow in microchannels", Energies, 12(13), 2556, 2019.

[13] G. Stella, M. Barcellona, L. Saitta, C. Tosto, G. Cicala, A. Gulino, M. Bucolo, M.E. Fragalà, "3D Printing Manufacturing of Polydimethyl-Siloxane/Zinc Oxide Micro-Optofluidic Device for Two-Phase Flows Control", Polymers 14, 2113, 2022.

[14] F. Yeshaiahu, L.P. Lee, D. Psaltis, C. Yang, "Optofluidics Fundamentals, Devices, and Application", McGraw-Hill, 2010.

[15] M. Brammer, T. Mappes, "Modular platforms for opto-microfluidic systems", Optofluidics 1, 2010.

[16] F. Cairone, S. Gagliano, D. Carbone,G. Recca, M. Bucolo, "Micro-optofluidic switch realized by 3D printing technology", Microfluidics and Nanofluidics 20: 61, 2016.

[17] F. Cairone, S. Davi, G. Stella, F. Guarino, G. Recca, G. Cicala, "3D-Printed micro-optofluidic device for chemical fluids and cells detection", Biomed Microdevices 22, 37, 2020.

[18] F. Cairone, F. Gallo Afflitto, G. Stella, G. Cicala, M. Ashour, M. Kersaudy-Kerhoas, M. Bucolo, "Micro-Optical Waveguides Realization by Low-Cost Technologies", Micro 2, 123-136, 2022.

[19] F. Cairone, G. Stella, S. Gagliano, M. Bucolo, "Data-Driven Modelling of Fast Slug Flows in Micro-channels", in 15th European Workshop on Advanced Control and Diagnosis, Springer, Cham., 405-422, 2022.

On the control of MIMO systems with uncertain control direction

G. BARTOLINI, A. PISANO

***Abstract*— This paper discusses the problem of stabilizing MIMO system whose high-frequency gain matrix contains elements of unknown signs. This problem is commonly referred to as the control problem of systems with "uncertain control direction" and it has not been satisfactorily addressed yet in the MIMO setting. We present some preliminary results involving 2-nd order MIMO systems where we develop a geometric framework to solve the underlying stabilization problem in finite time by a discontinuous feedback control inspired to the so-called "unit vector" method.**

I. Introduction

The control of single-input single-output (SISO) systems with high frequency gain of unknown sign has been the subject of many investigations [2], [1], [3], [5]. An early popular solution makes use of the so-called Nussbaum functions [4] to build an adaptive high-gain stabilizer known as the "universal controller". The transition from single to multi-input system is far from being straightforward even in the linear time-invariant case; existing solutions are based upon the satisfaction of certain strong structural assumptions regarding the high-frequency gain matrix $\mathbf{G}$ such as $\mathbf{G}$ diagonally dominant, $\mathbf{G} > 0$, $\mathbf{G} + \mathbf{G}^T > 0$.

Often it is tautologically assumed to know a constant matrix $\mathbf{K}$ that transforms the high-frequency gain control matrix $\mathbf{G}$, through right-multiplication, in a matrix falling into one of the above classes. It is noteworthy that the knowledge of $\mathbf{K}$ is a quite restrictive assumption that shrinks the considered class of uncertain dynamics.

A breakthrough in the area was the introduction of techniques that only requires the knowledge of an "unmixing set" for $\mathcal{D}(\mathbf{G})$. We say that a set $\mathrm{U} \subset GL(m, \Re)$ is *unmixing* $\mathcal{D}(\mathbf{G})$ is for any $M \in \mathcal{D}(\mathbf{G})$ there is at least one element $U \in \mathrm{U}$ such that $\sigma(MU) \subset C_0$. Existence of unmixing sets with finite cardinality (called "finite spectrum unmixing sets") has been proven in [11] for any dimension.

In [6] it is assumed that this set is known a-priori to the designer. The control is expressed as an high-gain adaptive output-feedback where the gain-matrix belongs to the unmixing set and a suitable strategy for cycling through the elements of this set is provided. Even if further steps have been performed, the prior knowledge of an unmixing set is generally postulated in the current literature. Some examples of how to build an unmixing set can be found in [11], [10]. Unfortunately, the cardinality of the unmixing sets given by the general construction in [11] is far too large than would be reasonable for applications, and hardly anything is known on the minimum cardinality of the unmixing sets. For the case $m = 2$ an unmixing set of cardinality 6 is given in [11]. Zhu [10] has constructed an unmixing set having cardinality 32 for the case $m = 3$. In this paper we present a control strategy which can be viewed as the efficient construction of an unmixing set of lower cardinality with respect to the state-of-the-art literature. The proposed control strategy is an extension to the multi-input case of the approach in [1], were the control of nonlinear single input systems with unknown sign of the high-frequency gain was dealt with. We take an approach whose main ingredients are the polar decomposition Theorem, the unit vector control law, and a geometrical viewpoint on the analysis of the closed loop trajectories. In this note we present some preliminary results involving second-order MIMO systems.

G. Bartolini and A. Pisano are with: the Department of Electrical and Electronic Engineering (DIEE), University of Cagliari, Italy. E-mail: apisano@unica.it

II. Problem statement and its solution

Consider a 2nd-order square system

$$\dot{\mathbf{y}} = \mathbf{\Phi}(\mathbf{y}, t) + \mathbf{G}\mathbf{u}, \qquad \mathbf{y}, \mathbf{u} \in R^2 \tag{1}$$

where $\mathbf{\Phi}(\mathbf{y}, t)$ is an uncertain drift term and $\mathbf{G}$ is the uncertain high-frequency gain (HFG) matrix, nonsingular by assumption. Assume what follows.

Assumption 1: There exist a known function $f(\mathbf{y}, t)$ such that $\|\mathbf{\Phi}(\mathbf{y}, t)\| \leq f(\mathbf{y}, t)$

The nonsingular HFG matrix $\mathbf{G}$ can be factorized as follows (polar decomposition Theorem)

$$\mathbf{G} = \mathbf{P}\mathbf{R}, \tag{2}$$

with $\mathbf{P} = \mathbf{P}^T, \quad \mathbf{P} > 0, \quad \mathbf{R} \in O(2)$.

The symmetric positive definite (SPD) matrix $\mathbf{P}$ and the orthogonal matrix $\mathbf{R}$ take the explicit representation

$$\mathbf{P} = [\mathbf{G}\mathbf{G}^T]^{1/2} \qquad \mathbf{R} = [\mathbf{G}\mathbf{G}^T]^{-1/2}\mathbf{G} \tag{3}$$

and are supposed to be unknown in the present treatment.

The next Lemma establishes the condition on matrix $\mathbf{G}$ under which the polar decomposition (2) involves a special orthogonal matrix $\mathbf{R} \in SO(2)$, i.e., a rotation matrix.

Lemma 1: A nonsingular matrix $\mathbf{G}$ with positive determinant admits the polar decomposition (2) with $\mathbf{P} = \mathbf{P}^T$, $\mathbf{P} > 0$, and $\mathbf{R} \in SO(2)$.

Proof of Lemma 1. Letting $\Delta = det(\mathbf{G})$, exploiting well-known properties of matrix determinants one derives from the expression of $\mathbf{R}$ in (3) that

$$det(\mathbf{R}) = sign\Delta$$

□

Let $\mathbf{G}$ be nonsingular and with positive determinant. Let Assumption 1 holds, and let t_0 be the initial time. We choose the control input as follows

$$\mathbf{u} = -\rho(t)\left[kf(\mathbf{y},t) + h^2\right]\frac{\mathbf{y}}{\|\mathbf{y}\|}, \qquad h \neq 0 \tag{4}$$

where $\rho(t)$ is a scalar gain defined as follows

$$\rho(t) = \begin{cases} 1 & t \in (t_0, t_1) \\ -1 & t \geq t_1 \end{cases} \tag{5}$$

where t_1 is the first time instant successive to t_0, if any, such that relation $\|\mathbf{y}(t_1)\| > \eta\|\mathbf{y}(0)\|$, $\eta > 1$, holds, and η and k are positive tuning gains to be defined.

Consider the following Lyapunov candidate function

$$V = \frac{1}{2}\mathbf{y}^T\mathbf{P}^{-1}\mathbf{y} \tag{6}$$

Computing the derivative of (8) along the solutions of (1), (4) yields

$$\begin{aligned} \dot{V} &= \mathbf{y}^T\mathbf{R}\mathbf{u} + \mathbf{y}^T\mathbf{P}^{-1}\mathbf{\Phi}(\mathbf{y},t) \\ &= -\rho(t)\left[kf(\mathbf{y},t) + h^2\right]\frac{1}{\|\mathbf{y}\|}\mathbf{y}^T\mathbf{R}\mathbf{y} \\ &\quad + \mathbf{y}^T\mathbf{P}^{-1}\mathbf{\Phi}(\mathbf{y},t) \end{aligned} \tag{7}$$

Here we take advantage of the geometric meaning of R as a rotation matrix. Notice that the term $\mathbf{y}^T\mathbf{R}\mathbf{y}$ is the crucial one in determining the stability features of the underlying closed loop system, being the only term potentially capable of making $\dot{V}$ negative. Such term is actually the scalar product between the output vector $\mathbf{y}$ and the rotated output vector $\mathbf{R}\mathbf{y}$. By exploiting well-known properties of the scalar product it turns out that

$$\mathbf{y}^T\mathbf{R}\mathbf{y} = \|\mathbf{y}\|^2 cos(\theta) \tag{8}$$

where θ is the rotation angle associated to matrix $\mathbf{R}$.

Let $\theta \neq \pm\pi/2$. With k and η chosen large enough one can straightforwardly show what follows

- By manipulating (7) one derives that $\forall t \in (t_0, t_1)$ there exist $\mu_1, \mu_2 > 0$ such that

$$\begin{array}{ll} \dot{V} \leq -\mu_1\sqrt{V} & if\ cos(\theta) > 0 \\ \dot{V} \geq \mu_2\sqrt{V} & if\ cos(\theta) < 0 \end{array} \tag{9}$$

- If $cos(\theta) > 0$ then $\mathbf{y}$ approaches the origin in a finite time T_1 and $\rho(t) = 1, \ \forall t \in (0, \infty)$
- If $cos(\theta) < 0$ then $V(t)$ is growing and there is t_1 such that $\rho(t) = -1, \ \forall t \geq t_1$ whence it follows that

$$\dot{V} \leq -\mu_1\sqrt{V}, \ \ t \geq t_1 \tag{10}$$

  Thus, $\mathbf{y}$ approaches the origin in a finite time T_2

The above sequence of steps implies that $\theta \neq \pm\pi/2$. If, however, after a time T_2 the norm of vector $\mathbf{y}$ is found to be nonzero this means that $\theta = \pm\pi/2$. The application, from $t = T_2$ on, of the control (4) premultiplied by the matrix

$$R^* = \begin{bmatrix} cos(\pi/4) & sin(\pi/4) \\ -sin(\pi/4) & cos(\pi/4) \end{bmatrix} \tag{11}$$

adds $\pi/4$ to the current value of θ thereby removing the "pathological" situation $\theta = \pm\pi/2$.

III. Conclusions

The generalization of the present reasoning to higher-order systems is not straightforward. In the Automatica.it 2022 presentation some preliminary results involving third order systems will also be presented.

References

[1] Bartolini G, Ferrara A., Giacomini L. "A switching controller for systems with hard uncertainties", *IEEE Trans. Circ. and Syst. - I Fund. Th. and Applic.*, **50**, 8, 984–990 (2003)

[2] E.P. Ryan (Guest Editor). Special Issue on Universal Stabilizers and High-gain Adaptive Control, *IMA J. Math. Contr. & Informat.*, **8**, 321–439 (1990)

[3] T. R. Oliveira, L. Hsu and J. Peixoto. "Output-feedback global tracking for unknown control direction plants with application to extremum-seeking control", *Automatica*, **47**, 9, 2029–2038 (2011)

[4] R. Nussbaumm "Some remarks on a conjecture in parameter adaptive control", *System and Control Letters*, **3**, 5, 243–246 (1983)

[5] T. Guo, Y. Liu and Y. Man. "Adaptive controller of nonlinear systems with unknown control directions and unknown input powers", *Int. J. Robust Nonlinear Control*, **30**, 17, 7670–7689 (2021)

[6] E.P. Ryan. "Adaptive stabilization of multi-input nonlinear systems", *Int. J. Robust Nonlinear Control*, **3**, 169–181 (1993)

[7] E.P. Ryan. "A nonlinear universal servomechanism", *IEEE Trans. Automatic Control*, **39**, 753–761 (1994)

[8] H. Logemann and A. Ilchmann "An adaptive servomechamism for a class of infinite-dimensional systems", *SIAM J. Contr. & Optimiz.*, **32**, 917–936 (1994)

[9] A. Ilchmann "Non-identifier based adaptive control of dynamical systems: a survey", *IMA J. Math. Contr. & Informat.*, **8**, 321–366 (1991)

[10] Zhu X.-J "A finite spectrum unmixing set for GL(3,ℜ)", in "Computation and Control III", Bower and Lund eds., Birkhäuser, Boston, p. 403-410, 1989.

[11] Martensson B., "The unmixing problem", *IMA J. Math. Contr. & Informat.*, **8**, 367–377 (1991)

[12] Martensson B., "Adaptive stabilization of multivariable nonlinear ystems", *Contemporary Mathematics*, **68**, 191–225 (1987)

Functional Iterative Learning Control for Linear Systems

Franco Angelini[1], Cosimo Della Santina[2,3]

***Abstract*— Many linear dynamic systems can usually be modeled in continuous time. However, to simplify the learning phase of Iterative Learning Control, the system output signal is frequently sampled, while the input is discretized, de-facto obtaining a discrete-time system. This work aims at preserving the continuous nature of the system, while tracking sampled outputs. To this end, we model the input signal as an element of a functional subspace, exploiting its infinite-dimension. Simulation results are presented.**

I. Introduction

A classic approach to execute repetitive tasks is Iterative Learning Control (ILC) [1]. This strategy refines the control action to perform the desired motion closing the loop not in the time domain but in the iteration one. The application of ILC to continuous linear systems introduces the requirement of high order derivatives [2]. To avoid this issue, ILC is typically implemented on a discretized model of the system. However, this inevitably constrains the exploration space of the learning rule, because the input is limited to be piece-wise constant.

The approach we propose to avoid this drawback, is to choose the feedforward control input as an element of a functional subspace. A similar approach has already been considered in [3]–[5] to enhance the ILC extrapolation behavior. However, these works perform the functional expansion directly on the discrete system instead of an alternative to zero-order holding. Other approaches are terminal ILC (TILC) [6], [7] and Point-to-Point ILC (P2PILC) [8], [9], which still present piece-wise constant inputs, but sampled with higher frequency w.r.t. the output. Moreover, the input is updated relying only on the measurements of the tracking error at the samples of interest instead of its whole evolution. Moreover, these works do not exploit the oversampling of the input to learn inputs for systems with more outputs than inputs.

To summarize, in this work we propose a novel ILC framework for non-square linear systems, which learns a continuous control input in a functional space (Fig. 1). This solution allows to track sampled outputs without constraining the input to be piece-wise, and it allows to choose a functional space large enough to cope with systems with fewer inputs than outputs. Necessary and sufficient conditions for ILC convergence are presented.

This research is partially supported by the European Union's Horizon 2020 Research and Innovation Programme under Grant Agreement No. 101016970 (Natural Intelligence) and in part by the Ministry of University and Research (MUR) as part of the PON 2014-2021 "Research and Innovation" resources – Green Action - DM MUR 1062/2021.

[1]Centro di Ricerca "Enrico Piaggio" and Dipartimento di Ingegneria dell'Informazione, Università di Pisa, Pisa, Italy.

[2]Department of Cognitive Robotics, Delft University of Technology, Delft, The Netherlands.

[3]Institute of Robotics and Mechatronics, German Aerospace Center (DLR), Wessling, Germany. Contact emails: franco.angelini@unipi.it,c.dellasantina@tudelft.nl.

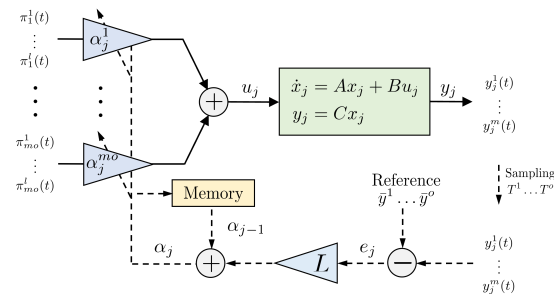

Fig. 1. Functional Iterative Learning Control scheme: u_j is the continuous input signal with iteration index j. The output y_j is sampled at o instants. We aim at having $y_j(T^1) \dots y_j(T^o)$ equal to the reference $\bar{y}^1 \dots \bar{y}^o$. The learning strategy is divided into two phases: i) u_j is modeled as a linear combination of iteration-independent basis functions $\pi_1 \dots \pi_{mo}$; ii) the weights $\alpha_j^1 \dots \alpha_j^{mo}$ are iteratively learnt through proportional error feedback.

II. Functional Iterative Learning Control

a) Problem definition: We refer to the model of a continuous time linear system

$$\dot{x}_j = Ax_j + Bu_j, \quad y_j = Cx_j, \tag{1}$$

with iteration index j, $A \in \mathbb{R}^{n\times n}$, $B \in \mathbb{R}^{n\times l}$, $C \in \mathbb{R}^{m\times n}$, $x_j \in \mathbb{R}^n$, $u_j \in \mathbb{R}^l$, $y_j \in \mathbb{R}^m$, with the classic meaning. It should be noted that (1) is usually not square. We consider a finite set of time instants $\{T^1, \dots, T^o\}$; the superscript is an index, and $T^0 = 0$ is the starting time. The desired output values at the given times are defined as $\bar{y}^1 \dots \bar{y}^o \in \mathbb{R}^m$. The objective of this work is to design a learning law such that $u_j(t)$ leads to

$$\lim_{j\to\infty} y_j(T^k) = \bar{y}^k, \quad \forall k \in \{1 \dots o\}. \tag{2}$$

b) Main Result: We focus on the evolution of the input u_j. The key idea behind our framework is to make the ILC problem square by learning u_j in a large enough subspace of a functional space. Specifically, the space of all possible continuous functions is infinite-dimensional. We can parametrize a generic element of this space as follows

$$u_j(t) = \pi(t)\alpha_j, \quad \pi = \left[\pi^1 \dots \pi^o\right] \in \mathbb{R}^{l\times mo}, \tag{3}$$

with $\pi^i(t) \in \mathbb{R}^{l\times m}$ and $\alpha_j \in \mathbb{R}^{mo}$. This parametrization allows to achieve two objectives. First, the time-dependent and the iteration-dependent components of $u_j(t)$ that are separated. Second,instead of learning a generic u, we can simply find a learning rule for the vector α_j. Theorem 1 presents such a learning law and provides conditions for convergence.

Theorem 1. *Consider the linear learning rule*

$$\alpha_{j+1} = \alpha_j + L \begin{bmatrix} \bar{y}^1 - y_j(T^1) \\ \vdots \\ \bar{y}^o - y_j(T^o) \end{bmatrix}, \tag{4}$$

with $L \in \mathbb{R}^{mo\times mo}$. The combination of (3) *and* (4) *fulfills* (2)

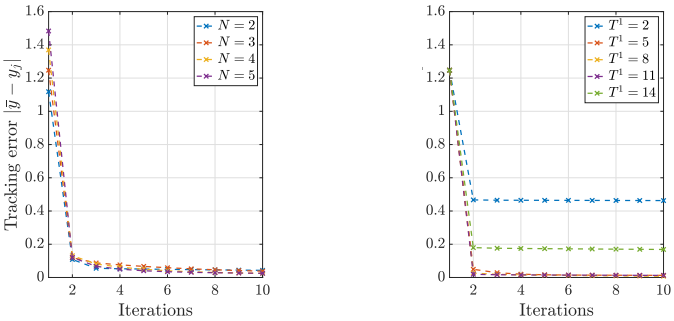

(a) $T^1 = 8$ and N variable. (b) $N = 3$ and T^1 variable.

Fig. 2. Tracking error evolutions across iterations.

with $x_j(0) = x_0$ for all j, if and only if

$$\rho\left(I - LH\right) < 1, \tag{5}$$

where ρ is the spectral radius of the argument, and

$$H = \begin{bmatrix} \int_0^{T^1} Ce^{A(T^1-\tau)}B\pi(\tau)\mathrm{d}\tau \\ \vdots \\ \int_0^{T^o} Ce^{A(T^o-\tau)}B\pi(\tau)\mathrm{d}\tau \end{bmatrix} \in \mathbb{R}^{mo\times mo}. \tag{6}$$

Proof. Please refer to [10] for the proof. □

At this point, to define the learning rule we need two choose two variables: the set of functions $\pi(t)$ and the learning gains L. The former can be freely chosen provided that H is non singular. This shifts the problem to finding L. Eq. (4) is formally equivalent to standard linear learning rules, and condition (5) is analogous to convergence conditions typically found in the literature [1]. As a result, classic ILC algorithms can be transferred into this framework with little modification.

III. Simulations

We validate the proposed framework on the challenging case of controlling all the $2N$ states of a system using only one input. The system under analysis is an interconnection of N masses ($m = 1$) constrained to a single direction of motion. These bodies are linked by linear springs $\kappa = 2$ and dampers $\beta = 1$, and they are actuated by a single force u_j applied at the last body. The system dynamics is not reported here for the sake of space, but it can be found in [10]. The output is the full stats, i.e., N positions and N velocities. We sample it three times T^1, T^2, T^3, with $T^2 = 18$s and $T^3 = 20$s. We simulate an increasing number N of masses and $T^1 = 8$, and we simulate a fixed number of masses $N = 3$ and $T^1 \in \{2, 5, 8, 11, 14\}$. The desired outputs are $\bar{y}^1 = (1/N, 2/N, \ldots, 1, 0, \ldots, 0)$, $\bar{y}^2 = (0, \ldots, 0, 0, \ldots, 0)$, and $\bar{y}^3 = \bar{y}^2$. The base functions π are chosen as $6N$ Gaussians, with variance $T^3/(12N)$ and shifted in time such that they homogeneously cover the interval $[0, T^3]$. This choice leads to a full rank H for all the tested values, but it presents a condition number too large when $N > 5$. We set the learning gain as $L = (H^\top H + S)^{-1}H^\top$, with $S = 10^{-2}I$. Fig. 2 shows the evolution of the error over iterations. The error converges to values close to zero after few iteration in all the tests except for $T^1 = 2$ and $T^1 = 14$. This is due to the fact that the number of Gaussians being in their variance range is less than three in these two seconds spans. Fig. 3 shows the whole simulation

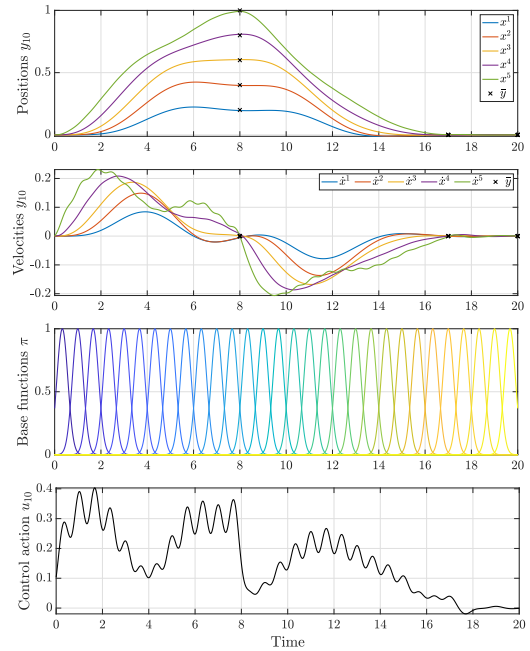

Fig. 3. Simulation at 10th with $T^1 = 8$ and $N = 5$. Black crosses indicate the reference values.

with $T^1 = 8$ and $N = 5$. The reference is precisely tracked with a reasonable control input.

IV. Conclusions

This work presented the Functional ILC framework, which enables the learning of continuous inputs to regulate the output of a linear system at discrete instants. Future work will extend this method to industrial robots.

References

[1] D. A. Bristow, M. Tharayil, and A. G. Alleyne, "A survey of iterative learning control," *IEEE control systems magazine*, vol. 26, no. 3, pp. 96–114, 2006.

[2] L. Cenceschi, F. Angelini, C. Della Santina, and A. Bicchi, "Pi$^\sigma$ - pi$^\sigma$ continuous iterative learning control for nonlinear systems with arbitrary relative degree," in *2021 European Control Conference (ECC)*. IEEE, 2021.

[3] J. van de Wijdeven and O. H. Bosgra, "Using basis functions in iterative learning control: analysis and design theory," *International Journal of Control*, vol. 83, no. 4, pp. 661–675, 2010.

[4] J. Bolder and T. Oomen, "Rational basis functions in iterative learning control—with experimental verification on a motion system," *IEEE Transactions on Control Systems Technology*, vol. 23, no. 2, pp. 722–729, 2014.

[5] L. Blanken, G. Isil, S. Koekebakker, and T. Oomen, "Flexible ilc: Towards a convex approach for non-causal rational basis functions," *IFAC-PapersOnLine*, vol. 50, no. 1, pp. 12 107–12 112, 2017.

[6] R. Chi, Y. Liu, Z. Hou, and S. Jin, "Data-driven terminal iterative learning control with high-order learning law for a class of non-linear discrete-time multiple-input–multiple output systems," *IET Control Theory & Applications*, vol. 9, no. 7, pp. 1075–1082, 2015.

[7] X. Dai, Q. Quan, J. Ren, Z. Xi, and K.-Y. Cai, "Terminal iterative learning control for autonomous aerial refueling under aerodynamic disturbances," *Journal of Guidance, Control, and Dynamics*, vol. 41, no. 7, pp. 1577–1584, 2018.

[8] T. D. Son and H.-S. Ahn, "Terminal iterative learning control with multiple intermediate pass points," in *Proceedings of the 2011 American Control Conference*. IEEE, 2011, pp. 3651–3656.

[9] R. Chi, Z. Hou, S. Jin, and B. Huang, "An improved data-driven point-to-point ilc using additional on-line control inputs with experimental verification," *IEEE Transactions on Systems, Man, and Cybernetics: Systems*, vol. 49, no. 4, pp. 687–696, 2017.

[10] C. Della Santina and F. Angelini, "Iterative learning in functional space for non-square linear systems," in *2021 60th IEEE Conference on Decision and Control (CDC)*. IEEE, 2021, pp. 5858–5863.

Safe and physically-consistent identification of robot payload in collaborative applications: an approach exploiting dynamic motion planning, mixed-reality and sensor fusion

Saverio Farsoni, Jacopo Rizzi, Marcello Bonfè, Silvio Simani

Department of Engineering, University of Ferrara.

Email: saverio.farsoni@unife.it

Abstract: The accurate knowledge of the inertial properties (i.e. mass, center of mass and inertia tensor) of the payload attached to an industrial manipulator is of fundamental importance to enable human-robot collaborative applications as e.g. hand guidance. Traditional methods to identify an unknown payload require the generation of fast and random robot motions, that are incompatible with the safety requirement of a collaborative workcell. Our research activities aim at designing a dynamic motion planning algorithm to allow the execution of identification motions taking care of avoiding collisions with monitored humans inside the robot workspace. Data acquired during such motions from a force/torque (F/T) sensor attached to the robot end-effector are then used to perform the identification of the payload inertial parameters by solving a constrained non-linear optimization problem that guarantees the physical consistency of the results. Ongoing activities investigate the usage of mixed reality to test and validate the safety of the trajectories generated by the planner.

Keywords: Human-robot collaboration, identification, optimization, inertial parameters, mixed reality

Introduction

It has been demonstrated [1] that a proper approach to identifying an unknown payload attached to an industrial manipulator requires fast and random robot motions, in particular sinusoidal trajectories with high frequency and amplitude can provide the proper excitation of the inertial parameters. Such an assumption is incompatible with the safety requirements of the collaborative application for which their knowledge is needful. Indeed, the mass, the center of mass and the inertia tensor introduces non-negligible effects during motions to be compensated in the control scheme of e.g. hand guidance applications. Typical identification approaches consist in solving a least-squares problem that takes into account the presence of noise in the data matrix [1]. An interesting aspect that has been recently investigated is the physical consistency of the identified parameters. In [2] the authors propose a constrained optimization problem whose solution ensures that the set of identified inertial parameters can always belong to a rigid body. We firstly develop a method to identify the parameters using specific test motions that do not take into account humans that move inside the robot workspace during the procedure [3]. Therefore, our aim, as proposed in [4], is the design of a dynamic motion planner that merges together the need to properly excite the payload inertial parameters and the requirement of avoiding collisions with humans, promptly reacting to unpredictable, but monitored, human movements inside the robot workspace. Then, we propose the usage of mixed reality, understood as the integration of real elements into a virtual scene, to safely compute, test and validate the motion planner output. For this purpose, we propose the usage of a bank of multi-rate Kalman filters, whose implementation is described in [5], to estimate the current pose of the human bones by fusing the measurements coming from a depth camera monitoring the workcell and from wearable devices containing IMUs and fixed to the human bones. Finally, we perform a physically-consistent identification of the payload parameters on the basis of the measurements acquired from a F/T sensor mounted on the robot end-effector.

Methods

We designed a sensor fusion algorithm to provide the estimation of the pose of the human bones inside the robot workspace. Such an algorithm consists in a bank of multirate Kalman filters that merge on one side the measurements coming from custom-made wearable IMU boards and, on the other, the estimation of a skeleton tracking algorithm, that makes use of point-cloud data coming from a depth camera. On the basis of such estimations, we project the real

human into a virtual scene where a virtual robot can be used to compute and validate the motion of the real robot ensuring the safety of the human. Indeed, the motion planner, living in the virtual scene, compute the command to be provided to the real robot, generating a repulsive potential field that pushes away the robot from the nearest human bone and, at the same time, an exciting potential field that allows the generation of proper identification data. While the robot is executing its motions, a parallel process is in charge of performing the identification of the inertial parameters of the payload, by solving a constrained non-linear optimization problem, whose solution guarantees the physical consistency of the parameters. Figure 1 depicts the block diagram of the proposed architecture and a screenshot of the virtual scene with the projection of real contents.

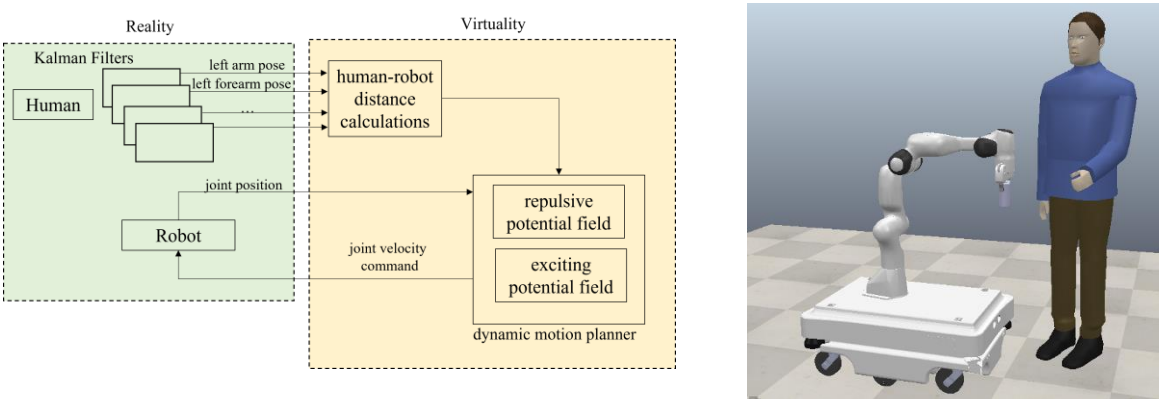

Figure 1. The proposed architecture and the virtual scene with the projection of real elements (the human and the robot)

Results

The simulations we performed demonstrated the feasibility of the approach. The motion planner has been always able to generate robot motion that avoided collision with registered human motions. Furthermore, the results of the identification of an unbalanced cylinder show a percentage error of less than 0.1% on mass and on the center of mass, and less than 10% on the elements of the inertia tensor.

Conclusion and further developments

We showed that mixed reality can be a valuable tool to compute, test and validate robot motions, assuming an accurate registration of the real contents into the virtual scene. We proposed a sensor-fusion algorithm to increase the accuracy of the human skeleton tracking and a dynamic motion planner to generate collision-free robot motions that also can properly excite the inertial parameters. Finally, a constrained non-linear optimization problem has been solved to provide a set of physically-consistent inertial parameters. Ongoing activities investigate the problem of integrating more suitable collision-avoidance algorithms, such as control barrier functions, into the motion planner and we also aim at improving the planning algorithm for 7-DOF robots, exploiting the redundancy of the robot to optimize the feasibility of the planned motions.

References

[1] Kubus, D., T. Kroger, and F. M. Wahl. "On-line estimation of inertial parameters using a recursive total least-squares approach." *2008 IEEE/RSJ International Conference on Intelligent Robots and Systems*.

[2] Traversaro, Silvio, et al. "Identification of fully physical consistent inertial parameters using optimization on manifolds." *2016 IEEE/RSJ International Conference on Intelligent Robots and Systems (IROS)*. IEEE, 2016.

[3] Farsoni, Saverio, Federica Ferraguti, and Marcello Bonfè. "Safety-oriented robot payload identification using collision-free path planning and decoupling motions." Robotics and Computer-Integrated Manufacturing 59 (2019): 189-200.

[4] Farsoni, Saverio, and Marcello Bonfè. "Complete and Consistent Payload Identification During Human-Robot Collaboration: A Safety-Oriented Procedure." *Human-Friendly Robotics 2021*. Springer, Cham, 2022. 15-28.

[5] Farsoni, Saverio, et al. "Real-time identification of robot payload using a multirate quaternion-based kalman filter and recursive total least-squares." *2018 IEEE International Conference on Robotics and Automation (ICRA)*. IEEE, 2018.

Decision Modeling in Markovian Multi-Agent Systems

Carl-Johan Heiker and Paolo Falcone

In our paper [1], we model a decision-making process involving a set of interacting agents using Markovian opinion dynamics, where each agent switches between decisions according to a continuous-time Markov chain (CTMC). Existing opinion dynamics models are extended by introducing attractive and repulsive forces that act within and between groups of agents, respectively. Such an extension enables the resemblance of behaviours emerging in networks where agents make decisions that depend both on their own preferences and the decisions of specific groups of surrounding agents. The considered modeling problem and the contributions in this paper are inspired by the interaction among road users (RUs) at traffic junctions, where each RU has to decide whether to go or to yield.

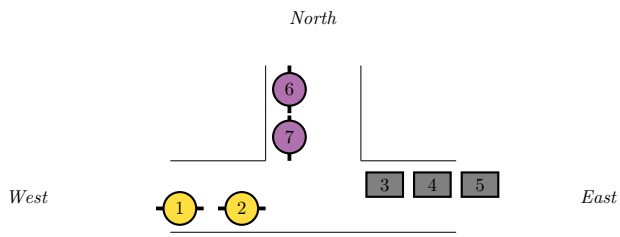

Figure 1: Unsignaled T-junction with cyclists (1-2 and 6-7) and drivers (3-4).

Traffic intersection problem

As a motivation for our model, we consider the case seen in Fig. 1. A set of RUs approach the intersection at t_0, at which time their initial decisions are known with some probability. The task is to predict the evolution of the the RUs' most likely decisions at $t \geq t_0$. To solve this problem, we start by modeling the decision process of a single agent (RU).

Markovian agents

An agent r can switch between states in the decision state set

$$\mathcal{S} = \{s_i | i = 1, 2, \ldots, M\}, \tag{1}$$

at any point in continuous time. In our traffic intersection problem, each agent r chooses between $s_1 = \textit{Yield}$ and $s_2 = \textit{Go}$ as a CTMC over the set $\mathcal{S}$, with $\pi_i^r(t)$ being the probability that r is in s_i at time t. With state probability vector

$$\Pi^r(t) = \begin{bmatrix} \pi_1^r(t) & \pi_2^r(t) & \ldots & \pi_M^r(t) \end{bmatrix}^T, \tag{2}$$

the CTMC of r is fully defined for a state set $\mathcal{S}$, a transition rate matrix $Q^r \in \mathbb{R}^{M \times M}$ and an initial state probability distribution $\Pi^r(0)$.

Interaction through transition rate modulation

In [2] and [3], agents increase their transition rates toward states that their neighbors select. In our model, we allow for a more intricate form of influence by dividing our agents into groups and defining *attractive* and *repulsive* force functions ψ and ξ for rate modulation,

$$\psi_j^{\mathcal{A}}(r) = \eta^r \lambda^{\mathcal{A}} \sum_{k_1 \in \mathcal{A}} \Lambda_{r,k_1}^{\mathcal{A}} I_j^{k_1}(t), \tag{3a}$$

$$\xi_j^{\mathcal{A}\mathcal{R}_\ell}(r) = \frac{\eta^r \gamma^{\mathcal{A}\mathcal{R}_\ell}}{|R|} \sum_{k_2 \in \mathcal{R}_\ell} \Gamma_{r,k_2}^{\mathcal{A}\mathcal{R}_\ell} \big(1 - I_j^{k_2}(t)\big), \tag{3b}$$

where I_i^k is an indicator function for when an agent k is in s_i. Through attraction, agent r increases its rates toward s_j proportional to the number of agents k_1 in its own group $\mathcal{A}$ that are in s_j at time t. Conversely, repulsion causes a rate increase toward s_j depending on the number of agents k_2 from conflicting groups $\mathcal{R}_\ell$ who are *not* in s_j. The matrices $\Lambda^{\mathcal{A}}$ and $\Gamma^{\mathcal{A}\mathcal{R}_\ell}$ describes agent-to-agent interaction strength for the attraction and repulsion, respectively. Additionally, η^r, $\lambda^{\mathcal{A}}$ and $\gamma^{\mathcal{A}\mathcal{R}_\ell}$ are parameters for agent confidence, attraction strength and repulsion strength. Lastly, $|R|$ is the number of groups that $\mathcal{A}$ is repulsed by.

We construct an M^N interactive agent network state CTMC model that can be reduced to an MN state linear marginalized model describing the rate of change in the probability that each agent is in each state as

$$\dot{\Pi}_m(t) = (Q_m + A_m + R_m)\Pi_m(t) + E_m \tag{4}$$

where Q_m, A_m and R_m with E_m describes isolated, attractive and repulsive interaction respectively.

State probabilities in traffic

In our traffic example, we predict the probabilities that RUs in two groups of cyclists (agents 1-2 and 6-7) and one group of drivers (agents 3-5) either yields or goes through an intersection. The cyclists are highly confident, while drivers change their decisions easily. We then show the effect of the attractive and repulsive forces by comparing the stationary state solutions of (4) in two cases. First, RUs are non-communicative, implying that A_m, R_m and E_m are identically zero in (4). The result is shown in Fig. 2a, where most RUs prefer the *Go* state with varying probabilities. Second, attractive and repulsive is included in (4). Fig. 2b shows that the drivers 3-5 are predicted to stop with high probability, and that the cyclists 1-2 and 6-7 will go with slightly higher probability.

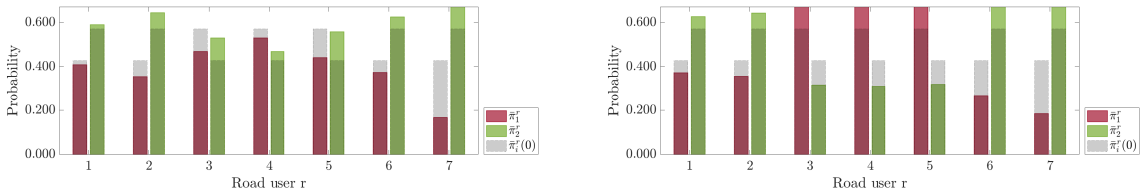

(a) Personal preferences only.

(b) Attractive and repulsive forces added.

Figure 2: Stationary state probabilities to *Yield* (red, left column) and *Go* (green, right column) in two cases.

Conclusions and future work

We have used Markovian opinion dynamics as a framework for modeling decision processes between stochastic agents, inspired by a traffic intersection problem in which road users collectively determine who should yield or go. Agents are divided into groups, and emerging behaviors such as peer pressure and polarization regarding decisions are modeled using attractive and repulsive forces.

In vehicle path planning problems, the stationary solution of our method could be used to predict road user behavior based on a complete traffic scene, whereas the transient solution may be used to express how such a prediction evolves over time.

References

[1] Carl-Johan Heiker and Paolo Falcone. "Collective Decision Making using Attractive and Repulsive Forces in Markovian Opinion Dynamics". In: *RESEARCH.chalmers.se preprint* (2022). URL: `https://research.chalmers.se/publication/529147`.

[2] P. Bolzern, P. Colaneri, and G. De Nicolao. "Opinion dynamics in social networks with heterogeneous Markovian agents". In: *2018 IEEE Conference on Decision and Control (CDC)*. Miami, USA, Dec. 2018, pp. 6180–6185.

[3] Paolo Bolzern, Patrizio Colaneri, and Giuseppe De Nicolao. "Opinion influence and evolution in social networks: A Markovian agents model". In: *Automatica* 100 (2019), pp. 219–230. ISSN: 0005-1098. DOI: `https://doi.org/10.1016/j.automatica.2018.11.023`.

Distributed Mode Computation in Open Multi-Agent Systems

Zoreh Al Zahra Sanai Dashti[1], Gabriele Oliva[2], Carla Seatzu[1],
Andrea Gasparri[3], and Mauro Franceschelli[1]

***Abstract*— Allowing Multi-Agent Systems (MAS) to compute the mode of the agents' initial values (i.e., the value with largest cardinality) represents a highly valuable building block for the development of complex decision-making tasks, as it allows agents to identify the central tendency of data or to implement majority voting processes while considering categorical opinions for which average or median values might not be possible to compute. This is especially challenging in the context of Open Multi-Agent Systems (OMAS), where agents are free to join or leave the network during the algorithm execution, as in this case the outcome of the mode computation process may vary depending on the current participants to the network. In this abstract, we present a novel OMAS distributed mode computation framework where agents currently participating in the network select a value from a finite set of alternatives, and compute the mode via the execution in parallel of a novel average-preserving distributed consensus procedure for each of the different alternatives. No distributed mode computation algorithm has been developed in the context of OMAS: we aim to fill this gap. The main building block of the proposed approach is a novel average-preserving consensus process that is suitable for OMAS, in that it allows to compute the average of the initial conditions of agents that are currently participating in the network. In this view, agents first implement multiple instances of the average-preserving consensus process (i.e., one for each discrete value), and then compute the mode by locally selecting the value associated with the largest among the scalar consensus outcomes.**

I. Introduction

Computation of the *mode* of a set of values is a fundamental building block for decision-making, as it allows to identify the central tendency when considering categorical data for which it is not possible to compute average or median values. Interestingly, the computation of the mode finds application also in *ensemble learning* [1] and has been theorized to represent a major underlying function of the brain's neocortex [2].

In the context of *Multi-Agent Systems* (MAS), examples of distributed mode computation or majority voting approaches can be found in [3], [5]. Such algorithms are shown to converge with high probability.

Distributed mode computation is particularly challenging in the context of *Open Multi-Agent Systems* (OMAS), where agents are free to join or leave the network. A fair amount of distributed consensus approaches for OMAS scenarios have been developed [6]–[13]. In [10], [11], agents estimate the time-varying average of a set of reference signals. In [13], a consensus algorithm for OMAS has been developed where agents track the median of time-varying reference signals.

[1] Department of Electrical and Electronic Engineering, University of Cagliari, Piazza D'Armi, 09123, Cagliari, Italy.
[2] University Campus Bio-Medico of Rome, via A. del Portillo 21, 00128 Rome, Italy.
[3] University Roma Tre, via della Vasca Navale 79, 00146 Rome, Italy.

II. Problem Statement and proposed method

We consider an undirected time-varying graph $\mathcal{G}(t) = \{\mathcal{V}(t), \mathcal{E}(t)\}$. Agents join the network by creating links in an arbitrary way with agents that are already present. Once created, the links do not change unless one of the endpoint agents is disconnected. In case an agent is disconnected, all its incident links are removed.

The *neighborhood* of agent i at time t is $\mathcal{N}_i(t) = \{j \in \mathcal{V}(t) \,|\, (i,j) \in \mathcal{E}(t)\}$. The set $\mathcal{R}(t)$ denotes agents remaining in the network at time t, the set $\mathcal{A}(t)$ denotes the agents joining the network and the set $\mathcal{D}(t)$ the agents leaving the network.

Each agent is provided with a value h_i selected from a finite set $\mathcal{H}$ of possible values, with $|\mathcal{H}| = b \geq 2$, i.e., $\mathcal{H} = \{1, \dots, b\}$. For each time instant t, let us use $\boldsymbol{h}(t) \in \mathbb{R}^{|\mathcal{V}(t)|}$ to denote the stack of the values h_i for the agents $i \in \mathcal{V}(t)$ and let us use $\gamma_j(t)$ to denote the cardinality of the set of agents in $\mathcal{V}(t)$ holding the value j. The *mode* of $\boldsymbol{h}(t)$ is

$$m(t) = \arg\max_{j=1,\dots,b} \{\gamma_j(t)\};$$

in other words, $m(t)$ is the value that appears most often in $\boldsymbol{h}(t)$, it is a function of time due to the agents joining and leaving the network. Our objective is thus to compute and track $m(t)$ in distributed fashion.

Let us define $c(t) = \frac{1}{|\mathcal{V}(t)|} \sum_{i \in \mathcal{V}(t)} h_i$, i.e., $c(t)$ is the average of $h(t)$ belonging to the agents that are participating in the network at time t, $c(t)$ varies as agents join and leave the network.

A. Proposed Protocol

We consider positive edge weights $W_{ij}(t) > 0$ chosen so that the resulting matrix encoding of the graph denoted $I + W(t)$ is a doubly stochastic matrix at all times. Moreover, let us consider boolean variables $\phi_i(t), \psi_i(t)$ defined as follows:

$$\phi_i(t) = \begin{cases} 1, & \text{if } i \in \mathcal{R}(t); \\ 0, & \text{otherwise,} \end{cases} \qquad \psi_i(t) = \begin{cases} 1, & \text{if } i \in \mathcal{A}(t); \\ 0, & \text{otherwise.} \end{cases}$$

Within the proposed protocol, at each time instant t each agent i that is participating in the network (either because it was already participating at time $t-1$ or because it joins the network at time t) maintains and updates an auxiliary variable $z_{ij}(t)$ for each of its neighbors in $\mathcal{N}_i(t)$. As discussed later, such a variable will represent the main ingredient to guarantee average-preservation in spite of the openness of

the multi-agent system. In more detail, the protocol proposed for each agent $i \in \mathcal{V}(t+1)$ (i.e., considering only the agents that need to perform an update at time $t+1$) is as follows

$$x_i(t+1) = \psi_i(t)h_i + \phi_i(t)x_i(t) + \phi_i(t)\underbrace{\left(\sum_{j\in\mathcal{N}_i(t)\cap\mathcal{R}(t)} W_{ij}(t)\big(x_j(t)-x_i(t)\big) + \sum_{j\in\mathcal{N}_i(t)\cap\mathcal{D}(t)} z_{ij}(t)\right)}_{u_i(t)}. \quad (1)$$

Moreover, each agent $i \in \mathcal{V}(t+1)$ maintains and updates auxiliary variable $z_{ij}(t)$ with the following dynamics

$$z_{ij}(t+1) = \phi_i(t)\phi_j(t)\left(z_{ij}(t) - W_{ij}(t)(x_j(t)-x_i(t))\right). \quad (2)$$

In other words, $z_{ij}(t+1)$ is zero whenever either $i \notin \mathcal{R}(t)$ or $j \notin \mathcal{R}(t)$ (or both). In the proposed approach, each agent must maintain $O(|\mathcal{N}_i(t)|b)$ variables at each time instant.

B. Convergence Analysis

We are able formally to show, as reported in Theorem 1 in [14], that the sum of the initial conditions of agents participating in the network is preserved at all times despite the OMAS framework and that, as reported in Theorem 2 in [14], if the network becomes fixed at some time instant t^*, the state $x_i(t)$ of the agents in $\mathcal{V}(t^*)$ asymptotically reaches the average of the initial conditions of the agents in $\mathcal{V}(t^*)$.

III. Numerical Example

We consider an OMAS featuring a maximum of 30 agents, each provided with a value h_i chosen among four possible alternatives, i.e., $b = 4$. The graph is a connected Erdös-Rényi graph with link formation probability $p = 0.35$. At time $t = 30$, a subset of 15 agents leaves the network, while at time $t = 61$, ten agents that left the network join it again. Table I reports the distribution over time of the cardinalities $\gamma_j(t)$ for the different values $j \in \mathcal{H}$ chosen by the agents, along with the mode $m(t)$.

	$\gamma_1(t)$	$\gamma_2(t)$	$\gamma_3(t)$	$\gamma_4(t)$	$m(t)$
$t \in [0, 29]$	6	4	9	11	4
$t \in [30, 60]$	5	3	3	4	1
$t \geq 61$	6	4	9	6	3

TABLE I: Cardinalities $\gamma_j(t)$ and mode $m(t)$ over time.

Figure 1 shows the presented numerical example. We observe that the agents are able to compute $m(t)$ as being equal to four for $t \in [0, 29]$, to one for $t \in [30, 60]$ and, again, to four for $t \geq 61$.

IV. Conclusions

We presented a distributed strategy to allow agents in an OMAS to track the mode of the initial conditions of those agents that are currently participating in the network. The approach is based on a novel average-preserving distributed consensus protocol used to cancel out the influence of agents leaving the network.

Future work will explore applications of these ideas to multi-agent ensemble learning.

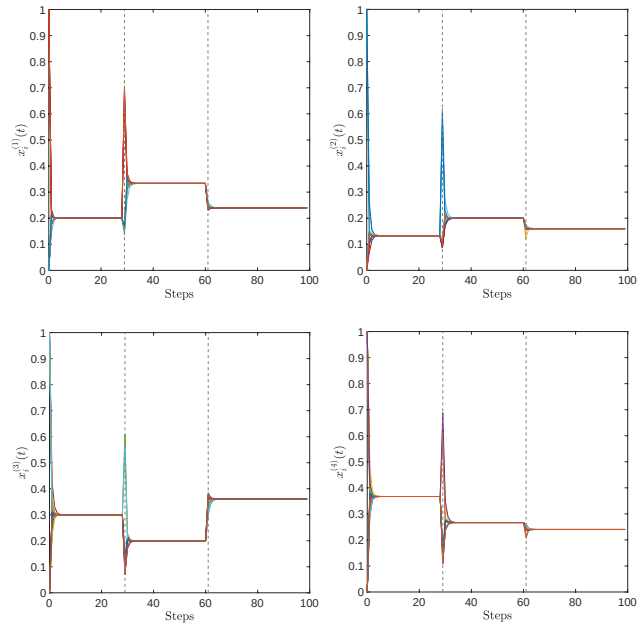

Fig. 1: Numerical example. The dotted vertical lines correspond to the time instants $t = 30$ and $t = 61$, respectively, where some of the agents leave and/or join the network.

References

[1] L. Breiman, "Random forests," *Machine learning*, vol. 45, no. 1, pp. 5–32, 2001.

[2] J. Hawkins, *A thousand brains: A new theory of intelligence*. Basic Books, 2021.

[3] M. A. Abdullah and M. Draief, "Global majority consensus by local majority polling on graphs of a given degree sequence," *Discrete Applied Mathematics*, vol. 180, pp. 1–10, 2015.

[4] S. Salehkaleybar, A. Sharif-Nassab, and S. J. Golestani, "Distributed voting/ranking with optimal number of states per node," *IEEE Transactions on Signal and Information Processing over Networks*, vol. 1, no. 4, pp. 259–267, 2015.

[5] B. Ghojogh and S. Salehkaleybar, "Distributed voting in beep model," *Signal Processing*, vol. 177, p. 107732, 2020.

[6] J. M. Hendrickx and S. Martin, "Open multi-agent systems: Gossiping with deterministic arrivals and departures," in *54th Annual Allerton Conference on Communication, Control, and Computing (Allerton)*, Sept 2016, pp. 1094–1101.

[7] ——, "Open multi-agent systems: Gossiping with random arrivals and departures," in *57th IEEE Conference on Decision and Control (CDC)*, Dec 2017.

[8] C. Monnoyer de Galland, S. Martin and J. M. Hendrickx, "Modelling Gossip Interactions in Open Multi-Agent Systems", arXiv, 2009.02970v2, 2022.

[9] M. Abdelrahim, J. M. Hendrickx, and W. P. M. H. Heemels, "Max-consensus in open multi-agent systems with gossip interactions," in *57th IEEE Conference on Decision and Control (CDC)*, Dec 2017.

[10] M. Franceschelli and P. Frasca, "Stability of open multi-agent systems and applications to dynamic consensus," *IEEE Transactions on Automatic Control*, vol. 66, no. 5, pp. 2326 - 2331, 2021.

[11] M. Franceschelli and P. Frasca, "Proportional dynamic consensus in open multi-agent systems," in *58th IEEE Conference on Decision and Control (CDC)*, Dec. 2018.

[12] V. S. Varma, I. C. Morarescu, and D. Nesic, "Open multi-agent systems with discrete states and stochastic interactions," *IEEE Control Systems Letters*, vol. 2, no. 3, pp. 375–380, July 2018.

[13] Z. A. Z. Sanai Dashti, C. Seatzu, and M. Franceschelli, "Dynamic consensus on the median value in open multi-agent systems," in *58th IEEE Conference on Decision and Control (CDC)*, Dec 2019.

[14] Z. A. Z. Sanai Dashti, G. Oliva, C. Seatzu, A. Gasparri and M. Franceschelli, "Distributed Mode Computation in Open Multi-Agent Systems," in *IEEE Control Systems Letters*, vol. 6, pp. 3481-3486, 2022.

Further characterizations of integral input-to-state stability for hybrid systems

Antonio Russo, Alberto Cavallo

I. Introduction

For modern control problems, there exists a wide variety of dynamical systems which exhibits both continuous and discrete behaviors. These dynamical systems can be best described as the so-called hybrid automata or *hybrid systems*. The study of hybrid systems is not new. Recently, a framework developed in [1], [2] defines hybrid systems as the composition of four elements: a flow set, a jump set, a differential inclusion regulating the system's continuous dynamics and a difference inclusion regulating the system's discrete dynamics. Such framework not only allows to model a wide range of hybrid systems, but it also paves the way to the study of stability and robustness for such systems.

Furthermore, stability analysis of dynamical systems in the presence of exogenous inputs has also been an important research topic over the last few decades. One of the well-known achievement is the introduction of *input-to-state stability* (ISS) in [3], which generalizes the notion of H_∞ stability for nonlinear continuous-time systems. A variant of the ISS notion, called *integral input-to-state stability* (iISS), was introduced in [4] extending H_2 stability to nonlinear systems. The iISS property has been investigated both for continuous-time systems in [5] and for discrete-time systems in [6]. Regarding the stability analysis for hybrid systems in terms of iISS property, to the best of the authors' knowledge, except for the work [7] where a Lyapunov characterization of iISS hybrid systems is proposed, the notion of iISS is only studied for some particular types of hybrid systems (e.g., [8] for switched systems, [9] for impulsive systems and [10] for a combination of the two).

As a result, this theoretical work aims at filling in the gaps in the characterization of iISS for hybrid systems. In particular, inspired by the study of the equivalence between *0-input global uniform asymptotic stability* (0-GUAS) plus *uniform bounded energy bounded state* (UBEBS) and iISS for continuous-time systems in [11], in this work we want to examine the same equivalence for hybrid systems. Meanwhile, as motivated by our previous observation in [12], where it was shown that a switched system is iISS under slow switching if and only if it is both locally iISS and practically iISS under slow switching, we would like to verify if such equivalence also holds for hybrid systems in general. We remark that although the former equivalence is verified for switched time-varying systems in [13], the regularity assumptions on the vector fields in that work are strictly stronger than those assumed on the hybrid systems. Moreover, the dynamics of hybrid systems are given by the combination of differential/difference inclusions rather than differential/difference equations, and stability properties that we investigate are defined with respect to a compact set rather than merely to the origin. These technical differences make the approaches adopted in previous works for showing the equivalent characterizations infeasible here. To tackle these difficulties, some necessary conditions for 0-GUAS and UBEBS of the hybrid systems are investigated at first. Such necessary conditions provide a non-smooth Lyapunov function for the hybrid system. While the Lyapunov theorem for iISS hybrid systems presented in [7] requires the Lyapunov function to be smooth, and smoothing the obtained non-smooth Lyapunov function turns out to be tedious, in this work we will alternatively show iISS by directly proving a non-smooth Lyapunov theorem. Finally, with the help of the aforementioned equivalence between 0-GUAS plus UBEBS and iISS, the combination of local iISS and practical iISS is also shown to be equivalent to iISS under one condition on the local and practical quantifiers.

A. Russo and A. Cavallo are with the Department of Engineering, Università degli Studi della Campania "Luigi Vanvitelli", Aversa, Italy.

II. Preliminaries

The adopted notation and some stability definitions are presented in the following. Consider a hybrid system $\mathcal{H} := \mathcal{H}(\mathcal{C}, \mathcal{D}, \mathcal{F}, \mathcal{G})$ with state $x \in \mathcal{X} \subset \mathbb{R}^n$ and input $u \in \mathcal{U} \subset \mathbb{R}^m$

$$\mathcal{H} := \begin{cases} \dot{x} \in \mathcal{F}(x,u) & (x,u) \in \mathcal{C}, \\ x^+ \in \mathcal{G}(x,u) & (x,u) \in \mathcal{D}. \end{cases} \tag{1}$$

The *flow* and *jump* sets are denoted by $\mathcal{C}$ and $\mathcal{D}$, respectively. Basic regularity assumptions borrowed from [14] are imposed for the hybrid system $\mathcal{H}$:

- A1 the set $\mathcal{X}$ is open, $\mathcal{U}$ is closed and $\mathcal{C}$ and $\mathcal{D}$ are relatively closed sets in $\mathcal{X} \times \mathcal{U}$.
- A2 The set-valued map $\mathcal{F} \colon \mathcal{C} \rightrightarrows \mathbb{R}^n$ is outer semi-continuous and locally bounded, and $\mathcal{F}(x,u)$ is nonempty and convex for all $(x,u) \in \mathcal{C}$.
- A3 The set-valued map $\mathcal{G} : \mathcal{D} \rightrightarrows \mathcal{X}$ is outer semi-continuous and locally bounded, and $\mathcal{G}(x,u)$ is nonempty for all $(x,u) \in \mathcal{D}$.

We refer to the assumptions A1–A3 as *Standing Assumptions*.

The set of all maximal solution pairs (x,u) to $\mathcal{H}$ with initial condition x_0 is designated by $\mathfrak{s}_u(x_0)$.

Let a hybrid input $v : \operatorname{dom} v \longrightarrow \mathcal{U}$ be given. Let $(t,j) \in \operatorname{dom} v$ be such that $(0,0) < (t,j)$. Define the collection of hybrid time of jumps as

$$\Gamma(v) := \{(t,j) \in \operatorname{dom} v : (t, j+1) \in \operatorname{dom} v\}.$$

For any $\gamma \in \mathcal{K}$, define

$$\|v\|^\gamma_{(t,j)} := \int_0^t \gamma\big(|v(s,i(s))|\big)\mathrm{d}s + \sum_{\substack{(t',j') \in \Gamma(v), \\ (0,0) \leqslant (t',j') \leqslant (t,j)}} \gamma\big(|v(t',j')|\big).$$

For any $l \in \mathbb{R}_{>0}$, we denote the set of all hybrid inputs with $\|v\|^\gamma_{(t,j)} \leqslant l$ for all $(t,j) \in \operatorname{dom} v$ by $\mathcal{L}_\gamma(l)$. We also denote the set of all hybrid inputs with $\|v\|^\gamma_{(t,j)} < \infty$ for all $(t,j) \in \operatorname{dom} v$ by $\mathcal{L}^e_\gamma$.

Let $\mathcal{A} \subset \mathcal{X}$ be a nonempty and compact set. Here we provide some stability definitions with respect to the set $\mathcal{A}$, which will be discussed in this work.

Definition 1. *A hybrid system $\mathcal{H}$ is* integral-input-to-state stable *or iISS if there exist functions $\beta \in \mathcal{KLL}$, $\chi \in \mathcal{K}_\infty$ and $\gamma \in \mathcal{K}$ such that for all $x_0 \in \mathcal{X}, u \in \mathcal{L}^e_\gamma$, each solution pair $(x,u) \in \mathfrak{s}_u(x_0)$ satisfies for all $(t,j) \in \operatorname{dom} x$*

$$|x(t,j;x_0,u)|_{\mathcal{A}} \leqslant \beta(|x_0|_{\mathcal{A}}, t, j) + \chi(\|u\|^{\gamma}_{(t,j)}). \tag{2}$$

Definition 2. *A hybrid system $\mathcal{H}$ is* uniform bounded energy bounded state *or UBEBS, if there exist functions $\alpha, \kappa \in \mathcal{K}_\infty, \gamma \in \mathcal{K}$ and $c \in \mathbb{R}_{>0}$ such that for all $x_0 \in \mathcal{X}, u \in \mathcal{L}^e_\gamma$, each solution pair $(x,u) \in \mathfrak{s}_u(x_0)$ satisfies for all $(t,j) \in \operatorname{dom} x$*

$$\alpha(|x(t,j;x_0,u)|_{\mathcal{A}}) \leqslant \kappa(|x_0|_{\mathcal{A}}) + \|u\|^{\gamma}_{(t,j)} + c. \tag{3}$$

Definition 3. *Let $l \in \mathbb{R}_{>0}$. A hybrid system $\mathcal{H}$ is l-*locally iISS *if there exist functions $\beta \in \mathcal{KLL}$, $\chi \in \mathcal{K}_\infty$ and $\gamma \in \mathcal{K}$ such that for all $x_0 \in \mathbb{B}(\mathcal{A}, l), u \in \mathcal{L}_\gamma(l)$, each solution pair $(x,u) \in \mathfrak{s}_u(x_0)$ satisfies (2) for all $(t,j) \in \operatorname{dom} x$.*

Definition 4. *Let $p \in \mathbb{R}_{\geqslant 0}$. A hybrid system $\mathcal{H}$ is p-*practically iISS *if there exist functions $\beta \in \mathcal{KLL}$, $\chi \in \mathcal{K}_\infty$ and $\gamma \in \mathcal{K}$ such that for all $x_0 \in \mathcal{X}, u \in \mathcal{L}^e_\gamma$, each solution pair $(x,u) \in \mathfrak{s}_u(x_0)$ satisfies for all $(t,j) \in \operatorname{dom} x$*

$$|x(t,j;x_0,u)|_{\mathcal{A}} \leqslant \beta(|x_0|_{\mathcal{A}}, t, j) + \chi(\|u\|^{\gamma}_{(t,j)}) + p. \tag{4}$$

III. Main results

In this section the main results are presented together with some intermediate results describing necessary conditions for 0-GUAS and UBEBS of hybrid systems.

Theorem III.1. *Consider a hybrid system $\mathcal{H}$ and suppose that the Standing Assumptions hold. The following facts are equivalent:*

1) *The system is iISS.*
2) *The system is 0-GUAS and UBEBS.*
3) *The system is l-locally iISS and p-practically iISS with $l > p$.*

A. Necessary conditions for 0-GAS

Lemma III.2. *A hybrid system $\mathcal{H}$ is 0-GUAS if and only if there exist a smooth Lyapunov function $V\colon \mathcal{X} \longrightarrow \mathbb{R}_{\geqslant 0}$, functions α_1, α_2, $\alpha_3 \in \mathcal{K}_\infty$, $\lambda \in \mathcal{K}$ and a nonzero function $q\colon \mathbb{R}_{\geqslant 0} \longrightarrow \mathbb{R}_{>0}$ with the property that $q(s) \equiv 1$ for all $s \in [0,1]$ such that*

$$\alpha_1(|x|_{\mathcal{A}}) \leqslant V(x) \leqslant \alpha_2(|x|_{\mathcal{A}}) \quad \forall x \in \mathcal{X}, \tag{5}$$

$$\max_{f \in \mathcal{F}(x,u)} \langle \nabla V(x), f \rangle \leqslant -\alpha_3(|x|_{\mathcal{A}}) + \lambda(1/q(|x|_{\mathcal{A}}))\lambda(|u|) \quad \forall (x,u) \in \mathcal{C}, \tag{6}$$

$$\max_{g \in \mathcal{G}(x,u)} V(g) - V(x) \leqslant -\alpha_3(|x|_{\mathcal{A}}) + \lambda(1/q(|x|_{\mathcal{A}}))\lambda(|u|) \quad \forall (x,u) \in \mathcal{D}. \tag{7}$$

Lemma III.3. *If a hybrid system $\mathcal{H}$ is 0-GUAS with respect to $\mathcal{A}$, then it is also locally iISS with respect to $\mathcal{A}$.*

B. Necessary conditions for UBEBS

Lemma III.4. *Suppose that a hybrid system $\mathcal{H}$ is 0-GUAS. Then the following properties are equivalent:*

a) *The system satisfies along all trajectories an estimate of the following type, for suitable functions $\alpha_1, \alpha_2, \alpha_3 \in \mathcal{K}_\infty$ and $\hat{\gamma} \in \mathcal{K}$:*

$$\alpha_1(|x(t,j;x_0,u)|_{\mathcal{A}}) \leqslant \alpha_2(|x_0|_{\mathcal{A}}) + \alpha_3(\|u\|^{\hat{\gamma}}_{(t,j)}). \tag{8}$$

b) *The system satisfies along all trajectories an UBEBS-like estimate with $c = 0$:*

$$\alpha(|x(t,j;x_0,u)|_{\mathcal{A}}) \leqslant \kappa(|x_0|_{\mathcal{A}}) + \|u\|^{\gamma}_{(t,j)}. \tag{9}$$

c) *The system is UBEBS.*

C. A non-smooth iISS Lyapunov theorem for hybrid systems

Theorem III.5. *Consider a hybrid system $\mathcal{H}$ and suppose that the Standing Assumptions hold. The system $\mathcal{H}$ is iISS if and only if there exist a function $\bar{V}(x) : \mathcal{X} \longrightarrow \mathbb{R}_{\geqslant 0}$, functions $\bar{\alpha}_1, \bar{\alpha}_2 \in \mathcal{K}_\infty, \bar{\gamma} \in \mathcal{K}$ and $\rho \in \mathcal{PD}$ such that*

$$\bar{\alpha}_1(|x|_{\mathcal{A}}) \leqslant \bar{V}(x) \leqslant \bar{\alpha}_2(|x|_{\mathcal{A}}) \quad \forall x \in \mathcal{X}, \tag{10}$$

$$\bar{V}(x(t,j;x_0,u)) \leqslant \bar{V}(x_0) - \int_0^t \rho(|x(\tau, i(\tau); x_0, u)|_{\mathcal{A}})\, \mathrm{d}\tau - \sum_{\substack{(t',j') \in \Gamma(x), \\ (0,0) \leqslant (t',j') \leqslant (t,j)}} \rho(|x(t',j';x_0,u)|_{\mathcal{A}}) + \|u\|^{\bar{\gamma}}_{(t,j)} \quad \forall x_0 \in \mathcal{X}, u \in \mathcal{L}^e_{\bar{\gamma}}, (t,j) \in \operatorname{dom} x. \tag{11}$$

References

[1] R. Goebel, R. G. Sanfelice, and A. R. Teel, *Hybrid Dynamical Systems: Modeling, Stability, and Robustness*, 2012.

[2] R. G. Sanfelice, *Hybrid Feedback Control*, 2021.

[3] E. D. Sontag, "Smooth stabilization implies coprime factorization," vol. 34, no. 4, pp. 435–443, Apr 1989.

[4] ——, "Comments on integral variants of ISS," vol. 34, no. 1, pp. 93 – 100, 1998.

[5] D. Angeli, E. D. Sontag, and Y. Wang, "A characterization of integral input-to-state stability," vol. 45, no. 6, pp. 1082–1097, June 2000.

[6] D. Angeli, "Intrinsic robustness of global asymptotic stability," vol. 38, no. 4, pp. 297–307, 1999.

[7] N. Noroozi, A. Khayatian, and R. Geiselhart, "A characterization of integral input-to-state stability for hybrid systems," vol. 29, no. 3, p. 13, Jun 2017.

[8] J. Mancilla-Aguilar and R. García, "On converse Lyapunov theorems for ISS and iISS switched nonlinear systems," vol. 42, no. 1, pp. 47 – 53, 2001.

[9] J. P. Hespanha, D. Liberzon, and A. R. Teel, "Lyapunov conditions for input-to-state stability of impulsive systems," vol. 44, no. 11, pp. 2735 – 2744, 2008.

[10] S. Liu, A. Tanwani, and D. Liberzon, "ISS and integral-ISS of switched systems with nonlinear supply functions," pp. 1–1, 2021.

[11] D. Angeli, E. D. Sontag, and Y. Wang, "Further equivalences and semiglobal versions of integral input to state stability," *Dynamics and Control*, vol. 10, no. 2, pp. 127–149, Apr 2000.

[12] S. Liu, A. Russo, D. Liberzon, and A. Cavallo, "Integral-input-to-state stability of switched nonlinear systems under slow switching," pp. 1–1, 2021.

[13] H. Haimovich and J. L. Mancilla-Aguilar, "A characterization of integral ISS for switched and time-varying systems," vol. 63, no. 2, pp. 578–585, Feb 2018.

[14] C. Cai and A. R. Teel, "Characterizations of input-to-state stability for hybrid systems," vol. 58, no. 1, pp. 47 – 53, 2009.

Learning with Bayesian Frequentist Bounds

G. Baggio, A. Carè, A. Scampicchio, G. Pillonetto *

poster presentation

Summary. Learning a function from noisy measurements is a crucial problem in statistics and engineering, with an impact on machine learning predictions and identification of dynamical systems. Existing results are derived by constraining the estimates to belong to a deterministic function space; however, the resulting bounds are often overly conservative and, hence, of limited applicability. An alternative is to use a Bayesian framework. The regions thereby obtained however require complete specification of prior distributions whose choice may significantly affect the probability of inclusion. Building on the Sign-Perturbed Sums (SPS) paradigm [1], we propose a framework for the effective computation of regions that include the unknown function with exact probability. In our setting, the users not only have the freedom to modulate the amount of prior knowledge that informs the constructed regions but can, on a different plane, finely modulate their commitment to such information. The result is a versatile certified estimation framework capable of addressing a variety of problems, ranging from parametric estimation (where the probabilistic guarantees can be issued under no commitment to the prior information) to non-parametric problems (that call for fine exploitation of prior information).

Problem formulation. We consider the measurement model

$$y = A\theta^0 + B\nu \tag{1}$$

where $A \in \mathbb{R}^{n\times m}$ and $B \in \mathbb{R}^{n\times n}$ are known matrices, both assumed full rank, $y \in \mathbb{R}^n$ are the collected data, $\theta^0 \in \mathbb{R}^m$ is the unknown vector while ν contains the noise components. We model both θ^0 and ν as (independent) random vectors. The unknown vector θ^0 is the sum of a (known) vector $\mu \in \mathbb{R}^m$ and the output of a linear system described by the $m \times m$ (known, full rank) matrix C fed with noise ω:

$$\theta^0 = \mu + C\omega. \tag{2}$$

we will make use of the following mild assumption on the noises ν and ω.

Assumption 1 *The components of ν and ω are independent and divided into two distinct sets. The first, denoted by $\mathcal{A}$, contains random variables of known probability distribution. The second, named $\mathcal{B}$, contains random variables with probability densities just known to be symmetric around zero.*

Our objective is to construct regions, based on the measurements collected in vector y, containing the true vector θ^0 with prescribed probability $\alpha \in (0, 1)$. In particular, any realization of our regions will be guaranteed to contain the estimate

$$\begin{aligned}\hat{\theta} &= \arg\min_{\theta}\ (y-A\theta)^\top\Sigma_v^{-1}(y-A\theta)+(\theta-\mu)^\top\Sigma_\theta^{-1}(\theta-\mu)\\ &= \mu + (A^\top\Sigma_v^{-1}A + \Sigma_\theta^{-1})^{-1}A^\top\Sigma_v^{-1}(y - A\mu)\end{aligned} \tag{3}$$

where $\Sigma_v = BB^\top$ and $\Sigma_\theta = CC^\top$. We stress that if the components of ν and ω are all mutually uncorrelated, with zero mean and unit variance, (3) is the minimum variance linear estimator of θ^0. In addition, (3) can capture any sampled version of the infinite-dimensional estimates returned by kernel-based learning methods [3, 4, 2].

*G. Baggio and G. Pillonetto are with the Department of Information Engineering, University of Padova, Padova, Italy. E-mails: {baggio,giapi}@dei.unipd.it. A. Carè is with the Department of Information Engineering, University of Brescia, Brescia, Italy. E-mail: algo.care@unibs.it. A. Scampicchio is with the Institute for Dynamic Systems and Control, ETH Zürich, Zürich, Switzerland. E-mail: ascampicc@ethz.ch.

Bayesian Frequentist Bounds. We define $\Omega \in \mathbb{R}^{N\times m}$, $z \in \mathbb{R}^N$, and $\epsilon \in \mathbb{R}^N$, where $N = n + m$, respectively, as

$$\Omega = \begin{bmatrix} B^{-1}A \\ C^{-1} \end{bmatrix}, \quad z = \begin{bmatrix} B^{-1}y \\ C^{-1}\mu \end{bmatrix}, \quad \epsilon = \begin{bmatrix} \nu \\ \omega \end{bmatrix}. \tag{5}$$

For $i = 1, 2, \ldots, r-1$ and $t = 1, 2, \ldots, N$, we use $\{\xi_t^i\}$ to denote a sequence of $(r-1)N$ independent random variables satisfying

$$\begin{cases} \mathbb{P}(\xi_t^i = 0) = 1 & \text{if } \epsilon_t \in \mathcal{A}, \\ \mathbb{P}(\xi_t^i = -1) = \mathbb{P}(\xi_t^i = 1) = \frac{1}{2} & \text{if } \epsilon_t \in \mathcal{B}. \end{cases} \tag{6}$$

Further, for $i = 1, 2, \ldots, r-1$, we use ζ^i to indicate independent random vectors whose components ζ_t^i, $t = 1, 2, \ldots, N$, are samples from the distribution of ϵ_t if $\epsilon_t \in \mathcal{A}$, and zero with probability one if $\epsilon_t \in \mathcal{B}$. The quantities introduced above allow us to define randomized copies of the vector ϵ: its components in $\mathcal{B}$ will be perturbed by random signs, while those in $\mathcal{A}$ will be drawn from their prior distribution. Finally, we let $\pi = (\pi(0), \pi(1), \ldots, \pi(r-1))$ denote a uniformly distributed random permutation of the set $\{0, 1, \ldots, r-1\}$. The proposed uncertainty regions, termed Bayesian Frequentist Bounds (BFB), are constructed as illustrated in Algorithm 1.

Algorithm 1 BFB of probability $\alpha = 1 - 1/r$

Compute

$$Q_i = \frac{1}{N}\sum_{t=1}^{N} \xi_t^i \Omega(t,:)^\top \Omega(t,:),$$

$$\psi_i = \frac{1}{N}\sum_{t=1}^{N} \xi_t^i \Omega(t,:)^\top z_t + \frac{1}{N}\sum_{t=1}^{N} \Omega(t,:)^\top \zeta_t^i$$

for $i = 1, 2, \ldots, r-1$, where $\Omega(t,:)$ is the t-th row of Ω.

Define the sets

$$\mathcal{E}_i = \{\theta \in \mathbb{R}^m \ : \ \theta^\top A_i \theta + 2\theta^\top b_i + c_i \leq_{\pi,i} 0\},$$

for $i = 1, 2, \ldots, r-1$, where $R_N = \frac{1}{N}\Omega^\top\Omega$, $A_i = R_N - Q_i R_N^{-1} Q_i, b_i = Q_i R_N^{-1}\psi_i - R_N\hat{\theta}$, $c_i = \hat{\theta}^\top R_N \hat{\theta} - \psi_i^\top R_N^{-1}\psi_i$. Here, $\hat{\theta}$ defined as in (3), and "$\leq_{\pi,i}$" stands for "$\leq$" if $\pi(0) < \pi(i)$, and "$<$" otherwise.

Return the region

$$\Theta(y) = \bigcup_{i=1}^{r-1} \mathcal{E}_i. \tag{4}$$

Our main result states that BFB are guaranteed to contain the unknown parameter θ^0 with exact probability $\alpha = 1 - 1/r$, where r is a tunable positive integer.

Theorem 1 (Exact inclusion probability) *Consider the model in (1)-(2) and Assumption 1. Then, the Bayesian frequentist region $\Theta(y)$ defined through Algorithm 1 is a union of convex sets, contains (3) if non-empty, and satisfies*

$$\mathbb{P}(\theta^0 \in \Theta(y)) = 1 - 1/r. \tag{7}$$

The proposed uncertainty bounds have been applied to several problems, ranging from Bayesian LASSO to heteroscedastic Gaussian regression, and compared with alternative approaches. The numerical analysis shows that BFB are often informative in terms of tightness while being computationally cheap.

References

[1] B. C. Csáji, M. C. Campi, and E. Weyer. Sign-perturbed sums: A new system identification approach for constructing exact non-asymptotic confidence regions in linear regression models. *IEEE Transactions on Signal Processing*, 63(1):169–181, 2014.

[2] G. Pillonetto and G. De Nicolao. A new kernel-based approach for linear system identification. *Automatica*, 46(1):81–93, 2010.

[3] T. Poggio and F. Girosi. Networks for approximation and learning. In *Proceedings of the IEEE*, volume 78, pages 1481–1497, 1990.

[4] G. Wahba. *Spline models for observational data*. SIAM, Philadelphia, 1990.

Mechanical Fault Detection of CNC Milling Machines

Marino Pavone, Nicola Epicoco, Giordano Pola,
Elena De Santis, Maria Domenica Di Benedetto

Authors are with the Department of Information Engineering, Computer Science and Mathematics and with the Center of Excellence DEWS, University of L'Aquila, Italy

Cyber-physical health management systems are very important tools that typically use so-called "Health Indicators", i.e., components of the state of a general system that can be analytically treated to (see, e.g., [1]): 1) understand how far from healthy/safety conditions the system is currently working (i.e., Health Management); 2) detect or predict anomalies that can be linked to some (usually well-known) incipient fault conditions (i.e., Fault Detection); 3) estimate the Rest Useful Life of the entire system (or a single component) and update such esteem as far as a new sample of the same health indicator is available (i.e., Prognostic). The simultaneous application of all concepts above to physical systems that are naturally subject to possible failures or degradation phenomena is called Predictive Maintenance (PM). Over the last two decades, the interest in this topic has constantly increased [2], mainly because efficiency has become even more important than performance optimization, particularly in modern industrial environments, characterized by a growing application of automation. In fact, having information about the healthy state of a system, beyond any safety reason related to preventing dangerous failures, is of paramount importance to reduce costs related to machine downtime and the consequent process interruption. Moreover, cyber-physical health management systems can increase the reliability of the industrial process and supply information to optimally plan maintenance works [3], which makes PM one of the most important paradigms of Industry 4.0.

The application of PM relies on the use of sensors that measure system characteristics, such as vibration, current, noise, temperature, or any kind of the so-called "medium for incipient faults". When such data are treated through a model-based approach, health indicators are computed via equations that describe the healthy work condition of the analyzed system with respect to its current working parameters. This approach is really accurate and reliable [4]; however, it requires deep knowledge and understanding of the physics behind the system functioning and can be affected by the environmental conditions which reduce the effective scalability and reusability of the method.

As a consequence, the growing market of IoT-based communication infrastructures, and the continuous evolution of Artificial intelligence (AI) and big data technologies, made Data Driven (DD) PM approaches the best choice for many industrial applications [5]. Basically, DD approaches consist in collecting data from experiments directly performed on the system both in normal functioning conditions and in some artificially induced fault situations. The acquired data are then processed by AI algorithms to realize a model that describes the healthy conditions of the system, only considering the medium measures and current parameters, and without requiring a deep knowledge of the system dynamics. As a matter of fact, nowadays good results have been reached by the application of DD methods in several fields, such as, for instance, bearing PM, battery health management, or electrical motors PM [1].

In this context, our research is focused on a specific cyber-physical health management system, which has never been studied before in the relevant literature, that is, a cartesian robot for planar machining. The reason behind this choice relies on the needs of a machine-tool manufacturing company (namely, Protek S.r.l. [6]) to reduce the number of repair requests from the technical assistant office. Clearly, such a milling machine can be affected by several different failures, such as, broken bearing, misalignment, gear wheels failure, and so on. Therefore, we firstly focused on the most common kind

of failure, that is, the degradation of the working tool, which clearly impacts on the final workpiece quality.

According to [7], vibrations are the most effective medium for mechanical applications. Hence, 200Hz accelerometric sensors have been positioned in suitably selected points of the machine. The infrastructure has been equipped with an acquisition board that collects all the measured data and acts as a gateway for sending these samples to the cloud, thus making them remotely available for all actors involved in their analysis.

We schedule a very wide set of experiments under different conditions (selected among the most commonly used ones) and each experiment is replicated in both normal and faulty conditions. More in detail, we first consider a milling process on different materials (that is, aluminium, forex, and plexiglass panels), and for each material we perform four different tool trajectories (in straight line, along the diagonals, sawtooth, and in circle). Moreover, all the trajectories are repeated at three different speeds (low, medium, and high), five times per speed so as to increase the data redundancy.

In all the experiments vibration signals are measured and stored on a dataset which covers as many working conditions as possible.

Data pre-processing and Feature Selection (FS) aims at processing collected data in order to highlight faulty characteristics, thus simplifying the subsequent Machine Learning modelling. In fact, being vibrations an oscillatory phenomenon, row data from sensors are typically chaotic and really hard to be interpreted. Thus, a FS technique is applied in order to extract time-frequency information, which allows identifying the specific fault and localizing it in time.

Currently, we are still performing some experiments, but preliminary results are promising. In particular, we are comparing the most popular time-frequency resolution techniques [8], such as Empirical Mode Decomposition, wavelet, and Hilbert Transformation as well as different machine learning tools, such as Neural Networks, Support Vector Machine, random forest, and decision trees in order to identify the most suitable pre-processing tool.

The final goal is to evaluate the accuracy and robustness of the method, based on the different coupling between the Feature Selection technique and the machine learning algorithm.

Once the methodology will be tuned on the considered working conditions, we plan to test it on other failures of interest.

References

[1] K.L. Tsui, N. Chen, Q. Zhou, Y. Hai, W. Wang, "Prognostics and Health Management: A Review on Data-Driven Approaches", Mathematical Problems in Engineering, vol. 2015, art. 793161, 2015.

[2] V.M. Catterson, J.J.A. Costello, G.M. West, S.D.J. McArthur, C.J. Wallace, "Increasing the Adoption of Prognostic Systems for Health Management in the Power Industry", Chemical Engineering Transactions, vol. 33, pp. 271-276, 2013.

[3] A. Prajapati, J. Bechtel, S. Ganesan, "Condition based maintenance: A survey", Journal of Quality in Maintenance Engineering, vol. 18 (4), pp. 384-400, 2012.

[4] Z. Gao, C. Cecati, S.X. Ding, "A Survey of Fault Diagnosis and Fault-Tolerant Techniques - Part I: Fault Diagnosis With Model-Based and Signal-Based Approaches", IEEE Transactions on Industrial Electronics, vol. 62 (6), pp. 3757-3767, 2015.

[5] S.J. Qin, "Survey on data-driven industrial process monitoring and diagnosis", Annual Reviews in Control, vol. 36 (2), pp. 220-234, 2012.

[6] https://www.protek.it/

[7] T.D. Lopes, A. Goedtel, R.H.C. Palácios et al., "Bearing fault identification of three-phase induction motors bases on two current sensor strategy", Soft Computing, vol. 21, pp. 6673-6685, 2017.

[8] B. Venkatesh and J. Anuradha, "A Review of Feature Selection and Its Methods", Cybernetics and Information Technologies, vol.19 (1), pp.3-26, 2019.

Data-driven Output Regulation via Gaussian Processes and Luenberger Internal Models

Lorenzo Gentilini, Michelangelo Bin, Lorenzo Marconi

Abstract: This paper deals with the problem of adaptive output regulation for multivariable nonlinear systems by presenting a learning-based adaptive internal model-based design strategy. The approach builds on the recently proposed adaptive internal model design techniques based on the theory of nonlinear Luenberger observers, and the adaptation side is approached as a probabilistic regression problem. In particular, Gaussian processes priors are employed to cope with the learning problem. Unlike the previous approaches in the field, here only coarse assumptions about the friend structure are required, making the proposed approach suitable for applications where the exosystem is highly uncertain.

1. PROBLEM SET-UP

In this work, we aim to design a learning-based adaptive internal model solving the problem of approximate output regulation for a class of nonlinear systems of the form

$$\begin{aligned} \dot{z} &= f_0\left(w, z, e\right), \\ \dot{e} &= Ae + B\left(q\left(w, z, e\right) + b\left(w, z, e\right) u\right), \\ y &= Ce, \end{aligned} \tag{1}$$

in which $z \in \mathbb{R}^{n_z}$ together with the error dynamics $e \in \mathbb{R}^{n_e}$ represent the overall state of the plant. The quantities $u \in \mathbb{R}^{n_y}$ and $y \in \mathbb{R}^{n_y}$ are the control input and the measured output respectively, while $w \in \mathbb{R}^{n_w}$ is an exogenous input, $f_0 : \mathbb{R}^{n_w} \times \mathbb{R}^{n_z} \times \mathbb{R}^{n_e} \mapsto \mathbb{R}^{n_z}$, $q : \mathbb{R}^{n_w} \times \mathbb{R}^{n_z} \times \mathbb{R}^{n_e} \mapsto \mathbb{R}^{n_y}$, $b : \mathbb{R}^{n_w} \times \mathbb{R}^{n_z} \times \mathbb{R}^{n_e} \mapsto \mathbb{R}^{n_y \times n_y}$ are continuous functions, and A, B, and C are in prime form, for some $r \in \mathbb{N}$.

Assumption 1. The function f_0 is locally Lipschitz and the functions q and b are $\mathcal{C}^1$ functions, with local Lipschitz derivative.

Assumption 2. There exists a $\mathcal{C}^1$ map $\pi : \mathcal{P} \subset \mathbb{R}^{n_w} \mapsto \mathbb{R}^{n_z}$, with $\mathcal{P}$ an open neighborhood of $\mathcal{W}$, satisfying

$$L^{(w)}_{s(w)} \pi\left(w\right) = f_0\left(w, \pi\left(w\right), 0\right),$$

with $L^{(w)}_{s(w)} \pi\left(w\right) = \frac{\partial \pi(w)}{\partial w} s(w)$, such that the system

$$\dot{w} = s\left(w\right), \; \dot{z} = f_0\left(w, z, e\right),$$

is Input-to-State Stable (ISS) with respect to the input e, relative to the compact set $\mathcal{A} = \{(w, z) \in \mathcal{W} \times \mathbb{R}^{n_z} : z = \pi\left(w\right)\}$.

Assumption 3. There exists a known constant nonsingular matrix $\boldsymbol{b} \in \mathbb{R}^{n_y \times n_y}$ such that the inequality

$$\left\| (b(w, z, e) - \boldsymbol{b})\boldsymbol{b}^{-1} \right\| \leq 1 - \mu_0,$$

holds for some known scalar $\mu_0 \in (0, 1)$, and for all $(w, z, e) \in \mathcal{W} \times \mathbb{R}^{n_z} \times \mathbb{R}^{n_e}$.

In this framework, we now recall a result based on (Bin et al., 2020, Theorem 1). Let Assumption 1, 2, and 3 hold, and let $\mathcal{M} = \{\psi(\theta, \cdot) : \mathbb{R}^{n_\eta} \mapsto \mathbb{R}^{n_y} | \theta \in \Theta\}$, with Θ a finite-dimensional normed vector space, be a finite-dimensional model set where γ is supposed to range. Consider the following regulator structure

$$\begin{cases} \dot{\zeta} = 1 \\ \dot{\eta} = F\eta + Gu \\ \dot{\hat{e}} = A\hat{e} + B\left(\hat{\xi} + \boldsymbol{b}u\right) + \Lambda(l) H\left(y - \hat{e}_1\right) \\ \dot{\hat{\xi}} = -\boldsymbol{b}\psi\left(\theta, \eta, u\right) + l^{r+1} H_{r+1}\left(y - \hat{e}_1\right) \\ \dot{\varsigma} = 0 \end{cases}$$

$$\left(\zeta, \eta, \hat{e}, \hat{\xi}, \varsigma, \theta, y\right) \in C_\zeta \times \mathbb{R}^{n_\eta + n_e + n_y} \times \Sigma \times \Theta \times \mathbb{R}^{n_y},$$

$$\begin{cases} \zeta^+ = 0, \quad \eta^+ = \eta \\ \hat{e}^+ = \hat{e}, \quad \hat{\xi}^+ = \hat{\xi} \\ \varsigma^+ = \varphi\left(\varsigma, \eta, u\right) \end{cases}$$

$$\left(\zeta, \eta, \hat{e}, \hat{\xi}, \varsigma, \theta, y\right) \in D_\zeta \times \mathbb{R}^{n_\eta + n_e + n_y} \times \Sigma \times \Theta \times \mathbb{R}^{n_y},$$

with $\theta = \vartheta\left(\varsigma\right)$ and output $u = \boldsymbol{b}^{-1}\mathrm{sat}(-\hat{\xi} + \kappa_s\left(\hat{e}\right))$. Where A, B, $\boldsymbol{b}$ are the same in (1) and Assumption 3, while (F, G) and n_η are defined as in Marconi et al. (2007), and Σ finite-dimensional normed vector space. The sets $C_\zeta = \left[0, \overline{\mathrm{T}}\right]$, $D_\zeta = \left[\underline{\mathrm{T}}, \overline{\mathrm{T}}\right]$ with $\overline{\mathrm{T}}$, $\underline{\mathrm{T}} \in \mathbb{R}_+$, satisfying $0 < \underline{\mathrm{T}} \leq \overline{\mathrm{T}}$. Furthermore, $\Lambda(l) = \mathrm{diag}\left(lI_{n_y}, l^2 I_{n_y}, \ldots, l^r I_{n_y}\right)$, $H = \mathrm{diag}\left(H_1, \ldots, H_r\right)$, and $H_i = \mathrm{diag}\left(h_i^1, \ldots, h_i^{n_y}\right)$ with $\{h_1^j, h_2^j, \ldots, h_{r+1}^j\}$ for all $j = 1, \ldots, n_y$ coefficients of a Hurwitz polinomial, and $l \in \mathbb{R}_{>0}$ is a control parameter. Let the tuple $(\mathcal{M}, \Sigma, \psi, \Theta, \vartheta)$ be such that the *identifier requirements*, relative to a given cost function $\mathcal{J}$, are satisfied (Bin et al. (2020)). Then, for each compact sets $Z_0 \subset \mathbb{R}^{n_z}$, $E_0 \subset \mathbb{R}^{n_e}$, and $S_0 \subset \mathbb{R}^{n_e} \times \mathbb{R}^{n_{n_y}}$ of initial conditions for z, e, and $(\hat{e}, \boldsymbol{b})$ respectively, there exists $l_s^\star > 0$ such that if $l > l_s^\star$ then the aggregate state $\boldsymbol{x} = (\zeta, w, z, e, \eta, \hat{e}, \hat{\xi}, \varsigma, \theta)$ of the closed-loop system is bounded. Moreover, there exists a $\alpha_{\boldsymbol{x}} > 0$ and for each $\underline{\mathrm{T}} > 0$, an $l_\epsilon^\star > 0$, such that if $l > l_\epsilon^\star\left(\underline{\mathrm{T}}\right)$ then

$$\limsup_{t \to \infty} |y(t)| \leq \alpha_{\boldsymbol{x}} \limsup_{t+j \to \infty} |u^\star(w) - \psi(\theta^\star, \tau(w))|.$$

The key idea behind the proposed approach consists in modeling the unknown function γ as the realization of a Gaussian process, supposing to have access to a dataset of samples collected at different time instants $t_i \in \mathbb{R}_{>0}$, $\mathcal{DS} = \{(\eta, u) \in \mathbb{R}^{n_\eta} \times \mathbb{R}^{n_y} : \eta = \eta(t_i), u = u(t_i) \text{ with } i = 1, \ldots, N\}$, with each pair $(\eta, u) \in \mathcal{DS}$ obtained as $u(t_i) = \gamma(\eta(t_i)) + \varepsilon(t_i)$ with $\varepsilon(t_i) \sim \mathcal{N}(0, \sigma_n^2 I_{n_y})$

white Gaussian noise with known variance σ_n^2. Denoting $\boldsymbol{\eta} = (\eta(t_1), \ldots, \eta(t_N))^\top$ and $\boldsymbol{u} = (u(t_1), \ldots, u(t_N))^\top$, the regression is then performed as (Rasmussen (2003))

$$\begin{aligned} \mu(\eta) &= \boldsymbol{\kappa}(\eta)^\top \left(\boldsymbol{\mathcal{K}} + \sigma_n^2 I_N\right)^{-1} \boldsymbol{u}, \\ \sigma^2(\eta) &= \kappa(\eta,\eta) - \boldsymbol{\kappa}(\eta)^\top \left(\boldsymbol{\mathcal{K}} + \sigma_n^2 I_N\right)^{-1} \boldsymbol{\kappa}(\eta), \end{aligned} \tag{2}$$

where $\boldsymbol{\mathcal{K}} \in \mathbb{R}^{N\times N}$ is the *Gram matrix* whose (k,h)-th entry is $\boldsymbol{\mathcal{K}}_{k,h} = \kappa(\boldsymbol{\eta}_k, \boldsymbol{\eta}_h)$, with $\boldsymbol{\eta}_k$ the k-th entry of $\boldsymbol{\eta}$, and $\boldsymbol{\kappa}(\eta) \in \mathbb{R}^N$ is the kernel vector whose k-th component is $\boldsymbol{\kappa}_k(\eta) = \kappa(\eta, \boldsymbol{\eta}_k)$. In the following, we exploit the commonly adopted *squared exponential kernel*, which can be expressed as

$$\kappa(\eta,\eta') = \sigma_p^2 \exp\left(-(\eta-\eta')^\top \Lambda^{-1} (\eta-\eta')\right) \tag{3}$$

for all $\eta, \eta' \in \mathbb{R}^{n_\eta}$, where $\Lambda = \mathrm{diag}(2\lambda_{\eta_1}^2, \ldots, 2\lambda_{\eta_{n_\eta}}^2)$, $\lambda_{\eta_i} \in \mathbb{R}_{>0}$ is known as *characteristic length scale* relative to the i-th signal, and σ_p^2 is usually called *amplitude*.

2. THE PROPOSED REGULATOR

The proposed regulator reads as follows

$$\begin{cases} \dot{\zeta} = 1 \\ \dot{\eta} = F\eta + Gu \\ \dot{\hat{e}} = A\hat{e} + B\left(\hat{\xi} + \boldsymbol{b}u\right) + \Lambda(l)H(y - \hat{e}_1) \\ \dot{\hat{\xi}} = -\boldsymbol{b}\left(\dot{\mu}(\eta,\varsigma,\theta)\right) + l^{r+1}H_{r+1}(y-\hat{e}_1) \\ \dot{\varsigma} = 0 \end{cases}$$

$$\left(\zeta, \eta, \hat{e}, \hat{\xi}, \varsigma, \theta, y\right) \in \mathcal{C},$$

$$\begin{cases} \zeta^+ = 0, \quad \eta^+ = \eta \\ \hat{e}^+ = \hat{e}, \quad \hat{\xi}^+ = \hat{\xi} \\ \varsigma^+ = (S \otimes I_N)\varsigma + (B \otimes I_N)\left[\eta \ u\right]^\top \end{cases}$$

$$\left(\zeta, \eta, \hat{e}, \hat{\xi}, \varsigma, \theta, y\right) \in \mathcal{D},$$

with $\theta = \vartheta(\varsigma)$ and output $u = \boldsymbol{b}^{-1}\mathrm{sat}(-\hat{\xi} + \kappa_s(\hat{e}))$. Where A, B, and $\boldsymbol{b}$ are the same as in (1) and Assumption 3, while F, G, n_η, $\Lambda(l)$, and H are defined as in Section 1 with $l \in \mathbb{R}_{>0}$ a free control parameter fixed later to a sufficiently large number, while the matrices $S \in \mathbb{R}^{N(n_\eta+n_y)\times N(n_\eta+n_y)}$ and $B \in \mathbb{R}^{N(n_\eta+n_y)}$ have the shift form. The flow and jump set are defined as $\mathcal{C} = \left\{(\zeta,\eta,\hat{e},\hat{\xi},\varsigma,\theta,y) \in \mathbb{R}_{>0} \times \mathbb{R}^{n_\eta+n_e+n_y} \times \Sigma \times \Theta \times \mathbb{R}^{n_y} : 0 \le \zeta \le \overline{\mathrm{T}}, \sigma^2(\eta,\varsigma,\theta) \le \sigma_{\mathrm{thr}}^2\right\}$ and $\mathcal{D} = \left\{(\zeta,\eta,\hat{e},\hat{\xi},\varsigma,\theta,y) \in \mathbb{R}_{>0} \times \mathbb{R}^{n_\eta+n_e+n_y} \times \Sigma \times \Theta \times \mathbb{R}^{n_y} : \underline{\mathrm{T}} \le \zeta \le \overline{\mathrm{T}}, \sigma^2(\eta,\varsigma,\theta) \ge \sigma_{\mathrm{thr}}^2\right\}$ respectively, where $\Sigma \subset \mathbb{R}^{N(n_\eta+n_y)}$, $\Theta \subset \mathbb{R}^N$ with $N \in \mathbb{N}_{>0}$, and $\underline{\mathrm{T}}, \overline{\mathrm{T}}, \sigma_{\mathrm{thr}}^2 \in \mathbb{R}_{>0}$ satisfying $\underline{\mathrm{T}} \le \overline{\mathrm{T}}$ and $\sigma_p^2\sigma_n^2(\sigma_p^2+\sigma_n^2)^{-1} < \sigma_{\mathrm{thr}}^2 \le \sigma_p^2$. The functions $\mu(\eta,\varsigma,\theta)$ and $\sigma^2(\eta,\varsigma,\theta)$ are the a posteriori GP estimate mean and variance, respectively, after the collection of N samples. Denoting $\varsigma = (\varsigma_\eta, \varsigma_u)^\top$, the latter functions read to

$$\begin{aligned} \mu(\eta,\varsigma,\theta) &= \boldsymbol{\kappa}(\eta)^\top \theta, \\ \sigma^2(\eta,\varsigma,\theta) &= \kappa(\eta,\eta) - \boldsymbol{\kappa}(\eta)^\top \left(\boldsymbol{\mathcal{K}} + \sigma_n^2 I_N\right)^{-1} \boldsymbol{\kappa}(\eta) \end{aligned}$$

with $\theta = \left(\boldsymbol{\mathcal{K}} + \sigma_n^2 I_N\right)^{-1} \varsigma_u$.

3. NUMERICAL SIMULATION

To test the proposed regulator performances we consider the problem of synchronizing the output of a Van der Pol oscillator, with unknown parameter, with a triangular wave with unknown frequency. The forced Van der Pol oscillator is described by the following equations

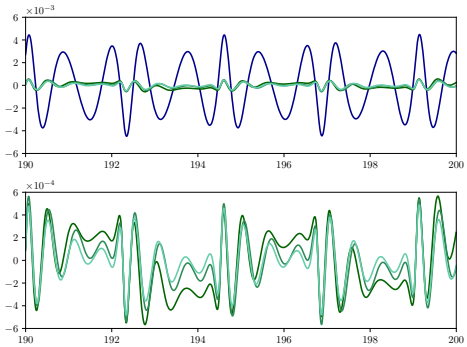

Fig. 1. Steady-state evolution of the tracking error $y(t)$ in the two cases obtained by employing a linear identifier (blue line), and a gaussian-based identifier with $N = 50$ (dark green line), $N = 100$ (green line), and $N = 200$ (light green line)

$$\begin{aligned} \dot{\chi}_1 &= \chi_2, \\ \dot{\chi}_2 &= -\chi_1 + a\left(1 - \chi_1^2\right)\chi_2 + u, \end{aligned} \tag{4}$$

with a scalar unknown parameter regulating the system damping. Furthermore, a triangular wave can be generated by an exosystem of the form

$$\dot{w}_1 = w_2, \ \dot{w}_2 = -\varrho w_1,$$

with output

$$\chi^\star(w) = \frac{2\sqrt{w_1^2+w_2^2}}{\pi} \arcsin\left(\frac{w_1}{\sqrt{w_1^2+w_2^2}}\right),$$

with scalar parameter ϱ the unknown oscillating frequency. The goal is to steer the output χ_1 of (4) to the reference $\chi^\star(w)$. The simulations reported in Figures 1 show the proposed regulator applied with $a = \varrho = 2$ in three cases with $N = 50$, $N = 100$, and $N = 200$. The obtained results are then compared with the regulator proposed by Bin et al. (2020) where the identifier is chosen as a least-squares identifier working on the model set $\mathcal{M} = \left\{\psi(\theta,\eta) : \mathbb{R}^{n_\eta} \mapsto \mathbb{R}^{n_y} | \psi(\theta,\eta) = \theta^\top\eta, \theta \in \Theta \subset \mathbb{R}^{n_\eta}\right\}$. In all simulations the GP parameters has been kept fixed at $\sigma_n^2 = 0.01$ and $\sigma_{\mathrm{thr}}^2 = \sigma_p^2 = 1$, while the kernel hyper-parameters $\boldsymbol{\lambda} = (\lambda_{\eta_1}, \ldots, \lambda_{\eta_{n_\eta}})$ has been estimated via log-likelihood minimization (Rasmussen (2003)) yielding to the values of $\boldsymbol{\lambda} = (7.7, 34.3, 19.9, 0.4, 133.6, 1.2)$. As emerges from Figure 1, the proposed approach reduces the maximum error of more than 100 times compared to the case with least-square identifier.

REFERENCES

Bin, M., Bernard, P., and Marconi, L. (2020). Approximate nonlinear regulation via identification-based adaptive internal models. *IEEE Transactions on Automatic Control*, 66(8), 3534–3549.

Marconi, L., Praly, L., and Isidori, A. (2007). Output stabilization via nonlinear luenberger observers. *SIAM Journal on Control and Optimization*, 45(6), 2277–2298.

Rasmussen, C.E. (2003). Gaussian processes in machine learning. In *Summer school on machine learning*, 63–71. Springer.

Resilient Constrained Optimization in Multi-Agent Systems

Mojtaba Kaheni, Elio Usai, and Mauro Franceschelli

***Abstract*—We consider resilient decentralized constrained optimization in multi-agent systems where some agents due to cyberattacks become adversaries. We show that the proposed method is resilient despite the persistent influence of up to F anonymous adversaries in the complete graphs. Our approach improves the approximation of the optimal solution compared to the current literature. Furthermore, if the agents' objectives are $2F$ redundant, then the algorithm converges to the optimal solution. In addition to current literature, we consider a constrained optimization problem.**

I. Introduction

DISTRIBUTED optimization in multi-agent systems refers to a group of agents with individual objective functions that cooperatively agree on the global optimizer of the sum of these functions. The agents gather information from their neighbors in a graph and then update their values according to a state update rule [1, 2, 3, 4].

As discussed in [5], distributed optimization methods can be easily disrupted by adversarial agents that can arise due to faults or cyberattacks. The methods proposed to deal with the destructive effects of adversarial agents on distributed optimization fall into two general categories. The first consists of methods that propose algorithms to detect and isolate the adversarial agents to prevent the outcome from being diverted to the attackers' desired value [6, 7]. The second category consists of methods that converge to a solution that the adversarial agents can not influence, thus without the need to detect and isolate [5, 8, 9]. The second category is referred to as *resilient distributed optimization*. In this abstract, we present the idea we published in [10] about resilient constrained optimization in multi-agent systems. Consider the constrained optimization problem

$$\min_{x\in X}\sum_{i=1}^{n} f_i(x). \tag{1}$$

The optimal solution of (1) in an adversarial environment is to ignore the adversarial agents and find the optimizer among the set V_r of regular agents with nominal behavior

$$\min_{x\in X}\sum_{i\in V_r} f_i(x). \tag{2}$$

The algorithms introduced in [5, 9, 11], instead of solving (2), find an approximate solution which consists in obtaining the optimal solution to the next problem:

$$\min_{x\in X}\sum_{i=1}^{n}\alpha_i f_i(x), \quad \sum_{i\in V_r}\alpha_i=1, \quad \forall i\in V\backslash V_r \rightarrow \alpha_i=0. \tag{3}$$

Mojtaba Kaheni, Elio Usai, and Mauro Franceschelli are with the Department of Electrical and Electronic Engineering (DIEE), University of Cagliari, Italy. {mojtaba.kaheni, elio.usai, mauro.franceschelli}@unica.it

where the coefficients α_i are arbitrary and unknown. The problem in (3) provides a good approximation of (2) only when the objective functions of each agent are the same or very similar to each other. On the other hand, if each objective function f_i is different, i.e., if their minimum value occurs for different values of x, then the solution obtained from solving (3) can be significantly different from the solution of (2). We pose the next important question: is it possible to find the solution of (2) despite the presence of adversarial agents?

In [12], the authors define the concept of *redundancy* in distributed optimization problems. They prove that the necessary condition for finding the solution of (2) in a network with the possibility of the presence of up to F adversarial agents is that the agents' cost functions have the *2F-redundancy* property. *2F-redundancy* means that for any subset of regular agents, Ω, where $|\Omega| = n - 2F$ we have

$$\operatorname*{argmin}_{x\in X}\sum_{i\in V_r} f_i(x) = \operatorname*{argmin}_{x\in X}\sum_{i\in \Omega} f_i(x). \tag{4}$$

In [13], the authors consider 2F-redundant unconstrained problems in complete graphs and propose an algorithm to find the exact optimal solution of (2) in the presence of up to F adversarial agents. In contrast, we propose an algorithm that reaches the same results in constrained problems.

II. Main Results

A. Problem statement

We consider a multi-agent framework to solve the constrained optimization problem, introduced in (1), and we consider up to F agents which distribute false state information at all times. These agents are unknown during the execution of our algorithm. We call these agents as *adversarial agents* and denote their set as V_a. An agent exhibiting adversarial behavior at future time instants is still counted as an adversarial agent in our analysis. We assume that (1) satisfies the following assumptions.

Assumption 1. For all $i \in \{1, \ldots, n\}$ the local objective function, f_i, is convex. In addition, The set of constraints, X, is nonempty, closed and convex. ■

Assumption 2. For all $i \in \{1, \ldots, n\}$, the gradient $d_i(x)$ of each objective f_i is continuous and bounded by

$$|d_i(x)| \leq L, \quad \forall i \in V.$$

■

Algorithm 1: Resilient Decentralized Constrained Optimization

1: Initialization: $x_i(0) \in X, \forall i \in V$
2: **Repeat**
3: Each agent gathers the state value of all others and builds the next three sets of neighbors:
$V_h(k) = \{F \text{ vertices with highest values}\}$,
$V_l(k) = \{F \text{ vertices with lowest values}\}$,
$V_n(k) = \{\text{Other vertices}\}$.
4: Each agent assigns weights to edges according to:
$(q = n - 2F)$
If $i \in V_n(k)$ then $a_{ij}(k) = \begin{cases} \frac{1}{q} & \text{if} \quad j \in V_n(k) \\ 0 & \text{otherwise.} \end{cases}$
Elseif $i \in V_h(k) \cup V_l(k)$, then
$a_{ij}(k) = \begin{cases} \frac{1}{q} & \text{if} \quad j \in \{V_n(k) \setminus i_r^k\} \\ \frac{1}{q} & \text{if} \quad j = i \\ 0 & \text{otherwise.} \end{cases}$
where i_r^k is the vertex with lowest state value in $V_n(k)$ if $i \in V_l(k)$ and the vertex with highest state value in $V_n(k)$ if $i \in V_h(k)$.
5: $v_i(k) = \sum_{j=1}^{n} a_{ij}(k) x_j(k)$.
6: $x_i(k+1) = P_X[v_i(k) - c(k) d_i(k)]$.
7: **Until stopping criterion is satisfied.**

Assumption 3. The total number of adversaries, F, is small enough to satisfy the following inequality

$$\lfloor \frac{n+1}{2} \rfloor \geq 2F + 1$$

■

Assumption 4. Each agent can interact with all others (complete graph). ■

Assumption 4 does not imply that it does because some agents are discarded; thus, the state updates evolve according to a directed graph.

B. Proposed Algorithm

Our proposed solution to (1) is Algorithm 1. The main idea behind Algorithm 1 is that each agent discards extreme values received from its in-neighbors.

C. Accuracy of the Approximation

Theorem 1 and Corollary 1 present the accuracy of the results achieved by executing Algorithm 1. More details on proofs and auxiliary lemmas can be found in [10].

Theorem 1. Consider the optimization problem (1) and a multi-agent system that executes Algorithm 1. Consider the power set $P(V_r)$ of regular agents V_r, which are indeed unknown during the execution of Algorithm 1, and let $V_\Omega = \{\Omega \in P(V_r) || \Omega| = n - 2F\}$ be the set of all possible subsets of regular agents of cardinality $n - 2F$.

Let Assumptions 1-4 be satisfied. If the number of adversaries is equal to or less than F, then the regular agents converge to an approximate solution $\bar{x}$ bounded by the minimum of an objective function that is guaranteed to be a combination of $n - 2F$ objectives of regular agents, thus such that $x_m \leq \bar{x} \leq x_M$, where

$$x_m = \min_{\Omega \in V_\Omega} \left\{ \operatorname*{argmin}_{x \in X} \sum_{i \in \Omega} f_i(x) \right\},$$
$$x_M = \max_{\Omega \in V_\Omega} \left\{ \operatorname*{argmin}_{x \in X} \sum_{i \in \Omega} f_i(x) \right\}. \quad ■$$

Next, we identify an interesting case where Algorithm 1 converges to the actual optimal solution of (1).

Corollary 1. Under the assumptions of Theorem 1 and the 2F-redundancy condition in (4), the solution $\bar{x}$ achieved by executing Algorithm 1 satisfies $\bar{x} \in x^\star$ where $x^\star$ is the set of optimal solutions of (1). ■

III. Conclusions

We presented a novel resilient decentralized algorithm for constrained optimization problems in complete graphs. We proved convergence to an approximate solution guaranteed to be bounded by a combination of $n - 2F$ objectives of regular agents. Further works will aim to consider less stringent topological constraints on the communication graph.

References

[1] A. Nedic, A. Ozdaglar, and P. A. Parrilo, "Constrained consensus and optimization in multi-agent networks," *IEEE Transactions on Automatic Control*, vol. 55, no. 4, pp. 922–938, 2010.

[2] A. Nedic and A. Ozdaglar, "Distributed subgradient methods for multi-agent optimization," *IEEE Transactions on Automatic Control*, vol. 54, no. 1, pp. 48–61, 2009.

[3] A. Nedić and A. Olshevsky, "Distributed optimization over time-varying directed graphs," *IEEE Transactions on Automatic Control*, vol. 60, no. 3, pp. 601–615, 2015.

[4] M. Kaheni, E. Usai, and M. Franceschelli, "A distributed optimization and control framework for a network of constraint coupled residential besss," in *2021 IEEE 17th International Conference on Automation Science and Engineering (CASE)*, 2021, pp. 2202–2207.

[5] S. Sundaram and B. Gharesifard, "Distributed optimization under adversarial nodes," *IEEE Transactions on Automatic Control*, vol. 64, no. 3, pp. 1063–1076, 2019.

[6] F. Pasqualetti, F. Dörfler, and F. Bullo, "Attack detection and identification in cyber-physical systems," *IEEE Transactions on Automatic Control*, vol. 58, no. 11, pp. 2715–2729, 2013.

[7] N. Ravi, A. Scaglione, and A. Nedić, "A case of distributed optimization in adversarial environment," in *ICASSP 2019 - 2019 IEEE International Conference on Acoustics, Speech and Signal Processing (ICASSP)*, 2019, pp. 5252–5256.

[8] L. Su and N. H. Vaidya, "Byzantine-resilient multiagent optimization," *IEEE Transactions on Automatic Control*, vol. 66, no. 5, pp. 2227–2233, 2021.

[9] K. Kuwaranancharoen, L. Xin, and S. Sundaram, "Byzantine-resilient distributed optimization of multi-dimensional functions," in *2020 American Control Conference (ACC)*, 2020, pp. 4399–4404.

[10] M. Kaheni, E. Usai, and M. Franceschelli, "Resilient constrained optimization in multi-agent systems with improved guarantee on approximation bounds," *IEEE Control Systems Letters*, vol. 6, pp. 2659–2664, 2022.

[11] W. Xu, Z. Li, and Q. Ling, "Robust decentralized dynamic optimization at presence of malfunctioning agents," *Signal Processing*, vol. 153, pp. 24–33, 2018.

[12] N. Gupta and N. H. Vaidya, "Fault-tolerance in distributed optimization: The case of redundancy," in *Proceedings of the 39th Symposium on Principles of Distributed Computing*, 2020, pp. 365–374.

[13] N. Gupta, T. T. Doan, and N. H. Vaidya, "Byzantine fault-tolerance in decentralized optimization under 2f-redundancy," in *2021 American Control Conference (ACC)*, 2021, pp. 3632–3637.

Road User Position Prediction using Averaging*

Angelos Toytziaridis[1], Paolo Falcone[2], Jonas Sjöberg[3]

***Abstract*—A weighted average model(WAM) of previously observed data of road user(RU) state trajectories is considered for predicting the future position of a target RU given its current state. WAM takes as input only the current position and velocity of the target and is six orders of magnitude simpler, in terms of number of parameters, than state-of-the-art while achieving similar performance when predicting the future position of pedestrians. Due to its simplicity WAM is significantly more transparent in how it calculates predictions than state-of-the-art. Simplicity and transparency are necessary features of a reliable prediction model as they reduce the risk of erroneous output.**

***Index Terms*—Intelligent vehicles, prediction, weighted average**

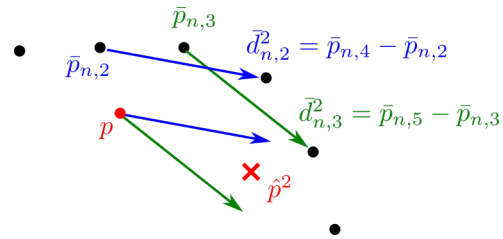

Fig. 1. Black dots are previously observed RU's positions. Red dot and cross are current position p and 2-step predicted position $\hat{p}^2$ of a target RU. Position p is closest, and thus most similar, to $\bar{p}_{n,2}$ and $\bar{p}_{n,3}$. Therefore, in this example, the prediction $\hat{p}^2$ is the position closest to $p+\bar{d}^2_{n,2}$ and $p+\bar{d}^2_{n,3}$.

I. Introduction

For an intelligent vehicle to safely navigate it must predict the future state of the environment using measurements from sensors. An assumption in prediction is that RUs track certain paths [1]. Complex paths are difficult to specify, hence [2] formulate a path planning problem. An alternative to reference tracking is to assume that RUs switch between operational modes, [3], [4]. Others use simpler dynamics and reachability analysis [5]. Complex models are in [6], [7] constructed by imposing structure on a flexible black box model. Work [8] uses a model-free method; a prediction is based on the state transitions most frequently occuring in data. Another model-free method is a Nadaraya-Watson(NW) estimator, which is a weighted average with weights having a particular structure. This has previously been explored in [9] using laboratory data. This work formulates prediction of a target RU's future position given its current position and velocity as a NW estimator, i.e. as a WAM, resulting in an interpretable model with few parameters. This contrasts complex neural networks with many parameter, that can produce erroneous outputs when their inputs are subject to small perturbations, [10]. This work's main contribution is to be the first work on RU position prediction to apply a NW estimator on real traffic data.

II. Methodology

Let the current state of a *target RU* be $R = (p, s, o)$, with $p \in \mathbb{R}^2$ the position in an inertial reference frame, $s \in \mathbb{R}$ the speed and $o \in \mathbb{R}^2$ the orientation. The orientation is a unit vector whose direction defines the forward direction of a RU. Let a collection $\mathcal{C} = \{\mathcal{C}_n\}_{n=1}^N$ consist of previously observed trajectories $\mathcal{C}_n = \{\bar{R}_{n,t}\}_{t=1}^{T_n}$ of RUs' states, where $\bar{R}_{n,t} = (\bar{p}_{n,t}, \bar{s}_{n,t}, \bar{o}_{n,t})$ denotes the t-th sample of the n-th trajectory. The RU position prediction problem is:

Problem 1: Given a target RU's current state R and a collection $\mathcal{C}$ of previously observed RUs' state trajectories, determine a prediction $\hat{p}^H$ of the target RU's position at H samples later, where H is called the *prediction horizon*.

To solve Problem 1 observe that if R is *similar*, in some sense, to the sample $\bar{R}_{n,t}$, then a prediction $\hat{p}^H$ is likely to be *similar* to the position $p + (\bar{p}_{n,t+H} - \bar{p}_{n,t})$. Fig. 1 illustrates such a prediction when similarity between R and $\bar{R}_{n,t}$ is measured by the distance between positions p and $\bar{p}_{n,t}$. Hence, a *similarity function*, taking the current state R of a target RU and a sample $\bar{R}_{n,t}$ and relating them to a real number representing similarity between R and $\bar{R}_{n,t}$ is to be introduced.

Call $\bar{p}_{n,t+H} - \bar{p}_{n,t}$ an *H-step displacement* and denote it by $\bar{d}^H_{n,t}$ and introduce the H-step predicted displacement $\hat{d}^H$ such that

$$\hat{p}^H = p + \hat{d}^H, \tag{1}$$

where $\hat{d}^H$ is closer to $\bar{d}^H_{n,t}$ the more similar R is to $\bar{R}_{n,t}$. Once the similarity between R and $\bar{R}_{n,t}$ is expressed by a function $\sigma(R, \bar{R}_{n,t})$, that is non-negative, the predicted displacement $\hat{d}^H$ is defined as a Nadaraya-Watson estimator:

$$\hat{d}^H = \sum_n \sum_t \frac{\sigma(R, \bar{R}_{n,t})}{\sum_m \sum_\tau \sigma(R, \bar{R}_{m,\tau})} \bar{d}^H_{n,t}. \tag{2}$$

Fig. 1 suggests that the smaller the distance between p and $\bar{p}_{n,t}$ is, the higher the similarity $\sigma(R, \bar{R}_{n,t})$ should be. For a state R, the similarity is assumed to monotonically decrease with the difference in position $\|p - \bar{p}_{n,t}\|$, speed $\|s - \bar{s}_{n,t}\|$, and orientation, defined as the angle $\bar{\theta}_{n,t}$ between o and $\bar{o}_{n,t}$. The similarity function is defined as a Gaussian kernel:

$$\sigma(R, \bar{R}_{n,t}) = \exp(-(a\|p - \bar{p}_{n,t}\|^2 + b|s - \bar{s}_{n,t}|^2 + c|\bar{\theta}_{n,t}|^2)), \tag{3}$$

with $a,\ b,\ c \in \mathbb{R}^+$ being parameters.

*This work was supported by Vinnova FFI project "5G for Connected Autonomous Vehicles in Complex Urban Environments", reference number 2018-05005.

[1,2,3] All authors are with the Mechatronics group at the Department of Electrical Engineering, Chalmers University of Technology, Gothenburg, Sweden. {angelos.toytziaridis, paolo.falcone, jonas.sjoberg}@ chalmers.se

[2] Paolo Falcone is with Engineering Department "Enzo Ferrari", University of Modena and Reggio Emilia, Italy. falcone@unimore.it

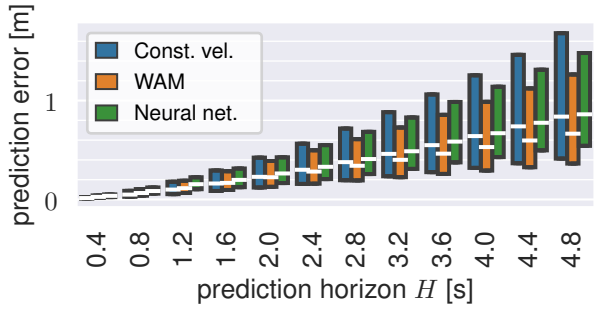

Fig. 2. Statistics of H-second prediction errors at location B. White lines are medians. Lower and upper sides of a rectangle are first and third quartiles.

III. Experiments

WAM is tested on the InD dataset [11], consisting of trajectories of pedestrians at four urban intersections, enumerated as A, B, C, and D. A portion of the dataset is used used as training data to identify the parameters a, b, c using 5-fold cross-validation. The rest of the dataset is used as test data.

Fig. 2 compares statistics of WAM and two baseline models; the constant velocity model and a neural network with a single hidden layer. It is seen that WAM outperforms the baselines. To gain confidence in the statistical results qualitative results are shown in Fig. 3, which plots positions of target RUs versus corresponding 4.8-second prediction errors smoothed using nearest neighbor regression. Fig. 3 reveals that both WAM and the neural network suffer in situations where having accurate predictions is most important, e.g. at crossings.

Table I compares WAM and the state-of-the-art method SCOUT [6]. The models are compared by their average 4.8-second prediction error, called the *Final Displacement Error*(FDE), and by their average of the averages of a 0.4-second prediction error, 0.8-second prediction error, $\ldots$, 4.8-second prediction error, called the *Average Displacement Error*(ADE). SCOUT assumes that the future position of a target RU depends on the current and past states of the target RU as well as those of surrounding RUs. Hence, the input consists of past and current positions and headings of both a target RU and surrounding RUs. Interaction between the target RU and surrounding RUs is modeled with a Graph Attention Network having around $1\,000\,000$ parameters. In contrast, WAM takes as input only current position, speed and orientation of a target RU, and has only 3 easily interpretable parameters, meaning that WAM is significantly simpler and less vurnable to erroneous behavior.

Unsurprisingly, WAM performs worst at locations A and D, which are the locations with least data, while the methods perform similarly at locations B and C. In the latter locations SCOUT still outperforms WAM. Although, by the principle of parsimony such complexity is unmotivated when the difference in FDE at location B is only 0.2 meters.

IV. Conclusion

WAM shows promising results in pedestrian position prediction when compared to a state-of-the-art model and two baseline models on the InD dataset. This motivates further exploring WAM as a solution to the RU position prediction problem. Specifically how to formulate WAM in a frame of reference independent of location and how to include as input the position of surrounding road users. A more comprehensive study of WAM is provided in [12].

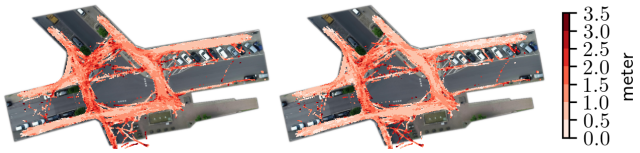

Fig. 3. Left is the baseline neural network. Right is WAM. Pixels are colored in proportion to the average magnitude of the 4.8-second prediction errors evaluated at positions within 0.25 meters of a pixel.

TABLE I
Comparison with state-of-the-art on ADE/FDE scores, units is meter. Score of [6] was originally reported in [6].

Location: Model:	A	B	C	D
WAM	1.30 / 2.50	0.72 / 1.41	0.71 / 1.42	0.91 / 1.75
SCOUT [6]	0.50 / 1.12	0.54 / 1.21	0.52 / 1.15	0.41 / 0.84

References

[1] I. Batkovic, M. Zanon, N. Lubbe, and P. Falcone, "A computationally efficient model for pedestrian motion prediction," in *2018 Eur. Control Conf. (ECC)*, pp. 374–379.

[2] V. Karasev, A. Ayvaci, B. Heisele, and S. Soatto, "Intent-aware long-term prediction of pedestrian motion," in *2016 IEEE Int. Conf. Robot. Automat. (ICRA)*, pp. 2543–2549.

[3] J. F. Kooij, F. Flohr, E. A. Pool, and D. M. Gavrila, "Context-based path prediction for targets with switching dynamics," *Int. J. Comput. Vision*, vol. 127, no. 3, pp. 239–262, 2019.

[4] R. Q. Mínguez, I. P. Alonso, D. Fernández-Llorca, and M. A. Sotelo, "Pedestrian path, pose, and intention prediction through gaussian process dynamical models and pedestrian activity recognition," *IEEE Trans. Intell. Transp. Syst.*, vol. 20, no. 5, pp. 1803–1814, 2018.

[5] M. Koschi and M. Althoff, "Set-based prediction of traffic participants considering occlusions and traffic rules," *IEEE Trans. Intell. Veh.*, vol. 6, no. 2, pp. 249–265, 2021.

[6] S. Carrasco, D. F. Llorca, and M. Sotelo, "Scout: Socially-consistent and understandable graph attention network for trajectory prediction of vehicles and vrus," in *2021 IEEE Intell. Vehicles Symp. (IV)*.

[7] H. Cheng, W. Liao, X. Tang, M. Y. Yang, M. Sester, and B. Rosenhahn, "Exploring dynamic context for multi-path trajectory prediction," in *2021 IEEE Int. Conf. Robot. Automat. (ICRA)*, pp. 12 795–12 801.

[8] A. Toytziaridis, P. Falcone, and J. Sjöberg, "A data-driven markovian framework for multi-agent pedestrian collision risk prediction," in *2019 IEEE Intell. Transp. Syst. Conf. (ITSC)*.

[9] R. F. Martin and D. R. Parisi, "Data-driven simulation of pedestrian collision avoidance with a nonparametric neural network," *Neurocomputing*, vol. 379, pp. 130–140, 2020.

[10] N. Akhtar and A. Mian, "Threat of adversarial attacks on deep learning in computer vision: A survey," *IEEE Access*, vol. 6, pp. 14 410–14 430, 2018.

[11] J. Bock, R. Krajewski, T. Moers, S. Runde, L. Vater, and L. Eckstein, "The ind dataset: A drone dataset of naturalistic road user trajectories at german intersections," in *2020 IEEE Intell. Vehicles Symp. (IV)*, pp. 1929–1934.

[12] A. Toytziaridis, P. Falcone, and J. Sjöberg, "Road user position prediction in urban environments via locally weighted learning," *arXiv preprint arXiv:2201.12895*, 2022.

A discrete event approach for EVs' charging optimal scheduling

Giulio Ferro*, Riccardo Minciardi*, Luca Parodi*, Michela Robba*

Department of Informatics, Bioengineering, Robotics and Systems Engineering, University of Genoa, Genoa, Italy (email: giulio.ferro@unige.it,riccardo.minciardi@unige.it,luca.parodi@edu.unige.it, michela.robba@unige.it)

A significant contribution to emissions is represented by transport and logistics. Mass deployment of EVs may be a good solution, but, unfortunately, wide usage of EVs may cause technical problems [1]. As an example, the power grid can be harmfully affected by uncontrolled charging, long charging times, and interruptions.

In a scenario in which many vehicles may need a recharge, it is necessary to optimally schedule the operations to satisfy customers in terms of energy requests and desired readiness of the vehicle in terms of time. In the literature, the optimization models that regard the scheduling of EVs in local areas consider different issues such as the minimization of costs of the smart grid in which they are located, the minimization of carbon dioxide emissions, the integration of renewable energy sources, peak shaving and load shifting, etc. [2], [3]. Usually, optimization problems are formalized in the discrete-time representation. For example, in [4], the aim of the model is to optimally schedule the EV charging in a smart grid while examining customers' dissatisfaction cost and by considering the EV demand as deferrable. Other approaches, like in [5], are related to a discrete-event formalization, which offers the advantage of reducing the number of decision variables, though losing some details in the time domain representation.

In this contribution, we present the work published in [6] consisting of a discrete event approach for the optimal scheduling of electric vehicles in which vehicles are the customers and charging stations are the machines. We consider a charging station made of a charging unit plus a storage element and a renewable energy source. The charging unit may provide charging services simultaneously to various vehicles. The maximum number of vehicles that can be connected to the charging unit is N (we say that the charging station has N sockets). We suppose to know exactly the arrival time of the vehicles and the energy requested by each charging service. Some more assumptions are relevant to the power flows which are considered as average values on the time intervals, evaluated as the period between two completion services (which are decision variables). A case study with 10 vehicles and 3 sockets is then proposed to show the results of the optimization problem.

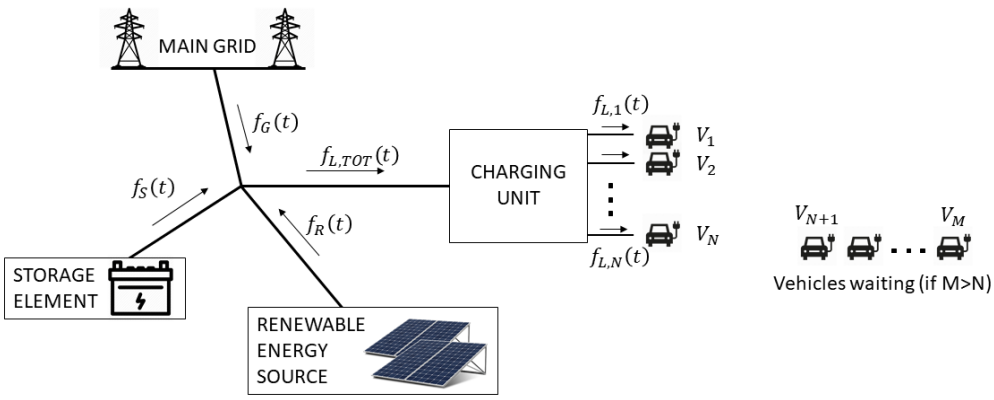

Figure 1 – System architecture.

Moreover, a further improvement to the model will be presented in this contribution. In fact, a piecewise linear characteristic for the EVs' battery has been introduced with a solution for the actual (continuous) power exchange with the EVs.

Figure 2 and Figure 3 show the EV battery characteristic curve and the real charging power, respectively.

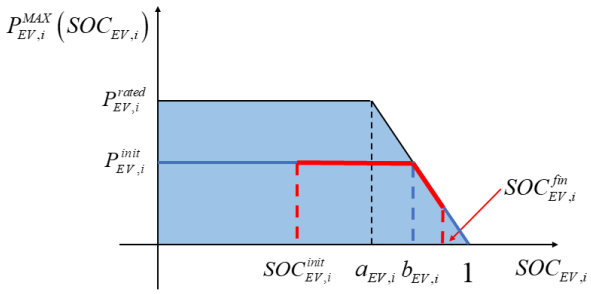

Figure 2 - Battery piecewise linear characteristic.

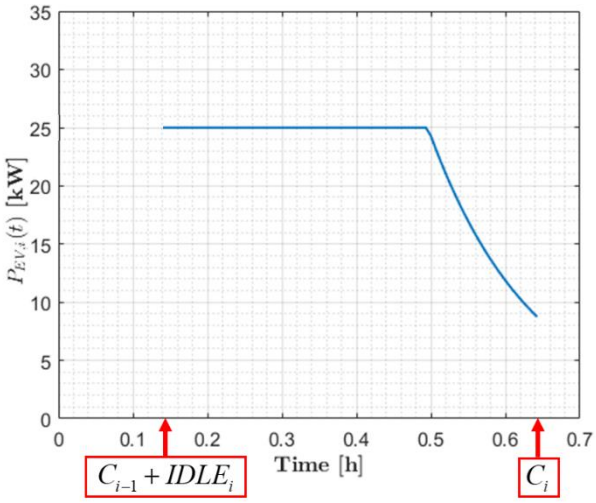

Figure 3 - Real power exchange with the EV.

Also some consideration about other applications of this discrete event formalization will be discussed. In fact, the formulation has been considered for periodic scheduling of bus fleets [7] which have the advantage of having predefined paths and periodic operation time schedules.

References

[1] F. Ahmad, A. Iqbal, I. Ashraf, M. Marzband, and I. khan, "Optimal location of electric vehicle charging station and its impact on distribution network: A review," *Energy Rep.*, vol. 8, pp. 2314–2333, Nov. 2022, doi: 10.1016/j.egyr.2022.01.180.

[2] J. Hu, H. Morais, T. Sousa, and M. Lind, "Electric vehicle fleet management in smart grids: A review of services, optimization and control aspects," *Renew. Sustain. Energy Rev.*, vol. 56, pp. 1207–1226, 2016, doi: 10.1016/j.rser.2015.12.014.

[3] S. R and V. Sankaranarayanan, "Optimal Scheduling of Electric Vehicle Charging at Geographically Dispersed Charging Stations with Multiple Charging Piles," *Int. J. Intell. Transp. Syst. Res.*, Jul. 2022, doi: 10.1007/s13177-022-00316-2.

[4] P. Aliasghari, B. Mohammadi-Ivatloo, M. Alipour, M. Abapour, and K. Zare, "Optimal scheduling of plug-in electric vehicles and renewable micro-grid in energy and reserve markets considering demand response program," *J. Clean. Prod.*, vol. 186, pp. 293–303, Jun. 2018, doi: 10.1016/j.jclepro.2018.03.058.

[5] G. Ferro, F. Laureri, R. Minciardi, and M. Robba, "A predictive discrete event approach for the optimal charging of electric vehicles in microgrids," *Control Eng. Pract.*, vol. 86, no. February, pp. 11–23, 2019, doi: 10.1016/j.conengprac.2019.02.004.

[6] G. Ferro, R. Minciardi, L. Parodi, and M. Robba, "Discrete event optimization of a vehicle charging station with multiple sockets," *Discrete Event Dyn. Syst.*, vol. 31, no. 2, pp. 219–249, 2021.

[7] V. Casella, G. Ferro, R. Minciardi, L. Parodi, and M. Robba, "Optimal charging of electric buses: a periodic discrete event approach," in *2021 29th Mediterranean Conference on Control and Automation (MED)*, 2021, pp. 208–213.

An iterative optimization-based approach to piecewise affine system identification

Simone Paoletti, Andrea Garulli, Antonio Vicino

***Abstract*— This note describes an iterative approach to PWA system identification. At each iteration, a single optimization problem is solved, performing simultaneously the estimation of the partition of the regressor domain, the assignment of data points to submodels, and the estimation of the submodel parameters. A nice feature of the proposed approach is that at each iteration it provides a classification of the data points that is linearly separable by construction, while guaranteeing that the value of the prediction error criterion is non-increasing along the iterations. The optimization problem solved at each iteration is a mixed integer program, where the classification involves only a fixed number of data points close to the boundaries of the partition estimated at the previous iteration. This number can be tuned to control the computational burden of the mixed integer program to be solved. The proposed technique can be applied to tackle an identification problem from scratch, or to refine the solution provided by other suboptimal techniques. This is shown through an application to the pick-and-place machine data set.**

I. Introduction

Piecewise affine (PWA) system identification has been the subject of intensive research in the last two decades, mainly due to the universal approximation properties of PWA maps, which makes them a suitable model class for nonlinear system identification. In spite of the appealing features of PWA models, their identification is generally a hard problem, that involves three tasks to be performed simultaneously: assignment of data points to submodels, estimation of the parameters of the affine submodels, and estimation of the hyperplanes defining the partition of the regressor domain. Hardness comes mainly from the first task, requiring the introduction of binary variables for data classification, thus leading to mixed integer programming formulations of the identification problem [1], [2]. Indeed, the problem of fitting optimally a PWA map to data is NP-hard, as shown in [2].

The intrinsic difficulty of identifying PWA regression models has motivated the interest of researchers in devising good heuristics and approximate techniques. The reader is referred to the survey papers [3], [4] and the book [2], for reviews of both established and emerging techniques at various stages of the research path on this topic. The common denominator of a large number of techniques is to start by classifying the data points and estimating the parameters of the submodels, on the basis of some hyperplane fitting criterion. The polyhedral partition of the regressor domain is not enforced "hardly" at this stage. It is rather taken into account "softly," by exploiting the proximity of the data points in the regressor domain. Given the clusters of regression vectors, standard two-class or multi-class linear separation techniques are applied to separate them. A drawback of this two-step approach is that the resulting classification may not be linearly separable. For this reason, the two steps are sometimes iterated to progressively improve the model and the classification.

The authors are with the Dipartimento di Ingegneria dell'Informazione e Scienze Matematiche, Università di Siena, Siena 53100, Italy (email: {paoletti, garulli, vicino}@diism.unisi.it).

II. Contribution

Consider a discrete-time dynamic system with input $u_t \in \mathbb{R}$ and output $y_t \in \mathbb{R}$. The contribution described in this note is an iterative, optimization-based approach to the identification of PWA models in the following form:

$$y_t = f(x_t; \Theta) + e_t, \tag{1}$$

where $f(\cdot;\Theta)$ is a PWA map, x_t is the regression vector at time t:

$$x_t = [\ y_{t-1}\ \dots\ y_{t-n_a}\ u_{t-1}\ \dots\ u_{t-n_b}\ ]', \tag{2}$$

with n_a and n_b fixed model orders, and e_t is an error term to be minimized. The PWA map is parameterized by the vector Θ, which encodes both the affine submodels and the partition of the regressor space. More specifically, one has

$$f(x;\Theta) = \begin{cases} \vartheta_1'\varphi & \text{if} \quad x \in \mathcal{X}_1 \\ \vdots & \qquad \vdots \\ \vartheta_S'\varphi & \text{if} \quad x \in \mathcal{X}_S, \end{cases} \tag{3}$$

where φ is the extended regression vector $\varphi = [x'\ 1]'$, ϑ_s is the parameter vector of the sth affine submodel, defined over the region $\mathcal{X}_s$, $s = 1, \dots, S$, and S is the number of submodels, which is assumed to be fixed. The regions $\mathcal{X}_s$ in (3) are assumed to be convex polyhedra defined by a piecewise linear (PWL) classifier [5], i.e.

$$\mathcal{X}_s = \big\{x \,:\, s = \arg \max_{r=1,\dots,S} w_r'\varphi\big\}, \tag{4}$$

where the vector $w_s \in \mathbb{R}^n$ defines the sth linear classification function. The parameter vector Θ of the PWA map (3) is then defined as $\Theta = [\vartheta'\ w']'$, where $\vartheta = [\vartheta_1'\ \dots\ \vartheta_S']'$ and $w = [w_1'\ \dots\ w_S']'$.

It is well known that the identification of the PWA model (1) can be formulated as a mixed integer linear program (MILP), implementing a prediction error minimization criterion with the l_1-norm. Unfortunately, such a formulation is tractable only for small instances [2]. The approach proposed in this note tries to cope with this issue by solving a sequence of MILPs of reduced size, which are affordable in terms of computational burden. It stems from the idea

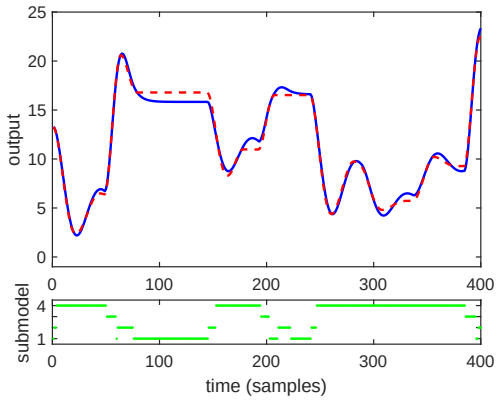

Fig. 1. Simulation results, initial PWA model. Top: Simulated output (solid line) and system output (dashed line). Bottom: Active submodel.

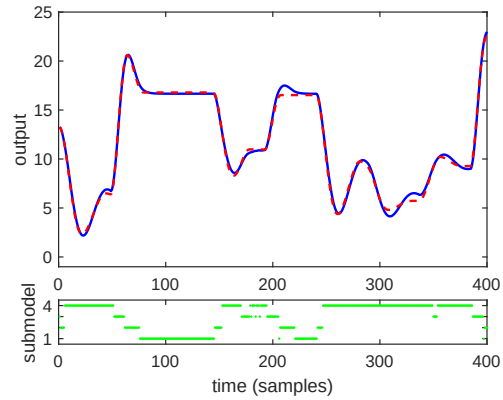

Fig. 2. Simulation results, final PWA model. Top: Simulated output (solid line) and system output (dashed line). Bottom: Active submodel.

of modifying the partition of the regressor space with the objective of decreasing the value of the cost function. The vector w is iteratively modified by allowing only the data points that are close to the hyperplanes defining the current partition to be reassigned to a different submodel. This leads to solving MILPs with a reduced number of binary variables, namely only those corresponding to the data points that can be reassigned. The number of free data points to be considered at each iteration, in the following denoted by n_{free}, is a hyperparameter of the proposed identification algorithm, that can be tuned to control the computational burden of the MILPs to be solved.

The proposed approach mimicks gradient-search methods, since at each step the weight vectors of the PWL classifier are updated in order to decrease the value of the objective function. Notice, however, that standard gradient-search methods cannot be applied to the problem at hand, because the cost function is piecewise constant with respect to w.

As compared to two-step approaches, the technique proposed here provides at each iteration a classification of the data points that is linearly separable by construction. The algorithm also features the property that the prediction error norm is non-increasing along the iterations. Since at each iteration the classification of only a subset of the data points can be modified, there is no guarantee that the algorithm converges to the global minimum. In order to explore new regions of the parameter space at each iteration, in search of better solutions, a suitable strategy is therefore developed.

III. Pick-and-place machine application

The iterative identification algorithm is applied to the identification of the electronic component placement process in a pick-and-place machine. The pick-and-place machine data set is a popular benchmark in PWA system identification. The reader is referred to [6], [7] for a description of the experimental setup, and of the data set used in this section. Here we recall only that the data set consists of $T = 1000$ estimation data points, and $T_v = 400$ validation data points. As in [6], we set $n_a = 2$, $n_b = 2$, and $S = 4$. We apply the iterative algorithm with $n_{free} = 20$, using as the initial data classification the one provided by the model identified in [6] for $S = 4$. The value of the cost function for the resulting initial model is $J_{initial} = 8.59$. The proposed algorithm runs 60 iterations, achieving a final value of the cost function $J_{final} = 7.33$, corresponding to a reduction of 14.66% with respect to $J_{initial}$. As in [6], the initial and the final PWA model are validated by evaluating the fit between the measured and the simulated responses using validation data. The measured and simulated responses are obtained by feeding the same inputs to the system and to the PWA model. They are shown in Fig. 1 (initial model) and Fig. 2 (final model). We obtain $FIT = 89.62\%$ for the former, and $FIT = 93.79\%$ for the latter. From the figures, it can be observed that the better fit of the final PWA model is mainly due to the fact that it estimates better the DC gain of the submodel active over the time interval (80,150). The positive effect of a better estimation of the partition of the regressor domain, is evident over the time interval (150,195), where the same submodel is always active for the initial model, leading to a noticeable overshoot. On the other hand, the final model switches several times between submodels 3 and 4 over the same time interval, thus following closely the behavior of the measured response.

References

[1] J. Roll, A. Bemporad, and L. Ljung, "Identification of piecewise affine systems via mixed-integer programming," *Automatica*, vol. 40, no. 1, pp. 37–50, 2004.

[2] F. Lauer and G. Bloch, *Hybrid System Identification*, ser. Lecture Notes in Control and Information Sciences. Springer, 2019, vol. 478.

[3] S. Paoletti, A. Lj. Juloski, G. Ferrari-Trecate, and R. Vidal, "Identification of hybrid systems: A tutorial," *European Journal of Control*, vol. 13, no. 2–3, pp. 242–260, 2007.

[4] A. Garulli, S. Paoletti, and A. Vicino, "A survey on switched and piecewise affine system identification," *IFAC Proceedings Volumes*, vol. 45, no. 16, pp. 344–355, 2012.

[5] K. P. Bennett and O. L. Mangasarian, "Multicategory discrimination via linear programming," *Optimization Methods and Software*, vol. 3, pp. 27–39, 1994.

[6] A. Bemporad, A. Garulli, S. Paoletti, and A. Vicino, "A bounded-error approach to piecewise affine system identification," *IEEE Transactions on Automatic Control*, vol. 50, no. 10, pp. 1567–1580, 2005.

[7] A. Lj. Juloski, W. P. M. H. Heemels, and G. Ferrari-Trecate, "Data-based hybrid modelling of the component placement process in pick-and-place machines," *Control Engineering Practice*, vol. 12, no. 10, pp. 1241–1252, 2004.

Multi-Trajectory Model Predictive Control for safe UAV Navigation in an Unknown Environment

Danilo Saccani, Leonardo Cecchin and Lorenzo Fagiano

***Abstract*—The talk will present an approach to address the problem of navigating an unmanned aerial vehicle (UAV) in an unknown environment with a novel model predictive control (MPC) formulation, named multi-trajectory MPC (mt-MPC). The objective is to safely drive the vehicle to the desired target location by relying only on the partial description of the surroundings provided by an exteroceptive sensor. This information results in time-varying constraints during the navigation among obstacles. The proposed mt-MPC generates a sequence of position setpoints that are fed to control loops at lower hierarchical levels. To do so, the mt-MPC predicts two different state trajectories, a safe one and an exploiting one, in the same Finite Horizon Optimal Control Problem (FHOCP). This formulation, particularly suitable for problems with uncertain time-varying constraints, allows one to partially decouple constraint satisfaction (safety) from cost function minimization (exploitation). Uncertainty due to modelling errors and sensors noise is taken into account as well, in a Set Membership framework. Theoretical guarantees of persistent obstacle avoidance are derived under suitable assumptions, and the approach is demonstrated experimentally out-of-the-lab on a prototype built with off-the-shelf components.**

***Index Terms*—Model Predictive Control, Safe Autonomous Navigation, Unmanned Aerial Vehicles, Uncertainty Quantification, Learning for Control.**

I. Introduction

In the last decade, technological advancements have showed that relatively cheap civil drones can take off, carry out complex missions, and land without any human intervention. At the same time, autonomous UAV missions belong to the spectrum of safety-critical applications, where the use of algorithms that do not account for uncertainty and robust constraint satisfaction can lead to catastrophic effects. The design of motion planning algorithms in safety-critical applications must trade-off a risk-aware approach, that guarantees the safety of the system and the environment, and the exploitation of the vehicle capabilities without falling into a too conservative behaviour. We consider here the problem of guaranteeing collision-free autonomous navigation from an initial point to a target position in an unknown environment. This problem presents several challenges: from rather usual requirements such as the compliance with actuator constraints and vehicle dynamics [1], to the need to guarantee collision avoidance despite uncertainties both in the environment and in the system dynamics and sensing capabilities, at the same time keeping computational complexity small enough to enable the real-time applicability of the algorithm in real-world tasks. When the environment is partially or totally unknown, or it could be different from the prior information, the algorithm must rely on local information collected by the available sensors to compute a feasible trajectory. Different approaches can be found in the literature that exploit directly the available information provided by exteroceptive sensors both to build a local map of the environment [2] or for reactive obstacle avoidance (see e.g [3]). However, the trajectory planning approaches available in the literature, despite providing an obstacle-free trajectory, only consider constraints on kinematic quantities and do not include in the problem setup the vehicle's dynamical response and the related uncertainty, due to, e.g., model mismatch or external disturbances (see e.g [4]). Other existing works dealing with this problem adopt Reinforcement Learning (RL) methods which employ directly the sensor measurements. All these methods often obtain good performance and the planning of obstacle-free trajectories but with little regard to safety guarantees, here considered in the form of constraint satisfaction and persistent obstacle avoidance. This problem indeed is particularly challenging since the feasible path must be re-planned on-line as new parts of the environment are discovered. In this case, the control logic has to balance two conflicting aspects: *safety*, that is to avoid the online discovered obstacles, and *exploitation*, i.e. to reach the desired target in short time. To deal with this balancing issue, in this work we propose a novel MPC approach that we find

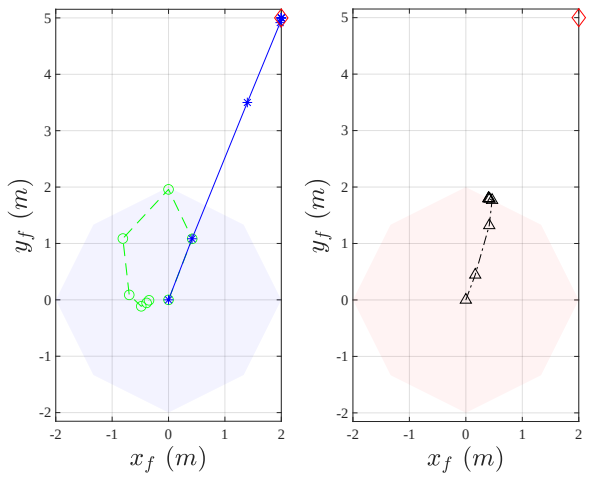

Fig. 1: Example illustrating the predicted state evolution with the multi-trajectory concept (left) vs. a single-trajectory one (right). Blue line with '*': exploiting trajectory; green line with '○': safe trajectory; black dash-dotted line with '△': single-trajectory approach. Red '◊': target. Colored polytopes represent the safe sets $\mathcal{S}(k)$.

This research has been supported by the Italian Ministry of University and Research (MIUR) under the PRIN 2017 grant n. 201732RS94 "Systems of Tethered Multicopters", and by the European Union's Horizon 2020 research and innovation programme under the Marie Skłodowska-Curie grant agreement No. 953348 "ELO-X - Embedded Learning and Optimization for the neXt generation of smart industrial control systems".

L. Fagiano and D. Saccani are with the Dipartimento di Elettronica, Informazione e Bioingegneria (DEIB), Politecnico di Milano, Italy. {danilo.saccani, lorenzo.fagiano}@polimi.it, L. Cecchin is with Robert Bosch GmbH, leonardo.cecchin@de.bosch.com

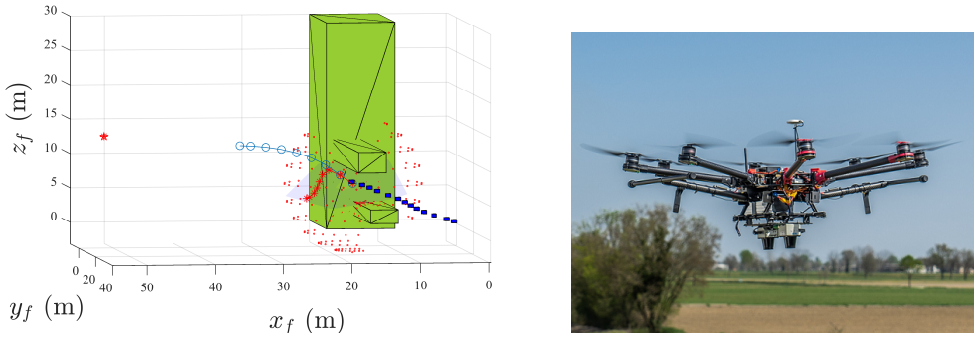

(a) (b)

Fig. 2: Simulation of the mt-MPC approach. Light blue polytope: set $\mathcal{S}(k)$. Red points: exteroceptive sensor measurements. Dashed red line with '$*$': safe trajectory. Solid blue line with '$\circ$': exploiting trajectory. Red star: target $\boldsymbol{p}_t$. Blue rectangles: past drone positions. Obstacles beyond the LiDAR's field of view are not shown.(2a). DJI S1000+ octocopter during field test. (2b).

particularly suitable for time-varying systems or constraints, named multi-trajectory MPC (mt-MPC). To trade-off safety and exploitation in an intuitive way, mt-MPC considers different future state trajectories in the same Finite Horizon Optimal Control Problem (FHOCP): a "safe" one, guaranteed to be contained in the safe set and to reach a safe state also considering the model uncertainty, and an "exploiting" one, which assumes that the current constraints are too conservative and can thus violate them. The two trajectories feature the same input at the current step and separate only afterwards in the prediction. To better illustrate this concept, let us consider the two-dimensional example in Fig. 1, showing on the left the multi-trajectory approach and on the right a standard, single-trajectory one. The shown trajectories are computed by solving a FHOCP and aiming to reach a target beyond the safe set. The single-trajectory approach forces all the predicted trajectory to lie within the safe set, minimizing the average distance from the target. This solution is optimal for the current safe set, but it does not consider a possible favorable evolution of the latter at the next time step. On the other hand, the multi-trajectory approach plans a much better (yet currently unfeasible) exploiting trajectory, but still retaining an alternative, guaranteed safe one in case the constraint set does not expand towards the target. Since the approach is implemented in receding horizon, the potential advantage is apparent by comparing the position reached at the first predicted time step by the two approaches, see Fig. 1. In this talk, we propose and demonstrate experimentally the use of mt-MPC to drive safely a multi-copter drone, equipped with an exteroceptive sensor, to a goal point in an a-priori unknown environment. The control structure is hierarchical: at low level, state-feedback controllers stabilize the vehicle's trajectories and track the set-points provided by the high-level mt-MPC. The navigation in an unknown environment leads to time-varying constraints, such that standard receding horizon strategies do not guarantee recursive feasibility anymore. To address this problem, we propose a modified receding horizon implementation and prove the existence of a feasible trajectory at each time step, hence persistent obstacle avoidance, under the assumption of time invariant environment. To guarantee this property also in presence of model-plant mismatch and disturbances, we quantify the model uncertainty in terms of bounds on the prediction error by exploiting a Set Membership framework [5]. All these aspects are relevant in real-world applications, yet they are rarely considered altogether in previous contributions, where the focus is either on the environment or on robust control starting from a given uncertainty model (e.g. disturbance bounds or model sets) without mentioning how this is derived. In addition, we address also two application-specific problems: the need to derive a convex under-approximation of the free space around the drone exploiting only local sensor measurements, in order to formulate the FHOCP as a convex QP, and the need to navigate around obstacles that stand between the drone and its target. Regarding the approximation of the free space, we present an approach that is computationally efficient and guarantees that the drone belongs to the derived set, which is needed to formally guarantee obstacle avoidance. The presentation material is related to a recent publication [6] and on ongoing research activities.

References

[1] S. Tang and V. Kumar, "Autonomous flight," *Annual Review of Control, Robotics, and Autonomous Systems*, vol. 1, pp. 29–52, 2018.

[2] S. Liu, M. Watterson, K. Mohta, K. Sun, S. Bhattacharya, C. J. Taylor, and V. Kumar, "Planning dynamically feasible trajectories for quadrotors using safe flight corridors in 3-d complex environments," *IEEE Robotics and Automation Letters*, vol. 2, no. 3, pp. 1688–1695, 2017.

[3] S. Hrabar, "Reactive obstacle avoidance for rotorcraft uavs," in *2011 IEEE/RSJ International Conference on Intelligent Robots and Systems*. IEEE, 2011, pp. 4967–4974.

[4] J. Tordesillas, B. T. Lopez, and J. P. How, "Faster: Fast and safe trajectory planner for flights in unknown environments," in *2019 IEEE/RSJ international conference on intelligent robots and systems (IROS)*. IEEE, 2019, pp. 1934–1940.

[5] M. Lauricella and L. Fagiano, "Set membership identification of linear systems with guaranteed simulation accuracy," *IEEE Transactions on Automatic Control*, doi: 10.1109/TAC.2020.2970146, 2020.

[6] D. Saccani and L. Fagiano, "Autonomous uav navigation in an unknown environment via multi-trajectory model predictive control," in *2021 European Control Conference (ECC)*. IEEE, 2021, pp. 1577–1582.

Potential evaluation of Model Predictive Control applied to Variable Speed Variable Displacement Pump systems

Leonardo Cecchin, Stefan Gering, Maximilian Manderla, Adrian Trachte, Moritz Diehl

***Abstract*—The use of Variable Speed Variable Displacement (VSVD) pumps has been proven to be advantageus with respect to constant speed or constant displacement solutions, and allows to exploit higher efficiency for a broad range of output requirements. This work presents an analysis of the performance obtainable in different load cases using a Model Predictive Controller. An overview of the system being controlled is provided, then a non linear Model Predictive Controller (nlMPC) formulation is described. At the end a comparison of nlMPC and other simpler control techniques is carried out through simulation.**

I. Introduction

Hydraulic powered machines are widely used in manufacuring industries, earth moving and construction vehicles. The hydraulic flow must be provided by a pumping unit, usually a variable displacement pump, which can be powered by an internal combustion engine, or an electric motor. A variable displacement pump is a unit in which it is possible, within a certain range, to change the amount of liquid that is displaced (e.g. pumped) for each rotation of the input shaft, therefore varying the resulting flow. The use of electric motors has numerous intuitive advantages, such as emissions and noise reduction, and allows to use the rotation speed as a control variable to change the output flow of the pump. The resulting system is called therefore Variable Speed Variable Displacement (VSVD) pump. With an appropriate control of speed and displacement VSVD pumps can be up to 15% more efficient than constant speed configurations, as shown in figure page 1, taken from [1]. The exploitation of the full potential, when working in static conditions (constant output flow and pressure), is quite simple, and can be obtained by computing the optimal system steady state through offline minimization of power losses, and then tracking that with commonly available controllers (e.g. PIDs).

When operating in dynamic conditions (e.g. varying output flow and/or pressure), the same control problem becomes much more complex: the dynamic behaviour of the system must be taken into account, following as precisely as possible the references, while at the same time keeping the power losses at a minimum. The problem is hard due to the non-linearity of the system, and the availability of some system equations only in the form of Look-Up Tables (LUTs). In most application cases of such pump system, moreover, the output load (e.g. the required output flow), is not known nor can be predicted, since it is dependent on operator-given control inputs.

This problem proves to be relevant from an industrial point of view, and at the same time offers interesting research challenges, mainly related to the use of LUTs inside the MPC problem formulation, and the implementation of the solver in embedded hardware.

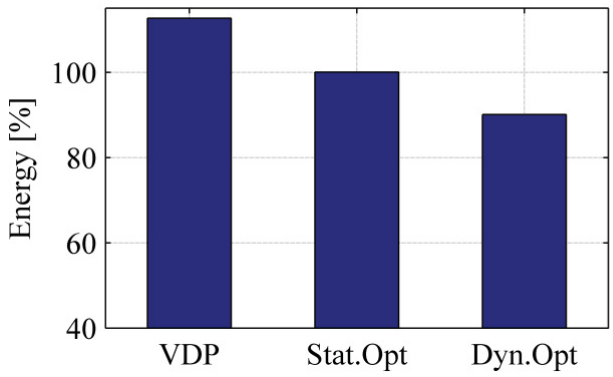

Fig. 1: Comparison of the potential of different pump systems: Variable Displacement Pump, at constant speed (VDP), VSVD pump with static optimization (Stat.Opt), VSVD pump with dynamic optimization (Dyn.Opt)

This project has received funding from the European Union's Framework Programme for Research and Innovation Horizon 2020 (2014-2020) under the Marie Sklodowska-Curie Grant Agreement No. 953348, and from DFG via Research Unit FOR 2401 and project 424107692

Leonardo Cecchin is with Corporate Research of Robert Bosch GmbH, Germany and Department of Microsystems Engineering (IMTEK), University of Freiburg. (e-mail: leonardo.cecchin@de.bosch.com)

Stefan Gering, Maximilian Manderla and Adrian Trachte are with Corporate Research of Robert Bosch GmbH, Germany. (e-mail: name.surname@de.bosch.com)

Moritz Diehl is with the Department of Microsystems Engineering (IMTEK) and Department of Mathematics, University of Freiburg. (e-mail: moritz.diehl@imtek.uni-freiburg.de)

References

[1] J. Willkomm, M. Wahler, and J. Weber, "Potentials of speed and displacement variable pumps in hydraulic applications," in *Proceedings of the 10th International Fluid Power Conference, Dresden, Germany*, 2016, pp. 8–10.

Chance-constrained sets approximation: A probabilistic scaling approach

M. Mammarella, V. Mirasierra, M. Lorenzen, T. Alamo, F. Dabbene

In real-world applications, the complexity of the phenomena encountered and the random nature of data makes dealing with uncertainty essential. In many cases, uncertainty arises in the modeling phase, in some others it is intrinsic to both the system and the operative environment, as for instance wind speed and turbulence in aircraft or wind turbine control [1]. Deriving results in the presence of uncertainty is of major relevance in different areas, including, but not limited to, optimization [2] and robustness analysis [3]. However, with respect to robust approaches, where the goal is to determine a feasible solution which is optimal in some sense for all possible uncertainty instances, the goal in the stochastic framework is to find a solution that is feasible for almost all possible uncertainty realizations, [4, 5]. In several applications, including engineering and finance, uncertainties in price, demand, supply, currency exchange rate, recycle and feed rate, and demographic condition are common. In these situations, it is acceptable, up to a certain safe level, to relax the inherent conservativeness of robust constraints enforcing probabilistic constraints. More recently, this probabilistic approach has been used also in unmanned autonomous vehicle navigation [6, 7] as well as in optimal power flow [8, 9]. In the optimization framework, constraints involving stochastic parameters that are required to be satisfied with a pre-specified probability threshold are called chance constraints (CC). In general, dealing with CC implies facing two serious challenges: the solution of difficult parameterized probability integrals and the nonconvexity of the ensuing constraints [10]. Consequently, while being attractive from a modeling view-point, problems involving CC are often computationally intractable, generally shown to be NP-hard, which seriously limits their applicability. However, being able to efficiently solve or approximate chance-constrained problems remains an important challenge, especially in systems and control. In the case of approximated solutions, there exists of course a fundamental trade-off between complexity of the approach and goodness of the approximation. The scientific community has devoted large research in devising computationally efficient approaches to deal with chance-constraints.

In this talk, we will present what we consider an important step forward in the sample-based approach. More precisely, our developments stem from the observation that, while in the general situation one is interested in finding an optimal solution to a chance-constrained problem, there exists a significant class of practical applications in which, instead, what it is really needed is being able to construct good approximation of the chance-constrained set. This is the case, for instance, of stochastic model predictive control (SMPC), where this approximation is necessary for post-processing in real time, see for instance [11, 12]. Motivated by these considerations, we propose a simple and efficient strategy to obtain a probabilistically guaranteed inner approximation of a chance-constrained set, with given confidence.

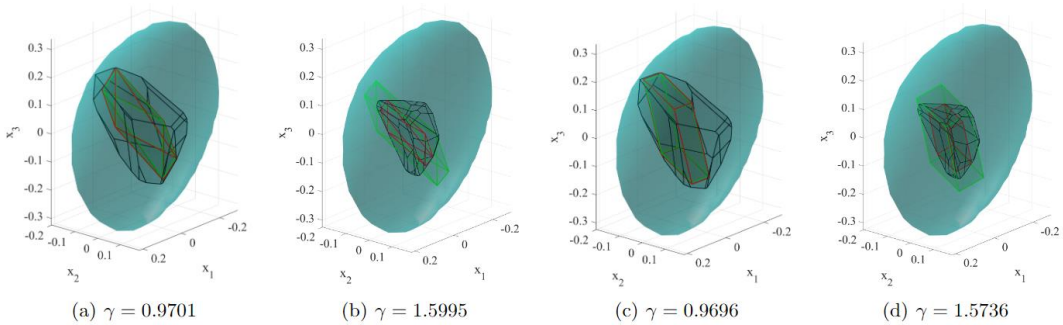

Fig. 1 Scaling procedure applied to (a) $\mathbb{S}_{\ell_1}$-SAS with $N_S = 100$, (b) $\mathbb{S}_{\ell_1}$-SAS with h $N_S = 1000$, (c) $\mathbb{S}_{\ell_\infty}$-SAS with $N_S = 100$, and (d) $\mathbb{S}_{\ell_\infty}$-SAS with h $N_S = 100$. The initial set is depicted in red, the final one in green. The sampled design polytope $\mathbb{S}_{N_S}$ is represented in black.

In particular, we describe a two-step procedure that involves: i) the preliminary approximation of the chance-constrained set by means of a so-called Simple Approximating Set (SAS); ii) a sample-used

scaling procedure that allows to properly scale the SAS so to guarantee the desired probabilistic properties. The proper selection of a low-complexity SAS allows the designer to easily tune the complexity of the approximating set, significantly reducing the sample complexity. We propose several candidate SAS shapes, grouped in two classes: i) sampled-polytopes; and ii) norm-based SAS. For example, in Fig. 1 we report two different norm-based SAS, and for each of them we consider two different values of fixed number N_S of *design* uncertainty samples. We can see that for larger N_S, the ensuing initial set becomes smaller. Consequently, we have a shrinkage process for small N_S and an inflating one for large N_S. Then, we also demonstrate the efficacy of the proposed approach with a numerical example in which the results of our research are applied to the probabilistic set membership estimation problem. Fig. 2 shows the results of both the point estimation and the probabilistic interval estimation.

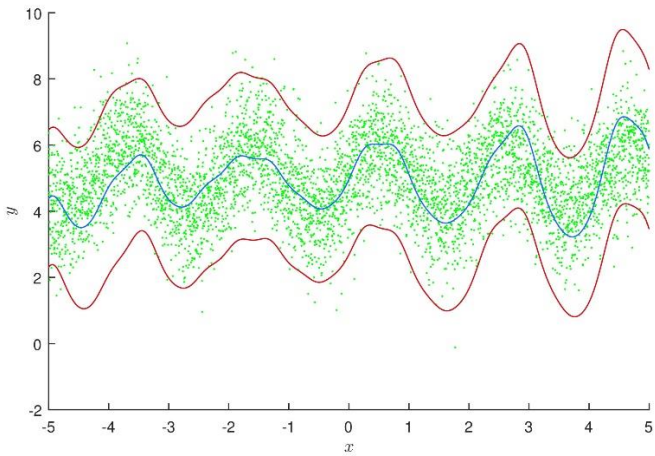

Fig. 2 Real values of y vs central estimation (blue) and interval prediction bounds (red).

References

[1] A. Pr´ekopa, Stochastic Programming. Kluwer Academic Publishers, 1995.

[2] N. V. Sahinidis, "Optimization under uncertainty: state-of-the-art and opportunities," Computers & Chemical Engineering, vol. 28, no. 6-7, pp. 971–983, 2004.

[3] A. Ben-Tal and A. Nemirovski, "Robust convex optimization," Mathematics of Operations Research, vol. 23, pp. 769–805, 1998.

[4] G. Calafiore, F. Dabbene, and R. Tempo, "Research on probabilistic methods for control system design," Automatica, vol. 47, pp. 1279–1293, 2011.

[5] R. Tempo, G. Calafiore, and F. Dabbene, Randomized Algorithms for Analysis and Control of Uncertain Systems: with Applications. Springer Science & Business Media, 2012.

[6] M. Mammarella, E. Capello, F. Dabbene, and G. Guglieri, "Sample-based SMPC for tracking control of fixed-wing UAV," IEEE Control Systems Letters, vol. 2, no. 4, pp. 611–616, 2018.

[7] J. Li, W. Zhan, Y. Hu, and M. Tomizuka, "Generic tracking and probabilistic prediction framework and its application in autonomous driving," IEEE Transactions on Intelligent Transportation Systems, vol. 21, no. 9, pp. 3634–3649, 2020.

[8] M. Chamanbaz, F. Dabbene, and C. Lagoa, Algorithms for Optimal AC Power Flow in the Presence of Renewable Sources. Wiley Encyclopedia of Electrical and Electronics Engineering, 2020, pp. 1–13.

[9] M. Chamanbaz, F. Dabbene, and C. M. Lagoa, "Probabilistically robust AC optimal power flow," IEEE Transactions on Control of Network Systems, vol. 6, no. 3, pp. 1135–1147, 2019.

[10] X. Geng and L. Xie, "Data-driven decision making in power systems with probabilistic guarantees: Theory and applications of chance-constrained optimization," Annual Reviews in Control, vol. 47, pp. 341–363, 2019.

[11] M. Lorenzen, F. Dabbene, R. Tempo, and F. Allg¨ower, "Stochastic MPC with offline uncertainty sampling," Automatica, vol. 81, no. 1, pp. 176–183, 2017.

[12] M. Mammarella, M. Lorenzen, E. Capello, H. Park, F. Dabbene, G. Guglieri, M. Romano, and F. Allg¨ower,

“An offline-sampling SMPC framework with application to autonomous space maneuvers,” IEEE Transactions on Control Systems Technology, vol. 28, no. 2, pp. 1–15, 2018.

Stability Analysis of a Class of Discontinuous Discrete-Time Systems

Francesco Ferrante and Giorgio Valmorbida

***Abstract*— The stability analysis of a class of discontinuous discrete-time systems is studied in this paper. The system under study is modeled as a feedback interconnection of a linear system and a set-valued nonlinearity. An equivalent representation, based on a constrained optimization problem, is proposed to represent the set-valued nonlinearity via a collection of linear and quadratic constraints. Relying on this description and on the use of a generalized quadratic set-valued Lyapunov functions, sufficient conditions in the form of linear matrix inequalities for global exponential stability are obtained. Numerical examples corroborate the theoretical findings.**

***Index Terms*— Nonlinear systems, Lyapunov stability, LMIs.**

I. Introduction

A. Motivation and background

The widespread availability and the decreasing costs of digital devices have promoted the implementation of control systems on digital platforms. However, embedded control systems when implemented on affordable devices also raise theoretical challenges in term of stability analysis and performance. Indeed, the presence of nonlinear elements in feedback control systems may lead to limit cycles, chaotic behaviors, which may induce poor performance and instability. A fundamental limitation in digital control systems consists of the use of finite alphabets to represent information such as inputs and outputs. The control of systems based on the use of finite alphabets has been largely investigated in the literature over the last years. A finite number of input values appears in quantized actuators followed by a saturation nonlinearity [1]. For example, in [2] the use of ternary controllers for multi agent systems consensus is proposed. Stabilization of nonlinear systems by a finite number of control or measurement values is studied in [3]. Formation control and consensus under the assumption of binary information exchanges has been pursued, respectively in [4] and [5]. Another application of ternary controllers for integrator coordination is featured in [6]. A predominant use of controllers taking values into finite alphabets arises in the literature of symbolic control in which control design is performed based on discrete abstractions; see, e.g., [7], [8].

B. Contributions and Outline of the Paper

In this paper, we focus on stability analysis of a class of discontinuous discrete-time control systems. In particular, we consider a scenario in which a linear plant is controlled via an affine static state feedback law taking values into the set $\{0,\delta_1\}\times\{0,\delta_2\}\times\ldots\{0,\delta_{n_u}\}$, where $n_u\in\mathbb{N}$ is the number of control inputs and $\delta_i\in\mathbb{R}$, for all $i\in\{1,2,\ldots,n_u\}$, are some given *levels*. More specifically, we focus on the following class of nonlinear discrete-time systems:

$$x^+ = Ax + B\Delta S(Kx+d) \tag{1}$$

Francesco Ferrante is with Department of Engineering, University of Perugia, Perugia, Italy. francesco.ferrante@unipg.it.

G. Valmorbida is with the Laboratoire des Signaux et Systèmes, CentraleSupélec, CNRS, Université Paris-Saclay, Gif-sur-Yvette 91192, France. He is also with Inria projet DISCO. giorgio.valmorbida@l2s.centralesupelec.fr.

where $A\in\mathbb{R}^{n_p\times n_p}$, $B\in\mathbb{R}^{n_p\times n_u}$, $K\in\mathbb{R}^{n_u\times n_p}$, $\Delta:=\operatorname{diag}\{\delta_1,\delta_2,\ldots,\delta_{n_u}\}$, $d\in\mathbb{R}^{n_u}$ are given and $S\colon\mathbb{R}^{n_u}\to\mathbb{R}^{n_u}$ is defined as follows:

$$S(u) := (s(u_1), s(u_2), \ldots, s(u_{n_u})) \tag{2}$$

where for all $v\in\mathbb{R}$

$$s(v) := \begin{cases} 1 & \text{if} \quad v>0 \\ 0 & \text{if} \quad v\le 0. \end{cases} \tag{3}$$

The above setup is rather general and allows one to capture, among others, the typical situation in which actuators may only deliver a finite set of input values. Since system (1) is assumed to be given, the goal of the paper is to provide a method for the stability analysis of the origin of (1). The expression for the input mapping s in (3) is a static nonlinearity, which is commonly studied by a sector description. In contrast with more classical absolute stability approaches, *we do not rely on any sector bound approach.* Moreover, we introduce a class of set-valued piecewise quadratic Lyapunov functions (LF), as opposed to the standard quadratic LF approaches.

C. Notation

The symbol $\mathbb{S}^n$ stands for the set of $n\times n$ symmetric matrices, $\mathbb{D}^n$ denotes the set of $n\times n$ diagonal matrices, and $\mathbb{P}^n$ is the set of $n\times n$ symmetric matrices with nonnegative entries. The identity matrix is denoted by I. The symbol $\mathbf{1}_n$ is the all-ones vector of $\mathbb{R}^n$. For a matrix $A\in\mathbb{R}^{n\times m}$, $A^\intercal$ denotes the transpose of A, and, when $n=m$, $\operatorname{He}(A)=A+A^\intercal$. The symbol $\odot$ stands for the Hadamard product. Let $A\in\mathbb{S}^n$, $A\preceq 0$ stands for negative semidefiniteness of A. Given $x\in\mathbb{R}^n$, $x\le 0$ indicates that the components of x are nonpositive. The symbol $\bullet$ stands for symmetric blocks in symmetric partitioned matrices. Given a matrix M with $\ker M\neq\{0\}$, $M_\perp$ stands for any matrix having as columns a basis of $\ker M$. The symbol $\bigoplus_{i=1}^n A_i$ stands for direct sum of matrices $A_1,A_2,\ldots,A_n$ and $A\otimes B$ indicates the Kronecker product of matrices A and B.

II. Problem setting and Key results

A. Modeling

Due to the discontinuity of S at zero, (1) is a discontinuous dynamical system. Although discontinuities in discrete-time dynamical systems do not lead to major technical problems as in their continuous-time counterpart (see, e.g., [9]), they generally lead to lack of robustness, with stability properties being fragile in the presence of vanishing perturbations; see [10, Example 4.4, page 76]. To overcome this drawback, in this work we consider the following set-valued *regularization* of (1):

$$x^+ \in Ax + B\Delta\mathbf{S}(Kx+d) \tag{4}$$

where the set-valued mapping[1] $\mathbf{S}\colon\mathbb{R}^{n_u}\rightrightarrows\mathbb{R}^{n_u}$ is defined as follows:

$$\mathbf{S}(u) := (\mathbf{s}(u_1), \mathbf{s}(u_2), \ldots, \mathbf{s}(u_{n_u})) \tag{5}$$

[1]The double arrow notation $\rightrightarrows$ is used to distinguish set-valued maps from functions.

with, for all $v \in \mathbb{R}$,

$$\mathbf{s}(v) := \begin{cases} 1 & \text{if} \quad v > 0 \\ 0 & \text{if} \quad v < 0 \\ [0,1] & \text{if} \quad v = 0. \end{cases} \tag{6}$$

Observe that solutions to (1) are solutions to (4). Thus, stability properties of (4) carry over (1).

B. Characterization of the mapping $\mathbf{S}$ *via quadratic constraints*

In this subsection we illustrate the key result of this paper. This result yields a tight characterization of the mapping $\mathbf{S}$ in (5) in terms of quadratic constraints. To achieve this goal, we pursue a similar approach as in [11] and rely on optimization-based representation of the mapping $\mathbf{S}$ along with Karush-Kuhn-Tucker (KKT) optimality conditions. To this end, observe that for all $v \in \mathbb{R}$, one can express (6) as

$$\mathbf{s}(v) \in \operatorname*{arg\,min}_{w \in [0,1]} \quad -vw. \tag{7}$$

Clearly, if $v < 0$, one has $\mathbf{s}(v) = 0$, if $v > 0$, one has $\mathbf{s}(v) = 1$, while when $v = 0$, $\mathbf{s}(v) \in [0,1]$, which is consistent with (6). Building upon this observation, one can obtain a characterization of the mapping $\mathbf{S}$ via the application of Karush-Kuhn-Tucker (KKT) optimality conditions to problem (7). This is formally stated in the result given next.

Theorem 1: Let $\mathbf{S}$ be defined as in (5), $u \in \mathbb{R}^{n_u}$, and $s \in \mathbb{R}^{n_u}$. Then, the following items are equivalent:

(*i*) $s \in \mathbf{S}(u)$

(*ii*) there exist $\lambda_1, \lambda_2 \in \mathbb{R}^{n_u}$ such that:

$$-u - \lambda_1 + \lambda_2 = 0 \tag{8a}$$
$$\lambda_1 \odot s = 0 \tag{8b}$$
$$\lambda_2 \odot (\mathbf{1}_{n_u} - s) = 0 \tag{8c}$$
$$-\lambda_1 \leq 0 \tag{8d}$$
$$-\lambda_2 \leq 0 \tag{8e}$$
$$-s \leq 0 \tag{8f}$$
$$-\mathbf{1}_{n_u} + s \leq 0 \tag{8g}$$

Theorem 1 shows that for all $u \in \mathbb{R}^{n_u}$ and $s \in \mathbf{S}(u)$, there exist $\lambda_1, \lambda_2 \in \mathbb{R}^{n_u}$ such that $\chi := (\lambda_1, \lambda_2, s, \mathbf{1}_{n_u} - s, u) \in \mathbb{R}^{5n_u}$ satisfies (8). In particular, the entries of the vector χ depend on u and s. Therefore, in the remainder of the paper, given $u \in \mathbb{R}^{n_u}$ and $s \in \mathbf{S}(u)$, we use the shorthand notation $\chi(u,s)$ to denote the corresponding vector satisfying (8). For compactness, next we rewrite the linear equality constraints in (8a) as $L\chi = 0$, where $L := \begin{bmatrix} -1 & 1 & 0 & 0 & -1 \end{bmatrix} \otimes I_{n_u}$. The remainder of the paper, for all $u \in \mathbb{R}^{n_u}$ we use the notation $\overline{\lambda}(u) = (r(-u), r(u))$.

C. Stability Analysis

We are now in a position to state the main result of this paper. This result provides sufficient conditions for global exponential stability of (4) in the form of matrix inequalities. These conditions are obtained by relying on the following set-valued Lyapunov function candidate:

$$V(x) := \bigcup_{s \in \mathbf{S}(Kx+d)} \left\{ \begin{bmatrix} x \\ s \\ \overline{\lambda}(Kx+d) \end{bmatrix}^{\mathsf{T}} P \begin{bmatrix} x \\ s \\ \overline{\lambda}(Kx+d) \end{bmatrix} \right\}$$

Theorem 2: Suppose that there exist $P \in \mathbb{S}^{n_p+3n_u}$, $M_1, M_2, M_3 \in \mathbb{P}^{8n_u+1}$, $\widehat{G}_i = (G_{i,1}, G_{i,2}) \in \mathbb{D}^{2n_u} \times \mathbb{D}^{2n_u}$, $c_i > 0$, with $i \in \{1,2,3\}$ such that

$$\begin{aligned} W_\perp^{\mathsf{T}}(V_u + T^{\mathsf{T}}\Psi(\widehat{G}_1)T + F^{\mathsf{T}}M_1F)W_\perp \preceq 0 \\ W_\perp^{\mathsf{T}}(V_l + T^{\mathsf{T}}\Psi(\widehat{G}_2)T + F^{\mathsf{T}}M_2F)W_\perp \preceq 0 \end{aligned} \tag{9a}$$

$$W_\perp^{\mathsf{T}}(\Xi + T^{\mathsf{T}}\Psi(\widehat{G}_3)T + F^{\mathsf{T}}M_3F)W_\perp \preceq 0 \tag{9b}$$

where for all $i \in \{1,2,3\}$:

$$\begin{aligned} &\Psi(\widehat{G}_i) := \operatorname{He}\left(\bigoplus_{j=1}^{2} \begin{bmatrix} 0_{2n_u,2n_u} & G_{i,j} & 0_{2n_u,n_u} \\ 0_{3n_u,2n_u} & 0_{3n_u,2n_u} & 0_{3n_u,n_u} \end{bmatrix} \right) \\ &\Xi := \begin{bmatrix} \Pi_1^{\mathsf{T}}\mathscr{V}_+^{\mathsf{T}} & \Pi_2^{\mathsf{T}} \end{bmatrix} \left(\begin{bmatrix} 1 & 0 \\ 0 & -1 \end{bmatrix} \otimes P \right) \begin{bmatrix} \mathscr{V}_+\Pi_1 \\ \Pi_2 \end{bmatrix} + c_3X \\ &V_l := -\Pi_2^{\mathsf{T}}P\Pi_2 + c_1X, V_u := \Pi_2^{\mathsf{T}}P\Pi_2 - c_2X, \end{aligned} \tag{10a}$$

and

$$\begin{aligned} &\mathscr{V}_+ := \begin{bmatrix} A & B\Delta & 0_{n_p,n_u} & 0_{n_p,2n_u} & 0_{n_p,2n_u} \\ 0_{n_u,n_p} & 0_{n_u,n_u} & I_{n_u} & 0_{n_u,2n_u} & 0_{n_u,2n_u} \\ 0_{2n_u,n_p} & 0_{2n_u,n_u} & 0_{2n_u,n_u} & 0_{2n_u,2n_u} & I_{2n_u} \end{bmatrix} \\ &F := \begin{bmatrix} 0_{4n_u,n_p} & [\, I_{4n_u} \ 0_{4n_u,n_u} \,] & 0_{4n_u,5n_u} & 0_{4n_u,1} \\ 0_{4n_u,n_p} & 0_{4n_u,5n_u} & [\, I_{4n_u} \ 0_{4n_u,n_u} \,] & 0_{4n_u,1} \\ 0_{1,n_p} & 0_{1,5n_u} & 0_{1,5n_u} & 1 \end{bmatrix} \\ &\Pi_1 := \begin{bmatrix} I_{n_p} & 0_{n_p,5n_u} & 0_{n_p,5n_u+1} \\ 0_{n_u,n_p} & H & 0_{n_u,5n_u+1} \\ 0_{n_u,n_p} & 0_{n_u,5n_u} & [\, H \ 0_{n_u,1} \,] \\ 0_{2n_u,n_p} & [\, I_{2n_u} \ 0_{2n_u,3n_u} \,] & 0_{2n_u,5n_u+1} \\ 0_{2n_u,n_p} & 0_{2n_u,5n_u} & [\, I_{2n_u} \ 0_{2n_u,3n_u+1} \,] \end{bmatrix} \\ &H := \begin{bmatrix} 0_{n_u,2n_u} & I_{n_u} & 0_{n_u,2n_u} \end{bmatrix}, X := I_{n_p} \oplus 0_{10n_u+1,10n_u+1} \\ &\Pi_2 := \begin{bmatrix} I_{n_p+n_u} & 0_{n_p+n_u,5n_u} \\ 0_{2n_u,(n_p+n_u)} & [\, 0_{2n_u,n_u} \ I_{2n_u} \ 0_{2n_u,2n_u} \,] \end{bmatrix} \Pi_1 \\ &W := \begin{bmatrix} R \\ (I_2 \otimes L)T \end{bmatrix}, T := \begin{bmatrix} 0_{10n_u,n_p} & I_{10n_u} & 0_{10n_u,1} \end{bmatrix} \\ &R := \begin{bmatrix} K & -Z & 0_{n_u,5n_u} & d \\ KA & KB\Delta J & -Z & d \\ 0_{n_u,n_p} & E & 0_{n_u,n_p} & -\mathbf{1} \\ 0_{n_u,n_p} & 0_{n_u,n_p} & E & -\mathbf{1} \end{bmatrix} \\ &E := \begin{bmatrix} 0_{n_u,2n_u} & I_{n_u} & I_{n_u} & 0_{n_u,n_u} \end{bmatrix} \\ &Z := \begin{bmatrix} 0_{n_u,4n_u} & I_{n_u} \end{bmatrix}, J := \begin{bmatrix} 0_{n_u,2n_u} & I_{n_u} & 0_{n_u,2n_u} \end{bmatrix}, \end{aligned} \tag{10b}$$

Then, the origin of (4) is GES.

References

[1] M. Fu and L. Xie, "The sector bound approach to quantized feedback control," *IEEE Transactions on Automatic Control*, vol. 50, no. 11, pp. 1698–1711, 2005.

[2] J. Cortés, "Finite-time convergent gradient flows with applications to network consensus," *Automatica*, vol. 42, no. 11, pp. 1993–2000, 2006.

[3] C. De Persis, "Robust stabilization of nonlinear systems by quantized and ternary control," *Systems & Control Letters*, vol. 58, no. 8, pp. 602–608, 2009.

[4] M. Jafarian and C. De Persis, "Formation control using binary information," *Automatica*, vol. 53, pp. 125–135, 2015.

[5] G. Chen, F. L. Lewis, and L. Xie, "Finite-time distributed consensus via binary control protocols," *Automatica*, vol. 47, no. 9, pp. 1962–1968, 2011.

[6] C. De Persis and P. Frasca, "Robust self-triggered coordination with ternary controllers," *IEEE Transactions on Automatic Control*, vol. 58, no. 12, pp. 3024–3038, 2013.

[7] P. Tabuada, *Verification and control of hybrid systems: a symbolic approach*. Springer Science & Business Media, 2009.

[8] A. Saoud, E. Ivanova, and A. Girard, "Efficient synthesis for monotone transition systems and directed safety specifications," in *Proceedings of the IEEE 58th Conference on Decision and Control*, 2019, pp. 6255–6260.

[9] J. Cortés, "Discontinuous dynamical systems," *Control Systems Magazine*, vol. 28, no. 3, pp. 36–73, 2008.

[10] R. Goebel, R. G. Sanfelice, and A. R. Teel, *Hybrid Dynamical Systems: Modeling, Stability, and Robustness*. Princeton University Press, 2012.

[11] J. Primbs, A. and M. Giannelli, "Kuhn-Tucker-based stability conditions for systems with saturation," *IEEE Transactions on Automatic Control*, vol. 46, no. 10, pp. 1643–1647, 2001.

Switching Observer for Finite State Machines and Its Application to Opacity

Naeimeh Fakhr Shamloo, Elena De Santis, *Senior Member, IEEE*, and Maria Domenica Di Benedetto, *Life Fellow, IEEE*

***Abstract*—In this paper, motivated by wide applications of observers in analyzing different properties of a system such as opacity, we propose the notion of switching observer and show how its use can reduce the computational cost of checking properties (such as opacity) of Finite State Machines (FSM) that need the design of an observer. We define the notion of total indistinguishability and use the notion of critical observability for the design of the switching observer, which is constructed by appropriately switching between a set of "sub-observers". The methodology is applied to check opacity, showing a significant complexity reduction in computation.**

I. Introduction

Reconstructing the internal behavior of a dynamic system based on the available information plays an important role in the study of Discrete Event Systems (DES). Depending on the model and the available output information, building an observer is often needed to verify system's properties such as detectability [1], diagnosability [2], or opacity [3]. Since complexity is one of the most important issues that must be overcome to make theoretical methodologies applicable to real industrial applications [4], in this work, we propose a method aimed at reducing the computational effort in designing observers for solving these problems.

Instead of building a traditional observer (see e.g. [5]), we propose the design of a *switching observer*, by appropriately switching between a set of "sub-observers" constructed on the basis of a decomposition of the given system. The decomposition is based on the notions of Total-indistinguishability and critical observability.

We then apply the proposed method to check the opacity of a given set, called the secret set for an FSM. Opacity is a rather recent field of research. A system is opaque if the evolution of its true states through a set of secret states remains opaque to an external intruder [6]. There are several ways, based on the design of a traditional observer, to verify different notions of opacity where the system is modeled as a DES and an intruder is modeled as a passive observer that monitors the behavior of the dynamic system via measured outputs [3]. In this work, we show that, for checking opacity, there is no need to construct all the sub-observers that compose the switching observer, thereby reducing the computational cost.

Naeimeh Fakhr Shamloo, Elena De Santis and Maria Domenica Di Benedetto are with the Department of Information Engineering, Computer Science and Mathematics, Center of Excellence DEWS, University of L'Aquila. (e-mail: {naeimeh.fakhrshamloo, elena.desantis,mariadomenica.dibenedetto}@univaq.it)

The research leading to these results has been partially supported by the Center of Excellence DEWS.

A. Abbreviations and Acronyms

For $a, b \in Z$, $[a, b] = \{x \in Z : a \leq x \leq b\}$ where Z denotes the set of nonnegative integer numbers. For a set Q the symbol $|Q|$ denotes its cardinality. For a set $Y \subset Q$, the symbol $\subset$ has to be understood as subset and the symbol $\bar{Y}$ denotes the complement of Y in Q. For $W \subset Q \times Q$, the symbol W^s denotes the symmetric closure of W, i.e. $W^s = \{(i_1, i_2) : (i_1, i_2) \in W \text{ or } (i_2, i_1) \in W\}$. The power set of a set Q is denoted by 2^Q. For two sets Q' and Q, let $Q' \backslash Q = \{i \in Q' | i \notin Q\}$.

II. Main Results

We consider DESs modeled as Finite-State Machines (FSMs). Let M be an FSM

$$M = (X, X_0, Y, H, \Delta) \tag{1}$$

where:
- X is the finite set of states;
- $X_0 \subset X$ is the set of initial states;
- Y is the finite set of outputs;
- $H : X \to Y$ is the output function;
- $\Delta \subset X \times X$ is the transition relation.

For $i \in X$, $succ\,(i) = \{j \in X : (i, j) \in \Delta\}$ and $pre\,(i) = \{j \in X : (j, i) \in \Delta\}$. Any finite or infinite string x with symbols in X that satisfies the condition $x\,(1) \in X$ and $x\,(k+1) \in succ\,(x\,(k))$, $k = 1, 2, ..., |x| - 1$ is called a state execution of the FSM M. Let $\mathcal{X}^*$ be the set of all state executions of M. For a given $\Psi \subset X$ we can define $\mathcal{X}$ the set of state executions $x \in \mathcal{X}^*$ with $x(1) \in X_0$ and $\mathcal{X}^\Psi$ the set of finite state executions $x \in \mathcal{X}^*$ with last symbol in Ψ.

The discrete output function H represents the accessible information. When no output information is available for some state i, we set $H(i) = \epsilon$, where ϵ denotes the null event. Let Υ be the set of strings with symbols in $\widehat{Y} = \{y \in Y : y \neq \epsilon\}$. Define $\mathrm{y} : \mathcal{X}^* \to \Upsilon$, the function that associates to a state execution the corresponding output execution, as $\mathrm{y}\,(x) = P\,(\sigma)$ where $\sigma = H\,(x\,(1))\,...H\,(x\,(n))$, $n = |x|$ if $|x|$ is finite and $P\,(\sigma)$ is the projection of the string σ, i.e. the string obtained from σ by erasing the symbol ϵ [7]. Otherwise if $|x|$ is infinite, $\mathrm{y(x)} = \mathrm{P}(\sigma_\infty)$ where σ_∞ is an infinite string recursively defined as $\sigma_1 = H(x(1)), \sigma_{k+1} = \sigma_k H(x(k+1)), k = 1, 2, ...$. Finally, $\mathrm{y}^{-1}(\mathrm{y(x)}) = \{\hat{\mathrm{x}} \in \mathcal{X} : \mathrm{y}(\hat{\mathrm{x}}) = \mathrm{y(x)}\}$, $x \in \mathcal{X}$.

In this work , we present a *switching observer* for an FSM M based on the notions of "Total-indistinguishability" and "Critical observability" which are defined in [8]:

Definition 1. *A pair* (i, j) *is called* Totally-indistinguishable *(T-indistinguishable) if for any finite state execution* $x \in \mathcal{X}$ *ending in* i *or in* j*, there exists a finite state execution* $x' \in \mathcal{X}$ *ending in* j*, or in* i*, respectively, with* x *and* x' *indistinguishable.*

Definition 2. *(Critical observability) The FSM* (1) *is critically observable with respect to a set* $\Omega \subset \mathrm{X}$ *(critically* Ω*-obs) if for any string* $x \in \mathcal{X}$*, whenever* $x(k) \in \Omega$*, it follows that for any string* $\hat{x} \in \mathrm{y}^{-1}\left(\mathrm{y}(x|_{[1,k]})\right)$*,* $\hat{x}\left(|\hat{x}|\right) \in \Omega$*. A set* Ω *is said to be critically observable if the FSM is critically* Ω*-obs).*

Since total indistinguishability is a transitive, reflexive and symmetric property we can group the states in X into equivalence classes. Let the symbol $\sim$ denote the total indistinguishability relation on the set X. For a state $i \in X$ its equivalence class is the set $\{j \in X : j \sim i\}$. The set of equivalences classes induces a partition of the state space X

$$X = X_1 \cup X_2 .... \cup X_L \tag{2}$$

with $L \leq N$. Let $\mathcal{T} = \{X_1, ..., X_L\}$.

Consider the FSM M and let O be a *traditional observer* for M, i.e. an observer constructed as described e.g. in [5].

Let $\mathcal{T}_C \subset \mathcal{T}$ be the collection of $X_i \in \mathcal{T}$ such that X_i is critically observable, $\mathcal{T}_C = \{X_i, i \in I_c \subset \{1, 2, ...L\}\}$.

Let M' be obtained from M by removing the transitions $(j, j') \in \Delta$ with $j' \in X_i \in \mathcal{T}_C$ for $i = 1, .., L$ and $M'|_i$ be the FSM M' with initial state set X_i. We define the FSMs M_i, $i \in I_c$ as $M_i = Ac(M'|_i)$ where $Ac(.)$ denotes the accessible part, as defined in [5]. Let O_i, $i \in I_c$, be the observer for M_i, also called "sub-observer". The switching observer, called $\mathcal{O}$, is constructed by appropriately switching between the observers in the family $\{O_i, i \in I_c\}$. Roughly speaking, consider a given finite state execution x, with $x(1) \in X_i$ for some $i \in I_c$. The observer at the first step is O_i and it will not change until the state execution reaches a different set in the family $\mathcal{T}_C$, say $X_j, i \neq j$. At this step, called the "switching step", the current observer becomes O_j, with the current observer state equal to X_j and it remains the same until the execution reaches the next different set in $\mathcal{T}_C$. Switching between the observers $\{O_i, i \in I_c\}$ following the state execution x.

Let k_h, k_{h+1} denote two consecutive switching steps, and define the intervals $I_h = [k_h, k_{h+1} - 1]$, $h = 1, 2, ...H$, with $I_H = [k_H, |x| + 1)$. Let us denote with $\mathcal{O}(h) \in \{O_i, i \in I_c\}$ the observer associated to the interval I_h.

Let $\hat{X}_O$ to be the set of states of the traditional observer O of M, $\hat{X}_{O_i}$ the set of states of the observer O_i of M_i and $\hat{X}_{\mathcal{O}}$ the set of states of the switching observer $\mathcal{O}$ of M. Then, we have:

$$\hat{X}_O = \hat{X}_{O_1} \cup ... \cup \hat{X}_{O_L} = \hat{X}_{\mathcal{O}}$$

By construction, the traditional observer and the switching observer are synchronized with the output execution of M, i.e. at each step the state of O is the same as the related state of the switching observer built following the algorithm above.

The following theorem presents this property formally:

Theorem 1. *For any execution of* M*, at each step, the state of* O *is equal to the state of* $\mathcal{O}$*.*

In this work, we use the proposed switching observer to check opacity for DES modeled by FSMs. We will show how the method proposed in the previous sections can be used to reduce the computational cost of opacity verification. The advantage of using the switching observer is that it is not necessary to build all the observers O_i to check if a set is opaque. In fact, consider the set of states X_i of M_i. Theorem presented in [9] for checking the opacity can be rewritten as:

Theorem 2. *A set* Υ_S *is opaque if and only if*

$$\hat{X}_{O_i} \cap 2^{\Upsilon_S} = \emptyset \tag{3}$$

for any $i \in I = \{i \in I_c$ *such that* $\Upsilon_S \cap X_i \neq \emptyset\}$.

Let $n = |X|$ and $n' = \sum_{i \in I} |X_i|$. Obviously $n' \leq n$ and therefore the order of computational cost can be reduced from (2^n) to $(2^{n'})$ by using the proposed method.

The examples and the algorithms that are necessary for building a switching observer are presented in the full version of this work.

III. Conclusions

In this work, we proposed notion of switching observer that can be considered as a decomposition in "sub-observers" of the traditional observer. Each sub-observer is designed for subsystems obtained by considering the critical observable total indistinguishable set as the initial state set. Then, we showed how using a switching observer can reduce the computational complexity in checking properties such as opacity. Examples demonstrate the efficiency of the proposed method and all the necessary materials is provided in the full paper .

References

[1] L. K. Carvalho, Y. C. Wu, R. Kwong and S. Lafortune, Detection and mitigation of classes of attacks in supervisory control systems, Automatica, vol. 97, 2018, pp. 121-133.

[2] J. Zaytoon and S. Lafortune, Overview of fault diagnosis methods for discrete event systems, Annual Reviews in Control. vol. 37, no. 2, 2013, pp. 308-320.

[3] Y. Tong, Z. Li, C. Seatzu and A. Giua, Current-state opacity enforcement in discrete event systems under incomparable observations, Discrete Event Dynamic Systems, vol. 28, no. 4, 2018, pp. 1-22.

[4] G. Pola, E. De Santis, M. D. Di Benedetto and D. Pezzuti, Design of decentralized critical observers for networks of finite state machines: A formal method approach, Automatica, vol. 86, 2017, pp. 174-182.

[5] C. G. Cassandras and S. Lafortune, Introduction to Discrete Event Systems. New York: Springer-Verlag, 1999, ch. 5.

[6] S. Lafortune, F. Lin and N. Hadjicostis, On the History of Diagnosibility and Opacity in Discrete Event Systems, Annual Reviews in Control, Elsevier, 2018.

[7] P. Ramadge and W. Wonham, The control of discrete-event systems. Proceedings of the IEEE, vol. 77, no. 1, 1989, pp. 81-98.

[8] E. De Santis and M. D. Di Benedetto, Observability and Diagnosability of Finite State Systems: A Unifying Framework. Automatica, vol. 81, 2017, pp. 115-122.

[9] A. Saboori and C. N. Hadjicostis, Notions of security and opacity in discrete event systems, 46th IEEE Conference on Decision and Control, 2007, pp. 5056-5061.

Switched ARX models: stability analysis and learning with guarantees

Vittorio De Iuliis, Francesco Smarra, Costanzo Manes, Alessandro D'Innocenzo

Extended Abstract

System identification has been described by Lennart Ljung as "the art and science of building mathematical models of dynamic systems from observed input-output data". Whilst the early developments of this field focused on estimating linear time-invariant models, which to some extent were also able to provide good accuracy dealing with mildly nonlinear dynamics, more recently the interest has shifted towards the problem of estimating dynamics to cope with large-scale systems in domains such as cyber-physical systems. Linear time-varying models or even nonlinear models have received significant attention from the research community. In particular, the class of switched models has offered an ideal choice due to the strong capability of such models to arbitrarily approximate complex nonlinear dynamics, and the availability of widespread methodologies for analysis and control purposes. The black-box identification problem is usually formulated on input-output data collected from a real system whose model is not available. Among general switching models, a significant attention has been devoted by the research community on the subclass of Switched AutoRegressive models with eXogenous inputs (switched ARX, or simply SARX). While SARX models are described in input-output form, both for analysis and control purposes, it may be interesting to represent them in state-space form.

This is indeed the strategy adopted by the recent contributions [1], [2], which introduce novel results on the analysis and estimation of SARX models, in the general case of multi-input multi-output (MIMO) systems. We survey such contributions starting from a stability analysis for SARX models under arbitrary switching and then show how the proposed results can be exploited to design learning algorithms with guaranteed stability. It is well known, indeed, that identification techniques can result in unstable models of stable systems due to high noise levels, plant disturbances, modeling error and finite sample constraints. The impact of this limitation, which has never been addressed for SARX models, may be negligible in a closed-loop regime, but preserving stability during an estimation procedure is a matter of consistency in terms of accuracy, and a fundamental requirement both in classical system identification and in recent learning-based methodologies.

The authors are with Dipartimento di Ingegneria e Scienze dell'Informazione, e Matematica, Università degli Studi dell'Aquila, Via Vetoio, 67100 Coppito (AQ), Italy (e-mail: vittorio.deiuliis@univaq.it)

Background on SARX models

A switched ARX model is a regressive model in input-output form described by:

$$y(k) = \Theta_{\sigma(k)}\phi(k) \tag{1}$$

where $y \in \mathbb{R}^q$ and $u \in \mathbb{R}^p$ are measured,

$$\phi(k) = [y(k-1)^\top \cdots y(k-\delta_y)^\top u(k)^\top \cdots u(k-\delta_u)^\top]^\top$$

is the vector of regressive terms, and $\Theta_{\sigma(k)} \in \mathbb{R}^{q\times[q\delta_y+p(\delta_u+1)]}$ is the switching matrix of parameters selected by $\sigma(k)$, with $\sigma : \mathbb{N}_0 \to \{1,\dots,h\}$.

Rewriting (1) as:

$$y(k) = [\Theta^y_{\sigma(k)}\Theta^u_{\sigma(k)}]\begin{bmatrix} y(k-1) \\ \vdots \\ y(k-\delta_y) \\ u(k-1) \\ \vdots \\ u(k-\delta_u)\end{bmatrix} + \Theta^{u_0}_{\sigma(k)}u(k) \tag{2}$$

and defining the state vector

$$x(k) = [y(k-1)^\top \cdots y(k-\delta_y)^\top u(k-1)^\top \cdots u(k-\delta_u)^\top]^\top \tag{3}$$

model (1) is realized in state-space form as follows:

$$\begin{aligned} x(k+1) &= A_{\sigma(k)}x(k) + B_{\sigma(k)}u(k) \\ y(k) &= C_{\sigma(k)}x(k) + D_{\sigma(k)}u(k) \end{aligned} \tag{4}$$

where:

$$A_{\sigma(k)} = \begin{bmatrix} \Theta^y_{\sigma(k)} & & \Theta^u_{\sigma(k)} & \\ I_{q(\delta_y-1)} & 0 & 0 & 0 \\ 0 & 0 & 0 & 0 \\ 0 & 0 & I_{p(\delta_u-1)} & 0 \end{bmatrix}, \tag{5}$$

$$B_{\sigma(k)} = \begin{bmatrix} \Theta^{u_0}_{\sigma(k)} \\ 0 \\ I_p \\ 0 \end{bmatrix}, \quad C_{\sigma(k)} = \begin{bmatrix} \Theta^y_{\sigma(k)} & \Theta^u_{\sigma(k)} \end{bmatrix}, \tag{6}$$

$$D_{\sigma(k)} = \Theta^{u_0}_{\sigma(k)}. \tag{7}$$

The identification problem is then solved jointly estimating matrices Θ_j selected by $\sigma(k) \in \{1, \dots, h\}$ and the switching rule σ. Also the the number h of sub-models selected by σ can be the object of the estimation, depending on the chosen technique and the class of models under investigation. The learning procedure is conducted starting from input-output measurements collected on the true system and it usually can be seen as a procedure consisting of two main steps: a clustering part, conducted under some technique, which divides i-o samples in regions; and a model-estimation part which builds a sub-model Θ_j (i.e., $\{A_j, B_j, C_j, D_j\}$) for each region. The second part is usually conducted using some variation of the least-squares method. A number of significant problems in identification and realization of SARX models are widely described in [3], [4]. Assessing some important properties (such as stability and stabilizability) of such models is challenging: the presence of switching dynamics requires sophisticated and computationally hard mathematical tools.

Contribution

The analysis we conduct in our work to prove stability results on SARX models and to constrain their estimation relies is built addressing the properties of a significant family of matrices: matrices in block companion form. Such matrices are known to arise in various theoretical and applicative domains such as delay systems and networked control systems, and constitute the auto-regressive part of the dynamical matrices of model (4).

Consider matrix A_j selected at time k by $\sigma(k) = j$. It is an upper block-triangular matrix, whose stability is only determined by the top-left block A_j^y:

$$A_j^y = \begin{bmatrix} \Theta_j^y & \\ I_{q(\delta_y-1)} & 0 \end{bmatrix} = \begin{bmatrix} \tilde{A}_{j,1} & \tilde{A}_{j,2} & \cdots & \tilde{A}_{j,\delta_y-1} & \tilde{A}_{j,\delta_y} \\ I_q & 0 & \cdots & 0 & 0 \\ 0 & I_q & \cdots & 0 & 0 \\ \vdots & \vdots & \ddots & \vdots & \vdots \\ 0 & 0 & \cdots & I_q & 0 \end{bmatrix}, \quad j = 1, \dots, h. \tag{8}$$

In fact, our works start showing that the stability of a system which arbitrarily switches among $\mathcal{A} = \{A_1, \dots, A_h\}$ is equivalent to the stability of the family of block companion matrices $\mathcal{A}^y = \{A_1^y, \dots, A_h^y\}$. The proof is obtained by algebraic considerations and exploiting the properties of the joint spectral radius (JSR), which is the key mathematical tool to analyze the stability of switching models. Moreover, due to the computational burden required to compute such JSR, and with the aim of obtaining simple stability conditions to constrain learning procedures, we show that a simple sufficient condition of arbitrary switching stability for MIMO SARX models (4) can be formulated by means of the existence of linear co-positive common Lyapunov functions (LCCLFs) on the dual family $(\mathcal{A}^y)^\top = \{(A_1^y)^\top, \dots, (A_h^y)^\top\}$, that is:

$$\exists v > 0 \ : \ |A_j^y|\, v < v, \quad j = 1, \dots, h, \tag{9}$$

where $|\cdot|$ stands for the component-wise absolute value of a matrix.

Indeed, we then show that an equivalent condition, at a much lower dimension, can be directly given on the matrices of the auto-regressive part Θ_j^y:

$$\exists v > 0 \ : \ \Big(\sum_{i=1}^{\delta_y} |\tilde{A}_{j,i}|\Big) v < v, \quad j = 1, \dots, h. \tag{10}$$

Condition (10) can be easily tested by means of Linear Programming, and can be adopted to constrain learning procedures so to only produce stable SARX models. When single-output models are considered (a subclass to which most of the literature is devoted), condition (9) is even more appealing, being equivalent to $\|\Theta_j^y\|_1 < 1$, which actually proves necessary and sufficient if Θ_j^y is a non-negative vector at all j [1].

Among the possible choices, we tested the conditions on a recent learning technique that leverages Regression Trees to derive switching models, showing remarkable predictive accuracy in real-life use cases [5]. The advantages of the novel technique are discussed to some extent and validated on a Building Automation System benchmark, showing better approximation capabilities with respect to the unconstrained methodology of [5], the k-LinReg algorithm of [6], and a family of nonlinear ARX models with wavelet nonlinearity.

References

[1] V. De Iuliis, F. Smarra, C. Manes, and A. D'Innocenzo, "On the stability of switched ARX models, with an application to learning via Regression Trees," *IFAC-PapersOnLine*, vol. 54, no. 5, pp. 61–66, 2021.

[2] ——, "Stability analysis of switched ARX models and application to learning with guarantees," *Nonlinear Analysis: Hybrid Systems*, 2022, to appear.

[3] A. Garulli, S. Paoletti, and A. Vicino, "A survey on switched and piecewise affine system identification," *IFAC Proceedings Volumes*, vol. 45, no. 16, pp. 344–355, 2012.

[4] S. Weiland, A. L. Juloski, and B. Vet, "On the equivalence of switched affine models and switched ARX models," in *Proceedings of the 45th IEEE Conference on Decision and Control*, 2006, pp. 2614–2618.

[5] F. Smarra, G. D. Di Girolamo, V. De Iuliis, A. Jain, R. Mangharam, and A. D'Innocenzo, "Data-driven switching modeling for MPC using Regression Trees and Random Forests," *Nonlinear Analysis: Hybrid Systems*, vol. 36, p. 100882, 2020.

[6] F. Lauer, "Estimating the probability of success of a simple algorithm for switched linear regression," *Nonlinear Analysis: Hybrid Systems*, vol. 8, pp. 31–47, 2013.

Internal Model-Based Online Optimization

Nicola Bastianello, Ruggero Carli, Sandro Zampieri

I. Online Optimization

In applications ranging from control, to signal processing, to machine learning, recent technological advances have made the class of *online optimization* problems of central importance [1], [2]. These problems are characterized by cost functions that vary over time, capturing the complexity of dynamic environments and changing optimization goals. Online problems require the design of solvers that can be applied in real time, with the objective of tracking the time-varying solution(s) within some precision.

Formally, an online problem is characterized by a discrete sequence of costs

$$\boldsymbol{x}_k^* = \arg\min_{\boldsymbol{x}\in\mathbb{R}^n} f_k(\boldsymbol{x}) \tag{1}$$

where a new cost is revealed every $T_\mathrm{s} > 0$ seconds, and where we assume that $\{f_k\}_{k\in\mathbb{N}}$ are $\underline{\lambda}$-strongly convex and $\bar{\lambda}$-smooth for any time $k \in \mathbb{N}$, with $0 < \underline{\lambda} \leq \bar{\lambda} < \infty$. Our goal then is to design online algorithms that track as closely as possible the optimal trajectory $\{\boldsymbol{x}_k^*\}_{k\in\mathbb{N}}$

A. *Unstructured* v. *structured*

We can classify online algorithms in two broad categories, *unstructured* and *structured* methods [2]. Unstructured algorithms are designed by repurposing methods from static optimization (say, gradient descent) by applying them to each problem in the sequence. In general we are able to prove their convergence to a neighborhood of the optimal trajectory, bounding its radius [1]. However, unstructured algorithms are in a sense passive with respect to the dynamic nature of online problems, since they treat each problem in the sequence as self-standing.

To remedy this fact, a broad part of the literature has been devoted to the design and analysis of *structured* algorithms, which aim to leverage knowledge of the problem in order to improve the performance by reducing the tracking error. Here we are interested in exploiting control-theoretical to design novel structured methods which can track the optimal trajectory with greater precision than unstructured methods, see [3].

II. Internal Model-Based Online Algorithm

We focus first on the *quadratic* problem

$$\boldsymbol{x}_k^* = \arg\min_{\boldsymbol{x}\in\mathbb{R}^n} f_k(\boldsymbol{x}) := \frac{1}{2}\boldsymbol{x}^\top \boldsymbol{A}\boldsymbol{x} + \langle \boldsymbol{b}_k, \boldsymbol{x}\rangle \tag{2}$$

N. Bastianello, R. Carli and S. Zampieri are with the Department of Information Engineering (DEI), University of Padova, Italy. nicola.bastianello@unipd.it, carlirug@dei.unipd.it, zampi@dei.unipd.it.

and we will later build on the insights gained in this particular case in order to solve more general problems. We assume to know a *model* of $\boldsymbol{b}_k$, specifically the *denominator* of its Z-transform[1]

$$\boldsymbol{B}(z) = \frac{\boldsymbol{B}_\mathrm{N}(z)}{B_\mathrm{D}(z)}, \quad B_\mathrm{D}(z) = z^m + \sum_{i=0}^{m-1} b_i z^i. \tag{3}$$

Tracking the optimal solution $\{\boldsymbol{x}_k^*\}_{k\in\mathbb{N}}$ can be achieved if $\boldsymbol{e}_k := -\nabla f_k(\boldsymbol{x}_k) \to 0$ as $k \to \infty$, where $\boldsymbol{x}_k$ is the output of our online algorithm. To this end, we employ the scheme in Figure 1, where we need to design the controller's Z-transform $C(z)$ in order to *(i)* achieve tracking and *(ii)* stabilize the feedback loop.

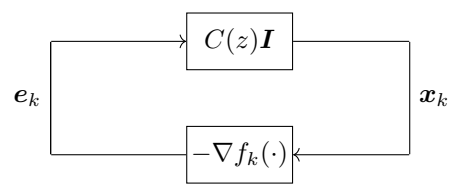

Fig. 1: The control scheme designed to solve (2) with time-varying linear term $\boldsymbol{b}_k$. Recall that $\nabla f_k(\boldsymbol{x}) = \boldsymbol{A}\boldsymbol{x} + \boldsymbol{b}_k$.

The first goal is attained by choosing the controller

$$C(z) = \frac{C_\mathrm{N}(z)}{B_\mathrm{D}(z)}, \quad \text{with} \quad C_\mathrm{N}(z) = \sum_{i=0}^{m-1} c_i z^i \tag{4}$$

where the denominator acts as *internal model* of $\boldsymbol{b}_k$. We now need to choose a nominator $C_\mathrm{N}(z)$ to guarantee stability. This problem can be translated into a *robust stability* problem, and (if it exists) we can design the controller by jointly solving two linear matrix inequalities that depend on $\underline{\lambda}$ and $\bar{\lambda}$, the strong convexity and smoothness moduli of f_k; see [3] for the details.

The resulting algorithm is characterized by

$$\boldsymbol{w}_{k+1} = \left(\begin{bmatrix} 0 & 1 & & \\ & & \ddots & \\ 0 & \cdots & 0 & 1 \\ -b_0 & \cdots & \cdots & -b_{m-1} \end{bmatrix} \otimes \boldsymbol{I} \right) \boldsymbol{w}_k + \begin{bmatrix} 0 \\ \vdots \\ 0 \\ 1 \end{bmatrix} \otimes \boldsymbol{e}_k \tag{5a}$$

$$\boldsymbol{x}_{k+1} = \left(\begin{bmatrix} c_0 & \cdots & c_{m-1} \end{bmatrix} \otimes \boldsymbol{I} \right) \boldsymbol{w}_{k+1} \tag{5b}$$

where, as defined above $\boldsymbol{e}_k = -\nabla f_k(\boldsymbol{x}_k) = -(\boldsymbol{A}\boldsymbol{x}_k + \boldsymbol{b}_k)$, and $\boldsymbol{w} \in \mathbb{R}^{nm}$ is a set of m auxiliary vectors. Notice that (5a) acts as internal model of $\boldsymbol{b}_k$.

[1] We *do not* assume to know the nominator.

A. Convergence results

The online algorithm (5) can indeed achieve exact tracking of the optimal trajectory of (2).

Proposition 1. *Consider problem* (2) *with* f_k *being* $\underline{\lambda}$*-strongly convex and* $\bar{\lambda}$*-smooth, and* $\boldsymbol{b}_k$ *having model* (3)*. Let* $\{\boldsymbol{x}_k\}_{k\in\mathbb{N}}$ *be defined by* (5)*, then it holds*

$$\limsup_{k\to\infty} \|\boldsymbol{x}_k - \boldsymbol{x}_k^*\| = 0.$$

While this result is promising, we remark that it requires exact knowledge of the denominator $B_{\mathrm{D}}(z)$ in (3). The following result shows that, even with an imperfect internal model, $\{\boldsymbol{x}_k^*\}_{k\in\mathbb{N}}$ can be tracked with some precision.

Proposition 2. *(Convergence with inexact model) Assume that algorithm* (5) *has access to the following,* inexact *model of* $B_{\mathrm{D}}(z)$ $\hat{B}_{\mathrm{D}}(z) = z^m + \sum_{i=0}^{m-1} \hat{b}_i z^i$*. Assume that there exists* $\beta > 0$ *such that, for any* $k \in \mathbb{N}$, $\|\boldsymbol{b}_k\| \leq \beta$*.*

Let $\{\boldsymbol{x}_k\}_{k\in\mathbb{N}}$ *be defined by* (5) *equipped with the inexact model, then it holds*

$$\limsup_{k\to\infty} \|\boldsymbol{x}_k - \boldsymbol{x}_k^*\| \leq C\beta \|\boldsymbol{d}\|$$

where $C > 0$[2] *and* $\boldsymbol{d} = \begin{bmatrix} b_0 - \hat{b}_0 & \cdots & b_{m-1} - \hat{b}_{m-1} \end{bmatrix}$.

B. Extensions

The previous results only apply to the online quadratic problem (2), and in this section we want to discuss the extension of our approach to more general problems.

It is clear that the scheme of Figure 1 can be applied to any problem (1), since it only requires an evaluation of the gradient. Of course, in this case $\boldsymbol{e}_k$ is not linear in $\boldsymbol{x}$, and stabilizing the loop becomes a non-linear control problem. However, we can still choose to apply the online algorithm (5), in which the controller is designed by choosing an approximate linear model for the non-linear $\boldsymbol{e}_k$; see [3]. The following numerical results show that this approach can still outperform unstructured methods, pointing to promising future research.

III. Numerical Results

A. Quadratic

We consider first the online quadratic problem (2), and in Figure 2 we report the tracking error $\|\boldsymbol{x}_k - \boldsymbol{x}_k^*\|$ of (5) against that of the unstructured online gradient $\boldsymbol{x}_{k+1} = \boldsymbol{x}_k - \alpha\nabla f_k(\boldsymbol{x}_k)$, when different models for the linear term are used. As predicted by the theoretical results, our control-based (structured) method outperforms the unstructured online gradient, achieving practically zero tracking error.

B. Non-quadratic

We consider now a more general, non-quadratic problem characterized by

$$f_k(\boldsymbol{x}) = \frac{1}{2}\boldsymbol{x}^\top \boldsymbol{A}\boldsymbol{x} + \langle \boldsymbol{b}, \boldsymbol{x}\rangle + \sin(\omega k T_{\mathrm{s}}) \log\left(1 + \exp\langle \boldsymbol{c}, \boldsymbol{x}\rangle\right). \tag{6}$$

[2]See [3] for a precise characterization.

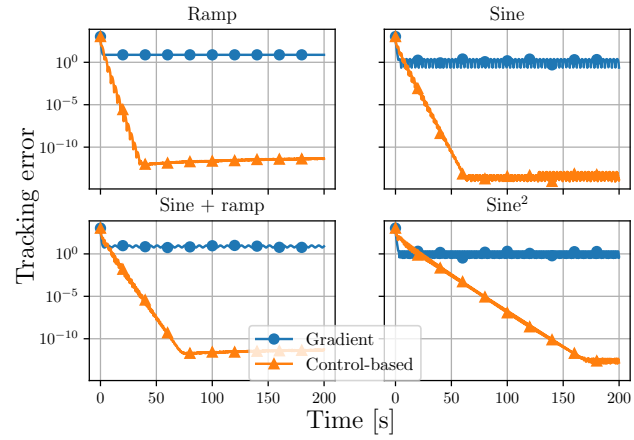

Fig. 2: Tracking error of the proposed algorithms applied to (2) with different models of $\boldsymbol{b}_k$.

In Figure 3 we report the tracking error of the proposed algorithm against the online gradient. In particular, the figure is derived by applying (5) with three different approximate linear models of order $L = 1, 2, 3$.

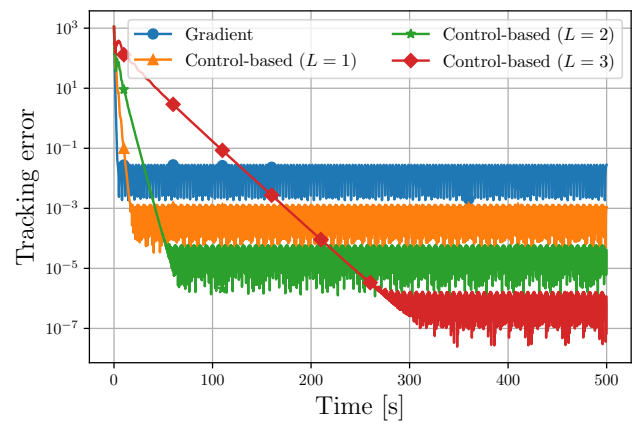

Fig. 3: Tracking error for the proposed algorithms applied to the non-quadratic (1) with (6).

Clearly, the proposed algorithm (5) outperforms the unstructured online gradient also for non-quadratic problems, with the performance being better the more complex the approximate internal model is.

References

[1] E. Dall'Anese, A. Simonetto, S. Becker, and L. Madden, "Optimization and Learning With Information Streams: Time-varying algorithms and applications," *IEEE Signal Processing Magazine*, vol. 37, no. 3, pp. 71–83, May 2020.

[2] A. Simonetto, E. Dall'Anese, S. Paternain, G. Leus, and G. B. Giannakis, "Time-Varying Convex Optimization: Time-Structured Algorithms and Applications," *Proceedings of the IEEE*, vol. 108, no. 11, pp. 2032–2048, Nov. 2020.

[3] N. Bastianello, R. Carli, and S. Zampieri, "Internal Model-Based Online Optimization," May 2022, arXiv:2205.13932. [Online]. Available: http://arxiv.org/abs/2205.13932

Bearing Rigidity Theory Applied to Robotic Formations

Giulia Michieletto and Angelo Cenedese

EXTENDED ABSTRACT

According to the most general definition, rigidity theory aims at studying the *stiffness* of a given system, understood as a reaction to an induced deformation.

Originally, the analysis of such a property applied to *physical* multi-element structures made up of different units interconnected by flexible linkages or hinges [1]. However, rigidity theory has recently enlarged its focus toward multi-agent systems wherein the connections among the group components are *virtual*, and represent sensing relations and sensing capabilities among the different units (see, for instance, [2] and the references therein). In this context, the rigidity properties leverage the establishment and/or the preservation of the agents (e.g., robots, with their actuation and sensing capabilities) interplay so that the available measurements are treated as constraints on the system dynamics. In particular, the literature discerns between *distance rigidity* and *bearing rigidity*. In the former case, the rigidity properties of a given formation rest on the range measurements gathered by the agents with respect to their neighbors (e.g., through onboard ToF sensors). Bearing rigidity, instead, refers to the case in which agents are equipped with sensors able to provide angular/bearing measurements (e.g., onboard cameras).

When dealing with *distance rigidity* theory applied to robotic formations, these are generally represented by means of *bar-and-joint models* where robots are modeled as points joined by bars whose lengths enforce the existing relative distance constraints [3], [4]. This constitutes a close contact point with the original rigidity theory application field, and for this reason the literature devoted to distance rigidity concepts applied to robotic multi-agent systems is wider as compared to the bearing one, which represents a more recent branch of knowledge. Nonetheless, the study of bearing rigidity theory is nowadays encouraged by the emerging control tasks for robotic formations and the wide employment of sensing systems that provide the related exploitable measurements (e.g. cameras). Indeed, the bearing rigidity framework fits for applications connected to the motion control of mobile robots and to the sensors cooperation for localization, exploration, mapping and tracking of a target.

When investigating the *bearing rigidity* properties of a robotic formation, the considered multi-agent system is typically modeled as a *framework* $(\mathcal{G}, \mathbf{x})$ embedded in a differential manifold $\bar{\mathcal{D}}$. The (directed or undirected) graph $\mathcal{G}$ describes the robots interplay so that any edge $e_k = e_{ij}$, $k \in \{1 \dots m\}$, between the i-th and j-th nodes, $i, j \in \{1 \dots n\}, i \neq j$, represents the capability of the i-th robot of retrieving the bearing measurement with respect to its j-th neighbor and eventually viceversa. The formation configuration $\mathbf{x} \in \bar{\mathcal{D}}$ (configuration domain), instead, collects the information on the robots controllable state depending on the adopted dynamic model. Hence, for homogeneous formations whose $n \geq 3$ components have the same actuation capabilities, it holds that $\bar{\mathcal{D}} = \mathcal{D}^n$ with $\mathcal{D}$ being the same controllable state space of any robot.

Along this direction, in [5] the bearing rigidity proprieties are discussed for homogeneous formations of n robots represented as *particle points* acting in 2D/3D space: these are modeled as frameworks in the Euclidean space $\mathbb{R}^{dn}$, with $d \in \{2, 3\}$. Dealing with more realistic scenarios, instead, in [6]–[10] robots are modeled as *rigid bodies* having a certain position and orientation with respect to a common global frame (which is generally assumed to be unavailable to the group) and a certain number of controllable degrees of freedom (dofs). In particular, in [6] bearing rigid theory is coded for homogeneous formations of robots having three dofs. This is, for instance, the case of a group of n ground robots treated as unicycle vehicles, which can be modeled as framework embedded in the Special Euclidean space $SE(2)^n = \mathbb{R}^{2n} \times SO(2)^n$. In [7] and [8], the study is extended to the 3D space although limiting the robots attitude kinematics to rotations along only one axis so that the controllable state of any formation component belongs to the four dimensional manifold $\mathcal{D} = \mathbb{R}^3 \times \mathbb{S}^1$. In particular, the attention is focused on homogeneous formation of quadrotors whose rotation dynamics is restricted to the rotations around the vertical yaw axis. Then, in [9], [10], fully actuated formations are considered by assuming to deal with systems of n robots having six independently controllable dofs, as, for instance, groups of tilted multi-rotor UAVs. In detail, in [9], the robotic formations are modeled as frameworks embedded in $\bar{\mathcal{D}} = SE(3)^n$, since the robots orientation is represented through rotation matrices; while in [10] the formation configuration is defined in $\bar{\mathcal{D}} = \mathbb{R}^{3n} \times (\mathbb{S}^3)^n$ due to the adoption of the quaternion attitude representation. Finally, a unified view on the bearing rigidity concepts is provided in [11], resting on the fact that any robot controllable space can be interpreted as a generic manifold embedded in $SE(3)$. Interestingly, this formalization yields a general groundwork to treat the rigidity properties of homogeneous formations modeled as framework in any manifold and paving the way towards extended methodological challenges to be faced and

G.Michieletto is with DTG - Department of Management and Engineering, University of Padova, Italy.
A.Cenedese is with DEI - Department of Information Engineering, University of Padova, Italy.
Contacts: giulia.michieletto@unipd.it,angelo.cenedese@unipd.it

suggestive application scenarios, as will be detailed later on.

From a more technical perspective, in all the aforementioned works, it is proved that necessary and sufficient condition to guarantee the rigidity properties of a given formation rests upon the rank of a suitably defined matrix summarizing the involved direction constraints on the interacting robots and generally called *(bearing) rigidity matrix*.

In detail, introducing the vector $\mathbf{b}_{\mathcal{G}}(\mathbf{x}) \in \bar{\mathcal{M}}$ (measurement domain) stacking all the available m bearing measurements in the considered formation and the vector $\mathbf{u} \in \bar{\mathcal{U}}$ (variation domain) depending on the robots controllable inputs so that $\dot{\mathbf{x}} = \mathbf{D}(\mathbf{x})\mathbf{u}$ with $\mathbf{D}(\mathbf{x}) \in \mathbb{R}^{|\bar{\mathcal{D}}|\times|\bar{\mathcal{U}}|}$, the rigidity matrix $\mathbf{B}_{\mathcal{G}}(\mathbf{x}) \in \mathbb{R}^{|\bar{\mathcal{M}}|\times|\bar{\mathcal{U}}|}$ describes the relation between $\mathbf{u}$ and the time-derivative of $\mathbf{b}_{\mathcal{G}}(\mathbf{x})$, linking the measurements dynamics to the system dynamics input. The null space of such a matrix outlines the configuration variations, i.e., the formation motions (called infinitesimal variations), which guarantee the preservation of the robots sensing interplay. When the set of the infinitesimal variations coincides with the null space of the rigidity matrix computed in correspondence to the same formation configuration $\mathbf{x}$ but accounting for the complete graph $\mathcal{K}$ associated to $\mathcal{G}$, then shape preservation is also ensured. In this case, the framework $(\mathcal{G}, \mathbf{x})$ models a so-called *infinitesimal bearing rigid* formation.

The rigidity matrix constitutes also a key synthesis tool to face *estimation and control issues* for the robotic multi-agent systems characterized by bearing sensing capabilities. Several recent works, indeed, propose bearing rigidity-based localization, formation stabilization and coordinated motion solutions for robotic formations. For instance, in [12], a distributed rigidity-based control law is designed to employ only bearing information for stabilizing a given formation of ground robots modeled as unicycle vehicles according to a set of desired measurements. A twofold control goal is faced in [13], where rigidity notions are exploited to steer a quadrotor group toward a desired formation, and to drive it along the motions preserving the formation shape. The same double control problem is tackled in [10] dealing with fully actuated UAV formations. In [13], it is also proposed a bearing-only localization algorithm having proved convergence guarantees; and a similar result is presented in [6] for a n-robot formation modeled as a framework in $SE(2)^n$.

Remarkably, the role of the rigidity matrix turns out to be crucial. Indeed, it characterizes the dynamics of the formation configuration estimation $\hat{\mathbf{x}} \in \bar{\mathcal{D}}$ when dealing with localization tasks: it generally holds that $\dot{\hat{\mathbf{x}}} = \mathbf{D}(\hat{\mathbf{x}})\ k_e \mathbf{B}_{\mathcal{G}}^{\top}(\hat{\mathbf{x}})\mathbf{b}_{\mathcal{G}}(\mathbf{x})$, where $k_e \in \mathbb{R}^+$ is a tunable gain. Furthermore, the rigidity matrix is involved in the definition of the *formation stabilization* (fs) control input $\mathbf{u}_{fs} = k_c \mathbf{B}_{\mathcal{G}}(\mathbf{x})^{\top}\mathbf{b}_{\mathcal{G}}(\mathbf{x}^d)$, whose application ensures the convergence toward a desired configuration $\mathbf{x}^d \in \bar{\mathcal{D}}$ modulated by the tunable gain $k_c \in \mathbb{R}^+$, and of the *coordinated motion* (cm) control input $\mathbf{u}_{cm} \in \text{null}(\mathbf{B}_{\mathcal{G}}(\mathbf{x}))$, which guarantees the shape preservation for bearing infinitesimal formations.

There still remain unexplored methodological aspects within rigidity theory that could unleash its potential in the development of distributed efficient and safe solutions for robotic formation scenarios. In this sense, our research directions include the following topics:

- *Heterogeneous multi-agent systems*: although most of the existing literature devoted to bearing rigidity is focused on homogeneous formations, many emerging tasks encourage the employment of robots having different actuation capabilities. The unified view proposed in [11] turns out to be useful to compute the rigidity matrix, and a first example of its application in solving heterogeneous formation control problems is given in [14] where a group of ground vehicles and aerial platforms is taken into account.
- *Role of noise*: in real world scenarios, bearing measurements are typically affected by noise. This reflects into the effectiveness of the bearing rigidity based estimation of formation configuration, as well as in the performance of the formation stabilization controllers.
- *New perspective in the rigidity features analysis*: observing the rigidity matrix spectral properties instead of merely the rank, rigidity can be interpreted as a more complex feature than a binary property entailing a shaded characterization of the formations properties.

References

[1] L. Asimow and B. Roth, "The rigidity of graphs," *Transactions of the American Mathematical Society*, vol. 245, pp. 279–289, 1978.

[2] H.-S. Ahn, *Formation Control: Approaches to Distributed Agents*. Springer Int. Publishing, 2020.

[3] M. F. Thorpe and P. M. Duxbury, *Rigidity theory and applications*. Springer Science & Business Media, 1999.

[4] J. Sidman and A. S. John, "The rigidity of frameworks: Theory and applications," *Notices of the AMS*, vol. 64, no. 9, 2017.

[5] S. Zhao and D. Zelazo, "Bearing rigidity and almost global bearing-only formation stabilization," *IEEE Transactions on Automatic Control*, vol. 61, no. 5, pp. 1255–1268, 2015.

[6] D. Zelazo, A. Franchi, and P. R. Giordano, "Rigidity theory in SE(2) for unscaled relative position estimation using only bearing measurements," in *European Control Conference (ECC)*, 2014, pp. 2703–2708.

[7] A. Franchi, C. Masone, V. Grabe, M. Ryll, H. H. Bülthoff, and P. R. Giordano, "Modeling and control of UAV bearing formations with bilateral high-level steering," *The International Journal of Robotics Research*, vol. 31, no. 12, pp. 1504–1525, 2012.

[8] R. Spica and P. R. Giordano, "Active decentralized scale estimation for bearing-based localization," in *IEEE/RSJ International Conference on Intelligent Robots and Systems (IROS)*, 2016, pp. 5084–5091.

[9] G. Michieletto, A. Cenedese, and A. Franchi, "Bearing rigidity theory in SE(3)," in *IEEE 55th Conference on Decision and Control (CDC)*, 2016, pp. 5950–5955.

[10] G. Michieletto and A. Cenedese, "Formation control for fully actuated systems: A quaternion-based bearing rigidity approach," in *18th European Control Conference (ECC)*, 2019, pp. 107–112.

[11] G. Michieletto, A. Cenedese, and D. Zelazo, "A unified dissertation on bearing rigidity theory," *IEEE Transactions on Control of Network Systems*, vol. 8, no. 4, pp. 1624–1636, 2021.

[12] D. Zelazo, P. R. Giordano, and A. Franchi, "Bearing-only formation control using an SE(2) rigidity theory," in *54th IEEE Conference on Decision and Control (CDC)*, 2015, pp. 6121–6126.

[13] F. Schiano, A. Franchi, D. Zelazo, and P. R. Giordano, "A rigidity-based decentralized bearing formation controller for groups of quadrotor UAVs," in *IEEE/RSJ International Conference on Intelligent Robots and Systems (IROS)*, 2016, pp. 5099–5106.

[14] B. Pozzan, G. Michieletto, A. Cenedese, and D. Zelazo, "Heterogeneous formation control: a bearing rigidity approach," in *60th IEEE Conference on Decision and Control (CDC)*, 2021, pp. 6451–6456.

Distributed control invariant set: the linear affine case

Davide Liuzza, Angel Molina Acosta, Paolo Falcone, Luigi Glielmo

---

An active research topic in the control community is the analysis and control of large-scale dynamical systems that arise when various subsystems are interconnected to form a complex one. Invariance is a well-studied property for (small-scale) dynamical systems. Control invariant (CI) sets are such that if the state of the system starts inside a CI set, then the state can be controlled to remain in said set for all future time by means of an admissible control input. For systems subject to disturbances, robust control invariant (RCI) sets provide the same guarantee in the face of disturbances. The maximal RCI set is the largest RCI possible inside a given region of the state space.

For discrete-time, linear, time-invariant systems subject to polyhedral constraints and bounded disturbances, the maximal RCI set can be determined exactly via a geometric approach that recursively computes the one-step backward reachable set [1]. This method relies on operations over polyhedra such as Minkowski sum and Pontryagin difference. These operations have in the worst case an exponential complexity that increases with the number of constraints and dimension of the polyhedra. Thus, computing the maximal RCI set for high-order systems, such as large-scale systems, can become prohibitively complex with the aforementioned geometric approach.

In this paper we present a novel method for decentralized computation of the maximal RCI set for large-scale systems with linear affine dynamics of arbitrary order subject to polytopic constraints and bounded additive disturbance. For this relevant class of systems, the paper customizes the general and abstract theory proposed in [2], where a theoretical equivalence is found between a centralized backward reachability problem for large-scale systems and its distributed counterpart. The results of this paper are applicable to linear systems that are interconnected via dynamic coupling among their states and/or inputs, as well as coupling via static constraints. No additional requirements or assumptions are made on the dynamical systems, the constraints and the network topology.

Our method relies on an iterative procedure to compute the one-step backward

reachable set in a distributed fashion. We propose an implicit representation of the backward reachable set as a polytope described with an algebraic system of equalities and inequalities. The nodes in the network of the large-scale system communicate constraints to their neighbours and then conduct specific operations on polytopic sets.

The fundamental concept behind the methods in this paper is the notion of distributed extrusion generated sets. Such sets are the result of an iterative exchange of information among the nodes in the network. Each node collects constraints over an appropriate subset of states and inputs and communicates those to the neighbouring nodes. Operations like extrusion, intersection, and projection are applied on the polytopic sets. This procedure converges to distributed sets that contain the minimum amount of information required to reconstruct the centralized set of constraints for the overall system.

An attractive feature of our approach is that it provides an equivalent result to that obtained via centralized computation of RCI sets but with fully decentralized operations. Each node in the network is provided with the minimum amount of information required to reconstruct the centralized RCI set for the large-scale system. Our method introduces no additional conservativeness. The distributed RCI set for the overall large-scale system is, by construction, the maximal one.

A numerical example is discussed to illustrate the advantages of the proposed method. In said example, a network of second order systems are coupled into a ring topology. Even for the low number of nodes and low order of the systems, computation of the maximal robust control invariant set in a centralized fashion proved to be intractable, while our distributed approach succeeded in the task.

References

[1] F. Borrelli, A. Bemporad, and M. Morari. *Predictive Control for Linear and Hybrid Systems.* Cambridge University Press, 2017.

[2] D Liuzza, Paolo Falcone, Massimo Tipaldi, and Luigi Glielmo. On the distributed backward reachability problem for large scale systems, 2021. http://arxiv.org/abs/2109.04856.

A new connection protocol for multi-consensus of discrete-time and sampled-data systems

Mattia Mattioni, Salvatore Monaco

Dipartimento di Ingegneria Informatica, Automatica e Gestionale A. Ruberti *(Università degli Studi di Roma La Sapienza), via Ariosto 25, 00185 Rome, Italy*
email: `mattia.mattioni@uniroma1.it, salvatore.monaco@uniroma1.it`

Dorothée Normand-Cyrot

Laboratoire de Signaux et Systèmes (L2S, CNRS and Univ. Paris-Saclay*); 3, Rue Joliot Curie, 91192, Gif-sur-Yvette, France email:*
`dorothee.normand-cyrot@centralesupelec.fr`

Abstract

In this presentation, a new connection protocol for consensus of multi-agent discrete-time systems under a general communication graph is proposed. In particular, the coupling is realized based on the outputs making each agent passive in the u-average sense so guaranteeing convergence to the agreement steady-state, with no need of mitigating the coupling gain, as typically done in concerned literature. The proposed connection rule is shown to apply for network dynamics under aperiodic sampling when the sampling sequence is known to all agents.

Keywords: Linear systems; Network analysis and control; Sampled-data control.

Consensus of multi-agent systems is nowadays fundamental as embedding different control problems spanning from several disciplines (e.g., Anderson and Ye (2019); Andreasson et al. (2014); You et al. (2009)). It is well known that, in general, when dynamical units exchange information through a communication graph, clusters arise and, under particular coupling functions, the corresponding trajectories might asymptotically converge to common behaviors (that is, multiconsensus Li et al. (2010); Mattioni and Monaco (2022)); such clusters and the number of consensuses are uniquely determined by the topology of the graph through the notion of almost equitable partitions.

In this setting, when considering scalar continuous-time integrator as agents of the network, the common neighbor-based coupling protocol Olfati-Saber et al. (2007); Monaco and Ricciardi Celsi (2019) ensures all agents converge to multi-consensus despite the strength of the connection. However, this does not hold for discrete-time systems in general, even when considering integrator-like units. As a matter of fact in this case, under the standard protocol, the coupling strength (i.e., the gain weighting the influence of the network on each agent) needs to be suitably set to ensure convergence to the agreement steady-state even when the network topology is fixed over time (e.g., Jadbabaie et al. (2003); Chen et al. (2011)). This results in conservative values for the gain which are generally inversely proportional to either the largest eigenvalue of the Laplacian (which must be known to all agents) or, alternatively, the number of agents involved in the network. Accordingly, the larger the network and the corresponding connectivity, the smallest is the necessary coupling gain which must be fixed for ensuring consensus so implying that the influence of the network over each agent must be significantly mitigated. This is not desirable in practice as discrete-time networks embed several classes of multi-agent systems as, to cite a few, communication systems and opinion dynamics Proskurnikov and Tempo (2017); Pietrabissa and Suraci (2017) for which the coupling strength of the network cannot be fixed small a priori, for both modeling and control reasons.

Motivated by these arguments, the objective of this presentation is to provide a new coupling protocol for discrete-time multi-agent systems forcing all agents to a common multi-consensus (uniquely fixed by the communication topology) despite the value of the interconnection strength which might be then tuned to control the convergence rate. The underlying idea is that, when considering integrator continuous-time dynamics, consensus is generally guaranteed since the neighbor-based interconnection is realized via a passive map for each agent. Unfortunately, this is not true in the discrete-time context when exploiting the same connection rule. The following question naturally arises: how to realize the neighbor-based connection via new suitably defined mappings guaranteeing consensus?

In detail, based the goal of this presentation is threefold.

(i) Based on the notion of average passivity introduced in Monaco and Normand-Cyrot (2011) for discrete-time systems at large, we construct a new neighbor-based coupling protocol by replacing the states of each agent with a new average passivating function which is directly depend-

ing on the coupling terms as well. The corresponding discrete-time network is proved to evolve with a new Laplacian-like matrix L_d which is structurally equivalent to the standard Laplacian L associated to the communication graph.

(*ii*) Under the proposed coupling, all agents asymptotically converge to the multi-consensus uniquely dictated by the communication graph (via the Laplacian) and the corresponding initial condition despite the connection strength. This extends the results in Monaco and Ricciardi Celsi (2019) and overcomes the need of small coupling gains Jadbabaie et al. (2003); Olfati-Saber et al. (2007).

(*iii*) The results are generalized to network agents under aperiodic (but synchronous) sampling under the assumption of known sampling sequences; i.e., when agents exchange information only at discrete-time instants sporadically spread over time. The proposed protocol allows large coupling strength and sampling periods, contrarily to the usual one (e.g., Hayashida et al. (2017); Mattioni (2020)).

More in detail, we first consider a multi-agent system exchanging information via a communication unweighted digraph $\mathcal{G} = (\mathcal{V}, \mathcal{E})$ where each vertex $\nu_i \in \mathcal{V}$ is a dynamical unit of the form

$$x_i(k+1) = x_i(k) + u_i(k) \tag{1}$$

with $x_i \in \mathbb{R}$ the state and $u_i \in \mathbb{R}$ the coupling terms. As well-known Jadbabaie et al. (2003); Olfati-Saber et al. (2007), the usual coupling rule

$$u_i = -\kappa \sum_{j:\nu_j \in \mathcal{N}(\nu_i)} (x_i - x_j) \tag{2}$$

ensures that the network system

$$x(k+1) = (I - \kappa L)x(k)$$

converges to the multi-consensus dictated by $\mathcal{G}$ provided that the coupling strength κ is small enough; namely, it must verify

$$\kappa < \frac{1}{2\lambda^\star}, \quad \lambda^\star = \max_{\lambda > 0}\{\lambda \in \sigma\{L\}\}.$$

The question we address is hence the following one.

Given the agent dynamics (1), is it possible to define a new discrete-time coupling rule (or consensus protocol)

$$u_i = -\kappa \sum_{j:\nu_j \in \mathcal{N}(\nu_i)} (y_i - y_j) \tag{3}$$

and a suitably defined output $y_i \in \mathbb{R}$, so that the corresponding multi-agent system converges to the (multi-)consensus associated to $\mathcal{G}$ for all $\kappa > 0$?

The answer we provide relies on passivity arguments for discrete-time systems; namely, we redefine the consensus protocol by defining the interconnection variable as a passifying output for all agents Monaco and Normand-Cyrot (2011). Based on this, we show that the new protocol for consensus can be fruitfully applied to sampled-data dynamics. In this latter case, we consider a network of N dynamical agents

$$\dot{x}_i(t) = u_i(t_k), \quad t \in [t_k, t_{k+1}) \tag{4}$$

with unweighted digraph $\mathcal{G}$. Let us assume that all agents exchange information at discrete-time instants $t_k \in \Delta$ and $\Delta = \{t_0, t_1, \dots\}$ the sampling sequence with bounded sampling periods $\delta_k := t_{k+1} - t_k \in [\delta_m, \delta_M]$ for some $\delta_M \geq \delta_m > 0$ and $k \geq 0$. Then, the sampled-data coupling protocol $u_i(k) := u_i(t_k)$ for $t_k \in \Delta$ defined starting from (3) as

$$u_i(t_k) = -\kappa \sum_{j:\nu_j \in \mathcal{N}(\nu_i)} (y_i(t_k) - y_j(t_k))$$

guarantees convergence to consensus independently on the sampling period and for all $\kappa > 0$.

A simulated example

Consider a network of $N = 8$ agents under the communication graph $\mathcal{G}$ with Laplacian

$$L = \begin{pmatrix} 1 & -1 & 0 & 0 & 0 & 0 & 0 & 0 \\ -1 & 1 & 0 & 0 & 0 & 0 & 0 & 0 \\ -1 & 0 & 1 & 0 & 0 & 0 & 0 & 0 \\ 0 & 0 & 0 & 1 & -1 & 0 & 0 & 0 \\ 0 & 0 & 0 & -1 & 1 & 0 & 0 & 0 \\ -1 & 0 & 0 & -1 & 0 & 3 & -1 & 0 \\ 0 & 0 & -1 & 0 & -1 & -1 & 3 & 0 \\ -1 & -1 & 0 & -1 & 0 & 0 & -1 & 4 \end{pmatrix}$$

and, in general, 4 consensuses. Simulations are reported in Figure 1) and are aimed at comparing the cases in which agents are: continuous-time integrators (for a benchmark behavior); sampled-data integrators under aperiodic sampling with $\delta_m = 0.1$ and $\delta_M = 2$ seconds; discrete-time integrators. In the latter case, two situations are reported: the network under the standard coupling; the network under the proposed coupling rule. In all scenarios, consensuses are spread according to the following clusters: $\rho_1 = \{\nu_1, \nu_2, \nu_3\}$, $\rho_2 = \{\nu_4, \nu_5\}$, $\rho_3 = \{\nu_6, \nu_7\}$ and $\rho_4 = \{\nu_8\}$. The results of the simulations are reported in Figure 1 when setting in all cases $\kappa = 1$ and initial conditions $x_i(0) = i$, for $i = 1, \ldots, 8$ so getting $x_s^1 = \frac{3}{2}$, $x_s^2 = \frac{9}{2}$, $x_s^{\delta,1} = 3$ and $x_s^{\delta,2} = \frac{21}{8}$. When using standard coupling, consensus is not guaranteed for $\kappa \geq \frac{1}{2}$ contrarily to the case in which the proposed connection is introduced.

References

Anderson, B.D., Ye, M., 2019. Recent advances in the modelling and analysis of opinion dynamics on influence networks. Int. Journal of Automation and Computing 16, 129–149.

Andreasson, M., Dimarogonas, D., Sandberg, H., Johansson, K., 2014. Distributed control of networked dynamical systems: static feedback, integral action and consensus. IEEE Transactions on Automatic Control 59, 1750–1764.

Chen, Y., Lü, J., Han, F., Yu, X., 2011. On the cluster consensus of discrete-time multi-agent systems. Systems & Control Letters 60, 517–523.

Hayashida, Y., Hetel, L., Oguchi, T., Richard, J.P., 2017. Stability of sampled-data systems with uncertain time-varying delays and its application to consensus control of multi-agent systems. IFAC-PapersOnLine 50, 1257–1262.

Jadbabaie, A., Lin, J., Morse, A.S., 2003. Coordination of groups of mobile autonomous agents using nearest neighbor rules. IEEE Transactions on Automatic Control 48, 988–1001.

Li, Z., Duan, Z., Chen, G., Huang, L., 2010. Consensus of multiagent systems and synchronization of complex networks: A unified viewpoint. IEEE Trans. on Circuits and Systems I: Regular Papers 57, 213–224.

Mattioni, M., 2020. On multiconsensus of multi-agent systems under aperiodic and asynchronous sampling. IEEE Control Systems Letters 4, 839–844.

Mattioni, M., Monaco, S., 2022. Cluster partitioning of heterogeneous multi-agent systems. Automatica 138, 110136.

Monaco, S., Normand-Cyrot, D., 2011. Nonlinear average passivity and stabilizing controllers in discrete time. Systems & Control Letters 60, 431–439.

Monaco, S., Ricciardi Celsi, L., 2019. On multi-consensus and almost equitable graph partitions. Automatica 103, 53–61.

Olfati-Saber, R., Fax, J.A., Murray, R.M., 2007. Consensus and cooperation in networked multi-agent systems. Proceedings of the IEEE 95, 215–233.

Pietrabissa, A., Suraci, V., 2017. Wardrop equilibrium on time-varying graphs. Automatica 84, 159–165.

Proskurnikov, A.V., Tempo, R., 2017. A tutorial on modeling and analysis of dynamic social networks. part i. Annual Reviews in Control 43, 65–79.

You, S., Kwon, D., Park, Y., Kim, S., Chung, M., , Kim, C., 2009. Collective behaviors of two-component swarms. Journal of Theoretical Biology 261, 494–500.

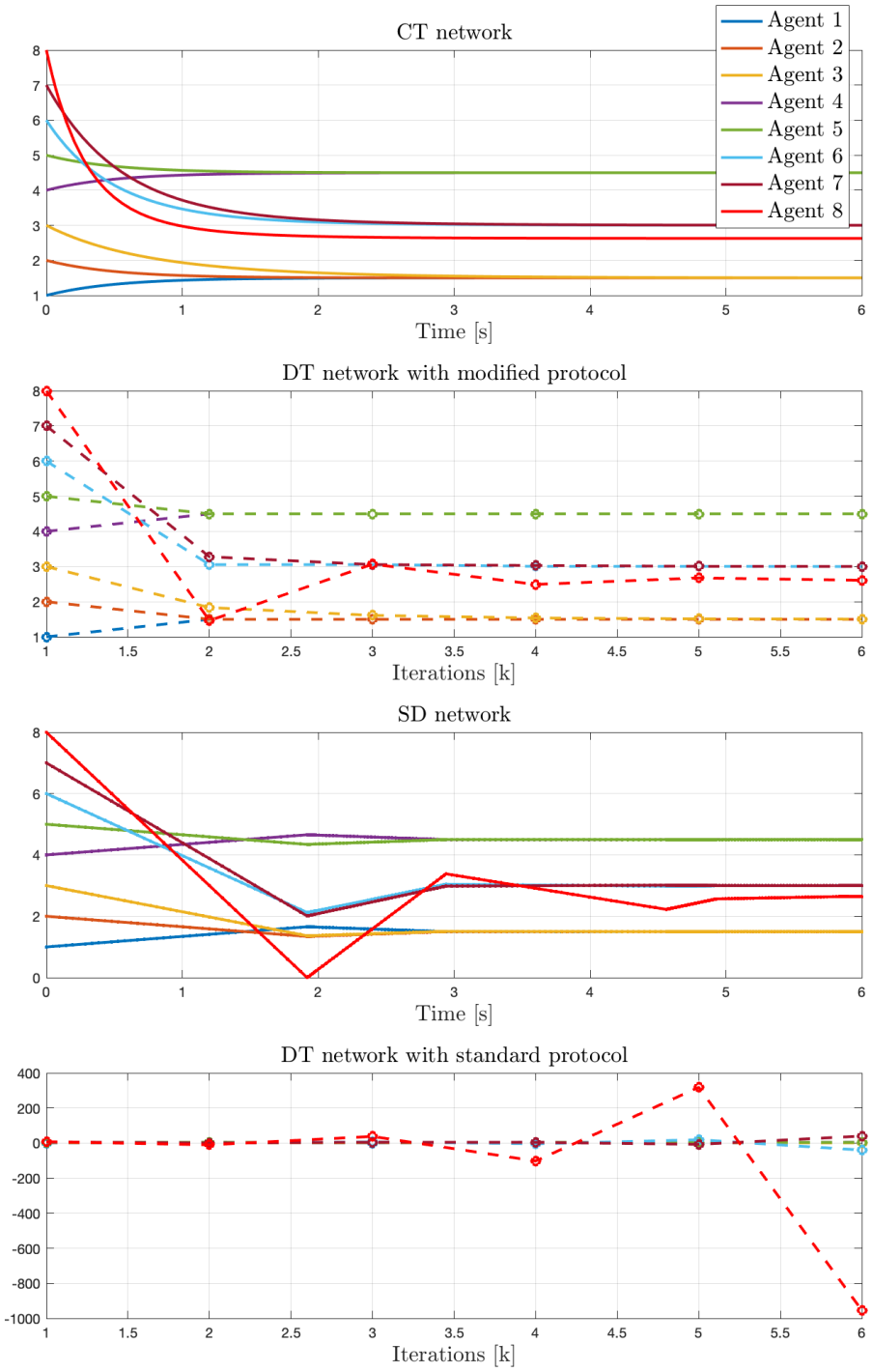

Figure 1: $\kappa = 1$, $x_i(0) = i$ for $i = 1, \ldots, 8$.

LS-SVM Identification of LPV Systems: Solution in Primal and Dual Space

Luca Cavanini[1], Francesco Ferracuti[2], Sauro Longhi[2] and Andrea Monteriù[2]

***Abstract*—Least Squares Support Vector Machine (LS-SVM) has been recently applied to non-parametric identification of Linear Parameter Varying (LPV) systems, described by the AutoRegressive with eXogenous input (ARX) structure and State-Space (SS) structure. Although the LS-SVM identification of LPV systems is mostly solved in its dual form, the problem can also be solved in the primal space by estimating a finite-dimensional feature map. Firstly, this paper compares the solution of LPV-ARX identification in primal and dual space. Secondly, the LPV identification is designed to handle very large data sets, since the finite-dimensional feature map allows computing of a sparse approximation by using only a subsample of selected support vectors from the entire data set. The advantage of the solution in primal space is that one can easily handle nonlinear estimation problems and obtain a low dimension solution reducing the computational time of the testing stage.**

I. Short Introduction

System identification in general is concerned with the identification of dynamic models from only the measurements of input/output signals. In particular, black-box models allow gathering nonlinear relationships using different approaches including machine learning techniques [1], [2]. Among non-parametric approaches, the LS-SVM framework [2] presents a way to bypass the difficulties associated with the selection of basis functions in LPV system identification. An LS-SVM-based method has been proposed in [3] to identify LPV-ARX models and a similar approach is also used to identify LPV-SS models [4]. Although the LPV system identification by LS-SVM framework is mostly solved in dual form, this paper present the estimation of LPV-ARX and LPV-SS systems in the primal space by estimating a finite-dimensional feature map. Another contribution of this paper is the introduction of fixed-size LS-SVM to the field of LPV system identification [1], [2]. With the fixed-size solution, it is possible to compute a sparse approximation by using only a subsample of selected support vectors from the entire data set. The advantage of this approach is to speed up the prediction in the regression problem by the estimation of a small weighting vector in terms of dimensionality.

II. Related works: LS-SVM Identification of LPV Systems in Dual Space

In this section, the identification procedure of LPV-ARX model, which is described in [3], [4], is briefly presented.

[1]Luca Cavanini is with Industrial Systems and Control Ltd, Culzean House, 36 Renfield Street, Glasgow G2 1LU, UK l.cavanini@isc-ltd.com

[2]Francesco Ferracuti, Sauro Longhi and Andrea Monteriù are with the Department of Information Università Politecnica delle Marche 60131 Ancona, Italy, {f.ferracuti, s.longhi, a.monteriu}@univpm.it

A discrete LPV system in ARX form is represented as follows:

$$y(k) + \sum_{i=1}^{n_a} a_i(\mathbf{p}(k))y(k-i) = \sum_{i=1}^{n_b} b_{i-1}(\mathbf{p}(k))u(k-i+1) + e(k) \tag{1}$$

where $k \in \mathbb{Z}$ is the discrete time index, n_a is the output order, n_b is the input order, $u : \mathbb{Z} \to \mathbb{U} \subseteq \mathbb{R}$ is the vector of input variables, $y : \mathbb{Z} \to \mathbb{Y} \subseteq \mathbb{R}$ is the vector of output variables, $\mathbf{p} : \mathbb{Z} \to \mathbb{P} \subseteq \mathbb{R}^{n_p}$ is the vector of scheduling variables and $e : \mathbb{Z} \to \mathbb{E} \subseteq \mathbb{R}$ is a vector of white stochastic noise processes. The time-varying parameters $a_i : \mathbb{P} \to \mathbb{R}$ and $b_i : \mathbb{P} \to \mathbb{R}$ have a static dependence on the scheduling parameter vector $\mathbf{p}$. The number of parameters to be estimated is $n_g = n_a + n_b$.

According to the identification approach presented in [3], [5], [6], the parameters a_i, b_i can be identified through LS-SVM approach, in particular, minimizing an LS-SVM-based cost function, the problem can be solved in the dual form by introducing the Lagrangian as defined in [3] and the output estimation in dual space is given by

$$\hat{y}(k) = \sum_{i=1}^{n_g} \left(\sum_{k=1}^{N} \left(\alpha(k) x_i(k) \boldsymbol{\phi}_i^T(\mathbf{p}(k)) \right) \boldsymbol{\phi}_i(\mathbf{p}(k)) x_i(k) + \gamma^{-1}\alpha(k) \right) \tag{2}$$

where $\boldsymbol{\alpha} = \left[\alpha(1), \ldots, \alpha(N)\right]^T \in \mathbb{R}^N$ is the vector of Lagrangian multipliers, γ is the regularization parameter of the LS-SVM problem, $\boldsymbol{\phi}_i$ is a set of real non-singular functions with static dependence on $\mathbf{p}$ and $\boldsymbol{\phi}_i(\cdot) : \mathbb{R}^{n_p} \to \mathbb{R}^{n_H}$ denotes an undefined, potentially infinite ($n_H = \infty$) dimensional feature map, such that the identification process is completely characterized by $\{\boldsymbol{\phi}_i(\cdot)\}_{i=1}^{n_g}$, N is the size of the identification dataset $\mathcal{D}_N = \{u(k), \mathbf{p}(k), y(k)\}_{k=1}^{N}$. Defining the vector $\mathbf{Y} = \left[y(1), \ldots, y(N)\right]^T$, Eq. (2) can be written in compact form

$$\mathbf{Y} = \left(\mathbf{K} + \gamma^{-1} I_N\right) \boldsymbol{\alpha} = \boldsymbol{\Omega}\boldsymbol{\alpha} \tag{3}$$

where I_N is the identity matrix of dimension N and the matrix $\mathbf{K} \in \mathbb{R}^{N \times N}$ is computed as

$$\mathbf{K} = \sum_{i=1}^{n_g} \mathbf{K}_i^g \circ \mathbf{K}_i^l \tag{4}$$

where $\mathbf{K}_i^g$ is a kernel matrix whose kernel function is defined *a priori*, whereas $\mathbf{K}_i^l$ is the kernel matrix of a linear kernel function. The positive kernel function $\mathbf{K}_i^g(\cdot)$ defines the inner product of $\langle \boldsymbol{\phi}_i(\mathbf{p}(\tilde{k})), \boldsymbol{\phi}_i(\mathbf{p}(k)) \rangle$ and characterizes the feature maps $\boldsymbol{\phi}_i(\cdot)$ in an efficient fashion [6]. Based on the kernel trick, the coefficient functions $a_i(\cdot)$ and $b_i(\cdot)$ are estimated without explicitly defining the involved feature maps.

The matrix $\mathbf{K}$ is used to compute the vector of Lagrangian multipliers $\boldsymbol{\alpha} = \boldsymbol{\Omega}^{-1}\mathbf{Y}$ representing the solution in dual space of Eq. (3) that corresponds to a form of ridge regression. The model coefficients are computed by the training dataset, the Lagrangian multipliers and the selected kernel functions.

III. LS-SVM Identification of LPV Systems in Primal Space

A. LPV-ARX system identification

Considering the LPV-ARX modeling in the LS-SVM setting, the parametrized model of system (1) is introduced as

$$\hat{y}(k) = \sum_{i=1}^{n_g} \boldsymbol{\omega}_i \boldsymbol{\phi}_i(\mathbf{p}(k)) x_i(k) \tag{5}$$

The discrete-time SISO LPV system in ARX form can be rewritten in compact form:

$$\hat{y}(k) = \boldsymbol{\omega}^T \boldsymbol{\varphi}(\mathbf{p}(k)) \tag{6}$$

where $\boldsymbol{\varphi}(\mathbf{p}(k)) = \left[\boldsymbol{\phi}_1(\mathbf{p}(k))x_1(k), \ldots, \boldsymbol{\phi}_{n_g}(\mathbf{p}(k))x_{n_g}(k)\right]^T \in \mathbb{R}^{n_g \cdot n_H}$ and $\boldsymbol{\omega} \in \mathbb{R}^{n_g \cdot n_H}$.

Once the feature maps $\boldsymbol{\phi}_i$ are estimated by using an approximation either using the full sample or using a sparse approximation based on a subsample, the model can be estimated in primal space. Consider the m-dimensional approximation $m << n_H$, based on the subsample of the feature maps $\boldsymbol{\phi}_i$ given by $\hat{\boldsymbol{\phi}}_i = \left[\hat{\phi}_i^1, \ldots, \hat{\phi}_i^m\right]$. The solution to the LS-SVM optimization problem can be written as the following linear system

$$\left(\hat{\boldsymbol{\Phi}}^T \hat{\boldsymbol{\Phi}} + \frac{\mathbf{I}}{\gamma}\right) \boldsymbol{\omega} = \hat{\boldsymbol{\Phi}}^T \mathbf{y} \tag{7}$$

where $\hat{\boldsymbol{\Phi}}$ is the m feature matrix of dimension $N \times (n_g \cdot m)$

$$\hat{\boldsymbol{\Phi}} = \begin{pmatrix} \hat{\boldsymbol{\phi}}_1(\mathbf{p}(1))x_1(1) & \ldots & \hat{\boldsymbol{\phi}}_{n_g}(\mathbf{p}(1))x_{n_g}(1) \\ \vdots & \ddots & \vdots \\ \hat{\boldsymbol{\phi}}_1(\mathbf{p}(N))x_1(N) & \ldots & \hat{\boldsymbol{\phi}}_{n_g}(\mathbf{p}(N))x_{n_g}(N) \end{pmatrix} \tag{8}$$

where I is the $m \times m$ identity matrix. The complexity of calculating the feature map and solving the linear system (7) is of order $\mathcal{O}(m^3 + m^2 N)$. The approximation solution permits to estimate a smaller weights vector $\boldsymbol{\omega}$ of dimension $n_g \cdot m << n_g \cdot n_H$. Once weights vector ω is estimated and the future maps $\boldsymbol{\phi}_i$ is estimated by approximation, then $\boldsymbol{\varphi}(\mathbf{p}(k))$ is calculated by the product between $\hat{\boldsymbol{\phi}}_i(\cdot)$ and $x_i(\cdot)$.

B. Approximation of the Feature Map

Approximation to the feature map $\boldsymbol{\phi}_i$ can be obtained by means of an eigenvalue decomposition of the kernel matrix $\mathbf{K}_i^g$ with entries $K_i^g(\mathbf{p}(\tilde{k}), \mathbf{p}(k)) = \boldsymbol{\phi}_i(\mathbf{p}(\tilde{k}))^T \boldsymbol{\phi}_i(\mathbf{p}(k))$ [2]. The Fredholm integral equation of the first kind defines the eigenvalues and eigenfunctions of the kernel function, and the Nyström method [7], [8] approximates the integral by means of the sample average. Based on this approximation, an explicit expression for the j-th entry of the approximated feature map $\hat{\boldsymbol{\phi}}_i = \left[\hat{\phi}_i^1, \ldots, \hat{\phi}_i^m\right]$ where $\hat{\phi}_i^j : \mathbb{R}^{n_p} \to \mathbb{R}$ is given by the approximation

$$\hat{\phi}_i^j(\mathbf{p}(k)) = \frac{1}{\sqrt{\lambda_{i,j}}} \sum_{\tilde{k}=1}^{N} u_{i,j,\tilde{k}} \mathbf{K}_i^g(\mathbf{p}(\tilde{k}), \mathbf{p}(k)) \tag{9}$$

where $\lambda_{i,j}$ is the j-th largest eigenvalue and $u_{i,j,\tilde{k}}$ is the $\tilde{k}$-th element of the j-th eigenvector of kernel function $\mathbf{K}_i^g(\cdot)$. This finite-dimensional approximation $\hat{\phi}_i^j$ can be used in the primal problem to finally estimate the weights vector $\boldsymbol{\omega}$ of dimension $n_g \cdot m << n_g \cdot n_H$.

C. Subset Selection and Sparseness

It is important to emphasize that the usage of the entire training sample of size N to compute the approximation of $\hat{\boldsymbol{\phi}}_i$ will yield at most N components. Each of these components can be calculated by means of (9). Considering large-scale problems, it has been motivated by [2] to choose a working set of fixed size $n\,(n << N)$ where the value n is related to the Nyström subsample and an entropy-based subset selection. In order to make a more suitable selection of the subsample instead of a random selection, an entropy-based criterion can be used as proposed in [2]. Indeed, the n support vectors can be selected by maximizing Rényi's entropy H_q of order q defined as

$$H_q = \frac{1}{1-q} \log \int p(x)^q dx \tag{10}$$

with $q > 1$, $q \neq 0$ and p the density of the selected support vectors. Further in this study, we set $q = 2$, which is also called quadratic Rényi entropy. The quadratic Rényi entropy can be approximated [9] by using

$$\int \hat{p}(x)^2 dx = \frac{1}{n^2} \mathbf{1}^T \mathbf{K}_i^g \mathbf{1} \tag{11}$$

where $\mathbf{1} = (1, \ldots, 1)^T$. By using such a criterion we can be sure that the selected subsample is well spread over the entire data region. Hence, the subsample will not be concentrated in a certain area of the entire data set. Note that the positive definiteness property is not required here for $\mathbf{K}_i^g$, since entropy estimation is related to density estimation.

IV. Results and Conclusions

The Silverbox model has been considered for testing the proposed approach. The mathematical model of the engine is based on the nonlinear system reported in [10]. The results will be presented in case of acceptance of the present extended abstract, during AUTOMATICA.IT 2022 in September, together with a detailed description of the algorithms previously reported.

References

[1] M. Espinoza, K. Pelckmans, L. Hoegaerts, J. A. Suykens, and B. De Moor, "A comparative study of LS-SVM's applied to the silver box identification problem," *IFAC Proceedings Volumes*, vol. 37, no. 13, pp. 369–374, 2004.

[2] K. De Brabanter, P. Dreesen, P. Karsmakers, K. Pelckmans, J. De Brabanter, J. Suykens, and B. De Moor, "Fixed-size LS-SVM applied to the Wiener-Hammerstein benchmark," *IFAC Proceedings Volumes*, vol. 42, no. 10, pp. 826–831, 2009.

[3] R. Tóth, V. Laurain, W. X. Zheng, and K. Poolla, "Model structure learning: A support vector machine approach for LPV linear-regression models," in *2011 50th IEEE Conference on Decision and Control and European Control Conference*. IEEE, 2011, pp. 3192–3197.

[4] S. Z. Rizvi, J. Mohammadpour, R. Tóth, and N. Meskin, "A kernel-based approach to MIMO LPV state-space identification and application to a nonlinear process system," *IFAC-PapersOnLine*, vol. 48, no. 26, pp. 85–90, 2015.

[5] R. Tóth, H. Hjalmarsson, and C. R. Rojas, "Order and structural dependence selection of LPV-ARX models revisited," in *2012 IEEE 51st IEEE Conference on Decision and Control (CDC)*, Dec 2012, pp. 6271–6276.

[6] D. Piga and R. Tóth, "LPV model order selection in an LS-SVM setting," in *52nd IEEE Conference on Decision and Control*, 2013, pp. 4128–4133.

[7] E. J. Nyström, "Über die praktische Auflösung von Integralgleichungen mit Anwendungen auf Randwertaufgaben," *Acta Mathematica*, vol. 54, pp. 185–204, 1930.

[8] C. Williams and M. Seeger, "Using the Nyström method to speed up kernel machines," *Advances in neural information processing systems*, vol. 13, 2000.

[9] M. Girolami, "Orthogonal series density estimation and the kernel eigenvalue problem," *Neural computation*, vol. 14, no. 3, pp. 669–688, 2002.

[10] T. Wigren and J. Schoukens, "Three free data sets for development and benchmarking in nonlinear system identification," in *2013 European Control Conference (ECC)*, 2013, pp. 2933–2938.

On Semi–Global Exponential Stability Under Sampling for Locally Lipschitz Time–Delay Systems *

M. Di Ferdinando, P. Pepe, and S. Di Gennaro

Department of Information Engineering, Computer Science, and Mathematics, University of L'Aquila, Via Vetoio (Coppito 1), 67100 L'Aquila, Italy
mario.diferdinando@univaq.it pierdomenico.pepe@univaq.it
stefano.digennaro@univaq.it

1 Extended Abstract

Nowadays, it is well-known that the utilization of digital technologies in practical engineering applications is more and more growing. This fact has consequently increased the attention of many researchers to the study of sampled–data control systems. In the literature concerning the sampled–data stabilization, many approaches have been provided for the stability analysis of linear, bilinear and nonlinear systems, also infinite dimensional. The reader can refer to [7] for an interesting survey on the topic.

As far as the sampled–data control problem of nonlinear time–delay systems is concerned, the results available in the literature are very few. Results concerning state feedback sampled–data controllers for nonlinear systems affected by time–delays in the input/output channels are provided in [8]. In [11], sufficient conditions for the uniform global pre–asymptotic stability preservation, under sampling of Continuous–time Dynamic Output Feedback (CDOF) controllers, are provided for nonlinear systems with state, input and output delays. An efficient methodology to analyse the upper bound of the sampling period is provided. In [4], sufficient conditions ensuring the semiglobal practical stability preservation for nonlinear systems with state–delays, by means of Emulated Dynamic Output Feedback (EDOF) controllers, are provided. Differently from [11], in [4] the dynamical part of the CDOF controller at hand is discretized by exploiting a family of discrete–time approximation models which are not used in [11] and allow for a very easy digital implementation of the continuous–time controller at hand avoiding also the requirement to solve a nonlinear infinite dimensional optimization problem as required when LMI approaches are used. On the other hand, differently from the results provided in [11], in [4] time–varying delays and problems related to the communication networks, such as finite bandwidth of the network and/or intermittent information update of the input/output channels, are not taken into account. In [5], it is shown that, if the continuous–time closed–loop system at hand is globally exponentially stable and the maps describing the plant and the CDOF controller are globally Lipschitz, then the Euler emulation, under suitably fast sampling, of the continuous–time controller preserves the global exponential stability of the sampled–data closed–loop system. As far as the semiglobal exponential stability under sampling for locally Lipschitz nonlinear time–delay systems is concerned, to our best knowledge no results are available in the literature, when CDOF controllers are emulated by the use of discrete–time approximation models. The main aim of this research work is to fill this gap.

In this contribution, it is shown that, under suitable conditions, for locally Lipschitz nonlinear time–delay systems there exists a maximum intersampling time such that the Euler

*This work has been partially supported by the: (i) Atheneum Project RIA 2020; (ii) the European Project ECSEL–JU RIA–2018 "Comp4Drones"; (iii) the Project "Coordination of autonomous unmanned vehicles for highly complex performances", SAAP3.

emulation of CDOF controllers yields semiglobal exponential stability, both for periodic or aperiodic samplings. The provided sufficient conditions are Lyapunov–Krasovskii based, and are highly inspired by the Lyapunov based conditions in [9] for the global asymptotic local exponential stability of delay–free systems, by which the author proves semiglobal asymptotic stability of nonlinear delay–free sampled–data systems. If emulation schemes other than the Euler one (e.g. the popular Runge–Kutta schemes) are chosen for the implementation of the CDOF controller, semiglobal practical exponential stability of the related sampled–data closed–loop system is guaranteed by suitably fast sampling, with arbitrarily small final target ball. The theory of the stabilization in the sample–and–hold sense [2, 4, 10], and Halanay's inequality [1, 6] are the main tools used for proving the results. Here, the intersampling system behaviour, as well as time–varying sampling intervals, are taken into account. The theoretical results are validated through examples, two of which concern important practical engineering applications. In particular, the considered applications address: (i) a chemical reactor system with recycle; (ii) the glucose regulation problem in type 2 diabetic patients. The presented research results have been recently published in [3].

References

[1] C.T.H. Baker and E. Buckwar. Exponential stability in pth mean of solutions, and of convergent Euler-type solutions, of stochastic delay differential equations. *Journal of Computational and Applied Mathematics*, 184:404–427, 2005.

[2] F. H. Clarke, Y. S. Ledyaev, E. D. Sontag, and A. I. Subbotin. Asymptotic controllability implies feedback stabilization. *IEEE Trans. Automat. Control*, 42:1394–1407, 1997.

[3] M. Di Ferdinando, P. Pepe, and S. Di Gennaro. On semi–global exponential stability under sampling for locally lipschitz time–delay systems. *IEEE Transactions on Automatic Control*, 2022.

[4] M. Di Ferdinando and P. Pepe. Sampled-data emulation of dynamic output feedback controllers for nonlinear time-delay systems. *Automatica*, 99:120–131, 2019.

[5] M. Di Ferdinando, P. Pepe, and E. Fridman. Exponential input-to-state stability of globally lipschitz time-delay systems under sampled-data noisy output feedback and actuation disturbances. *International Journal of Control*, 94:1682–1692, 2021.

[6] A. Halanay. Differential equations, stability, oscillations, time lags. *New York: Academic Press*, 1966.

[7] L. Hetel, C. Fiter, H. Omran, A. Seuret, E. Fridman, J.P. Richard, and S. I. Niculescu. Recent developments on the stability of systems with aperiodic sampling: An overview. *Automatica*, 76:309–335, 2017.

[8] I. Karafyllis and M. Krstic. Nonlinear stabilization under sampled and delayed measurements, and with inputs subject to delay and zero-order-hold. *IEEE Trans. Automat. Control*, 57:1141–1154, 2012.

[9] W. Lin. When is a nonlinear system semi-globally asymptotically stabilizable by digital feedback? *IEEE Transactions on Automatic Control*, 65:4584–4599, 2020.

[10] P. Pepe. On control Lyapunov-Razumikhin functions, nonconstant delays, nonsmooth feedbacks, and nonlinear sampled-data stabilization. *IEEE Transactions on Automatic Control*, 62:5604–5619, 2017.

[11] D. Tolić. Stabilizing transmission intervals and delays in nonlinear networked control systems through hybrid-system-with-memory modeling and Lyapunov-Krasovskii arguments. *Nonlinear Analysis: Hybrid Systems*, 36:100834, 2020.

Sparse learning with concave regularization: relaxation of the irrepresentable condition

V. Cerone, S. M. Fosson, D. Regruto

***Abstract*— The goal of sparse learning is to build parsimonious models, by identifying the most significant parameters and discarding the others. This can be achieved by solving suitable sparsity promoting optimization problems. In the framework of linear regression, Lasso is the most popular convex approach for sparse learning. For Lasso, it has been proven that the irrepresentable condition is sufficient and essentially necessary for a correct selection of the significant parameters of the model. In this work, we propose a different method based on concave regularization and we prove that it relaxes the irrepresentable condition. Moreover, we present numerical experiments that support the theoretical results.**

I. Introduction

Sparse learning is the science of building parsimonious models from data. The main motivation for sparse learning is the need of extracting relevant information from large collections of data, to prevent overfitting, redundancies, numerical complexity, and scarce understanding of the physical behavior of systems, see, e.g., [1]. Recently, sparse learning has been applied in different fields, ranging from system identification to neural networks; see, e.g., [2], [3].

Usually, sparse learning is formulated as an optimization problem where sparsity is promoted by a suitable regularization. In linear regression, the Lasso problem [4] is very popular, which consists in the minimization of an ℓ_1 regularized cost functional. The reliability of Lasso has been studied in terms of variable-selection consistency (VSC), i.e., the ability of identifying the significant parameters of the model. As illustrated in [5], [6], Lasso enjoys the VSC if the so-called irrepresentable condition holds; more precisely, this condition is sufficient and essentially necessary, see [7].

In this paper, we analyse an alternative approach to Lasso for sparse linear regression, based on a concave, semi-algebraic regularization. Recently, the use of non-convex regularizers has been gaining attention in sparse learning, see, e.g., [8] and reference therein. In the literature, it is shown via numerical experiments that the non-convex approach is often more effective than Lasso. Intuitively, this is due to the fact that the considered concave regularizers are closer to the ℓ_0 norm than the ℓ_1 norm; nevertheless, theoretical results are scarce. The goal of this paper is to fill this gap by providing a result that illustrates why a concave approach may be more reliable than Lasso, in terms of VSC.

II. Problem statement and background

Our goal is estimate a k-sparse vector $\widetilde{x} \in \mathbb{R}^n$ from

$$y = A\widetilde{x} + \eta, \tag{1}$$

where $A \in \mathbb{R}^{m,n}$ is known, and $\eta \in \mathbb{R}^m$ is an unknown measurement noise. In particular, we focus on the compressed case $m < n$, which is more challenging. We call $S \subset \{1, \dots, n\}$ the support of $\widetilde{x}$, and $\bar{S}$ its complementary. We assume that $\widetilde{x}_i \in [-d, d]$ for each $i \in S$. For any $v \in \mathbb{R}^n$, $v_S \in \mathbb{R}^k$ denotes the components of v in S. Similarly, A_S contains the columns of A indexed in S. For model (1), Lasso reads as follow: $\min_{x\in[-d,d]^n} \frac{1}{2}\|y - Ax\|_2^2 + \lambda\|x\|_1$ where $\lambda > 0$. In the literature, the VSC of Lasso is analysed by using the irrepresentable condition, see [1, Section 11.4.1].

Definition 1: **Irrepresentable condition (IRR)**
A satisfies (ω, S)-IRR if there exists $\omega > 0$ such that $\max_{j\in\bar{S}} \left\|A_j^T A_S (A_S^T A_S)^{-1}\right\|_1 \leq \frac{1}{\omega}$.
For Lasso, strong (ω, S)-IRR (i.e., $\omega > 1$) and weak (ω, S)-IRR (i.e., $\omega = 1$) respectively are sufficient and necessary for VSC, in the case $m \to \infty$, see [6]. In the non-asymptotic case, VSC is proven with large probability, under IRR and sufficiently large λ, see, e.g., [1, Theorem 11.3].

In the last years, different concave penalties have been proposed in sparse optimization, in particular, $\log(x)$, ℓ_p, with $p \in (0, 1)$, and minimax concave penalties (MCP, [9]). In this paper, we propose an MCP-based shrinkage and selection method, denoted as MCPS^2, which reads as follows.

$$\begin{aligned} \textbf{MCPS}^2: \quad & \min_{x\in[-d,d]^n} \mathcal{F}(x) := \frac{1}{2}\|y - Ax\|_2^2 + \lambda r(x) \\ & \text{where } r(x) := d\|x\|_1 - \frac{1}{2}\|x\|_2^2, \quad \lambda > 0. \end{aligned} \tag{2}$$

For our analysis, we exploit the restricted eigenvalue condition, see [1, Section 11.2.2]). Let us define the cone $\mathcal{C}(\alpha, S) := \{x \in \mathbb{R}^n : \|x_{\bar{S}}\|_1 \leq \alpha \|x_S\|_1\}$.

Definition 2: **Restricted eigenvalue condition (RE)**
A satisfies (α, ϕ, S)-RE if there exist $\alpha > 0$ and $\phi > 0$ such that $\frac{\|Av\|_2^2}{\|v\|_2^2} \geq \phi$ for any $v \in \mathcal{C}(\alpha, S) \setminus \{0\}$.
We remark that RE is generally weaker than IRR, see [10].

III. Theoretical analysis

In the following theorems, we analyse the VSC for MCPS^2 (2) for $m < n$. Specifically, we prove that a vector $x^\star$ with the same support of $\widetilde{x}$ is a local minimum of $\mathcal{F}$ in (2), under a relaxed (ω, S)-IRR (i.e., ω may be smaller than 1) and if (α, ϕ, S)-RE holds. Therefore, by implementing a descent algorithm that starts sufficiently close to $x^\star$ one can recover the right support. Furthermore, under additional conditions, $x^\star$ is proven to be the global minimum.

Theorem 1: Let $y = A\widetilde{x} + \eta$, where $\widetilde{x} \in [-d, d]^n$ has support S, with $|S| = k$. We assume $A_S^T A_S \succ 0$, with

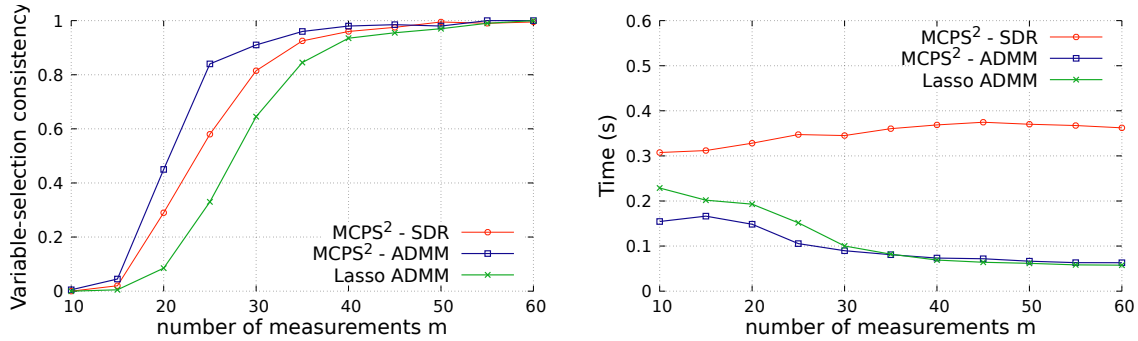

Fig. 1: Numerical results: comparison between MCPS^2, solved via SDR and ADMM, and Lasso, solved via ADMM.

minimum eigenvalue $\mathrm{a} > \lambda$. Let $\Omega := A_S^T A_S - \lambda I \succ 0$, $\mu := \frac{1}{d}\min_{i\in S}|\widetilde{x}_i| \in (0,1]$, and $\gamma := \lambda d(1-\mu) + \|A_S^T\eta\|_\infty$. We define $x^\star \in [-d,d]^n$ as follows:

$$x_S^\star := \widetilde{x}_S + \Omega^{-1}\left[\lambda\widetilde{x}_S - \lambda d\,\mathrm{sign}(\widetilde{x}_S) + A_S^T\eta\right]; \quad x_{\bar{S}}^\star := 0. \tag{3}$$

If $\gamma\sqrt{k} < \mu d(\mathrm{a}-\lambda)$, then $\mathrm{sign}(\widetilde{x}_S) = \mathrm{sign}(x_S^\star)$. Furthermore, given an arbitrarily small $\varepsilon > 0$, if the following conditions hold:

C1. A satisfies (ω, S)-IRR with $\omega > 1-\mu$,

C2. A satisfies (α,ϕ,S)-RE with $\phi > \lambda$,

C3. $\lambda d - \omega^{-1}\left(1 + \frac{\lambda\sqrt{k}}{\mathrm{a}-\lambda}\right)\gamma - \|A_{\bar{S}}^T\eta\|_\infty - \lambda\varepsilon\frac{1+\alpha}{\alpha} > 0$,

then, $x^\star$ is a local minimum of $\mathcal{F}(x)$, $x \in [-d,d]^n$.

We remark that C1 does not require $(1,S)$-IRR, which is necessary for Lasso. In other terms, MCPS^2 requires a relaxed IRR with respect to Lasso. Interestingly, in the limit case $\mu = 1$, no IRR is required, see [11]. The proof of Theorem 1 can be found in [11].

Proposition 1: Let $\theta = \|(y - Ax^\star)^T A\|_\infty$. Let us assume $\theta < \lambda d$. If A satisfies (α,ϕ,S)-RE with $\alpha \geq \frac{2\lambda d+\theta}{\lambda d-\theta}$, $\phi > \lambda$, and $\frac{2(\theta+2\lambda d)\sqrt{k}}{\phi-\lambda} \leq \varepsilon$, then, $x^\star$ defined in (3) is the global minimum of $\mathcal{F}$.

IV. Algorithms and Numerical Simulations

We propose two approaches to achieve a minimum of $\mathcal{F}$ as defined in (2): the semidefinite programming relaxation (SDR), see [12], and the alternating direction method of multipliers (ADMM, [13]). In the first approach, the global minimum is achieved by solving an SDR of sufficiently large order, see [12] for details. Nevertheless, the computational complexity increases with the order; in our experiments, we consider SDR of order 1. On the other hand, ADMM is an iterative algorithm that reaches a local minimum.

We illustrate some numerical simulations with SDR and ADMM and we compare them to Lasso, solved with ADMM. We consider the following setting: $n = 100$, $k = 5$, $\lambda = 10^{-2}$; for $i \in S$, $|\widetilde{x}_i| \in [\frac{1}{2}, 1]$. The available measurements are $y = A\widetilde{x} + \eta$, where $A \in \mathbb{R}^{m,n}$ has Gaussian independent entries $\mathcal{N}(0, \frac{1}{m})$, $m \in [10, 60]$. The measurement noise $\eta \in \mathbb{R}^m$ is Gaussian, with signal-to-noise-ratio SNR $= 25$ dB.

The results, averaged over 200 runs, are shown in Fig. 1. We see that MCPS^2 performs better than Lasso in terms of VSC, as expected from the proposed theoretical results. In Fig. 1, we also show the runtime of the different algorithms, SDR being a bit slower than ADMM.

As to MCPS^2, SDR and ADMM algorithms both suboptimal: on the one hand, SDR can be improved by increasing the relaxation order, now set to 1 to minimize the runtime; on the other hand, for ADMM, suitable initial conditions could be investigated to achieve the desired minimum.

V. Conclusions

In this work, we analyse MCPS^2, a non-convex optimization problem for sparse learning. Specifically, we study its variable-selection consistency and we obtain a relaxation of the weak irrepresentable condition, which is necessary for Lasso. In practice, this implies that MCPS^2 requires less measurements than Lasso.

References

[1] T. Hastie, R. Tibshirani, and M. Wainwright, *Statistical Learning with Sparsity: The Lasso and Generalizations*, 2nd ed. CRC press, 2015.

[2] S. Fattahi and S. Sojoudi, "Data-driven sparse system identification," in *Proc. Allerton Conf. Commun. Control Comput.*, 2018, pp. 462–469.

[3] S. L. Brunton and J. N. Kutz, *Data-Driven Science and Engineering: Machine Learning, Dynamical Systems, and Control*. Cambridge University Press, 2019.

[4] R. Tibshirani, "Regression shrinkage and selection via the lasso," *J. Roy. Stat. Soc. Series B*, vol. 58, pp. 267–288, 1996.

[5] J. J. Fuchs, "On sparse representations in arbitrary redundant bases," *IEEE Trans. Inf. Theory*, vol. 50, no. 6, pp. 1341–1344, 2004.

[6] P. Zhao and B. Yu, "On model selection consistency of Lasso," *J. Mach. Learn. Res.*, vol. 7, pp. 2541 – 2563, 2006.

[7] P. Bühlmann and S. van de Geer, *Variable selection with the Lasso*. Springer Berlin Heidelberg, 2011, pp. 183–247.

[8] V. Cerone, S. M. Fosson, and D. Regruto, "Sparse linear regression with compressed and low-precision data via concave quadratic programming," in *Proc. CDC*, 2019, pp. 6971–6976.

[9] C.-H. Zhang, "Nearly unbiased variable selection under minimax concave penalty," *Ann. Statist.*, vol. 38, no. 2, pp. 894–942, 2010.

[10] S. A. van de Geer and P. Bühlmann, "On the conditions used to prove oracle results for the Lasso," *Electron. J. Stat.*, vol. 3, pp. 1360–1392, 2009.

[11] V. Cerone, S. M. Fosson, D. Regruto, and A. Salam, "Sparse learning with concave regularization: relaxation of the irrepresentable condition," in *Proc. CDC*, 2020, pp. 396–401.

[12] J.-B. Lasserre, *An introduction to polynomial and semi-algebraic optimization*. Cambridge University Press, 2015.

[13] S. Boyd, N. Parikh, E. Chu, B. Peleato, and J. Eckstein, "Distributed optimization and statistical learning via the alternating direction method of multipliers," *Found. Trends Mach. Learn.*, vol. 3, no. 1, pp. 1 – 122, 2010.

New Automatic Motor Speed Reference Generators for Cruise and Lateral Control of Electric Vehicles with in-Wheel Motors

C.M. Verrelli, M. El Arayshi

***Abstract*—Motor speed reference generators have been first presented by the first author for the cruise control of electric vehicles powered by centralized electric motors: steady-state operation at a safe tire longitudinal slip is guaranteed to be achieved in the presence of uncertain external conditions. A generalization to electric vehicles that make use of two in-wheel motors and are required to perform a bend manoeuvre has been then provided by the same author: the two in-wheel rear motors provide propulsion, while being capable of acting as a rear differential. The common key point of the two aforementioned results (validated by both CarSim simulations and experiments) relies on the definition of suitable references for the motor speed, so that motor speed control algorithms can be directly inherited from the electric machine control literature and intrinsically robust motor speed control loops can be incorporated. The new step regards the last contribution. It is constituted by further including the use of a slight modification of the very recently defined *wheel angle*, in order to better rule the speed decrease in the presence of initial (transient) slip constraints violation.**

***Index Terms*—Electric vehicles; in-wheel motors; cruise and lateral control; slip constraints; wheel angle.**

I. Introduction

Vehicle control and estimation problems attract the interests of the research community. Such problems involve the design of: robust yaw moment controls to improve vehicle handling and stability; vision-based lane-keeping controls for non-autonomous and autonomous vehicles; integrated controls of front and rear active differentials to improve vehicle dynamics; sliding mode observer-based traction controllers to achieve a desired wheel slip for maximum deceleration in a minimum amount of time; cascaded wheel slip controls for wheel slip and acceleration regulation; decoupling controls on the front and rear steering angles for four-wheel steering vehicles; yaw stability controls; wheel slip controllers for automotive brakes; hierarchical algorithms for lane keeping assistance; differential braking controls; hybrid anti-lock brake systems with extended braking stiffness estimation (see the related references in [7]).

A green, energy-efficient, secure and safe transport technology is constituted by electric vehicles powered by electric motors. In particular, in-wheel motors lead to: simple packaging of the drive-train, with improved vehicle handling and safety (see [4] and [1]); the replacement of the mechanical differential with the electric differential (see [8] and references therein); improved safety, reduction in mass and increase of energy efficiency ([9]). Now, one typical goal in control problems concerning vehicles with electric motor propulsion is cruise control, i.e., the regulation of the vehicle longitudinal speed to a constant reference. Automatic speed control provides, in fact, the opportunity to increase safety by eliminating human errors that are the first cause of accidents. With this respect, a solution to the problem of regulating the vehicle longitudinal speed v_x to the corresponding constant reference v_{x*} has been presented in [6] and then extended to the case of slip constraints in [5]. In particular, the cruise control problem is transformed in [6] into the problem of regulating the motor speed ω to a suitable feedback-based motor speed reference, whose role is to exponentially estimate the uncertain motor speed reference ω_* corresponding to v_{x*}. Such motor speed reference ω_* is uncertain, owing to all the uncertainties characterizing the specific vehicle and the external conditions. However, the vehicle longitudinal speed reference v_{x*} is only exogenously given in [6]; it is not automatically (internally) adjusted *via* feedback in response to uncertain external conditions, such as tire-road adhesion coefficients and road slopes. The tire-longitudinal slip at steady-state is not guaranteed to be kept in safe regions. This limitation is then overcome in [5], in which the contraction theorem is applied to a smooth desired design function in the (ω, v_x)-plane in order to drive the pair (ω, v_x) into safe tire longitudinal slip- regions. However, only vehicles powered by a single electric motor (with fixed transmission gear ratio) have been taken into consideration in [6] and [5]: manoeuvres are restricted to be straight ones, whereas the yaw rate and lateral speed dynamics are not taken into account. In [7], whose contribution builds on the approach foreseen in [3], electric rear-wheel drive vehicles are considered. They are equipped with two independent rear motors (one per tire). These motors provide propulsion, while being capable of acting as a rear differential. The contribution of [7] is to extend the results in [6] and [5] to the more general case in which the vehicle is required to perform a bend manoeuvre (with constant curvature radius): treating the rotor speeds as independent control inputs allows for naturally addressing and solving the cruise and lateral control problem, even in the presence of slip constraints. No exact model knowledge, which is unreasonable due to the lumped nature of the approximated model used in the control design, is assumed. Furthermore, no lateral velocity measurements are required. Suitable reference signals for the motor speeds are generated by a contraction mapping algorithm and without any *a priori* knowledge about

C.M. Verrelli, M. El Arayshi are with the Electronic Engineering Department of the University of Rome Tor Vergata, Via del Politecnico 1, 00133 Rome, Italy. E-mails: verrelli@ing.uniroma2.it, elarayshi@ing.uniroma2.it.

the occurrence of a specific external condition. Such reference values converge to a steady-state operating point with safe tire longitudinal slips. Both realistic CarSim simulations (including electric motors dynamics) and experiments on an autonomous scaled vehicle (1:10) illustrate the effectiveness of such an approach, even in the presence of complex dynamics and practical aspects that have been neglected at the design stage.

The last original step of this research line is to incorporate a slight modification of the *wheel angle*, very recently defined in [2], in order to better rule the speed decrease in the presence of initial (transient) slip constraints violation and avoid too conservative values for the rotor speed.

II. Rotor speed generators under slip constraints

The idea originally proposed in [7] is described hereafter (see [7] for a detailed introduction of the meaning of the involved variables and parameters).

New speed reference generators are designed for fixed transmission gear ratio- electric vehicles. The key-idea relies on reducing to the (ω_L, v_x)-plane once the kinematic ω_L-constraint on ω_D:

$$\omega_D \equiv \frac{l_\omega r_*}{R_\omega} = \frac{l_\omega v_{x*}\delta}{R_\omega(l_f + l_r)} = \frac{l_\omega \omega_L \delta}{(l_f + l_r)} \qquad (1)$$

is imposed. The scenario in [5] is thus reproduced once ω_L replaces ω. For given external conditions and a given steering angle δ, the (ω_L, v_x)-steady-state operating conditions define a specific (ω_D-constrained) steady-state curve $g_{\mu,c}(\cdot)$ in the (ω_L, v_x)-plane.

Let $\Lambda_\mu = [\underline{\lambda}_\mu, \overline{\lambda}_\mu] \subset \mathbb{R}$ be the (connected) compact set representing the set of the desired, steady-state, safe tire longitudinal slip values for each uncertain external scenario μ. Let the (connected) compact set $\Omega = [\omega_{Lm}, \omega_{LM}] \subset \mathbb{R}^+$ be a domain of interest for the speed ω_L with $g_{\mu,c}(\cdot) : \Omega \to \mathcal{R}(g_{\mu,c})$ ($\mathcal{R}(f)$ generally denotes the range of function f). Let $f_O(\cdot) : \Omega \to \mathcal{R}(f_O)$ be a suitable smooth, strictly increasing function, whose $g_{\mu,c}(\cdot)$-intersection points $P_{\mu,c}$ are characterized by safe tire longitudinal slip values (i.e. both the corresponding λ_i, $_i \in \{_{r1}, _{r2}\}$, - computed at $P_{\mu,c}$ - belong to Λ_μ) and which exhibits the following properties (c_O is any sufficiently small positive real): 1) $f'_O(\cdot) \geq c_O > 0$; 2) $\max_\Omega\{|g'_{\mu,c}(\cdot)|\}/\min_\Omega\{f'_O(\cdot)\} \leq \alpha < 1$; 3) $\mathcal{R}(f_O) \supseteq \mathcal{R}(g_{\mu,c})$. By exploiting the features of the steady-state curves $g_{\mu,c}(\cdot)$ and the fast transients in motor speed tracking, a sequence of ω_L-reference values is defined as ($\omega_L^{*0} \in \Omega$):

$$\omega_L^{*0},\ \omega_L^{*1} = T(\omega_L^{*0}),\ \omega_L^{*2} = T(\omega_L^{*1}), \ldots, \qquad (2)$$

with the mapping

$$T(\cdot) = f_O^{-1}(g_{\mu,c}(\cdot)) \qquad (3)$$

being well defined since $\mathrm{dom}(f_O^{-1}) = \mathcal{R}(f_O) \supseteq \mathcal{R}(g_{\mu,c})$. According to the mean value theorem, the mapping $T(\cdot)$ is a contraction on Ω since $|T(\omega_L^{*1}) - T(\omega_L^{*2})| = |T'(\xi)||\omega_L^{*1} - \omega_L^{*2}|$, with $|T'(\xi)| \leq \alpha < 1$ and $\xi \in (\omega_L^{*1}, \omega_L^{*2})$. The above sequence (ω_L^{*i}) of the images of ω_L^{*0} under repeated application of $T(\cdot)$ remains in Ω; it is a Cauchy sequence that converges to a certain $\omega_L^{*a} \in \Omega$. This ω_L^{*a} is the unique fixed point of the mapping $T(\cdot)$ satisfying: $\omega_L^{*a} = T(\omega_L^{*a}) = f_O^{-1}(g_{\mu,c}(\omega_L^{*a}))$, that is $g_{\mu,c}(\omega_L^{*a}) = f_O(\omega_L^{*a})$. The sequence (ω_L^{*i}) thus drives the vehicle to the intersection point $P_{\mu,c}$ between the steady-state curve and the desired design function $f_O(\omega_L)$ in the (ω_L, v_x)-plane, which safe tire longitudinal slips correspond to. The vehicle speed can be thus automatically reduced when an abrupt change in tire-road adhesion coefficients occurs. In other words, it is possible to regulate the tire longitudinal slips to desired constant references that are actually uncertain, due their dependence on the specifically occurring uncertain external scenario [no slip estimation is in fact here performed]. It is straightforward to notice that when the two in-wheel motors collapse into one motor with straight manoeuvres being considered, only the longitudinal component ω_L survives ($\omega_D \equiv 0$), so that the above control strategy reduces to the one proposed in [5]. On the other hand, the application of $T(\cdot)$ to a sequence of motor speed values $\omega_L^j \in \Omega$ (which the sequence of vehicle speed values v_x^j corresponds to) is actually implementable since, by definition, $T(\omega_L^j) = f_O^{-1}(g_{\mu,c}(\omega_L^j)) = f_O^{-1}(v_x^j)$, with $f_O(\cdot)$ being a known invertible function with known inverse function. Anyway, the aforementioned intersection point $P_{\mu,c}$ between the steady-state curve and the desired design function $f_O(\omega_L)$ in the (ω_L, v_x)-plane exhibits tire longitudinal slips that can be too conservatively low, especially for curves corresponding to large μ. The new original improvement of this research line is constituted by further including the use of a slight modification of the *wheel angle* of [2] [i.e., by replacing the estimated load torque by the motor torque current], in order to better rule, by monitoring such an angle at each reduction step, the speed decrease in the presence of initial (transient) slip constraints violation.

References

[1] H. Alipour, M. Sabahi, M.B. Bannae Sharifian, Lateral stabilization of a four wheel independent drive electric vehicle on slippery roads, *Mechatronics*, 30: 275-285, 2015.

[2] G. Amato, R. Marino, Reconfigurable slip vectoring control in four in-wheel drive electric vehicles, *Actuators*, 10, 157, 2021.

[3] E. Coelingh, S. Solyom, All aboard the robotic road train, *IEEE Spectrum*, 8 November 2012.

[4] H.C. Lovatt, D. Elton, L. Cahill, D.H. Huynh, A. Stumpf, A. Kulkarni, A. Kapoor, M. Ektesabi, H. Mazumder, T. Dittmar, G. White, Design procedure for low cost, low mass, direct drive, in-wheel motor drivetrains for electric and hybrid vehicles, *IECON 2011 - 37th Annual Conference on IEEE Industrial Electronics Society*, pp. 4558-4562, 2011.

[5] R. Marino, L. Pasquale, S. Scalzi, C.M. Verrelli, Automatic rotor speed reference generator for electric vehicles under slip constraints, *IEEE Transactions on Intelligent Transporation Systems*, 16: 3473-3478, 2015.

[6] R. Marino, S. Scalzi, P. Tomei, C.M. Verrelli, Fault-tolerant cruise control of electric vehicles with induction motors, *Control Engineering Practice*, 21: 860-869, 2013.

[7] C. Pomponi, S. Scalzi, L. Pasquale, C.M. Verrelli, R. Marino, Automatic motor speed reference generators for cruise and lateral control of electric vehicles with in-wheel motors, *Control Engineering Practice*, 79, 126-143, 2018.

[8] Y.-P. Yang, X.-Y. Xing, Design of electric differential system for an electric vehicle with dual wheel motors, *Proceedings of the 47th IEEE Conference on Decision and Control*, pp. 4414-4419, 2008.

[9] G. Zhang, H. Zhang, X. Huang, J. Wang, H. Yu, R. Graaf, Active fault-tolerant control for electric vehicles with independently driven rear in-wheel motors against certain actuator faults, *IEEE Transactions on Control Systems Technology*, 24: 1557-1572, 2016.

A Consensus Protocol for Connecting Automated Vehicles at Signal-Free Intersection

Gianvito Difilippo, Maria Pia Fanti and Agostino Marcello Mangini

I. Introduction

Intersections represent a small percentage of the total road network, but they account for a relatively large proportion of road accidents and delays [1]. The adoption of Automated Vehicles (AVs) can be one solution to the aforementioned problem.

This work deals with the intersection management problem by using only V2V communication, i.e., without employing an external intersection management agent. The AVs apply a consensus protocol, which avoids collisions crossing the intersection and minimizes the delay or the anticipation with respect to a forecast exit time from the intersection.

The main contribution is the presented consensus protocol both to avoid the collisions and minimize delays or anticipations. Unlike [2], the proposed optimization technique is not centralized and does not need an intersection manager. Moreover, unlike [3], the consensus protocol does not need a coordinator vehicle inside the control zone.

II. Problem Formulation

A. System Description

We consider an intersection of four-way shown in Fig. 1: each AV coming to intersection can either turn right (R), turn left (L) or go forward (F). The intersection is divided in two regions: i) the Merging Zone (MZ), i.e., the area of potential collision; ii) the Control Zone (CZ), i.e.,the area where the AVs can communicate V2V.

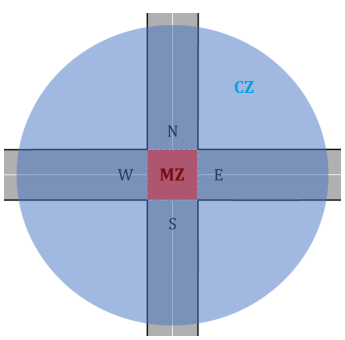

Fig. 1. Intersection.

The following assumption are imposed: 1) $n \leq 4$ AVs are considered in the intersection with one vehicle in each lane; 2) each AV $i \in N$ crosses the MZ at a constant speed $v_i \in [v_{MINi}, v_{MAXi}]$ at time instant τ_i; 3) each AV $i \in N$ enters the CZ with its velocity profile and forecasts to enter MZ at speed v_{0i} and at time instant τ_{0i}; 4) each AV $i \in N$ crosses the intersection area following either a straight line (if it does not modify its direction), or a quarter of circumference (if it modifies its direction), with center in a vertex of the square of the intersection area MZ.

Now, we define by $\mathbf{x}_i = [\tau_i, v_i]^T$ the decision variables for AV i. The position of AV i in the region MZ at time $t \in \Re^+$ with $t \in [\tau_i, \tau_i + \frac{v_i}{l_i}]$ is given by the coordinates in the plane of the intersection with respect to a specific coordinate system and is denoted by $\mathbf{p}_i(u_i(\mathbf{x}_i, t))$ where $u_i(\mathbf{x}_i, t) \in [0, 1]$ is the curvilinear coordinate of AV i on its trajectory curve. Denoting by l_i the length of the trajectory curve of AV i, $u_i(\mathbf{x}_i, t) = \frac{v_i}{l_i}(t - \tau_i)$.

For instance, considering a Cartesian system with origin in the center of the junction shown in Fig. 1, we describe the trajectories of an AV approaching from the lane S when it goes forward, turns right or turns left are indicated with p_{SN}, p_{SE} and p_{SW} respectively as follows:

$$p_{SN}(u_i) = \begin{bmatrix} 1 \\ -2 + 4u_i \end{bmatrix}, \; p_{SE}(u_i) = \begin{bmatrix} 2 - \cos\left(\frac{\pi}{2}u_i\right) \\ -2 + \sin\left(\frac{\pi}{2}u_i\right) \end{bmatrix},$$

$$p_{SW}(u_i) = \begin{bmatrix} -2 + 3\cos\left(\frac{\pi}{2}u_i\right) \\ -2 + 3\sin\left(\frac{\pi}{2}u_i\right) \end{bmatrix}.$$

The trajectories for the other lanes can be obtained by simply rotating the former ones. For the sake of simplicity in the following we denote $\mathbf{p}_i(u_i(\mathbf{x}_i, t)) = \mathbf{p}_i(\mathbf{x}_i, t)$.

B. Problem Statement

The primary condition is to ensure that no collision occurs during the crossing in MZ. To unsure the absence of any collision, we assume a predefined safe circle of vehicle i with radius ρ_i. For each pair of AVs $i, j \in N$, with $i \neq j$, crossing the intersection simultaneously, the following inequality must hold :

$$g_{i,j}(\mathbf{x}_i, \mathbf{x}_j, t) = \|\mathbf{p}_i(\mathbf{x}_i, t) - \mathbf{p}_j(\mathbf{x}_j, t)\|^2 - (\rho_i + \rho_j)^2 \geq 0 \quad \forall t. \tag{1}$$

Each vehicle may have a preferred arrival time and speed, so let $f_i(\mathbf{x}_i)$ be a cost function for AV i and let D_i denote the domain of the feasible values of $\mathbf{x}_i$. Then, the following optimization problem is obtained:

$$\min \sum_{i=1}^{n} f_i(\mathbf{x}_i)$$

$$\text{s.t.} \quad g_{i,j}(\mathbf{x}_i, \mathbf{x}_j, t) \geq 0 \quad \forall t \quad \forall i, j \in N, \; i \neq j$$

$$\text{and} \quad \mathbf{x}_i \in D_i.$$

This optimization problem falls into the category of Semi-Infinite Programming (SIP) because there are infinitely many constraints, due to the presence of time in the general

constraint expression. However, it can be transformed in a bi-level optimization problem, because just making sure the safety distance is respected in the moment of maximum proximity is enough to guarantee the absence of collisions. Let us denote by $t_{i,j}$ the time instant in which there is the maximum proximity between AVs i and j. Hence, it holds:

$$g_{i,j}(\mathbf{x}_i, \mathbf{x}_j, t_{i,j}) \leq g_{i,j}(\mathbf{x}_i, \mathbf{x}_j, t) \quad \forall t.$$

So, the problem is rewritten as:

$$\min \sum_{i=1}^{n} f_i(\mathbf{x}_i)$$
$$\text{s.t.} \quad g_{i,j}(\mathbf{x}_i, \mathbf{x}_j, t_{i,j}) \geq 0 \quad \forall t \quad \forall i, j \in N,\ i \neq j$$
$$\text{and} \quad \mathbf{x}_i \in D_i$$
$$\text{with} \quad t_{i,j}(\mathbf{x}_i, \mathbf{x}_j) = \underset{t}{\operatorname{argmin}}\, g_{i,j}(\mathbf{x}_i, \mathbf{x}_j, t).$$

In this work, we will assume that the goal of each vehicle is to cross the intersection experiencing the smallest delay or anticipation possible. This means that $f_i \equiv f, \forall i$. Since $\tau + l/v$ is the exit time of a generic vehicle and τ_0 and v_0 are the initial values of the decision variables, f is:

$$f(\mathbf{x}) = \frac{1}{2}\left(\tau + \frac{l}{v} - \left(\tau_0 + \frac{l}{v_0}\right)\right)^2. \tag{2}$$

III. The Proposed Solution

We propose a distributed algorithm that can be implemented by each AV. The solution strategy consists of two phases:

- first, an initial *feasible solution* is sought for allowing all vehicles to cross the intersection without collisions;
- second, an optimization procedure is carried out in the feasibility region seeking to optimize the function (2).

A. The Proposed Consensus Algorithm

At each iteration k, every AV $i \in N$ applies the consensus protocol. The main steps are summarized below.

Step 0: each AV i starts with the state $\mathbf{x}_i^{(1)} = [\tau_{0i}, v_{0i}]^T$.

Step 1: vehicle i computes for each AV j, the value of maximum proximity $t_{i,j}^{(k)}$, minimizing $g_{i,j}(\mathbf{x}_i^{(k)}, \mathbf{x}_j^{(k)}, t_{i,j}^{(k)})$.

Step 2: vehicle i computes each $c_{ij}^{(k)}$ on the basis of the values of $\mathbf{x}_j^{(k)}$ received from the AVs $j \in N$ ($c_{i,j}^{(k)} = 0$ if i and j will collide at the state of iteration k and $c_{i,j}^{(k)} = 1$ otherwise). If there exists a $c_{ij}^{(k)} = 0$, then vehicle i collides with j and we define the following function of the distances between the AVs that collide with such values of $t_{i,j}^{(k)}$:

$$G(\mathbf{x}_i^{(k)}) = \frac{1}{2} \sum_{j \in N_{Ci}^{(k)}} \|\mathbf{p}_i(\mathbf{x}_i^{(k)}, t_{i,j}^{(k)}) - \mathbf{p}_j(\mathbf{x}_j^{(k)}, t_{i,j}^{(k)})\|^2. \tag{3}$$

The goal is determining the values of $\tau_i^{(k)}$ and $v_i^{(k)}$ (i.e., $\mathbf{x}_i^{(k)}$) that maximize (3) in order to obtain $c_{i,j}^{(k)} = 1$ for all j. To solve this problem we use the gradient-based technique:

$$\nabla G(\mathbf{x}_i^{(k)}) = \sum_{j \in N_{Ci}^{(k)}} (\mathbf{p}_i(\mathbf{x}_i^{(k)}, t_{i,j}^{(k)}) - \mathbf{p}_j(\mathbf{x}_j^{(k)}, t_{i,j}^{(k)}))^T \nabla \mathbf{p}_i(\mathbf{x}_i^{(k)}, t_{i,j}^{(k)}). \tag{4}$$

If $C_i^{(k)} = \prod_{j \in N} c_{i,j}^{(k)} = 0$ then the state $\mathbf{x}_i^{(k)}$ is updated by the gradient (4):

$$\tau_i^{(k+1)} = \tau_i^{(k)} + \alpha \delta_\tau$$
$$v_i = v_i^{(k)} + \alpha \delta_v$$

where $\alpha > 0$ is an arbitrary real parameter. The value of $v_i^{(k+1)}$ is updated by v_i, considering also v_{MINi} and v_{MAXi}.

Step 3: If $C_i^{(k)} = \prod_{j \in N} c_{i,j}^{(k)} = 1$ then a feasible solution is found. At this point the vehicles start to optimize the cost function by making sure the collision constraints are not violated. To minimize f, a gradient-based method is again used:

$$\nabla f(\mathbf{x}_i^{(k)}) = \left(\tau_i^{(k)} + \frac{l}{v_i^{(k)}} - \left(\tau_{0i} + \frac{l}{v_{0i}}\right)\right) \begin{bmatrix} 1 \\ -\frac{l}{(v_i^{(k)})^2} \end{bmatrix}.$$

The new values of the state $\mathbf{x}^{(k+1)}$ are:

$$\tau_i = \tau_i^{(k)} + \beta \left(\tau_i^{(k)} + \frac{l}{v_i^{(k)}} - \left(\tau_{0i} + \frac{l}{v_{0i}}\right)\right)$$
$$\bar{v}_i = v_i^{(k)} - \beta \left(\tau_i^{(k)} + \frac{l}{v_i^{(k)}} - \left(\tau_{0i} + \frac{l}{v_{0i}}\right)\right) \frac{l}{(v_i^{(k)})^2}.$$

The new possible value of $\mathbf{x}^{(k+1)}$ is $[\tau_i, v_i]^T$, with $v_i = \bar{v}_i$ but considering also v_{MINi} and v_{MAXi}. In order to verify that the new values of $[\tau_i, v_i]^T$ guarantee to avoid collisions, the algorithm is again applied. As a result, if $C_i^{(k)} = 1$ then $\mathbf{x}^{(k+1)} = [\tau_i, v_i]^T$ else $\mathbf{x}^{(k+1)} = \mathbf{x}^{(k)}$, i.e. if a collision occurs the state is not updated by the new values.

IV. Conclusions

This work addresses the problem of controlling AVs crossing an intersection without any traffic signal. The objective is to minimize the difference between the obtained AV exit times from the intersection and the forecast ones, guaranteeing the safety constraints. **This work has been accepted for presentation at CDC 2022, 61st IEEE Conference on Decision and Control, that will be held in Cancun, Mexico, Dec. 6-9, 2022**. Future research will consider a larger number of vehicles.

References

[1] M. Bashiri and C. H. Fleming, "A platoon-based intersection management system for autonomous vehicles," in *2017 IEEE Intelligent Vehicles Symposium (IV)*, 2017, pp. 667–672.

[2] L. Wang, Y. Shi, X. Xiao, X. Cao, and F. Qu, "A scheduling algorithm for pass-through of connected and automated vehicle with different priorities in non-signalized intersection," in *2021 IEEE International Conference on Smart Internet of Things (SmartIoT)*. Los Alamitos, CA, USA: IEEE Computer Society, aug 2021, pp. 166–173.

[3] A. A. Malikopoulos, C. G. Cassandras, and Y. J. Zhang, "A decentralized energy-optimal control framework for connected automated vehicles at signal-free intersections," *Automatica*, vol. 93, pp. 244–256, 2018.

Distributed Estimation of All Distinct Eigenvalues of the Laplacian Matrix via Data-Driven Consensus Optimization

Claudia Congiu, Diego Deplano, Alessandro Giua, and Mauro Franceschelli

***Abstract*— This abstract introduces a distributed algorithm for discrete-time multi-agent systems (MAS) to compute all the distinct eigenvalues of the Laplacian matrix without any knowledge about the global undirected network topology. The algorithm resorts to an ingenious combination of standard techniques, such as wave equation on graphs, distributed optimization, and data-driven estimation. In a nutshell, the agents execute the wave equation so that each state trajectory persistently oscillates with modes that depend on the eigenvalues of the Laplacian matrix, then, exploiting the only knowledge of their own state trajectory, the agents solve a distributed optimization problem, from which a data-driven model of the whole system is determined and, in turn, the eigenvalues can be readily inferred.**

The main advantages of the proposed algorithm are: 1) the ability of each agent to estimate also eigenvalues corresponding to modes unobservable from its own state trajectory, and 2) a much greater numerical stability and therefore improved scalability to large networks with respect to competing approaches.

Different from the current literature, we combine the wave equation method and the formulation of a distributed optimization problem for improved numerical stability in large networks.

I. Introduction

Motivation. The behavior of a MAS is strongly influenced by the pattern of interaction among the agents in the network. Algebraic graph theory provides a number of powerful tools, in particular, the spectral properties of the Laplacian matrix associated to such graphs emerged as pivotal in the analysis and design of interconnected systems. Therefore, computing eigenvalues of a graph Laplacian in distributed fashion in the case where the full network topology is unknown is a key problem in MAS.

Literature review. One of the first distributed algorithms for eigenvalue computation in MAS took inspiration from the Power Iteration (PI) method [1]. Such methods usually involve successive matrix multiplications with a random initial vector and their normalization, which are centralized operation made distributed by exploiting consensus algorithm, as in [2], [3] for continuous-time systems.

Another strategy is to look at the past history of the agents while running specific distributed protocols in order to retrieve information about the Laplacian spectrum.

Both Charalambous *et al.* in [4] and Kibangou *et al.* [5] proposed distributed protocols based on the execution of a consensus protocol to enable the agents to compute in finite-time the set of observable eigenvalues, where the former deals with general weighted digraphs and the latter deals with undirected graphs. In contrast, a number of works force the agents' states to oscillate and then retrieve information about the eigenvalues via Fourier Transform [6]–[8].

These methods involve the estimation of the frequency at which the states' oscillates via peak-detection algorithms, which is not robust in large networks due to the occurrence of spectral leakage events. In addition, the agents can only estimate the eigenvalues associated with the modes that are observable and thus some agents may observe only a subset of the eigenvalues.

A last methodology employed for estimating the Laplacian spectrum is that of recasting the problem into a distributed optimization problem, such as in [9] for discrete-time systems and in [10] for continuous-time systems.

II. Distributed Spectrum Estimation

We consider Multi-Agent Systems (MASs) where n agents interact according to an undirected graph $\mathcal{G} = (\mathcal{V}, \mathcal{E})$, and denote with $L = \{\ell_{ij}\}$ the corresponding normalized Laplacian matrix.

The proposed algorithm consists in three main steps to be performed by each agent in the network, which are detailed in the next subsections.

A. Step 1: Local interaction based on wave equation

The agents execute

$$x_i(k+1) = 2x_i(k) - x_i(k-1) - c^2 \sum_{j \in \mathcal{N}_i} \ell_{ij} x_i(k).$$

In this way, each agent's state trajectory persistently oscillates at frequencies corresponding to the eigenvalues of the Laplacian matrix L. We claim that this strategy improves numerical stability for large networks if compared to the employment of standard consensus dynamics as in [4]. Although a formal proof of this claim is the object of current work, in this abstract we corroborate the claim by means of numerical simulations in Section III.

B. Step 2: Distributed Data-Driven Model Identification

By writing the wave equation in a compact form,

$$\underbrace{\begin{bmatrix} \boldsymbol{x}(k+1) \\ \boldsymbol{x}(k) \end{bmatrix}}_{\boldsymbol{z}(k)} = \underbrace{\begin{bmatrix} 2I_n - c^2 L & -I_n \\ I & \mathbf{0}_{n\times n} \end{bmatrix}}_{M} \underbrace{\begin{bmatrix} \boldsymbol{x}(k) \\ \boldsymbol{x}(k-1) \end{bmatrix}}_{\boldsymbol{z}(k-1)},$$

the relation between the modes of the oscillating network and the eigenvalues of the Laplacian matrix L is revealed. Then an equivalent representation in state-space form is given by

C. Congiu, D. Deplano, M. Franceschelli and A. Giua are with DIEE, University of Cagliari, 09123 Cagliari, Italy. Emails: claudia.congiu@unica.it, diego.deplano@unica.it, mauro.franceschelli@unica.it, giua@unica.it

the following difference equation of the same order of the system,

$$z(k) = \sum_{j=0}^{2n-1} \theta_{j+1} \boldsymbol{z}(k-2n+j),$$

which is usually employed in data-driven system identification [11]. With this representation, the eigenvalues of the matrix M correspond to the roots of the monic polynomial whose coefficients are the entries of the vector $\boldsymbol{\theta} = [\theta_1, \theta_2, \ldots, \theta_{2n}]^\top$. If the order of the system is not known but it is upper bounded by $m \in \mathbb{N}_+$, then the state $\boldsymbol{z}(k)$ can be approximated by $\hat{\boldsymbol{z}}(k)$ from a data-driven perspective as an Auto Regressive (AR) model where $\boldsymbol{\theta}$ is unknown but the values of $z(k)$ have been collected over a time window of observation of length $T_{obs} \in \mathbb{N}_+$. One can use the least-squares method to estimate the vector $\boldsymbol{\theta}$ that best makes $\hat{\boldsymbol{z}}(k)$ fit $\boldsymbol{z}(k)$, i.e., $\boldsymbol{\theta}$ is the solution to the following distributed optimization problem

$$\begin{aligned} \min_{\boldsymbol{\theta}_1,\ldots,\boldsymbol{\theta}_n} \quad & \sum_{i\in\mathcal{V}} \sum_{k=m+1}^{T_{obs}} \|\hat{\boldsymbol{z}}_i(k) - \boldsymbol{z}_i(k)\|^2, \\ \text{s.t.} \quad & \boldsymbol{\theta}_i = \boldsymbol{\theta}_j \quad \forall (i,j) \in \mathcal{E} \end{aligned}$$

where $\hat{\boldsymbol{z}}_i(k)$ is the local estimate of $\boldsymbol{z}_i(k)$ made by the i-th agent.

C. Step 3: Eigenvalue estimation procedure

Once the agents in the network have agreed upon a common vector of coefficients $\boldsymbol{\theta}^*$, they can estimate the eigenvalues of matrix L by computing the roots of the polynomial whose coefficients are the entries of $\boldsymbol{\theta}^*$, namely,

$$r^m - \theta_m^* r^{m-1} - \theta_{m-1} r^{m-2} - \ldots - \theta_2 r - \theta_1 = 0.$$

III. Numerical simulations

In this section we run our proposed method and Algorithm 3 in [4] over networks with line topology by increasing the number of agents $n = 3, 4, \ldots, 19, 20, 30, 40, \ldots, 100$. We consider 10 different instances of each problem with different initial conditions and show in Fig.1(left) the average results, by considering the estimation of an agent from which all the modes of the system are observable. With this setup, the comparison is made fair since both algorithms theoretically allow agent i^* to estimate all the eigenvalues of the Laplacian matrix.

Fig. 1 (right) shows that when our algorithm is executed by the MAS, the agent estimates all the eigenvalues for any network size and with a small error $\approx 10^{-8}$ that does not increase with the size of the network. On the other hand, Fig 1 shows that when Algorithm 3 in [4] is executed by the MAS, the agent can compute all the eigenvalues of the Laplacian matrix only for small networks, namely $n \leq 12$. However, for larger networks with $n > 12$, the agent fails in computing all the eigenvalues, meaning that some of the eigenvalues are not estimated at all and some eigenvalues are estimated with large error.

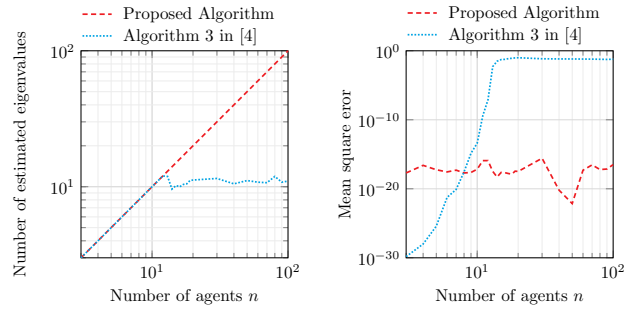

Fig. 1: Eigenvalue estimation in line networks: (left) number of estimated eigenvalue, (right) error made in the estimation.

IV. Conclusions

We have proposed a novel algorithm for the distributed estimation of the eigenvalues of the Laplacian matrix which improves numerical stability in large networks with respect to other similar methods. Currently, we are formalizing the characterization of the accuracy of the algorithm and reformulating the algorithm as an online distributed optimization problem.

References

[1] D. Kempe and F. McSherry, "A decentralized algorithm for spectral analysis," *Journal of Computer and System Sciences*, vol. 74, no. 1, 2008.

[2] P. Yang, R. A. Freeman, G. J. Gordon, K. M. Lynch, S. S. Srinivasa, and R. Sukthankar, "Decentralized estimation and control of graph connectivity for mobile sensor networks," *Automatica*, vol. 46, 2010.

[3] L. Sabattini, C. Secchi, N. Chopra, and A. Gasparri, "Distributed control of multirobot systems with global connectivity maintenance," *IEEE Transactions on Robotics*, vol. 29, no. 5, 2013.

[4] T. Charalambous, M. G. Rabbat, M. Johansson, and C. N. Hadjicostis, *Distributed Finite-Time Computation of Digraph Parameters: Left-Eigenvector, Out-Degree and Spectrum*.

[5] A. Y. Kibangou and C. Commault, "Decentralized laplacian eigenvalues estimation and collaborative network topology identification," *IFAC Proceedings Volumes*, vol. 45, 2012.

[6] M. Franceschelli, A. Gasparri, A. Giua, and C. Seatzu, "Decentralized laplacian eigenvalues estimation for networked multi-agent systems," in *48th IEEE Conference on Decision and Control (CDC)*, IEEE, 2009.

[7] T. Sahai, A. Speranzon, and A. Banaszuk, "Hearing the clusters of a graph: A distributed algorithm," *Automatica*, vol. 48, no. 1, 2012.

[8] M. Franceschelli, A. Gasparri, A. Giua, and C. Seatzu, "Decentralized estimation of laplacian eigenvalues in multi-agent systems," *Automatica*, vol. 49, 2013.

[9] T.-M.-D. Tran and A. Y. Kibangou, "Distributed estimation of laplacian eigenvalues via constrained consensus optimization problems," *Systems & Control Letters*, vol. 80, 2015.

[10] M. Zareh, L. Sabattini, and C. Secchi, "Distributed laplacian eigenvalue and eigenvector estimation in multi-robot systems," in *Distributed autonomous robotic systems*, Springer, 2018.

[11] S. Bittanti, *Model identification and data analysis*. John Wiley & Sons, 2019.

Water resources systems control and optimization: real case studies

Zanoli Silvia Maria, Pepe Crescenzo
LISA (Laboratory for Interconnected Systems Supervision and Automation)
DII (Dipartimento di Ingegneria dell'Informazione)
Università Politecnica delle Marche, Ancona (AN)
s.zanoli@univpm.it

Keywords – Advanced Process Control, Model Predictive Control, optimization, energy saving, Water Distribution Network, Hydroelectric Power Plant.

Among renewable sources, water is already largely exploited for energy production. However, a rational water usage is fundamental to target the objectives proposed by sustainable development, Agenda 2030 and smart cities. Water Distribution Networks (WDNs) and hydroelectric plants represent some examples of industries where a rational water usage would be obtained. LISA (Laboratory for Interconnected Systems Supervision and Automation) research group studies advanced techniques for process control and optimization. The research group developed many proprietary packages for different companies. Some of the first proprietary packages, developed in collaboration with i.Process, now Alperia group [1], refer to steel and cement industries (see [2], [3], [4]) where both energy savings and quality improvement were achieved. Here APC (Advanced Process Control) systems based on Model Predictive Control (MPC) techniques where applied. The experience gained on steel and cement industry sectors allowed a *cross fertilization* process to other sectors, in particular to the water resources sector [5]. The research activity initially focused on the control and optimization of a WDN and then on the water management of a hydroelectric power plant [5].
WDNs are complex systems generally composed of a large number of interconnected elements such as reservoirs, pipes, pumps, valves and other hydraulic elements. The presence of different conflicting objectives, e.g. fulfilling customers' water demand versus the minimization of energy consumption and water losses/leakages, represents an interesting challenge in the management of WDNs. Typically, a considerable number of pumps are used to convey water into elevated reservoirs from which the consumer demand is supplied. The high consumption of electrical energy associated with pumping activities, constitutes the largest expense for water utilities. A project aimed at the optimization of a subnet of an Italian WDN has been completed [6]. Two distinct phases have characterized the project: the first phase has been focused on the creation of District Metered Areas (DMAs) within the WDN while the design and installation of an APC system have been performed in the second phase. The APC system aims to improve the energy efficiency of the subnet through an automatic and smart management of the pumping stations involved, while minimizing the average pressure of the considered DMA (DMA1, see Fig. 1). The proposed average pressure minimization strategy is based on a two-layer MPC scheme that handles model uncertainties through a deadbeat Kalman filter. According to the authors' knowledge, this approach resulted innovative in WDNs field. In addition, tailored control strategies ("move suppression" factors and smart policies for process constraints handling) have been applied for the proposed pump stations scheduling algorithm which, according to the authors' knowledge, result innovative in WDNs pump scheduling applications [6], [7], [8]. After about three years from the commissioning, the service factor of the APC

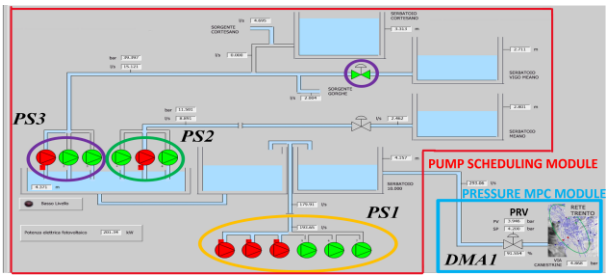

Figure 1 - Scheme of WDN APC system.

Table 1 - Global results: 2019-2020 WDN savings and benefits.

	2019	2020
BAC (Billed Authorized Consumption) [m^3]	6700000	
Water saved [m^3]	81474.46	136875.29
Electricity saved [kWh]	28480.26	52842.49
kg CO2 equivalents avoided [$kgCO_2$]	8770	16280
tep [tep]	5.33	9.88
Pressure reduction [%]	2.75	4.67
Loss reduction [%]	5.43	9.13

system is greater than 95%. Table 1 reports 2019-2020 saving and benefits related to DMA1 project. BAC (Billed Authorized Consumption) represents the billed water related to DMA1 (about 63% of the total water). Thanks to the developed project, a significant reduction of the average pressure with respect to the defined baseline (about 5.2 bar) has been achieved. In particular, 2.75% (2019) and 4.67% (2020) pressure reduction has been obtained. Thanks to this result, the maintenance interventions have been significantly reduced [8]. Finally, it is worth to note the significant water saving achieved, along with a substantial reduction in electricity demand [8].

A sector that strictly depends on the water resources is the hydroelectric one that is growing in global energy production. Hydroelectric energy is a renewable energy that transforms the movement of large water masses into electricity. Falling or moving water guarantees kinetic energy, which in turn is transformed into electricity thanks to turbines and alternators. In the hydroelectric power plant field, LISA research group developed a project where APC strategies have been designed and applied for the manipulation of a regulation gate on an Italian hydroelectric power plant [9], [10]. The considered regulation gate connects the two reservoirs of a hydroelectric power plant. In particular, thanks to the goodness of fit provided by the identified linear plant model, MPC technique has been selected, based on a Quadratic Programming (QP) problem. The project brought significant benefits to water management of the plant. The transition from the previous manual management to the automatic management of the regulation gate introduced by the APC system has brought benefits, e.g. implementing gradual variations on the regulation gate. The designed control system automatically adjusts the regulation gate respecting the control objectives for the downstream reservoir in order to ensure the expected energy production, ensuring the volumes of water necessary for implementation of the production plan. The ability to guarantee service and robustness in the different plant conditions, still leads today to obtain a service factor always greater than 90% [9], [10].

The specific hardware and software configuration of the developed APC systems is characterized by a PC, interconnected to the plant network, hosting the algorithms that supervise, control and optimize the process. These actions are performed generating the commands that are automatically sent to the plant. This type of configuration has been certified as Industry 4.0 compliant [1]. Further applications of the control and optimization tools developed concern district heating plants and HVAC (Heating, Ventilation and Air Conditioning) systems.

References

[1] https://www.alperia.eu/it

[2] S. M. Zanoli, F. Cocchioni, C. Valzecchi, C. Pepe, “Model Predictive Control of a Pusher Type Reheating Furnace,” Lecture Notes in Electrical Engineering (Proceedings of the 14th APCA International Conference on Automatic Control and Soft Computing, CONTROLO), vol. 695, 2020. doi: http://dx.doi.org/10.1007/978-3-030-58653-9_44

[3] S. M. Zanoli, C. Pepe, G. Astolfi, E. Moscoloni, "Analysis and Modeling of Steel Industry Reheating Furnace Billets Temperature," in: Proceedings of 2022 23rd International Carpathian Control Conference (ICCC), 2022, pp. 337-342. doi: http://dx.doi.org/10.1109/ICCC54292.2022.9805896

[4] S. M. Zanoli, L. Orlietti, F. Cocchioni, G. Astolfi, C. Pepe, “Optimization of the Clinker Production Phase in a Cement Plant,” Lecture Notes in Electrical Engineering (Proceedings of the 14th APCA International Conference on Automatic Control and Soft Computing, CONTROLO), vol. 695, 2020. doi: http://dx.doi.org/10.1007/978-3-030-58653-9_25

[5] S. M. Zanoli, C. Pepe, G. Astolfi, “Advanced Process Control applications to water resources systems: two industrial case studies,” accepted for publication in: 2nd IFAC Workshop on Control Methods for Water Resource Systems (CMWRS), 2022.

[6] S. M. Zanoli, G. Astolfi, L. Orlietti, M. Frisinghelli, C. Pepe, “Water Distribution Networks Optimization: a real case study,” IFAC-PapersOnLine, vol. 53, no. 2, 2020, pp. 16644-16650 (presented at 21st IFAC World Congress 2020). doi: https://doi.org/10.1016/j.ifacol.2020.12.794

[7] C. Pepe, G. Astolfi, L. Orlietti, C. Valzecchi, S. M. Zanoli, “Optimal Scheduling of Pumping Stations and Pressure Minimization of a Water Distribution Network,” Lecture Notes in Control and Information Science (Proceedings of the 15th European Workshop on Advanced Control and Diagnosis, ACD), 2019. doi: http://dx.doi.org/10.1007/978-3-030-85318-1_54

[8] S. M. Zanoli, C. Pepe, G. Astolfi, L. Orlietti, “Applications of Advanced Process Control techniques to an Italian Water Distribution Network,” waiting for review in: IEEE Transactions on Control of Network Systems (Special Issue on Smart City-Networks).

[9] S. M. Zanoli, C. Pepe, G. Astolfi, F. Luzi, "Model Predictive Control for Hydroelectric Power Plant Reservoirs," in: Proceedings of 2022 23rd International Carpathian Control Conference (ICCC), 2022, pp. 331-336. doi: https://doi.org/10.1109/ICCC54292.2022.9805881

[10] S. M. Zanoli, C. Pepe, G. Astolfi, I. Cervigni, “Model Predictive Control aimed at satisfying the production plan of a hydroelectric plant,” accepted for publication in: 17th IEEE International Conference on Control & Automation (ICCA), 2022.

sEMG-driven HITL Robotic Grasping: Soft-DTW Neural Networks Allow Minimally Supervised Regression-based Myocontrol

Alessandra Bernardini, Roberto Meattini, Gianluca Palli and Claudio Melchiorri

***Abstract*—In this study we present a novel method for regression-based sEMG-driven human-in-the-loop (HITL) control of robotic hands, i.e. myocontrolled robotic grasping. Specifically, we use a differentiable version of the Dynamic Time Warping (DTW) similarity measure as loss function to perform the training of a feed-forward neural network without the necessity of instant-by-instant data labelling. The absence of point-by-point labelling of the training dataset is the key advantage of the proposed architecture with respect to state-of-the-art sEMG-based supervised regression techniques, since it considerably simplifies training procedures. Results of both simulation and experimental studies demonstrate that the presented method allows successful myocontrol of artificial hands, reporting performances comparable with standard supervised regression approaches.**

***Index Terms*—Robotic grasping, robotic hands, myoelectric Control, telerobotics and teleoperation**

I. Introduction

Over the years, researchers have extensively developed control strategies for robotic grasping devices using surface electromyography (sEMG) signals. In particular, state-of-the-art supervised regression algorithms for robotic hand grasping control require point-by-point labelling of the training dataset. This often results in complicated and annoying training procedures, in which input-target misalignments can easily degrade system's performances [1]. To overcome this problem, we exploited the properties of the Dynamic Time Warping (DTW) similarity measure to develop a neural network architecture which can be trained even in presence of substantial temporal misalignments between sEMG trainset and related labelling, for human-in-the-loop (HITL) control of robot hands. The effectiveness of this method was assessed both with simulation and experimental studies, involving a group of 5 subjects.

II. Materials and Methods

A. sEMG Signals Acquisition and Processing

Forearm's sEMG signals were acquired using the 8-channel OYMotion gForcePro armband positioned in correspondence of the *Flexor Digitorum Superficialis* and *Extensor Digitorum Communis* muscles. To remove all the sources of noise that can negatively affect the sEMG signal, a 50 Hz notch filter was used to remove powerline interference, while a 20 Hz high pass filter was intended to reduce baseline noise. Lastly, the Root Mean Square (RMS) value of the signal was computed on a 200 ms sliding window with no overlapping.

B. Robotic Hand and Grasp Control

The performances of the proposed minimally supervised regression approach were evaluated using the simulator of the University of Bologna Hand version IV (UB Hand IV) [2], which is a five-fingered anthropomorphic robotic hand. The opening/closing motion of the hand can be regulated by modulating the hand closure level in the range [-1, 1], where 1 corresponds to the open configuration and -1 to the closed one. Incidentally, note that the hand closure level is simply the network output, that can be thus used to control the hand motion.

C. Soft-DTW Neural Network

To perform a minimally supervised regression of sEMG signals in continuous grasping control commands, we realized a feed-forward neural network to be trained with a soft-DTW based loss function. The soft-DTW divergence is a differentiable measure used to evaluate the similarity between time series independently from phase shifts and temporal distortions [3], which is nonnegative and minimized for identical temporal sequences. As a consequence, it can be used to construct a network robust to training target misalignments. In our application, the input of the network was the RMS value of the sEMG signals recorded by 8 bipolar surface electrodes, while the output was the grasp closure level used to regulate the opening/closing motion of the hand. Specifically, we trained the network using the soft-DTW divergence [3] as fitting loss between the network output and the reference target. Note that the target used to train the network is built a posteriori, once the training dataset has been recorded. More in detail, the user is first instructed to perform a certain number of power grasp opening/closing motions, without any visual reference and starting from the fully open hand. Then the target reference is built as a trapezoidal profile between 1 (hand fully open) and -1 (closed hand).

III. Simulation Study

As first step, we developed a Matlab simulation of the sEMG signals recorded by 8 bipolar surface electrodes placed on the forearm, during the execution of three repetitions of the

The authors are with the Dept. of Electrical, electronic and System Eng. (DEI), University of Bologna, Bologna, Italy.

This work was supported by the European Commission's Horizon 2020 Framework Programme with the project REMODEL under Grant agreement No. 870133.

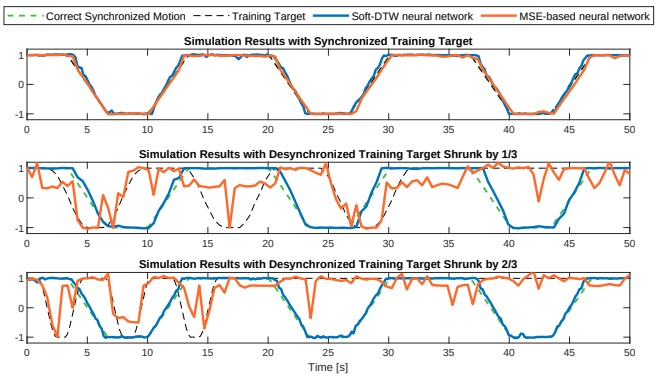

Fig. 1. Soft-DTW and MSE-based neural networks training outputs for the simulation study.

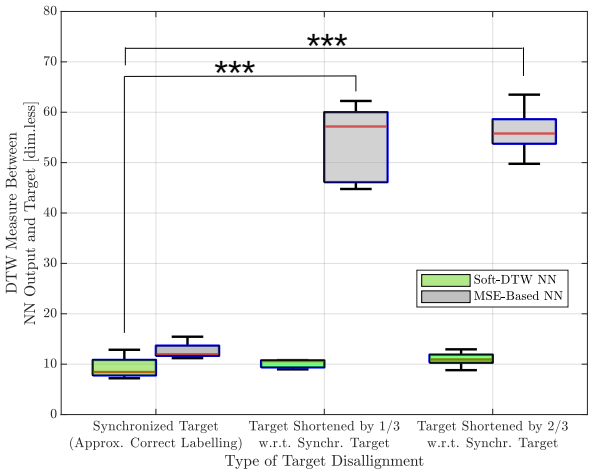

Fig. 2. Boxplot of the nested CV results over the five subjects (statistically significant difference is represented with the symbol "∗∗∗").

power grasp motion. To study the effectiveness of our soft-DTW neural network in extracting control commands from sEMG signals, we trained the network with three different targets: the *target synchronized* with the actual hand motion, the *target shrunk by 1/3* and the *target shrunk by 2/3*. The results obtained in the simulation study are reported in Fig. 1 along with the results obtained with a classical Mean Square Error (MSE)-based neural network. As can be observed in the figure, both neural networks were able to reconstruct the correct output in case of synchronized target, whereas the MSE-based neural networks trained with the target shrunk by 1/3 and 2/3 were not able to catch target desynchronization. Oppositely, the soft-DTW neural network performed well in all the cases.

IV. Experimental Session and Results

Furthermore, an experimental study was conducted to evaluate the performances of the proposed soft-DTW neural network with respect to target misalignments.

In a way similar to the simulation case, we considered three different case-study: the *target synchronized* with the actual hand motion, the *target shrunk by 1/3* and the *target shrunk by 2/3*. To this aim, the participants were asked to perform 5 repetitions of the power grasp motion, while their sEMG were recorded. The stored datasets were then used to conduct a nested cross-validation (nested CV) for each target type, consisting of a parameters tuning phase and a performance evaluation phase. The results of the nested CV over the 5 subjects are presented in the boxplots of Fig. 2. As illustrated, the outcomes of the soft-DTW neural network were compared with the outcomes of a classical MSE-based neural network trained with the same target signals, but using the MSE as loss function. The one-way ANOVA test conducted on these results showed a statistically significant difference between the results obtained with the soft-DTW neural network trained with the three targets and the MSE-based neural network trained with the synchronized target. These findings, together with the outcomes of the training phase reported in Fig. 3, show the robustness of the soft-DTW neural network with respect to

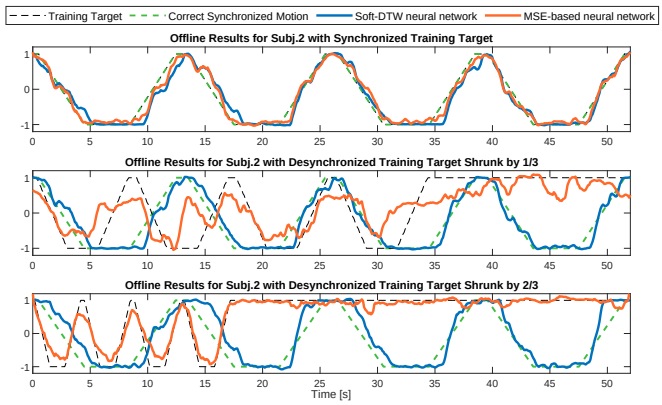

Fig. 3. Example of soft-DTW and MSE-based neural networks training outputs for the three different targets.

labelling misalignments. Indeed, as depicted in Fig. 3, the MSE-based neural network trained with the target shrunk by 1/3 and 2/3 is not able to manage labelling desynchronizations.

V. Conclusions

In this study we have presented a soft-DTW neural network to perform regression-based myocontrol of robotic hands without the need of an exact labelling of the training dataset. First, the feasibility of the proposed approach has been tested in a simulation study. Additionally, experiments were conducted to show the robustness of the proposed approach with respect to target misalignments.

References

[1] H. Hermens, S. Stramigioli, H. Rietman, P. Veltink, and S. Misra, "Myoelectric forearm prostheses: State of the art from a user-centered perspective," *J. Rehabil. Res. Dev.*, vol. 48, no. 6, p. 719, 2011.

[2] C. Melchiorri, G. Palli, G. Berselli, and G. Vassura, "Development of the ub hand iv: Overview of design solutions and enabling technologies," *IEEE Robotics & Automation Magazine*, vol. 20, no. 3, pp. 72–81, 2013.

[3] M. Cuturi and M. Blondel, "Soft-dtw: a differentiable loss function for time-series," in *International Conference on Machine Learning*. PMLR, 2017, pp. 894–903.

Physics Informed Gaussian Process Regression Methods for Robot Inverse Dynamics Identification

Giulio Giacomuzzo[1], Alberto Dalla Libera[1], Diego Romeres[2] and Ruggero Carli[1]

***Abstract*— In this extended abstract we present two recent contributions in the context of Physics Informed black-box inverse dynamics identification using Gaussian Processes (GPs). The first contribution consists in a novel kernel, named *Geometrically inspired Polynomial Kernel* (GIP) for single joint GP-based inverse dynamics identification. Driven by the fact that the inverse dynamics can be described as a polynomial function on a suitable input space, the GIP kernel restricts the regression problem to a finite-dimensional space which contains the inverse dynamics function, thus leading to improved data efficiency and generalization properties. The second contribution consists in the derivation of a multidimensional GP framework, named Lagrangian GPR, which overcomes the single joint approach and learns the inverse dynamics in a multidimensional setting. Exploiting the properties of GPs in connection with linear operators, Lagrangian GPR allows to impose by design the known symmetric structure of the Euler-Lagrange equation on the learned models. Moreover, since information is shared between different degrees of freedom (DOFs), this approach strongly improves data efficiency and generalization properties.**

I. INTRODUCTION

Inverse dynamics identification is a fundamental but challenging task in robotics. In the recent years black-box learning techniques have drawn the attention of the robotics community. Among them, a promising framework is represented by Gaussian Process Regression (GPR) [1]. Despite their ability to approximate very complex dynamics, however, GPR based black-box methods have two main limitations:

(i) they typically require large amount of samples and in general do not show satisfying generalization properties;
(ii) each torque component is typically modeled by an independent GP, which ignores the correlations and symmetries between different degrees of freedom (DOFs).

In order to address the aforementioned issues, a promising research line is represented by the so called *Physics-Informed* methods, which are based on the idea of embedding insights from physics as model prior. Instead of learning the inverse dynamics in a completely unstructured manner, which makes the problem unnecessarily hard, geometrical and physical properties are exploited both to improve learning performance and to impose physical consistency.

In this work we present our recent developments in the context of Physics-Informed GPR-based inverse dynamics identification of robot manipulators. In particular:

(i) inspired by the property of the inverse dynamics map components of being a polynomial function in an augmented input space, we proposed in [2] a novel black-box polynomial kernel named Geometrically Inspired Polynomial (GIP) kernel. This kernel aims at improving generalization and data efficiency by constraining the regression problem, for each DOF, into a finite dimensional space that contains the inverse dynamics equations.
(ii) Inspired by the fact that the inverse dynamics equations are obtained applying a linear operator to the Lagrangian function, we derived a multidimensional GPR framework, named Lagrangian GPR, where the inverse dynamics is learned considering correlation between different DOFs. Whitin this framework, symmetries of the system are imposed by design. Moreover, information is shared between different DOFs, which leads to improved data efficiency and generalization properties.

II. ROBOT INVERSE DYNAMICS

Consider a robotic arm with n joints, connected by $n+1$ links and let $\boldsymbol{q} \in \mathbb{R}^n$ be the vector of joint positions. The inverse dynamics is defined as the function mapping the robot state $\boldsymbol{x} = (\boldsymbol{q}, \dot{\boldsymbol{q}}, \ddot{\boldsymbol{q}}) \in \mathbb{R}^{3n}$ into the vector of generalized torques $\boldsymbol{\tau} \in \mathbb{R}^n$. Under the rigid body and energy conservation assumptions, the robot dynamics can be derived from the Lagrangian mechanics. Let the Lagrangian be the difference between kinetic energy T and potential energy V, namely $L = T - V$. Then, the system dynamics satisfies the Euler-Lagrange (EL) equation, expressed as

$$\boldsymbol{\tau} = \frac{d}{dt}(\nabla_{\dot{\boldsymbol{q}}} L(\boldsymbol{q}, \dot{\boldsymbol{q}})) + \nabla_{\boldsymbol{q}} L(\boldsymbol{q}, \dot{\boldsymbol{q}}) \tag{1}$$

where $\nabla_{\mathbf{x}} f(\cdot)$ denotes the gradient of f with respect to $\mathbf{x}$.

III. GAUSSIAN PROCESS REGRESSION

GPR can be employed to approximate an unknown function $f : \mathbb{R}^d \to \mathbb{R}$, given a training dataset $\mathcal{D} = \{X, \boldsymbol{y}\}$. The input samples are collected in $X \in \mathbb{R}^{Q \times N}$ while $\boldsymbol{y} \in \mathbb{R}^N$ contains the corresponding output measurements, with N being the number of observations and Q the input dimensions.

The output measurements $\boldsymbol{y}$ are assumed to be generated by the following probabilistic model

$$\boldsymbol{y} = \begin{bmatrix} f(\boldsymbol{x}_1) \\ \vdots \\ f(\boldsymbol{x}_N) \end{bmatrix} + \begin{bmatrix} w_1 \\ \vdots \\ w_N \end{bmatrix} = \boldsymbol{f}(X) + \boldsymbol{w}, \tag{2}$$

where $\boldsymbol{w}$ is i.i.d Gaussian noise with standard deviation σ. The unknown function f is modeled a priori as a zero-mean GP,

[1] Giulio Giacomuzzo, Alberto Dalla Libera and Ruggero Carli are with Department of Information Engeneering, University of Padova, Via Gradenigo 6/B, 35131 Padova, Italy [giacomuzzo@dei.unipd.it, alberto.dallalibera@unipd.it, carlirug@dei.unipd.it]

[2] Diego Romeres is with Mitsubishi Electric Research Laboratories (MERL), Cambridge, MA 02139 romeres@merl.com

namely $\boldsymbol{f}(X) \sim \mathcal{N}(0, \mathbb{K})$. Each element of the covariance matrix $\mathbb{K}$, known also as *kernel matrix*, is defined through a kernel function $k(\cdot,\cdot)$. In particular, the element of $\mathbb{K}$ in position (h, j) is equal to $k(\boldsymbol{x}_h, \boldsymbol{x}_j)$. Given the observations $\mathcal{D}$ and a new input location $\boldsymbol{x}_*$, it can be proved that the posterior distribution of $f(x_*)$ is Gaussian, with mean

$$\hat{f}_* = \boldsymbol{k}_*^T \boldsymbol{\alpha} \tag{3}$$

and covariance

$$\mathbb{V}[f_*] = k(\boldsymbol{x}_*, \boldsymbol{x}_*) - \boldsymbol{k}_*^T (\mathbb{K}^{(i)} + \sigma^2 I)^{-1} \boldsymbol{k}_*, \tag{4}$$

where

$$\boldsymbol{k}_* = [k(\boldsymbol{x}_*, \boldsymbol{x}_1), \ldots, k(\boldsymbol{x}_*, \boldsymbol{x}_N)]^T$$

and

$$\boldsymbol{\alpha} = (\mathbb{K} + \sigma_i^2 I)^{-1} \boldsymbol{y}.$$

The maximum a posteriori estimator coincides with the posterior mean $\hat{f}_*$. Within the GPR framework, a fundamental role is played by the kernel function: the whole complexity of GPR reduces to the choice of the correct kernel function for the problem at hand.

A. Single joint GPR Inverse dynamics identification

The GPR framework described above can be applied to the inverse dynamics identification problem. In particular, within the so called single-joint approach, each joint is considered individually and its torque $\boldsymbol{\tau}^{(i)}$ is modeled as an unknown function of the robot state $\boldsymbol{x} \in \mathbb{R}^{3n}$. Thus, the inverse dynamics identification problem reduces to solve n independents GPR problems.

IV. Geometrically Inspired Polynomial kernel

As already pointed out, the choice of the kernel is a crucial aspect in GPR. State of the art methods for single-joint Inverse dynamics identification rely on the so called *Squared Exponential* (SE) kernel [1]. This kernel function, however, capture only similarities between data and it ignores existing relations imposed by the physics and geometry of the problem. As a consequence, it shows the same data inefficiency and poor generalization issues mentioned above.

The Geometrically Inspired Polynomial (GIP) kernel, instead, is based on the property that each component $\boldsymbol{\tau}^{(i)}$ in eq. (1) is a polynomial function in a proper transformation of the GP input, fully characterized only by the type of each joint. Specifically, $\boldsymbol{q}$ is mapped in $\tilde{\boldsymbol{q}}$, the vector composed by the concatenation of the positions of prismatic joints and the sines and cosines of the positions of revolute joints. As proved in [2], the inverse dynamics eq. (1) is composed by polynomial functions in $\ddot{\boldsymbol{q}}$, $\dot{\boldsymbol{q}}$ and $\tilde{\boldsymbol{q}}$, where the elements of $\ddot{\boldsymbol{q}}$ have maximum relative degree of one, whereas the ones of $\dot{\boldsymbol{q}}$ and $\tilde{\boldsymbol{q}}$ have maximum relative degree two. To exploit this property, the GIP kernel is defined through the sum and the product of different polynomial kernels [3], hereafter denoted as $k_P^{(p)}(\cdot,\cdot)$ where p is the degree of the polynomial kernel. In particular,

$$K_{GIP}(\boldsymbol{x}, \boldsymbol{x}') = (k_P^{(1)}(\ddot{\boldsymbol{q}}, \ddot{\boldsymbol{q}}') + k_P^{(2)}(\dot{\boldsymbol{q}}, \dot{\boldsymbol{q}}'))k_Q(\tilde{\boldsymbol{q}}, \tilde{q}'). \tag{5}$$

where k_Q is given by the product of polynomial kernels with degree two. In this way, the GIP kernel allows defining a regression problem in a finite-dimensional function space where (1) is contained. From experimental results, the GIP kernel showed better data efficiency and generalization properties if compared to other black-box estimators. If compared to parametric models, instead, it shows similar generalization properties while requiring less prior information.

V. Lagrangian GPR Framework

The single joint approach is simpler and more computationally efficient, but it ignores known correlation between joints. As a result, the learned model is not guaranteed to respect the structure and symmetries imposed by the EL equation in (1). Our idea is to model the Lagrangian function as a zero-mean GP and then to exploit the invariance property of GPs under linear operators [4] to obtain a multidimensional GP framework for Inverse dynamics identification.

First, let $L(\boldsymbol{q}, \dot{\boldsymbol{q}}) \sim \mathcal{GP}(0, k_L(\boldsymbol{q}, \dot{\boldsymbol{q}}, \boldsymbol{q}', \dot{\boldsymbol{q}}'))$. Then consider the following proposition.

Proposition 1: Let $\boldsymbol{\mathcal{T}_x}$ be a linear operator and f be a GP such that

$$f(\boldsymbol{x}) \sim \mathcal{GP}(m(\boldsymbol{x}), k(\boldsymbol{x}, \boldsymbol{x}')). \tag{6}$$

Then, $g = \mathcal{T}_{\boldsymbol{x}} f$ is a (possibly multidimensional) GP such that

$$g(\boldsymbol{x}) \sim \mathcal{GP}(m_g(\boldsymbol{x}), k_g(\boldsymbol{x}, \boldsymbol{x}')) \tag{7}$$

with mean $m_g(\boldsymbol{x}) = \boldsymbol{\mathcal{T}_x} m(\boldsymbol{x})$ and kernel $k_g(\boldsymbol{x}, \boldsymbol{x}') = \boldsymbol{\mathcal{T}_x} k(\boldsymbol{x}, \boldsymbol{x}') \boldsymbol{\mathcal{T}_{x'}}$.

Defining the Lagrangian operator as $\mathcal{L}_{(\boldsymbol{q}, \dot{\boldsymbol{q}}, \ddot{\boldsymbol{q}})} = \frac{d}{dt} \nabla_{\dot{\boldsymbol{q}}} + \nabla_{\boldsymbol{q}}$, from eq. (1) we have that $\boldsymbol{\tau} = \mathcal{L}(\boldsymbol{q}, \dot{\boldsymbol{q}}, \ddot{\boldsymbol{q}}) L(\boldsymbol{q}, \dot{\boldsymbol{q}})$. Moreover, applying proposition 1 we obtain

$$\boldsymbol{\tau} \sim \mathcal{GP}(0, k_{\boldsymbol{\tau}}(\boldsymbol{x}, \boldsymbol{x}')) \tag{8}$$

with $k_{\boldsymbol{\tau}}(\boldsymbol{x}, \boldsymbol{x}') = \mathcal{L}_{(\boldsymbol{q}, \dot{\boldsymbol{q}}, \ddot{\boldsymbol{q}})} k_L(\boldsymbol{q}, \dot{\boldsymbol{q}}, \boldsymbol{q}', \dot{\boldsymbol{q}}')) \mathcal{L}_{(\boldsymbol{q}', \dot{\boldsymbol{q}}', \ddot{\boldsymbol{q}}')}$, where $\boldsymbol{x} = (\boldsymbol{q}, \dot{\boldsymbol{q}}, \ddot{\boldsymbol{q}})$ is the robot state. Note that this way we obtained a multidimensional GP. The extension of the GPR presented in section III to the multidimensional setting is straightforward [5].

Preliminary results showed that this approach provides improved data effeciency and generalization properties with respect to single joint methods. Moreover, the remaining degree of freedom represented by the choice of the lagrangian kernel k_L can be exploited to further improve the learning performances or to impose other constraints on the model, e.g. the positivity of the kinetic energy.

References

[1] C. E. Rasmussen, "Gaussian processes in machine learning," in *Summer school on machine learning*. Springer, 2003, pp. 63–71.

[2] A. Dalla Libera and R. Carli, "A data-efficient geometrically inspired polynomial kernel for robot inverse dynamic," *IEEE Robotics and Automation Letters*, vol. 5, no. 1, pp. 24–31, 2019.

[3] A. D. Libera, R. Carli, and G. Pillonetto, "A novel multiplicative polynomial kernel for volterra series identification," *arXiv preprint arXiv:1905.07960*, 2019.

[4] S. Särkkä, "Linear operators and stochastic partial differential equations in gaussian process regression," in *International Conference on Artificial Neural Networks*. Springer, 2011, pp. 151–158.

[5] Z. Chen, J. Fan, and K. Wang, "Remarks on multivariate gaussian process," *arXiv preprint arXiv:2010.09830*, 2020.

Tracking-based Distributed Aggregative Optimization for Cooperative Robotics

Guido Carnevale, Andrea Camisa, Giuseppe Notarstefano

Distributed optimization captures a variety of estimation and learning problems over networks. In most problems in distributed optimization, the cooperating agents share a common variable. However, in several scenarios of interest arising in cooperative robotics, such as multi-vehicle surveillance, the optimization variable is local to the agents and the cost functions depend not only on local information but also on some agregated form of it, such as the mean. This novel optimization framework, which is more suited for control applications, is recently gathering attention. Originally, it stems from distributed aggregative games where the objective is to compute a (generalized) Nash equilibrium rather than an optimal solution cooperatively. In our work, see [1], we focus on dynamic scenarios where online optimization problems arise due to, e.g., changing environmental state or time-varying robot positions. We propose a distributed optimization algorithm based on dynamic consensus techniques to reconstruct the global information and to optimize the overall cost function via gradient descent. The algorithm generalizes the recent work [2] by allowing for more general online set-ups and for the use of constant step-sizes. Thanks to refined steps in the algorithm evolution, we are able to prove tight bounds for the dynamic regret and linear convergence in case of time-invariant optimization problems. These stronger results are possible thanks to an analysis based on the evolution of a suitably defined dynamical system which has a Schur system matrix for certain choices of the parameters.

A. Online Aggregative Optimization Framework

The considered framework of distributed online aggregative optimization can be written in its general formulation as

$$\min_{\{x_i \in X_{i,t}\}_{\forall i}} \sum_{i=1}^{N} f_{i,t}(x_i, \sigma_t(x)), \tag{1}$$

in which each x_i is the decision vector associated to the i-th agent and $x := (x_1, \dots, x_N) \in \mathbb{R}^n$ is the global decision vector. At each time t, the i-th decision vector x_i is constrained to belong to a closed and convex set $X_{i,t}$. The objective functions $f_{i,t}$ consist of two arguments, where the first one is the local decision vector x_i and the second one is an aggregate information of the network, modeled with an *aggregation function* $\sigma_t(x)$ having the form

$$\sigma_t(x) := \frac{\sum_{i=1}^{N} \phi_{i,t}(x_i)}{N},$$

where each $\phi_{i,t}$ is a function modeling the contribution of the i-th agent to the aggregative variable at time t. It is assumed that the overall objective function, denoted as $f_t(x, \sigma_t(x))$, is strongly convex for all t. In the considered online optimization scenario, the objective is to minimize the so-called dynamic regret. For each time t, let $x_{i,t}$ be the solution estimate of the problem maintained by agent i and let $x_t^\star$ be the optimal solution of problem (1). Then, the dynamic regret is defined as

$$R_T := \sum_{t=1}^{T} f_t(x_t, \sigma_t(x_t)) - \sum_{t=1}^{T} f_t(x_t^\star, \sigma_t(x_t^\star)). \tag{2}$$

To concretize this online framework, we consider a surveillance task of a team of N robots aiming to protect a moving target from N moving intruders. The strategy of the team of robots is as follows. Each robot stays as close as possible to its associated intruder. Meanwhile, the whole team keeps its center of mass close to the target to be protected. A concept of this scenario is given in Fig. 1. To model this application using problem (1), one can proceed as follows. The decision vector x_i is the position of robot i, the aggregative variable $\sigma_t(x)$ is the team center of mass, while the i-th objective function weighs both the distance of robot i to its intruder and the distance of the center of mass to the target position at time t.

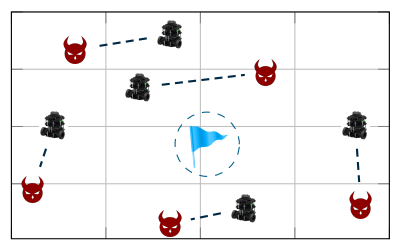

Fig. 1: Multi-robot surveillance scenario. The flag is the target to be protected. The black robots are the agents protecting the target, while devil icons denote intruders.

B. Projected Aggregative Tracking: Algorithm Description

In order to solve problem (1), one can use an online gradient method. The i-th block of such algorithm would read

$$x_{i,t+1} = x_{i,t} - \alpha[\nabla f_t(x_t, \sigma_t(x_t))]_i,$$

with an appropriate step size $\alpha > 0$. To this end, it is necessary to compute the gradient of the objective function. By applying the chain rule to problem (1), the gradient of $f_t(x, \sigma_t(x))$ reads

$$[\nabla f_t(x, \sigma(x))]_i = \tag{3}$$
$$= \nabla_1 f_{i,t}(x_i, \underbrace{\sigma_t(x)}_{\text{global}}) + \frac{\nabla \phi_{i,t}(x_i)}{N} \underbrace{\sum_{i=1}^{N} \nabla_2 f_{j,t}(x_j, \sigma_t(x))}_{\text{global}},$$

G. Carnevale, A. Camisa and G. Notarstefano are with the Department of Electrical, Electronic and Information Engineering, University of Bologna, Bologna, Italy, {guido.carnevale, a.camisa, giuseppe.notarstefano}@unibo.it. This result is part of the project "Distributed Optimization for Cooperative Machine Learning in Complex Networks" (No PGR10067) that has received funding from the Ministero degli Affari Esteri e della Cooperazione Internazionale.

where with $\nabla_1 f_{i,t}(\cdot,\cdot)$ and $\nabla_2 f_{i,t}(\cdot,\cdot)$ we denote the gradient of $f_{i,t}$ with respect to the first and the second argument respectively. However, note that the quantities highlighted with the braces are global information and none of the agents is aware of any of them. Indeed, in the considered distributed framework, each agent i is only aware of its locally available quantities, namely the objective function $f_{i,t}$, the contribution to the aggregative term $\phi_{i,t}$, and the constraint set $X_{i,t}$. Since in a distributed context agents are not allowed to share this information with a central server, this challenge is tackled by designing a suitable tracking mechanism.

Let us now introduce the proposed distributed algorithm, named Projected Aggregative Tracking. We assume the agents communicate according to a graph $\mathcal{G} := (\mathcal{V}, \mathcal{E})$, where $\mathcal{V} = \{1, \dots, N\}$ is the set of agents, $\mathcal{E} \in \mathcal{V} \times \mathcal{V}$ is the set of edges. Each agent i can exchange data only with its neighbors defined by $\mathcal{E}$. To the communication graph we associate a weighted adjacency matrix $\mathcal{A} \in \mathbb{R}^{N \times N}$, assumed to be doubly stochastic, i.e., such that $\sum_{j=1}^N a_{ij} = \sum_{j=1}^N a_{ji} = 1$ for all i. The tracking mechanism is as follows. Each agent i replaces the missing, global quantities in (3) with two auxiliary variables $s_{i,t}$ and $y_{i,t}$ that are iteratively updated according to a perturbed consensus dynamics. Hence, the algorithm at time t reads as

$$\tilde{x}_{i,t} = P_{X_{i,t}}\big[x_{i,t} - \alpha(\nabla_1 f_{i,t}(x_{i,t}, s_{i,t}) + \nabla \phi_{i,t}(x_{i,t}) y_{i,t})\big] \quad (4a)$$

$$x_{i,t+1} = x_{i,t} + \delta(\tilde{x}_{i,t} - x_{i,t}) \quad (4b)$$

$$s_{i,t+1} = \sum_{j=1}^N a_{ij} s_{j,t} + \phi_{i,t+1}(x_{i,t+1}) - \phi_{i,t}(x_{i,t}) \quad (4c)$$

$$y_{i,t+1} = \sum_{j=1}^N a_{ij} y_{j,t} + \nabla_2 f_{i,t+1}(x_{i,t+1}, s_{i,t+1}) - \nabla_2 f_{i,t}(x_{i,t}, s_{i,t}), \quad (4d)$$

where $\delta \in (0,1)$ a parameter. The update is composed as follows: (4a) performs a (projected) gradient descent step, while (4c) and (4d) are the updates of the trackers $s_{i,t}$ and $y_{i,t}$, which can be seen to converge to the two global quantities $\sigma_t(x_t)$ and $\sum_{j=1}^N \nabla_2 f_{j,t}(x_{j,t}, \sigma_t(x_t))$. Moreover, there is an additional convex combination step (4b), which turns out to be crucial to prove strong convergence properties for the algorithm.

C. Theoretical Properties of Projected Aggregative Tracking

In our work [1], we provide a thorough analysis of the algorithm. The first result regards the dynamic regret (2).

Theorem 1. *Let the agents run the steps of the distributed algorithm. Then, for sufficiently small step-size α and convex combinator δ, there exist constants $\lambda > 0, \rho \in (0,1)$ such that*

$$R_T \leq \frac{\lambda^2}{2}\left(\frac{\|z_0\|^2}{1-\rho^2} + 2\|z_0\| U_T + Q_T\right),$$

while $U_T, Q_T > 0$ depend on the variations of the problem with respect to time and the vector z_0 depends on the initial conditions of the algorithm (see (5)*).* □

As a corollary, when the algorithm is applied to a standard, time-invariant optimization problem, we obtain convergence to the optimal solution with a linear rate.

Corollary 1 (Static set-up)**.** *If the problem is static and α, δ are sufficiently small, then there exists constants $\lambda > 0, \rho \in (0,1)$ such that*

$$|f(x_t, \sigma(x_t)) - f(x^\star, \sigma(x^\star))| \leq \frac{\rho^{2t}\lambda^2}{2}\|z_0\|^2. \qquad \square$$

To perform the convergence analysis, we derive bounds for the following quantities: optimality error $\|x_t - x_t^\star\|$, consensus error of s_t, $\|s_t - \bar{s}_t\|$, and consensus error of y_t, $\|y_t - \bar{y}_t\|$, where $\bar{s}_t := \frac{1}{N}\sum_{i=1}^N s_{i,t}$ and $\bar{y}_t := \frac{1}{N}\sum_{i=1}^N y_{i,t}$ denote the mean of s_t and y_t. Let z_t be the vector with components

$$z_t := \begin{bmatrix} \|x_t - x_t^\star\| \\ \|s_t - \bar{s}_t\| \\ \|y_t - \bar{y}_t\| \end{bmatrix}. \quad (5)$$

It can be shown that z_t evolves as the perturbed linear system $z_{t+1} = A(\delta) z_t + B u_t$, where the entries of the matrices $A(\delta)$ and B depend on the problem parameters (such as, e.g., the strong convexity parameter of f_t) and u_t captures the variations of the problem with respect to time. One can see that, for sufficiently small $\delta > 0$, the matrix $A(\delta)$ is Schur.

D. Numerical Simulation

We show the results of a numerical simulation addressing the multi-robot surveillance scenario both in the online and static case. Specifically, we considered $N = 50$ agents and intruders, while, as regards the feasible sets, we picked a common box constraint. In the online case, the intruders, the target, and the constraint change according to randomly generated, piecewise linear trajectories. In the static case, the target and the intruder are placed in fixed, random locations. We performed 100 Monte Carlo trials with random initial positions of the agents. Fig. 2a shows the average dynamic regret R_t/t for the online case, while Fig. 2b shows the linear convergence of the solution error $\frac{\|x_t - x^\star\|}{\|x^\star\|}$ for the static problem, confirming Corollary 1.

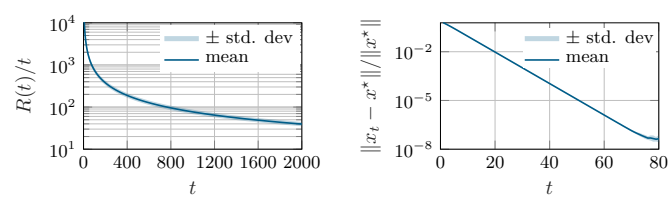

(a) Online case – Mean of the average dynamic regret and 1-standard deviation band.

(b) Static case – Mean of the solution error and 1-standard deviation.

Fig. 2: Numerical results of Montecarlo simulations on the multi-robot surveillance problem.

References

[1] G. Carnevale, A. Camisa, and G. Notarstefano, "Distributed online aggregative optimization for dynamic multi-robot coordination," *IEEE Transactions on Automatic Control*, 2022, to appear.

[2] X. Li, X. Yi, and L. Xie, "Distributed online convex optimization with an aggregative variable," *IEEE Transactions on Control of Network Systems*, 2021.

Motor Maps for legged locomotion control

Luca Patanè, Alessia Li Noce, Fabio Di Pietro, Paolo Arena

This research activity is part of an ongoing project focused on the design and development of model-free locomotion control systems for bio-inspired legged robots. Legged locomotion is considered a valid alternative to wheeled locomotion in such cases as minimally invasive exploration in unstructured and dangerous terrains and climbing tasks, but also for object manipulation [1], [2]. On the other side, locomotion control is a challenging task to be investigated, and different approaches are commonly adopted for controlling legged robots, requiring different subsystems devoted to handling multiple aspects such as leg coordination, travelling speed, balancing, reflexive behaviours (e.g., elevator and searching reflexes) and others. In our previous works, we highlighted the use of model-free approaches to handle some of the previously introduced domains. One of the adopted architectures was a Motor Map, successfully employed within an action-oriented perception system including weakly controlled chaotic dynamics [3] and for speed control in hexapod robots, also in presence of a *drosophila*-like biomimetic structure [4], [5].

Motor maps are neural structures proposed as an improvement of the more traditional Kohonen self-organising feature maps [6]. These are inspired by the topology-preserving maps identified in the brain, which encode the representation of sensory input signals into space-organised responding units; these, in turn, elicit an action in response to a given input stimulus. Motor maps expand the capabilities of Kohonen networks by adding the possibility to associate to a specific active neuron a required action to be executed [7].

In [3], an action-oriented perception loop was implemented via a bio-inspired architecture using a Motor Map controller (MMC). Perceptual meanings, useful for solving a given task (e.g. a foraging task implemented on an autonomous roving robot), can be autonomously learned, based on the environment-dependent patterns embedded into the controlled chaotic dynamics that are mapped into the robot actions through the MMC. An FPGA-based implementation of the whole control architecture was also proposed.

In [4], the CPG motor signals for controlling the locomotion in a *drosophila*-inspired hexapod robot, were modulated by the inputs provided by an MMC for speed control, also including reflexive paths. The MMC acts on the CPG by changing the phase displacement between the legs to converge towards stable free gaits able to guarantee the imposed reference speed.

In line with the results previously obtained, an MMC was recently adopted to compensate for attitude control errors in a simulated quadruped platform [8].

Luca Patanè is with the Department of Engineering, University of Messina, 98166, Italy (e-mail: lpatane@unime.it).

Paolo Arena, Alessia Li Noce and Fabio Di Pietro are with the Department of Electrical, Electronic and Computer Engineering, University of Catania, Italy

In literature, legged locomotion control is designed following a low-level and a high-level approach. The former imposes specific periodic trajectories to the robot legs, the latter is in charge of maintaining other references, such as attitude signals.

Traditional techniques mainly exploit the potentialities of convex model predictive control (MPC) to efficiently regulate the robot attitude while moving in unstructured environments. However, they are based on the knowledge of the analytical model of the robot.

It was demonstrated that the approximation of the complex nonlinear dynamics of quadruped robots through linear time-varying models can guarantee suitabletion and balance control in experesults riments involving running quadrupeds on flat terrains [9], [10]. However, the performance of the control action heavily relies on the feasibility of the prediction model. For this reason, in the literature, alternative strategies based uniquely on model-free, data-driven nonlinear structures, such as neural networks, were introduced into the control loop. Some examples of this approach refer to reinforcement learning techniques, for improving the capability of attitude maintenance while moving in unstructured environments [11], [12]. The main weakness of this solution is that, in principle, there is no guarantee of preserving stability in the control loop. Moreover, the knowledge of the system dynamics is completely discarded in the controller design. Our approach tries to merge model-based and model-free solutions to maintain the suitability of an MPC, adding compensation in case of unexpected disturbances through an MMC.

The quadruped robot taken into account to evaluate the performance of the proposed controller is the Mini Cheetah robot. It is a torque-controlled four-legged robot developed at the MIT Biomimetic Robotics Lab [9].

For controlling the pitch angle of the simulated Mini Cheetah, the pitch error and its derivative are considered as input signals for the MMC. Therefore, the MMC has two input units and twelve outputs, corresponding to the force components along the three orthogonal axes $f_{i,x}, f_{i,y}, f_{i,z}$ for each actuated leg ($i = 1, \cdots, 4$). Fig.1 shows a block scheme of the control loop. The MMC is added, as a feedforward block, to the underlying MPC. In particular, the leg control commands are generated in two different ways, according to the stance or swing phase of each leg. During the swing phase, the leg trajectory is simply planned using an interpolation of a series of waypoints using a Bezier curve approach. The stance phase is particularly relevant for stability and attitude control and it is realised using an MPC with the addition of a whole-body impulse controller (WBIC) [11], [9]. Here, the MPC computes the forces needed to maintain the body in a standing position, optimised on a $40Hz$ window; then these forces are used as input signals for a faster (i.e., $500Hz$) WBIC, which

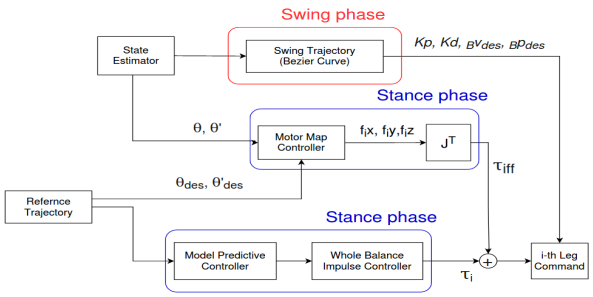

Fig. 1: The Mini Cheetah control scheme.

provides the stabilizing joint torques. During the stance phase, the MMC provides an additional nonlinear feedforward control action, in terms of forces, to be added to the underlying leg joint controller, after being transformed in joint torques $\tau_{i,ff}$ through the Jacobian matrix.

The most important aspect is the self-learning, model-free characteristic of the MMC. This can learn the right control law based on a *Reward Function* to be maximized. Its definition for the proposed application is here reported:

$$Reward = -(\Theta - \Theta_{ref})^2 - \frac{(\dot{\Theta} - \dot{\Theta}_{ref})^2}{(\Theta - \Theta_{ref})^4 + 1}\beta \qquad (1)$$

where Θ_{ref}, Θ, $\dot{\Theta}_{ref}$, $\dot{\Theta}$ are the reference and actual pitch, and the reference and actual pitch speed of the robot, respectively. The gain $\beta = 0.001$ was selected.

To assess the reliability of the learning process, a statistical analysis was performed, by running multiple trials of MMCs with a random weight initialization. The results obtained are depicted through the analysis of the Reward function, reported in Fig.2 (a). The outcome of a testing scenario is shown in Fig. 2 (b) where the pitch of the trotting robot is reported with and without the effect of the MMC (see Fig.2 (c)). It can be noticed that the traditional (MPC) controller alone is not able to compensate for a pitch error due to the presence of an unexpected load (i.e., about 25% of the robot weight) located on the front legs position.

The characteristics and advantages of the proposed controller are summarized below:

- The MMC is a nonlinear self-learning controller, uniquely based on measurements, without needing apriori knowledge of the robot physical characteristics, for the generation of the control law.
- Once the MMC is trained, the controller does not need internal iterations, since a static map is created. This generates a real-time, fast control action, suitable to be applied at different frequencies.
- Being a model-free approach, the MMC opens the possibility to be easily transferred to other robotic platforms.
- The nature of the MMC allows to create a nonlinear topographic representation of the system, for torque compensation. Suitable processing of the Kononen layer could be performed to explain the control action, along with the recent concept of explainable AI.
- The feedforward MMC action, injecting an additional torque signal focalised to compensate for disturbances, preserves the reliability of the underlying MPC-WBIC controller, previously designed.
- The most critical aspect to be taken into account is the Reward function definition, which is crucial for the MMC success. This has to be defined after a series of trials, together with the typical neural network parameters (i.e., neuron number, learning rate, etc.)

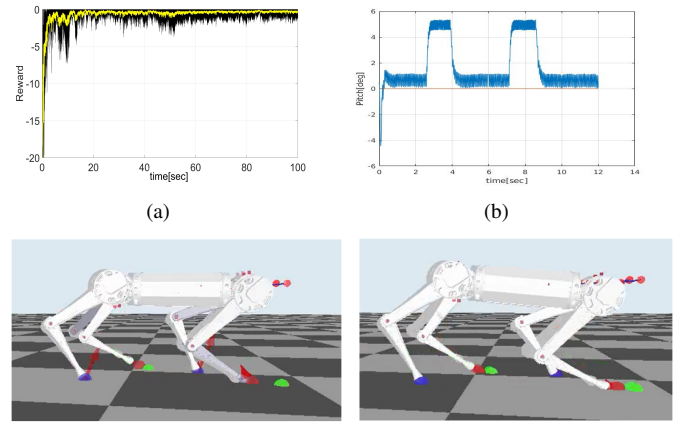

(a) (b)

(c)

Fig. 2: Effect of the MMC on the pitch control while the robot is trotting: (a) the mean and variance of the Reward function evaluated over 10 different trials; (b) trend of the pitch error during one trial; (c) snapshots showing the robot attitude in the sagittal plane when the MMC is active (left panel) and disabled (right panel). The MMC is disabled in the time intervals $[2.5,\ 4]s$ and $[7,\ 8.5]s$.

References

[1] M. Thor and P. Manoonpong, "Versatile modular neural locomotion control with fast learning," *Nat Mach Intell*, vol. 4, p. 169–179, 2022.

[2] J. Liu, M. Tan, and X. Zhao, "Legged robots: an overview," *Transactions of the Institute of Measurement and Control*, vol. 29, no. 2, pp. 185–202, 2007.

[3] P. Arena, S. De Fiore, L. Fortuna, and L. Patané, "Perception-action map learning in controlled multiscroll systems applied to robot navigation," *Chaos: An Interdisciplinary Journal of Nonlinear Science*, vol. 18, no. 4, p. 043119, 2008.

[4] E. Arena, P. Arena, and L. Patanè, *Robots and Lattice Automata*. London: Springer London, 2015, vol. 13, ch. Speed control on an hexapod robot driven by a CNN-CPG structure, pp. 97–116.

[5] P. Arena, L. Fortuna, M. Frasca, and G. Sicurella, "An adaptive, self-organizing dynamical system for hierarchical control of bio-inspired locomotion," *IEEE Transactions on Systems, Man, and Cybernetics, Part B (Cybernetics)*, vol. 34, no. 4, pp. 1823–1837, 2004.

[6] T. Kohonen, M. R. Schroeder, and T. S. Huang, *Self-Organizing Maps*, 3rd ed. Berlin, Heidelberg: Springer-Verlag, 2001.

[7] H. Ritter, T. Martinetz, and K. Schulten, *Neural Computation and Self-Organizing Maps; An Introduction*, 1st ed. USA: Addison-Wesley Longman Publishing Co., Inc., 1992.

[8] P. Arena, F. Di Pietro, A. Li Noce, and L. Patanè, "Attitude control in the mini cheetah robot via mpc and reward-based feed-forward controller," in *submitted to Syroco*, 2022.

[9] D. Kim, J. D. Carlo, B. Katz, G. Bledt, and S. Kim, "Highly dynamic quadruped locomotion via whole-body impulse control and model predictive control," *CoRR*, vol. abs/1909.06586, 2019.

[10] H. Sun, T. Fu, Y. Ling, and C. He, "Adaptive quadruped balance control for dynamic environments using maximum-entropy reinforcement learning," *Sensors*, vol. 21, p. 5907, 09 2021.

[11] G. Garcia, R. Griffin, and J. Pratt, "Time-varying model predictive control for highly dynamic motions of quadrupedal robots," in *2021 IEEE International Conference on Robotics and Automation (ICRA)*, 2021, pp. 7344–7349.

[12] J. Yue, "Learning locomotion for legged robots based on reinforcement learning: A survey," in *2020 International Conference on Electrical Engineering and Control Technologies (CEECT)*, 2020, pp. 1–7.

Generalized Simulink Model of PMSMs

Davide Tebaldi

Abstract

This extended abstract presents a generalized Simulink model for Permanent Magnet Synchronous Motors (PMSMs) equipped with a user-friendly interface allowing the User to select options and to input the model parameters.

1. Introduction

PMSMs are employed in a very large variety of industrial fields [1]-[2]. Different modeling approaches can be found in the literature, mainly in the d-q frame [3]. The typically proposed PMSM models are very useful but lack of flexibility to *select options*. In this work, the POG modeling technique [4] is used to propose a PMSM Simulink superblock [5]-[6] offering the following interesting functionalities: 1) straightforward compatibility with the PMSM parameters estimation Matlab App proposed in [5]; 2) both speed and torque control are incorporated in the model; 3) the user can choose whether to compute the three-phase voltages and currents or not, leading to heavier or lighter simulations; 4) the user can choose if the rotor mechanical dynamics has to be included or not; 5) easy control and understanding of the power flows within the system.

2. PMSM Superblock

The proposed PMSM superblock can be found in the IEEE DataPort [6]. The state-space equations implemented in the PMSM superblock are given by the POG block scheme in [5]-Fig. 1. The mask interface of the PMSM superblock is reported in Fig. 1, and it is subdivided into two containers: "Machine Parameters" and "Tunable Popups". The "Machine Parameters" container minimal configuration is shown in Fig. 1, reporting the parameters that always have to be defined, whereas more parameters appear selecting the different options in the "Tunable Popups" container. The parameters meaning is described in the "Help" section of the PMSM superblock interface. The parameters to be defined in the "Tunable Popups" container are: Star-Connected Phases? Yes or No $\Rightarrow$ {Yes, No}, Torque Limit? $\Rightarrow$ {Tq_Limit_On, Tq_Limit_Off}, Speed Control/Torque Control? $\Rightarrow$ {Speed_Control, Torque_Control}, ThreePhase/dq_Frame? $\Rightarrow$ {ThreePhase, dq_Frame}, Mechanical Dynamics: Yes or No? $\Rightarrow$ {Mech_Dynamics_Yes, Mech_Dynamics_No}. The names of the popups reflect their meaning, and more details are also given in the "Help" section of the PMSM superblock interface, together with the new parameters to be defined in the "Machine Parameters" container when selecting the different "Tunable Popups" options. The tunable popup "Star-Connected Phases? Yes or No" must be set to "Yes" in order to interface the PMSM superblock with the parameters estimation routine proposed in [5]. The external view of the PMSM superblock also changes depending on the options selected for the tunable popups. For the sake of brevity, only the external view of the PMSM superblock with one popups configuration is shown in this abstract, see Fig. 2. The Reader is invited to try the other options in the Simulink block schemes `EM_Speed_Control_slx.slx` and `EM_Torque_Control_slx.slx` in [7]\`PMSM_Superblock`.

3. Simulations

As an example, a simulation applying a torque control is performed using fictitious machine parameters. Some results for the considered simulation are reported in Fig. 3. From the upper subplot, it is possible to see the good superposition between the desired and actual torque characteristics, highlighting the effectiveness of the control.

4. Conclusion

In this abstract, a generalized PMSM Simulink superblock with a user-friendly interface has been in-

Davide Tebaldi is with the Department of Engineering "Enzo Ferrari", University of Modena and Reggio Emilia, Modena, Italy. `davide.tebaldi@unimore.it`

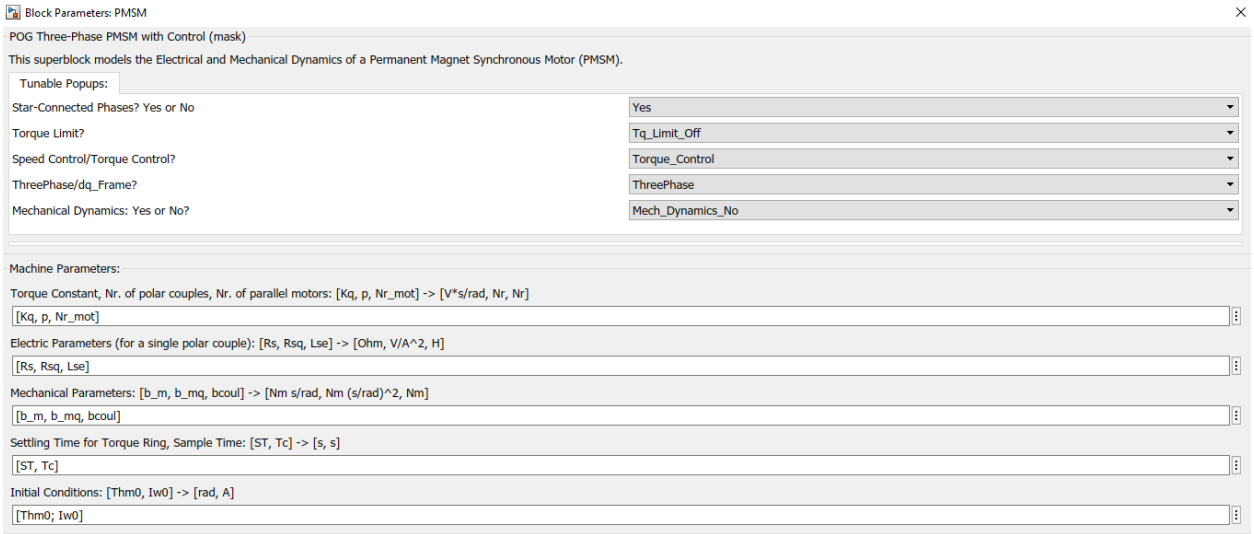

Figure 1: PMSM superblock user interface.

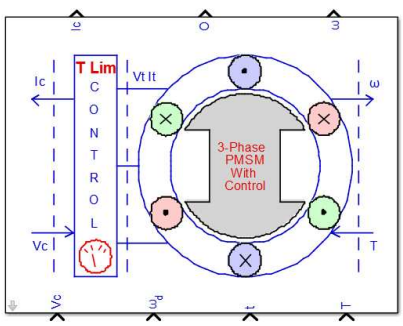

Figure 2: PMSM superblock external view when "Tq_Limit_On", "Speed_Control", "ThreePhase" and "Mech_Dynamics_Yes" are selected.

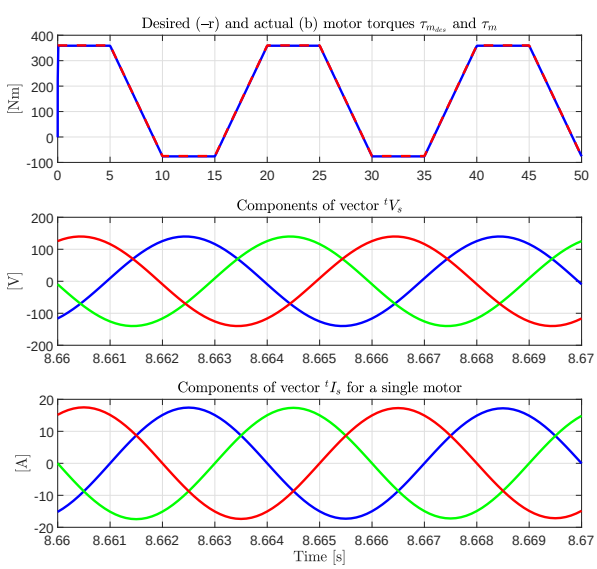

Figure 3: Torque control simulation results.

troduced. The PMSM superblock is compatible with the parameters estimation Matlab App in [5], allows both speed and torque control, and lets the user choose whether to compute the three-phase currents and voltages and if the rotor mechanical dynamics has to be included in the simulation or not. The results of a simulation performed on the PMSM superblock are finally reported and commented.

References

[1] Z. Ping, T. Wang, Y. Huang, H. Wang, J.-G. Lu, Y.-Li, "Internal model control of PMSM position servo system: theory and experimental results", *IEEE Trans. Ind. Informat.*, vol. 16, no. 4, pp. 2202-2211, Apr. 2020.

[2] S. Murshid, B. Singh, "A multiobjective GI-based control for effective operation of PV pumping system under abnormal grid conditions", *IEEE Trans. Ind. Informat.*, vol. 16, no. 11, pp. 6880-6891, Nov. 2020.

[3] S.-K. Kim, C. Ki Ahn, "Active-damping speed tracking technique for permanent magnet synchronous motors with transient performance boosting mechanism", *IEEE Trans. Ind. Informat.*, vol. 18, no. 4, pp. 2171-2179, 2022.

[4] R. Zanasi, "The power-oriented graphs technique: system modeling and basic properties", *IEEE Vehicle Power and Propulsion Conference (VPPC)*, Lille, France, Sep. 1-3, 2010.

[5] D. Tebaldi, Efficiency Map-Based PMSM Parameters Estimation Using Power-Oriented Modeling, *IEEE Access*, vol. 10, pp. 45954 - 45961, Apr. 2022.

[6] D. Tebaldi, PMSM Simulink Superblock and Matlab App for PMSM Parameters Estimation, *IEEE DataPort*, 2022, DOI: 10.21227/yn64-6c31.

[7] Link of the Supplementary Material:

`http://www.dii.unimo.it/~zanasi/PMSM/Suppl_M.zip`

MARTe2 porting for the ARM Architectures Design and challenges: towards novel generations of magnetic fusion plants

G. Avon[1], A. Buscarino1, A.C. Neto[2], F. Sartori[2], Zanon F.[3], De Marchi E.[3]

[1] Università degli Studi di Catania, Dipartimento di Ingegneria Elettrica, Elettronica e Informatica (DIEEI)
[2] Fusion for Energy, ITER Development, CODAC Group
[3] ENI S.P.A. MAFE Group

Abstract

MARTe2 is a modular framework for the development of real-time control applications. MARTe, its predecessor, is used in many fusion experiments (e.g., the JET Tokamak). Thanks to its modular nature, MARTe2 allows the rapid development of real-time control applications. MARTe2 is a portable framework, with no dependencies upon specific libraries and is bundled with an extensive set of components which ease the development of applications. The scope of this work is to describe the porting activity from the MARTe2 developer point-of-view. The purpose of the porting is to implement a control and data acquisition platform for the ITER magnetics diagnostic project, where the collection, processing and distribution of the sensor data coming from magnetic sensors distributed in the tokamak is accomplished by MARTe2 instances running on ARM Cortex-A53 APUs.

Introduction to MARTe2 porting

MARTe2 is a C++ framework built for the development of real-time control systems application. It is deployed in many fusion plants real-time control systems (e.g. JET Tokamak). MARTe2 framework is highly structured, also from the developer point-of-view. A first degree of organisation is based on *Tiers:* BareMetal, Filesystem and Scheduler. A second degree, furtherly divides each *Tier* in *Layers*. While tiers organise the code and modules by their operation area, layers organise the abstraction level, from the lower hardware/middleware/OS-bound (data types, files, network stack and sockets) to the higher functional layers.

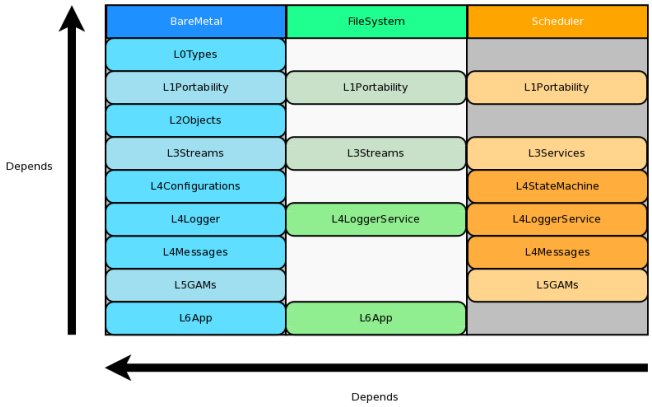

Figure 1 Code Organisation Diagram
Taken from the official MARTe2 website documentation

Thanks to this highly structured architecture, the porting activity is a well-defined process. The code porting is implemented into the lowermost layers (L0 and L1 with dependencies on the hardware, on the middleware and on the Operating System) and in the uppermost layer (L6 with dependencies again on the OS/Platform to manage the program entry-point).

Two further organisational elements are included in porting-oriented layers: *Architecture* and *Environment*. While the first contains the hardware (architecture) bound aspects of the framework, the latter contains the software (environment i.e., OS/HAL BareMetal) bindings. [1] [2] [3] [4] [5] [6]

Porting activity fundamentals

The porting activity was mainly aimed at running the framework on the ARM Cortex-A53 APU, both in bare-metal (without operating system) and under FreeRTOS (real-time operating system). Like all multiple core microprocessors, two main configurations are allowed: SMP (Symmetrical Multi-Processing) and AMP (Asymmetrical Multi-Processing). SMP consists of running all the cores in an operating system orchestrated environment, where tasks are assigned by a scheduler entity which is in charge managing the time allocation on each of the available cores. Conversely, in AMP configurations, each core behaves totally unaware of the others: each core can run its software or OS. Both the MARTe2 portings (bare metal and FreeRTOS) are based on

the AMP scheme: each core runs a separate instance of MARTe2, which is totally independent from the others running on the remaining cores.

The bare-metal MARTe2 runs almost directly on hardware, core bindings in the lowermost layers are based on ARM intrinsics and on the libraries that are available for the platform, specifically FatFs for the filesystem access and lwIP for the TCP/IP stack. The bare-metal porting can run a single-task MARTe2 application. The FreeRTOS porting, runs on the real-time OS provided facilities (mutex, semaphores, tasks) and can run multiple tasks MARTe2 applications. While the baremetal is targeted at running a single, high performance (high frequency loop rates) control task by using the whole core processing power, the FreeRTOS porting is targeted at having a more flexible system, by trading a portion of the core performances. [7]

Side development activities

To support the previously described system, as in an AMP configuration each core runs isolated from the other, components to allow inter-core communication were developed either based on (1) a mutex resident on a shared portion of the On-Chip-Memory (OCM) and (2) on the Inter-Processor-Interrupt (IPI) system to manage the synchronisation of the communications. Moreover, a component to support data exchange between FPGA and ARM cores was developed, as part of the whole application for which the porting was developed. These components were developed as MARTe2 components to allow seamless operation inside the real-time control framework.

Main Purpose of the porting

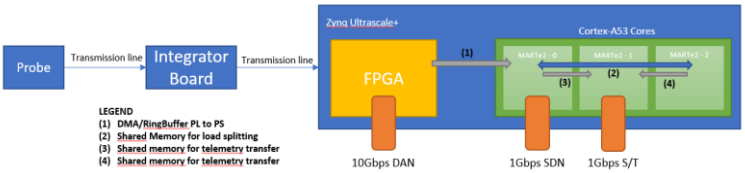

Figure 2 Logic block diagram of MARTe2 running on the Ultrascale+ SoM

The porting was specifically developed to operate in the ITER Magnetics Diagnostic system, where magnetic probes output a voltage proportional to the change of the magnetic field. These voltages are acquired by ADC boards which in turn are connected, via serial 128 MHz links to a Xilinx Ultrascale+ board. The System-On-Module houses an FPGA, the Cortex-A53 four core APU and a dual-core Cortex-R real-time processor. Each Xilinx Ultrascale+ board can be connected up to 30 ADC boards. The ADC board data is first processed by the FPGA logic at the original acquisition frequency of 2 MHz. This data is then filtered and downsampled to 10 kHz and transferred using DMA to a MARTe2 application that running on the first core. This interface makes use of the developed PL-to-PS component. The BareMetal MARTe2 application splits the processing task by transferring part of the data to the core 2, where another MARTe2 instance processes the remaining portion of the magnetic sensor data. Finally, data is collected again on the first core and streamed on the 1Gbps Synchronous Data Network. A third instance of MARTe2 running under FreeRTOS environment serves as control, telemetry and diagnostic for the two signal-processing instances, by using another dedicated 1Gbps network interface.

Achievements

The three MARTe2 instances process magnetic sensors data sampled from the ADC where two of them (baremetal) process a 10kHz x 30 channels ADC data and the third one (FreeRTOS) produces a 10 Hz telemetry and diagnostic stream aside keeping a control channel for the processing instances. The whole CPU + FPGA ensemble, running MARTe2 on this bespoke hardware and electronics will be integrated in a pipeline where the (1) incoming signal from the magnetic sensor is conditioned, (2) the filtered proportional and integrated signals are provided, (3) signals are validated, processed and provisioned to the plasma control system, to the interlock system and to the data storage networks for the post-pulse physics data analysis.

[1] D. Alves, A. C. Neto, D. F. Valcarcel, R. Felton, J. M. Lopez, A. Barbalace, L. Boncagni, P. Card, G. De Tommasi, A. Goodyear, S. Jachmich, P. J. Lomas, F. Maviglia, P. McCullen, A. Murari, A. Rainford, C. Reux, F. Rimini, F. Sartori, A. V. Stephen, J. Vega, R. Vitelli, L. Zabeo e D. Zastrow, «A new generation of real-time systems in the JET tokamak,» *IEEE Transactions on Nuclear Science,* pp. 711-719, 2014.

[2] T. Bellizio, G. De Tommasi, P. McCullen, A. C. Neto, F. Piccolo, F. Sartori , R. Vitelli e L. Zabeo, «The software architecture of the new vertical-stabilization system for the JET tokamak,» *IEEE Transactions on Plasma Science,* pp. 2465-2473, 2010.

[3] F. Janky, J. Havlicek, A. Batista, O. Kudlacek, J. Seidl, A. C. Neto, J. Pipek, M. Hron, O. Mikulin, A. Duarte, B. Carvalho, J. Stockel e R. Panek, «Upgrade of the COMPASS tokamak real-time control system,» *Fusion Engineering and Design,* pp. 186-194, 2014.

[4] G. Manduchi, A. Rigoni, T. Fredian, J. Stillerman, A. Neto e F. Sartori, «MARTe2 and MDSPlus integration for a comprehensive fast control and data acquisition system,» *Fusion Engineering and Design,* 2020.

[5] A. C. Neto, F. Sartori, F. Piccolo, A. Barbalace, R. Vitelli e H. Fernandes, «Linux real-time framework for fusion devices,» *Fusion Engineering and Design,* pp. 1408-1411, 2009.

[6] A. C. Neto, F. Sartori, F. Piccolo, R. Vitelli, G. De Tommasi, L. Zabeo, A. Barbalace, H. Fernandes, D. F. Valcarcel e A. J. N. Batista, «MARTe: A multiplatform real-time framework,» *IEEE Transactions on Nuclear Science,* pp. 479-486, 2010.

[7] G. Avon, A. Buscarino, A. C. Neto e F. Sartori, «MARTe2 embedded signal processing unit for the ITER magnetics diagnostics,» *IECON,* 2021.

AI-powered Distributed Stochastic MILP for Microgrid Control

Andrea Camisa and Giuseppe Notarstefano

In the last decade, the use of renewable energy sources is soaring and is creating new challenges in the field of microgrid control. These important structural changes of the power grid call for novel data-driven optimization approaches to take appropriately into account the energy produced by renewables. Optimization problems arising in power grids are intrinsically distributed, in the sense that the problem data are spatially scattered throughout the network. To this end, distributed optimization approaches allow for the solution of optimization problems with such properties while preserving the locality of the data and even resilience of the network in case of failures. In our work, we consider a distributed stochastic microgrid control problem consisting of several interconnected generators, renewable energy sources, storages and loads. Inspired by [1], the optimal control problem is formulated as a Mixed-Integer Linear Program (MILP). In order to deal with the uncertain nature of renewables, we apply a two-stage stochastic programming approach that allows for a distributed solution of the problem, that is, with a peer-to-peer protocol without a central coordinator. From an algorithmic point of view, these assumptions make the problem very challenging. We propose to tackle this distributed MILP using a primal decomposition approach inspired to the recent work on the deterministic case [2], with suitable changes to deal with the stochastic scenario. Note that MILPs are nonconvex and NP-hard, therefore large-scale instances can be solved within acceptable time windows only suboptimally. Interestingly, while [2] employs certain optimization variables to handle violations of the coupling constraints, here we reinterpret these variables as playing the role of second-stage variables in the stochastic scenario. We perform AI-enhanced realistic simulations by using open-source historical data, taken from the EU, on energy generation/consumption in South Italy. We train a Generative Adversarial Network (GAN) based on these data and use it to generate sample energy generation/consumption profiles. The synthesized data are used to perform a Monte Carlo numerical experiment on the Italian HPC CINECA infrastructure.

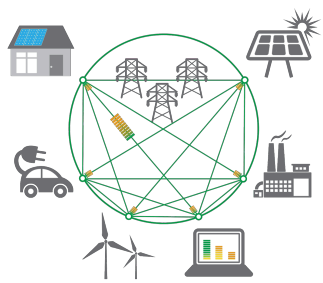

A. Mixed-Integer Microgrid Optimal Control Problem

A microgrid consists of N units, partitioned as follows. Storages are collected in $\mathbb{I}_{\text{STOR}}$, generators in $\mathbb{I}_{\text{GEN}}$, renewable energy sources in $\mathbb{I}_{\text{REN}}$, critical loads in $\mathbb{I}_{\text{LO}}$, controllable loads in $\mathbb{I}_{\text{CL}}$ and one connection with the utility grid in $\mathbb{I}_{\text{GRID}}$. Therefore, the whole set of units can be written as $\{1,\dots,N\} = \mathbb{I}_{\text{STOR}} \cup \mathbb{I}_{\text{GEN}} \cup \mathbb{I}_{\text{REN}} \cup \mathbb{I}_{\text{LO}} \cup \mathbb{I}_{\text{CL}} \cup \mathbb{I}_{\text{GRID}}$, By denoting the prediction horizon as $K \in \mathbb{N}$, the optimal control problem can be posed as

$$\begin{aligned}
\min_{u} \; & \sum_{k=0}^{K-1} \Big[J^k_{\text{GRID}}(u_{\text{GRID}}) + \sum_{i\in\mathbb{I}_{\text{GEN}}} J^k_{\text{GEN},i}(u_i) + \sum_{i\in\mathbb{I}_{\text{STOR}}} J^k_{\text{STOR},i}(u_i) \\
& \quad + \sum_{i\in\mathbb{I}_{\text{CL}}} J^k_{\text{CLOAD},i}(u_i) \Big] \\
\text{subj. to } & \sum_{i=1}^{N} P^k_i(u_i) = 0, \qquad \text{for } k = 0,\dots,K-1 \qquad (1)\\
& \text{(storage dynamics), (generator constraints)} \\
& \text{(controllable load constraints), (grid constraints)}
\end{aligned}$$

where $J^k_{\cdot,i}$ denotes a (linear) cost function of the i-th device of a certain type at time k, u_i denotes the decision variable associated to the i-th device, and P^k_i denotes the power exchanged by device i at time k. The mixed-integer nature of the problem is given by the fact that the dynamics of storages is piece-wise linear (for different charge/discharge rates), while generators and grid constraints comprise logical statements, such as minimum up/down time, different exchange prices for energy purchase and sell. The objective of solving problem (1) is to find an optimal scheduling of energy production/consumption of the microgrid, given the current state of storages and the energy that will be produced by renewables, which is uncertain, while satisfying the power balance constraint $\sum_{i=1}^{N} P^k_i(u_i) = 0$. Note that the terms $P^k_i(u_i)$ for $i \in \mathbb{I}_{\text{REN}}$, which represent the power generated by renewable i at the time step k of the prediction horizon, are unknown beforehand and must be modeled as stochastic variables having a certain probability distribution. Therefore, problem (1) is stochastic since the power balance constraint contains those terms. To deal with this complexity, we exploit a two-stage stochastic optimization approach, introduced next.

B. Two-stage Stochastic Optimization Approach

As we are interested in a distributed algorithm, instead of applying the two-stage stochastic approach directly to problem (1), we rather apply it to a distributed reformulation of problem (1). Indeed, it can be seen that with appropriate definitions the problem is equivalent to the stochastic MILP

$$\begin{aligned}
\min_{x_1,\dots,x_N} \; & \sum_{i=1}^{N} c_i^\top x_i \\
\text{subj. to } & \sum_{i=1}^{N} A_i x_i = b \qquad (2)\\
& x_i \in X_i^{\text{MILP}}, \qquad i = 1,\dots,N,
\end{aligned}$$

This result is part of the project "Distributed Optimization for Cooperative Machine Learning in Complex Networks" (No PGR10067) that has received funding from the Ministero degli Affari Esteri e della Cooperazione Internazionale. The authors are with the Department of Electrical, Electronic and Information Engineering, University of Bologna, Bologna, Italy, {a.camisa, giuseppe.notarstefano}@unibo.it.

where, for all $i \in \{1, \dots, N\}$, c_i is cost vector, x_i is the decision vector and the local constraint set X_i^{MILP} is a mixed-integer polyhedron. Moreover, the power balance constraint is encoded as a coupling among the variables, modeled with the matrices A_i and the *stochastic* vector b. Intuitively, the control scheme consists of choosing a set of decisions x_i, such as generated/stored power or power curtailments, in order to minimize the cost in an expected senses (since the value of b is not known), and then compensate for the violation of the power balance constraint by applying *recourse* actions with a certain cost. Denoting by ω the random vector collecting all the renewable energy generation profiles, the two-stage stochastic MILP can be formulated as

$$\begin{aligned} \min_{x_1,\dots,x_N} \quad & \sum_{i=1}^{N} c_i^\top x_i + \mathbb{E}[Q_\omega(x_1, \dots, x_N)] \\ \text{subj. to } \; & x_i \in X_i^{\text{MILP}}, \qquad i = 1, \dots, N, \end{aligned} \tag{3}$$

where the x_is are the *first-stage* variables and $Q_\omega(x_1, \dots, x_N)$ is the optimal value of the *second-stage* problem

$$\begin{aligned} Q_\omega(x_1, \dots, x_N) = \min_{\eta_+, \eta_-} \quad & \sum_{k=0}^{K-1} (q_+ \eta_{k+} + q_- \eta_{k-}) \\ \text{subj. to } \; & -\eta_- \leq \sum_{i=1}^{N} A_i x_i - b_\omega \leq \eta_+ \\ & \eta_+, \eta_- \geq 0. \end{aligned}$$

Here, b_ω represents a realization of b, while η_+, η_- are the vectors representing violations of the power balance constraint, i.e., recourse actions penalized in the cost with coefficients $q_+, q_- \geq 0$ (related to energy surplus and shortage).

C. Theoretical Guarantees of Distributed Algorithm

In this work, see paper [3], we proposed a distributed algorithm to solve the two-stage stochastic problem (3) inspired to the primal decomposition approach in [2]. Interestingly, while the inspiring method requires boundedness of the constraint sets X_i^{MILP} and considers a restriction mechanism of the coupling constraints $\sum_{i=1}^{N} A_i x_i \leq b$ with auxiliary variables, within the outlined two-stage stochastic approach the constraint sets X_i^{MILP} need not be bounded and the two-stage variables η_+, η_- play the role of the auxiliary variables for the algorithm (see [3] for details). These considerations allow us to prove a bound for the worst-case violation of the mixed-integer solution computed asymptotically by the distributed algorithm, where R is the total number of scenarios in the stochastic problems.

Theorem 1 ([3]): Denote by $(x_1^\infty, \dots, x_N^\infty)$ the asymptotic solution computed by the distributed algorithm. There exists a subset of agents $I_\mathbb{Z} \subset \{1, \dots, N\}$, with cardinality at least $N - 2RK$, and a scalar d^{MIN} such that the worst-case violation of the power balance constraint is equal to

$$\sum_{i \in I_\mathbb{Z}} \eta_i^{\text{LP}} + \sum_{i \notin I_\mathbb{Z}} \frac{c_i^\top (x_i^{\text{L}} - x_i^\infty) + d^\top \eta_i^{\text{L}}}{d^{\text{MIN}}} \mathbb{1},$$

where η_i^{LP} and x_i^{L} are suitably defined vectors [3]. □

D. Numerical Experiments

The proposed framework has been validated through large-scale numerical computations performed with the DISROPT package [4] on the Italian HPC CINECA infrastructure. We replace the expected value appearing in problem (3) with the empirical mean of extracted scenarios. The generation profiles of renewables are synthesized using a deep Generative Adversarial Network (GAN) trained on EU historical data using the data series provided by Open Power System Data. The power profiles generated by the GANs are quite realistic as it can be seen from Figure 1. To test the proposed framework,

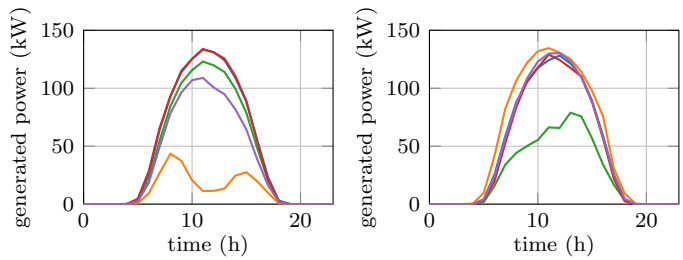

Fig. 1. Five examples of solar power generation profiles. Left: synthesized data, right: historical data.

we performed 100 Monte Carlo simulations in which we run the algorithm on different energy generation scenarios (i.e., realizations of b). The considered microgrid consists of 180 units with randomly initialized states. As an example, in Figure 2, we show the total power exchanged with storage units (a positive value means that, overall, the storage units are charging) and the global level of stored power. The solution provided by the algorithm is such that storages accumulate as much energy as they can during the peaks of power produced by the renewables. This energy is then released during the subsequent hours of the day.

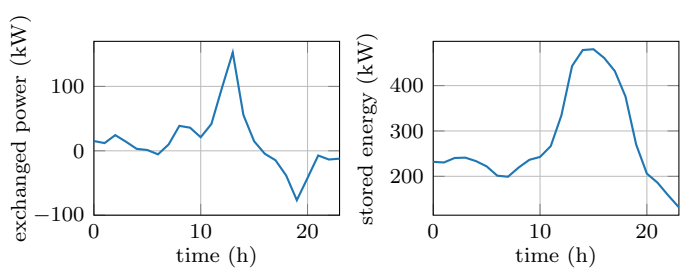

Fig. 2. Left: total average power exchanged by storage units. Right: level of total stored power.

References

[1] A. Parisio, E. Rikos, and L. Glielmo, "Stochastic model predictive control for economic/environmental operation management of microgrids: an experimental case study," *J. of Process Control*, vol. 43, pp. 24–37, 2016.

[2] A. Camisa, I. Notarnicola, and G. Notarstefano, "Distributed primal decomposition for large-scale MILPs," *IEEE Transactions on Automatic Control*, vol. 67, no. 1, pp. 413–420, 2021.

[3] A. Camisa and G. Notarstefano, "A distributed mixed-integer framework to stochastic optimal microgrid control," *IEEE Transactions on Control Systems Technology*, 2022.

[4] F. Farina, A. Camisa, A. Testa, I. Notarnicola, and G. Notarstefano, "DISROPT: A Python framework for distributed optimization," *IFAC-PapersOnLine*, vol. 53, no. 2, pp. 2666–2671, 2020.

A surrogate-based scheme for black-box and preference-based optimization with a controller calibration application

Davide Previtali[†], Mirko Mazzoleni[†], Antonio Ferramosca[†], Fabio Previdi[†]

I. Introduction

In the past two decades, *Black-Box Optimization (BBO)* and *Preference-Based Optimization (PBO)* methods have been used to calibrate the parameters of the controllers of several different control systems applications. The BBO framework is designed to find the *global solution(s)* of an optimization problem wherein the cost function is unknown/a black-box (e.g. the relationship between the controller parameters and a performance indicator), while PBO is tasked with searching for the calibration that is most preferred by a human *Decision-Maker (DM)*. In particular, in PBO, the DM compares two different tunings at a time and states a *preference*, such as "this calibration is better than that one" [1]. Notably, using notions of *utility theory* [2], the PBO problem equates to maximizing a (latent) function, called the *utility function* of the DM.

Most black-box and preference-based algorithms rely on a *surrogate model*, which is an approximation of either the black-box cost function or the utility function of the decision-maker, and for this reason are referred to as *surrogate-based methods*. The surrogate model is *exploited* to drive the search towards more promising calibrations (i.e. with lower cost or that are more preferred by the DM). At the same time, *exploration* of the space of all possible calibrations is needed to ensure the convergence towards the global solution(s) of the optimization problem. Surrogate-based methods are iterative procedures which operate as follows: (i) build a surrogate model of the objective function using only the information at hand (i.e. the cost function measures or the preferences of the DM), (ii) propose a new calibration to be evaluated, trading off exploration and exploitation, (iii) repeat until a maximum number of calibrations have been tried. *The goal of surrogate-based methods is to obtain a "sufficiently good" tuning using the least amount of function evaluations/queries to the DM as possible*.

II. Problem statement

Both black-box and preference-based optimization aim to solve the following *global optimization problem*:

$$\begin{aligned} \boldsymbol{x}^* &= \arg\min_{\boldsymbol{x}} f(\boldsymbol{x}) \\ \text{s.t.} \quad & \boldsymbol{x} \in \Omega, \end{aligned} \tag{1}$$

where $\boldsymbol{x} \in \mathbb{R}^n$ is the *decision vector*, $\boldsymbol{x}^* \in \Omega$ is the global solution, $f : \mathbb{R}^n \to \mathbb{R}$ is either a black-box cost function or the (negative) utility function of a human decision-maker and Ω is a *compact set of constraints*. In PBO, we consider the *preference function* $\pi : \mathbb{R}^n \times \mathbb{R}^n \to \{-1, 0, 1\}$ defined in [1]. Given two calibrations, $\boldsymbol{x}_i, \boldsymbol{x}_j \in \mathbb{R}^n$, $\pi(\boldsymbol{x}_i, \boldsymbol{x}_j)$ returns -1 if $\boldsymbol{x}_i$ is preferred to $\boldsymbol{x}_j$, 0 if the DM deems both tunings equally as good, and 1 otherwise.

[†]Department of Management, Information and Production Engineering, University of Bergamo, Via G. Marconi 5, 24044 Dalmine (BG), Italy. Email to: davide.previtali@unibg.it.

Surrogate-based methods start from a set of samples $\mathcal{X}$ as in:

$$\mathcal{X} = \{\boldsymbol{x}_i : i = 1, \dots, N, \boldsymbol{x}_i \in \Omega, \boldsymbol{x}_i \neq \boldsymbol{x}_j, \forall i \neq j\}. \tag{2}$$

Each point $\boldsymbol{x}_i \in \mathcal{X}$ is evaluated, either by measuring the values of $f(\boldsymbol{x})$ (BBO), obtaining:

$$\mathcal{Y} = \{y_i : y_i = f(\boldsymbol{x}_i), \boldsymbol{x}_i \in \mathcal{X}\}, \tag{3}$$

or by letting the DM compare couples of different samples $\boldsymbol{x}_i, \boldsymbol{x}_j \in \mathcal{X}, \boldsymbol{x}_i \neq \boldsymbol{x}_j$ (PBO), as highlighted by the sets

$$\mathcal{B} = \{b_h : h = 1, \dots, M, b_h \in \{-1, 0, 1\}\}, \tag{4}$$

$$\begin{aligned} \mathcal{S} = \Big\{ & (\ell(h), \kappa(h)) : \ h = 1, \dots, M, \ell(h), \kappa(h) \in \mathbb{N}, \\ & b_h = \pi\left(\boldsymbol{x}_{\ell(h)}, \boldsymbol{x}_{\kappa(h)}\right), b_h \in \mathcal{B}, \boldsymbol{x}_{\ell(h)}, \boldsymbol{x}_{\kappa(h)} \in \mathcal{X} \Big\}. \end{aligned} \tag{5}$$

$\mathcal{S}$ is a mapping set that highlights which samples have been compared to to obtain the preferences in (4). In particular, $\ell : \mathbb{N} \to \mathbb{N}$ and $\kappa : \mathbb{N} \to \mathbb{N}$ are two mapping functions that associate the indexes of the samples in $\mathcal{X}$ to the preferences in $\mathcal{B}$.

III. A surrogate-based scheme for BBO and PBO

We propose a surrogate-based procedure that is an extension of the recent `GLIS` [3] and `GLISp` [1] algorithms. The proposed scheme can be summarized as follows [4], [5]:

1) Generate a set of $N_{init} \in \mathbb{N}$ initial samples, $\mathcal{X}, |\mathcal{X}| = N_{init}$, using a suitable experimental design;
2) In BBO, measure the values of the cost function $f(\boldsymbol{x})$ at each $\boldsymbol{x}_i \in \mathcal{X}$, obtaining the set $\mathcal{Y}$ in (3). Instead, in PBO, let the DM express $M \in \mathbb{N}$ preferences, $1 \leq M \leq \binom{N_{init}}{2}$, described by the sets $\mathcal{B}, \mathcal{S}$ in (4), (5).
3) Repeat until $|\mathcal{X}| = N \leq N_{max}$, where $N_{max} \in \mathbb{N}, N_{max} > N_{init}$ is the *budget* (i.e. the maximum number of calibrations that we are willing to try):
   a) Build the surrogate model $\hat{f} : \mathbb{R}^n \to \mathbb{R}$ of $f(\boldsymbol{x})$ in Problem (1). We follow the rationale of algorithms `GLIS` [3] and `GLISp` [1] , which use a *radial basis function expansion* as $\hat{f}(\boldsymbol{x})$:
   $$\hat{f}(\boldsymbol{x}) = \sum_{i=1}^{N} \beta^{(i)} \cdot \varphi\left(\epsilon \cdot \|\boldsymbol{x} - \boldsymbol{x}_i\|_2\right). \tag{6}$$
   $\epsilon \in \mathbb{R}_{>0}$ is the shape parameter while $\varphi : \mathbb{R}_{\geq 0} \to \mathbb{R}$ is a radial function. $\boldsymbol{\beta} = \begin{bmatrix}\beta^{(1)} & \dots & \beta^{(N)}\end{bmatrix}^\top \in \mathbb{R}^N$ is a vector of weights that needs to be computed so that either $\hat{f}(\boldsymbol{x})$ in (6) (roughly) interpolates the points $(\mathcal{X}, \mathcal{Y})$ or correctly describes the preferences in $\mathcal{B}$ and $\mathcal{S}$, see [3], [1].
   b) Look for a new candidate sample $\boldsymbol{x}_{N+1} \in \Omega$ by solving
   $$\begin{aligned} \boldsymbol{x}_{N+1} &= \arg\min_{\boldsymbol{x}} a(\boldsymbol{x}) \\ \text{s.t.} \quad & \boldsymbol{x} \in \Omega, \end{aligned} \tag{7}$$

where $a : \mathbb{R}^n \to \mathbb{R}$ is the so-called *acquisition function*, which trades off exploration and exploitation. In particular [4], [5]:

$$a(\boldsymbol{x}) = \delta \cdot \hat{\bar{f}}(\boldsymbol{x}) + (1-\delta) \cdot \bar{z}(\boldsymbol{x}). \tag{8}$$

$\hat{\bar{f}}(\boldsymbol{x})$ is the min-max rescaled surrogate in (6) and similarly for $\bar{z}(\boldsymbol{x})$, see [4]. $z : \mathbb{R}^n \to (-1, 0]$ is the IDW distance function proposed in [3]:

$$z(\boldsymbol{x}) = \begin{cases} 0 & \text{if } \boldsymbol{x} \in \mathcal{X} \\ -\frac{2}{\pi} \cdot \arctan\left\{\left[\sum_{i=1}^{N} \|\boldsymbol{x} - \boldsymbol{x}_i\|_2^{-2}\right]^{-1}\right\} & \text{otherwise} \end{cases}. \tag{9}$$

$\delta \in [0, 1]$ in (8) is the exploration-exploitation trade-off.

c) Evaluate the new candidate sample, obtaining either $y_{N+1} = f(\boldsymbol{x}_{N+1})$ (BBO) or the preference $b_{M+1} = \pi(\boldsymbol{x}_{N+1}, \boldsymbol{x}_{\boldsymbol{best}}(N))$ (PBO), where $\boldsymbol{x}_{\boldsymbol{best}}(N)$ is best candidate when $|\mathcal{X}| = N$;

d) Update the sets $\mathcal{X}$ and $\mathcal{Y}$ or $\mathcal{B}, \mathcal{S}$.

We propose to cycle δ in (8) following a sequence of $N_{cycle} \in \mathbb{N}$ weights, $\Delta_{cycle} = \langle \delta_0, \ldots, \delta_{N_{cycle}-1} \rangle$, as follows. Suppose that at a certain iteration of the proposed scheme $\delta = \delta_k \in \Delta_{cycle}$. Assume that $\boldsymbol{x}_{N+1}$ obtained from Problem (7) improves the current best candidate $\boldsymbol{x}_{\boldsymbol{best}}(N)$, then δ is kept unchanged for the next iteration. Viceversa, we set $\delta = \delta_{(k+1) \bmod N_{cycle}}$. This rationale is referred to as *greedy δ-cycling*. In [4], [5] we prove that, under mild assumptions on $f(\boldsymbol{x})$, *if $\exists \delta_k \in \Delta_{cycle}$ such that $\delta_k = 0$, then the proposed scheme converges asymptotically to the global minima of Problem* (1). At the moment, no such proof of convergence is available for algorithms `GLIS` [3] and `GLISp` [1] .

IV. Case Study

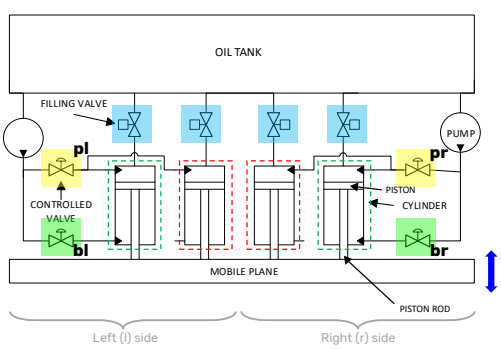

Fig. 1: Hydraulic scheme of the press under study.

We consider a simulator of the *hydraulic press* depicted in Fig. 1. The *mobile plane* of the press is mechanically connected to the *piston rods* of four *hydraulic cylinders*, which cause its motion. The inner cylinders are single-acting whereas the outer ones are double-acting. The force produced by each hydraulic cylinder depends on the pressure inside its chambers and on its constructive parameters. The pressure is generated by *pressurized oil*, which flows to the cylinders through several different pipes. The flow rates of the oil inside each pipe are regulated by different valves. The *filling valves* (cyan) regulate the oil throughput from the tank to the upper chambers of the hydraulic cylinders. These valves can either be completely open or completely closed and can handle high flow rates. Instead, the *pressing valves* (yellow) and the *balance valves* (green) allow for a continuous regulation (between 0% and 100%) of the oil throughput but possess lower nominal maximum flow rates. Furthermore, the pressing valves regulate the fluid flow rates to the upper chambers of the single-acting and double-acting hydraulic cylinders whereas the balance valves handle the lower chambers of the double-acting ones.

In this case study, we *tune the PI controllers of the balance valves for the fast descent phase of the hydraulic press*. In the fast descent phase, the mobile plane is lowered towards the work-piece at high speeds, following a position setpoint $SP(t)$. Throughout this stage, the pressing valves are left closed, therefore we only need to calibrate the regulators of the balance valves. Furthermore, the PI controllers on the left and the right side of the press share the same calibration, hence the decision vector is simply $\boldsymbol{x} = \begin{bmatrix} K_p & K_i \end{bmatrix}^\top$, with $0.1 \leq K_p \leq 2$ and $0.1 \leq K_i \leq 10$.

The *control specifications* are:

1) The position trajectory tracking must be "good enough". A possible indicator is:

$$pos_NMAE_l(\boldsymbol{x}) = \frac{\sum_{t=1}^{T} |SP(t) - pos_l(t; \boldsymbol{x})|}{\sum_{t=1}^{T} |SP(t) - \text{avg}_t[SP(t)]|}, \tag{10}$$

where $pos_l(t; \boldsymbol{x})$ is the position of the left side of the press at time t.

2) The downward motion of the mobile plane of the hydraulic press during the fast descent phase must be "as smooth as possible". A possible indicator is:

$$acc_std_l(\boldsymbol{x}) = \text{std}_t[acc_l(t; \boldsymbol{x})], \tag{11}$$

where $acc_l(t; \boldsymbol{x})$ is the acceleration of the left side of the press at time t.

In practice, (10) and (11) are two *conflicting criteria* which need to be traded off. Also, the indicators are averaged between the left and the right side of the press.

We optimize $f(\boldsymbol{x})$ defined as in (10) and (11) (BBO), using the scheme described in Section III. Furthermore, we also perform PBO; the first author of this paper plays the role of the DM, who compares different calibrations by taking a look at the position and acceleration signals. The hyper-parameters for the BBO/PBO algorithm are selected as in [3], [1], [4], $N_{init} = 4$ and $N_{max} = 50$. Fig. 2 depicts the performances of the best calibrations. Notice how *PBO achieves a trade-off between the two control specifications*.

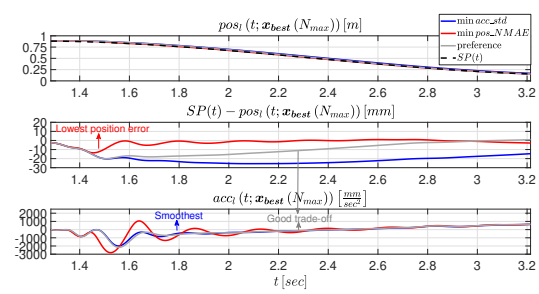

Fig. 2: Performances achieved by the tunings found by BBO and PBO.

References

[1] A. Bemporad and D. Piga, "Global optimization based on active preference learning with radial basis functions," *Machine Learning*, vol. 110, pp. 417–448, Feb 2021.

[2] E. A. Ok, *Real analysis with economic applications*. Princeton University Press, 2011.

[3] A. Bemporad, "Global optimization via inverse distance weighting and radial basis functions," *Computational Optimization and Applications*, vol. 77, pp. 571–595, Nov 2020.

[4] D. Previtali, M. Mazzoleni, A. Ferramosca, and F. Previdi, "Glisp-r: A preference-based optimization algorithm with convergence guarantees," 2022.

[5] D. Previtali, M. Mazzoleni, A. Ferramosca, and F. Previdi, "A unified surrogate-based scheme for black-box and preference-based optimization," 2022.

Simultaneous Design of Passive and Active Spacecraft Attitude Control via Black-Box Optimization

Lorenzo Sabug, Jr., Gian Paolo Incremona, Mara Tanelli, Fredy Ruiz, Lorenzo Fagiano
Politecnico di Milano

In the past decades, there has been a renewed interest in space systems, due to increased demand for data for earth observation, communications, and monitoring purposes. The miniaturization of electronics and decreasing costs of components has opened access to space for governments, academics, and hobbyists alike. One of the most important milestones in the "New Space" era is the introduction of the CubeSat standard, which sets a uniform specification for small spacecraft, with the standard unit size of 1U (with 10 cm x 10 cm x 10 cm). CubeSats are now the most common mode of entry to space for universities and research institutes, mainly for their low launch costs and short development timeframes.

One of the most common missions using CubeSats is Earth observation, which entails taking images of a target area on the ground, for environmental analysis or monitoring. Spacecraft for Earth observation are usually designed for three main goals:

(1) good camera pointing performance (minimizing tracking error),
(2) reliable data connectivity with the ground station (GS) assumed near the North pole, and
(3) low power consumption, up to a maximum power budget.

As an optical mission requires an accurate pointing, we require the CubeSat attitude controller to have good reference tracking performance. On the other hand, to transfer the images from CubeSat to a GS, we require antenna pointing to the GS to establish a reliable connection. However, the antenna pointing accuracy does allow for wider tolerances, owing to the relatively wide beamwidth of the antenna used. Hence, we propose the use of passive attitude compensation (magnets and hysteretic material) along the satellite, passively aligning it with the Earth's magnetic field. This alignment can then allow for the antenna to point to the GS without using any electrical power, which otherwise would have to be extracted from the (small) batteries. The use of a combination of active attitude control and passive attitude compensation has been proposed in one previous study, but no efforts have been made yet regarding sizing them. This is a particularly interesting problem because of the inherent trade-offs involved, in which putting too much priority to one design goal can inadvertently affect the other ones.

The trade-off among the different attitude actuators become apparent when we define the problem at a high level. For example, oversizing the passive attitude compensators to achieve goal (2) can lead to aggressive alignment response to the Earth's magnetic field, and sometimes can lead to instability. An oversized passive magnet along the CubeSat can orient it to near nadir-pointing at the Arctic region (because of the nature of geomagnetic field lines) and help with the passive pointing to the GS. However, the same thing forces the CubeSat to align to zenith-pointing at the South hemisphere, needing for more aggressive design of the active controllers to achieve (1). This, in turn, leads to more power consumption, affecting goal (3).

This study investigates the simultaneous design of attitude control and compensation mechanism for a spacecraft using black-box optimization with black-box constraints. Since the mission-level objective (1) and practical constraints (2), (3) are not analytically available, they are learned from simulation-derived data in the optimization process. The black-box optimization is carried out with a recent algorithm based on Set Membership theory, which trades off exploitation around the best feasible parameters and exploration of the search space, finding the optimum combination of the required attitude control and compensation parameters. The proposed approach is finally assessed in a realistic simulation of a 3U CubeSat system equipped with both a passive magnetic attitude compensation and an active reaction wheel-based control.

In the proposed presentation, we describe in detail the system model of the CubeSat, and we cast the goals into an objective function (for goal (1)), and black-box constraints (for goals (2), (3)). We introduce the black-box optimization algorithm we used, and discuss the design process we take, entailing the design of varied experiments for evaluation of the fitness w.r.t. mission goals, and performing repeated experiments on a simulation platform. We finally present the resulting controller, and we compare its performance with other common design approaches, including sequential design, and independent design. Statistical results show the superiority of the black-box optimization-based method for the simultaneous design of the active and passive attitude control for the CubeSat, satisfying both good pointing performance, and satisfaction of requirements for GS data connectivity and power consumption.

Implementation of a fully analog feedback loop with a Carbon-Black-based Fractional Order Controller

R. Caponetto[1,2], L. Patanè[2], and M. G. Xibilia[2]

[1]UniCT
[2]UniME

July 5, 2022

Abstract

Fractional calculus is a mathematical framework that has attracted considerable interest from mathematicians, physicists, and engineers, [1]. Among its applications, the use of fractional calculus in the automatic control field has led to interesting results, such as more robust controllers, compared to their integer-order counterparts. The proposed work utilizes the physical realization of a solid-state fractional-order capacitor for the implementation of a fractional-order lead compensator. The proposed capacitor is realized using a carbon black-based dielectric, [2]. Therefore, a fully analog closed-loop system implementation is realized. A suitable case study is conducted to validate the controller performance, both from simulations and experimentally. The obtained results demonstrate the suitability of using an intrinsic fractional-order device for analog closed-loop control. Among its applications, the use of fractional calculus has led to interesting results, such as more robust controllers, compared to their integer order counterparts. The fractional order capacitor used in the proposed closed-loop system is shown in Fig. 1. This is realized by diffusing carbon black nanoparticles inside a polydimethylsiloxane (PDMS) matrix.

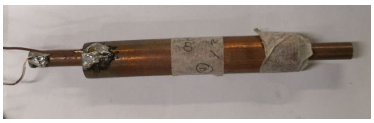

Figure 1: Picture of the C130B fractional-order capacitor

In Fig. 2 the closed FOC system is reported. The feedback is implemented using the first opamp with $R = 1K\Omega$, the second opamp is used

to implement the FOC block, and the remaining opamps implement the plant.

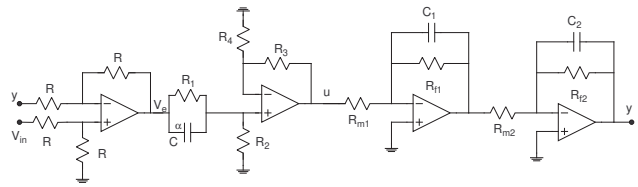

Figure 2: Electronics schematics of the full analog closed loop system

Five experiments, related to plant gain variation, are presented in Fig. 3. No significant differences were detected between the actual and simulated systems. In particular, the time differences between the first (i.e., k=800) and the last response (i.e., k = 1200) of both the real and simulated systems are comparable, approximately Ω. The iso-damping property of the proposed controller, [3] was demonstrated both in simulations and experiments. Research is in progress with the aim of defining the precise CPE fabrication parameters and reduced-size packaging.

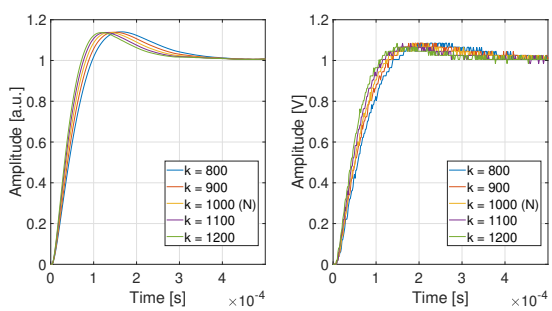

Figure 3: Comparison between simulated and real FO-closed-loop systems for the investigated values of k

References

[1] R. Caponetto, G. Dongola, L. Fortuna and I. Petras, "Fractional Order Systems: Modeling and Control Applications, World Scientific, 2010.

[2] K. Biswas, R. Caponetto G. Di Pasquale, S. Graziani, A. Pollicino and E. Murgano., "Realization and characterization of carbon black based fractional order element.", *Microelectronics Journal*, 2018;82:22-28.

[3] M. Beschi, F. Padula, A. Visioli, "The generalised isodamping approach for robust fractional pid controllers design.", *International Journal of Control*, 2017;90(6):1157-1164.

This article has been accepted for inclusion in a future issue of this journal. Content is final as presented, with the exception of pagination.

Symbolic Control Design of an Artificial Pancreas for Type-2 Diabetes

Alessandro Borri, *Senior Member, IEEE*, Giordano Pola, *Senior Member, IEEE*, Pierdomenico Pepe, *Senior Member, IEEE*, Maria Domenica Di Benedetto, *Life Fellow, IEEE*, and Pasquale Palumbo, *Member, IEEE*

***Abstract*— Diabetes is a widespread disease characterized by chronic hyperglycemia so that diabetic individuals usually require the administration of exogenous insulin for survival. As a consequence, in the context of the so-called artificial pancreas, many glucose control methods have been presented in the last few years. In this work, we focus on type-2 diabetes and propose a novel model-based glucose control technique based on the use of symbolic models, which are finite approximations of complex dynamical systems. This framework allows taking into account nonlinearities and delays in the dynamics, uncertainties, and input bounds, as well as nonidealities coming from the interaction between physical plant and digital environment. The methodology is extensively validated over a virtual patient model, broadly accepted as a substitute to animal trials in the preclinical testing of closed-loop glucose control strategies. The results show the effectiveness and the robustness of the approach.**

***Index Terms*— Artificial pancreas (AP), formal methods, hybrid systems, *in silico* validation, nonlinear time-delay systems, symbolic control.**

I. Introduction

DIABETES is a widespread disease affecting several million individuals worldwide and characterized by defects in the insulin production and/or in its efficacy [1], [2]. Insulin is the most important hormone involved in the regulation of blood glucose concentration (glycemia); since glucose is the main source of energy in the human metabolism and is introduced at every meal, its concentration needs to be regulated carefully to avoid serious issues due to chronic hyperglycemia, including retinal, renal, microvascular, and neurological complications [3].

Manuscript received June 12, 2021; revised October 12, 2021; accepted December 10, 2021. Manuscript received in final form December 11, 2021. This work was supported in part by the Center of Excellence for Research DEWS, University of L'Aquila, L'Aquila, Italy. Recommended by Associate Editor D. Raimondo. *(Corresponding author: Alessandro Borri.)*

Alessandro Borri is with the CNR-IASI Biomathematics Laboratory, National Research Council of Italy, 00168 Rome, Italy (e-mail: alessandro.borri@iasi.cnr.it).

Giordano Pola, Pierdomenico Pepe, and Maria Domenica Di Benedetto are with the Center of Excellence DEWS, Department of Information Engineering, Computer Science and Mathematics, University of L'Aquila, 67100 L'Aquila, Italy (e-mail: giordano.pola@univaq.it; pierdomenico.pepe@univaq.it; mariadomenica.dibenedetto@univaq.it).

Pasquale Palumbo is with the Department of Biotechnologies and Biosciences, University of Milano-Bicocca, 20126 Milan, Italy (e-mail: pasquale.palumbo@unimib.it).

Color versions of one or more figures in this article are available at https://doi.org/10.1109/TCST.2021.3135320.

Digital Object Identifier 10.1109/TCST.2021.3135320

In diabetic people, glucose regulation fails and an effective way to cope with this problem is to supplement insulin exogenously. While, for decades, diabetic patients have managed their insulin by self-administering a few doses per day, adjusting them on the basis of the expected glucose income and under the supervision of a physician, in the last few years, much attention and research effort have been devoted to the problem of automatic control of plasma glycemia [4], [5]. Glucose regulation is a tricky control problem since, while exogenous insulin administration prevents the long-term effects of diabetes, excessive insulin dosage may induce a too low glycemia concentration (hypoglycemia [6]), which may lead to short-term dangerous effects, including coma and possibly death.

In the last decades, many groups around the world successfully contributed to the theoretical and technological development of the so-called artificial pancreas (AP), whose meaning is not just limited to the first devices made available in the last 3–4 years [7] but, more in general, to the corpus of control strategies developed for the sake of closed-loop glycemia regulation (see, e.g., [8]–[11] and references therein). In the AP context, while model-less control strategies have given some advantages in reproducing experimental behaviors by means of controllers based on simplified strategies [12]–[14], model-based approaches to glucose control [15] recently brought some advantages in the fact that model and control parameters have a physical/physiologic meaning (see, e.g., [16], [17]), and the effectiveness of control algorithms can be tested in silico. Examples of model-based glucose regulation exist, for example, in the context of robust control [18], adaptive control [19], control of nonlinear [9], [20] and nonlinear time-delay systems [21]–[23], and model predictive control (MPC) [10], [11], [24]–[29], where the effect of meals is also accounted for [30].

In this work, we focus on type-2 diabetes, which is the most common type of diabetes mellitus, related to an insufficient insulin production and to insulin resistance, and propose an alternative approach with respect to those existing in the literature, and based on the use of symbolic models and control [31]–[33], widely exploited in the context of formal methods and, to the best of our knowledge, never used in the context of the control in biological and biomedical settings. The symbolic approach relies on the construction of finite approximations of complex systems, which are able to

1063-6536 © 2021 IEEE. Personal use is permitted, but republication/redistribution requires IEEE permission.
See https://www.ieee.org/publications/rights/index.html for more information.

Authorized licensed use limited to: Pasquale Palumbo. Downloaded on December 30,2021 at 11:34:38 UTC from IEEE Xplore. Restrictions apply.

This article has been accepted for inclusion in a future issue of this journal. Content is final as presented, with the exception of pagination.

approximately preserve some properties of the original systems, in particular with respect to the proximity of trajectories, based on the use of the approximate simulation relation [34]. In the AP context, some major advantages deriving from applying research results on symbolic models and control include the possibility of considering inherent uncertainties [35], [36] and state delay in the system dynamics [37], the sampled and quantized nature of output measurements [38] and insulin administration, as well as additional nonidealities arising in the digital environment [39], such as possible actuation delays and nonzero computation and communications lags. To the best of our knowledge, none of the existing techniques can consider all the aforementioned nonidealities at once in a systematic framework. Furthermore, symbolic control allows to address complex specifications, as, for example, possible concatenations of reachability and safety properties (useful to track time-varying zones in glucose control) set avoidance, language, and logic specifications, which are difficult to enforce by means of conventional control design methods [33]. Finally, the utilization of a delay differential equation (DDE) (infinite-dimensional) model of the glucose–insulin dynamics allows to reproduce, among the other features, an explicit delay in the secondary pancreatic insulin release, which is frequently observed in individuals exhibiting an endogenous insulin secretion [17], [40].

The aforementioned advantages of the symbolic approach are balanced by the fact that it is computationally demanding with respect to some more classical methods, especially the model-less approaches including PID controllers (see, e.g., [12]–[14], [41]) and the model-based nonlinear controllers designed in continuous time (see, e.g., [18], [21], [42]), which may also exhibit simpler analytical expressions. Computational complexity is mitigated by adopting an integrated approach [38], [39], [43], which allows for the construction of a symbolic controller solving the specification starting from a set of initial conditions, without building the whole symbolic model. With respect to the MPC glucose control literature (see, e.g., [10], [11], [24], [25], [27]–[29]), whose examples also exhibit nonnegligible computational costs, we do not explicitly solve any optimization problems regarding the rate of administered exogenous insulin, although the MPC approach often employs linearized discrete-time models to compute a solution.

Some preliminary results of the application of the symbolic framework to glucose control are contained in our conference paper [44], where the satisfaction of safety glycemic bounds is formally guaranteed for the adopted model of the glucose–insulin system [17], [40] in fasting conditions. This work introduces some major modifications and a more mature version of the approach, by considering the following points.

1) An improved model is introduced, incorporating a subcutaneous compartment and a meal digestion model; this allows considering the more widespread implementation of the AP via subcutaneous insulin infusion (replacing intravenous administration) [45] and a more realistic rate of glucose appearance due to food absorption [30].
2) From the theoretical viewpoint, we design finite (symbolic) models for possibly unstable time-delay systems with multiplicative disturbances, modeling a percentage uncertainty on the meal glucose content; symbolic models are the cornerstone of the proposed symbolic closed-loop control of glycemia in an AP setting.
3) An extensive simulation/validation campaign is carried out, aiming at evaluating the performance of symbolic glucose regulation along a full day (with three meals) over an extended high-dimensional virtual patient (VP) model [41], [46], which well describes both type-1 and type-2 diabetic patients and constitutes the core of the UVA/Padova Type-1 Diabetes Simulator, approved by the Food and Drug Administration (FDA) as a substitute to animal trials in the preclinical testing of AP control strategies [47].

For the sake of compactness of the model under consideration, we consider a simplified meal digestion model with respect to those proposed, e.g., in [48], [49], which considers different kinds of nutrients and the role of other hormones for different purposes. Moreover, with respect to the recent work [42], [50], while the approach to the validation procedure is somewhat similar, the glucose control strategy we propose here is completely different and formally considers meal digestion and subcutaneous insulin administration.

This article is organized as follows. In Section II, we introduce an integrated time-delay model jointly accounting for glucose regulation, insulin absorption, and meal digestion. Section III illustrates the symbolic control approach for the integrated model restated as an uncertain nonlinear-time-delay system and solve a glucose control problem over a 24-h horizon in an ideal setting. Section IV provides a thorough validation of the theoretical framework on a broadly accepted VP simulator. Section V offers some concluding remarks and leaves some problems open for future investigation. The Appendix includes the technical results developed in a general time-delay system framework, with full proofs.

II. Modeling

To build up the model, we exploit three distinct submodules, each referring to a specific compartment involved in the glucose–insulin dynamics (see Fig. 1). These modules are properly modified to make their interconnection consistent:

1) a two-compartment model of meal digestion, introduced in [51], later exploited also in [52];
2) a two-compartment model of insulin absorption introduced in [53], later exploited in [24];
3) a glucose–insulin DDE model introduced in [17], [40].

For the parameters of the first two submodels, we refer to the unifying notation adopted in [30].

In particular, as shown in Fig. 1, the meal digestion submodel (D_1, D_2) is forced by an exogenous meal input rate $\tilde{d}(t)$ [mmol/kgBW/min] (kgBW stands for kg of body weight), which we will assume to be known up to a relative uncertainty

$$\begin{cases} \dot{D}_1(t) = -\dfrac{1}{\tau_m} D_1(t) + K_{\text{Bio}} \tilde{d}(t) \\ \dot{D}_2(t) = -\dfrac{1}{\tau_m} D_2(t) + \dfrac{1}{\tau_m} D_1(t) \end{cases} \tag{1}$$

Authorized licensed use limited to: Pasquale Palumbo. Downloaded on December 30,2021 at 11:34:38 UTC from IEEE Xplore. Restrictions apply.

This article has been accepted for inclusion in a future issue of this journal. Content is final as presented, with the exception of pagination.

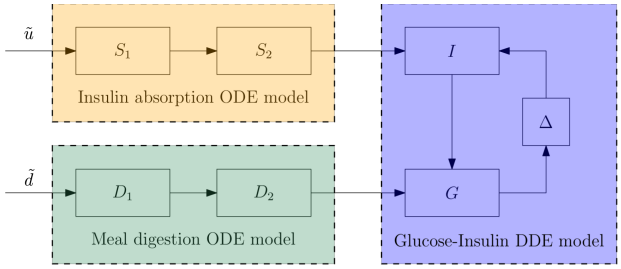

Fig. 1. Illustration of the model (1)–(3). The model is composed by the interconnection of three different submodels describing meal digestion, insulin absorption, and plasma glycemia and insulinemia.

where $D_1(t)$ and $D_2(t)$, expressed in [mmol/kgBW], model the digestion of glucose (CHO) ingested with the meal. While the work [52] considers impulsive meals (Dirac delta functions), we consider that the CHO quantity is assumed in a finite (nonzero) interval (with constant rate).

Similarly, the submodel (S_1, S_2), representing the absorption of subcutaneous insulin, is forced by the insulin control input rate $\tilde{u}(t)$ [pmol/kgBW/min]

$$\begin{cases} \dot{S}_1(t) = -\dfrac{1}{\tau_i} S_1(t) + \tilde{u}(t) \\ \dot{S}_2(t) = -\dfrac{1}{\tau_i} S_2(t) + \dfrac{1}{\tau_i} S_1(t) \end{cases} \tag{2}$$

where $S_1(t)$ and $S_2(t)$ are expressed in [pmol/kgBW].

The model in (1)–(2) is coupled with a modification of the one introduced in [17] and [40], properly modified to consider the rates of glucose and insulin appearance, $D_2(t)/\tau_m$ and $S_2(t)/\tau_i$, respectively, in the plasma

$$\begin{cases} \dot{G}(t) = -K_{xgi} G(t) I(t) + \dfrac{T_{gh}}{V_G} + \dfrac{D_2(t)}{\tau_m V_G} \\ \dot{I}(t) = -K_{xi} I(t) + \dfrac{T_{\text{iGmax}}}{V_I} h(G(t-\Delta)) + \dfrac{S_2(t)}{\tau_i V_I} \end{cases} \tag{3}$$

where $G(t)$ [mmol/L] denotes the plasma glucose concentration at time t, $I(t)$ [pmol/L] is the plasma insulin concentration at time t, and the nonlinear Hill function

$$h(G) = \frac{(G/G^*)^\gamma}{1 + (G/G^*)^\gamma}$$

represents the endogenous pancreatic insulin delivery rate (IDR).

Parameters are listed in Table I with their values and units of measurement (note that 1 M = 1 mol/L). The parameters of (1) have been calibrated with respect to the 3-D nonlinear digestion model in [54]. The value of τ_i in (2) is the one of $t_{\max,I}$ in [24]. The parameters of (3) are taken from [55].

It can be readily shown that system (1)–(3) is positive, i.e., the evolution of its state variables from nonnegative initial conditions and nonnegative disturbance and control inputs assumes nonnegative values at all times [56]; this model will be reformulated in the context of nonlinear time-delay systems in Section III.

TABLE I
MODEL PARAMETERS

Symbol	Quantity	Nominal Value
τ_i	time-to-maximum insulin of absorption of subcutaneously injected insulin	55 min
τ_m	digestion time constant	50 min
K_{Bio}	carbohydrates bioavailability in the meal	0.75
K_{xgi}	insulin-dependent glucose uptake rate by tissues per unit of plasma insulinemia	$3.15 \cdot 10^{-5}$ min^{-1}pM^{-1}
T_{gh}	net balance between hepatic glucose output and insulin-independent zero-order glucose tissue uptake	0.0023 min^{-1}·mmol/kgBW
V_G	apparent distribution volume for glucose	0.18 L/kgBW
K_{xi}	apparent linear insulin clearance rate	0.038 min^{-1}
T_{iGmax}	maximal second-phase insulin release rate	1.695 min^{-1}·pmol/kgBW
V_I	apparent distribution volume for insulin	0.25 L/kgBW
Δ	delay in the glucose action on pancreatic Insulin Delivery Rate (IDR)	6.5 min
γ	progressiveness of the pancreas reaction to circulating glucose concentrations	15.92
G^*	glycemia corresponding to half-maximal insulin release rate	9 mM

III. INTEGRATED SYMBOLIC AP DESIGN

This section is devoted to an illustration of the symbolic approach for nonlinear time-delay systems, which is a class of systems, including the model described in Section II. A novel result is provided regarding the construction of symbolic models for possibly unstable nonlinear time-delay systems with multiplicative uncertainties. Although the theoretical framework is here specialized to the AP context, the results have general validity, as further detailed in the appendixes, which also include a deeper explanation of the required notation and preliminaries. A glucose control problem is then formalized and solved.

A. AP Model as an Incrementally Forward Complete Uncertain Time-Delay System With Quantized Output

We preliminary define the (nonnormalized) state variables $\tilde{x}_1(t) := G(t)$, $\tilde{x}_2(t) := I(t)$, $\tilde{x}_3(t) := S_1(t)$, $\tilde{x}_4(t) := S_2(t)$, $\tilde{x}_5(t) := D_1(t)$, and $\tilde{x}_6(t) := D_2(t)$. Initial conditions are assumed constant on a hyper-rectangular set $\tilde{X}_0 = \times_{i=1}^{6} [\tilde{x}_{0i,\min}, \tilde{x}_{0i,\max}]$. The choice of $\tilde{X}_0$ affects the computation of the bounds $\tilde{x}_{i,\max}$, $i = 1, \ldots, 6$, of the working region of system (1)–(3), whose computation is needed to construct symbolic models according to the procedure described later in this section. To this end, note also that the linear time-invariant subsystems (1) and (2) are 0-GAS [57], which implies the ISS property; this, in turn, readily allows for defined uniform bounds $\tilde{u}_{\max}$ and $\tilde{d}_{\max}$ on the control and on the disturbance inputs, respectively, to also compute uniform bounds for the state variables (see, e.g., [57]), whose solutions are positive and bounded (following the reasoning illustrated in [40]).

The model (1)–(3) is then adimensionalized, to define later symbolic models with the same number of quantized values

Authorized licensed use limited to: Pasquale Palumbo. Downloaded on December 30,2021 at 11:34:38 UTC from IEEE Xplore. Restrictions apply.

This article has been accepted for inclusion in a future issue of this journal. Content is final as presented, with the exception of pagination.

for all the state dimensions, and can readily restated as an uncertain nonlinear time-delay system (TDS) with quantized output measurements in the general form (see Appendix I-B)

$$\begin{cases} \dot{x}(t) = f(x_t, u(t-r), d(t)), & t \in \mathbb{R}^+, \text{ a.e.} \\ x(t) \in \mathcal{X}_0, & t \in [-\Delta, 0] \\ y(t) = [z(t)]_\lambda, \text{ with } z(t) = [\, I_p \quad 0 \,]x(t), & t \in \mathbb{R}_0^+ \end{cases} \tag{4}$$

with the following particular choices.

1) $r = 0$ (input delay).
2) $x(t) \in X = [0, 1[^6 \subseteq \mathbb{R}^n$, with $n = 6$, is a vector in the form

$$\begin{aligned} x(t) &= \begin{bmatrix} x_1(t) & x_2(t) & x_3(t) & x_4(t) & x_5(t) & x_6(t) \end{bmatrix}^T \\ &= \begin{bmatrix} \frac{\tilde{x}_1(t)}{\tilde{x}_{1,\max}} & \frac{\tilde{x}_2(t)}{\tilde{x}_{2,\max}} & \frac{\tilde{x}_3(t)}{\tilde{x}_{3,\max}} & \frac{\tilde{x}_4(t)}{\tilde{x}_{4,\max}} & \frac{\tilde{x}_5(t)}{\tilde{x}_{5,\max}} & \frac{\tilde{x}_6(t)}{\tilde{x}_{6,\max}} \end{bmatrix}^T. \end{aligned} \tag{5}$$

3) $\mathcal{X}_0 \subseteq \mathcal{X}$ (initial functional states) is the set of constant functions on $[-\Delta, 0]$ with values in $X_0 = \times_{i=1}^{6}[x_{0i,\min}, x_{0i,\max}]$, with $x_{0i,\min} = (\tilde{x}_{0i,\min}/\tilde{x}_{i,\max})$ and $x_{0i,\max} = (\tilde{x}_{0i,\max}/\tilde{x}_{i,\max})$ for all i.
4) $\mathcal{X} = C^0([-\Delta, 0]; X)$ (set of functional states), which is forward invariant starting from an initial condition in $\mathcal{X}_0$, i.e., $x_0 \in \mathcal{X}_0$ implies $x_t \in \mathcal{X}$ for all $t \geq 0$.
5) Control input $u(t) = (\tilde{u}(t)/\tilde{u}_{\max}) \in U = (1/\tilde{u}_{\max})\mathbb{Z} \cap [0, 1[\subseteq \mathbb{R}^m$, at all times $t \in [-r, +\infty[$, accounting for the input quantization, with $m = 1$ (input dimension).
6) Disturbance input $d(t) = (\tilde{d}(t)/\tilde{d}_{\max}) \in D = [0, 1] \subseteq \mathbb{R}^q$, at all times $t \in \mathbb{R}_0^+$, with $q = 1$ (disturbance dimension), resulting in $\bar{D} = [0, (1/(1+\bar{\alpha}))]$, in agreement with the general formalism in Appendix I-B; the disturbance $d(t)$ is composed by a known meal quantity rate $\bar{d}(t)$ affected by an unknown bounded multiplicative (percentage) uncertainty α, i.e., $d(t) = (1+\alpha)\bar{d}$, $\alpha \in [-\bar{\alpha}, \bar{\alpha}]$, $\bar{d} \in \bar{D}$; D and $\bar{D}$ are then referred to as unknown and known disturbance sets, respectively.
7) $p = 1$ (output dimension), implying that quantized glycemia is the only measurable quantity; this assumption complies with most of the state-of-the-art technologies involved in real-time control input actuation, such as the insulin pumps in the AP [7].
8) $f : \mathcal{X} \times U \times D \to \mathbb{R}^n$ defined as $f(\phi, u, d)$, as shown at the bottom of the page.

Note that there exists a constant functional state $\phi_e \in \mathcal{X}$ such that $f(\phi_e, 0, 0) = 0$, with ϕ_e in the form

$$\phi_e(s) = x_e := \begin{bmatrix} \frac{G_b}{\tilde{x}_{1,\max}} & \frac{I_b}{\tilde{x}_{2,\max}} & 0 & 0 & 0 & 0 \end{bmatrix}^T, \quad s \in [-\Delta, 0]. \tag{6}$$

The quantities G_b and I_b are called basal glycemia and insulinemia values.

In relation to the TDS in (4), generalized in (15) to the case of positive constant input delay $r \in \mathbb{R}_0^+$, we consider the class of piecewise-constant control and disturbance input functions, denoted as $\mathcal{U}$ and $\mathcal{D}$, obtained as the concatenation of constant control and disturbance input functions belonging to $\mathcal{U}_\tau$, and $\mathcal{D}_\tau$, respectively, where $\tau \in \mathbb{R}^+$ is a sampling time parameter. Namely, $\mathcal{U}_\tau$ is defined as the collection of functions from $[-r, -r+\tau[$ to U with $u(t) = u(-r)$ for any $t \in [-r, -r+\tau[$, while $\mathcal{D}_\tau$ (resp. $\bar{\mathcal{D}}_\tau$) collects the functions from $[0, \tau[$ to D (resp. $\bar{D}$), with $d(t) = d(0)$ for any $t \in [0, \tau[$, $d(0) \in D$ (resp. $\bar{D}$). In many concrete applications, such as the AP studied in this article, controllers are implemented via digital devices (see, e.g., the recent contribution to the control on embedded AP in [58]) and this motivates our interest for the class of piecewise-constant control inputs. Similarly, disturbance inputs are also assumed to be piecewise-constant but taking value in the compact set D since the CHO quantity in the meal may vary in a continuous set. For simplicity, we assume a constant meal rate over a fixed time interval, which is an alternative more realistic choice than considering impulsive inputs [54].

A time-delay system in the form (4) is said to be forward complete (FC) if every solution is defined on $[0, +\infty[$. In the further developments, we refer to a time-delay system as in (4) by means of the tuple

$$\Sigma = (X, \mathcal{X}, \mathcal{X}_0, U \times D, \mathcal{U} \times \mathcal{D}, \mathbb{R}^p, f) \tag{7}$$

where each entity has been defined above.

We now introduce some assumptions that are made to derive our results. The following definition is a natural extension to time-delay systems of the one given for nonlinear systems in [59].

$$f(\phi, u, d) = \begin{bmatrix} -K_{xgi}\tilde{x}_{2,\max}\phi_1(0)\phi_2(0) + \frac{T_{gh}}{V_G\tilde{x}_{1,\max}} + \frac{\tilde{x}_{4,\max}}{\tau_m V_G \tilde{x}_{1,\max}}\phi_4(0) \\ -K_{xi}\phi_2(0) + \frac{T_{\text{iGmax}}}{V_I\tilde{x}_{2,\max}}h\big(\tilde{x}_{1,\max}\phi_1(-\Delta)\big) + \frac{\tilde{x}_{6,\max}}{\tau_i V_I \tilde{x}_{2,\max}}\phi_6(0) \\ -\frac{1}{\tau_m}\phi_3(0) + \frac{K_{\text{Bio}}\tilde{d}_{\max}}{\tilde{x}_{3,\max}}d \\ -\frac{1}{\tau_m}\phi_4(0) + \frac{\tilde{x}_{3,\max}}{\tau_m\tilde{x}_{4,\max}}\phi_3(0) \\ -\frac{1}{\tau_i}\phi_5(0) + \frac{\tilde{u}_{\max}}{\tilde{x}_{5,\max}}u \\ -\frac{1}{\tau_i}\phi_6(0) + \frac{\tilde{x}_{5,\max}}{\tau_i\tilde{x}_{6,\max}}\phi_5(0) \end{bmatrix}$$

Authorized licensed use limited to: Pasquale Palumbo. Downloaded on December 30,2021 at 11:34:38 UTC from IEEE Xplore. Restrictions apply.

This article has been accepted for inclusion in a future issue of this journal. Content is final as presented, with the exception of pagination.

Definition 1: A time-delay system in the form (7) is incrementally forward complete (δ-FC) if it is forward complete and there exist continuous functions $\beta : \mathbb{R}_0^+ \times \mathbb{R}_0^+ \to \mathbb{R}_0^+$ and $\gamma : \mathbb{R}_0^+ \times \mathbb{R}_0^+ \to \mathbb{R}_0^+$ such that, for every $s \in \mathbb{R}_0^+$, $\beta(\cdot, s)$ and $\gamma(\cdot, s)$ belong to class $\mathcal{K}_\infty$, and for any time $t \in \mathbb{R}_0^+$, any initial conditions $\xi_1, \xi_2 \in \mathcal{X}$, any control input $u \in \mathcal{U}$, and any disturbance inputs $d_1, d_2 \in \mathcal{D}$, the following inequality holds:

$$\|x_t(\xi_1, u, d_1) - x_t(\xi_2, u, d_2)\|_\infty \leq \beta(\|\xi_1 - \xi_2\|_\infty, t) + \gamma(\|d_1 - d_2\|_\infty, t). \quad (8)$$

The δ-FC property requires the distance between two arbitrary trajectories to be bounded by two terms capturing the mismatch between the initial conditions and the mismatch between the disturbance functions. This notion is rather mild; as discussed in [59] for the delay-free case, all linear systems are δ-FC and, for example, most unstable nonlinear systems not exhibiting finite escape time enjoy the δ-FC property. In addition, linear time-invariant systems with constant discrete time delays are δ-FC.

We conclude this section with the result, proven in the appendix, that the AP system (1)–(3), restated in the adimensionalized form of time-delay system in (4), is incrementally forward complete.

Theorem 1: The system (1)–(3), restated as (4), is δ-FC.

B. Construction of Symbolic Models

In this section, we derive some results for the construction of symbolic (finite) models approximating the extended time-delay glucose–insulin model Σ in the sense of alternating and also of (nonalternating) approximate simulation. These results generalize those in [44] and [60] by addressing incrementally forward complete time-delay systems with outputs and multiplicative disturbances.

Given the time-delay system Σ, we define the following system (see Definition 4) that considers the different (known and unknown) components of the disturbances:

$$S(\Sigma) = (X, X_0, L, \longrightarrow, Y, H)$$

where $X = \mathcal{X}$, $X_0 = \mathcal{X}_0$, $L = U \times \bar{D} = \{(u, \bar{d}) \in \mathcal{U}_\tau \times \bar{\mathcal{D}}_\tau \mid x_\tau(x, u, (1+\alpha)\bar{d})$ is defined for all $x \in \mathcal{X}$, for all $\alpha \in [-\bar{\alpha}, \bar{\alpha}]\}$, $x \xrightarrow{(u,\bar{d})} x'$ if $x_\tau(x, u, (1+\alpha)\bar{d}) = x'$, with $\alpha \in [-\bar{\alpha}, \bar{\alpha}]$, $Y = \mathbb{R}^p$, and $H(x) = [z]_\lambda$, with $z = [\, I_p \;\, 0\,]x(\tau)$, for all $x \in X$.

System $S(\Sigma)$ captures the evolution of Σ only at times $t = k\tau$ with $k \in \mathbb{N}_0$. In this sense, $S(\Sigma)$ can be viewed as a time discretization of Σ. By definition of X, system $S(\Sigma)$ is metric. In the sequel, we use the metric $\mathbf{d}(x, x') = \|x - x'\|_\infty$, $x, x' \in X$. Note that $S(\Sigma)$ is not symbolic because the set of states X is a functional space and $\bar{D}$ is an infinite set. Furthermore, note that only the known part of the disturbance is parameterized by means of the label $\bar{d}$, while, with respect to the relative uncertainty α, for a given state x and label pair $(u, \bar{d})$, multiple successors are considered.

The construction of symbolic models for time-delay systems relies upon approximations of the set of reachable states. Let $R_\tau(\Sigma) \subseteq \mathcal{X}$ be the set of reachable states of Σ at times $t = 0, \tau, \ldots, k\tau, \ldots$, i.e., the collection of all states $x \in \mathcal{X}$ for which there exist $k \in \mathbb{N}_0$, a control input $u \in \mathcal{U}$, and a disturbance input $d \in \mathcal{D}$ such that $x = x_{k\tau}(\xi_0, u, d)$, for some $\xi_0 \in \mathcal{X}_0$. The set $R_\tau(\Sigma)$ corresponding to[1] X in $S(\Sigma)$ is a functional space and therefore needs to be approximated. To this purpose, we assume the existence of a countable approximation $\mathcal{A}_\mathcal{X}$ of $R_\tau(\Sigma)$, see Definition 3. Map $\mathcal{A}_\mathcal{X}$ naturally induces a countable approximation $\mathcal{A}_{\mathcal{X}_0}$ of $\mathcal{X}_0$ because $\mathcal{X}_0 \subset R_\tau(\Sigma)$ (in the following, we will derive conditions ensuring existence and effective construction of $\mathcal{A}_\mathcal{X}$). We now define system $S_{\lambda,\mu}(\Sigma)$ that approximates $S(\Sigma)$.

Definition 2: Suppose that Σ in (7) is δ-FC and for any accuracy $\lambda \in \mathbb{R}^+$ and any disturbance quantization $\mu \in \mathbb{R}^+$, define the system

$$S_{\lambda,\mu}(\Sigma) = (X_\lambda, X_{0,\lambda}, L_{\lambda,\mu}, \underset{\lambda,\mu}{\longrightarrow}, Y_\lambda, H_\lambda) \quad (9)$$

where $X_\lambda = \mathcal{A}_\mathcal{X}(\lambda)$, $X_{0,\lambda} = \mathcal{A}_{\mathcal{X}_0}(\lambda)$; $L_{\lambda,\mu} = U \times [\bar{D}]_\mu$; $x_\lambda \xrightarrow[\lambda,\mu]{u,\bar{d}} x'_\lambda$ if $\|x_\tau(x_\lambda, u, (1+\alpha)\bar{d}) - x'_\lambda\|_\infty \leq \beta(\lambda, \tau) + \gamma((1+\alpha)\mu, \tau) + \lambda$, for some $\alpha \in [-\bar{\alpha}, \bar{\alpha}]$, with β and γ the functions appearing in (8); $Y_\lambda = [\mathbb{R}^p]_\lambda$; and $H_\lambda(x_\lambda) = [z_\lambda]_\lambda$, with $z_\lambda = [\, I_p \;\, 0\,]x_\lambda(\tau)$, for all $x_\lambda \in X_\lambda$.

In the sequel, we use the symbol x_λ to denote a state of $S_{\lambda,\mu}(\Sigma)$. If there exists a countable approximation $\mathcal{A}_\mathcal{X}$ of $R_\tau(\Sigma)$, system $S_{\lambda,\mu}(\Sigma)$ is countable. By definition of X_λ, system $S_{\lambda,\mu}(\Sigma)$ is metric; we use for $S_{\lambda,\mu}(\Sigma)$ the same metric $\mathbf{d}$ as the one used for $S(\Sigma)$. The following result establishes some relations between $S(\Sigma)$ and $S_{\lambda,\mu}(\Sigma)$ (see Definition 5 in Appendix I-D).

Theorem 2: Suppose that Σ is δ-FC and that there exists a countable approximation $\mathcal{A}_\mathcal{X}$ of $R_\tau(\Sigma)$. For any accuracy $\lambda \in \mathbb{R}^+$ and any disturbance quantization $\mu \in \mathbb{R}^+$ satisfying

$$\mu = \hat{\mu}_{\bar{D}}/n_{\bar{D}} \quad (10)$$

for some integer $n_{\bar{D}}$, the following statements hold.

1) $S_{\lambda,\mu}(\Sigma) \preceq_\lambda^{s,\text{alt}} S(\Sigma)$ with strong AλA simulation relation $\mathcal{R} \subseteq X_\lambda \times X$ defined by $(x_\lambda, x) \in \mathcal{R} \Leftrightarrow \|x_\lambda - x\|_\infty \leq \lambda$.
2) $S(\Sigma) \preceq_\lambda^s S_{\lambda,\mu}(\Sigma)$ with strong λA simulation relation $\mathcal{R}' \subseteq X \times X_\lambda$ defined by $\mathcal{R}' = \mathcal{R}^{-1}$.
3) $\|H(x) - H_\lambda(x_\lambda)\| \leq \lambda$, for any $(x_\lambda, x) \in \mathcal{R}$.

We now give results to approximate the set of reachable states $R_\tau(\Sigma)$ of the time-delay system Σ, thereby providing tools for the effective construction of the system $S_\lambda(\Sigma)$ proposed in Definition 2. To this end, consider a Lipschitz on bounded set functional $\bar{f}(\phi, 0, 0) := f(\phi + \phi_e, 0, 0)$, with $f(\phi_e, 0, 0) = 0$ and ϕ_e constantly equal to x_e as defined in (6) (see Appendix I-B). Then, the following assumptions are readily verified.

(A.1): The TDS Σ in (7) is δ-FC, from Theorem 1.
(A.2): The set $X = [0, 1[^6$ is bounded.
(A.3): The functional $\bar{f}$ is Fréchet differentiable in $C^0([-\Delta, 0]; \mathbb{R}^n) \times \mathbb{R}^m \times \mathbb{R}^q$.
(A.4): The Fréchet differential $J(\phi, u, d)$ of $\bar{f}$ is continuous and bounded on bounded subsets of $C^0([-\Delta, 0]; \mathbb{R}^n) \times \mathbb{R}^m \times \mathbb{R}^q$.

[1]In fact, the set X of states of $S(\Sigma)$ is $\mathcal{X}$ and not $R_\tau(\Sigma)$. However, all states in $\mathcal{X} \backslash R_\tau(\Sigma)$ will never be reached and this is the reason why we will approximate $R_\tau(\Sigma)$ rather than $\mathcal{X}$.

Authorized licensed use limited to: Pasquale Palumbo. Downloaded on December 30,2021 at 11:34:38 UTC from IEEE Xplore. Restrictions apply.

This article has been accepted for inclusion in a future issue of this journal. Content is final as presented, with the exception of pagination.

This implies that the following bounds are well defined:

$$\begin{aligned} B_X &= \sup_{x\in\bar{X}} \|x\|, \quad B_U = \max_{u\in U} \|u\|, \quad B_D = \max_{d\in D} \|d\| \\ B_J &= \sup_{(\phi,u,d)\in C^0([-\Delta,0];\bar{X})\times U\times D} \|J(\phi,u,d)\| \\ M &= (B_X + B_U + B_D)\kappa B_J \end{aligned} \tag{11}$$

where $\bar{X} = \{x - x_e, x \in X\}$, κ is the Lipschitz constant of functional $\bar{f}$ in the bounded set $C^0([-\Delta, 0]; \bar{X}) \times U \times D$ and $\|J(\phi, u, d)\|$ denotes the norm of the operator $J(\phi, u, d) : C^0([-\Delta, 0]; \mathbb{R}^n) \times \mathbb{R}^m \times \mathbb{R}^q \to \mathbb{R}^n$. We can now give the following technical lemma that is instrumental to provide the main result of this article.

Lemma 1: Suppose that Σ satisfies (A.1)–(A.4) and the following conditions hold [referred to as (A.5)].

(A.5.1): $\xi_0 \in C^0([-\Delta, 0]; \bar{X}) \cap PC^2([-\Delta, 0]; \mathbb{R}^n)$, for any $\xi_0 \in \mathcal{X}_0$.

(A.5.2): $\|D^2\xi_0\|_\infty \leq M$, for any $\xi_0 \in \mathcal{X}_0$.

(A.5.3): $\tau > 2\Delta$.

Then, for any $x_{k\tau} \in R_\tau(\Sigma)$ with $k \in \mathbb{N}_0$, the following conditions hold.

1) $x_{k\tau} \in C^0([-\Delta, 0]; \bar{X}) \cap PC^2([-\Delta, 0]; \mathbb{R}^n)$.
2) $\|D^2 x_{k\tau}\|_\infty \leq M$.

As a direct consequence of Lemmas 1 and 2 reported in Appendix I-C, we obtain the following.

Proposition 1: Consider the time-delay system Σ, satisfying Assumptions (A.1)–(A.5). Then, the set $\mathcal{A}_\mathcal{X}$ defined for any $\lambda \in \mathbb{R}^+$ by

$$\mathcal{A}_\mathcal{X}(\lambda) = \psi_{\lambda,M}(R_\tau(\Sigma)) \tag{12}$$

with $\psi_{\lambda,M}$ as in (19), is a symbolic approximation of $R_\tau(\Sigma)$. Given $\theta \in \mathbb{R}^+$ and $N \in \mathbb{N}$, consider the system $S_*(\Sigma) := S_{\lambda,\mu}(\Sigma)$ for $\lambda = \Lambda(N, \theta, M)$. We conclude by giving the main theoretical result of this article, establishing the relation between the time discretization $S(\Sigma)$ of the time-delay system Σ and the symbolic model $S_*(\Sigma)$.

Theorem 3: Suppose that the time-delay system Σ is δ-FC and that it satisfies Assumptions (A.1)–(A.5). For any quantization parameter $\lambda \in \mathbb{R}^+$ and any disturbance quantization $\mu \in \mathbb{R}^+$ satisfying (10) for some integer $n_{\bar{D}}$, pick $\theta \in \mathbb{R}^+$ and $N \in \mathbb{N}$ satisfying the following inequality:

$$\Lambda(N, \theta, M) \leq \lambda \tag{13}$$

with Λ as in (18) and M as in (11). Then, the following statements hold.

1) $S_*(\Sigma)$ is symbolic.
2) $S_*(\Sigma) \preceq_\lambda^{s,\text{alt}} S(\Sigma)$ with strong AλA relation $\mathcal{R} \subseteq X_\lambda \times X$ defined by $(x_\lambda, x) \in \mathcal{R} \Leftrightarrow \|x_\tau - x\|_\infty \leq \Lambda(N, \theta, M)$.
3) $S(\Sigma) \preceq_\lambda^s S_*(\Sigma)$ with strong λA relation $\mathcal{R}' \subseteq X \times X_\lambda$ defined by $\mathcal{R}' = \mathcal{R}^{-1}$.
4) $\|H(x) - H_\lambda(x_\lambda)\| \leq \Lambda(N, \theta, M)$, for any $(x_\lambda, x) \in \mathcal{R}$.

Proof: It shows the direct application of Proposition 1 and Theorem 2. ■

C. Integrated Control Synthesis for the AP

While the theoretical procedures reported above allow to infer the existence of uniform bounds, tighter bounds have been determined numerically for the model (1)–(3) (via over-approximation of reachable sets) for a choice of maximal insulin administration rate $\tilde{u}_{\max} = 90$ (as in [42]) and maximal meal ingestion rate $\tilde{d}_{\max} = 0.5$, computed as an upper bound for a VP of an average weight of 70 kg and accounting for a maximum meal size of 70 g + 25% (the work [61] reports that carbohydrate counting has an estimation error of around 20%). The numerical values for the rectangular bounds on initial conditions are set to $\tilde{x}_{01,\min} = 2$, $\tilde{x}_{01,\max} = 17$, $\tilde{x}_{02,\min} = 20$, $\tilde{x}_{02,\max} = 100$, $\tilde{x}_{0i,\min} = 0$ for $i = 3, 4, 5$, and 6, $\tilde{x}_{03,\max} = 1000$, $\tilde{x}_{04,\max} = 500$, $\tilde{x}_{05,\max} = 3$, and $\tilde{x}_{06,\max} = 2$ (see Section II for the units of measurements of all variables). This leads to bounds for the state variables of system (1)–(3) given by $\tilde{x}_{1,\max} = 20$, $\tilde{x}_{2,\max} = 1000$, $\tilde{x}_{3,\max} = 2000$, $\tilde{x}_{4,\max} = 1000$, $\tilde{x}_{5,\max} = 10$, and $\tilde{x}_{6,\max} = 5$. Properties (A.1)–(A.5) in Section III-B are satisfied for $B_X = B_U = B_D = 1$, $B_J = 0.32$, $\kappa = 0.0015$, and $M = 0.0014$, where the sampling time $\tau = 15$ [min] is chosen, which is a multiple of a common sampling interval (5 minutes) characterizing many off-the-shelf continuous glucose monitoring (CGM) devices [62]. The value of the disturbance quantization is fixed at $\mu = 1/24$. We set $\lambda = 0.005$ and choose $N = 2$ and $\theta = 0.001$ satisfying (13).

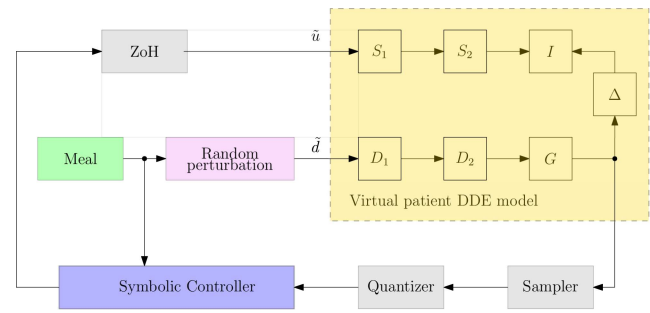

Fig. 2. Illustration of the closed-loop system consisting of the VP model (1)–(3) controlled by means of a symbolic controller in a digital environment, including a sampler and a ZoH, with sampling time τ, and a quantizer, with (percent) quantization λ.

We now refer to the digital control scheme shown in Fig. 2 and to the experiment in [42, Scenario 3], where a full-day time horizon is considered and three meals of 45, 70, and 70 g are administered at time 8, 12, and 20 h, respectively, corresponding to $t = 480$ min (breakfast), $t = 720$ min (lunch), and $t = 1200$ (dinner) min. The meals are assumed to be provided with constant meal rate in a period equal to one sampling interval for breakfast and to two sampling intervals for lunch and dinner. In this context, we assume a 25% uncertainty on each meal ($\bar{\alpha} = 0.25$), and the system starts from the equilibrium point x_e as in (6) with control law applied at time 0, with $G_b = 8.85$ and $I_b = 59.85$ satisfying (3) at the equilibrium.

The computed symbolic model is employed to solve a glucose control problem whose specification is described in natural language as follows.

1) *Excellent All-Time Safety:* $G(t) \geq 3.3$ at all times.
2) *Excellent Efficacy in Fasting Conditions:* $G(t) < 6$ after the first 3 hours of treatment (no meals).

Authorized licensed use limited to: Pasquale Palumbo. Downloaded on December 30,2021 at 11:34:38 UTC from IEEE Xplore. Restrictions apply.

This article has been accepted for inclusion in a future issue of this journal. Content is final as presented, with the exception of pagination.

TABLE II
CONTROL SAFETY SPECIFICATION

Safety level	Time with $G(t) \geq 3.3[mM]$	Time with $G(t) < 2[mM]$
Excellent	100%	0%
Good	$\geq 95\%$	0%
Satisfactory	$\geq 80\%$	0%
Unsatisfactory	otherwise	otherwise

TABLE III
CONTROL EFFICACY SPECIFICATION

Efficacy level	$t \in [3, 8]$ $[h]$ Fasting condition	$t \in [10, 12] \cup [14, 20] \cup [22, 24]$ $[h]$ Post-prandial condition
Excellent	$G(t) < 6$	$G(t) < 8$
Good	$G(t) \in [6, 7)$	$G(t) \in [8, 9.5)$
Satisfactory	$G(t) \in [7, 8)$	$G(t) \in [9.5, 11)$
Unsatisfactory	$G(t) \geq 8$	$G(t) \geq 11$

3) *Excellent Efficacy in Postprandial Conditions:* $G(t) <$ 8 mmol/L. after 2 h from meal and during the period before the possible next meal.

It corresponds to joint fulfillment of excellent safety and excellent efficacy as formalized in Tables II and III.

In order to solve this control problem, the previous time-varying specification has been restated in terms of a concatenation of "reach and stay" specifications, which can be solved by using supervisory control type algorithms [63], [64] on the symbolic model built according to the procedure in Section III-B. In more detail, the symbolic control procedure is computed off-line following the following steps (see, e.g., Appendix I-D and [39]).

1) The specification is reformulated in terms of a nondeterministic system $S(Q)$ (see Definition 4).
2) A symbolic controller S_{C^*} is computed as the maximal nonblocking subsystem[2] S_C of $S_*(\Sigma)$ such that $S_C \preceq_{\mu_\lambda} S(Q)$ and $S_C \preceq_0^{s,\text{alt}} S_*(\Sigma)$ (see Definition 5).
3) The symbolic controller S_{C^*} is refined (see, e.g., [39, Th. 3]) into a dynamic, nondeterministic symbolic controller C^* in the form

$$C^* : \begin{cases} \xi_k \in f_C(\xi_{k-1}, y_k, \bar{d}_k), \quad \xi_k \in \Xi_C, \ k \in \{0, 1, \ldots\} \\ u_k^* = h_C(\xi_k), \quad u_k \in U, \ k \in \{0, 1, \ldots\} \\ \xi_{-1} \in \Xi_C^0 \end{cases} \tag{14}$$

where Ξ_C is the finite set of states of the controller, $\Xi_C^0 \subseteq \Xi_C$ is the set of initial states of the controller, $f_C : \Xi_C \times [0, 1[_\lambda \times [0, 1[_\mu \to 2^{\Xi_C}$, and $h_C : \Xi_C \to U$.

In real-time glucose control, consider a general interval $[k\tau, (k+1)\tau[$, $k \in \{0, 1, \ldots\}$: as soon as the controller receives as input the measurement sample $y_k = [y(k\tau)]_\lambda$ and the known disturbance value $\bar{d}_k$, it updates its internal state to ξ_k and then returns the control sample $u_k^* = h_C(\xi_k) \in U$ as its output. Model (1)–(3) runs in the interval $[k\tau, (k+1)\tau[$ with constant control input (see the zero-order hold (ZoH) in Fig. 2)

$$\tilde{u}(t) = \tilde{u}_{\max} u_k^*, \quad t \in [k\tau, (k+1)\tau[$$

[2]Here, maximality is defined with respect to the preorder induced by the notion of subsystem.

Algorithm 1 Symbolic Real-Time Glucose Control

Init: C^*, $\xi_{-1} \in \Xi_C^0$, $G(s) = G_b \quad s \in [-\Delta, 0]$,
$I(0) = I_b$, $S_1(0) = S_2(0) = 0$, $D_1(0) = D_2(0) = 0$;
for $k \in \{0, 1, ..., k_{\max} - 1\}$ **do**
  Measure the glycemia sample $G(k\tau)$;
  Compute the normalized output $y_k = \left[\frac{G(k\tau)}{\bar{x}_{1,\max}}\right]_\lambda$;
  Compute the announced (normalized) meal $\bar{d}_k \in \bar{D}$;
  Update the controller state $\xi_k \in f_C(\xi_{k-1}, y_k, \bar{d}_k)$;
  Compute the control sample $u_k^* = h_C(\xi_k) \in U$;
  Perturb the meal $\alpha_k \in [-\bar{\alpha}, \bar{\alpha}]$ (uniformly distributed)
  $d_k = (1 + \alpha_k)\bar{d}_k$;
  Run system (1)–(3) in the time interval $[k\tau, (k+1)\tau)$ with insulin control input rate $\tilde{u}(t) = \tilde{u}_{\max} u_k^*$, and exogenous meal input rate $\tilde{d}(t) = \tilde{d}_{\max} d_k$.

and uniformly randomly perturbed unknown disturbance input

$$\tilde{d}(t) = \tilde{d}_{\max}(1 + \alpha_k)\bar{d}_k, \quad \alpha_k \in [-\bar{\alpha}, \bar{\alpha}], \ t \in [k\tau, (k+1)\tau[.$$

The closed-loop evolution over $k_{\max}$ sampling intervals of the VP in (1)–(3) and controlled by means of the symbolic controller C^* is formalized in Algorithm 1 for a random realization of the meal uncertainty.

Estimates of the space complexity in constructing the symbolic model $S_*(\Sigma)$ amount to more than 4×10^{15} states and about 2×10^{19} transitions, which makes the construction of the whole model computationally unfeasible. Instead, following an integrated approach (see, e.g., [38], [39], [43]), we just construct the part of the model that can solve the specification starting from the given initial conditions. Furthermore, it was not needed to employ a spline-based approximation for all the variables in the model equations, but just for the normalized glycemia $x_1(t)$ (since the other variables do not appear with delay in the model equations). The resulting controller has been built in the MATLAB suite in 2482 s on an ASUS UX303UB laptop with 2.5-GHz Intel Core i7 CPU and 12-GB RAM and has a memory occupation of 131 750 32-b integers. Fig. 3 shows the closed-loop performance of the symbolic controller applied to the VP model (1)–(3), with parameters in Table I, for a random realization of the meal uncertainty (see Algorithm 1), showing that the specification is met. The interested reader is mostly referred to [39], for a more detailed account of the control problem definition in the presence of uncertainties, and to [38] and [43], for integrated control strategies for systems with outputs, with additional ideas and details, in particular with relation to computational complexity issues.

IV. VALIDATION

We here validate the performances of the controller on a more qualitative and quantitative basis in a nonideal environment. As in the case of the results shown in Fig. 3, also the simulations in this section are run in the MATLAB suite on an ASUS UX303UB laptop with 2.5 GHz Intel Core i7 CPU and 12 GB RAM. The validation setting is a modification of the one proposed in [42].

Authorized licensed use limited to: Pasquale Palumbo. Downloaded on December 30,2021 at 11:34:38 UTC from IEEE Xplore. Restrictions apply.

This article has been accepted for inclusion in a future issue of this journal. Content is final as presented, with the exception of pagination.

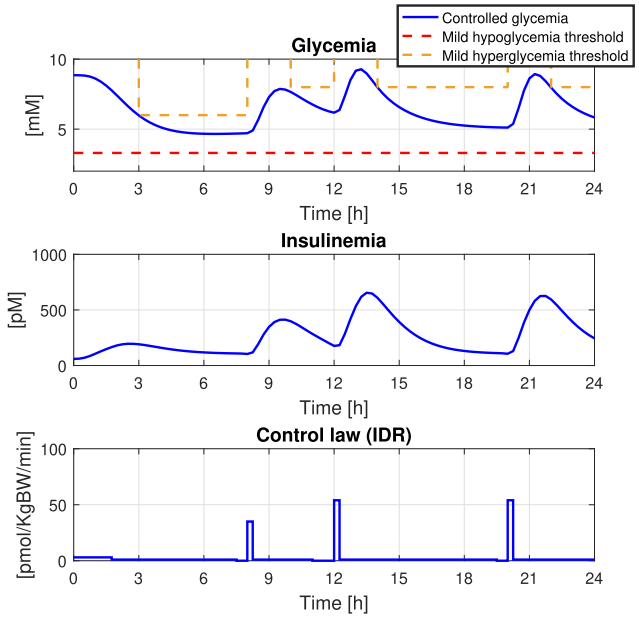

Fig. 3. Closed-loop behavior of the VP modeled by (1)–(3) and controlled by means of the symbolic control design illustrated in Section III for a random realization of the meal uncertainty (see Algorithm 1). The hypoglycemia/hyperglycemia thresholds in the top panel correspond to the excellent safety and efficacy values as formalized in Tables II and III.

We now consider a population of 10 000 type-2 diabetic VPs, each represented by an extended high-dimensional VP model [41], [46], which well describes both type-1 and type-2 diabetic patients and constitutes the core of the UVA/Padova Type-1 Diabetes Simulator, approved by the FDA as a substitute to animal trials in the preclinical testing of AP control strategies [47]. This model assumes insulin sensitivity 25% lower in the evening meal compared with breakfast and lunch and beta-cell responsivity to glucose 25% lower both at lunch and evening meals compared with breakfast since these quantities are not constant during the day, as detailed in the same paper [46]. In the validation phase, the model in [41] and [46] simply replaces (1)–(3) in step 9 of Algorithm 1, starting from the corresponding initial conditions. The parameters are randomly perturbed according to log-normal distributions with a coefficient of variation CV = 5% with respect to the nominal values in the average patient model [41], [46]. According to the modified parameters, each patient has a perturbed equilibrium with respect to (G_b, I_b), and we assume to start each simulation from the corresponding equilibrium. The parameter perturbation produces a quite heterogeneous population of T2DM VPs, with basal glycemia spanning from a minimum of 7 mM (threshold for diabetes) to a maximum of 12.47 mM. Similarly, meals are uniformly randomly perturbed with a maximum 25% variation with respect to the nominal meal values. This results in an interpatient variability of the average (daily) control input in the range [6.49, 11.13] pmol/kgBW/min, showing a good flexibility of the symbolic controller in adapting to the different individual conditions. Furthermore, a health monitoring system (HMS) [65] is implemented, preventing the administration of further exogenous insulin if glycemia is detected to be under a threshold (3.9 mM) and decreasing at a speed higher than 0.01 mM/min.

TABLE IV
SAFETY AND EFFICACY RESULTS

Level	Safety	Label efficacy	Fractional efficacy
Excellent	99.97%	23.67%	93.68%
Good	0%	72.47%	6.21 %
Satisfactory	0.03%	3.86%	0.11%
Unsatisfactory	0%	0%	0%

Tables II and III show the quantitative assessment of safety (with respect to hypoglycemia) and efficacy (with respect to hyperglycemia) for the virtual population. Safety is evaluated according to the fraction of time each VP spends in the severe hypoglycemia zone ($G(t) < 2$ mM) and in the mild hypoglycemia zone ($G(t) \in [2, 3.3)$ mM).

The evaluation of efficacy is more complex. Consider the set of efficacy levels L = {unsatisfactory,satisfactory, good, excellent}, with the strict order relation

$$\text{unsatisfactory} < \text{satisfactory} < \text{good} < \text{excellent}$$

reflecting the qualitative efficacy. With respect to the specification in Table III, we then perform two kinds of assessments [55].

1) *Fractional (Percentage) Efficacy:* Each VP is evaluated according to the fraction of time spent in each of the glycemic zones corresponding to the levels in L.
2) *Label Efficacy:* Each VP is uniquely labeled according to the least satisfactory efficacy level reached, i.e., as the lowest level in L (according to the efficacy order) where a nonzero fraction of time is spent.

Table IV and Fig. 4 summarize the simulation results. It is readily seen that there is 0% of unsatisfactory cases with respect to safety and efficacy, i.e., no patients enter the dangerous zones referred to severe hypoglycemia/hyperglycemia conditions. All the controlled patients readily decrease their glycemia (due to the control action) below the hyperlycemic threshold, and no (severe) hypoglycemiae are detected for the considered virtual population at any time. The number of simulated HMS alarms (insulin pump suspension events) was equal to 85 in the whole population.

Fig. 5 reports the control variability grid analysis (CVGA) [66], according to which each patient is evaluated in terms of minimal and maximal attained glycemia during the day. Note that the CVGA bounds, separating differently colored zones in Fig. 5, are standard and different from those defined in Section III and in Fig. 4 and Tables II and III. In particular, values in the range [2.8, 3.9] mM are regarded in CVGA as overcorrections of hyperglycemia, although these values are considered safe. In more detail, just 116 VPs (1.16% of the whole population) are in the lower C–D zones (1 VP in the lower D zone and 115 VPs in the lower C zone) of Fig. 5, but just 3 of them exhibit a mildly hypoglycemic behavior (below 3.3 mM) and none of them is severely hypoglycemic (below 2 mM).

Finally, we refer to the recent standardized CGM indices for good glucose control published in the International Consensus reports [67], [68] to further evaluate the control performance. Table V reports a performance comparison (on the same virtual population) between the symbolic technique and a digital PID

Authorized licensed use limited to: Pasquale Palumbo. Downloaded on December 30,2021 at 11:34:38 UTC from IEEE Xplore. Restrictions apply.

This article has been accepted for inclusion in a future issue of this journal. Content is final as presented, with the exception of pagination.

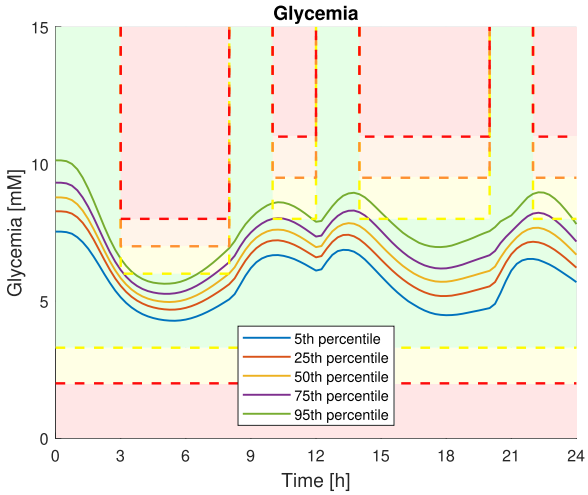

Fig. 4. Closed-loop behavior in terms of percentiles of the population of 10 000 VPs generated as random perturbations of the VP model in [41] and [46] and controlled by means of the symbolic control design illustrated in Section III for random realizations of the meal uncertainty. The dashed hypoglycemia thresholds correspond to the constant bounds equal to 3.3 [mM] (yellow) and 2 [mM] (red), as in Table II. The dashed hyperglycemia thresholds correspond to the bounds of good (yellow), satisfactory (orange), and unsatisfactory (red) efficacy performances, as in Table III.

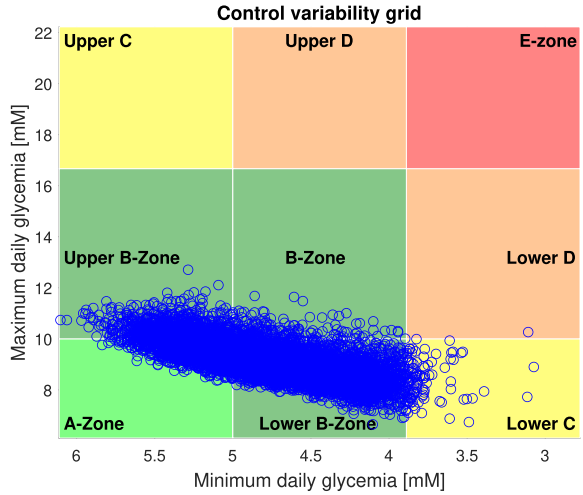

Fig. 5. CVGA for the population of 10 000 VPs generated as random perturbations of the VP model in [41] and [46] and controlled by means of the symbolic control design illustrated in Section III for random realizations of the meal uncertainty.

controller with insulin feedback (IF) (see [14, eqs. (6)–(10), (14), and (15)]) for the case of subcutaneous insulin administration (parameters taken from [12]).

The closed-loop performance results of the symbolic approach with respect to the considered CGM indices are better detailed in the following.

1) The population exhibits a mean glycemia equal to 6.62 mM, with a standard deviation equal to 0.45 over the population (CV = 7%). The corresponding average glucose management indicator (GMI) is 6.16%, with just one individual exceeding the recommended 7% threshold and none exceeding the 7.5% threshold.
2) The mean glycemic variability on the 24-h period over the population is equal to 18.19% (CV), with just one individual exceeding the 33% threshold (providing additional protection against hypoglycemia) and none exceeding the maximal recommended 36% threshold.
3) The time in range (TIR) is equal to 99.57% of the total simulation time, with 8675 individuals (86.75% of the whole population) spending 100% of the simulation time in the recommended zone [3.9, 10] mM.
4) The time above range (TAR), level 1, is equal to 0.38% of the total simulation time, with 1211 individuals (12.11% of the whole population) spending 3.17% of their simulation time (on average) in the range [10.1, 13.9] mM. No individuals exceed the maximal recommended TAR value equal to 25%.
5) The time below range (TBR), level 1, is equal to 0.05% of the total simulation time, with 116 individuals (1.16% of the whole population) spending 3.41% of their simulation time (on average) in the range [3, 3.8] mM. Only three individuals exceed the maximal recommended TBR value equal to 4%.
6) *TAR, Level 2:* No individuals (0% of the whole population) exceed the hyperglycemic threshold 13.9 mM at any time.
7) *TBR, Level 2:* No individuals (0% of the whole population) exceed the hypoglycemic threshold 3 mM at any time.

TABLE V
SYMBOLIC CONTROL EVALUATION VIA CGM INDICES AND COMPARISON WITH THE DIGITAL PID WITH IF IN [12] AND [14]

CGM index	Symbolic Controller	Digital PID+IF (from [14], [12])
Mean glycemia	6.62 mM	7.70 mM
Glucose management indicator (GMI)	6.16%	6.62%
Mean glycemic variability (CV)	18.19%	25.75%
Time in range (TIR)	99.57%	81.20%
Time above range (TAR), level 1	0.38%	15.10%
Time below range (TBR), level 1	0.05%	0%
Time above range (TAR), level 2	0%	3.70%
Time below range (TBR), level 2	0%	0%

The comparison between symbolic and PID-IF results reported in Table V shows, on the one hand, that the digital PID approach in [12] and [14] is more conservative and cautious in the exogenous insulin administration (no time is spent even in the mild hypoglycemia zone, TBR level 1, for any patients in the virtual population); on the other hand, the symbolic approach exerts a tighter glucose control, since, for example, the mean glycemia is lower and there are no violations of the high hyperglycemic threshold 13.9 mM (TAR level 2), despite several violations exhibited by the virtual population controlled by the digital PID.

In conclusion, the previous analysis highlights that the symbolic controller is able to jointly compensate for the hyperglycemic behavior and avoid dangerous conditions, providing significant performance improvements with respect to standard techniques (such as PID controllers) with respect to the efficacy metrics. Moreover, the symbolic controller behaves robustly with respect to (limited) model and parameter variations.

V. DISCUSSION

In this work, we proposed a novel model-based glucose control technique in the context of formal methods for the

Authorized licensed use limited to: Pasquale Palumbo. Downloaded on December 30,2021 at 11:34:38 UTC from IEEE Xplore. Restrictions apply.

This article has been accepted for inclusion in a future issue of this journal. Content is final as presented, with the exception of pagination.

AP. The approach is based on the use of symbolic models, which are finite approximations of complex dynamical systems and allow considering from the beginning the nonlinearities and delays appearing in the dynamics, uncertainties, and input bounds, and nonidealities coming from the interaction between physical plant and digital environment. The methodology is extensively validated over a VP model broadly accepted as a substitute to animal trials in the preclinical testing of closed-loop glucose control strategies [47], showing the effectiveness and the robustness of the approach, also in comparison to existing techniques. In more detail, the following conditions hold.

1) The model considered in this article considers subcutaneous (and not intravenous) insulin administration by properly accounting for the delayed/filtering effect of the subcutaneous compartment on the insulin input. Because of its reduced invasivity with respect to intravenous delivery, subcutaneous administration is currently the most common route of insulin delivery in the context of the AP [8], [11].
2) In order to compensate (partially) for the delay in the input action, this article considers the so-called "meal announcement," in which the controller knows (with uncertainty) the size of the ingested meals [30]. The delayed effect of meals on the glycemia dynamics is also considered in the system by means of a proper compartment.
3) Time-varying (synchronization) specifications are considered in the control design and not just verified afterward.
4) Sampling and quantization parameters (not required to be small enough) can be codesigned starting from the requirements coming from the digital environment.
5) In the performed preclinical validation, the time-varying glycemic safe bounds are never violated and the overall efficacy performance results, assessed by means of recent standardized CGM indices, are satisfactory despite the bounds on the control input, the sampled and quantized nature of the glycemic measurements, and the variability of the simulation conditions.

Further investigation on this topic will consider mixed meals (CHO and fats) as well as an extended validation spanning multiple days.

Appendix I
Notation, Definitions, and Existing Results

A. Notation and Basic Definitions

The symbols $\mathbb{N}$, $\mathbb{N}_0$, $\mathbb{Z}$, $\mathbb{R}$, $\mathbb{R}^+$, and $\mathbb{R}_0^+$ denote the set of natural, nonnegative integer, integer, real, positive real, and nonnegative real numbers, respectively. Given $a, b \in \mathbb{Z}$, we denote $[a; b] = [a, b] \cap \mathbb{Z}$. Given a set X, the symbol 2^X denotes the power set of X. Given a pair of sets X and Y and a relation $\mathcal{R} \subseteq X \times Y$, the symbol $\mathcal{R}^{-1}$ denotes the inverse relation of $\mathcal{R}$, i.e., $\mathcal{R}^{-1} = \{(y, x) \in Y \times X : (x, y) \in \mathcal{R}\}$. Given a function $f : X \to Y$, the symbol $f^{-1} : Y \to 2^X$ denotes the inverse map of f, i.e., $f^{-1}(y) = \{x \in X : y = f(x)\}$ for all y in the codomain of f. Given f and $X' \subseteq X$, the symbol $f(X')$ denotes the image of X' through f, i.e., $f(X') = \{y \in Y | \exists x \in X' \text{ s.t. } y = f(x)\}$. Similarly, given $Y' \subseteq Y$, the symbol $f^{-1}(Y')$ denotes the inverse image of Y' through f, i.e., $f^{-1}(Y') = \{x \in X | f(x) \in Y'\}$. A continuous function $\gamma : \mathbb{R}_0^+ \to \mathbb{R}_0^+$ is said to belong to class $\mathcal{K}$ if it is strictly increasing and $\gamma(0) = 0$; function γ is said to belong to class $\mathcal{K}_\infty$ if $\gamma \in \mathcal{K}$ and $\gamma(r) \to \infty$ as $r \to \infty$. Symbol I_r denotes the identity matrix in $\mathbb{R}^r$. Given a vector $x \in \mathbb{R}^n$, we denote by $x(i)$ the ith element of x and by $\|x\|$ the infinity norm of x. Given $a \in \mathbb{R}$ and $X \subseteq \mathbb{R}^n$, the symbol aX denotes the set $\{y \in \mathbb{R}^n | \exists x \in X \text{ s.t. } y = ax\}$. Given $\mu \in \mathbb{R}^+$ and $x \in \mathbb{R}^n$, we denote $\mathcal{B}^n_{[-\mu,\mu[}(x) = \{y \in \mathbb{R}^n | y(i) \in [-\mu + x(i), \mu + x(i)[, i \in [1; n]\}$. Note that for any $\mu \in \mathbb{R}^+$, the collection of $\mathcal{B}^n_{[-\mu,\mu[}(x)$ with x ranging in $2\mu\mathbb{Z}^n$ is a partition of $\mathbb{R}^n$. Given a positive $n \in \mathbb{N}_0$ and quantization parameter $\mu \in \mathbb{R}^+$, the quantizer in $\mathbb{R}^n$ with accuracy μ is a function $[\cdot]_\mu : \mathbb{R}^n \to 2\mu\mathbb{Z}^n$ associating to any $x \in \mathbb{R}^n$ the unique vector $[x]_\mu \in 2\mu\mathbb{Z}^n$ such that $x \in \mathcal{B}^n_{[-\mu,\mu[}([x]_\mu)$. As a consequence, $\|x - [x]_\mu\| \leq \mu$. Definition of $[\cdot]_\mu$ naturally extends to sets $A \subseteq \mathbb{R}^n$ when $[A]_\mu$ is interpreted as the image of A through function $[\cdot]_\mu$. Consider a set A given as a finite union of hyperrectangles, i.e., $A = \bigcup_{j\in[1;J]} A_j$, for some $J \in \mathbb{N}$, where $A_j = \bigtimes_{k\in[1;n]}[\underline{a}_{j,k}, \overline{a}_{j,k}[\subseteq \mathbb{R}^n$ with $\underline{a}_{j,k} < \overline{a}_{j,k}$, $\underline{a}_{j,k}, \overline{a}_{j,k} \in \hat{\mu}_A\mathbb{Z}$ for some $\hat{\mu}_A \in \mathbb{R}^+$. By construction, for any integer $n_A \in \mathbb{N}$, by setting $\mu = \hat{\mu}_A/n_A$, we get that for any $a \in A$, $\|a - [a]_\mu\| \leq \mu$ and $[a]_\mu \in A$, implying that $[A]_\mu \subseteq A$. Given a measurable and essentially bounded function $f : \mathbb{R}_0^+ \to \mathbb{R}^n$, the (essential) supremum norm of f is denoted by $\|f\|_\infty$; we recall that $\|f\|_\infty := \text{(ess)sup}\{\|f(t)\|, t \geq 0\}$. For a given time $\tau \in \mathbb{R}^+$, define f_τ so that $f_\tau(t) = f(t)$, for any $t \in [0, \tau[$, and $f(t) = 0$ elsewhere; f is said to be locally essentially bounded if for any $\tau \in \mathbb{R}^+$ and f_τ is essentially bounded. Given $k, n \in \mathbb{N}$ with $n \geq 1$ and $I = [a, b] \subseteq \mathbb{R}$, $a, b \in \mathbb{R}$, $a < b$ let $C^k(I; \mathbb{R}^n)$ be the space of functions $f : I \to \mathbb{R}^n$ that are continuously differentiable k times. Given $k \geq 1$, let $PC^k(I; \mathbb{R}^n)$ be the space of $C^{k-1}(I; \mathbb{R}^n)$ functions $f : I \to \mathbb{R}^n$ whose kth derivative exists except in a finite number of reals, and it is bounded, i.e., there exist $\gamma_0, \gamma_1, \ldots, \gamma_s \in \mathbb{R}^+$ with $a = \gamma_0 < \gamma_1 < \cdots < \gamma_s = b$ so that $D^k f$ is defined on each open interval (γ_i, γ_{i+1}), $i = 0, 1, \ldots, s-1$ and $\max_{i=0,1,\ldots,s-1} \sup_{t\in(\gamma_i,\gamma_{i+1})} \|D^k f(t)\| < \infty$. For any continuous function $x(s)$, defined on $-\Delta \leq s < a$, $a > 0$, and any fixed t, $0 \leq t < a$, the standard symbol x_t will denote the element of $C^0([-\Delta, 0]; \mathbb{R}^n)$ defined by $x_t(\theta) = x(t + \theta)$, $-\Delta \leq \theta \leq 0$. Finally, ODE stands for ordinary differential equation(s), DDE is short for delay differential equation(s), 0-GAS stands for globally asymptotically stable or global asymptotic stability of the origin, and ISS means the input-to-state stability.

B. Time-Delay Systems

We consider uncertain nonlinear time-delay systems with quantized output measurements in the form

$$\begin{cases} \dot{x}(t) = f(x_t, u(t-r), d(t)), & t \in \mathbb{R}^+, \text{ a.e.} \\ x(t) \in \mathcal{X}_0, & t \in [-\Delta, 0] \\ y(t) = [z(t)]_\lambda, \text{ with } z(t) = [\, I_p \quad 0 \,]x(t), & t \in \mathbb{R}_0^+ \end{cases} \tag{15}$$

Authorized licensed use limited to: Pasquale Palumbo. Downloaded on December 30,2021 at 11:34:38 UTC from IEEE Xplore. Restrictions apply.

This article has been accepted for inclusion in a future issue of this journal. Content is final as presented, with the exception of pagination.

where $\Delta \in \mathbb{R}_0^+$ is the maximum involved state delay, $r \in \mathbb{R}_0^+$ is the constant input delay, $x(t) \in X \subseteq \mathbb{R}^n$, $x_t \in \mathcal{X} \subseteq C^0([-\Delta, 0]; X)$ is the state at time $t \in \mathbb{R}_0^+$, $u(t) \in U \subseteq \mathbb{R}^m$ is the control input at time $t \in [-r, +\infty[$, $d(t) \in D \subseteq \mathbb{R}^q$ is the disturbance input at time $t \in \mathbb{R}_0^+$, and $y(t) \in \mathbb{R}^p$ is the output at time $t \in \mathbb{R}_0^+$, obtained as the quantization with accuracy $\lambda \in \mathbb{R}^+$ of $[\, I_p \;\, 0 \,]x(t)$, with $x(t)$ the last value of state x_t, f is a functional from $\mathcal{X} \times U \times D$ to $\mathbb{R}^n$, and $\mathcal{X}_0 \subseteq \mathcal{X}$ is the set of initial states.

Control inputs are assumed to be piecewise-constant and take value in U that is assumed to be a finite set. Disturbance inputs are also assumed to be piecewise-constant but taking value in the compact set D. Furthermore, we consider the disturbance to be affected by an unknown bounded multiplicative (percentage) uncertainty, so D takes the particular form

$$D = \{(1+\alpha)\bar{d},\ \alpha \in [-\bar{\alpha}, \bar{\alpha}],\ \bar{d} \in \bar{D}\} \tag{16}$$

where $\bar{\alpha} \in [0, 1[$ is the maximum relative uncertainty and $\bar{D}$ is the known disturbance set. Assume $\bar{D}$ to be given as a finite union of hyperrectangles $\bar{D} = \bigcup_{j \in [1;J]} \bar{D}_j$, for some $J \in \mathbb{N}$, each in the form $\bar{D}_j = \bigtimes_{k \in [1;n]} [\underline{d}_{j,k}, \overline{d}_{j,k}[$, with $\underline{d}_{j,k} < \overline{d}_{j,k}$, $\underline{d}_{j,k}, \overline{d}_{j,k} \in \hat{\mu}_{\bar{D}}\mathbb{Z}$ for some $\hat{\mu}_{\bar{D}} \in \mathbb{R}^+$.

From (15), we are assuming that the output variables of the system are the quantization of a selection of the state variables. The general case of nonlinear output functions can be considered at the expense of a heavier notation, as done in [38]. We suppose that f is Lipschitz on bounded sets, i.e., for every bounded set $K \subset \mathcal{X} \times U \times D$, there exists a constant $\kappa \in \mathbb{R}^+$ such that $\|f(x_1, u_1, d_1) - f(x_2, u_2, d_2)\| \leq \kappa(\|x_1 - x_2\|_\infty + \|u_1 - u_2\| + \|d_1 - d_2\|)$, for all $(x_1, u_1, d_1), (x_2, u_2, d_2) \in K$. We assume that there exists a constant function (state) $\phi_e \in \mathcal{X}$ such that $f(\phi_e, 0, 0) = 0$. Multiple discrete noncommensurate as well as distributed delays can appear in (15). Assumptions on f ensure existence and uniqueness of the solution of the differential equation in (15). In the following, $x(t, \xi_0, u, d)$ and $x_t(\xi_0, u, d)$ will denote the solution in X and $\mathcal{X}$, respectively, of the time-delay system with initial condition $\xi_0 \in \mathcal{X}_0$, input $u \in \mathcal{U}$, and disturbance $d \in \mathcal{D}$ at time t. With an abuse of notation, we will also use the expressions $x(t, \xi_0, u, d)$ and $x_t(\xi_0, u, d)$, with $u \in U$ and $d \in D$, to denote the solutions with constant input and disturbance functions $u(-r+\theta) = u$, $d(\theta) = d$, $\forall \theta \in [0, t]$.

C. Spline-Based Approximations of Functional Spaces

In this section, we briefly recall from [60] some results for approximating functional spaces, which are based on spline analysis (see, e.g., [69]). We start by defining countable/symbolic approximations.

Definition 3 [60]: Consider a functional space $\mathcal{Z} \subseteq C^0(I; Z)$ with $Z \subseteq \mathbb{R}^n$, $I = [a, b]$, $a, b \in \mathbb{R}$, $a < b$. A map $\mathcal{A} : \mathbb{R}^+ \to 2^{C^0(I;Z)}$ is a countable approximation of $\mathcal{Z}$ if for any desired accuracy $\lambda \in \mathbb{R}^+$, the following conditions hold.

1) $\mathcal{A}(\lambda)$ is a countable set.
2) For any $z \in \mathcal{Z}$ there exists $z' \in \mathcal{A}(\lambda)$ such that
$$\|z - z'\|_\infty \leq \lambda. \tag{17}$$
3) For any $z' \in \mathcal{A}(\lambda)$ there exists $z \in \mathcal{Z}$ such that (17) holds.

When condition 1) is replaced by $\mathcal{A}(\lambda)$ is a finite set, the map $\mathcal{A}$ is said to be a symbolic approximation of $\mathcal{Z}$.

Let us consider the space $\mathcal{Z} \subseteq C^0(I; Z)$ with $Z \subseteq \mathbb{R}^n$, $I = [a, b]$, $a, b \in \mathbb{R}$ and $a < b$. Given $N \in \mathbb{N}$, consider the following functions (see [69]):

$$s_0(t) = \begin{cases} 1 - (t-a)/h, & t \in [a, a+h] \\ 0, & \text{otherwise} \end{cases}$$

$$s_i(t) = \begin{cases} 1 - i + (t-a)/h, & t \in [a+(i-1)h, a+ih] \\ 1 + i - (t-a)/h, & t \in [a+ih, a+(i+1)h] \\ 0, & \text{otherwise} \end{cases}$$
$$i = 1, 2, \ldots, N$$

$$s_{N+1}(t) = \begin{cases} 1 + (t-b)/h, & t \in [b-h, b] \\ 0, & \text{otherwise} \end{cases}$$

where $h = (b-a)/(N+1)$. Functions s_i called splines are used to approximate $\mathcal{Z}$. The approximation scheme that we use is based on two steps.

1) We first approximate function $z \in \mathcal{Z}$ by the piecewise linear function z_1, obtained as the linear combination of the $N+2$ splines s_i, centered at time $t = a + ih$ with amplitude $z(a+ih)$.
2) We then approximate function z_1 by the piecewise linear function z_2 obtained as the linear combination of the $N+2$ splines s_i, centered at time $t = a + ih$ with amplitude $\tilde{z}_i$ in the lattice $[Z]_\theta$, which minimizes the distance from $z(a+ih)$, i.e., $\tilde{z}_i = \arg\min_{z \in [Z]_\theta} \|z - z(a+ih)\|$.

The first step above allows approximating the infinite dimensional space $\mathcal{Z}$ by the finite dimensional space Z^{N+2}, while the second step allows approximating the finite dimensional space Z^{N+2} by the countable space $([Z]_\theta)^{N+2}$, which becomes a finite set when the set Z is bounded.

Given any $N \in \mathbb{N}$ and $\theta, M \in \mathbb{R}^+$, let[3]

$$\Lambda(N, \theta, M) := h^2 M/8 + (N+2)\theta \tag{18}$$

with $h = (b-a)/(N+1)$. Function Λ will be shown hereafter to be an upper bound for the error associated with the proposed approximation scheme.

It is readily seen that, for any $\lambda \in \mathbb{R}^+$ and any $M \in \mathbb{R}^+$, there always exist $N \in \mathbb{N}$ and $\theta \in \mathbb{R}^+$ such that

$$\Lambda(N, \theta, M) \leq \lambda.$$

Let $N_{\lambda,M}$ and $\theta_{\lambda,M}$ be such that $\Lambda(N_{\lambda,M}, \theta_{\lambda,M}, M) \leq \lambda$. For any $\lambda \in \mathbb{R}^+$ and $M \in \mathbb{R}^+$, define the operator $\psi_{\lambda,M} : \mathcal{Z} \to C^0([a, b]; Z)$ that associates to any function $z \in \mathcal{Z}$ the following function:

$$\psi_{\lambda,M}(z)(t) := \sum_{i=0}^{N_{\lambda,M}+1} \tilde{z}_i s_i(t), \quad t \in [a, b] \tag{19}$$

where $\tilde{z}_i \in [Z]_{\theta_{\lambda,M}}$ and $\|\tilde{z}_i - z(a+ih)\| \leq \theta_{\lambda,M}$, for any $i = 0, 1, \ldots, N_{\lambda,M}+1$. Note that operator $\psi_{\lambda,M}$ is not uniquely defined. For any given $M \in \mathbb{R}^+$ and any given accuracy $\lambda \in \mathbb{R}^+$, define

$$\mathcal{A}_{\mathcal{Z},M}(\lambda) := \psi_{\lambda,M}(\mathcal{Z}). \tag{20}$$

[3]The real M is a uniform bound on the norm of the second derivative of functions in $\mathcal{Z}$ and its role will become clear hereafter.

Authorized licensed use limited to: Pasquale Palumbo. Downloaded on December 30,2021 at 11:34:38 UTC from IEEE Xplore. Restrictions apply.

This article has been accepted for inclusion in a future issue of this journal. Content is final as presented, with the exception of pagination.

Lemma 2 [60]: Suppose that $\mathcal{Z} \subseteq PC^2(I; Z)$ and there exists $M \in \mathbb{R}^+$ such that $\|D^2 z\|_\infty \leq M$ for any $z \in \mathcal{Z}$. Then, $\mathcal{A}_{\mathcal{Z},M}$ as defined in (20) is a countable approximation of $\mathcal{Z}$. Moreover, when Z is bounded, $\mathcal{A}_{\mathcal{Z},M}$ is a symbolic approximation of $\mathcal{Z}$.

D. Systems and Approximate Relations

In this article, we consider the notion of system as a unifying paradigm to describe time-delay systems as well as logic systems modeling controllers and specifications.

Definition 4 [31]: A system is a tuple $S = (X, X_0, L, \longrightarrow, Y, H)$ consisting of a set of states X, a set of initial states $X_0 \subseteq X$, a set of inputs L, a transition relation $\longrightarrow \subseteq X \times L \times X$, a set of outputs Y, and an output function $H : X \to Y$.

In the sequel, a transition $(x, l, x') \in \longrightarrow$ of S is denoted by $x \xrightarrow{l} x'$. For later purposes, given $x \in X$, define $L(x)$ as the collection of $l \in L$ for which there exists a transition $x \xrightarrow{l} x'$ for some $x' \in X$. The evolution of systems is captured by the notion of state run. Given a sequence $x_0 \xrightarrow{l_0} x_1 \xrightarrow{l_1}, \ldots, \xrightarrow{l_{l-1}} x_l$ of transitions of S, with $x_0 \in X_0$, the sequence $r_X :, x_0, x_1, \ldots, x_l$ is called a state run of S. System S is said to be countable if X and L are countable sets, symbolic if X and L are finite sets, and metric if X is equipped with a metric $\mathbf{d} : X \times X \to \mathbb{R}_0^+$.

In order to provide symbolic approximations of the time-delay system Σ, we need to recall the following notions.

Definition 5 [39], [70]: Consider a pair of metric systems

$$S_i = (X_i, X_{0,i}, L_i, \underset{i}{\longrightarrow}, Y_i, H_i), \quad i = 1, 2 \tag{21}$$

with $X_1, X_2 \subseteq X$ for some set X equipped with metric $\mathbf{d}$, and let $\eta \in \mathbb{R}^+$ be a given accuracy. Consider a relation $\mathcal{R} \subseteq X_1 \times X_2$, satisfying the following conditions.

1) $\forall x_1 \in X_{0,1} \exists x_2 \in X_{0,2}$ such that $(x_1, x_2) \in \mathcal{R}$.
2) $\forall (x_1, x_2) \in \mathcal{R}$, $\mathbf{d}(x_1, x_2) \leq \eta$. Relation $\mathcal{R}$ is a strong η-approximate (strong ηA) simulation relation from S_1 to S_2 if it enjoys conditions 1)–3).
3) $\forall (x_1, x_2) \in \mathcal{R}$ if $x_1 \xrightarrow[1]{l_1} x_1'$, then $\exists x_2 \xrightarrow[2]{l_2} x_2'$ with $l_2 = l_1$ such that $(x_1', x_2') \in \mathcal{R}$.

System S_1 is strongly η-simulated by S_2, denoted $S_1 \preceq_\eta^s S_2$, if there exists a strong η-approximate simulation relation from S_1 to S_2.

Relation $\mathcal{R}$ is a strong alternating η-approximate (strong $A\eta A$) simulation relation from S_1 to S_2 if it enjoys conditions 1), 2) and the following one.

3′) $\forall (x_1, x_2) \in \mathcal{R}$ $\forall l_1 \in L_1(x_1)$, $l_2 = l_1 \in L_2(x_2)$, and $\forall x_2 \xrightarrow[2]{l_2} x_2'$ $\exists x_1 \xrightarrow[1]{l_1} x_1'$ such that $(x_1', x_2') \in \mathcal{R}$.

System S_1 is strongly alternatingly η-simulated by S_2, denoted $S_1 \preceq_\eta^{s,\text{alt}} S_2$, if there exists a strong $A\eta A$ simulation relation from S_1 to S_2.

Appendix II
Novel Technical Results and Proofs

A. Checking δ-FC via Lyapunov–Krasovskii Inequalities

We now show that the δ-FC property (Definition 1) can be checked via Lyapunov–Krasovskii functional-type inequalities. We start with a general definition.

Definition 6: A Lipschitz on bounded sets functional $V : C^0([-\Delta, 0]; \mathbb{R}^n) \times C^0([-\Delta, 0]; \mathbb{R}^n) \to \mathbb{R}_0^+$ is said to be a δ-FC Lyapunov–Krasovskii functional for Σ in (15) if there exist functions α_1 and α_2 of class $\mathcal{K}_\infty$, σ_u, and σ_d of class $\mathcal{K}$ and $p \in \mathbb{R}$ such that, for any $\phi, \psi \in \mathcal{X}$, any $u \in U$, and any $d, \tilde{d} \in D$, the following inequalities hold.

$$\begin{aligned}
&1)\ \alpha_1(\|\phi(0) - \psi(0)\|) \leq V(\phi, \psi) \leq \alpha_2(\|\phi - \psi\|_\infty)\\
&2)\ D^+V\big((\phi, u, d), (\psi, u, \tilde{d})\big) \leq pV(\phi, \psi) + \sigma_d(\|d - \tilde{d}\|)\\
&3)\ D^+V\big((\phi, u, d), (\phi_e, 0, 0)\big) \leq pV(\phi, \phi_e) + \sigma_u(\|u\|)\\
&\qquad\qquad + \sigma_d(\|d\|)
\end{aligned} \tag{22}$$

where

$$\begin{aligned}
&D^+V\big((\phi, u, d), (\psi, u, \tilde{d})\big)\\
&\qquad = \limsup_{h \to 0^+} \frac{V(\phi_{h,u,d}, \psi_{h,u,\tilde{d}})}{h}\\
&D^+V\big((\phi, u, d), (\phi_e, 0, 0)\big)\\
&\qquad = \limsup_{h \to 0^+} \frac{V(\phi_{h,u,d}, \phi_e)}{h}\\
&\phi_{h,u,d}(s) = \begin{cases} \phi(s+h), & s \in [-\Delta, -h)\\ \phi(0) + (s+h) f(\phi, u, d), & s \in [-h, 0] \end{cases}\\
&\psi_{h,u,\tilde{d}}(s) = \begin{cases} \psi(s+h), & s \in [-\Delta, -h)\\ \psi(0) + (s+h) f(\psi, u, \tilde{d}), & s \in [-h, 0]. \end{cases}
\end{aligned} \tag{23}$$

Theorem 4: If there exists a δ-FC Lyapunov–Krasovskii functional for Σ in (15), then Σ is δ-FC, with, for $s, t \in \mathbb{R}_0^+$

$$\beta(s, t) = \alpha_1^{-1}(2e^{p(t+\Delta(h(p)-1))}\alpha_2(s)) \tag{24}$$

$$\gamma(s, t) = \begin{cases} \alpha_1^{-1}\left(2\dfrac{e^{p(t+\Delta(h(p)-1))} + 1}{|p|}\sigma_d(s)\right), & \text{if } |p| \neq 0\\ \alpha_1^{-1}(2t\sigma_d(s)), & \text{if } p = 0 \end{cases} \tag{25}$$

where $h : \mathbb{R} \to \{0, 1\}$ denotes the Heaviside function.[4]

Proof: First, let us show that, for any $\phi \in \mathcal{X}$, any $u \in \mathcal{U}$, and any $d \in \mathcal{D}$, the corresponding solution $x_t(\phi, u, d)$ exists for $t \in \mathbb{R}_0^+$. Let this solution $x_t(\phi, u, d)$ be defined on a maximal time interval $[0, b)$, $0 < b \leq +\infty$. Let, for $t \in [0, b)$, $w(t) = V(x_t(\phi, u, d), \phi_e)$. Then, considering that $f(\phi_e, 0, 0) = 0$ and condition 3), the following inequality holds, for any $t \in [0, b)$ (see [71], [72]):

$$D^+w(t) \leq pw(t) + \sigma_u(\|u(t)\|) + \sigma_d(\|d(t)\|). \tag{26}$$

From [57, Lemma 3.4], it follows that for $t \in [0, b)$

$$w(t) \leq e^{pt}w(0) + \int_0^t e^{p(t-s)}(\sigma_u(\|u(s)\|) + \sigma_d(\|d(s)\|)ds. \tag{27}$$

From condition 1), it follows that

$$\|x(t, \phi, u, d) - \phi_e(0)\| \leq \alpha_1^{-1}(w(t)), \quad t \in [0, b). \tag{28}$$

[4]We recall that $h(\cdot)$ is defined by $h(p) = 1$, if $p \geq 0$, and $h(p) = 0$, otherwise.

Authorized licensed use limited to: Pasquale Palumbo. Downloaded on December 30,2021 at 11:34:38 UTC from IEEE Xplore. Restrictions apply.

This article has been accepted for inclusion in a future issue of this journal. Content is final as presented, with the exception of pagination.

From (27) and (28) and from the boundedness-implies-continuation property of the system described by (15), it follows that $b = +\infty$ (i.e., Σ is forward complete).

Now, let $\phi, \psi \in \mathcal{X}$ be two initial states and $u \in \mathcal{U}$, let $d, \tilde{d} \in \mathcal{D}$ be two disturbance functions, and let $x_t(\phi, u, d)$ and $x_t(\psi, u, \tilde{d})$ be the corresponding solutions in $\mathbb{R}_0^+$. Let $w(t) = V(x_t(\phi, u, d), x_t(\psi, u, \tilde{d}))$, $t \in \mathbb{R}_0^+$. Then, for any $t \in \mathbb{R}_0^+$, the inequality $D^+ w(t) \leq p w(t) + \sigma_d(\|d(t) - \tilde{d}(t)\|)$ is implied (see [71], [72]). Lemma 3.4 in [57] implies that

$$w(t) \leq e^{pt} w(0) + \int_0^t e^{p(t-s)} \sigma_d(\|d(s) - \tilde{d}(s)\|) ds$$

and from conditions 1), one gets

$$\|x(t, \phi, u, d) - x(t, \psi, u, \tilde{d})\| \leq \beta_1(\|\phi - \psi\|_\infty, t) + \gamma_1(\|d - \tilde{d}\|_\infty, t) \quad (29)$$

where, for $s, t \in \mathbb{R}_0^+$, $\beta_1(s, t) = \alpha_1^{-1}(2e^{pt}\alpha_2(s))$, $\gamma_1(s, t) = \alpha_1^{-1}(2((e^{pt} + 1)/|p|)\sigma_d(s))$ if $|p| \neq 0$ and $\gamma_1(s, t) = \alpha_1^{-1}(2t\sigma_d(s))$ if $p = 0$. From (29), it can be shown that $\|x_t(\phi, u, d) - x_t(\psi, u, \tilde{d})\|_\infty \leq \beta(\|\phi - \psi\|_\infty, t) + \gamma(\|d - \tilde{d}\|_\infty, t)$, $t \in \mathbb{R}_0^+$, where functions β and γ are as in (24) and (25).

B. Proof of Theorem 1

The δ-FC property of the system (1)–(3) can be readily shown by applying Theorem 4 to the TDS (4) restated in the form (7). For any $\phi, \psi \in \mathcal{X}$, we consider a δ-FC Lyapunov–Krasovskii functional

$$V(\phi, \psi) = \sum_{i=1}^{6} \gamma_i [\phi_i(0) - \psi_i(0)]^2 + \bar{\gamma} \int_{-\Delta}^{0} [\phi_1(\tau) - \psi_1(\tau)]^2 \times e^{\mu\tau} d\tau \quad (30)$$

as in Definition 6, with γ_i, $\bar{\gamma}$, and μ to be chosen (positive), which readily satisfies condition 1) of Definition 6.

Then, for any $u \in U$, for any $d, \tilde{d} \in D$, we get

$$\begin{aligned}
&D^+ V((\phi, u, d)(\psi, \bar{u}, \bar{d}) \\
&= -2\gamma_1 K_{xgi} \tilde{x}_{2,\max} (\phi_1(0) - \psi_1(0))(\phi_1(0)\phi_2(0) \\
&\quad - \phi_1(0)\psi_2(0) + \phi_1(0)\psi_2(0) - \psi_1(0)\psi_2(0)) \\
&\quad + \frac{2\gamma_1 \tilde{x}_{4,\max}}{\tau_m V_G \tilde{x}_{1,\max}} (\phi_1(0) - \psi_1(0))(\phi_4(0) - \psi_4(0)) \\
&\quad - 2K_{xi}\gamma_2(\phi_2(0) - \psi_2(0))^2 - \frac{2\gamma_3}{\tau_m}(\phi_3(0) - \psi_3(0))^2 \\
&\quad + \frac{2\gamma_2 T_{\mathrm{iGmax}}}{V_I \tilde{x}_{2,\max}} (\phi_2(0) - \psi_2(0)) \\
&\quad \times \Big(h\big(\tilde{x}_{1,\max}\phi_1(-\Delta)\big) - h\big(\tilde{x}_{1,\max}\psi_1(-\Delta)\big)\Big) \\
&\quad + \frac{2\gamma_2 \tilde{x}_{6,\max}}{\tau_i V_I \tilde{x}_{2,\max}} (\phi_2(0) - \psi_2(0))(\phi_6(0) - \psi_6(0)) \\
&\quad + \frac{2\gamma_3 K_{\mathrm{Bio}} \tilde{d}_{\max}}{\tilde{x}_{3,\max}} (\phi_3(0) - \psi_3(0))(d - \bar{d}) \\
&\quad - \frac{2\gamma_4}{\tau_m}(\phi_4(0) - \psi_4(0))^2 - \frac{2\gamma_5}{\tau_i}(\phi_5(0) - \psi_5(0))^2 \\
&\quad + \frac{2\gamma_4 \tilde{x}_{3,\max}}{\tau_m \tilde{x}_{4,\max}} (\phi_3(0) - \psi_3(0))(\phi_4(0) - \psi_4(0)) \\
&\quad + \frac{2\gamma_5 \tilde{u}_{\max}}{\tilde{x}_{5,\max}} (\phi_5(0) - \psi_5(0))(u - \bar{u}) \\
&\quad - \frac{2\gamma_6}{\tau_i}(\phi_6(0) - \psi_6(0))^2 \\
&\quad + \frac{2\gamma_6 \tilde{x}_{5,\max}}{\tau_i \tilde{x}_{6,\max}} (\phi_5(0) - \psi_5(0))(\phi_6(0) - \psi_6(0)) \\
&\quad + \bar{\gamma}(\phi_1(0) - \psi_1(0))^2 - \bar{\gamma} e^{-\mu\Delta}(\phi_1(-\Delta) - \psi_1(-\Delta))^2 \\
&\quad + \mu\bar{\gamma} \int_{-\Delta}^{0} (\phi_1(\tau) - \psi_1(\tau))^2 e^{\mu\tau} d\tau.
\end{aligned}$$

We exploit the following facts [40].

1) The system is positive and bounded.
2) $h(\cdot)$ (Hill function) has finite derivative, which we call $h'_{\max}$, implying that $h(r) - h(s) \leq h'_{\max}|r - s|$.
3) $(a \pm b)^2 \geq 0 \Rightarrow a^2 \pm 2\,ab + b^2 \geq 0 \Rightarrow 2|ab| \leq a^2 + b^2$.

To get

$$\begin{aligned}
&D^+ V((\phi, u, d)(\psi, \bar{u}, \bar{d}) \\
&\leq \sum_{i=1}^{6} p_i \gamma_i (\phi_i(0) - \psi_i(0))^2 \\
&\quad + \left(\frac{\gamma_2 T_{\mathrm{iGmax}} \tilde{x}_{1,\max} h'_{\max}}{V_I \tilde{x}_{2,\max}} - \bar{\gamma} e^{-\mu\Delta}\right)(\phi_1(-\Delta) - \psi_1(-\Delta))^2 \\
&\quad + \mu\bar{\gamma} \int_{-\Delta}^{0} (\phi_1(\tau) - \psi_1(\tau))^2 e^{\mu\tau} d\tau \\
&\quad + 2\gamma_5 \tilde{u}_{\max}|u - \bar{u}| + 2\gamma_3 K_{\mathrm{Bio}} \tilde{d}_{\max}|d - \bar{d}|
\end{aligned}$$

where $p_1 = (\bar{\gamma}/\gamma_1) + (\tilde{x}_{4,\max}/(\tau_m V_G \tilde{x}_{1,\max}))$, $p_2 = ((\gamma_1 K_{xgi} \tilde{x}_{2,\max})/\gamma_2) + (\tilde{x}_{6,\max}/(\tau_i V_I \tilde{x}_{2,\max})) + ((T_{\mathrm{iGmax}} \tilde{x}_{1,\max} h'_{\max})/(V_I \tilde{x}_{2,\max})) - 2K_{xi}$, $p_3 = (\gamma_4 \tilde{x}_{3,\max})/(\tau_m \gamma_3 \tilde{x}_{4,\max})) - (2/\tau_m)$, $p_4 = ((\gamma_1 \tilde{x}_{4,\max})/(\tau_m \gamma_4 V_G \tilde{x}_{1,\max})) + ((\tilde{x}_{3,\max})/(\tau_m \tilde{x}_{4,\max})) - (2/\tau_m)$, $p_5 = ((\gamma_6 \tilde{x}_{5,\max})/(\tau_i \gamma_5 \tilde{x}_{6,\max})) - (2/\tau_i)$, and $p_6 = ((\gamma_2 \tilde{x}_{6,\max})/(\tau_i \gamma_6 V_I \tilde{x}_{2,\max})) + ((\tilde{x}_{5,\max})/(\tau_i \tilde{x}_{6,\max})) - (2/\tau_i)$

Now, set the following.

1) $p := \max\{p_1, p_2, p_3, p_4, p_5, p_6, \mu\}$.
2) $\sigma_u(s) := 2\gamma_5 \tilde{u}_{\max} s$, $\sigma_d(s) := 2\gamma_3 K_{\mathrm{Bio}} \tilde{d}_{\max} s$.
3) $\gamma_2 \in (0, ((V_I \tilde{x}_{2,\max} \bar{\gamma} e^{-\mu\Delta})/(T_{\mathrm{iGmax}} \tilde{x}_{1,\max} h'_{\max}))]$ so that

$$\begin{aligned}
&D^+ V((\phi, u, d)(\psi, \bar{u}, \bar{d}) \\
&\leq p\left(\sum_{i=1}^{6} \gamma_i [\phi_i(0) - \psi_i(0)]^2 + \bar{\gamma} \int_{-\Delta}^{0} [\phi_1(\tau) - \psi_1(\tau)]^2 e^{\mu\tau} d\tau\right) \\
&\qquad + \sigma_u(|u - \bar{u}|) + \sigma_d(|d - \bar{d}|) \\
&\leq p V(\phi, \psi) + \sigma_u(|u - \bar{u}|) + \sigma_d(|d - \bar{d}|).
\end{aligned}$$

Thus, $V(\phi, \psi)$ satisfies condition 2) and 3) of Definition 6. This concludes the proof.

C. Proof of Theorem 2

(Proof of Statement 1)):

(Proof of Condition 1) in Definition 5): Consider any $x_\lambda \in X_\lambda$. Since $X_\lambda = \mathcal{A}_{\mathcal{X}}(\lambda)$, by condition 3) in Definition 3, we get that there exists $x \in X$ such that

$$\|x_\lambda - x\|_\infty \leq \lambda \quad (31)$$

from which $(x_\lambda, x) \in \mathcal{R}$.

(Proof of Condition 2) in Definition 5): Trivially true by definition of relation $\mathcal{R}$.

Authorized licensed use limited to: Pasquale Palumbo. Downloaded on December 30,2021 at 11:34:38 UTC from IEEE Xplore. Restrictions apply.

This article has been accepted for inclusion in a future issue of this journal. Content is final as presented, with the exception of pagination.

(Proof of Condition 3′) in Definition 5): Consider any $l = (u, \bar{d}) \in L_{\lambda,\mu}(x_\lambda)$. First, note that $l = (u, \bar{d}) \in L(x)$. Now, consider the transition $x \xrightarrow{(u,\bar{d})} x'$ in $S(\Sigma)$, implying that $x' = x_\tau(x, u, (1+\alpha)\bar{d})$ for some $\alpha \in [-\bar{\alpha}, \bar{\alpha}]$. By definition of X_λ and by condition 2) in Definition 3, there exists $x'_\lambda \in X_\lambda$ such that

$$\|x'_\lambda - x'\|_\infty \leq \lambda. \tag{32}$$

By the δ-FC property of Σ and by (31), we get

$$\|x' - x_\tau(x_\lambda, u, (1+\alpha)\bar{d})\|_\infty \leq \beta(\lambda, \tau). \tag{33}$$

By combining (32) and (33) and by using the triangle inequality, we obtain $\|x_\tau(x_\lambda, u, (1+\alpha)\bar{d}) - x'_\lambda\|_\infty \leq \beta(\lambda, \tau) + \lambda$, from which $x_\lambda \xrightarrow[\lambda,\mu]{(u,\bar{d})} x'_\lambda$ in $S_{\lambda,\mu}(\Sigma)$. Moreover, by (32), $(x', x'_\lambda) \in \mathcal{R}$, from which condition 3′) holds.

(Proof of Statement 2)):

(Proof of Condition 1) in Definition 5): Consider any $x \in X$. Since $X_\lambda = \mathcal{A}_{\mathcal{X}}(\lambda)$, by condition 2) in Definition 3, we get that there exists $x_\lambda \in X_\lambda$ such that condition (31) holds, from which $(x_\lambda, x) \in \mathcal{R}$.

(Proof of Condition 2) in Definition 5): Trivially true by definition of relation $\mathcal{R}$.

(Proof of Condition 3) in Definition 5): Consider any $l = (u, \bar{d}) \in L(x)$ and consider the transition $x \xrightarrow{(u,\bar{d})} x'$ in $S(\Sigma)$, implying that $x' = x_\tau(x, u, (1+\alpha)\bar{d})$ for some $\alpha \in [-\bar{\alpha}, \bar{\alpha}]$. By definition of X_λ and condition 2) in Definition 3, there exists $x'_\lambda \in X_\lambda$ such that

$$\|x'_\lambda - x'\|_\infty \leq \lambda. \tag{34}$$

Define $\tilde{d} = [\bar{d}]_\mu$ such that $\tilde{d} \in \bar{D}$ from (10), implying that $(u, \tilde{d}) \in L_{\lambda,\mu}(x_\lambda)$. By the δ-FC property of Σ and by (31), we get

$$\|x' - x_\tau(x_\lambda, u, (1+\alpha)\tilde{d})\|_\infty \leq \beta(\lambda, \tau) + \gamma((1+\alpha)\mu, \tau). \tag{35}$$

By combining (34) and (35) and by using the triangle inequality, we obtain $\|x_\tau(x_\lambda, u, (1+\alpha)\tilde{d}) - x'_\lambda\|_\infty \leq \beta(\lambda, \tau) + \gamma((1+\alpha)\mu, \tau) + \lambda$ from which $x_\lambda \xrightarrow[\lambda,\mu]{(u,\tilde{d})} x'_\lambda$ in $S_{\lambda,\mu}(\Sigma)$. Moreover, by (34), $(x', x'_\lambda) \in \mathcal{R}$, from which condition 3) holds.

(Proof of Statement 3)): For any $(x_\lambda, x) \in \mathcal{R}$, we get

$$\begin{aligned}\|H(x) - H_\lambda(x_\lambda)\| &= \|\begin{bmatrix} I_p & 0 \end{bmatrix}(x(\tau) - x_\lambda(\tau))\| \\ &\leq \|x(\tau) - x_\lambda(\tau)\| \leq \|x - x_\lambda\|_\infty \leq \lambda\end{aligned}$$

where the last inequality holds by definition of $\mathcal{R}$.

D. Proof of Lemma 1

It suffices to show that $x_{k\tau}$ satisfies the same properties of $\xi_0 \in \mathcal{X}_0$, i.e., conditions (A.5.1) and (A.5.2) hold with ξ_0 replaced by $x_{k\tau}$. First, note that the function $t \to \dot{x}(t)$, $t \in [0, \tau]$, is uniformly continuous in the (compact) set $[0, \tau]$. By (A.5.3), it follows that $x_{\tau+\theta} \in C^1([-\Delta, 0]; \mathbb{R}^n)$, $\theta \in]-\Delta, 0[$, i.e., the derivative $\dot{x}_{\tau+\theta} \in C^0([-\Delta, 0]; \mathbb{R}^n)$. By (A.2), $\|x_t\|_\infty \leq B_X$, $t \in [0, \tau]$. By considering the Lipschitz constant κ (computed on the bounded set $\bar{X} \times U \times D$) of functional $\bar{f}$, the following chain of inequalities holds:

$$\begin{aligned}&\|\dot{x}_{\tau+\theta}\|_\infty \\ &= \sup_{\alpha\in[-\Delta,0]} \|\bar{f}(x_{\tau+\theta+\alpha}, u(\tau+\theta+\alpha-r), d(\tau+\theta+\alpha))\| \\ &\leq \kappa \sup_{\alpha\in[-\Delta,0]} (\|x_{\tau+\theta+\alpha}\|_\infty + \|u(\tau+\theta+\alpha-r)\| \\ &\qquad + \|d(\tau+\theta+\alpha)\|) \\ &\leq \kappa(B_X + B_U + B_D), \quad \theta \in]-\Delta, 0[.\end{aligned} \tag{36}$$

As far as the second derivative is concerned, the following equality holds, for $\theta \in]-\Delta, 0[$

$$\frac{d^2 x_\tau(\theta)}{d\theta^2} = J(x_{\tau+\theta}, u(\tau+\theta-r), d(\tau+\theta)) \begin{pmatrix} \dot{x}_{\tau+\theta} \\ 0 \\ 0 \end{pmatrix}.$$

From the continuity of the Fréchet differential J and from the fact that $\dot{x}_{\tau+\theta} \in C^0([-\Delta, 0]; \mathbb{R}^n)$, it follows that $x_\tau \in PC^2([-\Delta, 0]; \mathbb{R}^n)$. Moreover, by considering the bound B_J on the Fréchet differential J, the bound on the derivative $\dot{x}_{\tau+\theta}$ in (36), and the definition of M in (11), we obtain $\|D^2 x_\tau\|_\infty \leq M$. Thus, $x_{k\tau}$ satisfies conditions (A.5.1) and (A.5.2).

Acknowledgment

The authors would like to thank Andrea De Gaetano, Simona Panunzi, and Mario Di Ferdinando for fruitful discussions on the topic of the present work.

References

[1] P. Zimmet, K. Alberti, and J. Shaw, "Global and societal implications of the diabetes epidemic," *Nature*, vol. 414, no. 6865, p. 782, 2001.

[2] K. Ogurtsova *et al.*, "IDF diabetes atlas: Global estimates for the prevalence of diabetes for 2015 and 2040," *Diabetes Res. Clin. Pract.*, vol. 128, pp. 40–50, Jun. 2017.

[3] National Diabetes Data Group, "Classification and diagnosis of diabetes mellitus and other categories of glucose intolerance," *Diabetes*, vol. 28, no. 12, pp. 1039–1057, Dec. 1979.

[4] R. Hovorka, "Closed-loop insulin delivery: From bench to clinical practice," *Nature Rev. Endocrinol.*, vol. 7, no. 7, p. 385, 2011.

[5] B. Kovatchev, W. V. Tamborlane, W. T. Cefalu, and C. Cobelli, "The artificial pancreas in 2016: A digital treatment ecosystem for diabetes," *Diabetes Care*, vol. 39, no. 7, pp. 1123–1126, 2016.

[6] P. E. Cryer, S. N. Davis, and H. Shamoon, "Hypoglycemia in diabetes," *Diabetes Care*, vol. 26, no. 6, pp. 1902–1912, 2003.

[7] L. H. Messer *et al.*, "Optimizing hybrid closed-loop therapy in adolescents and emerging adults using the MiniMed 670G system," *Diabetes Care*, vol. 41, no. 4, pp. 789–796, Apr. 2018.

[8] C. Cobelli, E. Renard, and B. P. Kovatchev, "Artificial pancreas: Past, present, future," *Diabetes*, vol. 60, no. 1, pp. 2672–2682, 2011.

[9] A. Borri, P. Palumbo, C. Manes, S. Panunzi, and A. De Gaetano, "Sampled-data observer-based glucose control for the artificial pancreas," *Acta Polytech. Hungarica*, vol. 14, no. 1, pp. 79–94, 2017.

[10] A. Chakrabarty, S. Zavitsanou, I. F. Doyle, and E. Dassau, "Event-triggered model predictive control for embedded artificial pancreas systems," *IEEE Trans. Biomed. Eng.*, vol. 65, no. 3, pp. 575–586, Mar. 2017.

[11] M. Messori, G. P. Incremona, C. Cobelli, and L. Magni, "Individualized model predictive control for the artificial pancreas: In silico evaluation of closed-loop glucose control," *IEEE Control Syst. Mag.*, vol. 38, no. 1, pp. 86–104, Feb. 2018.

[12] S. Laxminarayan, J. Reifman, and G. M. Steil, "Use of a food and drug administration-approved type 1 diabetes mellitus simulator to evaluate and optimize a proportional-integral-derivative controller," *J. Diabetes Sci. Technol.*, vol. 6, no. 6, pp. 1401–1412, 2012.

[13] G. M. Steil, "Algorithms for a closed-loop artificial pancreas: The case for proportional-integral-derivative control," *J. Diabetes Sci. Technol.*, vol. 7, no. 6, pp. 1621–1631, 2013.

[14] L. M. Huyett, E. Dassau, H. C. Zisser, and F. J. Doyle, III, "Design and evaluation of a robust PID controller for a fully implantable artificial pancreas," *I& EC Res.*, vol. 54, no. 42, pp. 10311–10321, 2015.

[15] F. Chee and T. Fernando, *Closed-Loop Control Blood Glucose*, vol. 368. Berlin, Germany: Springer, 2007.

Authorized licensed use limited to: Pasquale Palumbo. Downloaded on December 30,2021 at 11:34:38 UTC from IEEE Xplore. Restrictions apply.

This article has been accepted for inclusion in a future issue of this journal. Content is final as presented, with the exception of pagination.

[16] R. N. Bergman, Y. Z. Ider, C. R. Bowden, and C. Cobelli, "Quantitative estimation of insulin sensitivity," *Amer. J. Physiol.-Endocrinol. Metabolism*, vol. 236, no. 6, p. E667, Jun. 1979.

[17] S. Panunzi, P. Palumbo, and A. De Gaetano, "A discrete single delay model for the intra-venous glucose tolerance test," *Theor. Biol. Med. Model.*, vol. 4, no. 1, p. 35, Sep. 2007.

[18] L. Kovàcs, P. Szalay, Z. Almàssy, and L. Barkai, "Applicability results of a nonlinear model-based robust blood glucose control algorithm," *J. Diabetes Sci. Technol.*, vol. 7, no. 3, pp. 708–716, 2013.

[19] K. Turksoy, L. Quinn, E. Littlejohn, and A. Cinar, "Multivariable adaptive identification and control for artificial pancreas systems," *IEEE Trans. Biomed. Eng.*, vol. 61, no. 3, pp. 883–891, Mar. 2013.

[20] G. Cocha, O. Rodriguez, H. Mazzeo, J. Rapallini, C. Amorena, and C. E. D'Attellis, "Intelligent insulin pump design," in *Proc. Congreso Argentino de Ciencias de la Informática y Desarrollos de Investigación (CACIDI)*, Nov. 2018, pp. 1–4.

[21] P. Palumbo, P. Pepe, S. Panunzi, and A. De Gaetano, "Time-delay model-based control of the glucose–insulin system, by means of a state observer," *Eur. J. Control*, vol. 18, no. 6, pp. 591–606, 2012.

[22] A. Borri, P. Pepe, I. D. Loreto, and M. D. Ferdinando, "Finite-dimensional periodic event-triggered control of nonlinear time-delay systems with an application to the artificial pancreas," *IEEE Control Syst. Lett.*, vol. 5, no. 1, pp. 31–36, Jan. 2021.

[23] M. Di Ferdinando, P. Pepe, S. Di Gennaro, A. Borri, and P. Palumbo, "Quantized sampled-data static output feedback control of the glucose–insulin system," *Control Eng. Pract.*, vol. 112, Jul. 2021, Art. no. 104828.

[24] R. Hovorka *et al.*, "Nonlinear model predictive control of glucose concentration in subjects with type 1 diabetes," *Physiol. Meas.*, vol. 25, no. 4, p. 905, 2004.

[25] P. Soru, G. De Nicolao, C. Toffanin, C. Dalla Man, C. Cobelli, and L. Magni, "MPC based artificial pancreas: Strategies for individualization and meal compensation," *Annu. Rev. Control*, vol. 36, no. 1, pp. 118–128, Apr. 2012.

[26] S. Zavitsanou, A. Mantalaris, M. C. Georgiadis, and E. N. Pistikopoulos, "In silico closed-loop control validation studies for optimal insulin delivery in type 1 diabetes," *IEEE Trans. Biomed. Eng.*, vol. 62, no. 10, pp. 2369–2378, Oct. 2015.

[27] R. Gondhalekar, E. Dassau, and F. J. Doyle, III, "Velocity-weighting & velocity-penalty MPC of an artificial pancreas: Improved safety & performance," *Automatica*, vol. 91, pp. 105–117, May 2018.

[28] G. P. Incremona, M. Messori, C. Toffanin, C. Cobelli, and L. Magni, "Model predictive control with integral action for artificial pancreas," *Control Eng. Pract.*, vol. 77, pp. 86–94, Aug. 2018.

[29] P. S. Rivadeneira, J. L. Godoy, J. Sereno, P. Abuin, A. Ferramosca, and A. H. González, "Impulsive mpc schemes for biomedical processes: Application to type 1 diabetes," in *Control Applications for Biomedical Engineering Systems*. Amsterdam, The Netherlands: Elsevier, 2020, pp. 55–87.

[30] A. El Fathi, M. R. Smaoui, V. Gingras, B. Boulet, and A. Haidar, "The artificial pancreas and meal control: An overview of postprandial glucose regulation in type 1 diabetes," *IEEE Control Syst. Mag.*, vol. 38, no. 1, pp. 67–85, Feb. 2018.

[31] P. Tabuada, *Verification and Control of Hybrid Systems: A Symbolic Approach*. Springer, 2009.

[32] C. Belta, B. Yordanov, and E. A. Gol, *Formal Methods for Discrete-Time Dynamical Systems*, vol. 89. Springer-Verlag, 2017.

[33] G. Pola and M. D. Di Benedetto, "Control of cyber-physical-systems with logic specifications: A formal methods approach," *Annu. Rev. Control*, vol. 47, pp. 178–192, 2019.

[34] A. Girard and G. J. Pappas, "Approximation metrics for discrete and continuous systems," *IEEE Trans. Autom. Control*, vol. 52, no. 5, pp. 782–798, May 2007.

[35] G. Pola and P. Tabuada, "Symbolic models for nonlinear control systems: Alternating approximate bisimulations," *SIAM J. Control Optim.*, vol. 48, no. 2, pp. 719–733, 2009.

[36] A. Borri, G. Pola, and M. D. Di Benedetto, "Symbolic models for nonlinear control systems affected by disturbances," *Int. J. Control*, vol. 85, no. 10, pp. 1422–1432, Oct. 2012.

[37] G. Pola, P. Pepe, and M. D. Di Benedetto, "Symbolic models for time-varying time-delay systems via alternating approximate bisimulation," *Int. J. Robust Nonlinear Control*, vol. 25, no. 14, pp. 2328–2347, Sep. 2015.

[38] G. Pola, M. D. Di Benedetto, and A. Borri, "Symbolic control design of nonlinear systems with outputs," *Automatica*, vol. 109, Nov. 2019, Art. no. 108511.

[39] A. Borri, G. Pola, and M. D. D. Benedetto, "Design of symbolic controllers for networked control systems," *IEEE Trans. Autom. Control*, vol. 64, no. 3, pp. 1034–1046, Mar. 2019.

[40] P. Palumbo, S. Panunzi, and A. De Gaetano, "Qualitative behavior of a family of delay-differential models of the glucose-insulin system," *Discrete Continuous Dyn. Syst.-B*, vol. 7, no. 2, pp. 399–424, 2007.

[41] C. D. Man, D. M. Raimondo, R. A. Rizza, and C. Cobelli, "GIM, simulation software of meal glucose-insulin model," *J. Diabetes Sci. Technol.*, vol. 1, no. 3, pp. 323–330, 2007.

[42] M. Di Ferdinando, P. Pepe, P. Palumbo, S. Panunzi, and A. De Gaetano, "Semiglobal sampled-data dynamic output feedback controller for the glucose–insulin system," *IEEE Trans. Control Syst. Technol.*, vol. 28, no. 1, pp. 16–32, Jan. 2020.

[43] G. Pola, A. Borri, and M. D. Di Benedetto, "Integrated design of symbolic controllers for nonlinear systems," *IEEE Trans. Autom. Control*, vol. 57, no. 2, pp. 534–539, Feb. 2012.

[44] G. Pola, A. Borri, P. Pepe, P. Palumbo, and M. D. Di Benedetto, "Symbolic models approximating possibly unstable time-delay systems with application to the artificial pancreas," in *Proc. 18th Eur. Control Conf. (ECC)*, Jun. 2019, pp. 275–280.

[45] G. M. Steil, A. E. Panteleon, and K. Rebrin, "Closed-loop insulin delivery-the path to physiological glucose control," *Adv. Drug Del. Rev.*, vol. 56, no. 2, pp. 125–144, 2004.

[46] C. D. Man, R. A. Rizza, and C. Cobelli, "Meal simulation model of the glucose-insulin system," *IEEE Trans. Biomed. Eng.*, vol. 54, no. 10, pp. 1740–1749, Oct. 2007.

[47] B. P. Kovatchev, M. Breton, C. D. Man, and C. Cobelli, "In silico preclinical trials: A proof of concept in closed-loop control of type 1 diabetes," *J. Diabetes Sci. Technol.*, vol. 3, no. 1, pp. 44–55, 2009.

[48] S. Panunzi, A. Borri, P. Palumbo, L. Kovács, and A. De Gaetano, "Simulation of insulin regimen and glucose profiles in type 1 diabetic patient," in *Proc. IEEE Int. Conf. Syst., Man, Cybern. (SMC)*, Oct. 2014, pp. 2464–2469.

[49] J. G. Pires, A. Borri, A. De Gaetano, C. Manes, and P. Palumbo, "A short-term dynamical model for ghrelin," *IFAC-PapersOnLine*, vol. 50, no. 1, pp. 11011–11016, Jul. 2017.

[50] M. Di Ferdinando, P. Pepe, S. Di Gennaro, and P. Palumbo, "Sampled-data static output feedback control of the glucose-insulin system," in *Proc. IFAC World Congr.*, 2020, pp. 3626–3631.

[51] D. R. L. Worthington, "Minimal model of food absorption in the gut," *Med. Informat.*, vol. 22, no. 1, pp. 35–45, Jan. 1997.

[52] N. Magdelaine *et al.*, "A long-term model of the glucose–insulin dynamics of type 1 diabetes," *IEEE Trans. Biomed. Eng.*, vol. 62, no. 6, pp. 1546–1552, Jun. 2015.

[53] W. R. Puckett and E. N. Lightfoot, "A model for multiple subcutaneous insulin injections developed from individual diabetic patient data," *Amer. J. Physiol.-Endocrinol. Metabolism*, vol. 269, no. 6, pp. E1115–E1124, Dec. 1995.

[54] C. D. Man, M. Camilleri, and C. Cobelli, "A system model of oral glucose absorption: Validation on gold standard data," *IEEE Trans. Biomed. Eng.*, vol. 53, no. 12, pp. 2472–2478, Dec. 2006.

[55] P. Palumbo, G. Pizzichelli, S. Panunzi, P. Pepe, and A. De Gaetano, "Model-based control of plasma glycemia: Tests on populations of virtual patients," *Math. Biosci.*, vol. 257, pp. 2–10, Nov. 2014.

[56] L. Farina and S. Rinaldi, *Positive Linear Systems: Theory and Applications*, vol. 50. Hoboken, NJ, USA: Wiley, 2011.

[57] H. Khalil, *Nonlinear Systems*, 3rd ed. Upper Saddle River, NJ, USA: Prentice-Hall, 1996.

[58] A. Chakrabarty, E. Healey, D. Shi, S. Zavitsanou, F. J. Doyle, and E. Dassau, "Embedded model predictive control for a wearable artificial pancreas," *IEEE Trans. Control Syst. Technol.*, vol. 28, no. 6, pp. 2600–2607, Nov. 2020.

[59] M. Zamani, G. Pola, M. Mazo, Jr., and P. Tabuada, "Symbolic models for nonlinear control systems without stability assumptions," *IEEE Trans. Autom. Control*, vol. 57, no. 7, pp. 1804–1809, Jul. 2012.

[60] G. Pola, P. Pepe, M. D. Di Benedetto, and P. Tabuada, "Symbolic models for nonlinear time-delay systems using approximate bisimulations," *Syst. Control Lett.*, vol. 59, no. 6, pp. 365–373, Jun. 2010.

[61] V. Gingras, R. Rabasa-Lhoret, V. Messier, M. Ladouceur, L. Legault, and A. Haidar, "Efficacy of dual-hormone artificial pancreas to alleviate the carbohydrate-counting burden of type 1 diabetes: A randomized crossover trial," *Diabetes Metabolism*, vol. 42, no. 1, pp. 47–54, Feb. 2016.

Authorized licensed use limited to: Pasquale Palumbo. Downloaded on December 30,2021 at 11:34:38 UTC from IEEE Xplore. Restrictions apply.

This article has been accepted for inclusion in a future issue of this journal. Content is final as presented, with the exception of pagination.

[62] D. B. Keenan, J. J. Mastrototaro, G. Voskanyan, and G. M. Steil, "Delays in minimally invasive continuous glucose monitoring devices: A review of current technology," *J. Diabetes Sci. Technol.*, vol. 3, no. 5, pp. 1207–1214, Sep. 2009.

[63] C. Cassandras and S. Lafortune, *Introduction to Discrete Event Systems*. Boston, MA, USA: Kluwer, 1999.

[64] G. Pola, P. Pepe, and M. D. D. Benedetto, "Decentralized supervisory control of networks of nonlinear control systems," *IEEE Trans. Autom. Control*, vol. 63, no. 9, pp. 2803–2817, Sep. 2018.

[65] R. A. Harvey, E. Dassau, H. Zisser, D. E. Seborg, L. Jovanovič, and F. J. Doyle, III, "Design of the health monitoring system for the artificial pancreas: Low glucose prediction module," *J. Diabetes Sci. Technol.*, vol. 6, no. 6, pp. 1345–1354, 2012.

[66] L. Magni *et al.*, "Evaluating the efficacy of closed-loop glucose regulation via control-variability grid analysis," *J. Diabetes Sci. Technol.*, vol. 2, no. 4, pp. 630–635, 2008.

[67] T. Danne *et al.*, "International consensus on use of continuous glucose monitoring," *Diabetes care*, vol. 40, no. 12, pp. 1631–1640, 2017.

[68] T. Battelino *et al.*, "Clinical targets for continuous glucose monitoring data interpretation: Recommendations from the international consensus on time in range," *Diabetes Care*, vol. 42, no. 8, pp. 1593–1603, 2019.

[69] M. H. Schultz, *Spline Analysis*. Upper Saddle River, NJ, USA: Prentice-Hall, 1973.

[70] G. Pola, A. Borri, and M. D. Di Benedetto, "On symbolic control design of discrete-time nonlinear systems with state quantized measurements," in *Proc. IEEE 55th Conf. Decis. Control (CDC)*, Dec. 2016, pp. 6571–6576.

[71] R. D. Driver, "Existence and stability of solutions of a delay-differential system," *Arch. Rational Mech. Anal.*, vol. 10, no. 1, pp. 401–426, 1962.

[72] P. Pepe, "On Liapunov–Krasovskii functionals under carathéodory conditions," *Automatica*, vol. 43, no. 4, pp. 701–706, 2007.

Alessandro Borri (Senior Member, IEEE) received the B.Sc. and M.Sc. degrees *(summa cum laude)* in computer and control engineering and the Ph.D. degree in information engineering from the University of L'Aquila, L'Aquila, Italy, in 2004, 2007, and 2011, respectively.

He spent research periods at Ford Motor Company, Aachen, Germany, in 2007; the University of California at Berkeley, Berkeley, CA, USA, from 2008 to 2009; the University of California at Santa Barbara, Santa Barbara, CA, USA, from 2009 to 2010; and the Royal Institute of Technology (KTH), Stockholm, Sweden, in 2011. From 2011 to 2012, he was a Post-Doctoral Researcher at the University of L'Aquila, where he currently holds an external affiliation and is an Adjunct Professor of systems biology. In 2012, he joined the Institute for Systems Analysis and Computer Science "A. Ruberti," National Research Council of Italy (CNR-IASI), Rome, Italy, where he is currently a Researcher. He has coauthored over 80 peer-reviewed international publications. His research interests include hybrid systems, control applications, systems biology, and biomathematics.

Dr. Borri is a Senior Member of the IEEE Control Systems Society (CSS), an Academic Editor of *PLOS One*, an Associate Editor of *International Journal of Robust and Nonlinear Control*, and a member of the IEEE-CSS Conference Editorial Board (CEB). He was a co-recipient of the Premium Award 2018 for Best Paper in IET Systems Biology.

Giordano Pola (Senior Member, IEEE) received the Laurea degree in electrical engineering and the Ph.D. degree in electrical engineering and computer science from the University of L'Aquila, L'Aquila, Italy, in July 2000 and June 2004, respectively.

He was Visiting Scholar at the University of Cambridge, Cambridge, U.K., from 2002 to 2003, and an Assistant Researcher and a Research Fellow at the University of Twente, Enschede, The Netherlands, in 2003 and 2004, respectively. From April 2005 to September 2006, he was a Post-Doctoral Researcher at the University of L'Aquila. From October 2006 to December 2007, he was a Post-Doctoral Researcher at the University of California at Los Angeles, Los Angeles, CA, USA. From 2008 to 2018, he was an Assistant Professor at the University of L'Aquila, where he has been an Associate Professor since 2018. He has published around 100 research papers in archival journals, books, and refereed conference proceedings.

Pierdomenico Pepe (Senior Member, IEEE) is currently a Full Professor of automatic control at the University of L'Aquila, L'Aquila, Italy. He has authored or coauthored 70 journal articles, 100 conference papers, and book chapters. In 2000, 2001, and 2004, he previously held one-semester visiting scholar positions at the University of California at Berkeley, Berkeley, CA, USA; Georgia Tech, Atlanta, GA, USA; and Polytechnic University, New York, NY, USA, respectively. He is the coeditor of two multiauthor volumes in the Springer series LNCIS and ADD. His main research interests include stability theory, nonlinear control, observers, and optimal control, with special emphasis on systems with time delays and applications to biomedical, chemical, and electrical engineering.

Dr. Pepe served as an IPC member in several (IEEE, International Federation of Automatic Control (IFAC), and SIAM) international conferences. He was a recipient of the Kybernetika Editor's Award in 2013. In 2006, he was the Chairperson and the Co-Editor of the 6*th* IFAC Workshop on Time-Delay Systems, held in L'Aquila. He has served as an Associate Editor for IEEE TRANSACTIONS ON AUTOMATIC CONTROL from 2011 to 2014 and *Systems and Control Letters* from 2012 to 2016. He is serving as an Associate Editor for *SIAM Journal on Control and Optimization*, *Journal on Control and Decision* (Taylor & Francis), and IEEE CONTROL SYSTEMS LETTERS.

Maria Domenica Di Benedetto (Life Fellow, IEEE) received the master's degree *(summa cum laude)* in electrical engineering and computer science from the University of Roma "La Sapienza," Rome, Italy, in 1976, and the Docteur-Ingénieur and Doctorat d'Etat ès Sciences degrees from the Université de Paris-Sud, Orsay, France, in 1981 and 1987, respectively.

She held visiting positions at the Massachusetts Institute of Technology (MIT), Cambridge, MA, USA, the University of Michigan, Ann Arbor, MI, USA, and the Ecole Nationale Supérieure de Mécanique, Nantes, France. Since 1994, she has been a Professor of automatic control at the University of L'Aquila, L'Aquila, Italy. She has been an Adjunct Professor from 1995 to 2002 and a McKay Professor from 1990 to 1995 at the Department of Electrical Engineering and Computer Sciences, University of California at Berkeley, Berkeley, CA, USA. She was the Principal Investigator and the Director of the Center of Excellence for Research DEWS "Architectures and Design Methodologies for Embedded Controllers, Wireless Interconnect and System-on-Chip," University of L'Aquila, from 2001 to 2019. Her research interests are in the areas of nonlinear and hybrid systems control theory, diagnosability and predictability in cyber-physical systems, and applications to automotive, smart grids, and traffic control.

Dr. Di Benedetto is a fellow of International Federation of Automatic Control (IFAC). Since 2009, she has been the President of the European Embedded Control Institute. From 2013 to 2019, she has been the President of the Italian Society of Researchers in Automatic Control (SIDRA).

Pasquale Palumbo (Member, IEEE) received the Laurea and Ph.D. degrees in electrical engineering from the University of L'Aquila, L'Aquila, Italy, in 1995 and 2000, respectively.

He was a Researcher at the Institute of Systems Analysis and Computer Science "A. Ruberti," Italian National Research Council (IASI-CNR), Rome, Italy, from 2000 to 2019. He was a Visiting Professor at the University of L'Aquila, teaching courses on probability, systems and control theory, and systems biology, from 2000 to 2019. He has been an Associate Professor of systems and control theory at the University of Milano-Bicocca, Milan, Italy, since 2019. He is currently an Honorary Professor with Óbuda University, Budapest, Hungary. He has authored over 120 peer-reviewed publications in nonlinear filtering and control systems, mathematical modeling and control of the glucose–insulin system, and systems and synthetic biology.

Dr. Palumbo is a member of the IEEE Control Systems Society, the IEEE Technical Committees on Systems Biology and on Healthcare and Medical Systems, and the CSS Conference Editorial Board (CEB). He was a recipient of the Kybernetika Editor's Award in 2013 and the IET Systems Biology Premium Award in 2018. He is serving as an Associate Editor for *PLOS One* and *Mathematical Problems in Engineering*.

Authorized licensed use limited to: Pasquale Palumbo. Downloaded on December 30,2021 at 11:34:38 UTC from IEEE Xplore. Restrictions apply.

On Multi-Agent Cognitive Cooperation: a Reinforcement Learning Decentralized Multi-Agent Control Approach

Salvatore D'Avella[1], Gerardo Camacho-Gonzalez[1], Carlo Alberto Avizzano[1], Paolo Tripicchio[1]

Human beings interact with each other to solve complex problems establishing a social interaction to achieve a common objective. Whenever a problem is too difficult to be accomplished by a single person, humans learn how to collaborate or cooperate, building a common frame of reference (CFR), i.e., a common mental representation of the situation. By having a CFR, participants can infer the behaviors of the other participants and can organize their work to perform complementary actions to solve that problem. What allows to construct and update the CFR by exchanging the information is the grounding process (GP). GP and CFR enable cognitive cooperation, which is the collaboration of multiple individuals in the cognitive context of actions, perceptions, memory, and decision-making. Cognitive collaboration operates unconsciously without the need for learning, and it is considered useful for tasks that exceed the ability of a single individual. Such concepts are strictly related to the Theory of Mind (ToM), the term used in psychology to explain the possibility that a living being is able to understand others' intentions, beliefs, desires, and perspectives that are different from their own. On the other hand, Machine Theory of Mind (MToM) describes the type of algorithms that aim to model the behaviors of other virtual agents in a collaborative scenario.

In this work [1], both the ToM and MToM concepts are investigated with a two-fold collaborative cognitive experimental study. A novel multi-agent cognitive cooperation model is proposed: multiple entities that perceive different and complementary information necessary to complete a common goal have to interact with each other to succeed in the shared task. The study first examined the ToM aspect with an experiment that involved two humans. They were immersed in an on-purpose virtual shared environment having a GP constituted by cross-modality feedback based on vision and haptic information. The objective was to escape the maze they were immersed in by maximizing a score function that was dependent on the completion time and the accumulated bonus and malus along the path through the goal. The new proposed cognitive collaboration model expected that the one participant could perceive the walls and the goal while the other one the bonus and the malus but not the other information (Fig. 1). The experimental campaign showed that most of the groups involved in the tests were able to build a CFR learning cognitive collaboration skills even in the particular collaboration scenario. Fig. 2 depicts the best trial registered during the experimental campaign by one of the group.

The second experiment tried to mimic human behavior in a simpler synthetic scenario where the participants were replaced by virtual agents controlled with the tabular Q-learning technique

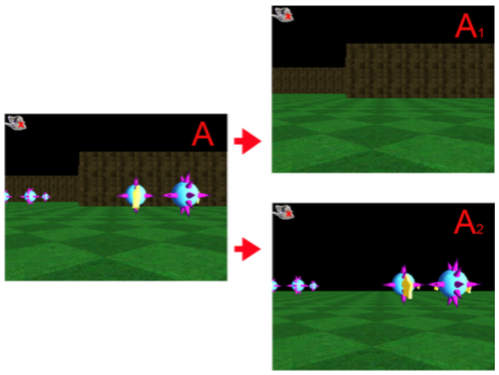

Fig. 1: Virtual maze seen by the two participants

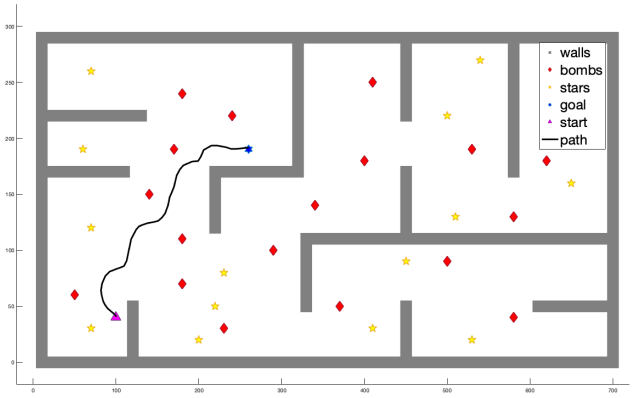

Fig. 2: Trajectory of group 4 in trial 3

having discrete action and state spaces. The proposed setting can be schematized as in Fig. 3. Two virtual agents implemented as tabular Q-learning perceive different and complementary cues of the environment necessary to an avatar to accomplish a certain task. Therefore, seeing different information could happen with a high probability that the agents perform different actions from each other. The combination of the two actions determines the behavior of the avatar in the environment. According to the movement of the avatar, the two virtual agents receive two different rewards. In particular, a simple maze scenario has been chosen to test this new MARL model, trying to resemble the same condition of the human experiment discussed in the previous section but reproduced in a discretized 2D space. In particular, the avatar moves in a confined maze with a wall, two bombs, and a goal. Virtual agent A can see the wall and the goal, while virtual agent B can see the bombs, like the human experiment. Each virtual agent can move only up, down, left, and right of one cell in the grid maze, while the avatar moves depending on the combination of $action_A$ and $action_B$.

The following definition presents in a more formal and general way the proposed setting described above.

[1]Salvatore D'Avella, Gerardo Camacho-Gonzalez, Carlo Alberto Avizzano and Paolo Tripicchio are with the Perceptual Robotics Laboratory, Department of Excellence in Robotics & AI, Institute of Mechanical Intelligence, Scuola Superiore Sant'Anna salvatore.davella@santannapisa.it

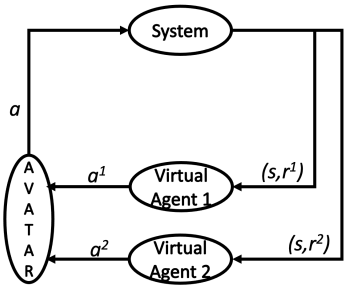

Fig. 3: Proposed MARL model

Definition 1. The proposed model is defined by a tuple $(N, S, \Omega, O, \{A^i\}_{i \in N}, A_v, P, \{R^i\}_{i \in N})$, where $N = 1, ..., n$ is the set of *virtual agents*, S is the state space, Ω is the set of observations, $O^i \subset \Omega$, is the observation space of agent i, where $\bigcup_{i=1}^{N} O^i = \Omega$, and A^i is the action space of agent i. If A is the cartesian product of the action of each agent ($A := A^1 \times A^2 \times ... \times A^n$), then $A_v \subset A$ contains only the set of feasible actions the single controlled *avatar* can do. Therefore, $P_a(s, s') : S \times A_v \times S \to \mathbb{R}$ represents the transition probability of going to any state $s' \in S$, being in any state $s \in S$ performing any joint action $a_v \in A_v$; $R^i_a(s, s') : S \times A \times S \to \mathbb{R}$ denotes the reward function that gives the immediate reward to each *virtual agent* i, given a transition from s to s' performing action a.

The performed tests exhibited promising outcomes demonstrating results similar to the human setting employing a two-step reward policy, i.e., after the normal reward, each agent gets an additional reward when their actions match in the same direction. Fig. 4 shows the learning process at different episodes.

The work has been improved further in [2] with continuous action and state spaces, proposing a multi-agent decentralized control approach. A more complex actor-critic architecture with a Proximal Policy Optimization (PPO) algorithm has been employed. The peculiarity is still that two virtual agents, sharing

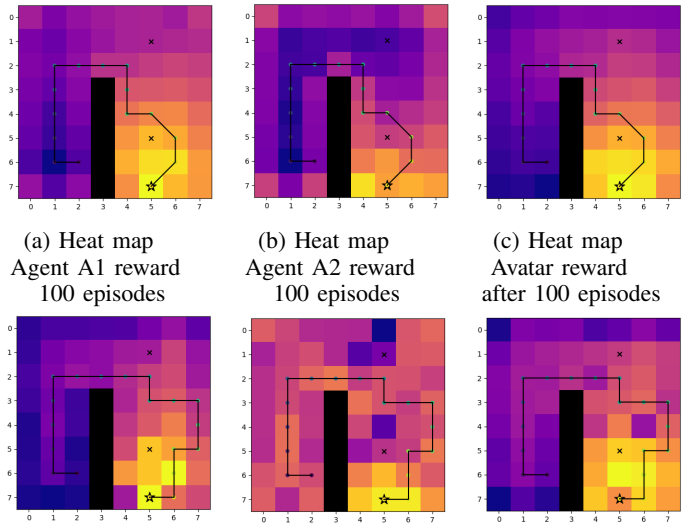

(a) Heat map Agent A1 reward 100 episodes
(b) Heat map Agent A2 reward 100 episodes
(c) Heat map Avatar reward after 100 episodes
(d) Heat map Agent A1 reward 50000 episodes
(e) Heat map Agent A2 reward 50000 episodes
(f) Heat map Avatar reward 50000 episodes

Fig. 4: Learning process using the two-step reward policy

(a) 1-walled map
(b) 2-walled map

Fig. 5: Rendered maps generated with SC2LE for continuous action space.

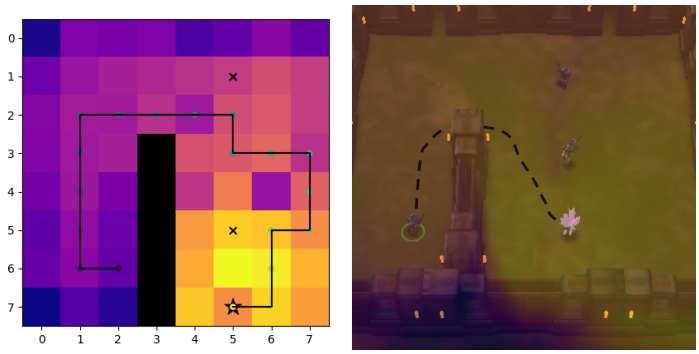

(a) QL merged value map
(b) Value from Critic map

Fig. 6: Comparison of the obtained value maps between the Q-Learning merged value map of the discrete environment from and the one from the critic network.

the same environment, control a single avatar but with access to complementary details necessary to finish the task. Each of them is responsible for solving a portion of the problem, and in order to efficiently solve the designed task, a collaboration should emerge among the virtual agents not to compete but to focus on the final goal. Furthermore, the actions of the two users are combined to control an avatar to achieve the highest possible performance. It is worth noticing that each virtual agent, performing individually, is not fully autonomous since it does not have a complete vision of the scene and needs the other one to properly command the avatar. In order to pursue such a goal, a 2D-maze-like environment has been designed using the StarCraft II Learning Environment (Fig. 5. An avatar is placed in the custom-designed map with collisions with enemies and walls as negative reward and reaching a goal as a positive reward. PPO was applied to enable the agents to learn the best actions to guide the avatar through the maze avoiding all enemies and reaching the goal successfully. Fig. 6 shows a comparison between the discrete and continuous action space setting.

References

[1] Salvatore D'Avella, Gerardo Camacho-Gonzalez, and Paolo Tripicchio. On multi-agent cognitive cooperation: Can virtual agents behave like humans? *Neurocomputing*, 480:27–38, 2022.

[2] Gerardo Camacho-Gonzalez, Salvatore D'Avella, Carlo Alberto Avizzano, and Paolo Tripicchio. A reinforcement learning decentralized multi-agent control approach exploiting cognitive cooperation on continuous environments. In *2022 IEEE 18th International Conference on Automation Science and Engineering*. IEEE, 2022.